Centre for
Energy Research

Progress Report on Research Activities 2022

CENTRE FOR ENERGY RESEARCH

29-33 KONKOLY-THEGE MIKLÓS ÚT

1121 BUDAPEST, HUNGARY

PROGRESS REPORT ON RESEARCH ACTIVITIES IN 2022

DEAR READER

Welcome to the 2022 yearbook published by the Centre for Energy Research (EK), summarising the scientific achievements of its three institutions and highlights in 2022. This booklet offers information also about the research personnel and equipment of departments as well as research groups working in the Centre.

In 2022 EK became a participating member of the Hungarian National Laboratory Program. In this structure, 26 National Laboratories have been set up across the country in four major focus areas (Healthy Living; Safety and Security; Digital Transformation of Economy and Society; and Green Transition) https://nkfih.gov.hu/fields-of-operation. The National Laboratory for Renewable Energy was set up from 8 universities and 2 research centres, one of them being EK. More information can be read here: https://nkfih.gov.hu/green-transition/national-laboratory-for-renewable-energy/about.

Three important research works are selected for highlights this year:

i) The ITER international fusion experiment is the world's largest scientific research collaboration, in which EK won the "broken pellet injection" technology test lab tender in 2020. Mitigation of the effects resulting from sudden plasma disruptions, causing a fast cooling of the hydrogen that stops fusion power production, can be achieved with 27 injectors, which will shoot a hydrogen projectile (a pellet with a temperature of minus ~268 °C). The Fusion Plasma Physics Department designed and built up a gun, which successfully shattered with large hydrogen pellets. Photo and video of the first successful shot of the gun can be seen in the News of the EK: https://www.ek.hun-ren.hu/en/2022/10/21/iter-pellet-fusion/.

ii) A team from EK, in collaboration with the University of Cambridge, has recently published a work that may help provide insights into the variable response of cells to radiation exposure and cancer radiotherapy. Scientists have looked at the effect of irradiating cells in culture for some years now, measuring the fraction of cells capable of cell division after radiation exposure. Surprisingly, many cell lines showed hyper-radiosensitivity at very low doses but paradoxically increased radioresistance at high doses. In order to understand the causes of this phenomenon 101 datasets were collected from 46 publications. Interestingly, the technical validation also identified some inconsistent datasets, which are now highlighted in the database, and call into question some previous findings. This work is an excellent example of the idea of FAIR data and greatly improves the value of the previous research. FAIR data means data, which are Findable, Accessible, Interoperable, and Reusable. More about this can be accessed at the URL https://www.ek.hun-ren.hu/en/2022/10/11/radiation-cells-database/.

iii) EK researchers found exotic magnetism in graphite when electrons crowd together on the surface. Rhombohedral Graphite (RG) is a topological semimetal and it's possibly the simplest material showing strong correlations between its electrons. Its simplicity stems from the fact that RG is made of only graphene sheets stacked in a special staggered fashion. Strong correlations are present in this surface state and according to Scanning Tunnel Microscopy (STM) measurements survive up to at least 16 Kelvin. Our STM measurements provide evidence that the ground state at charge neutrality is closely related to a quantum magnet. Important properties of this are a gapped and gapless state, which are degenerate and therefore form a domain structure on the surface of RG.

This year EK was also successful in winning 8 EU-funded projects and started to work on them besides many national and international ones. These new projects cover a wide spectrum of research topics, ranging from the biological effects of radiation to the aging of structural materials.

Ákos Horváth
Director General
horvath.akos@ek.hun-ren.hu

CONTENTS

MISSION STATEMENT OF THE CENTRE FOR ENERGY RESEARCH

- Research and development in the field of nuclear science and technology for facilitating the adoption and the safe use of nuclear technology in Hungary.
- To participate in international research effort aiming at the establishing a new generation of nuclear power plants and closing the fuel cycle.
- Maintaining and improving competence in nuclear science and technology, especially in the field of nuclear safety, security, health physics, nuclear and isotope chemistry.
- To guarantee the safe operation of Budapest Research Reactor (BRR), and to ensure the open access to the research facilities around the reactor operated by the Budapest Neutron Centre.
- Research activities to improve nuclear analytical and imaging methods and their applications for energy and materials science.
- Perform studies in the field of environmental physics related to energy generation, renewable energies, energy storage and their impact on public health, and on environmental safety.
- Research and development in the field of low carbon energy technologies and of energy saving in industrial technologies.
- Development of nuclear energy production processes based on nuclear fusion, research and development of related technological and physical issues.
- Development of manned mission space dosimetry and space weather measurement systems, furthermore, improvement of devices for space-biological, -chemical and -material science experiments.
- Interdisciplinary research on complex functional materials and nanometer-scale structures, exploration of their physical, chemical, and biological principles, exploitation their operations in integrated micro- and nanosystems, and in the development of characterization techniques.
- Dissemination of the results in international programs, education and industrial research.

ORGANIZATION STRUCTURE OF THE CENTRE FOR ENERGY RESEARCH (2022)

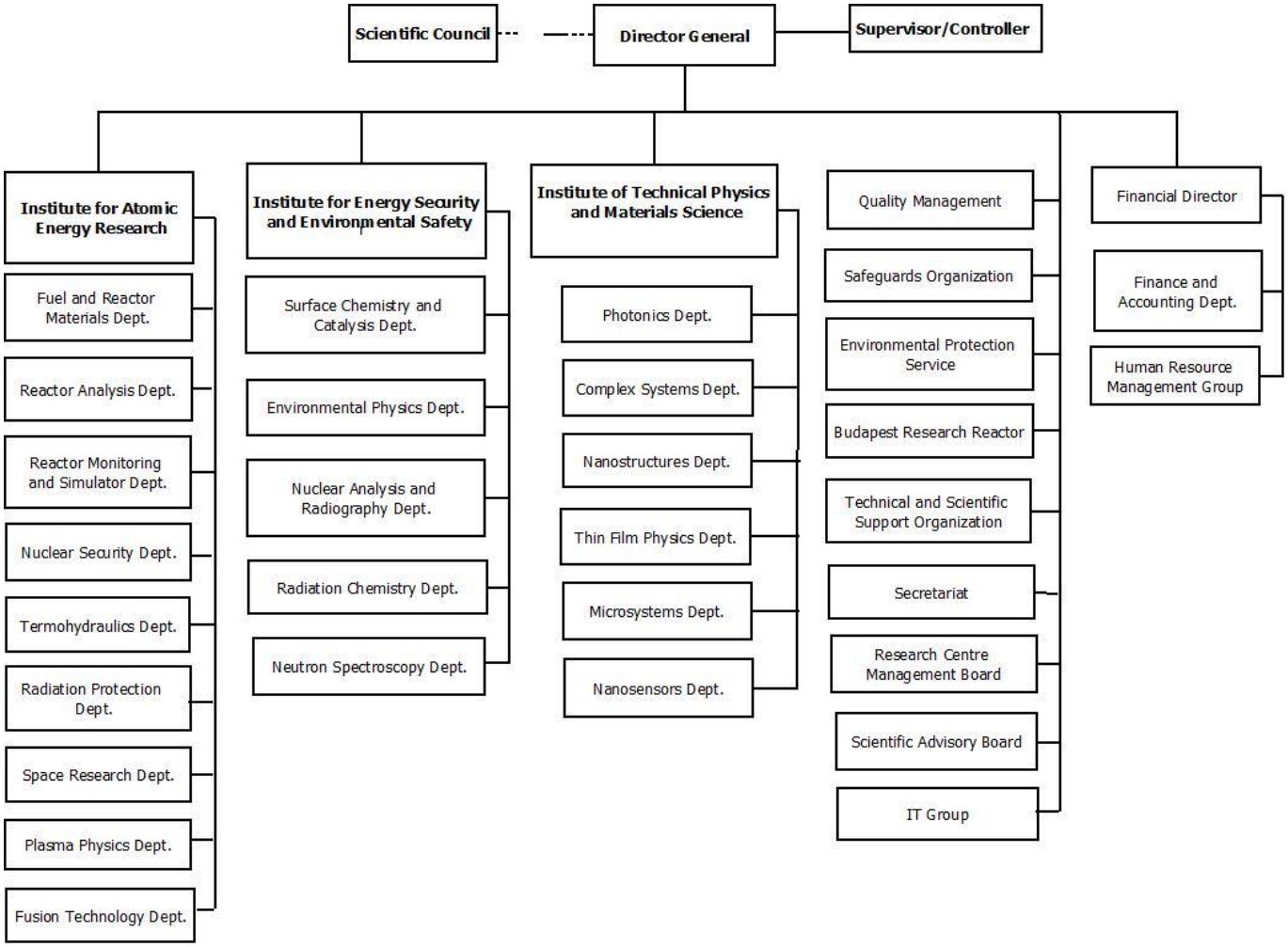

QUALITY MANAGEMENT

In order to achieve the highest quality of research, development, design, condition monitoring and valuation, engineering, contracting and managing in design, production, implementation and inspection, the Research Centre's quality management system has continuously been upgraded by the recommendations of ISO 9001 standard since 1994. Reviewing our QM system by integral audits and management reviews, evaluating improvement opportunities, maintaining project documentation, infrastructure, supporting communication, ensuring the competence of workers the management improves the Centre's QM system. For the new organization structure, our Quality Policy has been renewed. Many new employees induced a need to upgrade our QM tuition practice. We organized the work and fire safety educations. Our QM system has been certified by Hungarian Standards Institution, IQNet and MVM Paks NPP.


MAGYAR SZABVÁNYÜGYI TESTÜLET
HUNGARIAN STANDARDS INSTITUTION

TANÚSÍTÁSI OKIRAT
CERTIFICATE

Tanúsítjuk, hogy a
We certify that the Management System of

Energiatudományi Kutatóközpont
(kivéve az MFA és a Reaktorüzem)
H-1121 Budapest, Konkoly-Thege Miklós út 29-33.
Tanúsított székhely: H-1121 Budapest, Konkoly-Thege Miklós út 29-33.

MSZ EN ISO 9001:2015 (ISO 9001:2015)


THE INTERNATIONAL CERTIFICATION NETWORK

CERTIFICATE

Centre for Energy Research
(except Institute of Technical Physics and Materials Science (MFA) and Reactor Department (Reaktorüzem))
H-1121 Budapest, Konkoly-Thege Miklós út 29-33.
Certified headquarters: H-1121 Budapest, Konkoly-Thege Miklós út 29-33.

Quality Management System

research, development, design, condition monitoring and valuation, engineering, contracting and managing in design, production, implementation and inspection, independent technological expert activity in the field of application of nuclear energy

ISO 9001:2015

Issued on: 25-06-2020
First issued on: 22-06-1999
Expires on: 24-06-2023

Registration Number: HU-MSZT-503/0309(7)-97(7)

AZ MVM PAKSI ATOMERŐMŰ ZRT. IGAZOLJA, HOGY KÖVETELMÉNYEINEK AZ

ENERGIATUDOMÁNYI KUTATÓKÖZPONT

MINŐSÉGIRÁNYÍTÁSI RENDSZERE

MEGFELEL.

A MINŐSÍTÉS ÉRVÉNYESSÉGI IDEJE: 2023.07.31.

A MINŐSÍTÉS SZÁMA: KM 67/2020

Paks, 2020. július 31.

PUSKÁS LÁSZLÓ főosztályvezető

HORVÁTH GYÖRGY osztályvezető

Certifications by Hungarian Standards Institution, IQNet and MVM Paks NPP

Centre for Energy Research has complied with the requirements of the Hungarian Academy of Sciences which follow international standards. In 2019, the Hungarian Academy of Sciences thereby authorized the Centre for Energy Research to use the label MTA Centre of Excellence. This certificate was extended annually in 2020, 2021 and 2022.

BUDAPEST RESEARCH REACTOR

One of Hungary's most important strategic large-scale research facilities is the Budapest Research Reactor (BRR). It serves the needs of an extensive and diverse scientific community by supporting R&D opportunities, helping innovation and providing a strong foundation for training and education.

Bird's eye view of the Budapest Research Reactor

BRR is a VVR-type reactor that uses light water as moderator and cooling fluid. The power of the reactor is 10 MW provided from low enrichment uranium fuel, and its main purposes – as established during the feasibility/functionality study – are radioisotope production, production of thermal and cold neutron beams for research and applications in many areas of development of material sciences and nuclear physics.

The core is designed to have about 120 reactor days per year, having a time span of 4 days a week. We are committed to long-term safety and responsible operations, taking care of the wastes from the spent fuel coming from the reactor. Besides the temporary spent fuel storage pool, we also operate a long-term spent fuel storage building for the physical and environmental separation between the reactor and the spent fuel storage.

Top view of the research reactor

Layout of the BRR's facilities

The reactor hosts three kinds of activities: research activities utilizing neutron beams, production of radioisotopes for industrial, medical and research purposes, and providing national and international training. We are proud of our innovative flagship research topics, which are carried out by a network of neutron beam stations, including beam lines of thermal neutrons, experiments on powder and residual stress diffractometry, TOF neutron spectroscopy, radiography, biological irradiations, and beam lines of cold neutrons for experiments on small angle neutron scattering, reflectometry, prompt gamma activation analysis and nuclear data measurements. In accordance with recent worldwide trends, we are open to establishing new industrial relations and supporting innovation. The BRR's experimental facilities are open to science based on excellence for researchers from all around the world. We aim to increase our competence on special topics, implement new technologies and develop new materials, to promote and exploit our R&D capacity at the national, regional, as well as international levels. During the past years, BRR hosted several international schools on various technical and research topics, special trainings in the field of reactor physics, reactor operation, nuclear measurement techniques, and safety and environmental issues. Typical research fields are physics, chemistry, material sciences, engineering, life sciences and biotech.

BRR is used by groups of different scientific communities from medical, environmental, material, archaeological, nuclear sciences, and industry, as well as several Hungarian Universities. Neutron beams are uniquely suited to study the structure and dynamics of materials at the atomic level. The Budapest Neutron Centre (BNC) coordinates the scientific utilization of the research reactor. Some of the main research topics currently are as follows.

- Neutron scattering is used to examine changes in sample properties under different conditions such as variations in vacuum or pressure, high and low temperature and magnetic field, modelling real-world conditions.
- Using prompt and delayed neutron activation analysis makes it possible to measure the concentration of elements in ppm and ppb levels even for small samples. They decay by gamma-rays characteristic for each element that can be detected by suitable detectors.
- Neutron activation to produce different radioisotopes are widely used in industry and medicine production. For example, Y-90 microspheres to treat liver cancer are produced by bombarding Y-89 with neutrons, which capture them. Radioisotopes are produced for different applications such as medicine, sterilization and industrial use.
- Testing reactor materials are subjected to intense neutron irradiation, which causes radiation damage to their crystalline structure. For instance, some steels become brittle. Thus, the so-called high-entropy alloys resisting embrittlement are to be used in nuclear reactors instead.
- Applied research using neutron beams produce images of the material interior. Examples are the visualization of porosities in materials or changes of density inside the sample. Dynamic neutron radiography is capable of visualizing motion in materials. Examples are the viewing bubble forming in the cooling system of a refrigerator or the visualization of fuel burn in the engine system of a car.

BNC provides researchers with 15 neutron instruments; 13 of them are installed directly on the horizontal beam ports of the reactor or to the thermal and cold neutron guides, while the other 2 are placed at the vertical irradiation channels. The instruments are supported by a variety of sample environments, data acquisition hardware, analysis software, and visualization tools.

BNC provides access to the international neutron user community through a peer-review system. Local scientists assist researchers and industrial users in finding the appropriate neutron techniques that meet their research needs. The various neutron scattering instruments in BNC cater to a large number of users from Europe and have grown in strength and stature over the years. Since the COVID-19 pandemic, BNC accepts so-called remote users as well, which means that samples are sent by mail and the measurements are performed by the instrument scientists without the user and the results are forwarded to the users via electronic ways.

BNC is a member of the League of advanced European Neutron Sources (LENS) and CERIC-ERIC, and a partner in recent EU Framework Programme projects (H2020 IPERION HS, EURIZON, ARIEL, ReMade@ARI and TOURR).

BNC is strongly committed to the training of future professionals inland and all over the world in co-operation with the International Atomic Energy Agency. We cooperate with several Hungarian universities (Budapest University of Technology and Economics, Eötvös Loránd University (ELTE), Pannon University, Óbuda University and University of Pécs). BNC accommodates students for laboratory practice for studying nuclear-based techniques. A specialized course was developed for geology students of ELTE to introduce nuclear analytical techniques into their education. BNC organizes the Central European Training School on Neutron Scattering annually, which was cancelled this year due to the pandemic. The school provides insight into neutron scattering, element analysis and imaging techniques and their applications to study the structure and dynamics of condensed matter.

The Budapest Research Reactor is open to the public. Members of the local communities and high school and university students visit us regularly and learn more about the amazing nuclear science possibilities available at BRR.

ENVIRONMENTAL PROTECTION SERVICE

The main task in the Environmental Protection Service of the Centre for Energy Research (EK) is the environmental control of radiation protection of the KFKI Site.

Environmental control sampling station

Our Environmental Policy, developed on the basis of the relevant legislation, describes in detail that with what frequency and to what characteristics we have to examine the various sample types. These tests include monitoring of airborne gamma radiation, examinations of atmospheric fallout, and gamma spectrometry and total-beta activity of air aerosol particles. By the use of our own resources and tenders, we intend to develop our equipment and instrumentation in order to perform our tasks with high reliability.

Berthold LB790-5L-Lead type alpha-beta counting device

Environmental dose rate measuring probe

In addition to checking the external environment, we also monitor the external and internal radiation exposure of employees exposed to radiation. In addition to official TLD tests, the external radiation exposure is checked with the RADOS type thermoluminescent dosimeters used by the Service.

A detailed report of the work of the Service carried out in each year is available on the EK website.

Gáborné, Endrődi
Head of Service
endrodi.gaborne@ek-cer.mta.hu

I. RESEARCH ACTIVITIES SUPPORTED BY DOMESTIC AND INTERNATIONAL PUBLIC AGENCIES

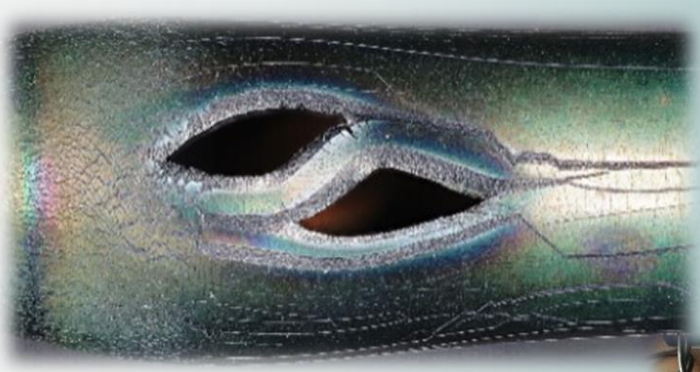

DEVELOPMENT OF ALLEGRO GAS-COOLED FAST REACTOR DEMONSTRATOR

János Gadó, Zoltán Hózer, Emese Slonszki, Bálint Batki, Petra Pónya, István Pataki, Attila Guba, István Panka, Gusztáv Mayer

Objective

ALLEGRO is a small power helium-cooled fast spectrum demonstrator reactor of the European gas-cooled GFR2400 reactor selected by the GEN IVth International Forum. The two primary goals of ALLEGRO are the demonstration of the helium-cooled fast reactor technology and the qualification of the new carbide refractory fuel. The starting fuel of the core is aimed to be MOX or UOX, and the final refractory core is proposed to be mixed carbide. Currently, EK actively participates in the Euratom SafeG project, which is dedicated to improving the safety of the Gas-cooled Fast Reactor (GFR) technology.

Methods

The current ALLEGRO design contains water on the secondary circuits of the Main Heat exchangers (MHX) and the Decay Heat Removal Heat exchangers (DHR HXs). For this reason, a primary-secondary break in the MHXs or the in DHR HXs may lead to water ingress into the primary circuit, which is better to be avoided. To solve this design issue, EK proposed a helium-cooled secondary circuit in the DHR HXs. In the newly developed model, the water on the DHR secondary circuit was replaced with pressurized helium at 65 bar. For the calculations, the French CATHARE thermal hydraulics code was used. The investigated initiating event was selected based on our previous work [1].

The first version of the ALLEGRO refractory core model based on the original Commissariat à l'énergie atomique et aux énergies alternatives (CEA) design was created in SERPENT and KIKO3DMG codes, and core safety parameters (reactivity coefficients, control rod worth, burn-up rates, and power distribution) were calculated. Results calculated by SERPENT and KIKO3DMG codes were compared. Since the material composition of the fuel and structural elements in the ALLEGRO ceramic core might change during the core optimization process or due to manufacturing reasons, a sensitivity analysis was performed to investigate the effect on neutronics aspects of the modification of isotopic composition. The analysis methods and results are detailed in Deliverable 1.2 of the SafeG project.

The first version of the deliverable "D4.1 GFR refractory fuel qualification options" in the framework of the EU SafeG project was reviewed by international experts from Slovakia, France, Hungary and Poland. The final version of the deliverable was produced, considering their comments. The technology readiness level approach was applied for GFR fuel composed of oxide pellets and SiC_f/SiC cladding.

Results

The CATHARE calculations for the helium-cooled DHR secondary side showed that the heating perimeter of the DHR HX tubes has to be increased by a factor of 4 if the same cooling capabilities are ensured as in the water-cooled case [2]. The higher HX surface can be ensured if the diameter of the DHR is roughly double in size, which raises some further design issues to be solved.

Reactivity coefficients, such as the Doppler coefficient, Doppler + fuel expansion coefficient, and void (coolant density) coefficient, were determined for the first version refractory core. Reactivity coefficients are more favourable in the MOX core than in the ceramic.

Results calculated by SERPENT and KIKO3DMG codes show good agreement. Control rod worth calculations showed that the reactivity worth of a single inner-positioned Control and Shutdown Device (CSD) assembly is significantly higher than that of a single outer-positioned CSD assembly. With β_{eff}≈350 pcm, the reactivity worth for one inner CSD is ~2300 pcm or ~6.5 dollars, which shall be optimized during the core design process.

Burn-up calculations of the refractory core show that the reactor can operate for about 560 days without refuelling, which is more than the required 1-year cycle length. The power distribution and the radial power peaking factor are similar to the CEA's MOX core design. The maximum assembly power is lower due to more fuel assemblies, which is advantageous considering safety limitations.

SERPENT's collision history-based approach was used to understand the change of the effective multiplication factor due to the material composition change. The numerical results can be used to estimate the reactivity change due to small changes in the isotopic composition, which can assist the core design optimization.

The refractory fuel qualification options were divided into two procedures: one for the carbide pellets in SiC_f/SiC cladding and another for oxide pellets in SiC_f/SiC cladding. The description of the role of the fuel supplier, the current status and the design of the fuel for ALLEGRO was extended. Requirements on the reprocessability of materials to close the fuel cycle and the capabilities to withstand long-term storage of spent fuel were included. The requirements for modelling the two fuel types in Design Extension Condition (DEC) by severe accident codes and high-temperature measurements to investigate ceramic fuel behaviour were also added.

Remaining work

The following step in the SafeG project is to define and finalize a new optimized refractory core supported by neutronics and thermal hydraulics calculations.

Related publications

[1] G. Mayer et al. *Selection of the enveloping transients of the ALLEGRO reactor at the beginning of the SafeG project.* The 19th International Topical Meeting on Nuclear Reactor Thermal Hydraulics (NURETH-19) Log nr.: 35548 *Brussels, Belgium, March 6 - 11, (2022)*

[2] G. Mayer and A. Guba, Investigation of water and helium-cooled decay heat removal systems in a gas-cooled fast reactor, The 20th International Topical Meeting on Nuclear Reactor Thermal Hydraulics, August 20–25, 2023 Washington, D.C. Washington Hilton

[3] Z. Hózer, E. Slonszki, J. Klouzal: *D4.1 GFR refractory fuel qualification options, version 2.0*, EU SafeG project, 2022.02.17.

FINAL RESEARCH REPORT ON GRANT NN 127102: V4 KOREA RADCON - THE EFFECT OF CHEMICAL COMPOSITION OF CONCRETE ON ITS LONG-TERM PERFORMANCE IN AN IRRADIATED ENVIRONMENT

Ildikó Harsányi, Zoltán Kis, Anita Horváth, Katalin Gméling, Veronika Szilágyi, László Szentmiklósi

Objective

Our goal was to recommend raw materials for radiation-resistant, durable concretes with low activation susceptibility for use in the future Paks II nuclear power plant (NPP). The chemical composition of concrete constituents is a key factor influencing the ageing of the NPPs, and hence the structural integrity (durability and service-lifetime), as well as the activation and radiation shielding properties of the concrete structures. It was advantageous to use Neutron Activation Analysis (NAA) and Prompt-Gamma neutron Activation Analysis (PGAA) techniques for the elemental analysis of the radiation susceptibility studies, since the basic principles of these nuclear analytical methods are reproducing the real situation inside the radiation shielding materials close to the reactor.

Results

1) Material characterization and radiation simulation of concrete raw materials

Sand and gravels, the fine and coarse aggregates taken from four major gravel mine regions (NWHR, SWHR, MDR, NEHR) of Hungary, which could be the major constituents of shielding concretes, were systematically analyzed for elemental composition, and considering different grain size fractions (0-4; 4-8; 8-16; 16-32 mm). We found that the major oxide contents of the examined sands and gravels are depleted relative to the average upper continental crust composition, except for their SiO_2 contents which are enriched. Based on these elemental concentration fingerprints, the claimed origin of an industrial raw material can be validated on a regional scale. The concentrations of the long-lived-isotope-forming elements is higher in Portland Cement (PC) than in the sand and gravel samples. The outcome of the geochemical survey pointed towards the conclusion that there are small amounts of trace elements that activate to rather long half-lives (2-13.5 y) in the examined aggregate constituents of concretes. It was also found that all analysed sand and gravel quarried in Hungary can be recommended to prepare low-activation shielding concrete; however, petrological, and geochemical studies revealed that the gravel and sand from the NW Hungarian region have the lowest induced activation (Fig. 1 a,b). The elemental concentration data were used as input for the FISPACT code to model changes in the activity of the samples over time. In our model, we assumed a radiation field typical of the near vessel region of a nuclear research reactor. The coarse aggregates, sand, and gravels contribute only to a small extent to the total activity and decay to the clearance level in 30 years (Fig. 1b), which is a reasonable time interval for decommissioning. [1]

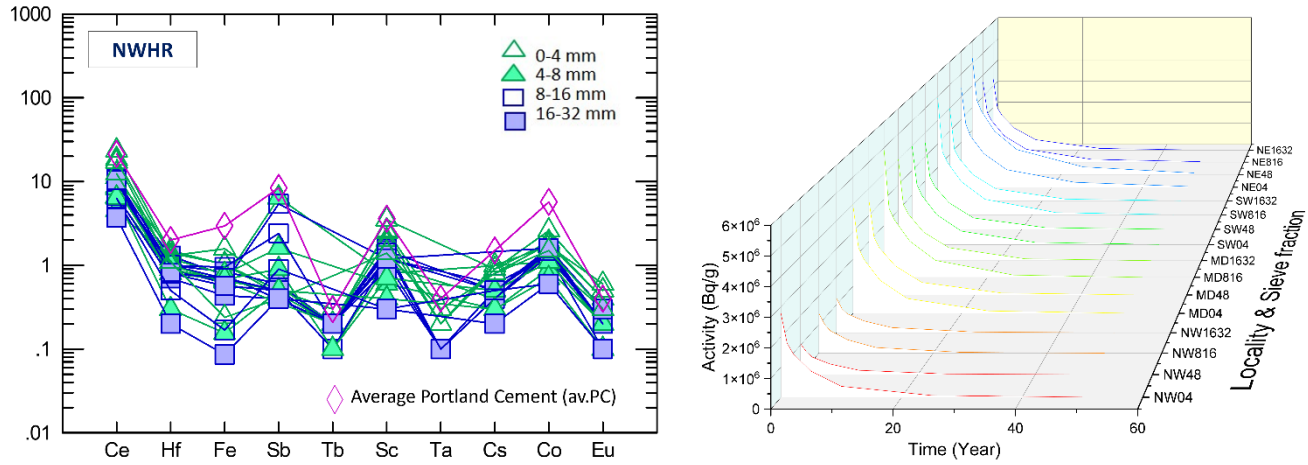

Figure 1: a) Trace element contents in µg/g on a logarithmic scale, and its distribution in the different grain size samples for the North-Western Hungarian Region (NWHR), which show the lowest induced activation. Elements from left to right have increasing half-lives. b) The decay of major long-lived isotopes of Co, Cs, and Eu in 60 years can be followed on the graphs by regions, and averages of grain size fractions. Note that the initial differences up to a factor of five diminish only after about 30 years.

2) Computer simulations to estimate the neutron-activation of concrete

The NEAAA method, i.e. the combination of i) experimental composition measurement by PGAA and NAA, ii) Monte Carlo N-Particle (MCNP)-based irradiation calculations, and iii) FISPACT based radioisotope inventory calculations, to predict the activation of targets placed into a vertical channel of the Budapest Research Reactor were worked out. The calculations were validated with irradiations at the No. 17 channel at 10 MW power (Figure 2).

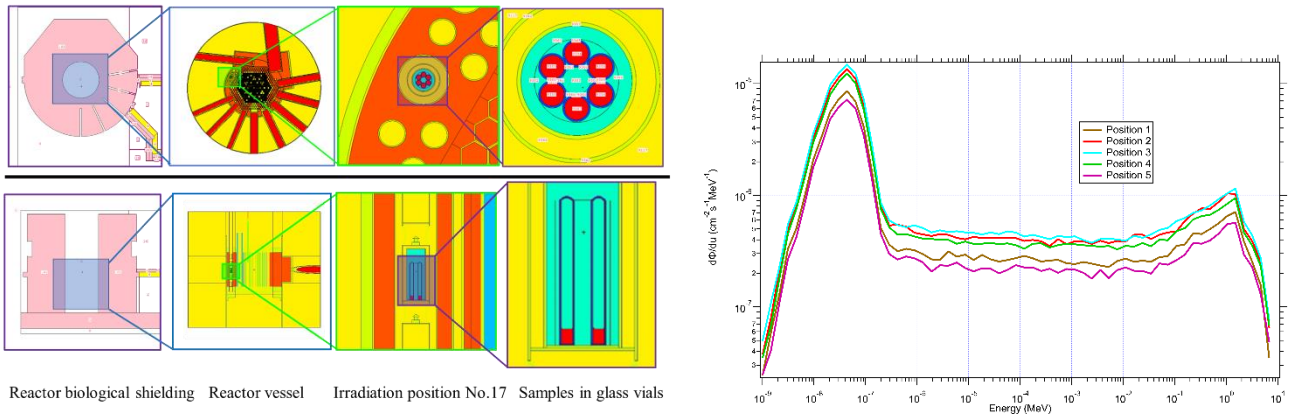

Figure 2: a) the geometry definition of irradiation channel No. 17 of the Budapest Research Reactor in MNCP, in both top and side views, and b) the neutron energy-distribution for the five vertical irradiation positions inside the No. 17 channel

Flux monitor foils, multi-component powdered NAA samples, and bulky mortar bars were tested, showing increasing complexity, and a decent agreement was achieved in all cases. The ratios of experimental and simulated activities agreed typically within 10%, while the uncertainty margin was about 5% (Figure 3). [2] Two counting measurements were done 4 days and 3 weeks after the irradiation.

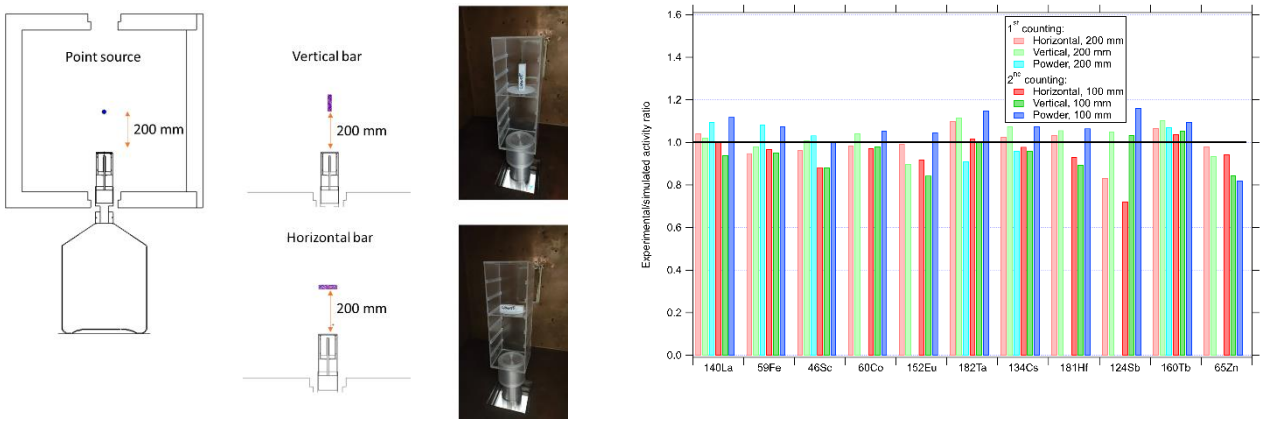

Figure 3. a) The MCNP model of the D5 gamma spectrometer to establish the efficiency transfer function of bulky samples. b) The ratios of the measured and FISPACT-predicted activities for the ground mortars loaded with various additives, in a point-source geometry. The first gamma measurement has been done at a 200 mm sample-to-detector distance, while the second at 100 mm.

Related publications

[1] I. Harsányi, A. Horváth, Z. Kis, K. Gméling, D. Jozwiak-Niedzwiedzka, M.A. Glinicki, L. Szentmiklósi: *Assessment of neutron-induced activation of irradiated samples in a research reactor,* Nuclear Engineering and Technology **55** (3), 1036-1044 (2022); https://doi.org/10.1016/j.net.2022.11.004

[2] K. Gméling, V. Szilágyi, I. Harsányi, L. Szentmiklósi: *Hungarian fine-to-coarse aggregate, a possible constituent of near-vessel structural concrete of nuclear power plants,* Materials **16** (9), 3520 (2023); https://doi.org/10.3390/ma16093520

LARGE FACILITY ANALYTICAL STUDIES OF POLISHED AND GROUND STONE ARTEFACTS

Zsolt Kasztovszky[1], Bálint Péterdi[2], Katalin T. Biró[3], György Szakmány[4], Veronika Szilágyi[1], Katalin Gméling[1], Kata Szilágyi[5], Ildikó Harsányi[1], Dóra Miklós[4], Erika Kereskényi[6], Tamás Sági[4], Zoltán Kovács [1]

[1]Centre for Energy Research, [2]Mining and Geological Survey of Hungary, [3]Hungarian National Museum, [4]Eötvös Loránd University, Department of Petrology and Geochemistry, [5]Móra Ferenc Museum, [6]Herman Ottó Museum

Objective

The project aims to identify the raw material sources of polished and ground stone artefacts in Hungary, delimiting the potential source areas as precisely as possible. Based on our former results, potential sources of some raw material types are located outside Hungary, even outside the Carpathian Basin. The research focuses on a systematic study of finds and raw materials that were not studied so far, as well as on supplementing former results by the application of new methods. We pay special attention to source-collected reference materials from the potential raw material source regions.

Methods

The unique and irreplaceable archaeological finds are analysed mostly by non-destructive Prompt-gamma Activation Analysis (PGAA) and "Original Surface" Scanning Electron Microscopy with Energy Dispersive X-Ray microanalysis (OS-SEM-EDX), while Neutron Activation Analysis (NAA) is used to measure the trace elements.

Results

The following archaeological collections have been studied: Öcsöd-Kováshalom (ELTE), Polgár-Csőszhalom (ELTE), Alsónyék-Bátaszék (ELKH Archaeological Institute), Aggtelek-Baradla cave, Hódmezővásárhely-Gorzsa. From these, the collection from Alsónyék comprises around 650 stone axes, chisels and maces. Measurements of objects from Szegvár-Tűzköves (Koszta József Museum, Szentes) have been done. Neolithic stone tool collection of the Wosinszky Mór Museum in Szekszárd and the archaeological site of "Lengyel sánc" in Tolna County have been visited.

To collect reference raw materials, field trips were organized: to Balaton Highland (Hungary) for alkaline basalt, to Little Carpathians (Pezinok-Pernek Crystalline Complex, Slovakia) for low and medium grade regional and contact metamorphic rocks (amphibolite, greenschist), to the Gemericum (SE Slovakia) for greenschist and amphibolite, to Mecsek mountains for olivine basalt, gabbro, phonolite rock samples from the Cretaceous volcanic area. Several earlier collected samples (metadolerites from the Maros valley from Szarvaskő (W-Bükk), and greenschists-amphibolite from Raho Crystalline Massif were also analysed.

Altogether around 1100 archaeological objects (mostly axes with or without shaft-hole, adzes, chisels, mace heads) and 23 geological reference samples have been selected for analysis. More than 150 thin sections have been studied by optical microscopy, 150 archaeological objects and raw materials by PGAA and 110 pieces by SEM-EDX to determine their mineralogical and geochemical composition. Study of the metadolerite samples proved that this rock type was procured from several localities of the Carpathian Basin (Szarvaskő, Maros valley) and probably from its wider surroundings (Serbian Mts., Alps). Forty-one red sandstone samples were studied by SEM-EDX, PGAA and NAA to determine the composition of the opaque minerals, tourmalines, apatites, amphiboles and garnets.

A web-based, user-friendly inventory and database framework has been created, and the scientific data have started to be uploaded by the task leaders and project members.

Remaining work

In the 4th project year, a fieldrip to North-Hungary and South-Slovakia is planned to collect basalt raw material. Artefacts from the Alsónyék archaeological site and pieces from Serbian Museums are also planned to be investigated.

Related publications

[1] Zs. Kasztovszky, B. Maróti, L. Szentmiklósi, K. Gméling: *Applicability of prompt-gamma activation analysis to determine elemental compositions of silicate-based cultural heritage objects and their raw materials*, Journal of Cultural Heritage **55,** 356–368 (2022)

[2] Kasztovszky Zs.: *Csiszolt kőeszköz és szerszámkő nyersanyagok nagyműszeres vizsgálata – egy NKFIH (OTKA) projekt rövid ismertetése,* Archeometriai Műhely XVIII/3 185–190 (2021). https//doi.org/10.55023/issn.1786-271X.2021-015

[3] Szilágyi K. & T. Biró K.: *Régészeti szempontok a Kárpát-medencéből és környékéről származó csiszolt kőeszközök és szerszámkövek eredetvizsgálatához*, Archeometriai Műhely XVIII/3 191–208 (2021) https//doi.org/10.55023/issn.1786-271X.2021-016

[4] Miklós D.G., Szakmány Gy., Józsa S., Starnini E. & Horváth F.: *Vörös homokkő nyersanyagú szerszámkövek Hódmező-vásárhely–Gorzsa késő neolit (Tisza kultúra) tell település leletanyagában*, Archeometriai Műhely XVIII/3 209–238 (2021). https//doi.org/10.55023/issn.1786-271X.2021-017

[5] Szilágyi V., Illés L., T. Biró K., Péntek A., Harsányi I., Sági T., Kovács Z., Fehér K. & Szakmány Gy.: *A Cserhát-Cserhátalja-Gödöllői-dombság-Mátraalja vidékéről származó csiszolt kőeszközök előzetes archeometriai vizsgálati eredményei*, Archeometriai Műhely XVIII/3 237–260 (2021). https//doi.org/10.55023/issn.1786-271X.2021-018

[6] T. Biró K., Hegedűs P., Szilágyi K.: *„Kigyla" - A „Csiszolt kőeszköz és szerszámkő nyersanyagok nagyműszeres vizsgálata a Kárpát-medence és környezete őskori távolsági és regionális kereskedelmi hálózatainak feltérképezéséhez" c. NKFIH projekt adatbázisa*, Archeometriai Műhely XVIII/3 261-272 (2021). https//doi.org/10.55023/issn.1786-271X.2021-019

[7] T. Biró K., Szakmány Gy., Szilágyi V., Kovács Z., Kasztovszky Zs., Harsányi I.: *The first greenstone axe in Hungary*, In: Dobrescu, Roxana; Boroneanț, Adina; Doboș, Adrian (szerk.) Scripta praehistorica. Miscellanea in honorem Mariae Bitiri dicata, Suceava, Románia : Editura Cetatea de Scaun pp. 517-528., 12 p. (2021)

[8] Miklós D.G., Szakmány Gy., Józsa S., Gméling K., Kasztovszky Zs., Harsányi I.: *The application of complex petrographic and geochemical analysis on red sandstone pebbles from clastic deposit*s. In: Ifjú Szakemberek ankétja LII - Előadáskivonatok, Orosháza-Gyopárosfürdő, 2022. 03. 25-26, 47-49. (2022)

[9] Miklós D.G., Józsa S., Szakmány Gy., Kovács Z.: *A felső perm Balatonfelvidéki Homokkő Formáció és a felső perm-alsó triász kelet-mecseki vörös homokkövek előzetes kőzettani és mikromineralógiai eredményei*. In: Fehér B., Molnár, K., Lukács R., Czuppon Gy., Kereskényi E. (szerk.): Calce et malleo - Mésszel és kalapáccsal: 12. Kőzettani és Geokémiai Vándorgyűlés, Miskolc, 2022. 09. 22-24., 102-105. (2022)

[10] Miklós D. G., Józsa S., Szakmány Gy., Kasztovszky Zs., Harsányi I., Gméling K., Kovács Z.: *Vörös homokkövek összehasonlító kőzettani, geokémiai és mikromineralógiai vizsgálati eredményei*. In: Piros O., Kercsmár Zs. (szerk.): Földtani és Geofizikai Vándorgyűlés - A Jövő Ösvényein, Budapest, 2022. 10. 14-16., 42-44. (2022)

[11] Péterdi B., Kovács Z., Szakmány Gy., Kasztovszky Zs., T. Biró K.: *Messziről jött balta nagy nyomásról regél (titánklinohumitos szerpentinit kőbalta archeometriai vizsgálatának előzetes eredményei)*. In: Fehér B., Molnár K., Lukács R., Czuppon G. és Kereskényi E. (szerk.): Calce et Malleo – Mésszel és kalapáccsal. 12. Kőzettani és Geokémiai Vándorgyűlés. Miskolc, 2022. szeptember 22-24. Csillagászati és Földtudományi Kutatóközpont, Földtani és Geokémiai Intézet, Budapest, 2022. p. 116-118. ISBN 978-963-7331-00-8

PARTICIPATION IN ESA MISSION TO JUPITER

János Nagy, László Hevesi, Zoltán Pálos, Gábor Tróznai, Pál Vizi, Bálint Sódor, Sándor Szalai, Lajos Dinnyés

Objective

The purpose of this work is to provide support for the activity covered by an earlier Contract: Design, Manufacturing, Validation, and Test of the Direct Current Converter (DCC) and Earth Ground Support Equipment (EGSEs) for Particle Environment Package (PEP) JUpiter ICy moons Explorer (JUICE) 4000124774 (former number: 4000123610, Acronym: JUICE PEP DCC&EGSE). JUICE investigates the Jupiter system as an archetype of gas giants, and investigates habitability around gas giants. JUICE will be launched in 2023 (by the present status), and the end of the mission is foreseen around 2032. JUICE is a European-led mission to the Jovian system. It will deliver 11 instruments to Jupiter, one of them is the PEP which was developed by broad international cooperation of Swedish, German, Swiss, American, Japanese and Hungarian institutes. Our job was to deliver a power supply unit for PEP, it is the DCC, which converts the onboard 28 V in the voltage ranges required by individual instruments with high efficiency.

The goal of our activity is to support ESA mission JUICE by supporting all DCC activities (document updating, tests, and integration) for PEP scientific instrument until the expected launch. PEP will help researchers to understand how three of Jupiter's icy moons are affected by the particles around Jupiter and search for the pre-conditions for life. We also delivered 15 EGSEs to test instruments separately and the communication between the PEP instrument and onboard SpaceWire bus. In one EGSE software improvement is ongoing in this work.

Methods

We took part in the evaluation of tests and in the calibration of housekeeping (HK) data and supported the new additional documentation needs of the PEP team.

Transformers and inductances were designed by Wigner Research Centre for Physics (Wigner FK) and manufactured by the company Flux and Wigner FK. During tests, Gate Drive and Current transformers had to be redesigned and remanufactured by Wigner FK. The brief account and detailed description of all transformers were collected and summarized with the main features and parameters in an Excel file. Altogether 32 transformers and inductances are used in one DCC. The test of transformers was executed in the DCC using the DCC-EGSE (Figure 1).

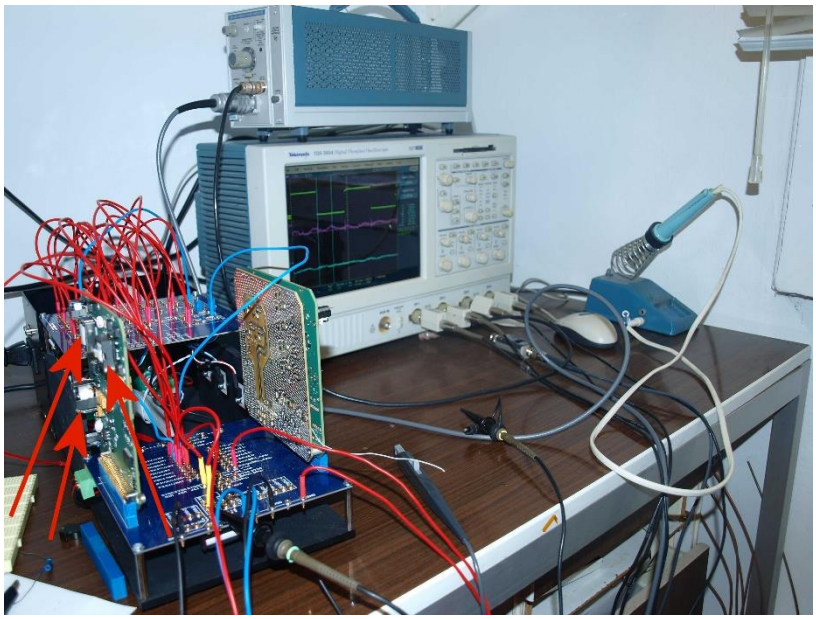

Figure 1: Test transformers of DCC cards with DCC-EGSE. Red arrows show transformers on the card.

In the previous phase, the simulation was performed for selected important circuit details, Over Voltage Protection (OVP) and main Latching Current Limiter (LCL) circuits. These simulations were partly performed by external experts, but their implementation should run and comply with our simulation package. During simulations, all parts were re-run and arranged with schematics, explanations, and updated models by modifications made during the tests. During the simulation, we used PSpice for Texas Instruments, which is a free compatible software with ORCAD PSpice. However, it has limited component base (only TI) so we have to import of several no TI components, which took considerable time.

In Digital Processor Unit DPU-EGSE, the SpaceWire cards and asynchronous cards were replaced because the previous cards sometimes caused data loss after a few hours of operation. Using the new cards required modifications to the individual card drivers.

The baseline of this task was to interpret the results obtained previously. It was a significant part of the task as EK had taken over software optimization from Wigner FK. A new free platform was chosen to complete our tasks. It was Lazarus in a Delphi compatible cross-platform IDE for Free Pascal of Lazarus firm Lazarus Homepage (lazarus-ide.org) for power control development. Lazarus' Free Pascal is a compiler that runs on Linux, Windows, macOS, FreeBSD, and others. The open-source Qt development software was used for handling SpaceWire part of EGSE. Qt is a cross-platform software for creating graphical user interfaces that run on various software and hardware platforms such as Linux and Windows.

Results

We prepared the update both in LINUX and Windows for DPU-EGSE software (Figure 2). According to end user suggestion, they prefer Linux version to Windows.

Documentation of DPU-EGSE software is about 60 pages with detailed description and illustrated with snapshots of screen. The results of simulations are collected and put into a common document of over 50 pages.

Detailed description of the used transformers is prepared.

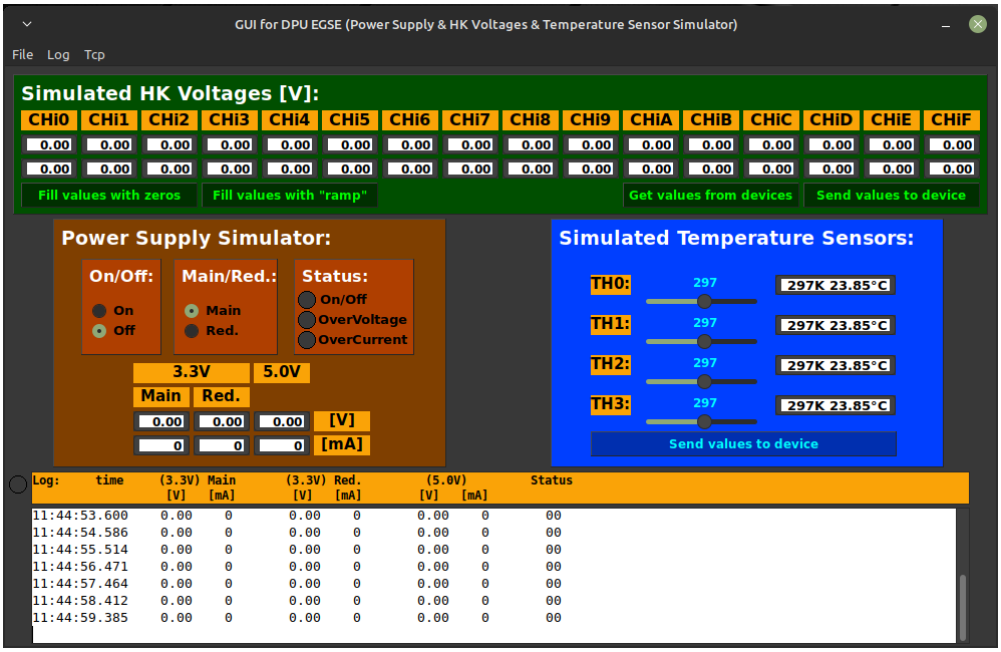

Figure 2: Screenshot of EGSE software controlling power of DPU and simulating House Keeping data of PEP sensors

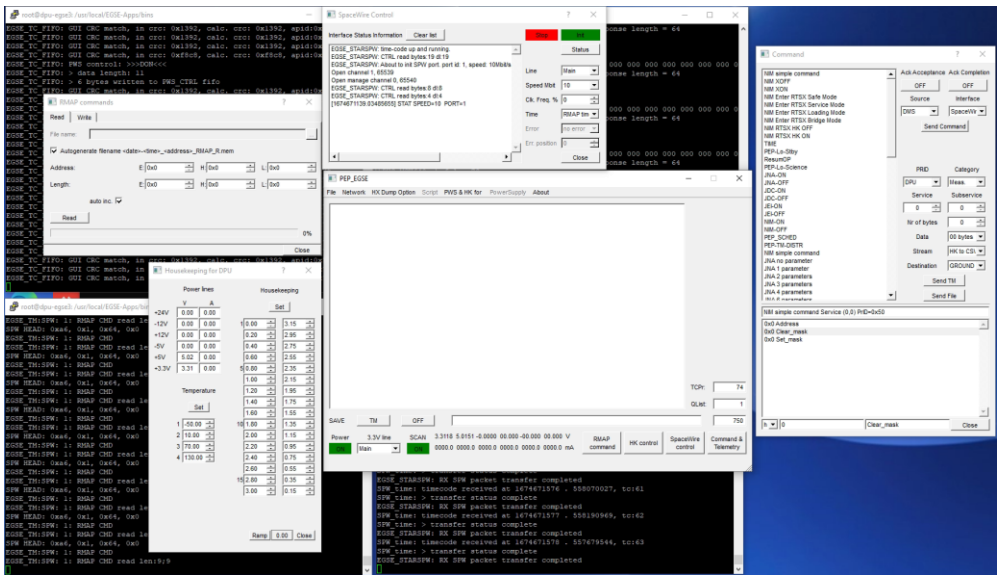

Figure 3: Screenshot of EGSE software simulating communication between onboard SpaceWire bus and DPU

Remaining work

Testing and possible refinement of the DPU-EGSE program will require time. The end user, the Finish Meteorological Institute (FMI) was busy with other jobs in 2022. There was a negotiation with FMI, and the end of February is reasonable.

We have recently received the PSpice model of Pulse With Modulation (PWM) chips from the manufacturer Renesas. By substituting the previously modelled chip, we would like to re-run the PWM simulation part with real PWM controller chips.

Related publications

[1] J. Nagy, L. Szalai at al: *Hungarian Participation in JUICE Project of European Space Agency*, Acta Polytechnica Hungarica **19(9),** 25-43 (2022); https://doi.org/10.12700/APH.19.9.2022.9.2

[2] Nagy J., Kerényi M., Frey S.: *Juice a Jupiterhez, Űrszonda magyar közreműködéssel*, Természet Világa **153,** 367-373 (2022)

RADONORM CITIZEN SCIENCE PILOT PROJECT IN HUNGARY

Veronika Groma, Endre Börcsök, Péter Füri, Balázs Madas

Objective

One of the objectives of the RadoNorm project is to establish a citizen science incubator for radon priority areas and a network of citizen science projects to address radon testing. For this, one of the tasks was to develop and test four citizen science pilot projects in France, Hungary, Ireland and Norway in order to propose a model for citizen science in EU Member States. The preliminary research questions defined by the Hungarian incubator project was that "How can high school students help to raise awareness on radon and promote remediation actions?". For this, our aim was to invite high school students to be citizen scientists from three institutions who can participate in the development of a toolkit which consists of various low-cost measurement sensors capable of measuring air quality, including radon. By engaging with the toolkit, we hoped students would gain first-hand experience of the impact of conscious behaviour on indoor environmental conditions, such as the importance of proper ventilation. Testing the toolkit and preliminary measurements at various locations (at school and at homes) were also planned.

Methods

One of the main objectives of the Hungarian citizen science project was to create a toolkit capable of detecting the atmospheric concentration of multiple air pollutant components besides radon with high time resolution. We carefully selected devices based on factors such as availability, cost, size, measurement range and time resolution. To ensure the reliability of the devices, we chose those that had already been verified in the literature. In addition to radon, the air pollutant components we investigated were size-fractionated aerosol number, carbon dioxide, methane and ozone concentration, as well as environmental parameters such as temperature and humidity. It is a feature of low-cost sensors that measurements using them is controlled with user-created code, so we developed our own software for both measurement control and data analysis. The Hungarian and English documentation of the toolkit, which includes the software, is available on the project's website (https://radonormcs.ek-cer.hu/).

Results

The toolkit was developed in several steps, however, it is still requiring some preliminary training for its operation. After the completion of the toolkit, measurements could be considered continuous. Since December 2022, students and staff from the rural school (Székesfehérvár) have been taking continuous measurements in their homes. So far, the measurement results at these locations have been very favourable in terms of both radon load and air pollution. In parallel, we carried out measurements at several locations of a school in Budapest. A picture of the developed toolkit and an example of measurement results are shown in Figure 1.

The inclusion of other air pollutants than radon in the measurement process had a positive impact on the citizen scientists' awareness and understanding of air pollution. By providing a context for the measurement results, they were able to comprehend the data more easily. Utilizing students as citizen scientists proved to be highly effective, especially when a specific timeline and purpose were given.

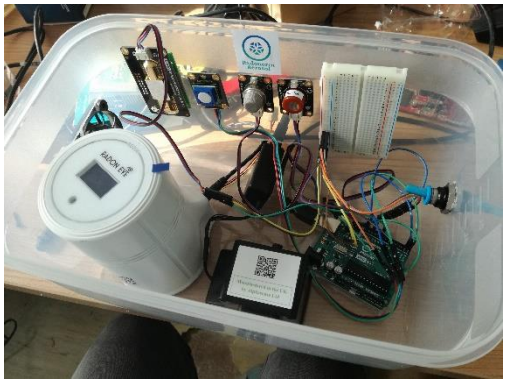

a)

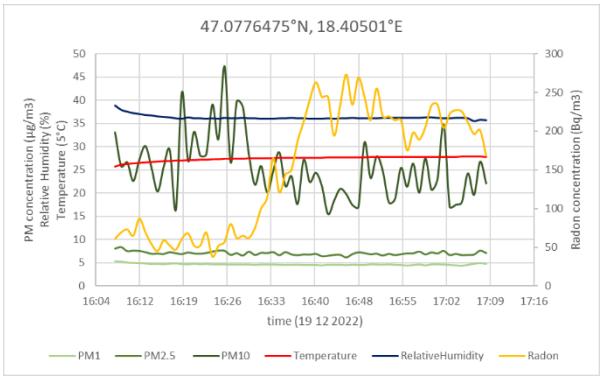

b)

Figure 1: a) picture of the toolkit, b) example of results measured at citizen scientist home

Remaining work

During the project work, it became clear that as long as the device is not Plug and Play (PnP), many errors can occur during the measurement, particularly data loss. To this end, we plan to improve the user-friendliness of the toolkit and provide guidance on data analysis. Our overarching objective is to create a framework that not only raises awareness but also improves the personal life circumstances.

During the next year, we plan to perform measurements with the toolkit at locations in Transylvania, in collaboration with the local citizen scientists' partners.

PIANOFORTE E-SURVEY ON PUBLIC UNDERSTANDING OF RADIATION PROTECTION ISSUES – PRELIMINARY ACTIVITIES

Veronika Groma, Balázs Madas

Objective

During the European Joint Program CONCERT, in the framework of a large public survey, radiation risk perception and attitudes towards various radiation protection issues have been explored in different public groups in different national languages. While these survey results indicated a reasonable level of public satisfaction with the available information regarding radiation risk, a potential for a follow up of the main radiological protection concepts has been clearly shown helping to understand the potential for further exploring the information availability and the development of knowledge over time, as well as better communication and stakeholder engagement in the creation and dissemination of knowledge. Therefore, an electronic survey was organized and launched within the PIANOFORTE partnership dedicated to exploring these specific issues within the area of general radiation protection and possible developments of public knowledge. The main objectives of the survey were to (i) gain insights on stakeholders' views and opinions on the main radiation protection issues previously explored in other projects, (ii) give different stakeholders (end users) opportunity to express their opinion on research topics that should be prioritized in the area of radiation protection (in Open Calls for R&I projects, but also in Strategic Research Agendas and Joint Roadmaps for future research in radiation protection), and (iii) provide more information about the PIANOFORTE partnership to the wider stakeholder community in first months of the partnership.

Methods

The survey was performed in English language and distributed to a compiled email address list, containing contacts from both national and international organisations, researchers, regulators, implementer groups, members of public, etc. It was implemented on SurveyMonkey platform, which is a cloud-based survey tool that helps users to create, send and analyze surveys.

To best tailor the questions to the identified audience (target groups), the survey was divided into different parts. The survey contained both closed and open-ended questions and covered information related to the PIANOFORTE partnership, research priorities for the partnership´s Open Calls and general radiation protection issues – understanding, concerns and views.

The e-survey contained three types of questions:

(1) General Background questions: participants were asked to mark which stakeholder groups they belong to or could identify with, their name, profession, email, and country (for the purpose of the geographical distribution analysis). Apart from the first consent question which was made mandatory, questions in all fields of this section, although providing valuable information about the respondent's background profile, have been set as non-mandatory due to data protection and ethical issues.

(2) PIANOFORTE related questions: participants were briefed and asked about the main features and activities of the partnership, identified research priorities for decision making on R&I project funding and expected stakeholder engagement in the partnership, as well as how they would like to be informed about the partnership's outcomes.

(3) Radiation protection questions: raised questions covered the main radiation protection topics and issues that are potentially of interest and/or concern to a wide range of stakeholders.

Results

The e-survey was developed during the early months of the partnership and launched on 22 November 2022, with a response period of just over two months, until 31st January 2023. The link for the PIANOFORTE e-survey was sent to 990 contacts in European countries, both participants and non-participants of the PIANOFORTE partnership. The contacts were also asked and encouraged to further distribute the survey link to other proper contact persons. In addition to personal e-mails, the survey was also announced on social media platforms.

The preliminary analysis of responses on questions related to specific radiation protection issues showed different views on various topics, with some interesting examples, such as:

The most important improvements needed in future in radiation protection, as seen by stakeholders, are related to research and development and their relationship to regulatory and management practice and the topic of international collaboration in the field of radiation protection.

The level of satisfaction with publicly available information on the given topics of radiation protection is the highest for use of ionizing radiation in medical purposes (71% of respondents answered that they are either rather or very satisfied). A high level of satisfaction (61-67% of respondents) was also expressed for available information on NORM and radon, emergency and preparedness as well as for radioecology and environmental radioactivity.

Remaining work

Specific response analysis as well as statistical analysis of responses and response cross-analysis will be provided for comprehensive and accurate conclusions.

INTEGRATED PLATFORMS FOR THE EUROPEAN RESEARCH INFRASTRUCTURE ON HERITAGE SCIENCE (IPERION HS)

Zsolt Kasztovszky, László Szentmiklósi, Boglárka Maróti, Ildikó Harsányi, Zoltán Kis, Veronika Szilágyi, Katalin Gméling, Katalin Bajnok, Adél Len, John Gait, László Rosta

Objective

IPERION HS integrates national facilities of recognized excellence in Heritage Science and aims at establishing a distributed Research Infrastructure (RI) with a sustainable plan of activities, including offering access to a wide range of high-level scientific instruments, methodologies, data and tools for advancing knowledge and innovation in Heritage Science. IPERION HS connects researchers in the Humanities and Natural Sciences and fosters a trans-disciplinary culture of exchange and cooperation for the growth of the European Research Area. IPERION HS pursues the integration of European world-class facilities to create a cohesive entity playing a leading role in the global community of Heritage Science. IPERION HS consists of partners from 23 countries clustered around their national nodes.

Methods

The Budapest Neutron Centre is an access provider in the FIXLAB platform, where FIXLAB means the large facilities of fixed locality. We offer Prompt Gamma Activation Analysis (PGAA) to determine the bulk elemental composition, and Prompt Gamma Activation Imaging (PGAI) to determine the elemental spatial distribution within a large heterogeneous sample. Neutron Activation Analysis (NAA) is to determine trace element concentrations in small samples. Neutron imaging on NIPS-NORMA and on RAD allows us to map the 2D or 3D macro-structure of the objects. Time-of-flight Neutron Diffraction (ToF-ND) and Small Angle Neutron Scattering (SANS) are for structure determination on atomic or on macromolecular scales.

Results

In 2022, five submitted research proposals were accepted by the Peer Review Panel and have been accomplished at the Budapest Neutron Centre (BNC). Two proposals were from Portugal, one from Romania, one from Germany and one from Slovenia. Each project's aim was to determine the provenance of various archaeological objects made of ivory, schist, glass, lapis lazuli or ceramics. For this purpose, the compositions of the archaeological objects were compared with reference samples of potential raw materials. In most projects, PGAA was used, occasionally complemented by NAA or Particle Induced X ray Emission (PIXE). The evaluation of the experimental results is in progress. For the Egyptian lapis lazuli amulets, the Afghanistan provenance is very likely. In some cases, the objects turned out to be made of a different material than lapis lazuli.

Table 1: List of the IPERION HS TNA research proposals accomplished at the BNC

Project Acronyme	Title	Affiliation	Country	BNC Instruments
ROMAN GLASS @ BLACK	Non-invasive compositional characterization of Roman glass finds from Black Sea Coast archaeological sites	Horia Hulubei National Institute for Nuclear Physics and Engineering, Magurele, Romania	RO	PGAA
FINGERCHALC	Fingerprinting Chalcolithic artefacts from ditched enclosures	Instituto Superior Técnico, Universidade De Lisboa	PT	PGAA, NAA, PIXE
IVORIST	Provenance and circulation issues of pre-historic ivory and schist remarkable artefacts	Instituto Superior Técnico, Universidade De Lisboa	PT	PGAA, NAA, PIXE
Egyptian Lapis Lazul	Egyptian Lapis Lazuli	Institute of Material Science, University of Stutgart	D	PGAA, Raman- and IR-Spectroscopy
MELB	Mobility and Exchange in Ljubljansko barje: non-destructive analyses of Copper age pottery of Ljubljana culture in Central Slovenia	ZRC SAZU Institute of Archaeology	SLO	PGAA

Remaining work

Other successful research proposals submitted to the BNC within the IPERION HS are being measured until the end of the project.

Related publication

[1] Sándor Sz.: *Roncsolásmentes analitikai módszerek alkalmazása lápisz lazuliból készült régészeti leletek eredetvizsgálatára (Application of non-destructive analytical methods to the provenance of archaeological finds made of lapis lazuli,* TDK / Students Scentific Association Research Work, – Eötvös Loránd University, 2022

TRAINING AND TUTORING FOR THE RADIATION PROTECTION AND NUCLEAR SAFETY EXPERTS OF NON-EU COUNTRIES

Tamás Pázmándi, Dorottya Jakab

Objective

The European Union (EU) supports the promotion of the effective nuclear safety and radiation protection culture, the safe management of spent nuclear fuels and radioactive waste, the establishment of efficient and effective safeguards for nuclear materials, and the implementation of the highest related standards in non-EU countries. These objectives are achieved through the European Instrument for International Nuclear Safety Cooperation (INSC). INSC includes Training & Tutoring (T&T) initiative aims at assisting the National Nuclear Regulatory Authorities (NRAs) and Technical Support Organizations (TSOs) of non-EU countries in capacity building to become competent, reasonably independent and adequately financed.

The 5th project phase („Training and tutoring for experts of the NRAs and their TSOs for developing or strengthening their regulatory and technical capabilities - MC3.01/20") of the EU-funded INSC T&T initiative, that follows up the previous project phases organized since 2012, has been launched in January 2022. It is implemented by an international consortium led by the Centre for Energy Research, and having members of NucAdvisor (France), Nuclear and INdustrial Engineering S.r.l. NINE (Italy), VUJE, a. s. (Slovakia), Uni-Energy Ltd. (Hungary), European Nuclear Education Network (ENEN) (Belgium). The responsible body overviewing the project implementation is the Directorate General for International Partnerships (DG INTPA) of the European Commission (EC).

Methods

The project supports the enhancement of capacities of NRAs and TSOs in non-EU countries through provision of training and tutoring aiming at transferring knowledge, EU expertise, experience and good practices to develop and maintain competences and skills by NRS/TSO staff related to the different areas of regulatory responsibilities and functions. During the nearly three years of the project tens of 1-2-week training courses are organized and tens of 1-2-month tutoring courses (on-the-job trainings) are held in EU NRAs/TSOs.

The project is implemented in 4+1 Tasks: Task 0 provides a general operational assistance, Tasks 1 and 2 prepare and implement the T&T Program, Task 3 evaluates the implementation for quality control and assurance and Task 4 operates a T&T Alumni Network to facilitate networking and global cooperation on nuclear safety regulation. The T&T courses are developed and delivered by prominent European experts of radiation protection, nuclear safety, emergency preparedness and responses, with the support of local experts from different regions around the world.

Results

In the first year of the project, great emphasis was put on the development, testing and validation, and subsequent improvement of the methodologies, approaches and tools to be used for the project implementation and course preparation and organization. As key results, the training and tutoring needs of the beneficiary countries and NRAs/TSOs were identified, and systematic analyses of the competence development needs were performed, on which basis a T&T Program was designed, that

- supports cognition and application of the best EU and international regulatory approaches with considering the local needs and specificities, too,
- provides underlying technical knowledge necessary to comprehend and apply scientific and technological fundamentals and concepts for effective nuclear safety regulation,
- best serves the identified competence development needs and with the defined topics and best suited delivery methods ensures that trained experts will maximize the use of the acquired knowledge in their daily work.

In 2022, two training courses in the topics of *Inspecting of Emergency Preparedness* and *Regulation of Radiation Protection in Medical Applications*, and one tutoring course in the topic of *EU Acquis, regulation and regulatory oversight of radiation protection* were successfully organized with 27 participants from 14 different countries.

Remaining work

The project lasts for 31 months and will be finished in 2024.

Disclaimer

This publication was produced with the financial support of the European Union. Its contents are the sole responsibility of the Contractor (Centre for Energy Research), the opinions expressed herein are those of the Contractor and do not necessarily reflect the views of the European Union and Commission.

Related publications

[1] T. Pázmándi, G. Bruna, Cs. Pesznyák, G. Cognet, A. Petruzzi, G. Pavel, M. Benke, B. Hatala, A. Van Den Brande, D. Jakab: *Training and Tutoring for the Experts of Nuclear Regulatory Authorities of Countries Outside the EU*, 10th European Commission Conference on EURATOM Research and Training in Safety of Reactor Systems, Lyon, France, 30 May - 3 June 2022

[2] T. Pázmándi, G. Bruna, Cs. Pesznyák, G. Cognet, A. Petruzzi, G. Pavel, M. Benke, B. Hatala, A. Van Den Brande, D. Jakab: *Training and Tutoring for the Experts of Nuclear Regulatory Authorities of Countries Outside the EU*, 6th European Congress on Radiation Protection (IRPA2022), Budapest, Hungary, 30 May - 3 June 2022

[3] T. Pázmándi, G. Bruna, Cs. Pesznyák, G. Cognet, A. Petruzzi, G. Pavel, M. Benke, B. Hatala, D. Jakab: *Training and Tutoring for the Experts of Nuclear Regulatory Authorities of Countries Outside the EU*, 4th European Congress of Medical Physics (ECMP 2022), Dublin, Ireland, 17–20 August 2022

[4] T. Pázmándi, G. Bruna, Cs. Pesznyák, G. Cognet, A. Petruzzi, G. Pavel, M. Benke, B. Hatala, D. Jakab: *Training and Tutoring for the Nuclear Safety Experts of Non-EU Countries*, 31st International Conference Nuclear Energy for New Europe (NENE2022), Portorož, Slovenia 12–15 September 2022

[5] T. Pázmándi, G. Bruna, Cs. Pesznyák, G. Cognet, A. Petruzzi, G. Pavel, M. Benke, B. Hatala, D. Jakab: *Training and Tutoring for the Radiation Protection and Nuclear Safety Experts of Non-EU Countries*, 8th International Conference VVER 2022, Řež, Czech Republic, 10-11 October 2022

[6] T. Pázmándi, G. Bruna, Cs. Pesznyák, G. Cognet, A. Petruzzi, G. Pavel, M. Benke, B. Hatala, D. Jakab: *Training and Tutoring for the Radiation Protection and Nuclear Safety Experts of Non-EU Countries*, European Radiation Protection Week 2022 (ERPW-2022) Estoril, Portugal, 9-14 October 2022

CHEMICAL EVOLUTION AND RADIONUCLIDE RETENTION STUDIES FOR HIGH-LEVEL RADIOACTIVE WASTE DISPOSAL

Margit Fábián, István Tolnai, János Osán, Ottó Czömpöly, Fruzsina Szabó

Objective

The aim of our work was to study the chemical evolution of a glass/steel/clay system held under conditions like those that could be predicted for a deep geological waste repository. Long-term exposure to repository conditions could result in significant alterations to the Engineered Barrier System (EBS) materials during the service life. The host media can be a source of oxygen, reactive ions and other species that can cause significant alterations to the system during its operation. The effects of radiation, temperature and mechanical stress must also be considered when various forms of degradation are calculated.

Scale model systems were assembled in such a way that close to real conditions were established. Our model EBS comprises borosilicate glass, modelling the waste matrix; iron, modelling the steel canister; and claystone, modelling the low permeability buffer surroundings. The main goal was to understand the characteristics, applicability, and stability of the whole system, from the structural properties of the vitrified waste to the clay response in the repository.

Quantifying the long-term entrapment of radionuclides (RN) in the solid phases of the host rock around the radioactive waste repository is a crucial step toward understanding diffusion and transport mechanisms. Hence, in a separate subproject, sorption and diffusion characteristics of a cation representing a key RN (Co^{2+}) were studied on clay-rich rock sections of the Boda Claystone Formation (BCF). Diffusion experiments involving nonradioactive ions of interest were especially performed for later microscopic investigations of the diffusion front on the typical oxidative section (albitic claystone) of a recent BCF core. The oxidation state of the redox-sensitive Co was studied non-destructively using synchrotron-radiation based X-ray absorption spectrometry. The influence of the presence of Ni^{2+} on the behaviour of Co^{2+} was also investigated.

Methods

To get information on the effect of the long-term exposure, a scaled-down model system was assembled with close to realistic expected disposal conditions in order to understand the chemical evolution of the contacting material surfaces, and the stability of the system, all the way from the structural and dissolution properties of the modelled vitrified waste to the clay response in the repository. Our experiment was carried out with three identical model setups containing glass, steel, and clay. To provide the necessary physical conditions, each prepared model setup was embedded into an external and an internal Teflon container. During the experiments all the three setups were fully saturated by synthetic BCF groundwater. The internal vessel contained a mixture of 1.4 g of powdered glass (borosilicate powder, with 50-86 μm particle size, 0.083 m^2 surface area), 0.7 g of steel (Fe powder, with 50-86 μm particle size, 0.008 m^2 surface area) and 27.9 g of claystone (crushed Boda albitic claystone, <100 μm fraction). The environmental conditioning of the model setup due to the Boda claystone groundwater was carried out at room temperature. The external vessel contained the enclosed internal vessel as well as 75.36 ml of groundwater. During the static experiments, the shape of the glass grains was assumed to be cubic so that the calculated surface area to volume ratio (SA/V) was 1108 m^{-1}. To ensure the continuous saturation of the powdered material, holes with 0.7 mm diameter were randomly drilled through the walls of the internal vessels. All the containers were filled with the same glass/steel/clay mixture and kept in an incubator at 80 °C. After periods of 3, 7 and 12 months one container was opened for post-mortem characterization and named as GFeC-3M, GFeC-7M and GFeC-12M, respectively. A portion of the initial glass/steel/clay mixture was preserved and kept dry for reference, and an initial sample of the groundwater mixture used was also preserved for similar purposes. Post-mortem characterizations of the solid phase were performed using Scanning Electron Microscopy (SEM), Energy Dispersive X-ray spectroscopy (EDX) and X-ray Photoelectron Spectroscopy (XPS). With the Inductively Coupled Plasma Optical Emission Spectroscopy (ICP-OES) and Ion Chromatography (IC) analyses of the liquid phase we predict the chemical durability of the system, thanks to the obtained leachates at each stage of the experiments.

Sorption and diffusion characteristics of the BCF host rock for Co^{2+} were also studied. Sorption of Co^{2+} was investigated both alone and in the presence of Ni^{2+} on both crushed rock samples and petrographic thin sections using conditioned synthetic BCF groundwater for the solutions holding the Co and Ni cations. Sorption isotherms (sorbed amount as a function of the equilibrium concentration, C_{eq}(M), in the liquid phase) were recorded through batch experiments in the 10^{-6}-10^{-2} M equilibrium concentration regime using non-radioactive ions of interest. Equilibrium concentrations in the liquid phase were determined using ICP-OES. Diffusion cells accommodating 4-8 mm thick slices of full diameter (62 mm) core sections and small hexahedral pieces (10×10×30 mm^3) were used. To monitor the diffusion in the rock, the changes in concentration of the Co during the experiment lasting several months were measured in the liquid phase using ICP-OES. At the end of the diffusion experiment, the rock sections were cut and the concentration profile which had developed inside the rock was mapped. On the solid samples, microscopic X-Ray Fluorescence (μXRF) and X-ray Absorption Near-Edge Structure (XANES) investigations were performed.

Results

During the SEM/EDX investigations – after 3, 7 and 12 months – the glass, Fe and clay materials could be identified based on their elemental composition and investigated separately (Fig. 1, Table 1). For the glass particles, the surface and borders do

not change significantly. The main elements contained in borosilicate glass are B, Si, O, Na, Zr, Ba, and all of them except boron were detected with EDX analysis after 3, 7 and 12 months (Table 1). (SEM/EDX analysis is not sensitive for boron.) Although, no secondary phases were identified and no alteration layer has been found on the borosilicate glass samples in any case within the resolution (~1 μm) of backscattered electron imaging at 20 keV, the elemental composition of the investigated material changes in rather small amounts. That means the average composition within its information depth (~2-3 μm) was not altered due to the experimental treatment. Since the composition of the glass surface to a depth of 2-3 μm was not affected, it can be assumed that the same is true for the whole volume of the glass particles.

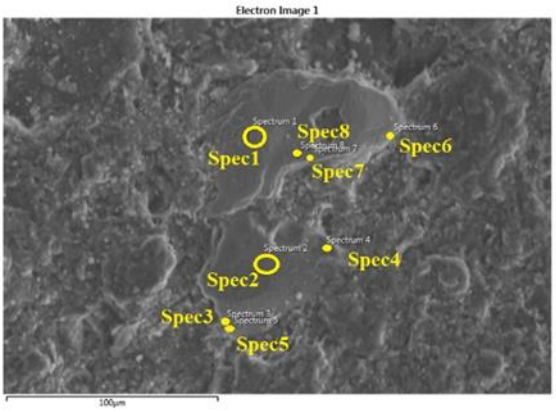

Figure 1: SEM secondary electron image on GFeC-12M sample, showing the topography of the sample surface.

Based on the recorded secondary electron image shown (Fig. 1) the structure of iron and glass did not change significantly during the experiment. Both the edges and the bulk phase remained uniform and homogeneous; no alteration layers were formed. Table 1 contains the major elemental composition for the selected positions, focusing on the iron and glass particles. The elemental composition of the glass particles was rather similar in the positions Spec 3,4,5 meaning that the average composition within the information depth (~2-3 μm) did not change as a result of the experimental treatment. Spectra 6,7 show that iron and clay are simultaneously present at the measured positions.

Table 1: SEM/EDX elemental composition at selected positions after 12 months (wt. %)

Elements	**Spec1** (Fe)	**Spec2** (gl)	**Spec3** (gl)	**Spec4** (gl)	**Spec5** (gl)	**Spec6** (Fe/clay)	**Spec7** (Fe/clay)	**Spec8** (Fe)
O	1.01	47.23	43.79	42.81	45.82	47.96	10.79	
Na		5.87	4.21	3.55	3.39	2.57	0.82	
Mg			0.21		0.25	2.41	1.01	
Al			0.72	0.74	1.10	7.90	3.26	
Si		26.04	27.25	28.06	26.81	21.49	6.48	
K			0.33	0.50	0.45	2.19	1.23	
Ca			0.26	0.55	0.26	0.72	1.33	
Fe	98.99		0.64	0.58	0.53	14.15	75.07	100.00
Zr		8.41	8.90	10.12	8.38			
Ba		12.44	13.70	13.08	13.01	0.60		
Total	100	100	100	100	100	100	100	100

Supplementary surface analysis was carried out for the samples whose evolution was stopped after shorter periods of time with XPS directly on the 55 mol`% SiO_2 - 10 mol% B_2O_3 - 25 mol% Na_2O – 5 mol% BaO – 5 mol% ZrO_2 matrix glass to observe changes and possibly formation of secondary phases. The results showed that for Si and O the atomic composition remained rather the same after 3 months, while Na and Ba decreased. The presence of boron within the information depth of the XPS method cannot be detected. The most significant finding was the precipitation of Mg and Ca on the surface of the borosilicate glass resulting from the synthetic porewater. The formation of this passive layer can be observed, which takes on an increasingly homogeneous structure as time progresses. The ICP-OES results shows that the released fraction of B increases in the liquid phase. The concentration of leached Ca and Mg among the glass-forming elements decreases, which correlates with the XPS results, while the concentration of K, Si and Na increases. Ion chromatography measurements for Cl^- and SO_4^{2-} ions in the final porewater are close to those of the conditioned SBPW but a slight increase was observed over time. The increase was less than 10% for Cl^- but more than 30% for SO_4^{2-}. According to the results, we can conclude that under the tested conditions (12 Months, 80 °C) the components used in the engineered barrier system do not have a significant effect on each other. Rather, they individually preserve their integrity, which is the basic principle of Defense in Depth. The borosilicate glass remains a stable glass under the tested conditions, no sign of secondary phase formation and no measurable physical/chemical

changes are observed. Fe flakes show no corrosion reaction. Based on our triplicate test, the minerals of BCF albitic claystone does not react with the other two engineered barriers and significantly slows down the structural transformation of the glass by delaying the alteration process [1, 2].

Results obtained from batch sorption experiments of Co^{2+} on crushed Boda Claystone are in line with sorption isotherms reported in the literature for other European argillaceous rocks. A correlation analysis of the µXRF results obtained for the thin sections which have undergone sorption experiments revealed that cobalt was primarily bound to areas of the same elemental composition as for typical clay minerals. Similar sorption properties of cobalt and nickel could also be confirmed by microscopic measurements, since the spatial distribution of Co and Ni was highly correlated. Synchrotron radiation XANES revealed that the majority of Co was found as Co^{2+} for BCF both in dispersed (crushed) and compact (thin section) forms (Fig. 2). Based on the XANES spectra, precipitation of cobalt chloride could be excluded (Fig. 2, right). Cobalt uptake by clay minerals occurred also at high concentrations (10^{-3} M). The diffusion experiments were launched in breakthrough geometry at different concentration between 10^{-2} and 10^{-5} M. With the initial concentration of 10^{-2} M, the diffusion coefficient appeared to be De=1.5×10^{-12} m²/s. A characteristic gradient profile of cobalt in the rock could be obtained using µXRF measurements [3].

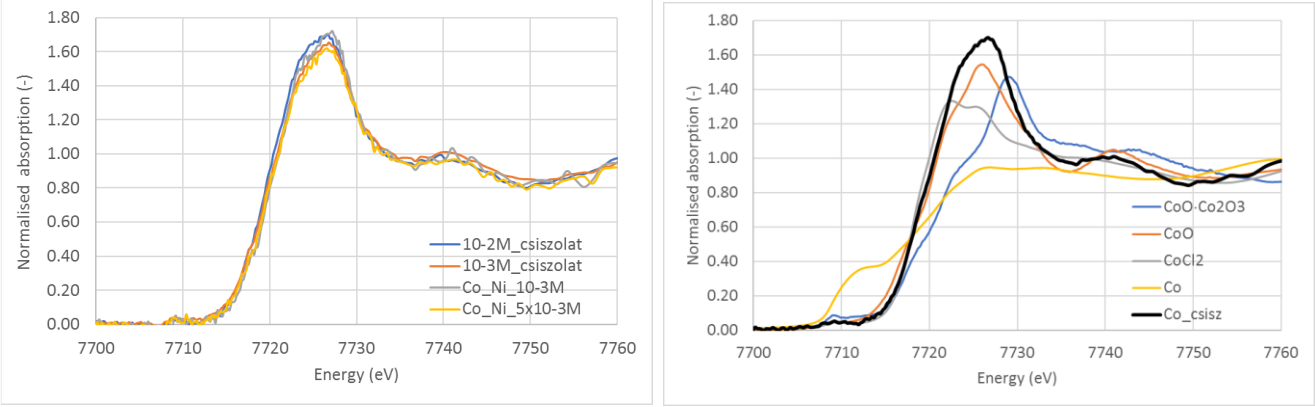

Figure 2: Co-K XANES spectra of BCF thin sections which have undergone sorption experiments with cobalt and cobalt/nickel (left) and comparison to spectra of reference compounds (right)

This work was supported by the H-2020 European Joint Program on Radioactive Waste Management (EURAD) – 847593.

Remaining work

This is the fourth year of a five-year project; we continue the well-prepared schedule.

Related publications

[1] M. Fabian, I. Tolnai, O. Czompoly, J. Osan and L.E. Aradi: *Characteristics of a Steel/Clay Model System Under Repository Conditions* In: ANS Proceedings, IHLRWM 2022 La Grange Park (IL), American Nuclear Society (ANS) (2022) pp. 900-905., DOI: 10.13182/T127-39306

[2] I. Tolnai, J. Osan, O. Czompoly, A. Sulyok and M. Fabian: *Glass/steel/clay interactions in a simulated radioactive waste geological disposal system*, Scientific Reports, submitted (2022)

[3] F. Szabó, O. Czömpöly and J. Osán: *Sorption and diffusion of cobalt on the potential host rock of a high-level radioactive waste repository,* Poster presented at the XIX. Nuclear Technical Symposium of the Hungarian Nuclear Society, 29-30 September 2022.

ACTIVITY RELEASE DURING STEAM GENERATOR TUBE RUPTURE IN A VVER-440 NUCLEAR POWER PLANT

Berta Bürger, Zoltán Hózer

Objective

In order to assess the consequences of Steam Generator Tube Rupture (SGTR) scenarios the activity release from defective fuel rods and from the primary coolant was simulated with SGTR boundary conditions in the framework of the EU R2CA project.

Methods

The primary coolant activity concentrations were calculated for two SGTR scenarios in a VVER-440 reactor:

- Break of 3 steam generator tubes,
- Collector cover opening event.

The following components (radionuclide groups) of the coolant activity were specified:

- Fission products,
- Transuranium elements,
- Corrosion products,
- Activation products.

The fission products originated from the defective fuel rods and from the tramp uranium deposited on the surface of fuel elements. The spiking effect was considered for the ^{131}I, ^{134}Cs and ^{137}Cs isotopes and calculated by the RING code. High water purification flowrate was used in setting up initial activity concentrations for the calculated iodine and caesium isotopes. For the other fission products and transuranium elements the steady state values from a simple model were taken into account, which is based on the core inventory and defines the maximum allowable activity concentrations for steady state operation at nominal power. Measured NPP data were used to set the corresponding values for the activity concentrations of corrosion and activation products. In case of activation products numerical models were also used.

In order to estimate the activity release to the steam generator additional calculations were carried out using the break and Emergency Core Cooling System (ECCS) flowrates and taking into account the decay of short lived isotopes.

Results

The calculated results showed that the activity release from leaking fuel rods was higher in the case of 3 tube generator ruptures compared to collector cover opening event (Fig. 1).

In the calculated scenarios 400 leaking fuel rods corresponded to the iodine activity concentration limits. According to the simulation of iodine spiking phenomena with the boundary conditions of the two scenarios 2.6% and 1.7% of fuel rod inventory was released to the primary coolant during the 3 tube break and collector cover opening transients, respectively.

During the calculated period (roughly 3 hours) ≈30-40% of the activity released from the fuel rods into the primary coolant was transferred to the secondary side of steam generator (Fig. 1).

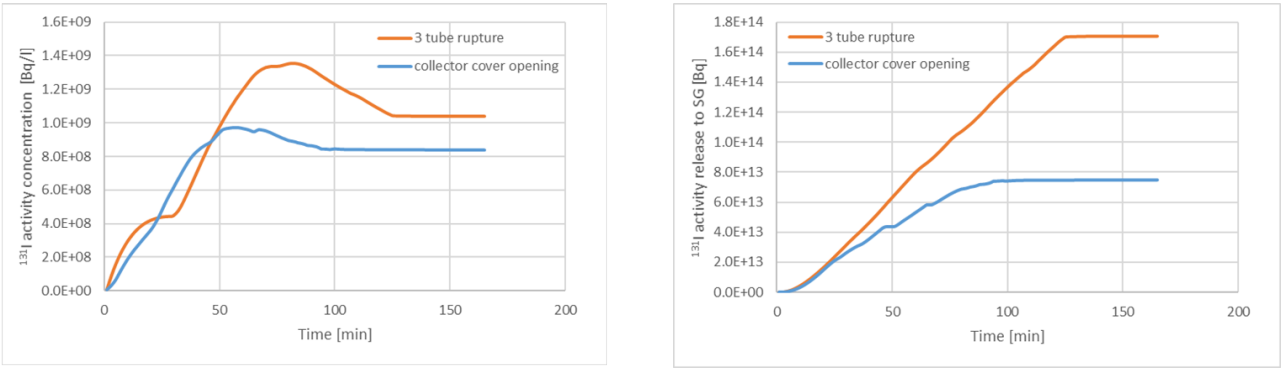

Figure 1: ^{131}I activity concentrations in the primary coolant (left) and integrated ^{131}I activity release to the secondary volume of steam generator

Remaining work

The planned calculations were completed.

Related publications

[1] B. Bürger, Z. Hózer: *Simulation of coolant activity concentrations during SGTR with the RING code,* EK-2022-437-1-1-M0 (2022)

[2] B. Bürger, Z. Hózer: *Reassessment of activity release during SGTR in a VVER-440 NPP,* EK-2022-437-1-2-M0 (2022)

FUSION RESEARCH AND DEVELOPMENT IN THE EUROFUSION PROGRAMME

Sándor Zoletnik

Objective

A coordinated research programme is being conducted in the European Union for the development of nuclear fusion energy production. It is managed by the Eurofusion consortium which includes participants from each Member State. From Hungary, the Centre for Energy Research is the member of Eurofusion, and the Wigner Research Centre for Physics and the Budapest University of Technology and Economics participate with some contributions as an "Affiliated Entity". The Eurofusion workprogram comprises two main elements: plasma physics research on existing experiments and development of the EU demonstration fusion power plant (DEMO) conceptual design.

Methods

In 2022 the Fusion Plasma Physics Department (FPL) participated in experiments on the Joint European Torus (JET, Culham, UK), the ASDEX Upgrade tokamak (Garching, D), the MAST Upgrade tokamak (Culham, UK) and the Wendelstein 7-X stellarator (Greifswald, Germany). On JET our researchers contributed by measuring the plasma edge density profile with the Lithium beam diagnostic. On ASDEX Upgrade a new diagnostic concept (imaging Heavy Ion Beam Probe, iHIBP) is being developed for measuring the magnetic field at the edge of the plasma by following the trajectory of injected impurity ions. The injector was built earlier by the FPL team, and this year trial measurements were done on the tokamak. On the MAST compact tokamak FPL researchers upgraded the Beam Emission Spectroscopy (BES) diagnostic and the first measurements were conducted this year. Participation in the Wendelstein 7-X program is the major plasma physics research activity of the department, since FPL staff have built and are operating two diagnostics: the 13-camera video system and the alkali beam diagnostic. After a 4-year shutdown, the commissioning phase of the experimental campaign started in September. Both diagnostics were manned by our team. A related project intends to develop real-time data processing capabilities based on the EDICAM video system[1] which is operating on Wendelstein 7-X and which is also installed and is waiting for experiments in the JT-60SA tokamak in Japan. The experimental work with beam-based diagnostics is supported by modelling activities [2] [3].

In the DEMO conceptual design program, the Fusion Technology Department (FTL) develops technologies for the maintenance of the blanket, the heat extraction and tritium production device in the future fusion power plant. Besides design and modelling, this also involved full size pipe brazing tests in the laboratory. FPL participated by designing various schemes for the replacement of the blanket segments in the tokamak. These involved scheme design, modelling, and some maintenance machine concept development. In the DEMO diagnostic setup, FPL is the task leader for the visible and UV diagnostics which measure radiation spectra and its spatial distribution in the divertor, during pellet injection, and for limiter protection. This work involves collaboration with several Eurofusion laboratories where specific works are performed. A mechanical engineer, Imre Katona, has won a position in the prestigious Eurofusion Engineering Grant to be trained as "ITER and DEMO optical diagnostic engineer". After the 3 year training period he is expected to be capable of designing DEMO diagnostics and forming a link between the physics and engineering community on DEMO diagnostics.

In future fusion reactors the device wall close to the hot plasma will receive a high neutron dose rate, which will destroy materials after a few year operation. As no existing neutron source can generate the dose and spectrum for the DEMO conditions the Eurofusion program is designing a large accelerator-based neutron source, DONES (Demo Oriented NEutron Source). FPL engineers are deeply involved in systems engineering [3], test cell, test system and liquid lithium system design.

Results

The JET tokamak is the only one in the World which can operate with Deuterium-Tritium mixture, the final fuel of fusion reactors. In the 2022 experimental campaign, with the contribution of EK researchers, it demonstrated record energy production from magnetic fusion. On ASDEX Upgrade, the iHIBP diagnostic achieved first results, showing that under specific plasma conditions it can collect the injected ions and detect magnetic field changes. This is also supported by earlier measurements of the FPL team on the COMPASS experiment in Prague. On MAST Upgrade, the BES diagnostic showed excellent signals, in agreement with expectations and has already detected signs of plasma turbulence, which is the main aim of the diagnostic. On the Wendelstein 7-X stellarator the video camera system provided a general overview of the experiment; it is a key diagnostic for plasma operation. The alkali beam diagnostic had some technical problems, and hence did not produce results in the commissioning, but a new spectroscopy observation has been successfully commissioned. Results are expected in the main part of the experimental campaign in 2023.

The DEMO and DONES design and development activities progressed as planned. These are long term projects involving collaboration with many EU laboratories. A DEMO conceptual design is expected to be completed in 2025.

The training activity under the auspices of the Eurofusion Engineering Grant progressed as expected. The trainee received education in optical detectors, electronics, optics design, radiation effects, and first mirror problems in ITER.

Remaining work

The data obtained from the JET and MAST Upgrade experiments will be evaluated in the coming year. JET will have its last campaign in 2023, when FPL researchers will continue to work on the edge density profile measurement. ASDEX Upgrade is closed now for a major upgrade. The future of the iHIBP diagnostic will be decided in 2023. There are already proposals from the FPL team to change the ion species to Potassium and optimize the observation system. On Wendelstein 7-X, the measurement campaign will be finished at the end of March and data evaluation will have to be done.

The DEMO and DONES works will continue following the present activities.

The Eurofusion Engineering Grant trainee will visit ITER for 3 months to work on a selected diagnostic engineering problem and thus gain experience in work on a reactor-class machine. He will also become gradually more involved in the DEMO diagnostic activities.

Related publications

[1] G. Cseh, et al: *Integrating EDICAM into the MARTe framework*, Fusion Engineering and Design **191,** 113516 (2023)

[2] P. Balazs, et al: *Special behaviour of alkali beam emission spectroscopy in low-ion-temperature plasma,* Fusion Engineering and Design **193,** 113650 (2023)

[3] C. C. Torregrosa-Martin, ... A. Zsakai: *Overview of IFMIF-DONES diagnostics: Requirements and techniques,* Fusion Engineering and Design **191,** 113556 (2023)

DISRUPTION MITIGATION SYSTEM FAST SHUTTER PROTOTYPE DEVELOPMENT

András Zsákai, Dániel Imre Réfy, Erik Walcz, Domonkos Nagy, Dénes Zoltán Oravecz, László Richárd Csiszár, Sándor Zoletnik

Objective

The project started at the beginning of 2022 with the aim to develop a fast shutter prototype that can effectively close off a 40 mm wide aperture in under a few milliseconds of time. The shutter will be part of the ITER Disruption Mitigation System (DMS), which protects the first wall of the device against plasma disruptions during high-power operations that could cause uncontrolled heat loads on the wall. This can be accomplished by launching and shattering cryogenic Hydrogen, Deuterium and Neon pellets close to the plasma. The technology is called Shattered Pellet Injection (SPI) and a support laboratory for its development is working at EK. It is important to avoid any contact between the flying pellet and the internal surfaces of the several-meter-long flight line to minimize the risk of premature pellet breakage. Therefore, the internal dimensions of the flight tube of the SPI are relatively large compared to the pellet, and hence provide a bypass for the propellant gas to overtake the pellet, resulting in a significant quantity of propellant gas arriving in the plasma ahead of the pellet. This would cause undesirable instability in the plasma and compromise the effectiveness of the disruption mitigation. One possible solution for this issue is the use of a fast-acting shutter in the flight line, which will close after the pellet has passed through it to hold back the propellant gas. Therefore, the need to build and test a prototype shutter has arisen and a grant was awarded for this to EK.

Methods

Initially, a requirement analysis and a study of various options have been conducted to find those options that could fulfil the specifications of the contractor. From this, a shutter consisting of an eddy current-based accelerator (copper coil – copper ring pair) and an eddy current-based decelerator (conductive plate – magnet stack pair) setup has been chosen [1]. Numerical calculations have been conducted and a test bench has been built to observe the performance of the accelerator-decelerator combination and to determine the optimal layout of the driving coil and the layout of the magnet stacks and conductive plate. The test bench also included diagnostics for detailed analysis (fast camera) and for automatic analysis (optical LED diagnostics) for cycle testing [2]. Currently, the prototype-related optimal layout is under design and a new test bench is also under development for it [3].

Results

The acceleration of the fast shutter was tested and proved to work efficiently and reliably. Even 1 ms of closing time over a 40 mm aperture could be achieved. However, the limiting factor is the deceleration capabilities of the shutter due to the tight space constraints. Based on numerical analysis, the decelerator setup can slow down the shutter and avoid a hard impact (by using a gradually slowing trajectory) while achieving an approximately 2.5 ms closing time. The decelerator setup uses a Halbach array layout (a special arrangement of magnets) and copper- or alumina-based conductive decelerator plates.

Remaining work

The project is continuing for the next year and the main work will be to design the prototype itself, based on the already achieved results, and to confirm this design by conducting the required tests on it as set by the contractor.

Related publications

[1] A. Zsákai et al.: *Fast Shutter optioneering study for the ITER Disruption Mitigation System,* Abstract accepted to ISFNT-15 (2023)

[2] D. I. Réfy et al.: *ITER DMS Fast Shutter development and laboratory testing,* Abstract accepted to ISFNT-15 (2023)

[3] L. R. Csiszár et al.: *Mechanical design of a Fast Shutter for the Disruption Mitigation System,* Abstract accepted to ISFNT-15 (2023)

REMOTE MAINTENANCE RELATED TASKS WITHIN THE DEMO PROJECT

Jenő Kádi, Ákos Szegedi, József Szőke, Márton Gregor, Miklós Palánkai

Objective

DEMO is set to be the first example of a commercial fusion power plant (Tokamak type) using the heat produced in the reactor to generate electricity. To successfully produce a fully operational, commercially viable Demonstration Fusion Power Plant (DEMO), the maintenance of the plant must be considered as an integral part of the overall design. Due to the nature of fusion reactors, almost all maintenance will, by necessity, be remote.

Methods

Within the Work Package Remote Maintenance (WPRM) project our tasks cover 3 different topics:

[1] Due to the thermal and nuclear loading on the first wall (closest to the plasma), the components will need to be removed and replaced periodically. Installation of new blankets requires the joining of their service pipes. Brazing is one of the alternatives that are being considered for joining the service pipes of the DEMO breeding blankets.

[2] DEMO contains a variety of different pipes transporting different materials necessary during the operation of the plant. They may need to transport gases or liquids for cooling or other purposes. The pipes within DEMO also come in a wide range of sizes (up to DN350 or even greater) which makes certain technologies preferable in some cases, while not reasonable in others. Some typical G1 pipes would be limiter port pipes, port cooling pipes, and manifold pipe connections among others.

[3] The work for 2022 advanced the development of welding, repair, and Non-Destructive Testing (NDT) techniques to be used ex-vessel in DEMO, as part of a programme of work that will achieve a validated concept design by the end of Framework Program 9 (FP9).

Results

The results obtained in the topics above:

[1] In order to realize in-bore brazing within DEMO, the first step is to test the heating method that has the most potential and to verify that the brazing filler metal can be evenly heated up to a specific melting temperature. We have been developing a brazing test station, which includes the design and optimization of a bespoke induction heater (Fig. 1 and 2.).

[2] Various pipe layout alternatives have been examined as well as the pipe arrangements related to the Electron Cyclotron system, and the required maintenance functions and risks for said systems have been examined. Suggestions have been made regarding the pre-concepts for the Equatorial Port Plug (EPP) Remote Maintenance designs and a preliminary evaluation and setup of a short-list of the design alternatives for both systems (G1 pipes and Electron Cyclotron) have been performed.

[3] Welding and NDT technologies were examined for remote maintenance operations inside the bio-shield, from which the most viable technologies were selected, and their commercially available alternatives were compared to our assumptions and requirements. From this information, sets of System Requirement Documents (SRD) and Context Definition Documents (CDD) were created, finally culminating in the creation of a risk register which examined the gaps between current and expected technological capabilities and the reality of the assumption that discrepancies between the two could be bridged, given our current timeframe and resources.

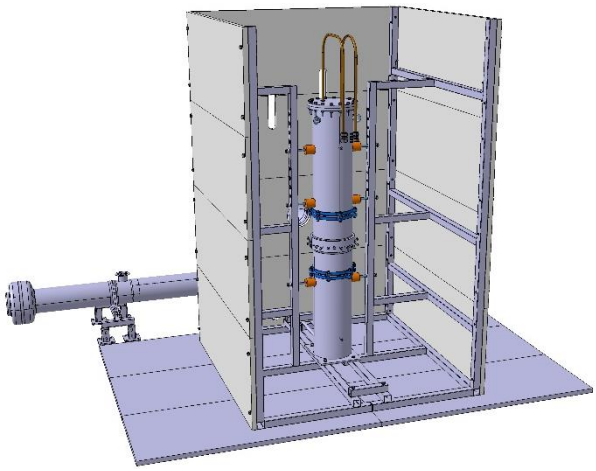

Figure 1: Brazing trial station

Figure 2: Brazing test station is being built in the lab.

Remaining work

In the following years our tasks will include:

[1] The optimization of the brazing heating technique and after that we are planning to conduct actual brazing tests of the DEMO DN200 cooling pipes,

[2] Further specifying the relevant applicable studies and constraints in regard to the physical layouts of the G1 and Electron Cyclotron pipes, once their geometric models are available,

[3] Study the remaining open questions related to the maintenance of the ex-vessel welds of the DEMO tokamak in order to obtain a concept design by the end of FP9.

Related publication

No publication yet.

SUPPORT LABORATORY FOR THE ITER DISRUPTION MITIGATION SYSTEM

Sándor Zoletnik, Erik Walcz

Objective

This project started at the end of 2020 with the aim of setting up a laboratory for the development of a "Shattered Pellet Injection" (SPI) technology for ITER [1]. The equipment consists of a cryogenic pellet injector [2], a flight tube and a shattering plate, where the solid Hydrogen, Deuterium and Neon pellets are broken into pieces, and finally their fragment size and velocity distributions are measured. This solid fragment cloud can inject material into an unstable ITER plasma much faster and deeper than in gaseous form, and therefore can more quickly cool the plasma, and prevent damage to the device wall from uncontrolled heat loads. The technology of reproducibly generating a suitable distribution fragment cloud is expected to be provided by the Support Laboratory, so that the 27 SPI injectors for ITER can be built and reliably operated.

Methods

The first 19x38 (diameter x length) pellet injection was achieved, without shattering, in December 2021. In 2022, the system was completed with the 4 m long flight tube, the shattering device and the analysis vacuum chamber. The whole setup is a 10 meter long vacuum system with roughly 2 m^3 volume. Two laser curtain diagnostics were installed in the diagnostic chamber for the measurement of the pellet fragment size and velocity distributions, by detecting light scattered by the fragments.

In the first part of 2022, experiments were conducted with 19 mm diameter Hydrogen, Deuterium and Neon pellets in order to explore the pellet production recipes[1][3][4]. In June, the injector was rebuilt for 28.5 mm diameter pellet production. Such large Hydrogen pellets had never been made before. In July, the first measurements with all three materials were successfully demonstrated with the larger pellets. In the second half of the year systematic experiments were conducted with Hydrogen and Neon. To better characterize the details of the pellet production and shattering processes, ITER extended the contract by funding the procurement of four new fast cameras and the modelling activity for the pellet production process. The new cameras were installed in November. An Optical Pellet Diagnostic (OPD), developed by Fusion Instruments Kft. in the framework of another ITER project, was also installed in the system, and a Schlieren optical diagnostic was also tested. This latter diagnostic is capable of revealing gas flow patterns around the pellet and might improve our understanding of the pellet launch process. The design and photographs of the setup are shown in the Figure 1 below.

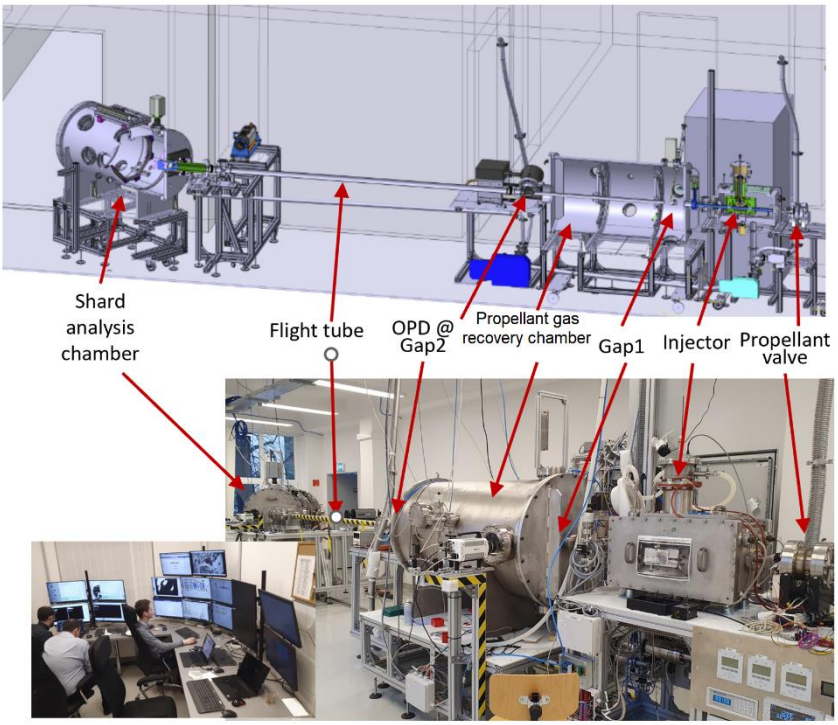

Figure 1: The design and photographs of the ITER DMS Support Laboratory

Results

The results obtained in the ITER DMS Support Laboratory showed that the technology and pellet size planned for the ITER Disruption Mitigation System is possible. Pellet production recipes were found, which develop a loose snow-like layer on the

pellet surface and enable launching the pellet with a moderate gas pressure [1]. The numerical pellet production model does not include this effect, but still reproduces the pellet production time within 50% to the experiment. The full diagnostic system was installed towards the end of the year and now it can fully characterize pellet quality, speed and rotation at three positions on their roughly 6 m long flight from the injector to the shattering device. Initial analysis of the laser curtain diagnostic data showed [3] that the fragment cloud is elongated parallel to the shattering plate.

Remaining work

The most urgent task in 2023 is to further develop the processing algorithms for the laser curtain data, and thus provide fragment size, flight direction and velocity distributions for various pellets. Solutions and tests for preventing the propellant gas from overtaking the pellet are also planned, as the gas would pre-cool the plasma edge, further destabilizing it. In this respect, regular operation of the Schlieren diagnostic is essential. The present open shattering head will be replaced by an ITER-like closed shattering device which will be installed in a second stage of injector development, and fragment distributions will be characterized with it. This project will continue for several years with the testing on different shattering heads and other components of the ITER setup.

Related publications

[1] S. Zoletnik, et al: *Shattered pellet technology development in the ITER DMS test laboratory,* Fusion Engineering and Design **190,** 113701(2023)

[2] E. Walcz, et al: *Development of a Shattered Pellet Injector test bench for the ITER DMS support laboratory,* Fusion Engineering and Design **191,** 113584 (2023)

[3] G. Kocsis, et al: *Fragment plume diagnostics for cryogenic pellet shattering studies*: *Development and first experimental results,* Fusion Engineering and Design **190,** 113515 (2023)

[4] T. Szepesi, et al: *In-situ pellet growth and quality monitoring diagnostics for the ITER DMS*

PREPARATION OF FORMING CARBON DIOXIDE NEUTRAL ENERGY SCENARIOS IN THE EUROPEAN REGION

Endre Börcsök and Veronika Oláhné Groma

Objective

One of the important objectives of the European Union is to create a carbon dioxide neutral energy sector. The realization of this extremely ambitious goal is currently unattainable without the use of nuclear energy. The development of nuclear energy based on fission has become politically controversial and has lost its social support in many member countries. Taking this into account, the European Union considers fusion energy development as a primary research and investment area. An important issue related to fusion power plant research is to determine what extent can be reached by an energy system that - based on long-term forecasts - will rely mainly on weather-dependent renewable energy sources. In the framework of the EUROfusion-WPSES project, as part of an international team, we have the opportunity to develop our energy model, which have been tested so far within national level. Our aim is to prepare the rescaling of our energy model on a European scale and to create relevant energy scenarios which are taking into account specific national criteria weights.

Methods

Within the framework of the EUROfusion-WPSES project, we joined the work of an international research group specializing in the creation of energy scenarios by applying multi-criteria decision analysis. Since the primary modelling tool used by the group (TIMES model) does not allow the application of a wide system of criteria, we decided to further develop our own model. The set containing 14 criteria was selected so that beside completeness, a good comparability of electricity production alternatives could be guaranteed. Since the evaluation aspects were assessed on a different scale, their values can only be considered as ratios. The starting points of the uniform scaling were the variable and fixed costs. The starting weight of the criteria was chosen so that their mean value was the same as the average of the variable costs, and then individual weighting was applied to the 14 aspects for each country with multipliers in the [0.1 ; 10] interval. Our aim was to implement the determination of the 36 country-specific weight vectors in such a way that the result of our model approximates the real production data. In this work, we rely on the ENTSO-E (European Network of Transmission System Operators) database and consider 20 electricity production alternatives, to which pumped storage was taken into consideration, too. The hourly resolution production data and frontier crossing values were all considered as target values of our model calculation, while the annual maxima were tend to be limiting conditions.

Results

Based on the literature data and the results of our previous research [1], we defined 14 criteria (Fix cost, Variable cost, Climate change effect, Air pollution, Hazardous waste, Waste quantity, Geo-political factors, Availability of fuel, Flexibility, Risk of accident, Long-term sustainability, Risk aversion, Land use and Jobs creation) for 20 alternatives of which the starting criteria weights for 6 alternatives are presented in Figure 1. Country-specific weights based on historical data series can be a realistic starting point for predictive calculations.

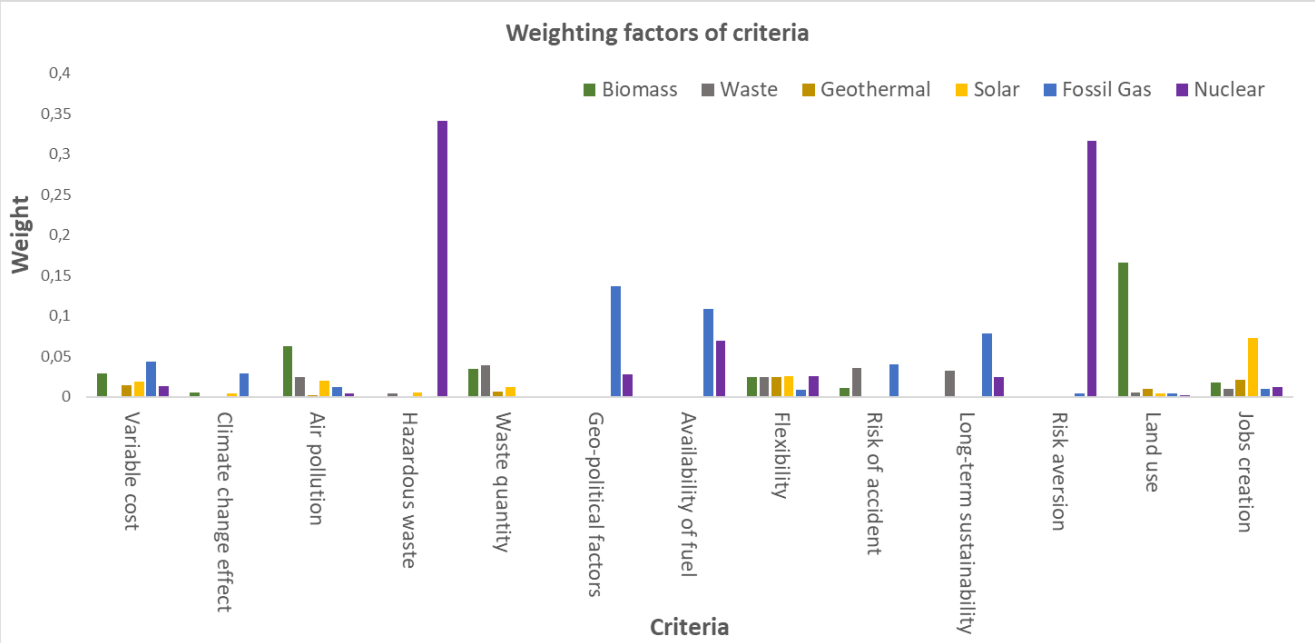

Figure 1: Starting weighting factors for some selected electricity production alternatives

Remaining work

Currently, our calculations cover one day, which we would like to expand to 28 days in order to publish stable results.

Related publication

[1] E. Börcsök, Z. Ferencz, V. Groma, Á. Gerse, J. Fülöp, S. Bozóki, J. Osán, S. Török, Á. Horváth: *Energy Supply Preferences as Multicriteria Decision Problems: Developing a System of Criteria from Survey Data*, Energies **13**, 3767 (2020)

TESTING DIFFERENT ACCIDENT TOLERANT FUEL CLADDINGS

Zoltán Hózer, Márton Király, Richárd Nagy, Péter Szabó, Erzsébet Perez-Feró, Tamás Novotny, Anna Csordás-Pintér, Levente Illés, Zoltán Kovács

Objective

In the framework of the IAEA Testing and Simulation for Advanced Technology and Accident Tolerant Fuels (ATF-TS) project testing of different cladding materials is carried out in order to characterize the behaviour of candidate materials and compare the new measured data with the parameters of traditional cladding alloys.

Methods

Comparative tests of cladding tubes for water cooled reactors were carried out using several cladding types:

- Zircaloy-4, ZIRLO™, optZIRLO™, Zr1%Nb tubes as references,
- Cr, CrN, CrN/Cr, TiAl coating on the external surface of Zr alloys,
- FeCrAl alloy.

The experimental program in 2022 included isothermal burst tests at 800-900 °C in inert atmosphere, with linear pressurization rates. Oxidation of specimens was carried out in steam at 1000 °C and 1200 °C. Scanning Electron Microscopy (SEM) was applied for the examination of cladding microstructure. Two scanning electron microscopes (LEO 1540XB and ThermoFischer Scientific Scios 2 types) were used for morphological studies. Secondary Electron (SE) images were taken on the outer side surface of the samples at 5 keV. The elemental composition and the distribution of the most interesting elements were investigated by Oxford X-MAX 20 type Energy Dispersive X-ray microanalyser (EDX) with silicon drift detector. For EDX analysis, 10 kV and 20 KV voltages were applied.

Results

According to the ballooning tests results, the burst of coated samples took place at slightly higher pressure compared to the uncoated reference samples. Significant cracking of the coating, long axial ridges were observed on the Cr coating post-test, not only at the burst location, but all along the tubes. The Cr-CrN multicoated Zr1%Nb had the least cracks. Strange double failure initiation could be seen on one sample (Fig. 1).

SEM examinations were carried out with as-received and oxidized samples. As an example the results for the as-received TiAl coated Zircaloy-4 are shown in Fig. 2. Elongated sample parts can be seen. There are thin gaps and cavities on the surface where various impurities (such as Fe, Na) can be detected. Individual particles with 100–600 nm lengths can be seen. These grains have slightly elongated shapes. A thin long feature with probable impurities can be identified on the top of small particles. Oxygen can be found everywhere. It seems that the TiAl layer was oxidized during manufacturing.

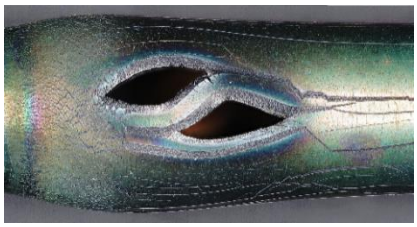

Figure 1: Burst of CrN coated Zr1%Nb cladding tubes tested at 900 °C

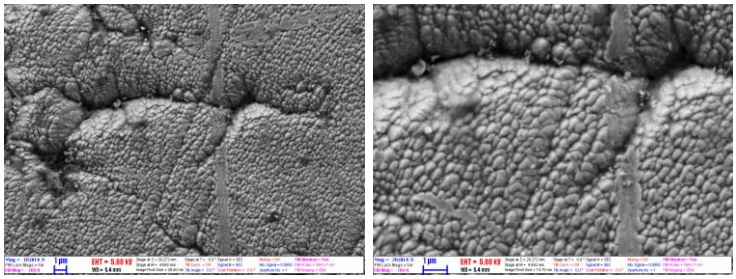

Figure 2: SEM images taken on TiAl coated Zircaloy-4 sample

Remaining work

It is planned for 2023 to continue the series with mechanical tests (mandrel, ring tensile) using the same cladding types.

Related publication

[1] Z. Hózer, M. Király, R. Nagy: *IAEA CRP ATF-TS Burst tests of coated claddings,* Consultancy Meeting of Coordinated Research Project "Testing and Simulation for Advanced Technology and Accident Tolerant Fuels (ATF-TS)", IAEA Headquarters Vienna and Cisco Webex, 15 - 18 August 2022

TESTING SiC_f/SiC COMPOSITE CLADDING TUBES FOR GAS-COOLED FAST REACTORS

Zoltán Hózer, Tatsuya Hinoki, Emese Slonszki, Anna Pintér-Csordás, Levente Illés, Márton Király, Zoltán Kovács, Márta Horváth, Róbert Farkas, Roland Mischl. Róbert Nagy, Erzsébet Perez-Feró, Tamás Novotny, Péter Szabó*

**Kyoto University*

Objective

In the framework of the EU SafeG project experiments and examinations of cladding microstructure were carried out in order to check the applicability of SiC_f/SiC composite cladding tubes for high temperature conditions in gas-cooled fast reactors.

Methods

The SiC_f/SiC tube samples were fabricated using *prepreg* sheets at the Kyoto University. Two series of samples were supplied for testing at EK. In the second series higher tension was applied during wrapping.

The following experiments and examinations with SiC cladding tubes were performed:

- high temperature treatment in He atmosphere (1000 °C, 7 h),
- high temperature oxidation in steam (1000 °C for 1 h, 1200 °C for 30 min),
- ring compression tests of as-received and heat treated samples,
- mandrel tests of as-received and heat treated samples,
- pressurization of 30 mm long tubes,
- Scanning electron microscopy of as-received and tested samples.

Results

The mechanical tests showed limited load bearing capability of the SiC cladding tubes. In both mandrel and ring compression tests, the failure of the cladding tubes took place at about 100 N load (with 8 mm long tubes). The high temperature treatment at 1000 °C in He atmosphere for 7 hours resulted in further embrittlement and significant reduction of load bearing capability. The pressurization tests indicated leakage at relatively low overpressure.

The first results with testing SiC_f/SiC composite tubes are promising and this is the primary candidate cladding material for the refractory fuel of gas-cooled fast reactors. However, the currently used fabrication procedure needs further improvement to overcome the observed weaknesses.

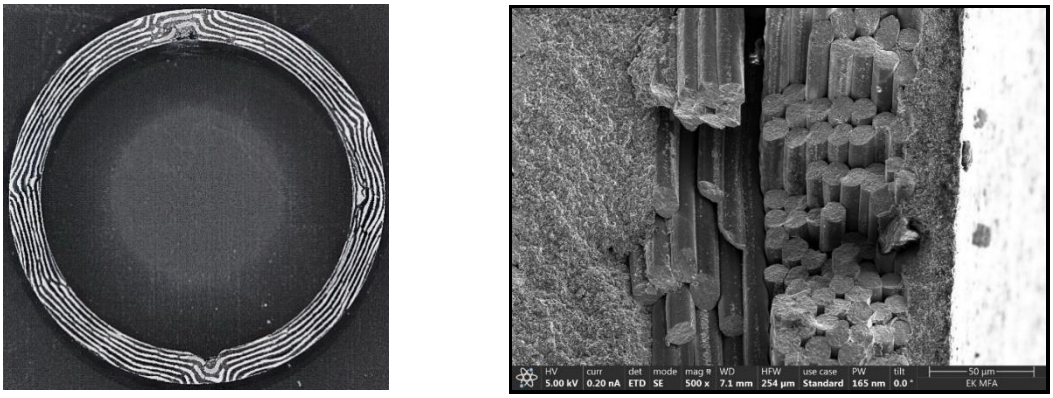

Figure 1: Cross section of as-received SiC_f/SiC sample (left) and SE image taken on the fracture surface of a broken sample (right)

Remaining work

The planned work was completed. The continuation will depend on the availability of new SiC cladding specimens.

Related publication

[1] Z. Hózer, T. Hinoki, E. Slonszki, A. Pintér-Csordás, L. Illés, M. Király., Z. Kovács, M. Horváth, R. Farkas, R. Mischl, R. Nagy, E. Perez-Feró, T. Novotny, P. Szabó: *D2.1 Innovative cladding materials testing, EU SafeG project*, Technical report EK-THL-2022-487-00-05-M0-A0 (2022)

MATERIALS SCIENCE RESEARCH FOR THE DEMO FUSION REACTOR

Ildikó Szenthe, Ferenc Gillemot, Márta Horváth, Szilvia Móritz, Dávid Cinger, Kristóf Andor Csikós and Balázs Hargitai

Objective

The next step in European fusion research after the ITER reactor is the development of the DEMO fusion reactor. In connection with the research on DEMO materials science issues, the Reactor Material Research Group has participated in the research activities inside the MAT-IREMEV work package of EUROfusion programme. The research group in 2022 continued the work in the materials-integrated radiation effects modelling and experimental validation field. The objective of the work is to research the radiation damage studies of fusion materials.

Methods

To supply base data for the elaboration of further testing, the previously irradiated EUROFER97 material specimens were tested. Further irradiation campaign was going on up to 2 dpa (displacement per atom, Fe) fast fluence, at 300-350 °C. The specimens were manufactured, coded and pre-fatigued according to the ASTM E-1820-18 standard. Hardness measurements were also performed, and all data were collected into a database. The target holder and the capsules were designed and manufactured. Four separate target box were prepared. Each box included one set of dosimetry monitor foils (Cu, Fe, Al-Co1%, Nb) to measure the fluence. The irradiation rig was filled with the specimens and inserted into the reactor core. All the heating and controlling connections were linked to the BAGIRA system.

Other task was to prepare the database of research results on functional materials. The aged material properties (mainly after neutron and gamma irradiation) were compiled from the yearly reports of the topic's research group. Advancement was achieved in the development of Material Handbook on Functional Materials summarizing the database content at a high level to support design of DEMO in-vessel components.

The newly developed potential structural materials as tungsten, Oxide Dispersion-Strengthened (ODS) steels are going to be investigated. To test the high temperature fracture toughness, bending- and tensile strength of high purity tungsten and ODS steels require specially designed samples. Sample preparation and pre-fatigue technology were developed.

Results

The irradiation of 32 pieces of compact tension and 32 pieces of tension specimens at two temperatures: 300 and 350 °C up to 0.5 dpa (Fe) was started in September. The irradiation is planned to be finished at the end of 2025.

In connection with the Functional Materials Database and Properties Handbook the work continued with the collection of the raw data based on the yearly reports of the "Functional Materials" research group. Functional materials were characterized with their optical and di-electrical properties such as absorption, reflectance, electrical conductivity, permittivity and loss tangent (dissipation factor). In 2022 the Functional Materials Material Property Handbook (MPH) has not only been extended with properties mentioned above, but thanks to the literature review of one of the research groups the thermal conductivity of some insulators (of non-irradiated and irradiated materials as well) was also included in the MPH, which section was quite incomplete till now. Furthermore, this year's great progress was made within the project as the first Designers Interface Meeting was held. The discussion covered topics such as system design and selection/use of functional materials, what additional material properties need to be investigated to finalize the design of the respective systems, and other corresponding requirements, such as irradiating functional materials by higher fluences.

For the measuring of tungsten and ODS steels, fracture toughness, bending- and tensile strength samples were manufactured. Our research group started to develop the design of special tools and equipment for future measurements.

Remaining work

To supply base data for the elaboration of further testing, measurement of the irradiated EUROFER97 material specimens will be performed in the near future. The results will be included into the updated Material Property Handbook. Further development of the Functional Material Property Handbook and underlying database is also carried out. The Reactor Material Research Group will participate in the development and testing of potential new fusion structural materials.

DIFFUSION BONDING OF CDS COMPOSITE WITH AL_2O_3 AND 316L STAINLESS STEEL AT GLEEBLE 3800 PHYSICAL SIMULATOR

Tétény Baross, Csaba Balázsi, Katalin Balázsi, Haroune Rachid Ben Zine, Gábor Veres

Objective

Diffusion bonding is a candidate joining method for flat metal parts of ITER First Wall components. The diffusion bonding is a well-known technology, however, the bonding capabilities of new materials like Ceramic Dispersion Strengthened (CDS) 316L stainless steels require investigations. The Centre for Energy Research has a unique capability to produce CDS specimens to be tested for suitability of use in fusion reactor conditions. As a continuation of our earlier work [1,2], where diffusion bonding of 316L specimens were tested on a Gleeble 3800 physical simulator, five CDS-316L specimens were diffusion bonded with 316L specimens within the temperature range of 950-1000 °C and axial mechanical pressures of 20 – 30 MPa. The CDS 316L specimens were prepared by powder technology via Spark Plasma Sintering (SPS) similarly to [3,4,5] with the following composition: Fe–16.8% Cr–12% Ni–2.5% Mo–1.5% Mn–0.6% Si (wt.%). For diffusion bonding two starting compositions were the following: 316L and 316L/1 wt% Al_2O_3. The goal of this project was to investigate the bonding applicability of CDS-316L specimens. One example for diffusion bonding can be seen on Figure 1, where between the two 316L stainless steel rods a CDS-316L specimen was successfully bonded.

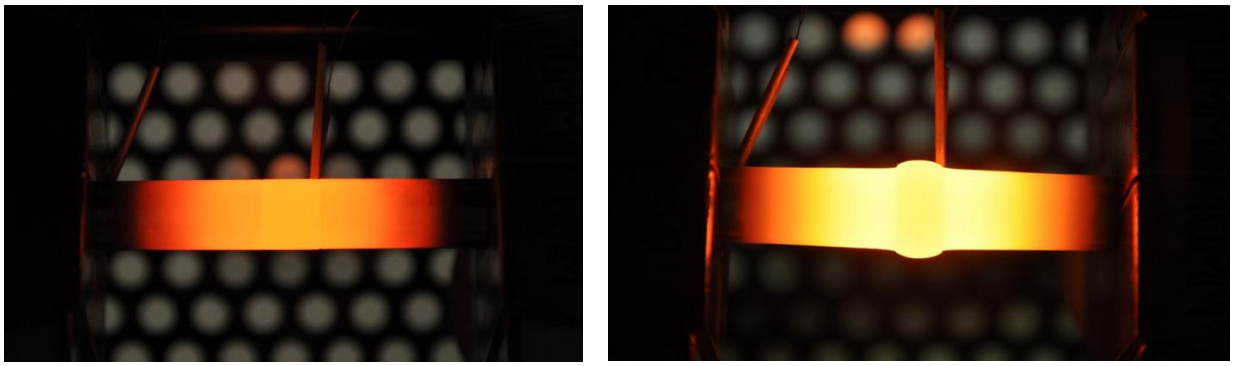

Figure 1: Diffusion bonding of a CDS-316L specimen between two SS316L spec., 1000C/30MPa/60min, a.) initiation b.) after 20 min

Methods

Four diffusion bonding experiments were prepared: 30 mm (316L rod) + 9 mm / 11 mm (CDS-316L) + 30 mm (316L rod) with diameter 12,5 mm. The measurements concluded much higher electrical resistance in CDS specimens, combined with a high creep deformation compared to the SS 316L. The high electrical resistance can be explained by the powder structure of the CDS specimens. During the earlier physical experiments, we found that the optimal temperature with acceptable deformations was around 975°C or less and the applied pressure was around 20-30 MPa.

The bonded surfaces were prepared by polishing, cleaning and etched by CITRANOX® to remove the oxides. The surface roughness was kept under (Rz = 0,2…0,7 micron). They were shipped under Ag gas, to avoid further oxidation and contamination before diffusion bonding. However, in this case 30-60 minutes passed after opening the vacuum chamber, until the vacuum pump down was started in the Gleeble chamber, therefore the oxidation was not avoidable.

Since the high strain rate at the CDS specimens were much higher compared to the 316L stainless steel, the first 10 minutes could be taken as only the strain of the CDS specimen. Related to the flow stress we have comparable results for the OALG4, OALG9. Table 1. summarizes the diffusion bonding test parameters.

Table 1: The diffusion bonding tests of CDS specimens with the altering parameters

Number	Test layout	T [C]	P [MPa]	t [min]	Useful length before and after bonding [mm]
6-7	316L rod / 11 mm CDS-316L sp. /316L rod	1000	30	40	71 / 57,03
16-17	316L rod / 9 mm CDS-316L(1 wt% Al_2O_3) /316L rod	975	20	40	69 / 60,94
10-13	316L rod / 9 mm CDS-316L(1 wt% Al_2O_3) /316L rod	975	30	40	69 / 65,3
14-15	316L r./ 9 mm CDS-316L(Al_2O_3)/ 11 mm CDS-316L/ /316L r.	950	20	60	80 / 76,5

Figure 2: Prepared and polished specimens for SEM and EDS investigations

The specimens were cut for microstructural investigation, it has been polished using abrasion paper up to 1200 grade. The Vickers micro-hardness has been measured across the samples where an average of 12 measurements have been performed on each zone. Basically, the three zones are the two 316L rods and in the middle the reference 316L and the CDS 316L with 1 wt% Al_2O_3 Discs.

Four bars from each bonded specimens have been used to test the flexural strength by 3-point bending tests. The results were between 440 - 550 MPa. The diffusion bonding between the CDS 316L and CDS 316L/1 wt% Al_2O_3 (Nr. 14-15) showed better properties with an average of 543.75 MPa. Some specimens (Nr. 6-7) were ductile and were not broken. The 10-13 samples broke in the CDS / bulk material interface due to the presence of an initial crack along the diffusion bonded interface as it was visible on the Scanning Electron Microscope (SEM) images.

The bonded zones have been investigated by SEM and Energy Dispersive X-ray Spectroscopy (EDS): a mixture of large grains and thin elongated grains surrounded by a darker phase was observed. The interface between the zones is well defined, no obvious diffusion zone has been observed within the investigated magnification. The 316L samples consists of a mixture of large and elongated grains surrounded by a darker area rich with Oxygen. The Alumina particles are distributed in the darker areas of the investigated samples (left image), whereas the Oxide could be observed on the right image. The SEM images can be seen in Figure 3.

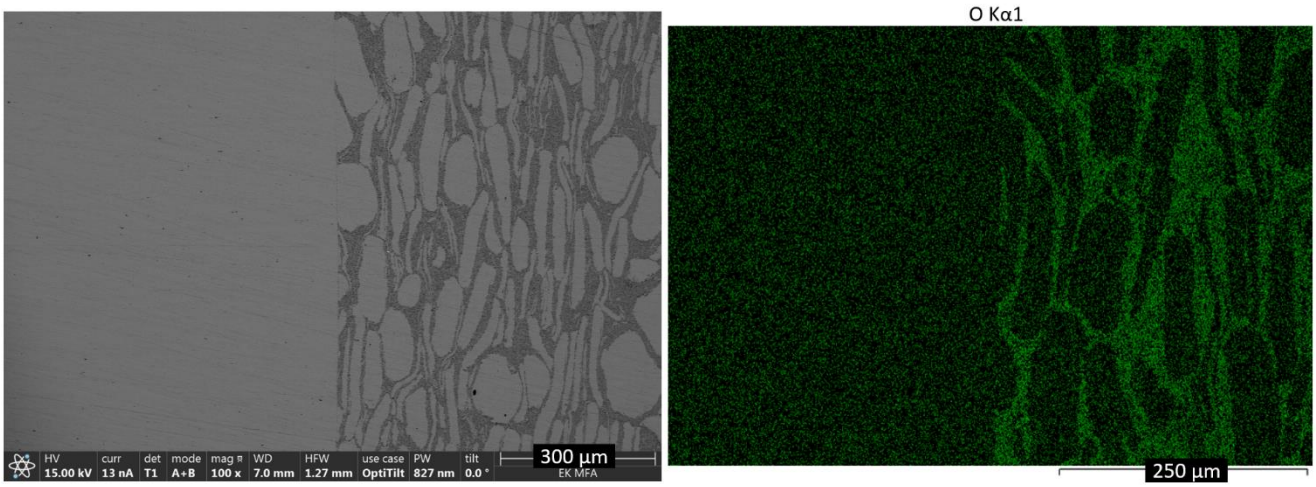

Figure 3: The SEM investigations of the CDS 316L and CDS 316L/1 wt% Al_2O_3 (Nr. 14-15) specimens

Results

CDS-316L and CDS-316L/1 wt% Al_2O_3 specimens were successfully diffusion bonded with standard 316L stainless steel rods. It was found that the creep properties of the CDS specimens at this combination of high temperature and high current density were much higher compared to the standard 316L steel. We supposed a high electrical resistivity inside the CDS specimens with larger volumetric heating during the welding process.

The addition of Alumina particles increased the microhardness of the 316L CDS steel. No diffusion zones have been observed within the investigated magnification for all composites, where the interfaces between the different zones were well defined at all bonded specimens.

The strain rate and the flow stress were investigated. A very slow and continuous axial deformation was found at a given stress, in this way we did not assume strain hardening, where the slow deformation can be the result of the diffusional creep.

Since the CDS bonding experiments were closely linked to the first authors' PhD work, the completion of the thesis was appointed as a goal. During this period the thesis was submitted to the doctoral school and defended at MATE University. During this time a summarizing article was published [2] related to the PhD work.

Remaining work

The authors plan to write an article about the main results in the Journal of Nuclear Materials or other relevant journal.

Related publications

[1] T. Baross, P. Bereczki, L. Jánosi, M. Palánkai, B. Sánta, G. Veres: *Diffusion bonding experiments of 316L steels in a Gleeble 3800 thermomechanical simulator for investigation of non-destructive inspection methods,* Fusion Engineering and Design, **160,** 111768 (2020) ISSN 0920-3796, https://doi.org/10.1016/j.fusengdes.2020.111768

[2] T. Baross, P. Bereczki, L. Jánosi, M. Palánkai, G. Veres: *316L mintákon végzett diffúziós hegesztési kísérletek Gleeble 3800 fizikai szimulátoron,* Nukleon, **15,** 241 (2022) ISSN: 1789-9613

[3] C. Balázsi, F. Gillemot, M. Horváth, F. Wéber, K. Balázsi, F. C. Sahin, Y. Onüralp, Á. Horváth: *Preparation and structural investigation of nanostructured oxide dispersed strengthened steels.* J. Mater Sci 46, 4598–4605 (2011) https://doi.org/10.1007/s10853-011-5359-1

[4] P. Jenei et al.: *The influence of carbon nanotube addition on the phase composition, microstructure and mechanical properties of 316L stainless steel consolidated by spark plasma sintering,* J Mater Res Technol. 8(1), 1141-1149 (2018) https://doi.org/10.1016/j.jmrt.2018.07.019

[5] P. Jenei, Cs. Balázsi, Á. Horváth, K. Balázsi And J. Gubicza: *The influence of BN additives on the phase composition, microstructure and mechanical properties of 316L steel consolidated by spark plasma sintering,* IOP Conference Series: Materials Science and Engineering, 426. ISSN 1757-8981 (2018)

MULTIPURPOSE ION BEAM ANALYSIS CHAMBER FOR FUSION MATERIAL SCIENCE APPLICATIONS

Jenő Kádi, Miklós Palánkai, József Szőke, Gábor Veres

Objective

In the fusion industry, there is a need for the development of new steel alloys, which could fulfil the requirements that are, in some cases, very much different from those of other fields of industry. High temperature and radiation levels alone are reasons why the currently available alloys could hardly be used in certain areas of a (e.g.) tokamak. In future fusion devices the utilization of novel steel compounds, such as Oxide Dispersion-Strengthened (ODS) alloys or reduced activation steels, would have considerable advantages over conventional steels. Diffusion bonding of ODS steels is a focus-area of research nowadays. The quality of the bonds can be investigated with non-destructive nuclear methods, such as Rutherford Backscattering Spectrometry (RBS), Particle Induced X ray Emission (PIXE) and Proton Induced Gamma-ray Emission (PIGE).

Methods

The assembly can be split into 3 main sub-assemblies. The first is the analysis chamber itself, which is responsible for carrying out the measurements. The second is a separate collimator chamber, the duty of which is to collimate the ion beam as precisely as possible. The last sub-assembly is a holder structure, which is capable of lowering and raising the analysis and collimator chambers to be able to set the desired beam height with respect to the floor between 100 and 180 cm. The scissor-like mechanism equipped with a stepper motor can move the chamber continuously and thus the height can be fine aligned to fit the inlet and outlet ports of the surrounding equipment.

The rotation feedthroughs, the stepper motor, the gate valves and the linear positioner can all be operated remotely. The services needed for operation is current and air supply, because the actuators work electrically, and the gate valves are pneumatic.

Results

We have successfully developed a very flexible multi-purpose analysis chamber that can perform multiple ion beam analysis measurements simultaneously. Access for sample replacement is very easy, owing to a large fast entry port.

The holder structure beneath the analysis chamber can adapt it to a wide beam height range.

Two separate sample holders were developed, the first being a nine-slot sample holder for thin films. This holder has one degree of freedom, which is the rotation around the feedthrough axis.

The unique sample holder for Time-of-Flight Elastic Recoil Detection Analysis (ToF-ERDA) measurements has 4 Depth of Field (DoF), thus making it possible to direct scattered particles from the small-sized samples precisely to the dedicated ports.

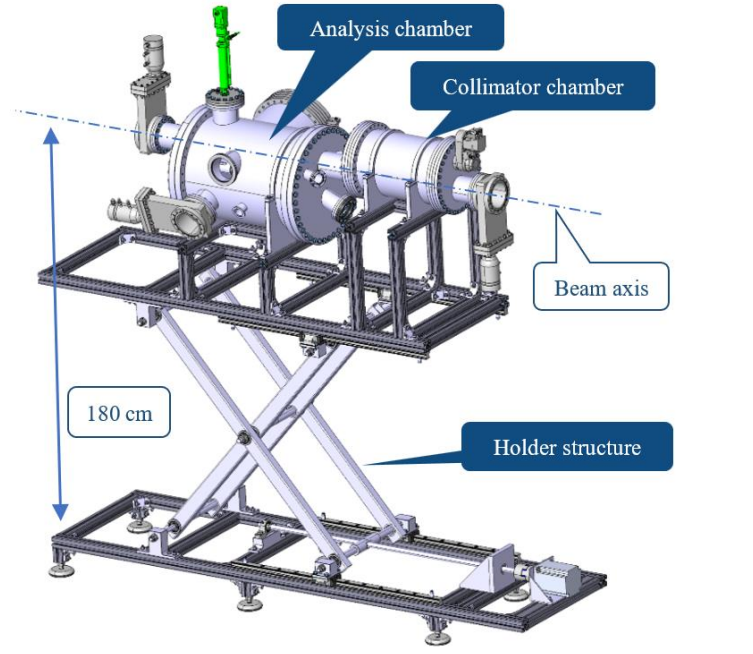

Figure 1: Overview of the analysis chamber

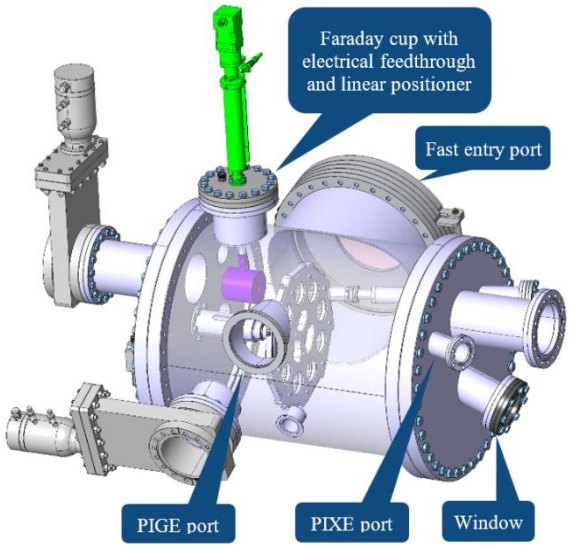

Figure 2: Ports of the vacuum chamber (isometric view)

Remaining work

The work was finished, the design documents were handed over to IAEA.

Related publication

[1] J. Kádi, M. Palánkai, J. Szőke, G. Veres: *Multipurpose Ion Beam Analysis Chamber for Fusion Material Science Applications*: Fusion Engineering and Design **191,** 113519 (2023) https://doi.org/10.1016/j.fusengdes.2023.113519

DEVELOPMENT OF THE IN-VESSEL OPTICAL BOX OF THE ITER EROSION DEPOSITION MONITOR

Miklós Palánkai, Tétény Baross, Bálint Papp, Zsolt Papp, Gábor Szarvas, Attila Bőhm, Gábor Veres, Mark Kempenaars, Govindarajan Jagannathan

Objective

The main function of the ITER Erosion Deposition Monitor (EDM) is to observe the erosion/deposition status of the divertor vertical targets as well as the topology change and surface damage that may occur due to the plasma-wall interaction at these vertical targets. The main function of the optical box of this diagnostic system, which is mounted under the divertor dome of one of the divertor cassettes, is to provide a stiff base and multi-functional shielding for the optical components located inside of it.

Methods

Since the optical box under the divertor dome is in a harsh environment, under high plasma, nuclear and electromagnetic (EM) loads, it becomes one of the critical parts of the ITER optical system. The design challenges involve the tight space between the surrounding parts, the manufacturing of the complex cooling channels, maintaining the optical tolerances and the adequate heat transfer between the different components. To produce a robust design and fulfil all the requirements, the optical box has gone through several design iterations and simulation stages.

Results

The EDM is an optical diagnostic system whose accuracy depends on the integrity of the mechanical parts. We report on the challenges of the development of the optical box itself, the mirror supports and the shutters. We present design solutions for key components that decrease the temperature of the optical box and its internal parts. These components are the cooling channels, which have been integrated into the walls to increase the cooling of the box, and the redesigned mirror supports, which have better heat transfer between the water-cooled walls and the mirrors.

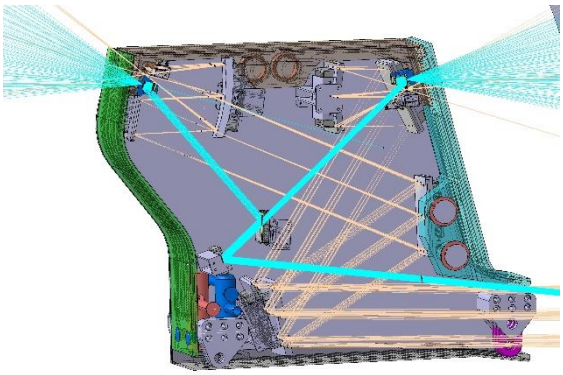

Figure 1: The inside of the optical box version #3 with the laser paths shown

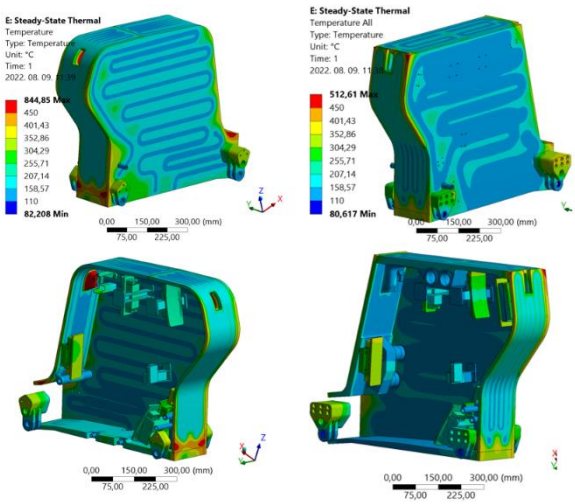

Figure 2: Temperature distributions in the solid region of two different designs, showing the outside and inside of each box

Remaining work

The next step in the development is the presentation of the result to the Preliminary Design Review panel, and to develop the system further, towards the Final Design.

Related publication

[1] M. Palánkai, T. Baross, B. Papp, Zs. Papp, G. Szarvas, A. Bőhm, G. Veres, M. Kempenaars, G. Jagannathan: *Development of the in-vessel optical box of the ITER Erosion Deposition Monitor*, Fusion Engineering and Design **189,** 113519 (2023) https://doi.org/10.1016/j.fusengdes.2023.113421

NON-DESTRUCTIVE, SPATIALLY-RESOLVED ELEMENT ANALYSIS OF STRUCTURED SAMPLES

László Szentmiklósi, Boglárka Maróti, Zoltán Kis

Objective

We use Prompt-Gamma Activation Imaging (PGAI) to characterize non-homogeneous and irregularly-shaped samples.

Methods

Composition measurements using PGAI-NT (Neutron Tomography), computer programming, Monte-Carlo modelling.

Results

Within the project K124068 funded by the NKFIH, we worked out and validated a comprehensive matrix-effect correction method to extend the applicability of the PGAA method to the study of non-homogeneous objects [1]. The correction is based on the MCNP 6.2 code with the nuclear data library Lib80x (based on the ENDF/B-VIII.0 database). The detailed geometries of the Budapest Neutron Centre's PGAA and Neutron-Induced Prompt Gamma-ray Spectroscopy (NIPS)-NORMA experimental stations, the energy distribution of the cold neutron beam, and the structure of the sample were implemented in the simulation environment to reproduce the real PGAA experiments.

Earlier, a set of benchmark objects were created comprising 3×3×3-unit cubes of materials typically found in the main fields of application as well as in the sample holders, including Cu, Fe, PTFE, graphite, Pb, Sn, and limestone (Figure 1). These represent the materials found in the major application fields of the Budapest PGAA facilities. They were measured in various geometrical arrangements using a well-collimated pencil neutron beam. We carried out the simulations this year to correct quantitatively the results. We compared the *a priori* analytic geometry definition to the voxelized calculations that uses pointwise material assignation from a segmented neutron tomogram. The simulations of both approaches gave adequate matrix-effect corrections even for such a complex object, so unbiased analytical results could be obtained [2].

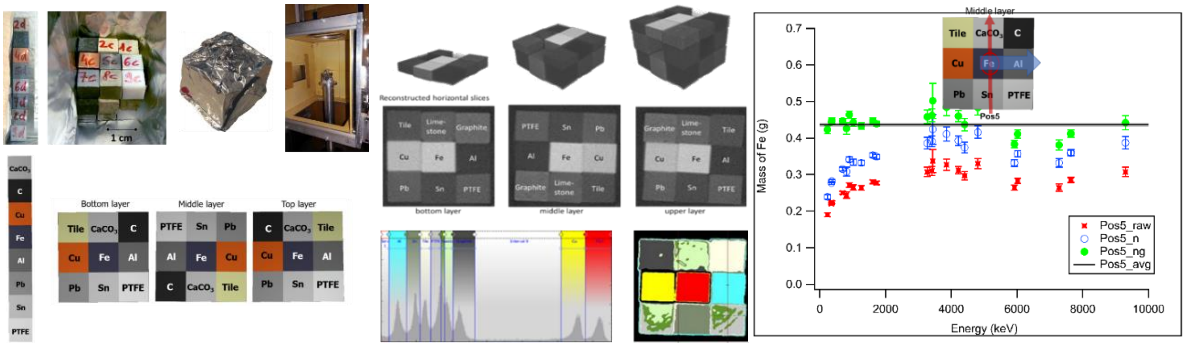

Figure 1: The segmentation of the test cube and the subsequent correction for the matrix effect on the measured raw data for the central Fe unit cube

In other cases, e.g. the non-destructive characterization of decorated porcelain artifacts, the object has only a surface inhomogeneity that is much thinner than the bulk. This requires the joint use of surface-analytical methods for the decorative surface pattern and methods of high penetration depth for the bulk-representative chemical composition. We used position-sensitive X-ray Fluorescence Spectrometry (XRF) and Prompt-Gamma Activation Analysis (PGAA), assisted by 3D structured-light optical scanning and dual-energy X-ray radiography. The proper combination of the near-surface and bulk element composition data can shed light on raw material use and manufacturing technology of ceramics [3].

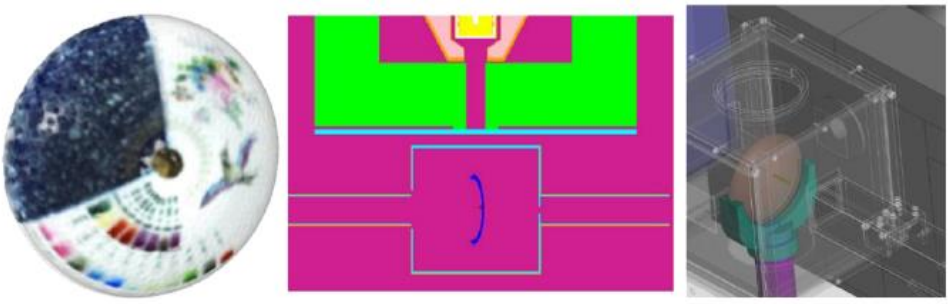

Figure 2: The 3D optical scan of the Sevres ceramic. The geometry for bulk PGAA simulations has been transferred to MCNP via voxelization

Related publications

[1] L. Szentmiklósi, Z. Kis, B. Maróti: *Integration of neutron-based elemental analysis and imaging to characterize complex cultural heritage objects*, in: D'Amico S., Venuti V. (eds) Handbook of Cultural Heritage Analysis. pp. 239-271 (2022) Springer, ISBN 978-3-030-60015-0 DOI 10.1007/978-3-030-60016-7_10

[2] L. Szentmiklósi, B. Maróti, Z. Kis: *Quantitative element analysis of 3D-structured samples*, Journal of Analytical Atomic Spectrometry **38,** 333–341 (2023) DOI: 10.1039/D2JA00316C

[3] L. Szentmiklósi, B. Maróti, Sz. Csákvári, T. Calligaro: *Position-sensitive bulk and surface element analysis of decorated porcelain artifacts*, Materials **15(15),** 5106 (2022) DOI: 10.3390/ma15155106

WIRELESS GAMMA RADIATION DETECTOR SYSTEM FOR ENVIRONMENTAL MONITORING, DOSE RATE MAPPING AND SEARCH FOR RADIOACTIVE SOURCES

Attila Hirn, István Apáthy, Sándor Deme, Erika Tunyogi, János Volk

Objective

The radiation detector system briefly described below is developed in the frame of an umbrella project on developing environmental monitoring sensors for use in emergency conditions. The main objective of the development is to create a wireless gamma radiation detector system for environmental monitoring, dose rate mapping and search for radioactive sources that can be of either fixed installation, mounted on unmanned or passenger vehicles, or even man-portable.

Methods

The detector system is based on the Geiger-Müller (GM) counter system developed by the EK Space Research Department for operation also aboard stratospheric balloons and sounding rockets in harsh environment and designed to be compatible with the environmental monitoring system of the Environmental Protection Service at the KFKI Campus. The equipment is designed to run on either batteries, solar cells, Universal Serial Port (USB) or mains electricity. Communication can be via direct connection through USB or Long-Range Wide Area Network (LoRaWAN), Global System for Mobile communication (GSM) or later the Unified Digital Radio Telecommunications (UDR) network of the Hungarian Government.

Results

Continuous data acquisition (with Global Positioning System (GPS) coordinates and timestamps), data download via USB and data transfer through LoRaWan were successfully tested on the prototype of the wireless gamma radiation detector system powered by batteries and solar panels. Data could be retrieved also directly from the internal memory card for post-processing. The detector housing with the USB interface and battery status indicator, and a barrel equipped with the detector system powered from batteries and solar cells used for environmental monitoring at fixed installation are shown in Fig. 1. This later setup was used for demonstrating the operation of the wireless gamma radiation detector system as element of the environmental monitoring system at the campus.

Figure 1: The portable wireless gamma radiation detector system (left) and the barrel equipped with solar cells and the detector system used for environmental monitoring at fixed installation (right)

Remaining work

In year 2023 prototyping of the wireless gamma radiation detector system shall be finished and its operation demonstrated for different applications (environmental monitoring, dose rate mapping, radiation source detection) and configurations (fixed installation, mounted on unmanned or passenger vehicles, man-portable measurements).

Acknowledgment

The activity reported in the present paper was conducted in the frame of the Thematic Excellence Program 2021, grant number TKP-16-6/PALY-2021.

EASI-STRESS PROJECT

Márton Markó, Gyula Török, Tamás Szabolics, László Rosta

Objective

The aim of doing stress measurement with neutrons is the mapping of the deformation within metallic structural materials arising from production methods, heat treatments, etc. in the bulk material.

The institute is a contributing member of the EASI-STRESS European project (European Activity for Standardization of Industrial residual STRESS characterization methods) aiming to create a standard for stress measurements at Large Research Infrastructures (LRI) such as neutron and synchrotron sources. Our contribution covers the development of the ATHOS instrument to be able to make stress measurements, performing experiments on standard, so called round robin samples and on industrial samples, the development of a general data treatment program intended to be used by both industrial users and physicists, and to make a contribution to the final proposal for a European standard. In this year, we continued the development of hardware and control software of our instrument, conducted experiments on round robin samples and produced the first version of the general data reduction program.

Results

Instrument development

The stress mapping with neutrons is based on the defining of the shift of the Bragg peaks at different points in the sample. This shift is much smaller than the resolution of the instrument. Hence, during the measurement any change in the instrument configuration causes an increase in the measurement time due to the need for repeated long, high precision calibrations. Since the measured volume (Gauge Volume (GV)) at a measurement point is below the surface, any uncontrolled moving of the sample e.g. by changing the position or orientation manually, has to be avoided.

This year, we improved accuracy of the setting and checking of the position of the measured volume (GV) in the sample by improving the optical system of the instrument, involving a higher resolution laser setting, and determining the optimal setup by using a theodolite. We have also designed an XYZ table for the sample movements, to use for a better determination of the position and the orientation of the sample. We also further developed the instrument control and data reduction/data treatment software to provide a faster visualization of the data obtained, so as to be able to monitor the quality of the measurement in real time. The data reduction and the automatic calculation of the relative strain (deformation) is integrated in the control program. The data treatment program calculates the stress and produces a nexus output file.

Development of the general data treatment program

The aim of the general data treatment program is to give a harmonized data structure containing measurement method, the strain and stress data as a function of the position in the sample. The data structure is easily understandable for all users, independent of the place and measurement method.

This year, together with the colleagues of other LRI-s, we defined the general input (NEXUS data structure with obligatory fields) and output (svg and NEXUS data structure) of the program and developed the first version of the program.

Measurement on round robin samples

We conducted experiments on bent steel samples under different strain conditions and on 3D printed samples after different heat treatments. In figure 1. a tensioned round robin sample and the results of the measurement are shown. The slopes of the measured strain distribution follows the calculated ones.

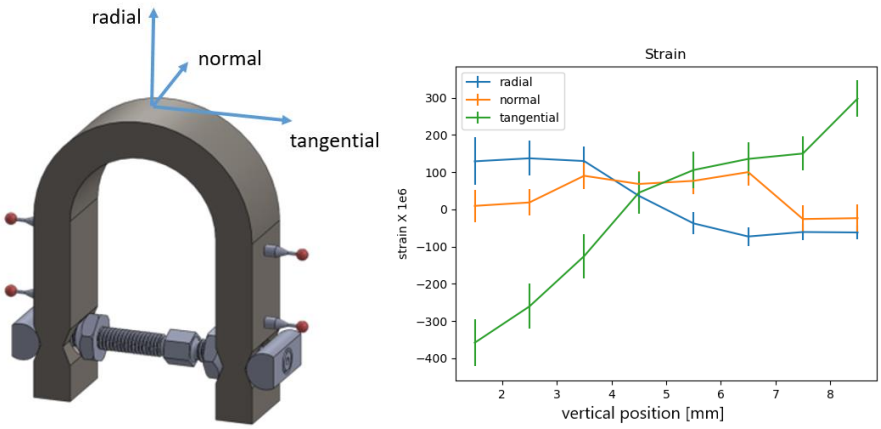

Figure 1. Left: round robin sample, Right: strain distribution measured in the middle of the sample downwards from the outer surface

Remaining work

In the remaining part of the project we will finalize the development of ATHOS, integrate the XYZ table into it, finalize the control software, finish the validation of the general data treatment program, and conduct measurements on industrial samples within the scope of the project. The standardization has just started, the final proposal for the standard will be ready at the end of the project.

POTENTIAL REFERENCE SAMPLES FOR ELEMENTAL ANALYSIS OF AEROSOL PARTICLES COLLECTED BY CASCADE IMPACTORS

János Osán, Csaba Dücső, Ottó Czömpöly, Veronika Groma

Objective

The combination of cascade impactor aerosol sampling with Total-Reflection X-ray Fluorescence (TXRF) analysis was found to be an effective tool to determine the chemical elements in size fractionated particulate matter. Due to low detection limits (in the range of 0.1-10 ng/m^3) an adequate time resolution of 1-4 h sampling time can be reached in urban environment, thus daily time trend of elements in size fractioned aerosol samples can be studied [1]. Internal standardization generally performed for droplet residues is not straightforward for direct TXRF analysis of cascade impactor samples, since the deposition pattern of the collected particles is generally different for various impactor types. May and Sioutas impactors collect the aerosol particles deposited as thin stripes, while Dekati impactors have series of round nozzles distributed around the centre of impactor plates.

Methods

The AEROMET II project aims at the development of potential reference samples for the TXRF analysis of aerosol particles collected by cascade impactors. These reference samples are designed to have known elemental composition and mass distributed along a lateral pattern similar to the aerosol particle deposits expected in the impactors. Test samples were prepared on round Si wafers of around 30 mm in diameter to be suitable for measurements in most commercial TXRF equipment. Two types of optical lithography, lift-off technique and wet etching, were applied for preparation of round Cr pads of 2-3 μm in diameter and 20-90 nm in height distributed randomly within the deposited areas. The shape and diameter of the pads and their uniformity were verified by scanning electron microscopy and the angular dependence of Kα X-ray intensities of Cr and Si were studied using Synchrotron Radiation X-Ray Fluorescence (SR XRF) at the XRF beamline of Elettra (Trieste, Italy).

Results

In order to eliminate the effect of orientation, patterns composed of circles around the centre of the wafers were developed (Fig. 1, left). The amount of particulate matter deposited on the impactor stages is also critical for TXRF quantification [2], therefore the potential reference samples were designed to contain low but quantifiable mass of Cr. The suitability of the test samples as candidate reference materials was investigated through the angular dependence of Cr-Kα X-ray intensities. Samples containing microparticles on a flat reflector surface are expected to show nearly constant X-ray intensities below the critical angle of total reflection (1.75° at a 10 keV excitation energy) which is double of the intensities above the critical angle. Test samples prepared using wet etching have the smallest dependence of Cr-Kα X-ray intensities in the range of 0.08°–0.12° generally used for TXRF (Fig.1, right). Lift-off technique resulted in less reliable samples especially with a small height of Cr pads (20 nm, sample 9.7). Optical lithography with wet etching was found to be the most promising technique for preparation of candidate reference samples with excellent production repeatability [3]. These samples are expected to be used as external standards for calibration of table-top TXRF equipment.

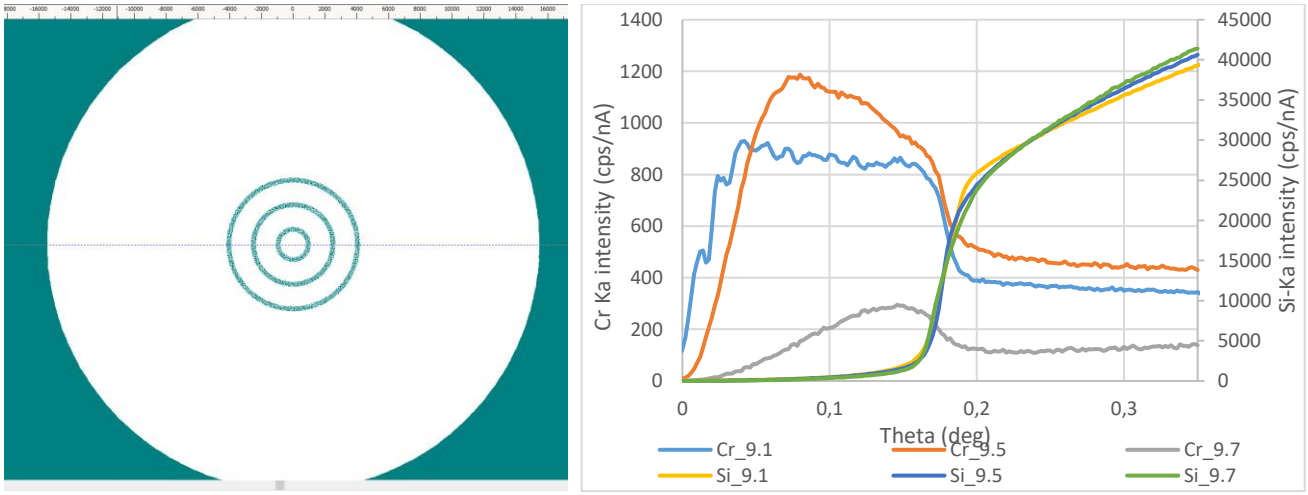

Figure 1: Layout of Cr pads randomly distributed within three circular rings for preparation of test samples (left), angular dependence of Cr-Kα and Si-Kα X-ray intensities measured on three test samples using SR-XRF (right; 9.1: etching; 9.5 and 9.7: lift-off)

This work was supported by the EMPIR program, co-financed by the Participating States and from the European Union's Horizon 2020 research and innovation program, through grant agreement 19ENV08 AEROMET II.

Remaining work

Development of calibration procedures for laboratory TXRF equipment used in elemental analysis of aerosol particles.

Related publications

[1] V. Groma, B. Alföldy, E. Börcsök, O. Czömpöly, P. Füri, A. Horváthné Kéri, G. Kovács, S. Török and J. Osán: *Sources and health effects of fine and ultrafine aerosol particles in an urban environment*, Atmospheric Pollution Research **13**, 101302 (2022)

[2] Y. Kayser, J. Osán, P. Hönicke and B. Beckhoff: *Reliable compositional analysis of airborne particulate matter beyond the quantification limits of total reflection X-ray fluorescence*, Analytica Chimica Acta **1192**, 339367 (2022)

[3] J. Osán, C. Dücső, O. Czömpöly, M. Gottschalk, S. Seeger, A. Gross, Y. Kayser and B. Beckhoff: *Development and characterization of potential reference samples for TXRF elemental analysis of aerosol particles collected by cascade impactors,* 11th International Aerosol Conference, Athens, Greece, 4-9 September 2022, SS-3-06 (2022)

SIMULATION OF FUEL CYCLES WITH A FLEET OF EPR AND GFR REACTORS APPLYING HIGH PU CONTENT IN GFR FUEL

Zoltán Hózer, Berta Bürger, Emese Slonszki

Objective

In the EU Plutonium Management for More Agility (PuMMA) project different aspects of plutonium management are investigated. In order to review the fuel cycle related questions in case of using high Pu content in nuclear reactors, EK carried out calculations with the SImulation TOol for modelling the Nuclear fuel cycle (SITON) code.

Methods

The numerical tool for the calculation was the SITON code developed by EK and BME NTI. The simulated scenario was based on the operation of a fleet of Evolutionary Power Reactor (EPR) reactors and later introduction of Gas-cooled Fast Reactors (GFRs).

The simulated scenario started with operation of eight EPRs (1550 MW_e) between 2030 and 2090. Gas-cooled fast reactors (GFR2400 with 1080 MW_e) are connected to grid in 2090 and will work for 100 years. Two scenarios were selected for the simulation:

A. The Mixed Oxide (MOX) fuel of GFR2400 reactors contains 15-16% plutonium and 2.3% minor actinides (MA). In this scenario two reactors are fed by the reprocessed spent fuel.

B. The MOX fuel of GFR2400 reactors contains 30-32% plutonium and 4.6% minor actinides. In this scenario only one reactor is fed by the reprocessed spent fuel.

In both scenarios the reprocessing of EPR fuel will start in 2077, the first loads of GFR2400 core are produced from depleted uranium (EPR fuel production) and plutonium (reprocessed fuel from EPR), minor actinides are added to GFR2400 MOX fuel and reprocessing of GFR2400 fuel starts in 2096.

The reprocessing of all spent EPR fuel produced 110 t plutonium and 25 t minor actinides, which was used for the production of fuel for GFR. In both scenarios the same amount of Pu and MA was used, since the fuel in the single reactor in scenario B had twice as much Pu and MA as the two GFRs in scenario A.

Results

The calculated results indicated that in case of lower Pu and MA content the mass of plutonium in the stocks would not decrease, due to breeding in the GFR. However, the higher Pu and MA – and the lower ^{238}U – content resulted in burning capacities and the Pu mass was decreasing (Figure 1). There was no significant difference between the two scenarios in terms of MA amount: slow trend of decrease could be observed in the last decades of GFR operation. Since only one GFR reactor was operated in the second scenario, the electric output was half of that of the first scenario with two reactors.

This example illustrated that the high Pu (≈30%) content of fast reactor MOX fuel can lead to fast decrease of accumulated plutonium stocks. However, the lower (≈15%) Pu content can be used in a more economical way due to better breeding capabilities.

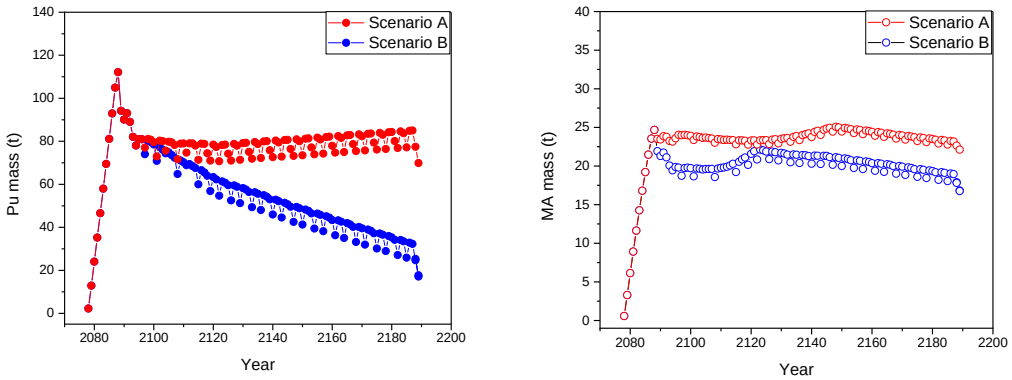

Figure 1: Calculated inventory of Pu (left) and minor actinides (right) in stocks

Remaining work

The planned calculations were completed.

Related publication

[1] Z. Hózer, B. Bürger, E. Slonszki: *Simulation of fuel cycles with a fleet of EPR and GFR reactors applying high Pu content in GFR fuel,* EK-FRL-2022-483-1-1-M0 (2022)

VALIDATION OF FAST REACTOR FUEL BEHAVIOUR CALCULATIONS TO EXPERIMENTS WITH HIGH PU CONTENT FUEL

Berta Bürger, János Gadó

Objective

In the EU Plutonium Management for More Agility (PuMMA) project different aspects of plutonium management are investigated. A work package is devoted to the validation of fast reactor fuel behaviour calculations to experiments performed with high Pu content fuel. In the first part of the project EK carried out calculations with the FUROM-FBR code.

Methods

Very limited experimental results are available for fuel with high (i.e. more than 25%) Pu content to be used in fast reactors. Three sets of data are provided within the framework of the project. These data will serve for the validation of various fuel behaviour codes developed and applied in European laboratories. EK participates in the comparative calculations with the FUROM-FBR code which is the fast reactor version of the FUROM code that has successfully been applied for VVER fuel calculations for more than 15 years. The code versions were developed in EK.

In the first phase of the project the results of calculations with the various codes have been compared with each other. Moreover, sensitivity of different quantities' parameters was studied in order to be prepared for the comparison with experiments.

Results

The gap conductance plays a crucial role in the calculations. On the one hand, it depends on the actual thermo-mechanical parameters, and, on the other hand, it has a strong influence on these parameters. Dependence of gap conductance from burn-up (practically from the irradiation time) is shown on **Hiba! A hivatkozási forrás nem található.**. This is a typical graph of the change of the gap conductance for a high Pu (≈30%) content fast reactor Mixed Oxide (MOX) fuel.

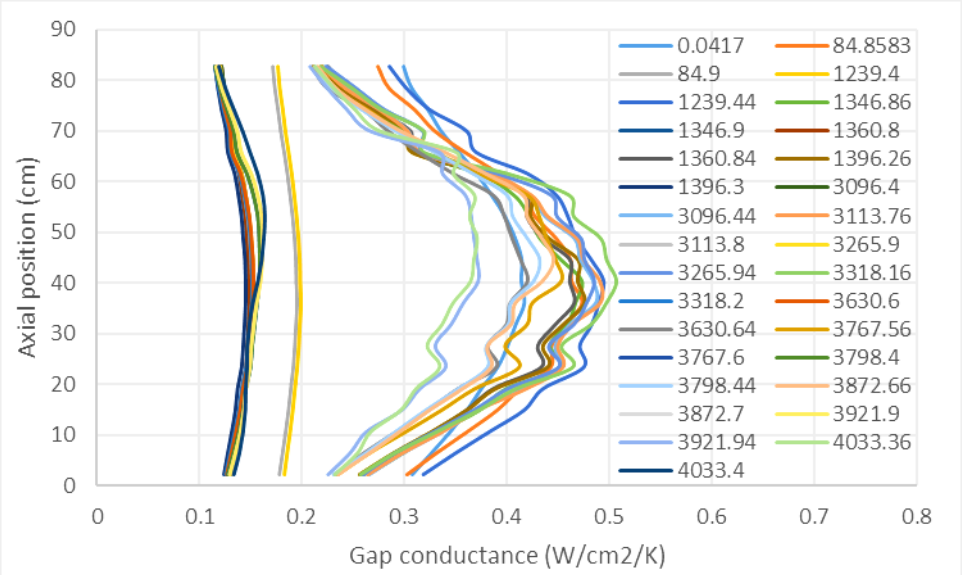

Figure 1: Gap conductance

Remaining work

In the second phase of the project the results of calculations will be compared with the experiments and conclusions for the need of further code development will be drawn.

Related publications

[1] J. Gadó: *Gap conductance calculation,* EK-FRL-2022-483-1-2-M0 (2022)

[2] J. Gadó, B. Bürger: *PuMMA sensitivity calculations by using the FUROM-FBR code,* EK-FRL-2022-483-1-3-M0 (2022)

STRUMAT: STRUCTURAL MATERIALS RESEARCH FOR SAFE LONG TERM OPERATION OF LIGHT WATER REACTOR NUCLEAR POWER PLANTS

Ildikó Szenthe, Ferenc Gillemot, Márta Horváth, Balázs Hargitai, Kristóf Andor Csikós, Szilvia Móritz, Dávid Cinger

Objective

One of the critical issues for long-term operation of pressurized water reactors is the embrittlement of the reactor pressure vessel wall, caused mainly by neutron irradiation. The goal of the project is understanding the unfavourable synergy between Nickel, Manganese and Silicon on the microstructure and mechanical properties of the reactor pressure vessel at high neutron fluences. This is needed to elucidate the irradiation effects toward the end of the life of the vessel. Existing embrittlement trend equations tend to underpredict the reactor vessel material embrittlement at higher fluence regimes. The suitability of a master curve approach at high fluences, together with the use of small/sub-sized test specimens characterize irradiation induced shifts in reference curves for bulk materials, needs to be further investigated.

Methods

An international collaborative research project with the participation of 17 European countries + Ukraine was set up to study these issues. The project is led by our institute. An irradiation campaign had been performed in the High Flux Reactor, Petten, Netherlands. A variety of different steel reactor vessel samples with systematic variations in Nickel, Manganese and Silicon contents have been irradiated to a high fluence which resembles reactor operation for greater than 60 years. EK undertook the management of the manufacturing and testing possibilities of irradiated small specimens.

Results

Different Embrittlement Trend Evaluation (ETE) curves based on the chemical composition of the material and the End Of Life (EOL) fluence were evaluated to compare their predicted neutron irradiation caused embrittlement and the thermal ageing of the Reactor Pressure Vessel (RPV) wall material. No present ETE is good enough to determine the irradiation-caused ageing shift of the VVER-440 RPV steel and weld. The reason is the high fluence and that the chemical composition (microstructure) is different from the other Pressurized Water Reactors (PWR-s). In another workpackage led by EK, fracture toughness testing specimens had been modified, prefatigued and tested. In 2022 the unirradiated model alloy specimens were investigated. Since the amount of available raw data increases as the project progresses, the evaluation of the correlations and synergies has begun. The relationship between the Nickel and Manganese content of the different types of model alloys and their hardness before and after irradiation is shown in Figure 1.

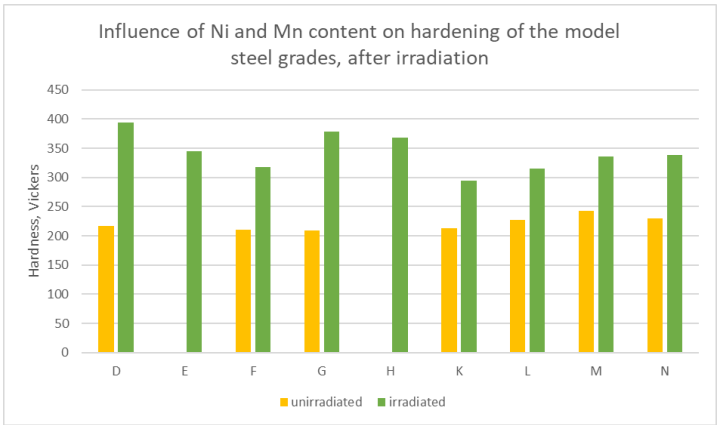

Figure 1: Influence of Ni and Mn content on hardening of the model steel grades named D, E, F, G, H, K, M types, after irradiation

Remaining work

Further study is required to decide whether the ageing of the VVER-1000 reactors can be described either with the ETE-s developed for other PWR-s, or whether there can be developed a common ETE with the inclusion of the VVER-440 steels. For the fracture toughness results and usage of the Master Curve, further evaluation will be available when the irradiated alloys will be tested for mechanical and microstructural properties.

Related publication

[1] R. Welschen, F. Gillemot, I. Simonovski, O. Martin, M. Adamech, J. Petzova, M. Kolluri: *Round Robin Analysis of Small Punch Testing on 15Kh2NMFA Reference Material,* In Pressure Vessels and Piping Conference (Vol. 86182, p.V04BT06A046). American Society of Mechanical Engineers) (2022 July)

TOWARDS OPTIMIZED USE OF RESEARCH REACTORS IN EUROPE

László Szentmiklósi

Objective

The TOURR Project is a EURATOM-funded coordination and support action aimed at proposing a strategy for the optimization of the European Research Reactor (RR) fleet and providing tools to facilitate the achievement of that objective.

This coordinated action is an answer to the challenge to assess the impact of the decreasing number of RRs, identify future needs (including new neutron sources), draw a roadmap for the upgrade of the existing RR fleet, and a model for harmonized resource management. The project is also looking into providing the research community the opportunity to coordinate the use of the Research Reactors and their Facilities in terms of access and experimental opportunities

Methods

Within Work Package 1, with the contribution of the EK representative, a detailed questionnaire has been prepared and distributed among operating RRs in Europe and it had an 84% response rate. We received data from Austria, Belgium, Czech Republic, France, Germany, Hungary, Italy, Netherlands, Poland, Romania, and Slovenia. A paper describing the work done on this questionnaire in detail has been published in the Nuclear Energy for New Europe (NENE) Conference Proceedings [1].

Results

A description of the general considerations that can be obtained from the questionnaire has been presented in the Deliverable 1.1 - Data Base of European RR fleet, publicly available at [2]. Given the very sensitive nature of the data collected via the questionnaire, a choice was made to provide only general considerations in a public deliverable. However, all collected data are available for consultation by the EC and the consortium members.

The collected data from the questionnaire were the basis of a gap analysis which highlighted gaps versus opportunities for Technological applications, Medical applications, and Education & training, as specified in Table 1.

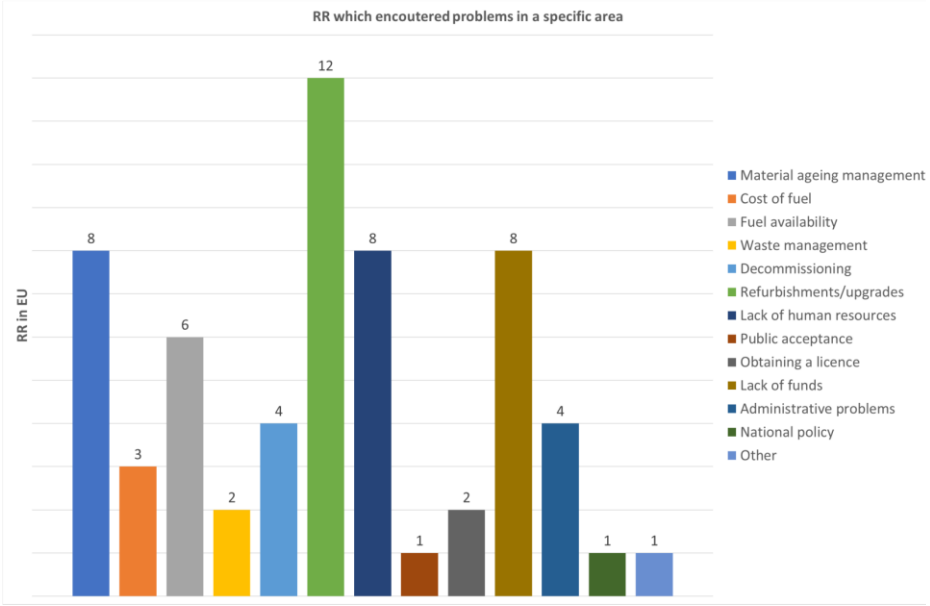

Figure 1: The main challenges of research reactors, based on the responses in the questionnaire

LIST OF IDENTIFIED GAPS:	LIST OF IDENTIFIED OPPORTUNITIES:
– Lack of long-term financial stability	– Nuclear-driven production and processing of chemicals (chemical transmutations in research reactors)
– Lack of manpower	– Radiation Hardness Testing
– Better communication to bridge the gap between customers and reactor operators and among the reactor operators themselves	– Fusion research
	– Neutron scattering community will need both reactor-based sources and spallation sources
	– Fuel cells, hydrogen storage, and batteries
	– Silicon doping

Table 1: The main results of the gap analysis

Related publications

[1] https://www.djs.si/nene2021/proceedings/pdf/NENE2021_318.pdf

[2] https://www.tourr.eu/fileadmin/user_upload/TOURR_D1.1_Data_Base_of_European_RR_fleet.pdf

FRACTESUS: FRACTURE MECHANICS TESTING OF IRRADIATED RPV STEELS USING SUB-SIZED SPECIMENS

Ildikó Szenthe, Ferenc Gillemot, Márta Horváth, Dávid Cinger, Balázs Hargitai, Kristóf Andor Csikós, Szilvia Móritz

Objective

The safety and operability of any nuclear systems heavily relies on a defence in depth strategy where the integrity of structural materials plays an essential role. Due to lack of availability of very much irradiated material, the use of small size specimens to obtain reliable measurements of the resistance to fracture is needed by the nuclear industry to comply with the Nuclear Safety Directives. Attempts to develop small-size specimen fracture toughness measurements (with a size ratio 1 : 0.16 to that previously used) has already succeeded. However further efforts are required to validate the results and achieve European regulatory acceptance of this approach. The goal of the project is to join European and International efforts to establish a solid base of small specimen fracture toughness procedures and data and to achieve changes in codes and standards at the national regulatory authorities.

Methods

Un-irradiated and irradiated real- and model Reactor Pressure Vessel (RPV) materials - available from the participants' stock - and representative of nuclear reactor walls had already been chosen. The selected materials have to already be well characterized by previously established standard tests. Small scale, compact tension specimens with 0.16 ratio have been fabricated from the original specimen remnants and tested by using specially designed clamping devices and measurement equipment. To enhance the testing quality, benchmark calculations and Round-Robin testing of un-irradiated (as received and irradiated materials was initiated.

Results

Based on the measured values the fracture toughnesses (K_{JC}) were calculated. NASA TOTEM software was used to calculate the T_0 reference temperature, on which the comparison is based, see below (Fig. 1).

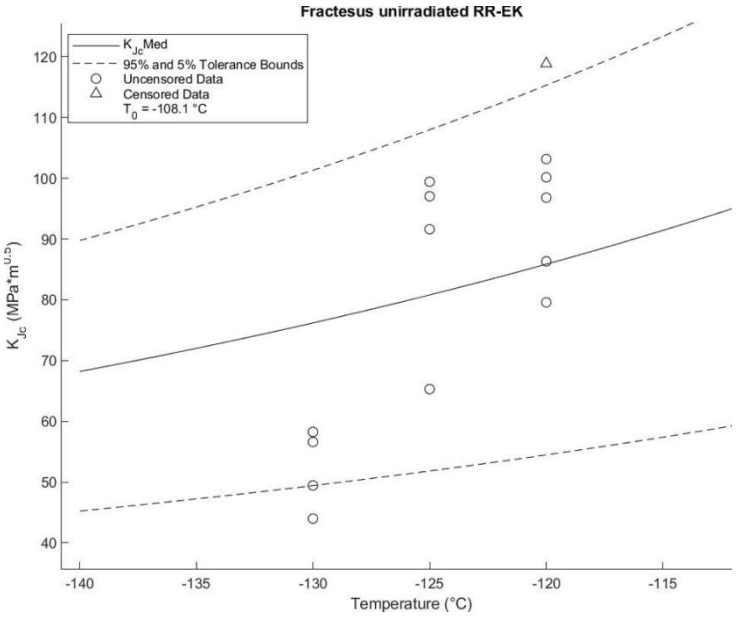

Figure 1: The T_0 determination using the NASA TOTEM software on the EK unirradiated RR 15H2MFA base material specimens

Remaining work

Mini compact tension specimens will be produced from the selected irradiated ones. The specimens will be pre-fatigued and tested. The results obtained by the different participants will be commonly evaluated, and published. Guidelines for Master Curve determination on mini compact tension specimens will be elaborated and discussed with the National Regulatory Bodies. Finally, a workshop for teaching the small size specimen fracture toughness testing and evaluation methods to young engineers and research fellows will be organized.

NOTE: A photo of one of the small specimens with it's clamps would add value to the report.

IMPLEMENTATION OF NUCLEAR AND RADIOLOGICAL EMERGENCY PREPAREDNESS AND RESPONSE REQUIREMENTS IN EU MEMBER STATES AND NEIGHBOURING COUNTRIES

Tamás Pázmándi, Péter Zagyvai

Objective

The objective of the work was to examine the arrangements for radiological emergency management in the event of a major nuclear accident on the European continent and to analyze the practical implementation of the Directives issued by the European Council, reviewing emergency management systems, stakeholder organizations, national protection strategies, cross-border cooperation and internal and public communication channels in order to identify areas for improvement. [1] EK participated in this project as one of the consortium members.

Methods

EU Member States (MS) and EU Neighbourhood countries were invited to participate in this Project in order to evaluate the practical implementation of national Emergency Preparedness and Response (EP&R) arrangements in all participating countries, including cross-border cooperation and coordination aspects and public confidence. Additionally, participants were asked to assist in the development of recommendations for future policy actions at the EU level.

The participating 25 EU Member States, 8 non-EU Members and other organizations involved in the EP&R field responded to questionnaires that were developed to obtain quality data on the practical implementation of national emergency management systems and contingency plans in their countries and on practical measures for coordination with other countries.

The work was conducted in four phases. In phase 1, to assess the practical implementation of EP&R arrangements a national-level review was conducted with questionnaires for each participating country. Three different questionnaires were established for safety authorities and civil protection organizations, nuclear utilities, civil society organizations and international organizations. In phase 2, the practical aspects of the EP&R arrangements were tested in the frame of a non-real-time exercise in order to evaluate the transborder issues during a simulation of a large-scale radiological accident scenario based on a succession of three stages (from INES 1 to INES 6). The responses of all the stakeholders were analyzed and used to identify the points of strength and weakness in managing an accident with transborder consequences. In phase 3, two workshops were organized to disseminate information and the outputs of the project. In the final phase, the best practices, challenges and recommendations were identified and formulated, and the final report of the study has been written. An overall synthesis of the international EP&R rules, regulations and guidelines, along with the findings and recommendations derived from all the past projects dealing with EP&R arrangements was performed.

Results

As a result of the work, six recommendations were formulated for future EU policy actions. The recommendations are as follows:

R1. The European Commission (EC) should launch an initiative in cooperation with Heads of the European Radiological Protection Competent Authorities/Western European Nuclear Regulators Association (HERCA/WENRA) to reach an appropriate mutual understanding between all concerned stakeholders and to achieve greater harmonization of the implemented protection strategies between neighbouring countries in Europe in case of radiological or nuclear emergencies.

R2. The EC should develop EU recommendations on joint drills or exercises between neighbouring countries to support MS implementation of the Basic Safety Standards (BSS) requirements on cooperation (i.e. Art 99).

R3. The EC should give consideration to extend the scope of existing European notification and information exchange systems to the phase prior to the declaration of an emergency.

R4. The EC should consider launching an initiative to formalize and harmonize citizen participation in emergency preparedness in the vicinity of nuclear installations in order to enhance communication and transparency with the official national and local bodies responsible for coordinating decisions and actions in case of a nuclear accident.

R5. The EC should give consideration to elaborate guidance in developing practicable strategies and arrangements for longer-term protective measures, such as relocation and decontamination.

R6. The EC should consider launching a study about the impact of a pandemic and other non-nuclear emergencies on nuclear/radiological emergency arrangements.

Related publication

[1] S. Madureira, F. Rocchi, T. Pázmándi, B. Hatala and J. Bohunova: *Implementation of nuclear and radiological emergency preparedness and response requirements in EU Member States and neighbouring countries*, ENER/2020/NUCL/SI2.838109 – Final Report (2023)

WEB SEARCH OF SOFTWARE DEVELOPERS

B. Katalin Szabó

Objective

The existence and the searchability of the Internet eases software development: developers do not have to "reinvent the wheel" all the time. If someone before them has already solved a particular programming task, and it is documented online, they only have to find the solution and use it (provided that legal constraints and other circumstances do not prevent the reuse). Therefore, web search for software development is an important skill of a developer, and, as such, a valid research area. Knowing how developers perform web search, and identifying good (and bad) practices may be of educational value and it could also be a starting point for further research.

The author, following the successful completion of a difficult programming task which involved lengthy web searches (especially for source code), started analyzing her own search and development diary, wanting to share the findings for educational purposes. Writing a scholarly article about the subject necessitated conducting a literature review as well.

Methods

For the article, a thorough literature search was conducted on how developers perform search on the web. The articles have been collected from queries to various scholarly search sites and also to general purpose search engines. Backward and forward snowballing (i.e. citation search) was performed from the papers which were found relevant. The most important publications were summarized in the literature review section of the article.

From the diary, data were extracted about the number, type and sources of relevant URLs found and recorded during the searches performed for the author's development work.

Lessons learned from this particular case and derived from the literature were formulated into search tips for developers.

Results

An article was written for an education journal, with the following content:

Articles about research on the subject, using numerous methods (analyzing search logs, interviewing developers, performing surveys) are discussed.

One article identified the most common search tasks of developers as searching for explanations for unknown terminologies, explanations for exceptions/error messages, reusable code snippets, solutions to common programming bugs, and suitable third-party libraries/services. The most difficult search tasks were searching for solutions to performance bugs, solutions to multi-threading bugs, public datasets to test newly developed algorithms or systems, reusable code snippets, best industrial practices, database optimization solutions, solutions to security bugs, and solutions to software configuration bugs.

The most researched type among developers' web searches is search for code, i.e., software. Developers look for ready-to-use software, linkable/includable code libraries, code examples, code samples, coding tips, bug fixing tips, also algorithms from which codes can be written. Developers prefer general-purpose search engines over any other information gathering means, specialized code search engines are not used too often.

One study has found that in comparison to other searches, code searches contained more words, the number of queries per search session was much higher, query modifications occurred more often, more websites were visited in a session, more time was spent on the search. This implies that searching for code is harder, and also that developers do not give it up easily.

Some authors emphasize the iterative nature of search, especially when the search is not for one specific piece of code or other information. Having a complex problem to solve, the developer is not entirely sure at the beginning what he/she is searching for. These exploratory searches may span months, as was indeed the case with the search reflected in the above mentioned diary. Such complex, exploratory searches by developers are hard to study, there are very few publications about them, so the diary was analyzed and the findings discussed: persistence, examining a high number of search results, thoroughly documenting and evaluating the search results all contributed to the success.

Finally, further search tips are shared with the reader, such as using multiple search engines, using certain advanced search options, searching for scholarly literature, and searching social media such as Q&A sites (especially Stack Overflow), forums, blogs, microblogs (Twitter) and collaboratory code repositories (SourceForge, GitHub etc.).

Related publication

[1] B. K. Szabó: *Web search of software developers - Characteristics and tips*, Frontiers in Education (2022). https://doi.org/10.3389/feduc.2022.908712

II. RESEARCH AND DEVELOPMENT RELATED TO NUCLEAR POWER PLANTS

ACTIVITIES OF EK AS MAIN CONSULTANT OF PAKS NPP

Zsolt Kerner, Katalin Kulacsy

Objective

EK, together with NUBIKI (Nuclear Safety Research Institute), has been the main consultant of Paks Nuclear Power Plant (NPP) for many years. The main consultant supports the NPP in solving safety-related technical issues and helps with strategic planning. The work is done by the most experienced and highly qualified members of the staff on the basis of individual orders. In 2022 EK undertook the following separate tasks, performed by different (groups of) experts:

- investigation of structural changes in the cladding of slim fuel rods,
- review of the water sampling gamma spectrometry evaluation procedure of Paks NPP.

Since there were several projects related to slim fuel rods, the report on the first topic can be found elsewhere in the present Yearbook, grouped with other research activities related to the slim fuel.

As regards laboratory gamma spectrometric testing of specimens sampled from power plant's systems, it is a routine plant control task. The activity of the media provides information on the sources of radiation, the cleanliness of the systems, the corrosion processes and the hermeticity of the fuel assemblies. The Apex Gamma software is used at Paks NPP to perform the measurements and evaluate the gamma spectra. The following steps of the evaluation are performed automatically after each measurement: peak search, deconvolution of overlapping peaks, determination of peaks area, background subtraction, peak identification based on a nuclide library, calculation of activities and detection limits, reporting. Results are uploaded to the power plant's IT system after data check by the laboratory personnel. In some case the nuclide identification is not perfect. In this work, the evaluation process (software settings and nuclide library) was reviewed.

Methods

A large number of spectra were evaluated manually, the results were compared with the report. The efficiency of the peak search was verified and the cases of typical nuclide misidentifications were revealed. The data in the nuclide library were compared with verified databases. The list of nuclides was revised. This was based partly on EK's previous analysis of the expected maximum activity of the fission products appearing in the primary circuit in the presence of leaking fuel assemblies, and partly on operational experience and literature. The origin of all possible nuclides was investigated taking into account the neutron capture cross-sections.

The following open data sources were used: Table of Radionuclides – Monography BIPM (Bureau International Des Poids et Mesures), Nucléide-Lara (Laboratoire National Henri Becquerel), The Lund/LBNL Nuclear Data Search, NuDat 3.0 (National Nuclear Data Center at Brookhaven National Laboratory) and Experimental Nuclear Research Data (IAEA).

Results

The peak search settings in the software were optimal. There were few false positives and there were hardly any peaks that were not found in the spectra. The vast majority of the physical data in the nuclide library was found to be accurate.

We found some peaks that were regularly misidentified or not identified. For example, the peak appearing at 159 keV was assigned as Ni-56 or Te-123m or Sc-47 randomly. Based on the detailed examination of the spectra and the probability of their formation, Sc-47 and Ni-56 could be ruled out. The absence of some natural radionuclides from the library also led to misidentifications. It was recommended to exclude 7 nuclides and add 6 nuclides to the library.

The gamma lines included in the library were reviewed taking into account the overlaps and the maximum expected primary circuit activities. We recommended adding 300 lines to the library that can help with nuclide identification. The number of single-line nuclides was reduced. The software provides the possibility to mark lines in the nuclide library that are only used for identification, not for activity calculation. This option was not used previously. We recommended excluding about a quarter of the lines of the extended library from the calculation.

The use of the renewed library presumably reduces the number of wrong nuclide identifications, provides more accurate results, thereby simplifies data verification.

Remaining work

Testing and possible refinement of the compiled nuclide library are planned in the framework of a future project.

SAFETY STUDIES INDICATED BY THE PERIODIC SAFETY REVIEW

Attila Guba, Áron Hegedüs

Objective

The Periodic Safety Review of the Paks NPP revealed the necessity of performing new safety studies.

One of the very important events in the NPP is the interface Loss of Coolant Accident (LOCA), where due to the break location the primary coolant bypasses the containment and reaches the environment more easily. Previously the "Primary to secondary leak" (PRISE) transient enveloped the category. In the safety enhancement program modifications were made so the occurrence of the PRISE transient was eliminated. The systematic review of the potential interface LOCAs other than PRISE indicated two possibilities. One is a multiple pipe break in a heat exchanger of the main circulating pump cooling system, the other is a break location connected to the primary letdown system. Besides the retention of the primary activity, the containment plays role in detecting the leak and consequently starting the safety systems ensuring adequate core cooling. In the case of interface LOCA the lacking safety signals need to be substituted by operator action. In the safety analysis, as a conservative assumption, the operator is assumed not to react in at least the first 30 minutes of the transient. It must be shown that the operator has enough time to react and manage successfully the core cooling.

Secondary side breaks were analyzed where depending on the break location several steam generators may depressurize. In the analysis of the possible damages made by the high energy jet at a break location revealed that in some special cases all types of the feedwater injection to all the steam generators may be lost. Consequently, the secondary side heat removal function is degraded. To restore the heat removal from the primary system the operator needs to initiate a primary "bleed-and-feed" procedure. The question is whether the operator action after 30 minutes of the transient is capable to maintain adequate core cooling.

The project aimed to investigate the above transients, prove that the operators are able, and have enough time to initiate protective measures to ensure suitable core cooling.

Methods

To perform the conservative safety studies RELAP5 thermohydraulic system code was used.

For the interface LOCA case, since the possible locations are all connected to the cold leg, cold leg breaks with nine different break sizes were assumed to cover the possible range.

In the secondary break case, total loss of all types of feedwater is assumed to be caused by the high energy jet from the break. Break may occur in different locations resulting in depressurization of different number of steam generators. Four depressurization arrangements were found that envelop all the possible situations. Depending on the break location there may be 6, 3, 1 or no steam generator depressurization. For all the four cases calculations have been performed to prove that no immediate operator action is needed in the first 30 minutes. In the next step the primary bleed-and-feed procedure is initiated at 30 minutes, in the calculations the pressurizer safety valve and relief valve were both tested as a device for the bleed.

Results

For the Interface LOCA analysis, conservative approach of assuming the break immediately at the cold leg and neglecting the following piping system is applied. When the break equivalent diameter is less than 14 mm the charging system can compensate the primary mass lost and can maintain the primary parameters constant. Calculations with larger break sizes show increase in the charging flow but it is not enough to compensate the break flow, therefore the pressurizer pressure and level start to decrease resulting in SCRAM and after about a minute High Pressure Safety Injection (HPSI) initiation. Depending on the break size the primary pressure stabilizes to a value where the break and the injected HPSI flow are equal. The HPSI injection cools at first the primary circuit then the secondary, too. The decreasing secondary pressure results in steam generator isolation and main circulation pump stop. At about 37 mm break equivalent diameter the first main circulation pump stop occurs later than an hour transient time. Since the expected break size is much less than the above value the operators have enough time to manage the transients.

The secondary break with damage caused by the break jet calculations indicated that the operator has well enough time to initiate the primary "bleed-and-feed" process to ensure sufficient core cooling. Parametric calculations indicated that both pressurizer safety valve and relief valve opening could successfully maintain the core cooling. The application of the larger safety valve resulted in quicker change of the system parameters, being demanding for the system parts. Using the smaller pressurizer relief valve gives more smooth variations, therefore that is the optimal solution for the primary bleed.

Remaining work

This project has been completed.

VALIDATION AND APPLICATION OF THE IN-HOUSE DEVELOPED KIKO3DMG AND KARATE CODES

Bálint Batki, György Hegyi, István Panka, István Pataki, Emese Temesvári

Objective

In the first case, the main aim was to validate the in-house developed KIKO3DMG nodal multigroup diffusion and Simplified Spherical Harmonics (SPN) code on experimental measurements of the China Experimental Fast Reactor (CEFR) start-up tests. Five start-up tests were selected from the IAEA CRP to validate the static calculations of the KIKO3DMG: fuel loading and first criticality, control rod worth, void reactivity, subassembly swap reactivity, and temperature reactivity measurements. In addition, the rod drop experiments are used to validate the code in dynamic cases. In the second case, the simulation of xenon transients of VVER-1200 reactors against the available measurements was finished. The new objective was to highlight the importance of the recriticality temperature during the main steam line break accident and to show a calculation methodology for VVER-1200 reactors using the KARATE-1200 code system.

Methods

For the CEFR tests, the full-core KIKO3DMG model of the CEFR core was set up, which consists of 712 sub-assemblies. Full-core Serpent models were also developed to provide reference calculation results of the experiments and to generate group constants in 6 energy groups. Additionally, a new reactivity curve smoothing method was implemented in the KIKO3DMG code to eliminate the cusping effect due to the movement of the absorber. The nodal calculations were performed using diffusion and SP3 solvers. In the case of the VVER-1200 reactor, the global calculation module of KARATE-1200 was used, and different loads of Novovoronezh NPP were modelled. Full core calculation methodology with 30 axial layers was applied to determine the recriticality temperature using different conservative emergency shutdown (scram) assumptions.

Results

In the case of the CEFR, the KIKO3DMG calculations were verified to reference Serpent Monte Carlo calculations, as it is demonstrated in Fig. 1. For the static calculations, with few exceptions, it was found that the SP3 solver fits the measurements and reference calculations better than the diffusion solver; however, the results were mostly within 2σ for both solvers. The simulated reactivity and neutron flux curves showed excellent agreement with the measurement values (see Fig.2) during the rod drop experiment simulation, demonstrating the code's dynamic simulation capabilities [1]. Concerning the VVER-1200 reactors, rather good agreements were gained by the KARATE-1200 code system for the xenon transients [2], and it was found that the recriticality temperature is below 100 °C at the equilibrium cycle [3]. It was concluded that the role of uncertainties may be significant, and some questions were raised which may be worthy of further research.

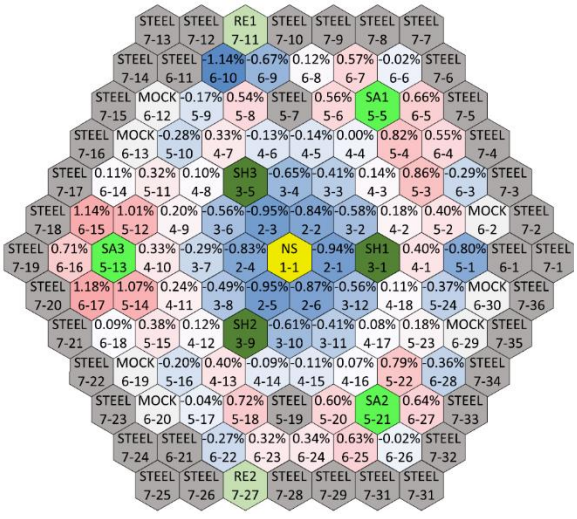

Figure 1: Distribution of the relative fuel subassembly power relative difference ($kq_{,KIKO3DMG}/kq_{,Serpent}$-1) between Serpent and KIKO3DMG calculations of the CEFR, SP3 solver [1]

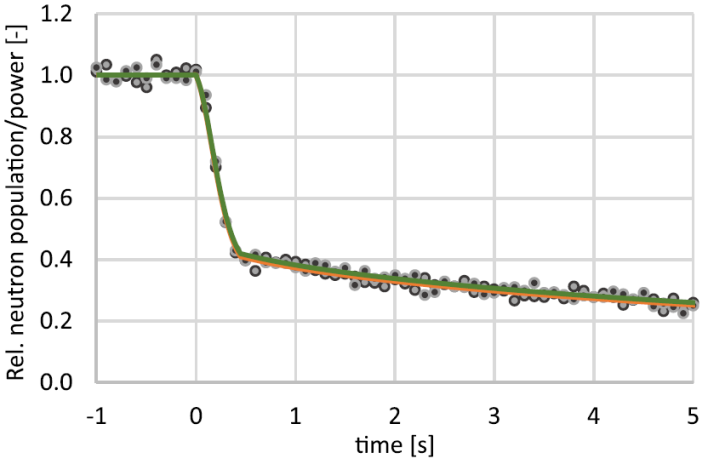

Figure 2: Measured relative neutron population and calculated relative power during rod drop measurement of a safety absorber [1], dots: measurements, green: KIKO3DMG SP3, orange: KIKO3DMG diffusion

Remaining work

The results of IAEA CRP concerning the CEFR should be published in an IAEA Technical Document in 2023. The calculation results and further investigation of the recriticality temperature in VVER-1200 reactors will be published in NUKLEON and in an international journal.

Related publications

[1] I. Pataki, B. Batki, M. Tóth, I. Panka: *Validation of the KIKO3DMG neutronics code on the CEFR start-up tests*, Annals of Nuclear Energy **180,** 109493 (2023)

[2] Gy. Hegyi, Cs. Maráczy, E. Temesvári: *Simulation of xenon transients in the VVER-1200 NPP using the KARATE code system*, Annals of Nuclear Energy **176,** 109258 (2022)

[3] E. Temesvári, Gy. Hegyi: *Investigation of the recriticality temperature in VVER-1200 reactors by using the KARATE-1200 code system*, MNT Symposium, 29-30 September 2022 (in Hungarian)

VALIDATION OF THE KARATE CODE SYSTEM AGAINST THE LATEST OPERATIONAL DATA AND STARTUP MEASUREMENTS

István Panka, György Hegyi

Objective

In the last decades, KARATE-440 was elaborated and developed continuously to calculate VVER-440 rector cores by coupled neutron physical - thermal hydraulics models. The main goal of the calculations is the core reload design, however, certain safety analyses amenable to a static code can also be analyzed by KARATE-440. The program serves economic core reload design so that the limitations demanded by the safety analysis should be observed. The latter function is utilized for the periodic independent check of the Paks Nuclear Power Plant (NPP) core design. On the other hand, in the last years several modifications of the VVER fuel construction and the corresponding core design aiming at more economic fuel utilization were introduced by Paks NPP, which made further development of the models necessary. Recently, the code system has also been applied for the licensing of the new water-to-uranium ratio optimized fuel, called "SLIM". Having regard to the above situation, continuous validation from year to year against the latest operational and start-up measurements is indispensable for the establishment of the uncertainties and the margins for the calculated safety related frame parameters. In 2022, the cycles of Paks NPP realized in 2021 were used for the validation.

Methods

Model validation, comparison of the calculated and measured data.

Results

The following parameters were used for the validation:

- core burnup dependent radial peaking factors based on the assembly-wise in-core temperature rises,
- core burnup dependent operational critical boron concentrations,
- critical boron concentrations measured at the Minimum Controllable Power,
- isothermal temperature reactivity coefficients measured at the start-up procedure,
- integral and differential efficiencies of the control rod groups.

According to the validation results, there are no significant changes of the deviations from the measurements as compared to the earlier cycles using Gd doped fuel. As an example, Fig. 1 shows the comparison of the measured and calculated isothermal temperature reactivity coefficients for Unit 3 using high enriched Gd doped fuel. The maximum deviation is about 1 pcm/°C, which is in the range of the measurement scattering.

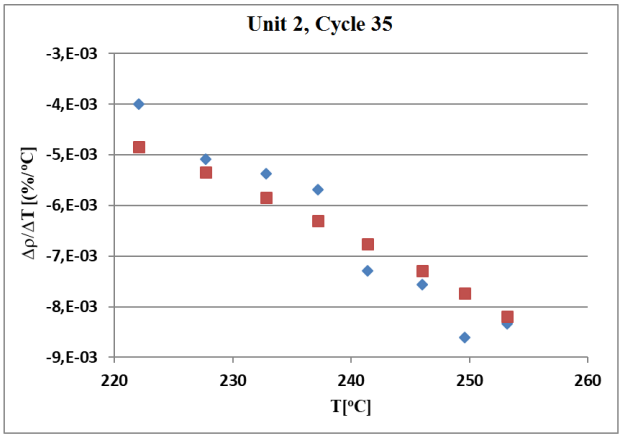

Figure 1: Measured (blue dots) and calculated isothermal temperature reactivity coefficient for Cycle 35 of Unit 2 vs temperature (T)

Remaining work

Continuous validation of the KARATE code system using the results of the measurements.

Related publications

[1] Gy. Hegyi, I. Panka: *Comparison of the KARATE 5.0 results with the measurements and C-PORCA calculations for the cycles of Paks NPP realized in 2021,* EK-RAL-2022-706-01-01-M0, in Hungarian (2022)

[2] Gy. Hegyi, I. Panka: *Determination of the accuracy of the moderator temperature coefficient and the rod worth of group No. 6 using the KARATE 5.0 code system,* EK-RAL-2022-706-01-02-M0, in Hungarian (2022)

USING HOT ZERO POWER STATES OF PAKS NUCLEAR POWER PLANT FOR THE VALIDATION OF BURNUP CREDIT CALCULATION, CONSIDERATIONS FOR CONVENTIONAL AND GD DOPED FUEL CYCLE

István Panka, György Hegyi, Gábor Hordósy, Emese Temesvári

Objective

The subcriticality analysis of a spent fuel storage facility is strongly influenced by the uncertainty of the calculated multiplication factor (k_{eff}) due to the uncertainties of nuclear cross section and technological data. Traditionally, this uncertainty was determined from comparison of calculated and measured k_{eff} values for a number of critical experiments.

This approach can easily be applied to cases with fresh fuel, because there are a number of publicly available critical experiments with fuel enrichment, moderator, geometry etc. similar to the storage facilities. However, when burnup credit is applied in the subcriticality analysis i.e. the change of reactivity due to the change of composition with burnup is considered, the problem arises that there are no such published critical experiments where the fuel composition is similar to the composition of the spent fuel.

A possible solution is to determine the discussed uncertainty by calculation using the covariance data of the cross sections as well as the uncertainties of the technological parameters and use the Hot Zero Power (HZP) states of operated NPP's for checking the calculations. In this case, an additional task is to assess how representative are the considered HZP states for the storage facility in connection with the fuel composition.

Methods

Concerning the statistical method, a Monte-Carlo type, sampling based methodology was used. At the first step, a sampling procedure for the selected isotopes, cross sections and technological parameter is performed many times, and subsequently, the elaborated statistical methodology is applied. Finally, one can get the estimated standard deviations or the results can be evaluated using the Wilks' method in case of small sampled values. In the latter case, the calculations can usually be characterized by tolerance intervals with 95%/95% probabilities.

Results

In 2022, the methodology and the full core MCNP model were improved for cycles using conventional or Gd doped fuel. First, real HZP states of Paks NPP were calculated by the new model. These results correspond to the so called best-estimate calculation. After that, the elaborated statistical methodology based on the Wilks' method was applied to determine the uncertainties of the effective multiplication factors. In case of the conventional fuel, the uncertainties of the composition of the fuel were also taken into account using the statistical version of the KARATE code system, as well.

In connection with the effective multiplication factor, some results are demonstrated in Table 1. It was found that the main source of uncertainty in the multiplication factor is the uncertainty in the nuclear data. The results concluded that the expectation that the true value of the multiplication factor should fall within the uncertainty interval around the calculated value is largely fulfilled in the cases studied.

*Table 1: Mean values and uncertainties of the effective multiplication factor for some HZP states (** means: without the uncertainties of the composition)*

	Mean	95%/95% lower limit	95%/95% upper limit
Cycle 24, Unit I, Gd, conventional fuel	1.00198	0.98301	1.01843
Cycle 20, Unit III, conventional fuel	0.99948	0.98053	1.01677
Cycle 38, Unit I, Gd doped fuel**	0.99647	0.98422	1.01233
Cycle 33, Unit III, Gd doped fuel**	0.99612	0.98409	1.01050

Remaining work

Investigations will continue to determine how representative the conditions of the HZP are for the storage facility.

Related publication

[1] Gy. Hegyi, G. Hordósy, I. Panka, E. Temesvári: *Accounting of burnup in the criticality calculation of storage and transport facilities - Calculation of HZP states No. 2,* EK-RAL-2022-708-01-02-M0, in Hungarian (2022)

CREEP AND BURST TESTS WITH SLIM FUEL CLADDING TUBES

Márton Király, Richárd Nagy, Péter Szabó

Objective

In this project the behaviour of SLIM (0.2 mm smaller outer diameter) fuel cladding tubes was investigated in normal operation and in accident conditions. This new fuel type was recently introduced in the MVM Paks NPP.

Methods

The thermo-mechanical creep was investigated using a pressure system and a three-zone tube furnace. The internal pressure of the cladding samples was set to 11 MPa, while the furnace maintained a 400 °C constant temperature in mostly inert atmosphere. The change in diameter was measured using a custom-built profilometer comprised of a laser micrometer and a linear module. The data were recorded in LabView and in Excel, the data processing was partially automated in Excel.

The ballooning and burst tests simulate the temperatures and pressures in a LOCA condition. The samples were at isothermal conditions in a custom tube furnace at temperatures between 800 °C and 1000 °C, while the pressure system increased the inner pressure at a constant rate up till the burst. The control and the data acquisition were done in LabView.

Results

The creep rate of the new SLIM cladding tube was found to be greater than that of the traditional type E110 cladding material. There were some discrepancies in the measurement, like applying the same pressure to the tubes of different diameter and wall thickness resulted in different stress states in the two cladding types. This was done in order to investigate the tubes in the same conditions, as the tests at similar radial stresses were already completed. The other major problem that arose during the test was the slight oxidation of the surface of the cladding tubes in air. This was not visible for the most part, but as the test continued for about 100 days, the slight oxidation cumulated and a broken oxide layer covered the surface, making the diameter measurement difficult (*Fig 1*). Control samples with no pressurization were also used, but those samples showed less oxidation than the pressurized ones. The furnace setup was modified to hold a constant inner pressure and getter materials were inserted to capture the air and water inside.

The burst tests showed that the new material behaved similarly to the traditional cladding alloy, in that the pressure of the burst at different temperatures was similar to the older test results. As the wall thickness is smaller, the burst pressure was expected to be lower by about 15%, but it was not the case. Additionally, the test results were compared to a correlation fitted to previous data and it also showed that the new material behaves differently than the other tested claddings. New tests with the old and the new material in similar conditions around 1000 °C are planned for the next year to understand the behaviour of these claddings in accident conditions.

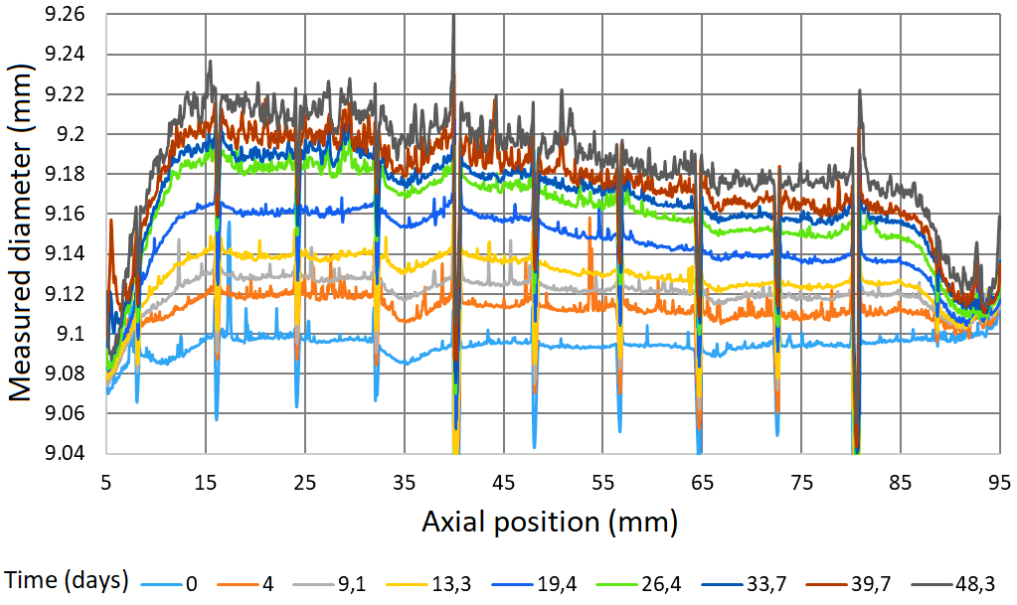

Figure 1: The diameter increase of the SLIM cladding tube during the creep test

Remaining work

Both the creep and the burst test will continue with additional tests in 2023. The new samples are prepared, the creep tests will initiate in January and the burst test will be completed in April 2023.

MECHANICAL TESTS WITH SLIM FUEL CLADDING

Erzsébet Perez-Feró, Márton Király, Márta Horváth,
Tamás Novotny, Péter Szabó

Objective

The aim of the project is to characterize the mechanical behaviour of the SLIM cladding in different pre-treated states (oxidized, heat-treated and hydrogenated) and to compare the results with those of measurements on E110 and E110G alloys.

Methods

As the first task of the project, mandrel tests were carried out on as-received and pre-treated SLIM specimens to evaluate deformation and ductility during pellet-cladding interaction. Some of the pre-treated samples were oxidized in high temperature steam, others were annealed in argon gas and some specimens were hydrogenated in a hydrogen atmosphere.

The second task of the project was to prepare additional samples for ring compression tests, in a high temperature furnace using steam oxidation. Since embrittlement of the cladding is mainly expected as a result of oxidation at 1000 °C and 1200 °C, our measurements were mainly performed at these two temperatures.

Results

First task: To evaluate the effect of oxidation, the results of samples oxidized in steam and heat-treated in an inert gas for the same time and temperature were compared. After oxidation at 800 °C, the maximum increase in internal diameter to fracture was reduced by 30%, in case of oxidation at 1000 °C the maximum increase in internal diameter was 20-70% lower compared to the heat treatment. Based on the obtained results, the oxidation clearly reduced the ductility of the SLIM cladding (Fig. 1). The maximum increase in internal diameter for both 800 °C and 1000 °C oxidation was similar for SLIM samples compared to E110 and E110G samples.

Hydrogenated SLIM samples became brittle above 1500 ppm hydrogen content and samples with higher hydrogen contents had lower residual ductility than previously tested E110 and E110G alloys.

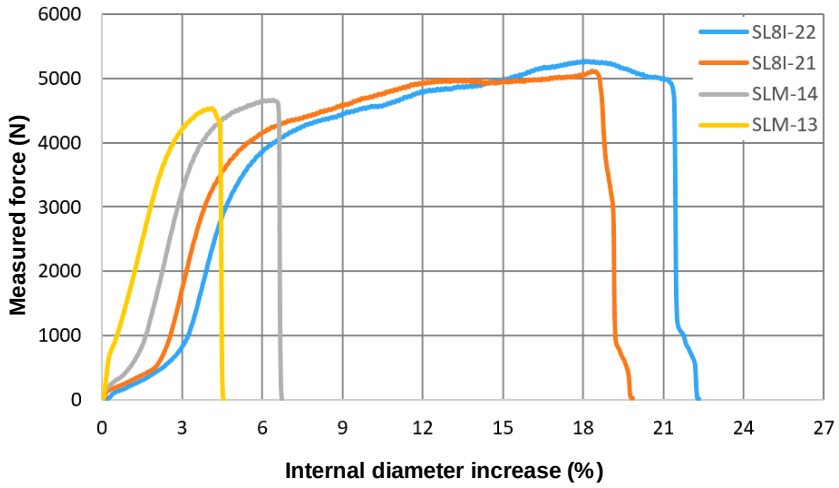

Figure 1: Force−diameter increase curves of SLIM samples heat-treated (SL8I-21 and SL8I-22) and oxidized (SLM-13 and SLM-14) for 690 s at 1000 °C

Second task: A total of 64 as-received and hydrogenated samples were oxidized at 1000 °C and 1200 °C. It can be concluded that the oxidation behaviour of the SLIM cladding at 1000 °C is better than that of the E110 cladding, which is susceptible to breakaway oxidation. The oxidation behaviour of SLIM and E110G is not significantly different, although their equivalent oxidation rates differ, but this is mainly due to the difference in wall thicknesses.

Remaining work

Next year, the 64 oxidized samples will be used for ring compression tests at 135 °C to investigate the ductile-brittle transition of thin-walled cladding. The research project runs until May 2023.

Related publications

[1] M. Király, E. Perez-Feró, M. Horváth, T. Novotny: *Mandrel measurements with slim fuel cladding*, EK-FRL-2022-701-1-1-M0, in Hungarian (2022)

[2] E. Perez-Feró, T. Novotny, P. Szabó: *Steam oxidation measurements with slim fuel cladding*, EK-FRL-2022-701-1-2-M0, in Hungarian (2022)

NEW APPLICATION IDEAS FOR ACOUSTIC EMISSION METHODS

Attila Gábor Nagy

Objective

At the beginning of the year 2021, our institute procured a new Acoustic Emissions (AE) measuring equipment, (including full software support) for the regular Paks NPP reactor tank tests. At the end of 2021, the tests were successfully completed, the equipment had perfectly passed the trial. These kinds of measurements are regular and mandated by law, so long-term usage of the equipment is assured. The aim of the project is to search for other purposes to use this hardware. In the application I had listed some ideas, but I have found a different purpose too, which better connects to the main profile (nuclear energy) of our institute. Our laboratory experiments had revealed details about the ballooning and burst of nuclear cladding tubes in accident conditions involving high temperature and high pressure before the actual event. With this new type of equipment and methodology, I could add a fresh perspective (involving AE tests) for these kinds of measurements.

Methods

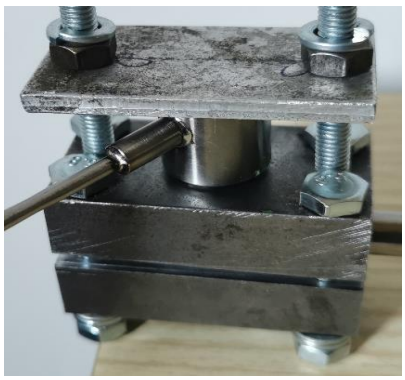

Figure 1: Sensor fixing on the tube

For achieving our goal, we had to design and build an adapter for the AE sensors so that they could be fixed to the tube(s). I have made the choice of using steel, because it has similar acoustic characteristics as the tubes themselves. I have planned to add two sensors to make the setup capable to detect the precise location of the signals, but until now, I could only add just one to the upper part. I intended to design the sensor clamping mechanism to make a very tight connection with the tube, so we used screws (Figure 1) and contact material, namely the same material that we use in the reactor tank measurements. I have made several measurements to test the sensitivity of the sensors in this setup. I'd find out that my clamping method on the tube reduces the signal by around <4dB. Larger, about 20dB signal loss occurs at the connection of the tubes. I could also test the signal quality by changing the force by which the sensors are screwed to the tubes—at the reactor measurements we have magnetic clamping, so we cannot change that force -, I have found out that this force can make a big difference, till a certain point. Also, for the reactor measurements we have heat resistant sensors so I had no problem in that regard. I had opted to use a separate pre-amplifier, in the usual 40dB setting.

Results

The point of the acoustic emissions measurement is that when a certain material is under stress, it emits acoustic signals in a specific frequency range and in my tests, I have used the aforementioned sensors to catch these signals. AE signals are indicators for major and rapid changes in the integrity of the material *before* they happen. In practice if a clear burst signal is detected during a pressure test, the user should consider to abort the test. In the ballooning tests, we have this kind of workload. In our testing, we had recorded burst type signals before and during the ballooning effects. The burst signals (Figure 2) before the ballooning were very definite, during the ballooning the elated acoustic background blurs the signals. These experiments showed the usefulness of this type of testing method, because we may predict the deformation of material before it even starts to happen. The other major benefit of the method was that we could detect leaks of the nuclear cladding tubes.

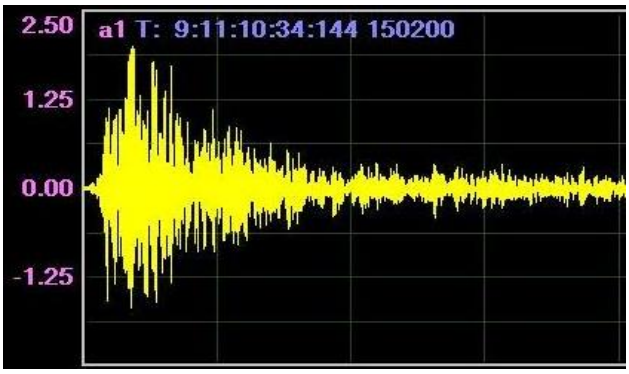

Figure 3: Burst signal marks the nearing ballooning

Remaining work

1. To do more measurements with multiple sensors to record the precise position of the signals,
2. Implement temperature and pressure measurements during the AE tests,
3. Find a generalized measurement methodology to collect burst signals before the ballooning effects,
4. Design measurement setup to detect leaks of the tubes, to determine the place of the leak, too,
5. Study the possibility to make these measurements useful in general practice,
6. Publish the results.

ENERGY STORAGE AND ENERGY RECOVERY FROM LOW-TEMPERATURE HEAT SOURCES

Attila R. Imre, Sindu Daniarta[1]

Objective

To have a sustainable society, the need to use renewable sources to produce power and heat is inevitable. Due to the weather dependence of some of these sources, utility-scale storage has to be used. These fluctuations range from minutes to whole seasons. Although short-time methods – especially for low-capacity storage – are already available, high-capacity seasonal storage must be solved for heat and power. Sometimes, the two goals (heat- and power storage) are strongly connected, therefore, novel Heat-to-Power methods – even for low-temperature heat sources – have to be developed, and the existing ones have to be improved [1]. Basic research problems related to these two fields often include selecting the right working fluid for the utilization of a given industrial waste heat source or selecting the right - often chemical - energy storage method for a heat-storage system. This research addresses problems related to these topics.

Methods

Thermodynamic data were taken from RefProp database and NIST Webbook for efficiency calculations. Calculations were done by our own codes.

Results

Our results can be divided into two interlocked parts: (i) energy storage and (ii) heat utilization; between them, one can find the transition by applying heat utilization in energy storage systems.

According to the present European regulation: "energy storage means, in the electricity system, deferring the final use of electricity to a moment later than when it was generated, or the conversion of electrical energy into a form of energy which can be stored, the storing of such energy, and the subsequent reconversion of such energy into electrical energy or use as another energy carrier" [2]. There are two important consequences for this definition:

- Power-to-Gas (and, in general, Power-to-Fuel) technologies have a green light because the last step of the original energy storage scheme (Fuel-to-Power), which is usually a low-efficiency step, can be omitted, and the fuel (mostly hydrogen or other gases, like methane or ammonia, produced from the primary hydrogen) can be used directly.
- Heat storage is "usually" not considered as energy storage, except when the heat is generated by power, and later the stored heat is used to generate power.

In the near future, demand for hydrogen is expected to increase sharply. Present demand is satisfied mostly by methods using fossil fuel (like steam reformation of the methane content of natural gas), but in the future, green hydrogen needs to satisfy the newly emerging needs (transport, energy storage). Although renewable-based power plays an important role in this field, one has to realize that presently reliable and predictable hydrogen production cannot be achieved based solely on conventional renewable electricity. Therefore, in the next few years or decades, carbon-free nuclear power should have an inevitable role in hydrogen production [3].

Although hydrogen seems to be the ultimate "green" fuel, storage and transportation are still difficult. Power-to-Methane method uses green hydrogen and non-fossil carbon dioxide (like the CO_2-content of biogas) to produce pure methane, which can be stored, transported and used, just like natural gas. When proper CO_2-sources are used, the method can be considered carbon-free [1].

The efficiency of the Power-to-Methane cycles is quite low; therefore, any method which can increase this efficiency even by a few percentage is useful. The storage efficiency of PtM may be increased either by maximizing the recovery of the stored electricity or by reducing the amount of electricity the PtM has to be charged with for a given amount of stored energy. A case study was presented for the latter by directly integrating an Organic Rankine Cycle (ORC) into the methanation technology. In this method, the waste heat of water electrolysis and biological methanation were used to generate power by the ORC. This power was channelled back to electrolysis, increasing the total storage efficiency by approximately two percentage points, see *Figure 1* [4]. In this way, energy storage and low-temperature heat utilization were integrated.

Liquefied Natural Gas (LNG) is gaining more and more popularity giving an alternate way for natural gas transportation. A fairly large amount of energy must be added to the system to liquefy natural gas. Although the reason for this energy input is not energy storage, still, part of this energy can be recovered when the liquid gas is vaporized back before further use. Therefore, LNG can also be handled as an energy storage system. The so-called "cold energy" can be utilized by various cryogenic power cycles. Since the composition of the LNG in selected countries (e.g., Algeria, Australia, Malaysia, Nigeria, Oman, Qatar, Trinidad and Tobago) is different, the gasification process – when the energy is "charged" into the system - and the energy recovery will differ as well. Comparing the recoverable energies by using direct expander from the typical LNG used in the listed countries, the most energy can be recovered from the LNG produced in Trinidad and Tobago (which consists of 96.9% Methane, 2.7% Ethane, 0.3% Propane, and 0.1% Butane) [5].

---

[1] Visiting student, START 2022 Program, Wroclaw University of Technology, Poland

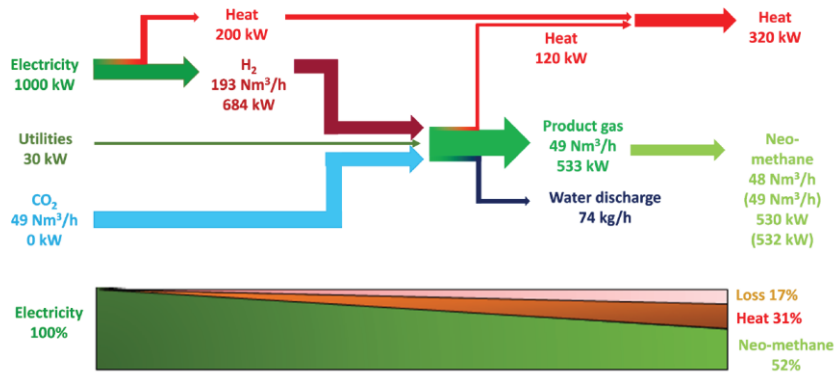

Figure 1: Mass and Energy balance of the reference methanation system. The approximately 320 kW_{th} low-enthalpy heat flow (upper right corner) goes to the ORC device, where – depending on the technology – 17-22 kW_e can be produced [4].

Although heat storage is officially not energy storage [2], there is a heat-storage-related method that fulfils all energy storage criteria. This is the so-called Carnot-battery method, when heat is generated by power, then stored and finally, power is recovered by using a thermodynamic cycle by utilizing the stored heat. Carnot battery technology offers a good solution for high-capacity, day-to-day energy storage. One of the disadvantages of the method is the low Heat-to-Power efficiency. For sufficiently high storage efficiency, one has to use state-of-art thermodynamic cycles specially designed for this purpose. A preliminary analysis of a specially designed Carnot battery configuration employing a novel reversible Rankine-based Thermodynamic Cycle (RRTC) has been reported [6].

In general, utilization of low-enthalpy heat sources with acceptable efficiency is still a challenge, therefore, the improvement of the thermodynamic efficiency of machines and devices applied for energy conversion is nowadays one of the most important research topics. To find a way to increase this efficiency, various novel subcritical and transcritical power cycles were analyzed [7]. Simulations were proceeded using selected wet (or ACZ type) working fluids for given maximal and minimal cycle temperatures. Novel markers were introduced in this study to provide a new perspective on the efficiency of subcritical and transcritical power cycles with predetermined temperature ranges. Engineers and scientists may obtain the greatest efficiency of the system based on a special configuration in the architecture or an enhancement in the present thermal power plant.

In the same way, the improvement of traditional Organic Rankine and Trilateral Flash Cycles (ORC and TFC) has been investigated using different working fluids, fitting to the maximal and minimal cycle temperatures determined by the given heat source. Thermodynamic analysis was performed for ideal and real ORC with various heat source temperatures and mass flow rates, using propane and R32 as working fluids; thermal efficiency, output energy, net earning, and payback period as output parameters were studied. The results indicated that all output parameters have higher values at certain subcritical temperatures, while they decrease with increasing cycle temperature close to critical temperature, refuting the original assumption that these parameters increase monotonously with the temperature [8, 9].

Finally, a simple carbon-dioxide cycle was investigated, which could be fitted to an internal combustion engine to generate power from the waste heat escaping with the exhaust gas. Special features of supercritical CO_2 make these cycles able to recover more energy than the traditional organic Rankine cycle. [10]

Related publications

[1] A. R. Imre: *Seasonal Energy Storage with Power-to-Methane Technology (Editorial)*, Energies, **15**, 712 (2022)

[2] DIRECTIVE (EU) 2019/944 OF THE EUROPEAN PARLIAMENT AND OF THE COUNCIL of 5th of June 2019 on common rules for the internal market for electricity and amending Directive 2012/27/EU, Chapter I, Article 2, point (59), https://eur-lex.europa.eu/legal-content/EN/TXT/?uri=celex%3A32019L0944, accessed: 11.18.2022

[3] Imre A. R., Horváth Á.: *Az atomerőművek szerepe a hidrogén-előállításban,* Anyagvizsgálók Lapja, II, 32 (2022)

[4] A. Groniewsky, R. Kustán and A. Imre: *Efficiency increase of biological methanation based Power-to-Methane technology using waste heat recovery with Organic Rankine Cycle*, Periodica Polytechnica Chemical Engineering, **66**, 595 (2022)

[5] S. Daniarta, A. R. Imre and P. Kolasiński: *A Comparative Study of Direct Expanders Utilizing Different Mixtures of Natural Gas*, IEEE Xplore, 8th International Youth Conference on Energy (IYCE), 1 (2022)

[6] S. Daniarta, P. Kolasiński and A. R. Imre: *A Preliminary Design and Modelling Analysis of Two-phase Volumetric Expanders for a Novel Reversible Organic Rankine-based Cycle for Carnot Battery Technology*, Applied Science, **12**, 3557 (2022)

[7] S. Daniarta, A. R. Imre, P. Kolasiński: *Thermodynamic efficiency of subcritical and transcritical power cycles utilizing selected ACZ working fluids*, Energy, **254**, 122432 (2022)

[8] A. M. Ahmed, A. R. Imre: *Critical temperature effect at the wet working fluids in the subcritical ORC performance*, Book of Proceedings, 13th International Exergy, Energy and Environment Symposium (IEEES-13) March 14 to 17, 2022, Makkah, Saudi Arabia, Editors: Abdullah A. AlZahrani, Naief Almalki, Kamel Guedri, Ibrahim Dincer, 229 (2022).

[9] A. M. Ahmed, A. R. Imre: *Investigation of thermal efficiency for subcritical Organic Rankine cycle (ORC) and Trilateral Flash Cycle (TFC) using super dry working fluids*, Energy Science & Engineering, accepted (2022).

[10] M. A. R. Atik, A. R. Imre, *Analysis of CO_2-based trans-critical power cycle in waste heat recovery*, Pollack Periodica, in press

EXPLORING TECHNICAL MEANS TO ACQUAINT SIGHT-IMPAIRED PERSONS WITH NUCLEAR POWER PLANTS

Hedvig Jung, B. Katalin Szabó

Objective

As nuclear energy is gaining importance in an era of climate change and energy crisis, it is advantageous to increase its acceptance by acquainting various groups of the population with it. With our project, we would like to explore means for bringing nuclear energy closer to a special group: sight-impaired persons. As their visual channel is restricted or non-operational, we have to communicate through other senses, namely, sound and touch.

Methods

A display providing touch experience is called haptic display. A static (non-changeable) haptic display can be a physical 3D model of e.g. a reactor vessel or a logical diagram. Such objects can be manufactured by 3D printing. We have made a few test 3D prints.

We have also searched for commercial dynamic haptic displays. We have found commercially available solutions based on moving mechanical pins, vibration and electrofriction. However, we have found no commercially available heat displays, even though numerous attempts have been documented in the scholarly literature. Most of these solutions are based on a relatively cheap semiconductor device: the Peltier element. Therefore, we have decided to make a systematic literature review on the use of Peltier devices for heat displays which are at least potentially usable by hand by sight-impaired users. First, we have established a collection of 37 papers through various non-systematic searches in the scholarly literature. Then we studied the literature on doing systematic reviews. We selected 19 information sources for our systematic review. The selection of these sites was based on whether their search produced significant results for the preliminary query "*thermal display*" *Peltier*. We created search queries capable of finding most of the papers in the collection. These queries had to be tailored to the syntax rules and limitations of the individual search tools. We have performed the queries and brought the results to uniform format by self-developed parser programs, establishing a database of the publications. We have excluded the trivially irrelevant results by manual evaluation. We have eliminated most of the duplicates (provided by several search tools or by multiple queries performed within the same search tool) with a self-developed program, then eliminated the remaining few duplicates by hand.

We have made a test program which queries the mouse coordinates and reads aloud the colour info of the point which corresponds to the mouse position on a picture. By moving the mouse, the user gets pixel-wise information.

Results

We have found that the 3D printing technology available at our research centre is sufficiently detailed not only for 3D models of real objects but also for Braille writing, which we intend to use in creating objects for demonstration.

The systematic literature search for Peltier-based heat displays yielded 6784 hits. After removing trivially irrelevant results and duplicates, 437 items remained.

35 of the 37 papers in the above mentioned preliminary collection could be found with our queries, the remaining 2 could be identified by backward snowballing (citation-following) from these hits.

The above mentioned test program is operational and conveys information to the blind and visually impaired user. The solution could be utilized for communicating the content of not only static explanatory diagrams but also the dynamic distribution of physical quantities such as pressure or velocity.

Remaining work

The systematic review will be continued by two researchers evaluating the 437 items independently and deciding on their relevance, according to pre-established inclusion and exclusion criteria. The decision will primarily be based on the abstract, but, when easily available, the full text as well. The judgments of the researchers will be compared, in case of discrepancy they will try to arrive at a consensus, when they cannot, a third researcher will act as arbiter. Then the full texts (when missing) of the selected papers will be obtained (if impossible, the paper will be left out of the review). One researcher will then perform forward and backward snowballing starting from the selected papers, and will obtain further papers, which will be added to the collection. This will be performed iteratively until no more new papers are found. After the other researcher's approval of the new papers, all relevant papers will be assessed and their most important features will be summarized in a report which could establish a basis for the development of a heat display of our own.

A journal article will be written about the process and the results of the systematic review.

We would also like to experiment further with the test program reading aloud the picture info. We would like to analyse, how much information the blind and visually impaired people can get from pictures of different image resolutions.

III. NUCLEAR SECURITY, DOSIMETRY AND SPACE RESEARCH

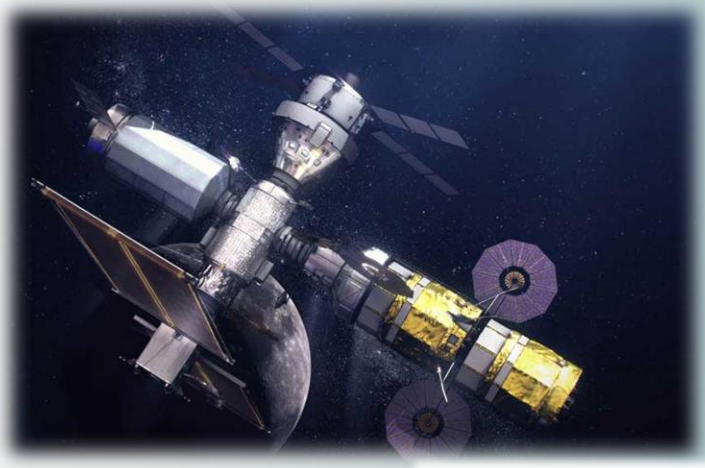

DEVELOPMENT OF NEW MODEL AND NUCLEAR MEASURING PROCEDURE FOR DETERMINATION OF BURNUP HISTORY OF NUCLEAR FUELS FOR SAFEGUARDS AND FORENSIC ANALYTICAL INVESTIGATIONS

Péter Kirchknopf, Imre Szalóki, Péter Völgyesi

Objective

The objective of this research is the development of a spent nuclear fuel characterisation method that relies on Non-Destructive Assays (NDA), mainly gamma-ray spectrometry. This study encompasses the measurement of power reactor spent fuel assemblies, evaluation of the measured data, and the testing of various data analysis techniques that can be used to predict some of the most important parameters of spent fuels: burnup, cooling time, initial enrichment, and the burnup history profile. The resulting method could be useful for Nuclear Safeguards inspectors and it could also provide a basis for Nuclear Forensics analysis of irradiated nuclear materials. This year's objectives were the further studying of the gamma-ray spectrometric dataset collected at Paks NPP between 2010 and 2021, the comparison of the burnup prediction methods for VVER-440 type and other PWR and BWR type spent fuel assemblies, and the development of a Monte Carlo (MC) particle transport simulation model in MCNP 6.2 to calculate the absolute detection efficiency of the spent fuel measurements at Paks NPP.

Methods

Non-linear regression and cluster analysis methods have been applied to the measured fission product activity ratios in order to determine the relationship between the ratios and the burnup, cooling time, and burnup history of VVER-440 type spent fuels [1]. The same regression procedure has been applied to experimental data available in the NEA SFCOMPO 2.0 spent fuel database for various PWR and BWR spent fuel assemblies [2]. Besides the commonly used fission product activity ratios (e.g., $^{134}Cs/^{137}Cs$, $^{154}Eu/^{137}Cs$), several more ratios were computed by multiplying the different powers of the ^{137}Cs normed ratios with exponents ranging from -3 to +3 [3]. For the determination of the detection efficiency, a full-scale simulation geometry of the measurements was created including the fuel assembly, service pit, shielding, collimator, and HPGe detector. Different variance reduction techniques available in MCNP 6.2 were tested and appropriate ones were used in the subsequent simulation runs to significantly reduce the needed computer times. Photon transport was simulated with many relevant starting energies and for each individual fuel pin to obtain efficiency calibration curves for all pins in the assembly. A deterministic calculation scheme employing numerical integration for a simplified one-pin geometry was also used to verify the MC simulation results.

Results

Analysis of the SFCOMPO 2.0 spent fuel data showed good agreement between the activity ratio – burnup characteristics of VVER-440 and other PWR type spent fuels. In particular, burnup prediction via the $^{134}Cs^2/(^{106}Ru^{137}Cs)$ compound activity ratio, which showed good performance for VVER-440 assemblies, may also be successfully applied to PWR assemblies (Fig. 1). The results seem less clear for BWR type assemblies, where the data points for the $^{134}Cs^2/(^{106}Ru^{137}Cs)$ ratio as function of fuel burnup scatter too much to give any usable formula for burnup prediction (Fig. 2).

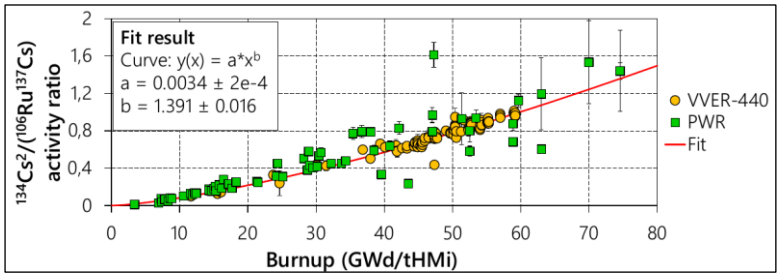

Figure 1: Comparison of VVER-440 and PWR assembly data for $^{134}Cs^2/(^{106}Ru^{137}Cs)$ as a function of burnup

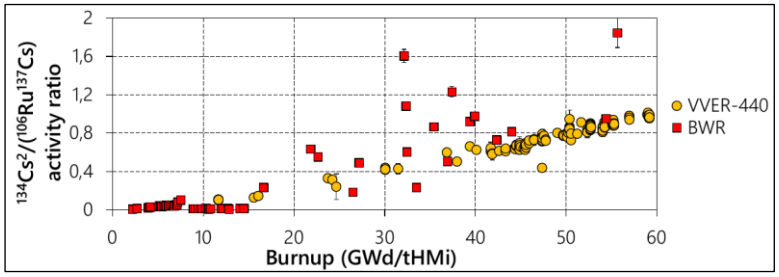

Figure 2: Comparison of VVER-440 and BWR assembly data for $^{134}Cs^2/(^{106}Ru^{137}Cs)$ as a function of burnup

It was found that out of 1200 different activity ratios, the previously found $^{134}Cs^2/(^{106}Ru^{137}Cs)$ ratio still performs best at predicting the fuel burnup, even in the case when the cooling time is unknown.

The MC simulation results for the simplified geometry agree well with the deterministic efficiency curve (Fig. 3). The pin-wise efficiency values at different gamma-ray energies indicate which parts of the assembly the spectral information is originating from (Fig. 4).

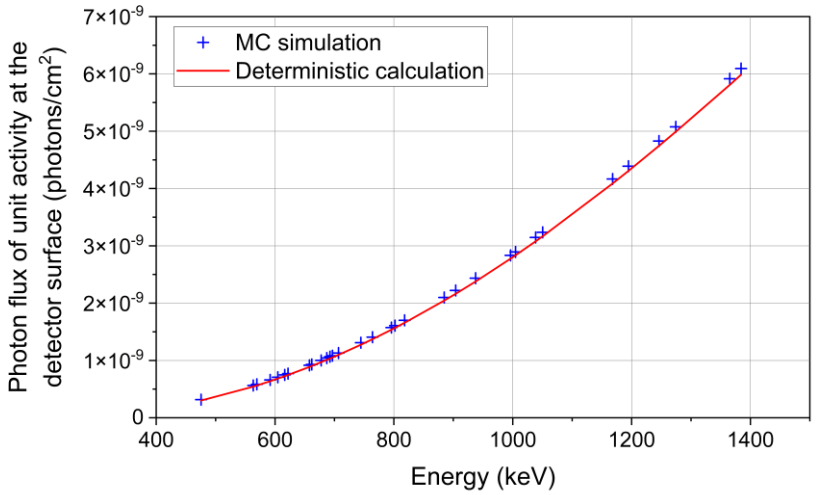

Figure 3: Verification of the MC simulated photon flux at the detector surface with deterministic calculation

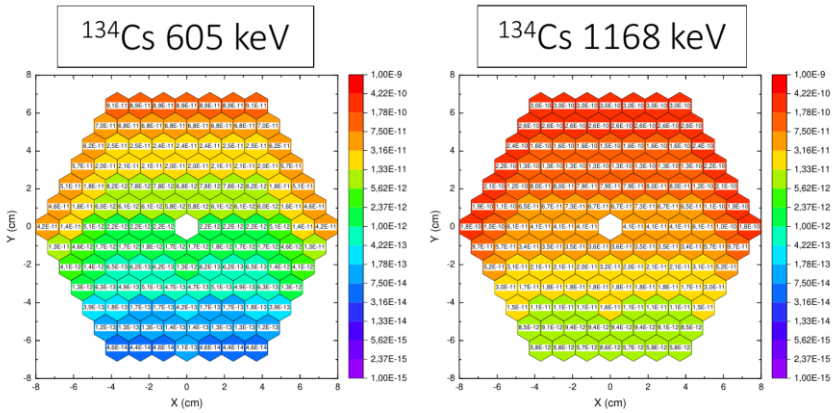

Figure 4: The different pin-wise efficiency maps of the 605 keV and 1168 keV gamma-rays of ^{134}Cs

Additionally, another set of spent fuel assemblies was successfully measured at Paks NPP at the end of this year. Of special importance are some assemblies that had very short cooling times at around 100 days, that will broaden the parameter limits of the available experimental dataset.

Remaining work

A paper is being prepared from the results of the MC simulation of the spent fuel measurements and the resulting manuscript will be submitted next year to a scientific journal.

The research effort will continue in 2023, with more focus on the analysis in detail of the spectral data, and on machine learning data analysis approaches.

Related publications

[1] P. Kirchknopf, I. Almási, G. Radócz, I. Nemes, P. Völgyesi and I. Szalóki: *Determining burnup, cooling time and operational history of VVER-440 spent fuel assemblies based on in-situ gamma spectrometry at Paks Nuclear Power Plant*, Annals of Nuclear Energy **170,** 108975 (2022)

[2] P. Kirchknopf, I. Almási, G. Radócz, I. Nemes, P. Völgyesi and I. Szalóki: *Gamma Spectrometric Investigation of Fission Product Activity Ratios to Calculate Burnup, Cooling Time and Power History of Spent Nuclear Fuels*, Poster presentation, 6th European Congress on Radiation Protection (IRPA2022), Budapest, Hungary, 2022.06.02.

[3] P. Kirchknopf, I. Almási, G. Radócz, I. Nemes, K. Zoltán, I. Szalóki, P. Völgyesi: *Kiégett fűtőelemek vizsgálata gamma-spektrometriával*, Oral presentation, XIX. MNT Nukleáris Technikai Szimpózium, Budapest, 2022.09.29.

DEVELOPMENT OF NUCLEAR FORENSIC ANALYTICAL METHODS FOR DETERMINING THE ORIGIN OF SMUGGLED MATERIALS

Csaba Tóbi, Péter Völgyesi

Objective

The aims of the PhD research are to determine the origin of nuclear materials, to identify new key parameters for origin assessment as well as to select from the already known parameters those with which a substance can be identified with certainty. It belongs to the research goal to find novel methodologies for nuclear forensic analysis, developing new methods and further development of existing methods, too.

Methods

Development of Rare Earth Element (REE) separation method for Inductively Coupled Plasma Mass Spectrometry (ICP-MS)

REE pattern is a high confidential signature to determine the origin of uranium containing materials in the nuclear forensic examination. In the literature there are many different REE separation techniques in the case of nuclear materials, but the reproducibility in the laboratory is usually difficult. The efficiency of the REE separation technique used at the Nuclear Security Department is not completely satisfactory. Therefore, the REE content of uranium ore concentrate and nuclear fuel pellet reference materials were examined together with the separation efficiency based on the following recipe:

- Dissolution of the samples: 300-500 mg sample in 9 ml 10 M HNO_3 for 24 hours.
- REE separation method:
  - Samples LOAD: 300 µl sample+ 900 µl MiliQ water.
  - Extraction chromatographic resin: 1,8 ml TRU (Triskem).
  - REE Separation: 1. Condition of the column with 10 ml 2 M HNO_3 2. Sample upload 3. Washing the column with 2 ml 2M HNO_3 3. Washing the REE fraction wit 1 ml cc. HCl, after that with 4 ml 4M HCl.
  - Evaporation of the samples on 130 °C with 2 ml of cc. HNO_3 and 200 µl H_2O_2.
  - Droplet pick up with 4 ml 1% HNO_3 solution.
- ICP-MS measurements of the samples.

Nuclear Forensic measurements on nuclear fuel pellets by Atomic Force Microscope (AFM)

The AFM has already been used for the examination of various nuclear materials, including nuclear forensic investigations. But the number of scientific articles dealing with this topic is very small and few of them have dealt with the comparison of the surface of nuclear fuel pellets.

The surface of the tested reference pellets is considered a rough surface for the instrument, so before the 3D-topographic scanning, the optimal parameters were identified in order to obtain adequate quality images. After the determination of the optimized settings for the optimal measurement of the instrument, 4 pellets were scanned. These topographic images were taken in a 10x10 µm area on the samples. If the scanning of the smaller area produced adequate results, a 50x50 µm area was scanned in the same way. All of the topographic scan images were edited using Gwyddion, an open-source professional cross-platform modular program for scanning probe microscopy data visualization and analysis.

Results

Development of Rare Earth Element separation method for ICP-MS

After the evaluation of the ICP-MS measurement results, the 24-hour nitric acid dissolution is not sufficient for the digestion of uranium ore concentrates and fuel pellets (Fig. 1). Therefore, it is necessary to investigate other digestion methods to properly dissolve the samples. Also, the efficiency of separation with TRU resin could be further increased. In addition to the TRU resin, several other resins have REE separation capabilities according to the literature, so examination of the resins should be considered.

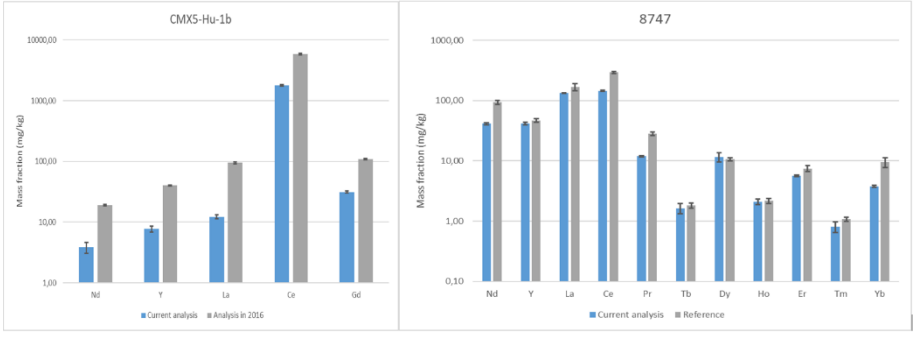

Figure 1: The reference REE concentrations in a nuclear fuel pellet and a uranium ore concentrate

Nuclear Forensic measurements on nuclear fuel pellets by Atomic Force Microscope

Based on the optimal instrument setting, evaluable topographic images were produced. In the case of the scanned images of the 4 fuel pellets from different origins (Fig. 2) it can be said that the surface of all four pellets show fine manufacturing processes. Furthermore, the pellets show large structural differences in both of the 10x10 µm and the 50x50 µm scanning's. In the aspect of the obtained results, scanning additional points is necessary and the topographic examination of one more reference pellet has to be done. The topographic images are acceptable, but the parameters for the scanning can be further optimized.

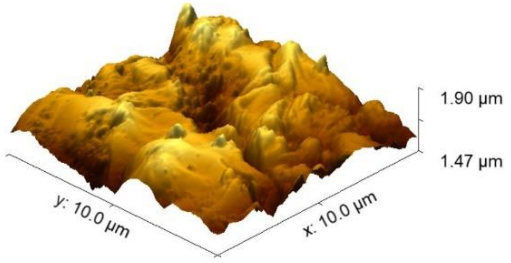

Sample 643 10x10 µm scan

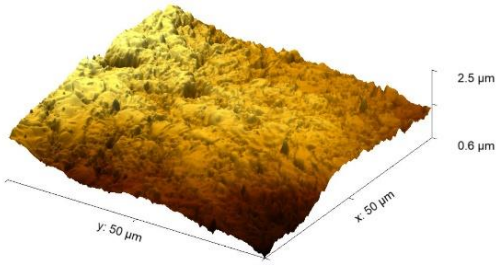

Sample 643 50x50 µm scan

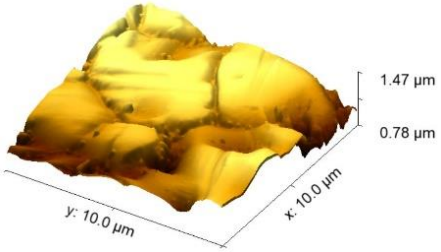

Sample 644 10x10 µm scan

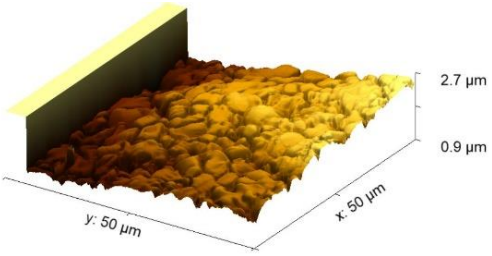

Sample 644 50x50 µm scan

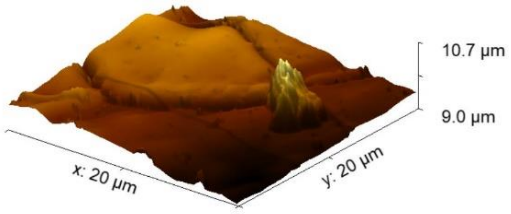

Sample CMX4-13-1 20x20 µm scan

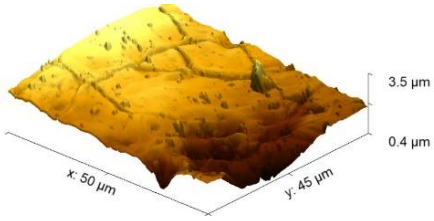

Sample CMX4-13-1 50x45 µm scan

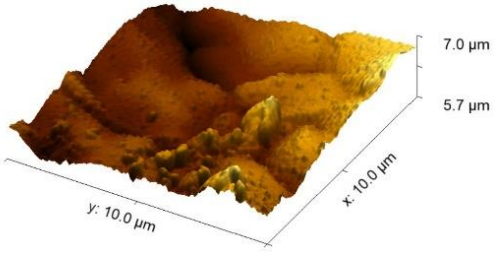

Sample CMX4-13-3 10x10 µm scan

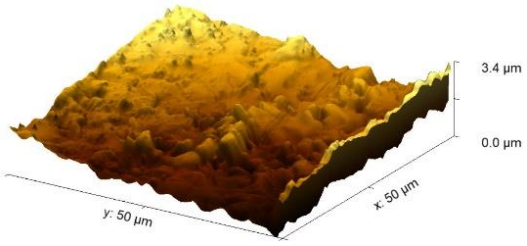

Sample CMX4-13-3 50x50 µm scan

Figure 2: AFM 3D-surface topography images of nuclear fuel pellets

Remaining work

Development of Rare Earth Element separation method: Continue the development of the REE separation method. The goal of the separation method development is to achieve a higher extraction level of REE in the case of uranium ore concentrates and uranium fuel pellets, which means the examination of different sample solution technics and chemical separation method for REE.

Nuclear Forensic measurements on nuclear fuel pellets by Atomic Force Microscope: Continue the AFM instrument optimization for the measurements and the 3D-surface topography scanning. Determine the height and friction signal of the pellets then compare the sample results. Comparison the fuel pellets based on their force curve to provide characteristic information from the surface of the pellets.

Related publications and conference presentations

[1] Cs. Tóbi, Z. Homonnay, K. Süvegh: *A novel methodology for Nuclear Forensic Examination: Positron annihilation Spectroscopy*, IAEA Technical Meeting on Nuclear Forensics: From National Foundation to Global Impact, Vienna Austria, 11-14.04.2022

[2] Cs. Tóbi, L. Illés, K. Fél, K. Süvegh, Z. Homonnay *Nuclear Forensic Examination of Uranium Ore Concentrate Samples* in: T. Kovács, E. Tóth-Bodrogi, G. Bátor, and R. Nagy, eds. (2022) VIII. Terrestrial Radioisotopes in Environment. International Conference on Environmental Protection. Book of Abstracts. Social Organization for Radioecological Cleanliness, Veszprém. ISBN 978-615-81632-2-4,

[3] K.L. LeBlanc, K. Nadeau, J. Meija, L. Yang, P.A. Babay, M.A. Bavio, Cs. Tóbi, Zs. Varga, Z. Mester at al: *Collaborative Study for Certification of Trace Elements in Uranium Ore Concentrate CRMs UCLO-1, UCHI-1, and UPER-1,* Journal of Radioanalytical and Nuclear Chemistry **331**, 4031–4045 (2022)

LOST RADIOACTIVE SOURCE EXPLORATION TRAINING CAPABILITIES AT THE CENTRE FOR ENERGY RESEARCH (EK)

Károly Bodor

Objective

One of the main tasks of the Nuclear Security Department (SBL) of EK is to explore, collect, identify, and store the lost orphan nuclear sources and materials in Hungary as delegated in the 490/2015. (XII.30.) governmental decree to EK. Also, this decree describes the required relevant intervention procedures and the steps of the intervention in such cases (when and which organization has to act).

The Centre for Energy Research is the Technical Support Organization of the Hungarian Atomic Energy Authority (OAH) and has also got cooperation programs with the following organizations:

- National Directorate for Disaster Management (OKF)
- Counter Terrorism Centre (TEK)
- Hungarian Defence Forces (MH)
- Hungarian Defence Forces "Görgey Artúr" Chemical Biological Radiological Nuclear Area Information Centre (MH GAVIK)
- Hungarian National Police, National Bureau of Investigation (NNI)
- National Tax and Customs Administration (NAV)

In case of confiscation or finding nuclear material with unknown origin, their identification and first characterization/categorization is performed in-field by the Mobile Expert Support Team (MEST) with the support of the Mobile Laboratory.

The Centre for Energy Research established an indoor and an outdoor training field at the EK premises for the training and harmonizing the different organization's procedures of exploring orphan radioactive sources/nuclear materials.

Methods

Several scenarios can be performed at these training fields utilizing the available laboratories and buildings like the „C" level isotope laboratory, a hangar with natural background and enhanced background supplemented with neutron field.

The indoor training site is an advanced one, where the orphan source exploration can be done in a special environment. Most of the real scenarios are not as difficult as at the indoor site, but when a first responder can successfully explore the sources then at any case the efficiency of the exploration can be high.

Results

At the indoor training site the EK and the Hungarian National Police, National Bureau of Investigation made a demonstration showing how a joint exercise takes place (Figure 1). The scenario was to find, collect and analyze radioactive material at an illegal laboratory. The whole work was done based on the common operating procedure.

Figure 1: Joint exploration exercise at illegal laboratory, exploration of illegal sources

For outdoor scenarios, the EK created an outdoor site at the KFKI campus (Figure 2). It is located inside a forest in concreted area. A hot zone can be designated, and an observer station is placed at the site. At the indoor site, several scenarios can be performed like parking lot, border control point, highway accident etc.

At the training sites Unmanned Ground Vehicle (UGV) and Unmanned Aircraft Vehicle (UAV) testing are also available. The EK also made UGV tests.

The outdoor site was tested by the National Directorate for Disaster Management, the scenario was a Border Control Point (BCP) event. At the test, the camera and streaming system were tested and the OKF tested their new backpacks and other measurement devices. Inside the vehicle several sources were hidden. The task was to find all sources in the car. The other task was to detect the sources at high vehicle speed when the backpacks were inside the van, and also when the sources were under the vehicle.

Figure 2: Radioactive source exploration under vehicle, backpack testing at high speed, outdoor site

At INCLUDING project's Hungarian Joint Action a complex scenario was demonstrated, where the Counter Terrorism Centre arrested a dangerous criminal who was dealing with ~~a~~ radioactive source (Figure 3). After the arrest, the MEST (the team from the Hungarian National Police, National Bureau of Investigation and the EK SBL) arrived at the house of the arrested person to investigate the location. At the scenario the above mentioned common operating procedure was demonstrated. Furthermore, several technical developments were presented to the INCLUDING team:

- Virtual system: Virtual Radioactive Source System (VRSS), virtual surface contamination,
- Border Control Point (BCP) with giant scintillation detectors & DOZIMOBIL system,
- Drone, UGV reconnaissance),
- Mobile laboratory.

Figure 3: Hungarian Joint Action, Counter Terrorism Centre& Rapid Response and Special Police Services& MEST action

Remaining work

In 2023 we are planning to do trainings with our partners.

Related publication

[1] K. Bodor, P. Zagyvai: *Lost Radioactive source exploration training capabilities at the Centre for Energy Research (EK)*, Biztonságtudományi Szemle Évf. 4. Szám 4. (2022)

ASSESSMENT OF THE CHARACTERISTICS OF RADIONUCLIDES AND DETERMINATION OF KEY NUCLIDES FOR RADIATION PROTECTION CALCAULTIONS: PART 1

Dorottya Jakab, Annamária Pántya, Tamás Pázmándi, Csilla Rudas, Péter Zagyvai

Objective

The goal of this work is to determine key nuclides contributing significantly to public doses that shall be considered in dose calculations. Based on these results the computational burden of such calculations could be reduced. However, for different nuclear facilities, various operation states and release scenarios the key nuclides could be different. These investigations require the work to spread over several years to be able to develop methods for determining the key nuclides for a wide range of circumstances.

Methods

In this first part of the work, assessments were conducted with the in-house developed CARC program to evaluate the contribution of different radionuclides to the public dose (the 7-day and 50-year committed effective dose) at 1 km, 3 km, 10 km and 30 km distances from the release point. In this report, we present the results of one of them as an example and note that the assessments can be done similarly for other operating states, fuel burn-up, accident conditions as well as for different nuclear facilities (e.g., research reactors). For hypothetical Design Basis Accidents (DBA4) scenario from a nuclear power plant, 10 release source terms were taken into account with consideration of 39 radionuclides. The release height was set to be 120 m. The atmospheric dispersion calculations were conducted with 12 different meteorological scenarios to cover various circumstances. The dose results were computed for different exposure pathways, the cloudshine, groundshine, inhalation and ingestion doses were calculated separately for each radionuclide and meteorological case, then the frequency of the resulting doses were counted where the contribution from each considered radionuclide to the dose was higher than a pre-defined percentage. From the 12 different meteorological cases, the average contribution was selected as the final result.

Results

The results obtained for the different source terms were similar. For brevity's sake, the nuclides and their aggregated contribution to only the 7-day dose are shown for the various distances for one of the selected release source terms in Table 1. The nuclides with contribution higher than 10% are indicated with italic and underlined font.

Table 1: Nuclides with contribution to the 7-day committed effective dose higher than 1%

Distance from the release point	**1 km**	**3 km**	**10 km**	**30 km**
Contribution from the selected radionuclides	91.9%	92.4%	92.8%	92.8%
Nuclides with contribution >1%	**15** Ba-140, *Ce-144*, Cs-134, *I-131*, I-132, *I-133*, I-135, Kr-88, La-140, Ru-103, Ru-106, Sr-90, Te-132, Xe-135, Zr-95	**16** Ba-140, *Ce-144*, Cs-134, *I-131*, I-132, *I-133*, I-135, Kr-88, La-140, Ru-103, Ru-106, Sr-90, Te-132, Xe-133, Xe-135, Zr-95		

By ranking the nuclides based on their contribution to the total dose, the key nuclides can be selected. It can be stated that the top 5 nuclides having the largest individual contributions to the 7-day dose are I-131, Ce-144, I-133, I-135 and La-140. In case of the 50 years dose, the top nuclides are I-131, Cs-137, Ce-144, Cs-134, I-133 and Sr-90. These nuclides are responsible for around 70% of the two dose quantities, thus these nuclides can be considered key ones for this specific release case.

Remaining work

In the next phases of the work, results for various conditions of nuclear power plants, such as operating states, fuel burn-up, accident conditions as well as source terms for different nuclear facilities (e.g. research reactors) will be investigated and compared. Similar evaluations of the contribution from different radionuclides to the public dose will be performed in order to identify the key nuclides for different facilities and conditions and to quantify the level of correction that is needed with the omission of a large number of radionuclides. Based on the results, recommendation can be formulated on which nuclides should be included in the assessment and which can be excluded, and a correction factor can be determined to compensate for the nuclides not included.

DEVELOPMENT OF A BIOKINETIC MODEL FOR THYROID DOSE ESTIMATION

Zsófia Rékasi, Tamás Pázmándi, Annamária Pántya, Péter Zagyvai

Objective

Iodine is a key element of the thyroid hormones, which regulate various essential processes in the human body, in particular in the thyroid organ. The thyroid function and the daily iodine uptake are influenced by several factors, such as age, diseases, lifestyle, and diet. In case of a nuclear reactor accident with environmental release, iodine-131 is one of the dominant contributors to internal dose of the public in the early phase of the emergency. For adequate dose estimation, knowledge of the iodine metabolism is imperative, which can be represented by biokinetic models. The aim of our study was to define a new biokinetic model of iodine metabolism that is able to take personal characteristics, such as age-dependent thyroid uptake or the effect of dietary iodine intake into account, the impact of which on the dose estimation has been investigated.

Methods

Biokinetic models previously published in the literature for thyroid dose estimation were reviewed and compared, their advantages and disadvantages were assessed, and a new mathematical model based on the existing ones has been developed for the studies. The ModelMaker4 program was used to implement the compartment model, structure of the new model can be seen in Fig. 1. The squares represent the compartments, and the arrows indicate the direction of exchanges between compartments. The exchange rate constants (k [h^{-1}]) together with the iodine contents (Q [mg]) determine the transfer rate between compartments. The time-dependent distribution of iodine in the body was determined, factors influencing the thyroid function were collected.

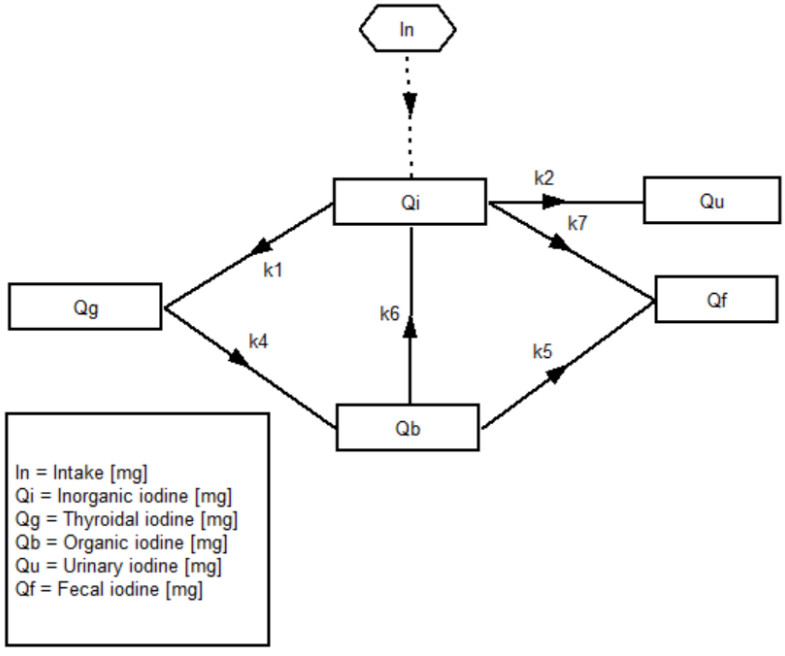

Figure 1: Structure of the developed model

Results

First, the effect of dietary iodine to the thyroid activity was investigated. If the dietary intake of iodine is less than adequate, it will cause iodine deficiency in the body. The iodine uptake of the thyroid will increase, so that the thyroid can maintain the normal hormone synthesis. Consequently, following a radioactive release to the environment the radioactive uptake of the thyroid will increase, as well. According to our results intake of radioactive iodine could be even 2-3 times higher than in normal iodine level, resulting in the same increase in the absorbed dose of thyroid.

Age-dependent radioiodine uptake to the thyroid was also investigated. The age-dependent rate constants were taken from literature, the thyroid activity in six age groups from the age of 3 months to adults were evaluated. Our study showed that the mean uptake to the thyroid increases with about 10% from the age of 3 months to adulthood.

Related publication

[1] Zs. Rékasi, T. Pázmándi, A. Pántya, P. Zagyvai: *Role of individual characteristics in thyroid dose estimation*, Poster, 6th European IRPA Congress (2022)

MATHEMATICAL MODELLING OF LOW DOSE HYPER-RADIOSENSITIVITY AND INDUCED RADIORESISTANCE

Szabolcs Polgár, Balázs Madas

Objective

Earlier, it was supposed that low dose hyper-radiosensitivity and induced radioresistance are the result of a tissue level minimization of mutation load. Due to ionizing radiation, cells suffer radiation damage in their DNA which increases the chance of mutation and thus endangers the long-term survival of the tissue. Each cell compares its own damage to the average damage of its neighbors (this information is obtained by chemical signalling) and if the given cell has more DNA damage than a threshold it goes into apoptosis and gives room for a division of a cell with less damage. This threshold is the sum of the environmental average and the average number of mutations per cell division. By replacing the most damaged cells, the tissue minimizes the risk of mutation at the cost of additional cell death at low doses. The aim of this work is to test the hypothesis of minimum mutation load by developing a new mathematical model and validating it with an experimental database constructed from published articles [1-3].

Methods

The model has been developed in Python programming language. A total of 600 cells are placed randomly in a circle with a given radius representing a dish. The cells are able to communicate their DNA damage by a signal. The concentration of this signal follows normal distribution, centered on the cell and the DNA damage of the cells follows Poisson distribution for a given dose. The fit parameters for the model were acquired by fitting with the Nelder-Mead method to the experimental data in each case. The parameter calculation consisted of two steps. First, the initial parameters were acquired using the starting slope and the local minimum of each dataset. With these parameters, a two-dimensional fit with the Nelder-Mead method was performed to reach the best fitting values. The results were then evaluated and compared to our model where there was a fit in the original article.

Results

While the fitting is still under way, the initial results show good fit to the experimental data. The first comparison was made between the widely used induced repair (IR) model fit and the fit of our model. Overall, 54 datasets were investigated. In 21 cases the IR model gave a better fit, in 19 cases it was worse, for the remaining 14 cases the two model gave similar results with no significant difference between them. It can be concluded that the model performed on the same level as the standard induced repair model did, with the additional benefit of having fewer variables (two instead of four) and they have biological meaning. The results also helped to identify those cases where the model fails to give a good fit. This happened most commonly if the data did not contain a local minimum and if the local minimum was really low (lower than 50% of cells survived). This second problem can be amended by changing the setup of the model (changing the cell number, signalling strength or cell size), while for the first problem further development of the model is required.

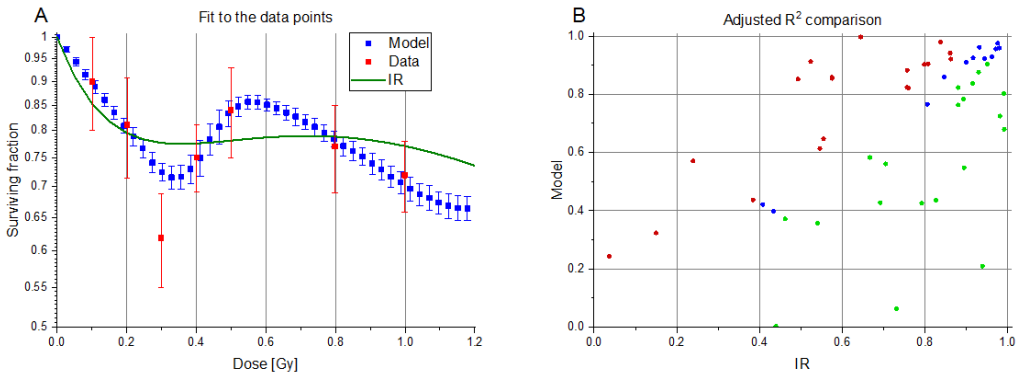

Figure 1: An example of the fit to the data with uncertainties (panel A). Comparison of R^2 values for each data set (panel B). The points are green if the IR model fit was significantly better, red if our model fit was significantly better and blue if there were no significant difference.

Related publications

[1] S. Polgár, P. N. Schofield, & B. G Madas: *Data collection and analysis on low dose hyper-radiosensitivity and induced radio-resistance*, STOREDB (2021) https://doi.org/10.20348/STOREDB/1163

[2] S. Polgár, P. N. Schofield, & B. G. Madas: *Datasets of in vitro clonogenic assays showing low dose hyper-radiosensitivity and induced radioresistance.* Sci. Data **9,** 555 (2022)

[3] S. Polgár, & B. G. Madas: *Kis dózisoknál megfigyelhető hiperszenzitivitással és indukált sugárrezisztenciával kapcsolatos adatok gyűjtése és közzététele.* 39-48, in Hungarian (2022)

DEVELOPMENT OF METHODS TO IMPROVE ACCURACY AND PRECISION OF THE MEASUREMENT RESULTS OF ENVIRONMENTAL RADIATION MONITORING SYSTEMS

Dorottya Jakab, Tamás Pázmándi, Péter Zagyvai

Objective

The aim of the project was to develop procedures to support the interpretation and appropriate use of measurement data in environmental radiation monitoring, with a primary focus on the measurement evaluation and statistical analysis of measurement data(sets). In the last part [4] of the multi-year work, we synthesized the main results and findings of the project [1][2][3] where we also addressed the changes that have occurred over the years of the project, coming, on the one hand, from the release of new relevant documents and concepts, and, on the other hand, from the continuously expanding body of knowledge and experience from our own developments and improved methodologies. As a key outcome we compiled a methodological guide [5] containing a set of procedures developed and recommended for practice, supporting not only the adequate, routine application of measurement evaluation and data analysis methods but also contributing to the harmonization of domestic environmental radiation monitoring activities.

Methods

One of the main focuses of our investigations in the course of this project was to examine the limitations and conditions of application of the most commonly used methods for measurement evaluation, including uncertainty assessment and determination of characteristic limits, and for statistical analysis, to be considered when applying in environmental radiation monitoring. This was done not only by reviewing the most relevant documents, such as the pertinent international and national standards and guidelines, and the mathematical interpretation of the corresponding theoretical models, but also by carrying out numerous example calculations and tests.

It was found that even concepts and approaches available for measurement evaluation may not easily be interpreted and put into practice by a general user, and the off-the-shelf evaluation software products are either used as black boxes (without understanding their computational functions and the mathematical foundations of them) or there may be a need for compromise on the features and functions available or missing in these software products. To help with these difficulties, an easy-to-use measurement evaluation procedure was defined that can be implemented in the most common software environment (Microsoft Excel) using its built-in functions available to all users by default, without requiring any special programing knowledge. Applicability of alternative or complementary methods that can be chosen for use depending on measurement circumstances and conditions, available computing capacities and capabilities and individual user needs or preference was also investigated.

Results

An 11-step measurement evaluation procedure was defined that among others allows for a) a step-by-step and transparent application, b) a complete and uncompromised implementation in terms of comprehensiveness of computational steps and functions, c) the inclusion of investigation steps to verify the adequacy of measurement evaluation procedures (based on uncertainty propagation and propagation of distributions using Monte Carlo Method). With the procedure, it is also possible to define the steps to be taken in the measurement evaluation, as appropriate and necessary, and the way in which the results are to be reported, particularly for the adequate subsequent analysis of datasets. The methodological guide describes the ideal procedure for measurement evaluation along these steps, supplemented with numerous explanations, examples, suggestions, and calculation schemes and aids.

The reports of the multi-year project [1][2][3] contain numerous findings and recommendations on the optimization of the monitoring systems and measuring methods, such as ways to reduce the measurement uncertainty and characteristic limits and improve the temporal and spatial representativeness of measurement results.

Related publications

[1] D. Jakab, T. Pázmándi, P. Zagyvai: *Development of methods to improve precision of the measurement results of environmental radiation monitoring systems – Part 1: Determination of uncertainties and characteristic limits of environmental radiation measurements,* EK-SVL-2019-270-01-01-01, In Hungarian (2019)

[2] D. Jakab, T. Pázmándi, P. Zagyvai: *Development of methods to improve precision of the measurement results of environmental radiation monitoring systems – Part 2: Methods for reduction of measurement uncertainties and characteristic limits of environmental radiation measurement*, EK-SVL-2019-270-02-01-01, In Hungarian (2020)

[3] D. Jakab, T. Pázmándi, P. Zagyvai: *Development of methods to improve precision of the measurement results of environmental radiation monitoring systems – Part 3: Integrated statistical analysis of environmental radiation measurements*, EK-SVL-2020-270-01-01-00, In Hungarian (2020)

[4] D. Jakab, T. Pázmándi, P. Zagyvai: *Development of methods to improve precision of the measurement results of environmental radiation monitoring systems – Part 4: Final report*, EK-SVL-2022-270-01-01-01, In Hungarian (2022)

[5] D. Jakab, T. Pázmándi, P. Zagyvai: *Development of methods to improve precision of the measurement results of environmental radiation monitoring systems – Methodological guide on the evaluation of environmental radiation measurements and the analysis of data series*, EK-SVL-2022-270-02-01-01, In Hungarian (2022)

EFFECTIVE USE OF DOSE PROJECTION TOOLS IN THE PREPAREDNESS AND RESPONSE TO NUCLEAR AND RADIOLOGICAL EMERGENCIES: PART 3

Tamás Pázmándi, Csilla Rudas

Objective

The research in this 3-years long project is focused on the assessment and application of dose projection software, and the main objective is the evaluation of uncertainties in atmospheric dispersion modelling and dose estimation in case of accidental radiological releases. In the third project phase [1], the uncertainty assessments were carried out based on the previously selected perturbation of the input parameters, the output uncertainties of the two codes were compared. The work was carried out in cooperation with the Nuclear Safety Research Institute (NUBIKI).

Methods

The uncertainty assessment was carried out with two different dose projection tools, the SINAC decision support system developed in the Centre for Energy Research and the MACCS engineering-level computer code developed at Sandia National Laboratories. A simple release scenario was assumed with consideration of spatially and temporally constant meteorological conditions and various dose quantities were computed at 3 km, 5 km, 10 km, 15 km and 30 km distances from the release point along the plume centreline. In the assessment, the release characteristics and meteorological parameters were perturbed along predefined wide and uncertainty ranges (Table 1)

Table 1: The perturbed parameters and their values used in the assessment

Group of parameters	Parameter	Default	Uncertainty range	Wide range
Release characteristics	Release height	50 m	±1 m	±50 m
	Release duration	~4 h (15000 s)	-	+4 h, +8 h
Meteorological parameters	Wind speed	1 m/s	±0.2 m/s	+4 m/s, +9 m/s
	Pasquill stability class	D	±1 class	–3 class, +2 class
	Precipitation intensity	1 mm/h	±1 mm/h	+9 mm/h

Results

In case of the uncertainty perturbations, the most influential parameter was the Pasquill stability class, one class difference resulted in an average variation around ±50% in the total 7-day dose. The second most influential parameter was the precipitation intensity (variation from 1 mm/h to 0 mm/h, 2 mm/h) causing an average variation of about ±15% in the total 7-day dose. The uncertainty perturbation of the other parameters (release height, release duration, wind speed) had only a minor effect on the total 7-day dose with average variations less than ±10% for each parameter.

Similarly, when the parameters perturbed within a wider range, the most influential one was again the Pasquill stability class, causing more than ±100% difference between the total 7-day doses computed with Pasquill D and F class. The second most influential parameter was the precipitation intensity (variation from 1 mm/h to 10 mm/h) resulting in an average difference of ±70% in the total 7-day doses. The other parameters perturbed within a wider range caused around or less than ±50% difference each in the total 7-day doses. The difference of the time integrated air activity concentrations at ground level computed with various Pasquill stability classes compared to the reference case is shown in Figure 1.

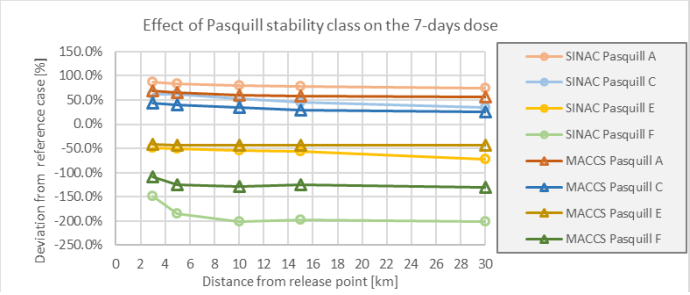

Figure 1: The time integrated air activity concentrations at ground level for selected nuclides

Related publication

[1] T. Pázmándi, Cs. Rudas, A. Bareith, G. L. Horváth, G. Lajtha: *Third Phase: Comparison of SINAC and MACCS calculations with perturbed input parameters*, EK-SVL-2022-345-01-01-00 (2022)

DEVELOPMENT OF THE CARC SOFTWARE AND SURVEY OF HABIT AND CONSUMPTION DATA OF THE PUBLIC

Csilla Rudas, Dorottya Jakab, Anikó Jécsai, Tamás Pázmándi

Objective

A new approach and software were developed for defining and calculating the atmospheric release criteria for nuclear safety analysis in line with the Council Directive 2014/87/Euratom about preventing the release of radioactive material from nuclear facilities. Even though international guidelines exist describing the requirements of environmental release criteria, the practical application of them differs from country to country. The objective of the new approach was to establish a methodology that could be applied in practice for existing and operating nuclear power plants and also for other nuclear facilities by being easy to implement. The usage of the developed simplified methodology would improve the comparability of such dose calculations in different countries and thus facilitate the harmonization of safety analyses so that the safety of different nuclear facilities could be assessed on the same basis. Another important goal was for the method to be capable of taking into account site specific input data such as long-term meteorological measurement data and habit and consumption data of the local population. [1]

Methods

The basis of the approach is that with appropriate boundary conditions, the characteristics of the release, the environmental dilution (atmospheric dispersion, deposition, etc.) and the exposure of the population can be separated and the dose at a receptor point can be computed with a simple multiplication according to the following schematic equation:

$$\Delta = S \cdot T \cdot E \tag{1}$$

where Δ is the dose representative of the radiation exposure, S is the source term of the released activity, T is the transport factor describing the environmental dilution and E is the exposure factor that contains the characteristics of the exposure of the population. With this separation, the compliance with the release criteria can be verified quickly if the appropriate T and E characteristics have already been determined for an installation. Despite the fact that these site-specific conditions might change over time, factors T and E should only be updated during a periodical safety analysis review, e.g. once in every 10 years, or when there is a significant change in the parameters. [1]

The CARC (Calculating Atmospheric Release Criteria) software was developed to apply the new methodology and is capable of calculating the consequences of radiological releases to the atmosphere from a nuclear facility. The atmospheric transport of the radioactive material is computed with a Gaussian plume model with Pasquill characterization of the atmospheric stability. Dry and wet deposition is considered with source depletion assumed to be uniform along the z-axis of the plume. Exposure pathways taken into account by the software include cloudshine and inhalation from plume passage, groundshine from deposited material and ingestion of contaminated foodstuff. Skin dose and inhalation of resuspended material are not taken into account. [1]

For comparison with the safety criteria, computations need to be conducted for all necessary release cases, pathways, distances and nuclides. The CARC software applying the new methodology determines the transport factor for all meteorological data points given in the input and computes a selected percentile for the air activity concentration and concentration of the deposited activity in the ground. Separate values of the transport factor are determined for each release case (c), distance (d) and nuclide (i). Then, the exposure due to unit concentration is computed for the selected nuclides (i), pathways (p) and residence times (t). These factors are multiplied with the release source term and summed up for all nuclides and pathways based on the following detailed expression:

$$\Delta^{c,d,t} = \gamma \sum_{p} \sum_{i} S_i^c T_i^{c,p,d} E_i^{p,d,t} \tag{2}$$

The γ safety factor compensates the uncertainty of some elements of the calculation. The criterion is fulfilled if all Δ values are below the limit.

Site-specific data can be considered by the model taking into account long-term meteorological measurement data from the actual site of the nuclear facility. Regarding the population data, different habit and consumption data can be provided for each receptor point where the resulting dose quantities are determined. [1]

To actualize the input data that describe the exposure of the population required by the CARC software to compute the dose consequences, an extensive literature review of the Hungarian census data and research papers was conducted. Based on the review it was found that most of the input data for the population that is needed for the precise calculation of public doses was not available at all, or was only available as average values for the entire country and not for specific regions around nuclear sites. To obtain precise population data that are needed to calculate the dose exposure with the CARC software, a survey was conducted to investigate the habit and consumption data of habitants living within a 30 km radius of the Paks Nuclear Power Plant (NPP) in Hungary.

The questionnaire used in the survey was developed to focus on the characteristics that influence the radiation exposure of the public. The survey and the evaluation of the results were carried out in cooperation with two market research companies. [2] [3]

Results

The survey questionnaire was developed to cover all of the parameters that are necessary for the dose calculations arranged in the following three topics:

- living conditions (such as building materials, floor of the residence, time spent near the Danube River, fishing, hunting, plant and livestock production);
- activities (such as time spent indoors and outdoors, time spent with activities of various intensities);
- consumption of foodstuff (such as vegetables, fruits, drinks, grain products, dairy products, meat, eggs).

The survey sample was selected to be representative of the population living within a 30 km radius of the Paks NPP. The unit of the survey was a household, and one adult was questioned in each household. If at least one infant or child was a resident of the household questions were also asked about their activities. The consumption of all household members was surveyed as well. The selection of the questioned 1000 households was based on stratification according to the following characteristics:

- size of settlement (small: population less than 1500, medium: population between 1500 and 10 000, large: population more than 10 000);
- distance from the NPP (less than 5 km, between 5-10 km, between 10-20 km beyond 20 km);
- location of settlement along the Danube River (left side identified with Kalocsa, right side identified with Paks).

As examples of the results, the time spent and the consumption are shown in Figure 1. and Figure 2. [1]

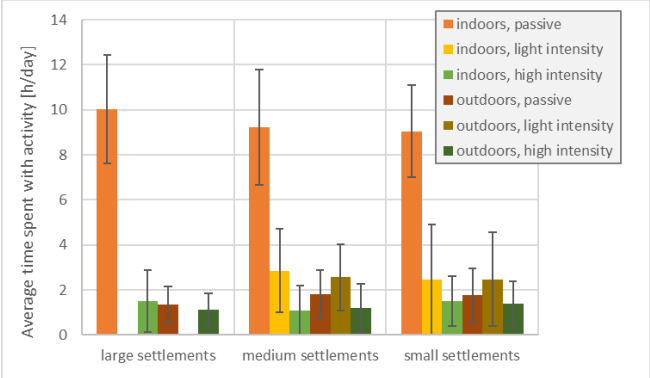

Figure 1: Average time spent with various activities grouped by settlement size (entire sample)

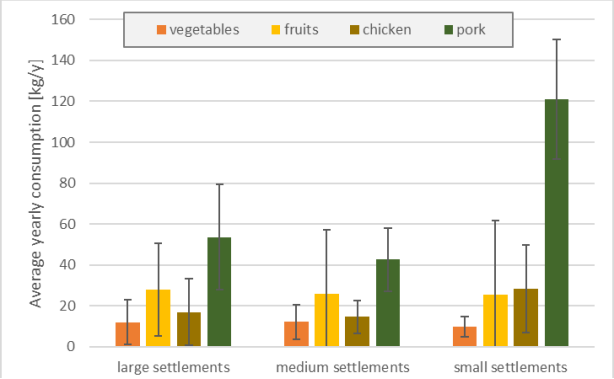

Figure 2: Average yearly consumption of various foodstuffs grouped by settlement size (entire sample)

Based on the results of the survey, the characteristics of the representative groups were determined by using statistical quantities such as the median values for three age groups and the entire survey sample. As an example, the parameter values of the time spent outdoors and indoors with activities of various intensities are shown in Table 1 for the three age groups. [3]

Table 1: Time spent outdoors and indoors with activities of various intensities for the representative groups

Parameter	Adults (>18 y)	Children (2-18y)	Infants (<2y)
Indoors, passive activity [h/day]	15.43	24.00	21.71
Indoors, light intensity activity [h/day]	3.43	0.00	0.00
Indoors, high intensity activity [h/day]	0.00	0.00	0.00
Outdoors, passive activity [h/day]	1.71	0.00	2.29
Outdoors, light intensity activity [h/day]	3.43	0.00	0.00
Outdoors, high intensity activity [h/day]	0.00	0.00	0.00

Dose calculations were performed for the determined representative groups with source terms of the new "slim" fuel assemblies optimized for the water-uranium ratio and for the DBC4 accident scenarios of the Paks NPP. [3]

Related publications

[1] Cs. Rudas, D. Jakab, E. Hann, L. Beck, A. Názer, D. Róna, E. Galgóczi, L. Kósa, O. Bajnay, A. Jécsai and T. Pázmándi: *New Method for Calculating Release Criteria for Nuclear Safety Analysis and Survey of Habit and Consumption Data of the Public*, 8th International Conference VVER 2022, Řež, Czech Republic, 10-11 October (2022)

[2] A. Jécsai, T. Pázmándi, Cs. Rudas, O. Bajnay, D. Róna and E. Szőke: *Actualization of input data used for assessment of environmental consequences – 3. Phase: Evaluation of data and derivation of input data required for the assessments,* EK-SVL-2022-742-01-01-00, in Hungarian (2022)

[3] T. Pázmándi, Cs. Rudas: *Actualization of input data used for assessment of environmental consequences – 4. Phase: Dose assessments with the input data obtained in the population survey,* EK-SVL-2022-742-01-02-00, in Hungarian (2022)

INTERNAL DOSIMETRY ARRAY FOR GATEWAY, THE SPACE STATION OF THE ARTEMIS PROGRAM

Balázs Zábori, Attila Hirn

Objective

The main objective of the Internal Dosimeter Array (IDA), the very first European-led internal payload to be hosted within the US Habitation and Logistics (HALO) module for Lunar Gateway early utilization is to monitor the internal space dosimetry environment in lunar orbit with the combination of existing and proven instrument technologies in an international collaboration. Dosimetry measurements for exploration mission are of utmost importance as the astronauts will not be protected by the Earth's magnetic field or the atmosphere; hence, they could be exposed to up to 700 times the radiation dose of an average human on Earth from space radiation. The IDA consortium is led by the Centre for Energy Research (EK).

Methods

The project is executed following a phased approach defined by the European Cooperation for Space Standardization (ECSS) standards. The instruments integrated in the IDA payload are the European Active Dosimeter (EAD) mobile unit from the German Aerospace Centre (DLR), MediPix from the Czech company ADVACAM s.r.o., the three-dimensional silicon detector telescope TRITEL from EK (subcontractor REMRED Ltd.), and D-SPACE detector system from the Japanese Exploration Space Agency (JAXA). The common Electronics Box (E-Box) interfacing with the Gateway subsystems is developed by REMRED Ltd. Structural and thermal design is elaborated by Airbus Defence and Space.

Results

The IDA Phase 0/I combined safety review conducted by the National Aeronautics and Space Administration (NASA) was passed. The Manufacturing Readiness Review (MRR) of the IDA Engineering Model (EM) in November 2022 was successful and the corresponding milestone was achieved. The data pack submitted for the review included, among others, management plans and interface control documentation. The rendered Computer Aided Design (CAD) model of the current design can be seen in Fig. 1. The total mass of the payload is less than 33 kg, dimensions are 0.5 m (W) x 0.25 m (L) x 0.42 m (D).

Figure 1: Rendered 3D CAD model of the IDA payload

Remaining work

IDA Design shall be frozen by mid-2023 concluded with a successful Critical Design Review (CDR). After the CDR has been accomplished, the project can enter into Phase D (verification and manufacturing of the proto-flight model).

Acknowledgment

The implementation of the IDA payload is conducted in the frame of the ESA Contract No. 4000136731/21/NL/AT.

COORDINATION OF THE HUNGARIAN TO ORBIT NATIONAL ASTRONAUT PROGRAM

Balázs Zábori, Attila Hirn, Gábor Béla Magyari, Klaudia Vivien Nagy

Objective

The Hungarian to Orbit (HUNOR) Astronaut Program was announced by the Ministry of Foreign Affairs and Trade (KKM) in 2021. The goal of the program is to boost Hungarian space research and space industry by establishing Hungarian astronaut capabilities. The next Hungarian research astronaut is planned to have his mission to the NASA operated segments of the International Space Station (ISS) in the year of 2024 in collaboration with US company AXIOM Space. The program is executed, lead and coordinated by the Space Research Department of the Centre for Energy Research, using the standards of the European Space Cooperation for Standardization (ECSS) as baseline applicable set of management, quality assurance and engineering requirements [1].

Methods

The astronaut selection was started by the closure of the official application and the initiation of a phased selection process. In the first phase, the applicants were down-selected subjected to online aptitude testing. Based on the results, the best ones were sent out to the German Aerospace Centre (DLR) for further medical testing in collaboration with the European Space Agency (ESA). In parallel, the national medical screening of the applicants was started by Semmelweis University. In the frame of the last phase, technical skills assessment of the astronaut candidates was conducted. In order to determine the physiological acclimatization capabilities, the candidates were exposed to accelerations from various directions and intensities, including an airborne G-acceleration exercise.

In the frame of the HUNOR Research & Development (R&D) Subprogram, eight dedicated experiment concepts were pre-identified by KKM as bases of the definition studies, which were executed and coordinated in accordance with ECSS standards to guarantee the proper outcome for the feasibility review. Axiom Space was involved on a regular base in the definition studies to provide all inputs for the development teams required for the proper execution.

In order to open the possibilities of the program to the scientific and the general public within Hungary, an open call was announced by EK in collaboration with KKM in the following categories: instrument development, laboratory experiments, public outreach activities. Experts form AXIOM Space, ESA, the Scientific Council on Space Research in Hungary and Centre for Energy Research participated in the feasibility review and the open call evaluation.

Results

More than 200 applications were received for the prospective astronaut selection program and 100 applicants were down-selected subjected to online aptitude testing. Almost half of them were selected to enter Phase 2. After completing the psychometrical, the psychological and the complex aeromedical tests, the best 8 candidates were subjected to the final selection phase, carried out at EK premises in early autumn supported by medical monitoring provided by Semmelweis University. The laboratory exercises used for technical skills assessment included thermo-vacuum and vibration testing, sub- and supersonic flow measurement, control of power on the simulator of a nuclear reactor, evaluation of passive detectors used for space dosimetry, basic life support and telemedicine exercise, mechanical tests and microstructure examinations on reactor materials' specimens, and radioactive source finding scenario at the radiological training facility. All tests have been conducted and the results successfully evaluated. Preliminary specification for the national astronaut training and payload centre was established. Such capabilities may be used later on at European level in collaboration with ESA or other partners, like countries of the Visegrad (V4) Group.

The Definition Study Phase and the concluding Feasibility Review was conducted and closed. 6 of the baseline experiment data packages were approved, or approved with actions to enter the contract negotiations for the development phase (Phase B2/C). 24 project proposals were received for the HUNOR Open Call. Proposals were received in all the main scientific and technological areas of the HUNOR program, the main ones being cosmic rays and space dosimetry, materials testing and materials technology, space biology and space medicine, space nutrition, telecommunication technologies, and science outreach and education. Applicants included space industry companies, universities, research institutes, non-profit professional and educational organizations. 11 proposals addressed scientific and technological developments, 9 proposals addressed scientific and educational outreach activities, while the remaining 4 proposed laboratory experiments for ISS.

Remaining work

In 2023, the final four astronaut candidates will be identified and will start basic training. The Development Phase of the baseline experiments will be conducted concluding with the National Aeronautics and Space Administration (NASA) Phase II Safety Review and the Critical Design Review. The open call will be made permanently open and approved ideas will be included in the HUNOR R&D portfolio.

Related publication

[1] B. Zabori, O. Ferencz, A. Hirn, G. B. Magyari and K. V. Nagy: *The Hungarian Astronaut Program HUNOR*, Proceedings of the 73rd International Astronautical Congress, Paris, France, 18-22 September (2022)

NEAR-SPACE RADIATION MEASUREMENTS ON BOARD A STRATOSPHERIC RESEARCH BALLOON

Attila Hirn, Adél Malatinszky, Balázs Zábori

Objective

Several near-space radiation experiments were conducted by the Centre for Energy Research (EK) in the stratosphere on board research balloons and sounding rockets launched from Esrange Space Centre, Northern Sweden, above the Arctic Circle. The results have shown that further in-situ measurements are needed to better characterize the stratospheric space radiation environment for future space weather nowcast and forecast capabilities. The objective of the Radiation Monitoring System (RADMOS) experiment was to perform radiation measurements that are comparable to measurements performed a decade ago from the very same location with similar instrumentation and measurement platform.

Methods

Primary cosmic rays reaching the Earth interact with the magnetosphere and the atmosphere of the planet providing a complex radiation environment. Cosmic ray fluxes vary with geomagnetic latitude and solar activity. Significant spatial and temporal variations could be observed influenced by the effects of the space weather.

In the frame of the RADMOS project EK proposed radiation measurements by using existing technologies already available at the research centre from similar stratospheric balloon and sounding rocket experiments. The measurement platform of the TECHDOSE experiment, performed in 2012 in the frame of the European Space Agency's (ESA) Balloon Experiments for University Students (BEXUS) program, was adapted to the zero-pressure balloon of HEMERA, a research infrastructure funded by the Horizon 2020 framework. The Geiger–Müller (GM) counters flown in the RADMOS experiment were identical to the ones used in the TECHDOSE experiment, while the 3-axis silicon detector system, TRITEL, was replaced by a linear radiation telescope, RADTEL, developed for space weather missions and comprising fully depleted silicon detectors similar to those used in TRITEL. Adaptation of the TECHDOSE measurement platform, integration of RADTEL into the system and execution of the experiment in Northern Sweden was done by EK's space industry subcontractor, REMRED Ltd.

Direct comparison of the count rates provided by the Geiger–Müller counters in the TECHDOSE and the RADMOS experiments was made, whereas, in the case of the silicon detectors, dose rates in the second (300-µm-thick) detector in the RADMOS/RADTEL telescope could be compared with the TECHDOSE/TRITEL data (same detector thickness, similar lower discrimination levels).

Results

The maximum of secondary radiation generation (Regener-Pfotzer maximum, RP maximum) was determined by fitting a 2nd order polynomial to the count rate data versus altitude of the balloon. Count rates measured by the GM counters in the RADMOS experiment are shown in Fig. 1. Comparison of the values of the RP maxima in the case of the TECHDOSE and the RADMOS experiment is given in Table 1. The mean planetary K (Kp_p) indexes for the duration of the flight are also included. The K_p index, ranging from 0 to 9, describes the global geomagnetic activity based on 3-hour ground-based measurements. Values below 4 indicate quiet geomagnetic conditions, whereas values greater than 4 indicate storm-level geomagnetic activity.

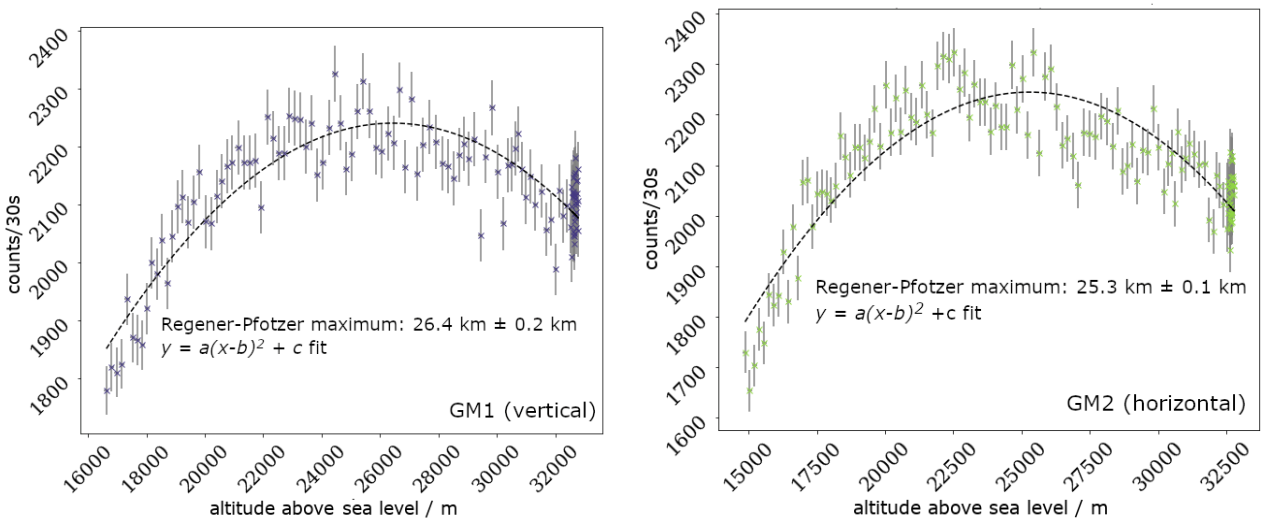

Figure 1: Count rates measured as function of altitude with a vertical and a horizontal GM counter

In both experiments, the RP maxima measured by the vertical GM counters were significantly higher than those with the horizontal ones (more sensitive in the zenith direction). The difference is due to the difference in the atmospheric thickness in the zenith direction and the direction of the horizon. The RP maxima during the RADMOS experiment were significantly higher than during the BEXUS experiment, which might be due to the difference in the space weather conditions.

The average dose rate calculated from the energy deposition spectra measured by the second (300-µm-thick) detector in the RADTEL telescope was 5.4±0.5 µGy/h and the value calculated from TRITEL measurements in the TECHDOSE experiment was (4.9 ± 0.2) µGy/h. The values are in good agreement considering that the average daily geomagnetic activity in the time of TECHDOSE did not differ significantly.

Table 1: Comparison of RP maxima during the TECHDOSE and the RADMOS experiments

Experiment	Mission	Date	Mean K_p index	Regener-Pfotzer maximum (km)	
				Vertical GM	Horizontal GM
TECHDOSE	BEXUS-14	24/09/2012	1.3 ± 0.8	22.4 ± 0.2	21.5 ± 0.2
RADMOS	SSC HEMERA ZPB 2022	07/09/2022	2.7 ± 0.7	26.4 ± 0.2	25.3 ± 0.1

Remaining work

Analysis of energy spectra measured with the RADTEL telescope will be performed in 2023.

Acknowledgment

The RADMOS Project is conducted in the frame of the ESA PRODEX Experiment Arrangement No. 4000128980 and utilized the HEMERA infrastructure and hence was supported by the European Commission in the frame of the UE Grant Agreement 730970.

DEVELOPMENT OF A COMPLEX SPACE DOSIMETRY SYSTEM FOR THE MARS SAMPLE RETURN MISSION EARTH RETURN ORBITER

Attila Hirn, Balázs Zábori, Boglárka Erdős, Gábor Albrecht, Julianna Szabó

Objective

The Mars Sample Return (MSR) campaign led by NASA/JPL (National Aeronautics and Space Administration / Jet Propulsion Laboratory) aims at conveying soil and atmospheric samples from the Mars surface to Earth by 2033. An important contribution of the European Space Agency (ESA) to the program is the Earth Return Orbiter (ERO) spacecraft. The Space Dosimetry System (SDS) experiment, composed of a space radiation monitor (RADTEL space radiation telescope) and a dosimetry monitoring system (TRITEL 3-dimensional silicon detector telescope), was proposed for ERO to monitor space radiation and related dosimetry quantities during the Earth-Mars cruise, in orbit around the Mars and during the trip back from Mars to Earth to support future human Mars missions. In year 2022, following the accomplishment of the definition study of the SDS, the preliminary experiment design was consolidated.

Methods

Engineering activities, including the electrical, the software, the mechanical and the thermal design, are performed by Hungarian sub-contractors with relevant space flight technology experience. Project management and product assurance requirements consolidation, roadmap development and experiment approach definitions, as well as radiation analyses are conducted by the Centre for Energy Research (EK).

Data product specification has been finalized based on scientific objectives and performance requirements. Albeit SDS provides primarily dosimetry information for future crewed interplanetary missions, and its radiation telescope is basically included to improve the quality of the dosimetry data products provided, the European space weather community has also expressed interest in the data provided by SDS, especially by that of the RADTEL telescope. Hence, requirements coming from ESA's space weather section have also been considered as far as feasible.

Finally, the updated preliminary design was reviewed by ESA experts to ensure that a robust and credible baseline experiment specification, design and plan exists to proceed into the critical design phase.

Results

In year 2022, the study phase was concluded with a successful feasibility review; the preliminary requirement specification, the instrument development roadmap and the experiment approach definition were delivered. A call was announced by ESA for the implementation of the project for which EK submitted a winning tender as a lead of a Hungarian space industry consortium. At the end of the reporting period, the consortium successfully passed the delta-preliminary design review and could enter into the critical design phase, at the end of which the design shall be frozen.

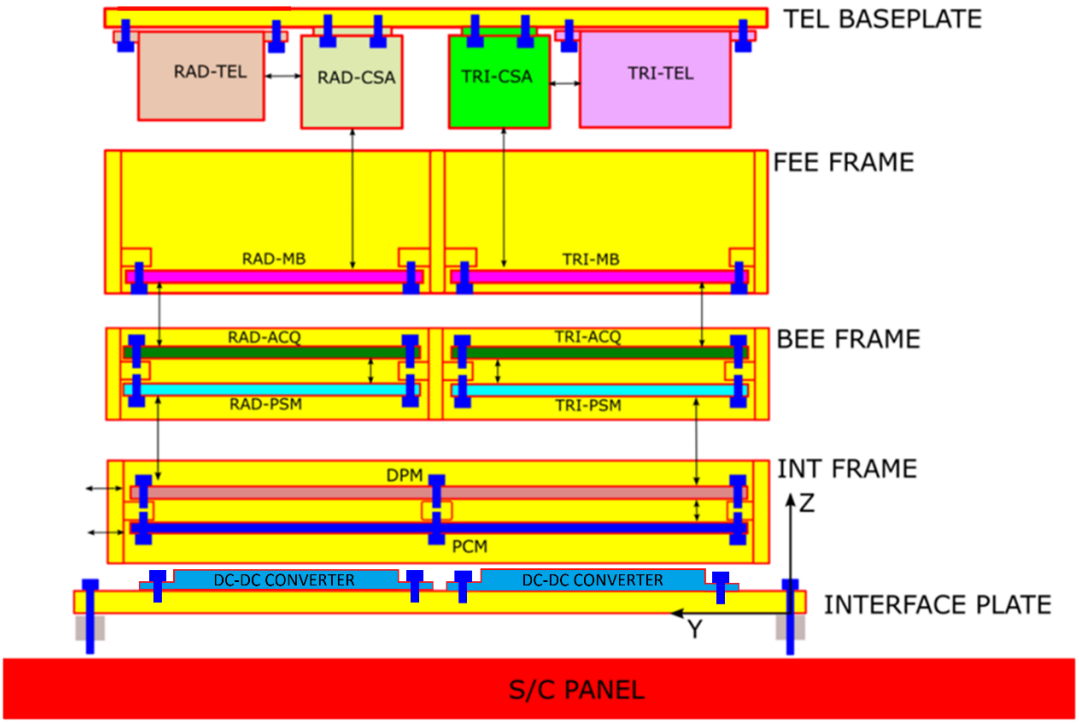

Figure 1: The main structural units of SDS on ERO

The SDS payload consists of five main structural units (Fig. 1), the Platform Interface Plate (PIP), the Interface Electronics frame (INT), the Back-End Electronics frame (BEE), the Front-End Electronics frame (FEE), and the Telescopes Baseplate (TEL). PIP provides the base for the whole SDS assembly, and it also accommodates the DC-DC converters. INT hosts a Digital Processing Module (DPM), which controls the instruments and provides scientific and housekeeping data for the ERO spacecraft, and a Power Converter Module (PCM), which converts the redundant 28 V input power to lower voltages. The BEE hosts the instrument power supply (TRI-PSU, RAD-PSU) and acquisition boards (TRI-ACQ, RAD-ACQ). The FEE is located above the BEE and hosts instrument motherboards (TRI-MB, RAD-MB). The FEE forms the instrument cavity and provides radiative surfaces. The Telescope Baseplate lays on the top of the SDS, above the FEE. It is a 3-mm-thick aluminium isothermal baseplate to host the TRITEL and RADTEL telescopes, and twelve Charge Sensitive Amplifier (CSA) boards. Operational temperature range is maintained by passive cooling through radiator surfaces, Multilayer Insulation (MLI) and active heating using Kapton foil heaters, and their sensors attached to the units' outer surfaces.

The raw (Level-0) data products provided by SDS in real time during the mission were defined in detail, including measurement ranges, time and energy resolution, binning (Table 1, Table 2). With 5-minute time resolution for energy deposition and linear energy transfer spectra, and 1-minute time resolution for each time spectra and RADTEL particle energy spectra (necessary in the case of solar particle events when particle fluxes change rapidly), the total data budget for 30 days, with 20% system margin, stays below 80 MB. 30 days are the duration for which the payload shall be capable of storing raw measurement data internally in the lack of data transmission to ground.

Table 1: SDS TRITEL Level-0 (raw science) data products

Data product groups	Depths (shielding at the telescope entrance window)	Range	Bins	Time resolution
Single detector total and coincidence energy deposition spectra	0 mm Al + MLI/ 1.2 mm Al / 13.1 mm Al	60 keV – 80 MeV (corresponding to: 0.2 keV/μm – 120 keV/μm in water)	128	300 s
Single detector total and coincidence time spectra		-	-	60 s

Table 2: SDS RADTEL Level-0 (raw science) data products

Data product groups	Depths (shielding at the telescope entrance window)	Range	Bins	Time resolution
Single detector total energy deposition spectra	0 mm Al + MLI/100 μm Si/ 400 μm Si/ 900 μm Si/ 3900 μm Si/ 4200 μm Si/ 4.2 mm Si + 7.0 mm Al	D1(100 μm): 150 keV- 126 MeV D2(300 μm): 60 keV- 84 MeV D3(300 μm): 60 keV- 84 MeV D4(3000 μm): 500 keV- 840 MeV D5(300 μm): 60 keV- 84 MeV D6(300 μm): 60 keV- 84 MeV	64	300 s
Energy spectra	0 mm Al + MLI	Protons: 3 MeV – 400 MeV	11	60 s
		Electrons: 0.3 MeV – 3.9 MeV	6	60 s
		He group: 3 MeV/n – 500 MeV/n	11	60 s
		CNO group: 6 MeV/n – 500 MeV/n	10	60 s
		Fe group: 63 MeV/n – 500 MeV/n	5	60 s
Single detector time spectra	0 mm Al + MLI/100 μm Si/400 μm Si/ 900 μm Si/ 3900 μm Si/ 4200 μm Si /4.2 mm Si + 7.0 mm Al	-	-	60 s
Proton, electron, He, CNO and Fe ions group time spectra	0 mm Al + MLI	-	-	60 s

Remaining work

In years 2023-2024, freezing of the system design responding to requirements, manufacturing, integration, verification and delivery will be performed.

Acknowledgment

The Definition Study of MSR-ERO-SDS was conducted in the frame of the ESA PRODEX Experiment Arrangement No. 4000132501. Implementation phase is financed in the frame of ESA Contract No. 4000137393/22/NL/DB.

IV. ENERGY SECURITY AND ENVIRONMENTAL STUDIES

CATALYTIC SYSTEMS FOR WATER ELECTROLYSIS

Tímea Benkó, Soma Keszei, Dávid Lukács, Sahir M. Al-Zuraiji, Krisztina Frey, Zsolt Kerner, Miklós Németh, Antal Koós, Levente Tapasztó, Tamás Ollár, József S. Pap

Objectives

Fe compounds as potential co-catalysts were immobilized on a bismuth vanadate semiconductor substrate to promote photoelectrochemical oxygen evolution from water and to reveal the role of the ancillary ligand.

Based on a thorough survey of the corresponding literature, several structurally homologue Cu complexes with redox-active ligands were thoroughly studied as catalysts for the Oxygen Evolving Reaction (OER) in order to understand dissolution and re-adsorption processes in the electrode reaction.

Molybdenum sulfide was decorated with Pt-nanoparticles to investigate the electrocatalytic capabilities of the composites in the Hydrogen Evolving Reaction (HER) and to highlight the mechanistic details. Four Fe(II) complexes containing bidentate ligands were also studied to understand how the predominant equilibrium species in solution affects the redox stabilisation of the reduced complex forms, and thus promotes HER. The work was supported by the NKFIH 132869/2019 and the NKFIH 128841/2018 grants, as well as the RRF-2.3.1-21-2022-00009 and the TKP2021-05 projects.

Methods

Synthesis of the Cu and Fe compounds was done according to published procedures. Electrochemical experiments were performed on a Bio-Logic SP-150 potentio-galvanostat. Boron Doped Diamond (BDD), Glassy Carbon (GC), Indium Tin Oxide (ITO), Fluorine-Doped Tin Oxide (FTO), or $BiVO_4$/FTO were used as working electrodes. For the HER, 2D-$MoS_{2-x}O_x$ was prepared on a Highly Oriented Pyrolytic Graphite (HOPG) support by the Chemical Vapour Deposition (CVD) method. Decoration with Pt was accomplished by electrodeposition.

The applied electrochemical methods were Linear Sweep- (LSV), Cyclic- (CV) and Square Wave Voltammetry (SWV), Electrochemical Impedance Spectroscopy (EIS) and Controlled Potential Electrolysis (CPE). Quantitative gas analysis of the O_2 and H_2 that was produced was done using a Shimadzu Tracera 2010 gas chromatograph, or an optical probe (Ocean Optics FOXY). The surfaces of the electrodes were analysed by Scanning Tunneling Microscopy (STM), X-ray Photoelectron Spectroscopy (XPS), Scanning Electron Microscopy (SEM) with Energy Dispersive X-ray (EDX), and Raman and infrared (IR) spectroscopy.

Results

Photoelectrochemical water splitting can be made more efficient by grafting co-catalysts on semiconductors which improve the interfacial OER. We used a simple non-noble metal pre-catalyst, $[Fe^{II}(PBI)_3]^{2+}$ (PBI is the 2-(2′-pyridyl)benzimidazole ligand) for this purpose on a nanopyramidal $BiVO_4$ semiconductor that was morphologically optimal for efficient light harvesting, but whose performance suffered from V-poor surface recombination sites. The $[Fe^{II}(PBI)_3]^{2+}$ transformed *in situ* to α-Fe_2O_3 nanoparticles on the V-vacant areas of $BiVO_4$, thus mending their photocurrent-limiting effect. Photoelectrochemistry at pH 8.3 confirmed that the α-Fe_2O_3 co-catalyst improved the charge transfer efficiency by an order of magnitude, suppressed the recombination in the bulk and reduced the charge transfer resistance. Overall, the α-Fe_2O_3 suppressed the recombination on the V-poor surface, while at high potentials it provided high-valent centers for the oxygen evolution. The resulting photocurrent density far exceeding that of $BiVO_4$ or of samples modified by $FeCl_3$ or $Fe(NO_3)_3$ underlines the metallochaperone-like effect of the PBI ligand [1].

Earlier, we have explored the redox-active and proton acceptor role of an isoindoline-based pincer ligand in electrocatalytic OER. Inspired by our findings, an overview focusing on redox cooperation between ligands and metals has been published [2]. Based on these preliminary studies, six structurally characterized Cu(II)-1,3-bis(arylimino)isoindoline complexes were investigated as potential water oxidation electrocatalysts and these studies revealed phenomena that helped elucidate the role of catalyst inhomogeneity. In the presence of bases, most of the compounds became insoluble in non-aqueous solvents, indicating a hydroxide complex form potentially relevant in OER electrocatalysis. With the immobilization of the complexes on ITO, during electrolysis in a buffered aqueous medium, a desorption-dissolution process produced micron-sized particles in chemical equilibrium with the dissolved monomeric forms. The re-adsorption process was hindered in borate buffer with pH 9.2, which allowed simplifying the problem on the dissolution product as the catalytically relevant species. At optimized concentration, the compounds could be ranked into two groups: those behaving as true immobilized molecular catalysts and those acting as a precursor a heterogeneous catalyst reflected in the lowered Faraday efficiency. A simple evaluation method was presented for the estimation of the lowest possible values of catalytic rates. The long-term stability of the immobilized molecular catalysts could be attributed to the redox-active pincer ligands that stabilize the metal centre in the copper(II) state over the catalytic cycle.

Concerning the HER electrocatalysis, the performance of Pt as a co-catalyst is beyond compare [4]. However, due to evident considerations, non-noble metal alternatives are intensely sought to catalytically activate the cathode. For this purpose, we investigated four Fe(II) complexes containing the bidentate ligands 2-(2′-pyridyl)benzoxazole (PBO, $\mathbf{L^O}$), 2-(2′-pyridyl)benzthiazole (PBT, $\mathbf{L^S}$), 2-(2′-pyridyl)benzimidazole (PBI, $\mathbf{L^{NH}}$) and 2-2′-bipyridyl (bpy, $\mathbf{L^{py}}$). In the ligand series, a

heterocyclic donor group by the 2-pyridyl function was systematically changed which was expected to define the predominant equilibrium species in solution and affect the redox stabilisation of the reduced complex forms. In fact, the differences in the redox behaviour of the compounds in acetonitrile correlated with the basicity of the ligands. Addition of trifluoroacetic acid as a proton source suggests that the **FeL^{S,O,NH}** complexes act as homogeneous catalysts with activities from k_{obs} (s^{-1}) = 0.03, 1.1 and 10.8 s^{-1} at overpotentials of 0.81, 0.76 and 0.79 V, respectively. The activity can be associated with the $[Fe(\mathbf{L^n})_2(S)_2]^{2+}$ form, where S stands for a monodentate solvent or substrate ligand. Kinetic studies and controlled potential electrolysis were used to explore the structure-activity relationships for the complexes. In contrast, **FeL^{py}** is inactive in catalysis, due to the persistence of the low spin $[Fe(\mathbf{L^n})_3]^{2+}$ species the reaction mixture [5].

Related publications

[1] T. Benkó, S. Shen, M. Németh, J. Su, Á. Szamosvölgyi, Z. Kovács, G. Sáfrán, S. M. Al-Zuraiji, A. Sápi, Z. Kónya, J. S. Pap: *$BiVO_4$ charge transfer control by a water-insoluble iron complex for solar water oxidation,* Appl. Cat. A (under review)

[2] T. Benkó, D. Lukács, M. Li, J. S. Pap: *Redox-Active ligands in artificial photosynthesis: a review,* Environ. Chem. Lett. **20,** 3657–3695 (2022) https://doi.org/10.1007/s10311-022-01448-3

[3] D. Lukács, T. Benkó, É. Kováts, N. May, L. Vayssieres and J. S. Pap: *Investigation of copper(II)-1,3-bis(arylimino)isoindoline complexes in water oxidation catalysis (work title)*, Catalysts, manuscript (80%)

[4] …, T. Ollár, J. S. Pap, A. Koós, L. Tapasztó: ready to submit

[5] S. Keszei, T. Ollár, M. Németh, K. Frey, L. Tapasztó, J. S. Pap: *Electrocatalytic hydrogen evolution by iron(II) complexes with bidentate aromatic N-donor ligand,* Dalton Trans., manuscript (90%)

CATALYTIC METHANE CONVERSION TO HYDROGEN OR SYNGAS

Andrea Beck, Miklós Németh, Tamás Korányi, Anita Horváth

Objective

Catalyst developments for the CO_2-free exploitation of the abundantly available natural gas/biogas producing i) syngas by methane dry reforming (DRM: $CH_4+CO_2 \rightleftharpoons 2CO+2H_2$) and (ii) H_2 and solid carbon by methane pyrolysis ($CH_4 \rightleftharpoons C+2H_2$) were continued.

Methods

For use in DRM reactions, new Ni or Ni-In/CeO_2 catalysts having various CeO_2 morphologies (cubic, polyhedral or commercial Aldrich ceria nanopowder) were prepared by wet impregnation, producing 3 wt% Ni and 0.3 wt% In loadings similar to our previous CeO_2-Al_2O_3 supported catalyst samples. Aldrich CeO_2 supported Ni and Ni-In samples were also prepared by the Deposition Precipitation (DP) method for comparison with the properties of the analogous CeO_2-Al_2O_3 supported catalysts published last year. The samples were calcined (650°C/air/2h) and then reduced (650°C/H_2/1h). Structural investigations were performed by Temperature Programmed Reduction (TPR) of the calcined samples and by CO adsorption on the reduced samples, followed by Diffuse Reflectance Infrared Fourier Transform (DRIFT) spectroscopy.

The three bimetallic Ni-Mo/MgO samples (7wt%Ni with Mo/Ni atomic ratio of 0.4 prepared at room temperature, 7wt%Ni with Mo/Ni=0.4 and 1.2 ratios prepared at 80 °C) and monometallic 7wt%Ni/MgO and 13 wt% Mo/MgO catalysts prepared and studied in methane pyrolysis last year were now investigated in more detail by X-ray Photoelectron Spectroscopy (XPS) in reduced states and by Raman spectroscopy after the pyrolysis reaction.

Preliminary experiments were done to introduce the "one-sample concept" microcombinatorial Transmission Electron Microscopy (TEM) method (developed and patented in EK) into catalysis research. According to this concept, as a first step, Ni films of linearly increasing thickness were grown on various TEM grids by DC magnetron sputtering. Then, these microcombinatorial samples were characterised by TEM in the as prepared state and again after a 600°C treatment in 10%H_2/Ar for 1h (to get a metallic Ni surface for the methane activation step). The final aim here is to optimize the composition of Ni based bimetallic catalysts for methane pyrolysis or dry reforming catalytic processes.

Results

Nickel oxide in the calcined CeO_2 supported samples could be reduced at temperatures below 450°C in all cases, e.g. at a much lower temperature than for the CeO_2-Al_2O_3 supported samples. The differing TPR profile of the CeO_2 supported materials produced by the two above mentioned preparation methods indicates a variation in the Ni or Ni-In particle sizes and also differences in the metal-support interaction. In accordance with this, the IR spectrum of the CO adsorbed on the reduced catalysts show significant differences in the positions and the intensity ratio of bridge and linear CO bands. In all bimetallic samples the Ni-In interaction was proven by the typical CO bands and their desorption phenomena during temperature increase.

The methane pyrolysis activity and lifetime of the three bimetallic Ni-Mo catalysts (a spectacular synergistic effect was detected last year) correlated well with the relative Mo/Ni surface concentrations determined by XPS. The detailed analysis of the Raman spectra suggests that the small amount of carbon formed on Ni/MgO and Mo/MgO is probably a 1-2 layer graphene and a highly defective nanographite type, respectively, with some amorphous carbon in both cases. The large amount of carbon produced by the bimetallic catalysts were dominantly defective multiwalled carbon nanotubes (MWCNT) with some amorphous carbon (more where the MWCNTs were more defective).

As for the microcombinatorial TEM approach, the sample production method and layer stability was studied by linearly increasing the size of monometallic Ni particles on carbon coated Au or Mo and non-coated Mo grids. Evaporated SiO_x thin films were applied as a barrier to avoid the interaction of Ni particles with the carbon layer on the TEM grid. Isolated Ni particles in the 2-25 nm size range were successfully produced, but above 25 nm size the particles were joined with each other. However, during the high temperature reduction pretreatment to get the metallic Ni sites needed for CH_4 dissociation, onion-like graphene layers were formed around Ni particles on carbon containing grids which is undesireable and could cause inactivity in the next methane activation step. Though Ni particles on the SiO_x overlayer on the bare Mo grid remained intact, this SiO_x film was not stable under electron beam bombardment. This means that such grids cannot be used for the catalytic optimisation. Thus, commercial Au grids with SiO_x will be purchased and used for further experiments.

Remaining work

Concerning DRM, the catalytic tests of the CeO_2 supported samples are still to be done. Assembly of the catalytic test station implemented with a precise, low flow liquid pump for bi-reforming is necessary. A paper on the methane pyrolysis results will be completed and submitted.

Related publications

[1] T.I. Korányi, M. Németh, A. Beck, A. Horváth: *Recent Advances in Methane Pyrolysis: Turquoise Hydrogen with Solid Carbon Production*, Energies **15,** 6342 (2022) https://doi.org/10.3390/en15176342

[2] A. Horváth, M. Németh, A. Beck, A. Pintar, V. La Parola: *Improvement of Ni-based catalysts via Indium promotion for dry reforming of methane* (oral presentation), 15th Pannonian International Symposium on Catalysis, 4-8.09.2022, Jastrzebia Gora, Poland

[3] A. Horváth, M. Németh, A. Beck, Gy. Sáfrán, G. Žerjav, A. Pintar: *Study of Metal-Support Interactions in Different Ni-In/CeO_2 Catalysts Designed for Methane Dry Reforming,* poster presentation, 28th Annual Meeting of the Slovenian Chemical Society, 21-23 September 2022, Portoroz, Slovenija

[4] A. Horváth, A. Beck, M. Németh, Gy. Safran, Zs. Horváth, T. Korányi: *Methane pyrolysis on NiMo/MgO catalysts: the influence of bimetallic nature on the carbon formation process*, manuscript under preparation

[5] B. Kalas, Zs. Zolnai, G. Sáfrán, M. Serényi, E. Agocs, T. Lohner, A. Németh, M. Fried, P. Petrik: *Micro-combinatorial sampling of the optical properties of hydrogenated amorphous $Si_{1-x}Ge_x$ for the entire range of compositions towards a database for optoelectronics:* www.nature.com/Scientific Reports **10,** 19266 (2020) https://doi.org/10.1038/s41598-020-74881-5

MONITORING OF ANTIBACTERIAL ACTIVITY IN RADIATION-INDUCED DEGRADATION OF SELECTED ANTIBIOTICS IN FOUR MATRICES

László Wojnárovits, Tünde Tóth, Krisztina Kovács, László Szabó, Renáta Homlok, Erzsébet Takács

Objective

To reduce the spread of antibiotic resistant bacteria, the elimination of antibiotics from purified wastewater is an important task. Purified wastewater contains a large variety of organic/inorganic compounds that strongly influence the efficiency of Advanced Oxidation Processes (AOP). In this study, we studied the elimination by irradiation of two frequently used β-lactam type antibiotics, oxacillin and cloxacillin and two tetracyclines, tetracycline and chlortetracycline. We investigated and compared the antibacterial activity in 0.1 mmol dm^{-3} concentration solutions after high-energy irradiation treatment in four different water matrices.

Methods

Samples containing a 0.1 mmol dm^{-3} antibiotic concentration were irradiated with 0.5, 1, 2 and 4 kGy doses in pure water, tap water, synthetic wastewater and purified wastewater matrices. The antibacterial potency of untreated and irradiated samples were investigated in agar diffusion tests. For the agar diffusion tests the Staphylococcus aureus strain (B.01755) was received from the National Collection of Agricultural and Industrial Microorganisms (NCAIM). The microbiological work was carried out under sterile conditions. In the agar diffusion assay, 1 cm^3 of the Staphylococcus aureus bacterial suspension at 10^6 CFU cm^{-3} (Colony Forming Unit) concentration and 25 cm^3 of Tryptone-glucose-yeast extract (TGYE) agar were mixed and poured into a Petri dish. Holes were punched in the agar (after the agar had solidified) using a metal tube with a diameter of 4 mm and the holes were filled with 0.08 cm^3 of antibiotic solution of 0.1 mmol dm^{-3} concentration. The samples were allowed to diffuse into the agar for 24 h in a 37 °C incubator.

Results

The antibiotic-containing solution was placed into the punched hole on the agar plate seeded with the test bacteria (Staphylococcus aureus strains). If the solution diffusing into the agar layer has antibacterial activity, a visible inhibition zone appears around the hole. The antibacterial activity, as usual, is characterized by the inhibition zone, defined as the diameter of the zone minus the hole diameter. Absence of any inhibition zone indicates the absence of any antibacterial effect. When the non-irradiated antibiotic solutions were tested in this way, inhibition zones with 17–31 mm diameters appeared around the punched 4 mm holes (Figure 1).

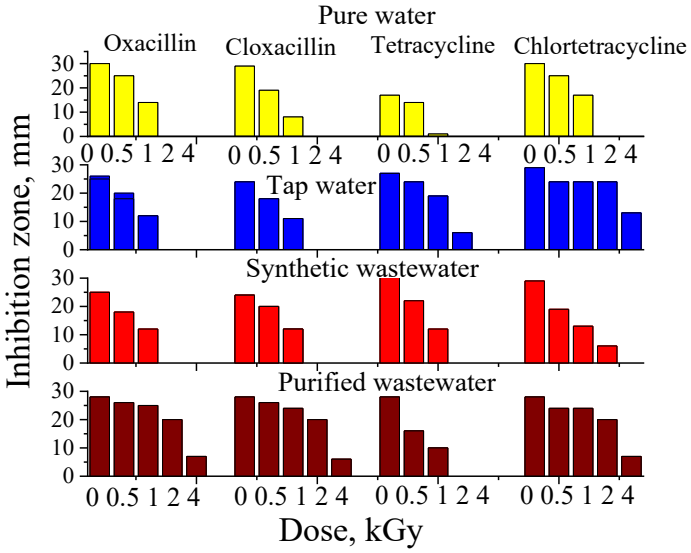

Figure 1: Inhibition zones in agar diffusion tests (mm) measured with 0.1 mmol dm^{-3} antibiotic solutions using Staphylococcus aureus strain (B.01755)

For the irradiated solutions, the diameters were smaller and in many cases, the inhibition disappeared when the dose was higher than 1 kGy. This was not true for oxacillin, cloxacillin, and chlortetracycline solutions prepared in purified wastewater matrices, where the halo around the punched hole was present even for solutions irradiated with a 4 kGy dose. In these solutions, due to the higher and (in AOP) poorly degradable organic molecule content of the matrix, either the degradation of

the antibiotic was decreased, or the purified and irradiated wastewater itself had antibiotic properties. Interestingly, we did not observe this phenomenon in the tetracycline solution prepared in purified wastewater. In the chlortetracycline tap water solution, the antibacterial activity also very slowly disappeared with the absorbed dose. These phenomena need further clarification in the future. The results of these diffusion tests indicate that the wastewater degradation products may have antibacterial potency, although a more accurate method, such as a broth microdilution assay would be necessary to confirm this.

Remaining work

We would like to extend our studies to a sensitive and a resistant *E. coli* strain.

Related publications

[1] R. Homlok, G. Kisko, A. Kovacs, T. Toth, E. Takacs, Cs. Mohacsi-Farkas, L. Wojnarovits, L. Szabo: *Antibiotics in a wastewater matrix at environmentally relevant concentrations affect coexisting resistant/sensitive bacterial cultures with profound impact on advanced oxidation treatment,* Science of the Total Environment **754,** 142181 (2021)

[2] E. Takács, J. Wang, L. Chu, T. Tóth, K. Kovács, A. Bezsenyi, L. Szabó, R. Homlok, L. Wojnárovits: *Elimination of oxacillin, its toxicity and antibacterial activity by using ionizing radiation,* Chemosphere **286,** 131467 (2022)

[3] L. Wojnárovits, JL. Wang, LB. Chu, T. Tóth, K. Kovács, A. Bezsenyi, L. Szabó, R. Homlok, E. Takács: *Matrix effect in the hydroxyl radical induced degradation of ß-lactam and tetracycline type antibiotics*. Radiation Physics and Chemistry: The Journal for Radiation Physics Radiation Chemistry and Radiation Processing **193,** 109980, 10 (2022)

CHARACTERISTICS OF AEROSOL PARTICLES DURING NON-MACHINING METAL MANUFACTURING

Szilvia Kugler, Endre Börcsök, Árpád Farkas, Péter Füri, Veronika Groma, János Osán

Objective

During the Additive Manufacturing (AM) processes, printing and casting of heavy non-ferrous metal alloys, mainly fine (d < 2.5 μm) and ultrafine (d < 100 nm) aerosol particles are produced. These aerosol particles are very small, but might have large surfaces, and hence could be highly dangerous to the operators of these activities. The aim of the present work was the physical and chemical characterization of the emitted aerosol particles (particle size distribution, shape, elemental content) during these activities in an industrial environment with an air extraction system. The oxidation state of metals was studied for aerosol samples collected near a 3D metal printer operated in the laboratory without an air extraction device.

Methods

The properties of the emitted aerosol particles were determined for two metal manufacturing processes in an industrial environment. One was a 3D metal printing process using H13 stainless steel feedstock powder, and the other was a tin casting process using both tin based metal blocks and powder. Previously the same 3D printer was applied in a small room of 26 m^2 without any air extraction system in laboratory. Size fractionated aerosol samples were collected with a 5-stage Sioutas cascade impactor. An Aerosol Particle Counter (APC) was operated in parallel to monitor particle mass and number concentrations in the 0.25–30 μm size range. Air extraction devices were operating at both industrial sites during the aerosol sampling. Elemental composition and morphology of the particles was determined by Total-Reflection X-Ray Fluorescence (TXRF) analysis and Scanning Electron Microscopy (SEM), respectively. X-ray Absorption Near-Edge Structure spectroscopy (XANES) at the XRF beamline of Elettra (Trieste, Italy) was used to determine the oxidation state of the metals in the aerosol samples of both the industrial and the laboratory environments.

Results

Particulate Matter (PM) monitoring results obtained by the APC at the two industrial sites revealed that mass concentrations were almost constant during the AM process, but were quite variable during Sn melting, depending on the phase of the process (preheating, loading and melting). Regarding the AM process in industrial conditions, the PM_1/PM_{10} mass ratio was found to be 0.85, which is in line with the laboratory experiments, where the vast majority of the emitted particles were below 100 nm using the same feedstock powder (H13 tool steel) [1,2]. APC results for the Sn melting were different, showing a PM_1/PM_{10} mass ratio of 0.11, which indicates the dominance of larger particles, mainly due to the resuspension of the loaded powder. TXRF results of the size-fractionated samples show that the main metals of the starting materials (Fe and Ni for AM and Sn and Pb for tin melting) had the highest concentration in the 2.5–10 μm fraction (Table 1). The concentration of Ca was comparable to that of Fe and Sn in both types of process. For AM, Ca originated from resuspension of dust originally present on the floor of the hall. For Sn melting, lime powder was added to the melt. For the AM process, in the size fraction under 1 μm, the Fe (and Cr and Mn) concentration increases with decreasing particle size in accordance with the laboratory results [1]. Regarding the Sn melting, the Pb and Bi content of the aerosols are also elevated, with the Bi/Pb ratio increasing with increasing particle diameter (Table 1).

A high enrichment of Cr and Mn was detected mainly in the lowest aerosol size fractions (0.07-0.25 μm) in the laboratory 3D printing experiments using H13 feedstock powder, mainly due to their high vapour pressure [1]. The average oxidation state of the following metals in different fractions was found to be +2.4 for Mn, +2.1 for Cr and +1.3 for Fe in the total aerosol, the most oxidized being in the ultrafine and the less oxidized being in the coarse fraction [1]. Regarding the Fe oxidation state of aerosols collected during the AM process using H13 feedstock powder, iron was more oxidized in the industrial aerosols in both the 0.25–0.5 μm and 2.5–10 μm fractions than in laboratory conditions.

Table 1: Elemental content of the aerosol particles during different activities

Elements	Concentration (ng/m³) during AM				Concentration (ng/m³) during Sn melting			
	0.25–0.5 μm	0.5–1 μm	1–2.5 μm	2.5–10 μm	0.25–0.5 μm	0.5–1 μm	1–2.5 μm	2.5–10 μm
Ca	7.1	7.0	7.1	14.5	166.5	271.7	661.0	1036.9
Cr	0.5	0.2	0.3	1.6	0.3	0.4	0.5	0.7
Mn	0.4	0.2	0.1	0.3	0.3	0.5	0.7	0.8
Fe	6.4	3.8	3.9	12.5	6.7	8.8	18.0	26.0
Ni	0.1	0.2	0.2	1.8	0.5	0.8	1.5	13.7
Sn					355.6	541.1	1389.5	2970.1
Pb	0.3	0.1	0.0	0.0	3.3	4.8	13.8	28.2
Bi					1.2	1.9	5.7	43.2

Related publications

[1] L. Péter, J. Osán, Sz. Kugler, V. Groma, S. Pollastri and A. Nagy: *Comprehensive Analysis of Two H13-Type Starting Materials Used for Laser Cladding and Aerosol Particles Formed in This Process,* Materials **15(20),** 7367 (2022)

[2] A. Nagy, Sz. Kugler, L. Péter, J. Osán, V. Groma and A. Czitrovszky: *Characterization of particle formation in intense laser-metal interaction, International Aerosol Conference, 05 09– 09 09 2022, Athens, Greece, AT-P3_007 (2022)*

BIOGENIC CARBON CONTENT DETERMINATION OF CATALYTICALLY CONVERTED BIOMASS MATERIALS

Tamás Korányi

Objective

The aim of this present study was the optimization of direct Liquid Scintillation Counting (LSC) measuring conditions for biomass originated samples for the determination of the biogenic carbon content of catalytically converted biomass.

Methods

The determination of the biocarbon content relative to fossil carbon in biomass containing Diesel fuels by radiocarbon (^{14}C) LSC was our goal. This determination depends on the fact that there is no ^{14}C in the fossil-carbon. The product mixture was dissolved directly in the scintillation cocktail and its biogenic carbon content was measured with a Tri-Carb 4810 TR LSC equipment. This method is only applicable using colourless or slightly coloured samples.

Results

Jenő Hancsók (Prof. Emeritus, Pannon University) provided to our group various diesel fuel samples with 0-10 % biocarbon content. The aim of these investigations was to determine the reliability of biogenic carbon content determination on these samples by our radiocarbon LSC method. Several samples were measured, the measuring conditions were varied systematically and they were optimized. Samples around 10 wt% biocomponent content provided reliable results with a less than 5 % dpm (disintegration per minute) error.

Remaining work

The Accelerator Mass Spectrometry (AMS) method is recommended in ASTM standards for the determination of biogenic carbon content of fuels. We plan to measure the biocarbon content of some of these samples by AMS in cooperation with Mihály Molnár (Atomki, Debrecen) in order to compare the precision of ^{14}C detection on biomass originated samples by LSC and AMS.

Related publications

[1] T.I. Korányi, B. Fridrich, A. Pineda and K. Barta: *Development of 'Lignin-First' Approaches for the Valorisation of Lignocellulosic Biomass,* Molecules **25**, 2815 (2020)

[2] A. Deneyer, E. Peeters, T. Renders, S. Van den Bosch, N. Van Oeckel, T. Ennaert, T. Szarvas, T.I. Korányi, M. Dusselier and B.F. Sels: *Direct Upstream Integration of Biogasoline Production into Current Light Straight Run Naphtha Petrorefinery Processes*, Nature Energy **3**, 969-977 (2018)

[3] J. Hancsók, T. Kasza and O. Visnyei: *Isomerization of n-C5/C6 Bioparaffins to Gasoline Components with High Octane Number*, Energies **13**, 1672 (2020)

[4] J. Hancsók, O. Visnyei, A. Holló, L. Leveles, A. Thernesz, G. Varga and J. Valyon: *Alternative Diesel Fuels with High Hydrogen Content in their Molecular Structures,* Renewable Energy **142**, 239-248 (2019)

DEGRADATION OF THE BETA-BLOCKER NADOLOL USING HIGH ENERGY IONIZING RADIATION IN AQUEOUS SOLUTIONS AND COMPARISON WITH THE REACTIONS OF PROPRANOLOL

Krisztina Kovács, Renáta Homlok, Tünde Tóth, Erzsébet Takács, László Wojnárovits

Objective

In our previous study we have investigated the radical reactions of the beta-blockers (Atenolol and Propranolol) [1,2]. As a continuation of these studies in 2022 we investigated the radiolytic degradation processes of another beta-blocker, Nadolol by pulse radiolysis with electron beam and gamma radiolysis, and compared it to the results obtained during the degradation of Propranolol.

Methods

Radiolysis experiments were performed in order to investigate the radical induced degradation reactions of Nadolol at 0.1 mmol dm^{-3} initial concentration. The transient intermediates of the degradation reactions were studied by pulse radiolysis technique using 4 MeV accelerated electrons with a pulse length (pulse duration) of 800 ns and an optical system with a 1 cm path length cell utilizing kinetic spectrophotometric detection. Radical scavenging (redox) experiments were used to identify and quantify the participating free radicals.

In the end-product experiments the irradiation was done in a panoramic type ^{60}Co-γ irradiation chamber (dose rate 10 kGy h^{-1}) under different conditions in order to study the effects of each radical. The starting molecules and their degradation products were characterized by the standard measurements we use in waste water analysis including UV-Vis spectrophotometry, Chemical Oxygen Demand (COD), Total Organic Carbon content (TOC) and toxicity measurements. The effect of reactive species (e_{aq}^-, •OH, H•) from the radiolysis of water on the degradation process was studied using a JASCO 550 UV-Vis spectrophotometer with a 1 cm long (path length) cell. The oxidation and mineralization reactions were monitored by COD and TOC measurements as a function of the absorbed dose using Behrotest TRS 200 and Shimadzu TOC-L CSH/CSN equipment, respectively. The toxicity of Nadolol and its degradation products were characterized to get a picture about the environmental impact of degradation products. The test organism used to measure this impact was *Vibrio fischeri* marine luminescent bacteria.

Results

Nadolol is one of the beta-blockers used for treatment of cardiovascular diseases. Similar to other beta-blockers, there is an oxypropanolamine side chain connected to the aryl group containing two polar OH groups in the case of our studied compound (Fig. 1). There are no radiolytic degradation results on Nadolol yet in the literature.

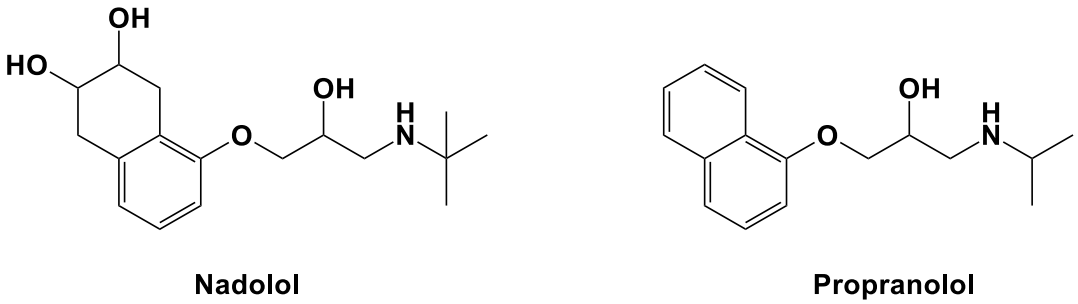

Figure 1: The chemical structure of Nadolol and Propranolol

In electron beam radiolysis experiments the reactions between Nadolol and •OH were investigated thoroughly at pH 7 and 12, supplemented by redox measurements (Fig. 2). At pH 7 the side chain is in protonated form with higher reactivity than in the deprotonated form. The preferred reaction takes place on the aryl ring *via* formation of hydroxycyclohexadienyl type radicals similar to Propranolol. Based on the chemical structure of the oxypropanolamine α-aminoalkyl, aminium, aminyl and ketyl type radicals may also form in •OH reactions. The presence of α-aminoalkyl, aminium and aminyl type radicals was confirmed by our measurements which show that pH may have an effect on the reactivity of the side chain. The rate constants of •OH reactions were 7.08×10^9 and 7.55×10^9 mol^{-1} dm^3 s^{-1} for Nadolol and Propranolol, respectively. Propranolol, possessing a condensed aromatic ring, has higher reactivity towards •OH.

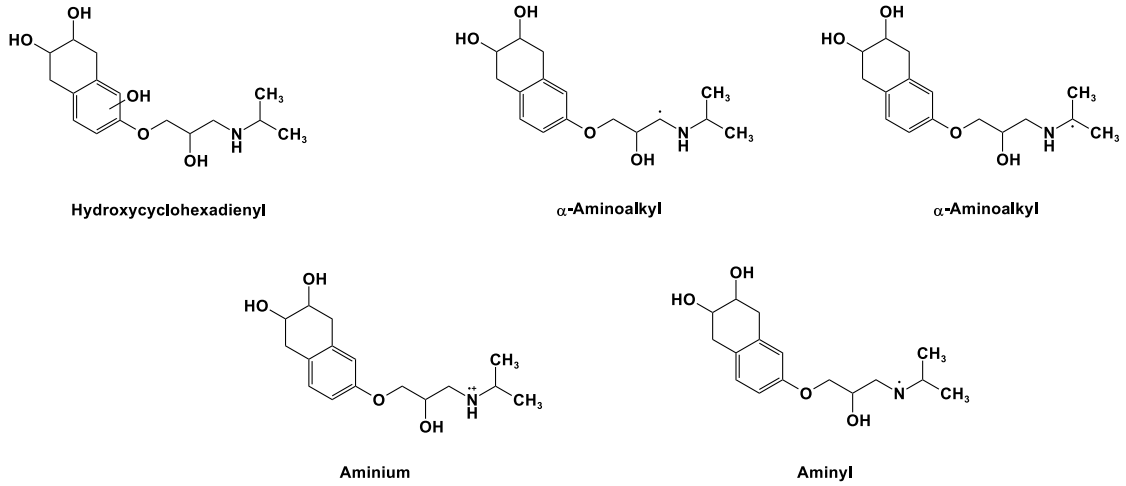

Figure 2: Possible radicals forming in •OH reaction with Nadolol

During the investigation of different reactive species formed in water radiolysis (•OH, e_{aq}^-, H•), the reactions with•OH were the most favoured for both Nadolol and Propranolol. The characteristic aromatic peaks in the UV-Vis spectra disappeared at 1 kGy or at more absorbed dose. The e_{aq}^- reactions were found to be highly various. The reaction between Propranolol and e_{aq}^- is almost as intensive as for the •OH reactions. However, e_{aq}^- degrades Nadolol slowly.

Oxidation and mineralization processes take place in parallel. Their rates were measured to be: 13 mg dm^{-3} O_2 kGy^{-1} and 1.4 mg dm^{-3} C kGy^{-1}, respectively. Compared to other beta-blockers possessing a simple aromatic ring like atenolol, oxidation and mineralization take place with higher rates in the cases of Nadolol and Propranolol. The presence of two OH groups on the aryl group for Nadolol and the condensed ring having high electron density in Propranolol may cause increased reactivity during degradation.

Based on the toxicity tests, the degradation products formed at low doses showed higher toxicity than the starting molecules in the cases of both compounds. Products forming from degradation of Propranolol were proven to be more toxic than those of Nadolol due to the formation of substituted naphthalene derivatives. Elimination of Nadolol and Propranolol can be achieved effectively using appropriate doses *via* radiolytic reactions.

Remaining work

During previous studies we obtained a wide-spread picture about radiolytic degradation processes of different beta-blockers. We intend to continue our work regarding the beta-blockers, looking for a relationship between the degradation efficiency and the chemical structure. Moreover, we plan to investigate in-detail the effect of the water matrix in degradation processes.

Related publications

[1] K. Kovács, Á. Simon, T. Tóth, L. Wojnárovits: *Free radical chemistry of atenolol and propranolol investigated by pulse and gamma radiolysis*, Radiation Physics and Chemistry **196**, 110141 (2022)

[2] K. Kovács, T. Tóth, L. Wojnárovits: *Evaluation of Advanced Oxidation Processes for ß-blockers degradation: a review*, Water Science and Technology **85 (2)**, 685 (2022)

VULNERABILITY ANALYSIS OF POWER GRIDS USING COMPLEX NETWORK ANALYSIS

Bálint Hartmann, Tamás Soha, Viktória Sugár

Objective

The project aims to contribute to the line of work, that was started in 2019, which focuses on the analysis of the vulnerability of power grids, using complex network analysis and geoinformatics.

Methods

The authors have assembled network data as a function of time using officially published data of transmission system operators, historical maps and yearbooks, and websites of selected research communities. Since none of the sources were consistent, some pre-processing and standardization of the data had to be made. In the database, a new node was created when a substation was first constructed, regardless of the installed switchgear and the type of the busbar. A new edge was created when a power line was put into operation. Power (or transmission) lines used by two systems are handled as single connections. Graph representations were made for each year, with the nodes being the power generators, transformers and substations, and the edges being transmission lines. From these graphs, as inputs, the authors have calculated the outputs of node degree distribution and average node degree, the diameter, the modularity metric, the average path length, the clustering coefficient and the small-world metric. Some of these outputs are related to measures of system vulnerability.

Results

The project made significant progress in two areas of the work. First, the simulation framework of the complex network analysis tools was generalized. The structure of the network database was redesigned. A set of MATLAB scripts were created to make automatic the calculations for a larger number of networks. The indices of vulnerability to be analyzed were selected. Second, the historical network database for four countries was extended to the Dutch and the Spanish power grids via international cooperation with Rens Baardman and José Lois Vázquez. An analysis of the latter networks was also finished and has supported the previous findings of the researchers that the small-world properties of power grids are the results of evolutionary processes and the existence of different voltage levels, and not of increase in network size.

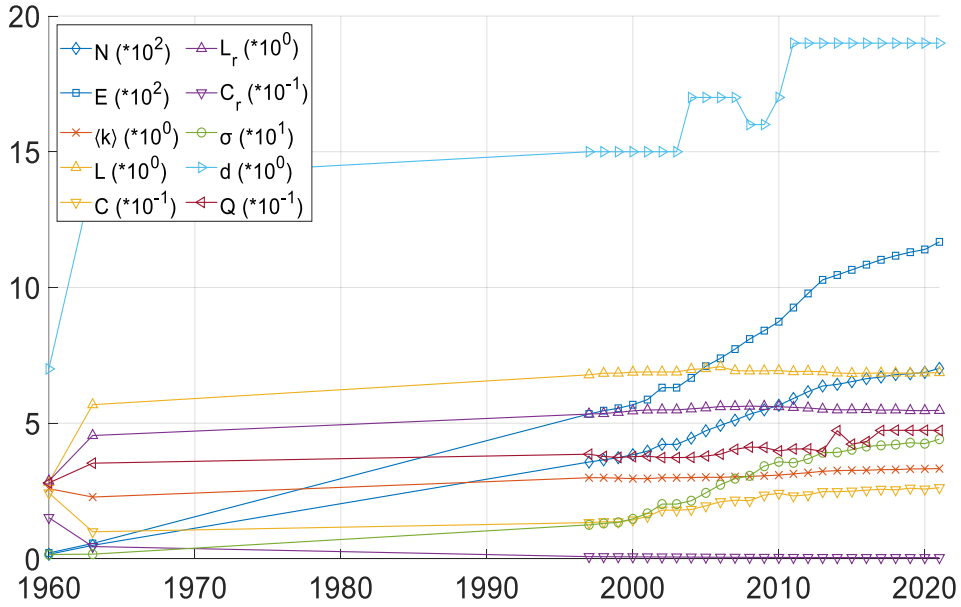

Figure 1: Evolution of the Spanish power grid between 1960 and 2021
N – number of nodes, E – number of edges, <k> - average node degree, L – average path length, C – clustering coefficient, Lr – average path length of reference random network, Cr – clustering coefficient of reference random network, σ – small world coefficient, d – distance, Q – modularity quotient

Results of the work were disseminated in a number of invited talks, including Power-Net 2022, a satellite of NetSci 2022 and the 20th Jubilee of the Student Association of Energy, where Bálint Hartmann presented as an invited plenary speaker.

Remaining work

The work is planned to be continued in 2023 with extending the analysis to other European power grids and with moving on to the evaluation of the vulnerability of those systems.

RADIONUCLIDE RETENTION PROPERTIES OF THE HOST ROCK OF A POTENTIAL HIGH-LEVEL RADIOACTIVE WASTE REPOSITORY

Ottó Sámuel Czömpöly, Margit Fábián, Tamás Korányi, György Nagy, István Tolnai, János Osán

Objective

High-Level Radioactive Waste (HLW) is planned to be disposed of in deep geological repositories in Europe. In addition to the multicomponent engineered barrier system, the surrounding rock of the repository serves as a natural barrier to contain the radionuclides. In several European countries, argillaceous rock formations are being considered as the site for the disposal of HLW. In Hungary, the potential host rock is the Boda Claystone Formation (BCF).

The main aim of the present work was to evaluate the radionuclide retention capacity of argillaceous rocks of the BCF, by studying sorption and diffusion properties of albitic claystone and pyritic sections of a recent drilling core (BAF-2). Sorption properties were studied for SeO_3^{2-} anion through an extension of the sorption isotherm to low concentrations (10^{-10} M). The reversibility of sorption was investigated through isotopic exchange using ^{75}Se tracer. Diffusion experiments were conducted for SeO_3^{2-} and UO_2^{2+} ions at different concentrations.

Methods

In order to study the sorption properties of SeO_3^{2-} (selenite ion) on BCF, the crushed rock was conditioned prior to the experiments using the dialysis technique. The experiments were conducted under atmospheric conditions. The suspensions were continuously shaken using an orbital shaker (Ohaus SHHD1619AL). For determining the time necessary to reach quasi-equilibrum conditions kinetic tests were performed. Sorption isotherms were collected in the 10^{-3}-10^{-10} M region using Inductively Coupled Plasma Optical Emission Spectrometry (ICP-OES) in the high concentration region (above 10^{-6} M) and Liquid Scintillation Counting (LSC) using ^{75}Se radiotracer in the whole concentration range. The reversibility of sorption was studied by isotopic exchange experiments, adding ^{75}Se radiotracer after reaching equilibrium with inactive SeO_3^{2-} and measuring the uptake using LSC. Sorption was also studied on petrographic thin sections prepared from claystone. The distribution of selenium and rock-forming elements were investigated using microscopic X-Ray Fluorescence (micro-XRF) with a spatial resolution of around 30 µm. The oxidation state of selenium was investigated using X-ray Absorption Near Edge Structure (XANES) spectrometry at the XRF beamline of Elettra (Trieste, Italy) both on thin sections and on crushed rock samples in the form of pressed pellets. To obtain the diffusion coefficient, through-diffusion experiments were launched with SeO_3^{2-} as well as UO_2^{2+} ions (at 10^{-3} – 10^{-5} M concentrations). After experiencing a break-through state, each diffusion cell was opened, the disc was cut and then investigated with micro-XRF and XANES.

Results

Regarding the kinetic tests, 21 days of intensive shaking was found to be sufficient to study the sorption properties with batch experiments. Microscopic measurements on thin sections showed a good spatial correlation between Se–Fe and Se–K which suggests that selenite is mostly sorbed on clay minerals. Results of ICP-OES and LSC methods of the liquid phase are in agreement and altogether show a typical sorption isotherm for selenite, comparable to those obtained for illite and illite-smectite in the literature, especially in the low concentration region (below 10^{-5} M). In the higher concentration regime the sorbed amount of selenium was found to be lower than on pure illite consistently with the clay mineral content of the BCF core sections studied (approx. 30–35 %). Isotopic exchange experiments using ^{75}Se radiotracer indicate reversibility of sorption in the 10^{-8}–10^{-4} M selenite concentration range.

With the initial SeO_3^{2-} concentration of 10^{-3} M, the effective diffusion coefficient was obtained as $D_e = (1–1.2)\times10^{-12}$ m²/s. A similar value ($D_e = 2\times10^{-12}$ m²/s) was obtained for UO_2^{2+} at an initial concentration of 10^{-4} M. Based on the diffusion profile of selenium inside the rock which was obtained using synchrotron-radiation micro-XRF, XANES measurements were then performed at selected representative positions. Overall, in each form of the studied rock (crushed rock, thin sections, compacted diffusion sample), no change in the oxidation state of selenium was experienced after sorption or diffusion experiments. However, at certain positions with enriched pyrite content, reduction to Se(0) could not be excluded [1,2].

Remaining work

Sorption–desorption experiments are planned to be conducted supplementary to the isotopic exchange experiments to study the reversibility of sorption. We'll study the diffusion profile and chemical state of uranium on the microscale.

Related publications

[1] O. Czömpöly, M. Fábián, I. Tolnai, S. Pollastri, I. Zizak and J. Osán: *Application of X-ray fluorescence methods in metal uptake studies of argillaceous rocks,* European Conference on X-Ray Spectrometry (EXRS-2022), Bruges, Belgium, 26 June – 1 July 2022.

[2] O. Czömpöly, M. Fábián, T. Korányi, G. Nagy, Z.E. Horváth, S. Pollastri, I. Zizak, M. Aertsens and J. Osán: *Adsorption and diffusion of selenite on Boda Claystone Formation*, Applied Clay Science **241**, 106997 (2023)

SYNTHESIS AND STRUCTURAL CHARACTERIZATION OF FUNCTIONAL XEROGELS AND AEROGELS

László Almásy, Zoltán Balogh, Zoltán Dudás, Adél Len, Dániel Pércsi

Objective

Synthesis and structural characterization of functional xero- and aerogels continues to be among the most important scientific topics. In 2022, the „Technology developments of functional aerogels" topic was selected by the International Union of Pure and Applied Chemistry (IUPAC) as being among the top ten emerging technologies in chemistry. The objectives of our group have been to synthetize functionalized silica xero- and aerogels for environmental remediation and catalytic purposes, to characterize the new materials in a systematic way using various laboratory techniques and large scale facilities, and to relate the mesostructure properties of the aerogels to the synthesis conditions. Several possible applications have also been tested.

Results

Nanoporous polymer-cross-linked alginate aerogels

Depending on the choice of the cross-linking triisocyanate reagent, polyurea-cross-linked Ca-alginate (X-Ca-alginate (alg)) aerogels showed distinct nanoscale morphologies. Cross-linking native Ca-alg wet gels with the aliphatic triisocyanate Desmodur N3300 yields aliphatic/flexible polyurea macromolecules in the final aerogel framework, while the aromatic triisocyanate Desmodur RE yields aromatic/rigid polyurea macromolecules. Probing the native Ca-alg aerogel together with the polyurea-cross-linked aerogels using low-voltage Scanning Electron Microscopy (SEM), N_2-sorption porosimetry, and contrast variation Small Angle Neutron Scattering (SANS) enabled the reconstruction of the nanomorphology of the aerogels (Fig. 1). Native Ca-alg aerogels are built from primary nanoparticles (8.3 nm in radius) that aggregate in mass-fractal secondary particles. Cross-linking reactions are realized after the formation of the Ca-alg nanostructure, while the different polyureas attach in different ways to the primary Ca-alg nanoparticles. Cross-linking with the flexible aliphatic Desmodur N3300 triisocyanate leads to the formation of a compact polyurea layer over the primary nanoparticles following the contours of the native Ca-alg skeletal framework (8.8 nm in radius). On the other hand, the rigid aromatic Desmodur RE triisocyanate forms a more rigid and randomly oriented polymer structure that fills loosely the empty space between the primary nanoparticles (10 nm in radius) within the secondary particles. Overall, both processes leave the primary Ca-alg structure practically undisturbed, while it does affect the structure at the most fundamental level, increasing the primary particle size and reducing the porosity. The different fundamental skeletal nanostructures of X-Ca-alg aerogels affect not only their material properties but also their potential for application in environmental remediation [1].

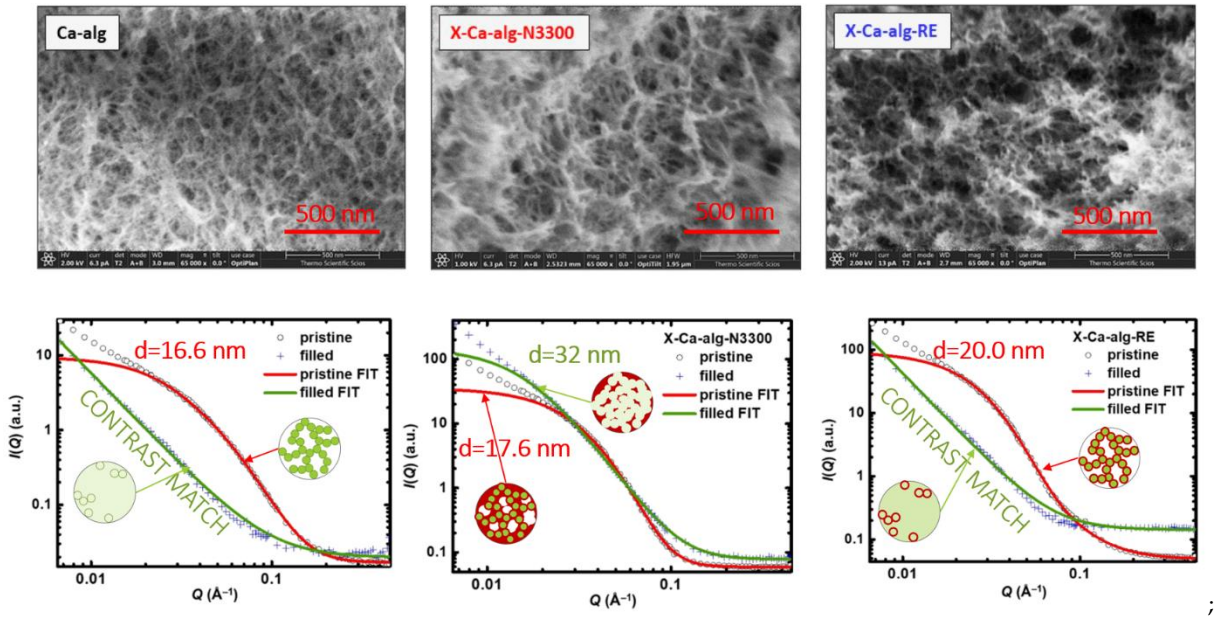

Figure 1: SEM images and SANS curves of the Ca-alg, X-Ca-alg-N3300 and X-Ca-alg-RE aerogels

Catalytic activities of dissolved and aerogel immobilized Cu(II) cyclen

Silica aerogel has been synthetized to serve as a chemically inert support for 1,4,7,10-tetraazacyclododecane [Cu(II)-cyclen] as it acts as a catalyst in the oxidation of aqueous phenol by H_2O_2. The morphology of the functionalized aerogel is very similar to that of the parent silica aerogel with an open interconnected mesoporous network. SANS measurements prove that the copper centres are dispersed quasi homogeneously in the silica matrix. There is no indication for the formation of individual

copper-rich structural regions at the nanometre scale. Electron Paramagnetic Resonance (EPR) spectroscopy measurements prove, as well, that the Cu(II) centres do not interact with each other, but the coordination mode of Cu(II) is somewhat different than in the dissolved Cu(II)-cyclen. Detailed kinetic experiments prove that a unified kinetic model is adequate to describe and benchmark both the homogeneous and the heterogeneous reaction systems. This approach clearly shows that the specific activity of the heterogeneous catalyst is somewhat lower than that of the homogeneous because of hindered mass transport, and not because of ineffective activation or new side reactions. Based on this characterization, the results highlight the fact that the effective separation of the catalytic centres and the accessible equatorial plane of Cu(II)-cyclen in the functionalized aerogel ensures the conservation of the catalytic activity of the complex, which is naturally advantageous for an immobilized catalyst [2].

Adsorptive recovery of Pd(II) using magnetic iron-oxide-silica nanocomposites

Magnetic Iron Oxide-silica shell Nanocomposites (IONP@SiO_2) have been prepared in a two-step procedure. Iron Oxide Nanoparticles (IONPs) were obtained by co-precipitation of iron salts, and coated by silica in a sol-gel method under sonication. Two IONP/silica ratios: 11% and 35% iron oxide content, and two drying methods: heating in an oven and supercritical CO_2 drying, were used. The samples were analysed using various nano- and mesostructure characterization methods. The iron oxide silica nanocomposites obtained via supercritical drying exhibited higher values of specific surface area and of saturation magnetization compared to the samples synthesized with the same iron oxide content, but dried in an oven at 60 °C. Pd(II) adsorption experiments were performed on the materials prepared by supercritical drying. Adsorption of Pd(II) ions took place at the surface of the material, as a spontaneous, endothermic process governed mainly by physisorption. The maximum adsorption capacity 6.5 mg/g showed that the materials can be used as a good and cheap adsorbent for palladium ions from an aquatic environment. Pd(II) could be efficiently recovered by adsorption on the nanocomposite obtained by supercritical drying, and its efficacy was comparable to the efficacy of similar materials presented in the literature [3].

Imidazolium Ionic Liquids as Designer Solvents Confined in Silica Nanopores

Based on their unique characteristics, with a high flexibility in varying the cations and the anions, the Ionic Liquids (ILs) have been generally referred to as designer solvents. In the present study, ILs with an imidazolium cation and different anions, tetrafluoroborate or chloride, were used for preparing composite xerogels. The xerogels were synthetized via the acid catalysed sol–gel route using tetraethoxysilan (TEOS) as the silica precursor, and 1-butyl-3-methylimidazolium tetrafluoroborate [BMIM][BF_4] or 1-butyl-3-methylimidazolium chloride [BMIM][Cl] ionic liquids, used simultaneously as co-solvents, catalysts and pore templates, at various IL-to-silica ratios. By using several structural characterization techniques, the differences in the morphology and thermal behaviour of the various IL-content composites were revealed. The xerogel synthetized without IL had both meso- and microporosity, while the IL-containing xerogels showed different characteristic dimensions of a mesoscopic structure. The homogeneous [BMIM][Cl] aqueous solution led to formation of a more homogeneous composite xerogel, whereas from the heterogeneous [BMIM][BF_4] solution a rather heterogeneous nanocomposite was formed. The present results contribute to the understanding of phase separation in the mixtures of the gel precursors and can serve for tailoring the design of templated xerogel composites.

Related publications

[1] P. Paraskevopoulou, G. Raptopoulos, A. Len, Z. Dudás, I. Fábián, J. Kalmár: *Fundamental Skeletal Nanostructure of Nanoporous Polymer-Crosslinked Alginate Aerogels and its Relevance to Environmental Remediation*, ACS Applied Nanomaterials **4**, 10575 (2021)

[2] A. Forgács, Z. Balogh, M. Andrási, A. Len, Z. Dudás, N. Nóra, P. Herman, L. Juhász, I. Fábián, L. Norbert, J. Kalmár: *Mechanistic Explanation for Differences Between Catalytic Activities of Dissolved and Aerogel Immobilized Cu(II) Cyclen*, Applied Surface Science **579**, 152210 (2022)

[3] C. Ianasi, E.-M. Piciorus, R. Nicola, A.-M. Putz, A. Negrea, M. Ciopec, A. Len, L. Almásy: *Synthesis and characterization of magnetic iron oxide–silica nanocomposites used for adsorptive recovery of palladium (II)*, Soft Materials **20**, S68–S75 (2022)

[4] A.-M. Putz, A. Len, L. Trif, Zs. E. Horváth, L. Almásy: *Imidazolium Ionic Liquids as Designer Solvents Confined in Silica Nanopores*, Gels **8**, 388 (2022)

ESTIMATING THE SOLAR ENERGY PRODUCTION POTENTIAL OF AN URBAN AREA USING THE CAD AND GIS METHODS

Viktória Sugár, Bálint Hartmann, Tamás Soha

Objective

One of the most important tasks presently is to reduce our energy usage and at the same time to increase the share of renewable energy in it. In this current research, the solar energy production opportunities are taken into account by considering the characteristics of the building structures and the urban fabric. By examining the potential of the surfaces that could be used for energy production, the aim is to determine the proportion of energy needs of buildings with different characteristics (size, degree of renovation, etc.) that can be met by renewable energy produced locally. We compare two methodologies used to estimate solar potential, one based on CAD building models and simulation and one using the Geographical Information System (GIS) method.

Methods

For the CAD method, REVIT 2018 software was used for simulations with the Insight plugin. The roof surfaces were simulated separately to estimate the incident solar irradiation as related to roof orientation. The software uses the data of the nearest weather station to the exact location of the building in the model. These weather stations include 'actual year' virtual weather stations and typical year weather stations based on 30-year averages. The simulation results were used as input data for calculations. The average annual irradiation, the cumulative annual irradiation, and the roof surfaces were acquired from the model. The net heated interior area of the building was calculated using the geometry input of the database. The GIS approach uses LiDAR (Light Detection and Ranging technology, a method for determining ranges by targeting an object or a surface with a laser) data, from which a DEM (Digital Elevation Model) was created. The DEM was utilized for evaluating the roof slope, aspect, and the global irradiation. The latter was modelled using local climatic characteristics and gave results with a 25 cm spatial and 1 hour temporal resolution, meaning that a very detailed database of insolation for each building was calculated. Solar potentials, available roof area, photovoltaic (PV) system capacities and estimated annual electricity production were derived from the GIS modelling. Two blocks of buildings were used in the detailed simulation.

Results

The CAD and GIS methods use different approaches to determine the solar power potential. With CAD, the chosen buildings were first modelled in 3D with their environment, while the GIS method uses observational LiDAR raster data to determine the geometry. However the two approaches can be compared by transforming the raster into a vector format. Both methods have their advantages, and their uncertainties are caused by different factors. The values of the raster derived surfaces are mostly agreeing with the CAD method's results in terms of the suitable areas and irradiation characteristics (Fig. 1) [1].

The comparing of methods was carried out on 30 buildings. The estimated irradiation on the roof surfaces resulted in values with a large standard deviation, indicating the need to extend the database used. In addition, the results indicate the necessity of on-site filed surveys in order to validate each of the approaches and to refine the modelled values.

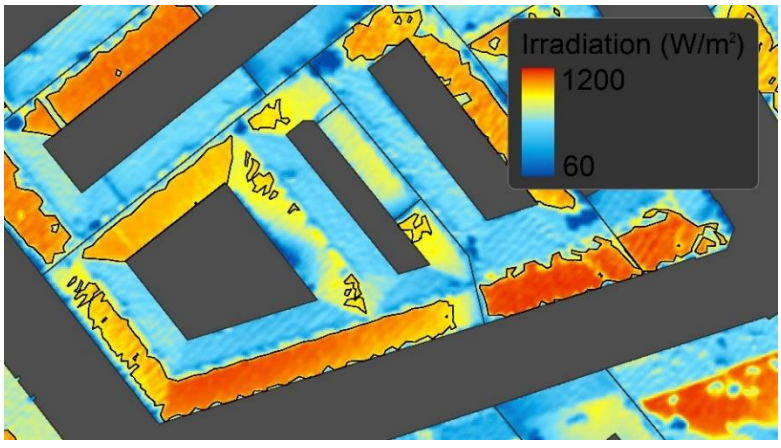

Figure 1: Irradiation on the roofs and the most suitable areas for PV systems determined with the GIS method

Remaining work

To continue our research, real-life solar irradiation data will be used to validate the methods and determine their usability in large-scale estimations.

Related publication

[1] V. Sugár, B. Hartmann, T. Soha: *Estimating solar potential in urban environment: comparing CAD and GIS methods,* Manuscript under preparation

ASSESSING THE IMMOBILIZATION CAPACITIES OF ORDINARY PORTLAND/SULFOALUMINATE CEMENT PASTE MIXTURES CONTAINING NOVEL RADIOACTIVE WASTE OF B–10 ENRICHED BORIC ACID AND NATURAL BORIC ACID

Margit Fábián, István Tolnai, Katalin Gméling, Mihály Óvári, Zsuzsanna Szabó-Krausz, Mojtaba Rostamiparsa, Iklaga Gabriel**

Objective

Natural Boric Acid (NBA) and B-10 Enriched Boric Acid (EBA) are solutions used for neutron absorption in Nuclear Power Plants (NPP). The aim of the present project was to assess the optimum Ordinary-Portland and Sulfoaluminate Cement (OPC & SAC) ratio in cement pastes for attaining effective immobilization of boric acid waste.

Methods

Cement paste sample preparation. The cement paste samples were made using ordinary OPC grade (R – 15796 CEM I 52.5 N) and SAC grade (R – 14734 ALI CEM GREEN) from CEMKUT Ltd in various ratios, using one of two boric acid solutions. Natural (20% B-10 isotopic abundance) (NBA) and B-10 enriched boric acid (80% B^{10} (EBA)) were used to synthesize the boric acid solutions. Boric acid solutions with elemental Boron concentrations ranging from 10g/l to 40g/l were prepared. Reference cement samples were also made with demineralized (DM) water, rather than a boric acid addition. Varying SAC ratios of 0% SAC (i.e. 100% OPC), 10% SAC, 20% SAC, 30% SAC and 40% SAC were used. The cement paste samples were poured into cylindrical molds of 43 x 25mm dimensions and cured at 20^0C for 28 days.

Leaching tests. After curing, the cement paste samples were subjected to a standardized reference leaching test (ASTM C1308-08_2021) for a total of 11 days. The leachates (the leachant was DM water) were replaced and sampled at 2, 5, 17 and 24 hours for the first day and then daily for the next 10 days.

Analytical techniques. The solidified cement samples before and after the leaching test, were analysed by compressive strength test, Scanning Electron Microscopy (SEM), X-Ray Diffraction (XRD) and Neutron Activation Analysis (NAA)/Prompt Gamma Activation Analysis (PGAA) methods. The initial boric acid solutions were examined by Raman-spectroscopy and the leachate solution samples coming out from the leaching tests were analysed by Inductively Coupled Plasma Optical Emission Spectroscopy (ICP-OES) using an inductively coupled plasma sector field mass spectrometer (ICP-MS).

Results

Raman-spectroscopy results of initial, simulated boric acid waste solutions

Based on the Raman-spectra measured, we find that the simulated EBA and NBA liquid wastes mostly contain boron in $\boldsymbol{B(OH)_4^-}$ and $\boldsymbol{B_5O_6(OH)_4^-}$ ions, but their mass ratio is higher in the EBA- than in the NBA-solution by up to 27%.

For the known bands of borate molecules at 521 cm^{-1} ($B_5O_6(OH)_4^-$) and 745 cm^{-1} ($B(OH)_4^-$), the ratio of their integrated areas ($RS_p = S_{p_{745}}/S_{p_{521}}$, and the relative comparison of RS_p between NBA and EBA at a fixed concentration ($\Delta RS_{p_{(EBA/NBA)}} = (RS_{P_{(EBA)}} - RS_{P_{(NBA)}})/RS_{P_{(EBA)}} \times 100$ [%]) were calculated. These two ratios give us the comparability of the molecular ratio of $B_5O_6(OH)_4^-$ and $B(OH)_4^-$ in the studied liquid wastes, where $S_{p_{745}}$ and $S_{p_{521}}$ are the integrated areas under the specific bands for $B(OH)_4^-$ and $B_5O_6(OH)_4^-$, and $RS_{P_{EBA}}$ is a measure of the percent difference in the ratios of the integrated areas of these two bands in the EBA and NBA solutions, respectively. For each boron concentration, the RS_p of the enriched sample ($RS_{P_{(EBA)}}$) is bigger than that of the natural sample $\left(RS\middle|P_{(NBA)}\right)$, and the percentage of this difference ($\Delta RS_{p(\ \ EBA/NBA)}$) is decreasing from 26.9 to 4.7% with an increase of the elemental boron concentration in the solution from 10 to 40 g/l. This difference affects the chemical reactions of the solutions with cement clinker [1] which is causing the difference in the stability of their cement pastes.

Compressive strength, SEM, XRD and NAA/PGAA results of solid specimens after leaching

Compressive strength results indicate that both NBA and EBA retard the hydration process of all the cement mixture ratios since the reference samples show higher compressive strength values. It was also observed that the largest compressive strength values gained after leaching belong to the cement mixtures with about 20% SAC.

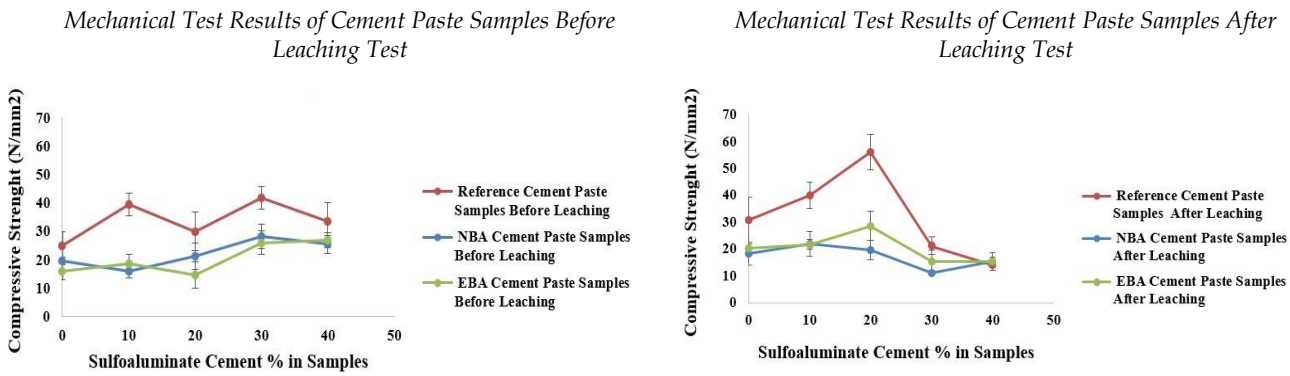

Figure 1: Compressive strength test results for the cement paste samples before (left) and after (right) the standard leaching test, indicating 0%, 10%, 20%, 30% and 40% SAC-content in cement mixed with DM water, NBA and EBA solutions. The results of our experiments showed that water diffuses from the surface into the interior parts of the cementitious matrices during the leaching test. Due to the large natural unbonded boron-salt solubility, most of the boron-bearing molecules get released from the NBA-specimens. However, only some of those molecules from the EBA-specimens are released from the affected depth of the solidified matrix, which is due to the higher stability of borate molecules in the EBA solidified specimens. During dissolution, the more that the boron-containing molecules are released from the cementitious structure (NBA-cementitious specimens in this study), the higher the porosity becomes, and consequently, the shorter durability of the simulated final waste specimens made with NBA is expected compared with the specimens made with EBA.

The SEM results of the cement paste samples before leaching (partially presented in Figure 2) indicate that the cement hydration process is retarded by the boric acid since the 40% SAC reference sample (MR4) shows fewer macro-fractures than the 40% SAC, NBA or EBA containing samples (MN4 and ME4, respectively). Observations of the samples after leaching indicate that the amount of clinker phases are reduced as the cement hydration process progresses during leaching. The backscattered-electron images of SEM measurements of the solid cement paste samples were analysed before leaching (ME4, MN4 and MR4-reference samples) and after leaching (LME4, LMN4 and LMR4) using ImageJ software, which is a versatile, open-source used for a variety of tasks, such as simple image enhancements and quantitative image analysis. The results of the analyses quantified the unhydrated surface areas of the samples before leaching as ME4 (239493.731 μm^2), MN4 (238675.265 μm^2), MR4 (53714.927 μm^2) whereas samples after leaching have LME4 (246095.847 μm^2), LMN4 (316751.896 μm^2) using a uniform surface area for the statistical analyses. These results seem to indicate a positive correlation between increasing boric acid concentration from 0 g/l in the reference samples to 40 g/l in the SE4 and SN4 samples, and the SEM results showing an increasing surface area of unhydrated clinker phases of 239493.731 μm^2 observed on the samples implying the possibility of increased hydration retardation with increasing boric acid concentration. Furthermore, the leaching tests seem to further increase the size of macro-fractures in the borated cement paste samples.

Before Leaching

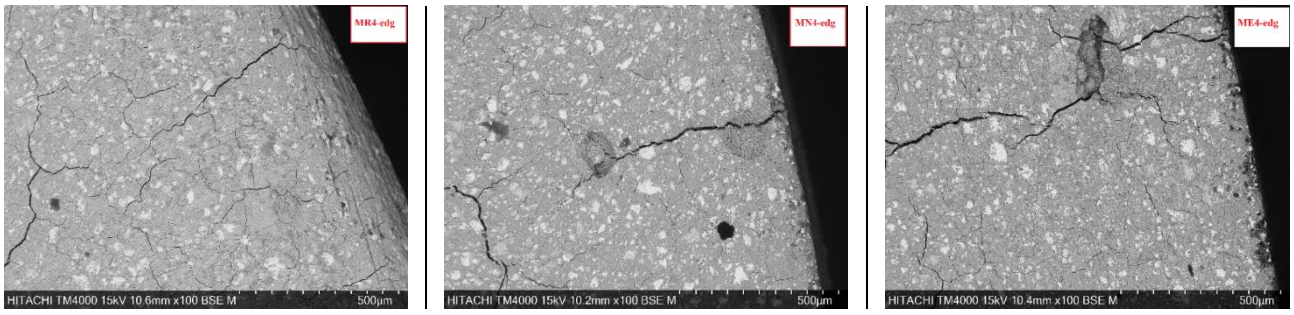

After Leaching

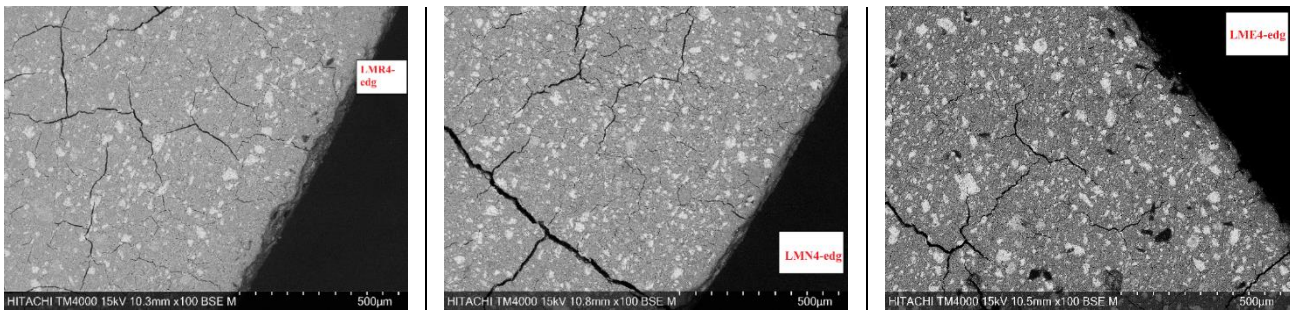

Figure 2: SEM observation of macro-fractures in the 40% SAC-content cement pastes, before and after the standard leaching test

The results from the XRD measurements also indicate that both NBA and EBA containing samples show retarded hydration when compared to the reference samples. This is based on the fact that in all the SAC percentage cases the OPC cement primary clinker phases e.g., alite and larnite, are used up more efficiently in the reference samples than in the NBA and EBA containing samples as secondary cement hydration progresses. The ettringite secondary hydration phase (Figure 3) is the most probable one to capture boron atoms in the samples and Fig. 3 confirms the above statement (since reference samples always contain more secondary ettringite phase, formed from alite and larnite) and it also shows an increasing amount as more SAC is added to the cement. Therefore, adding more SAC has a potential to bond boric acid more efficiently. The results also indicate that NBA samples always contain more ettringite than the EBA samples.

Ettringite XRD results Before Leaching *Ettringite XRD results After Leaching*

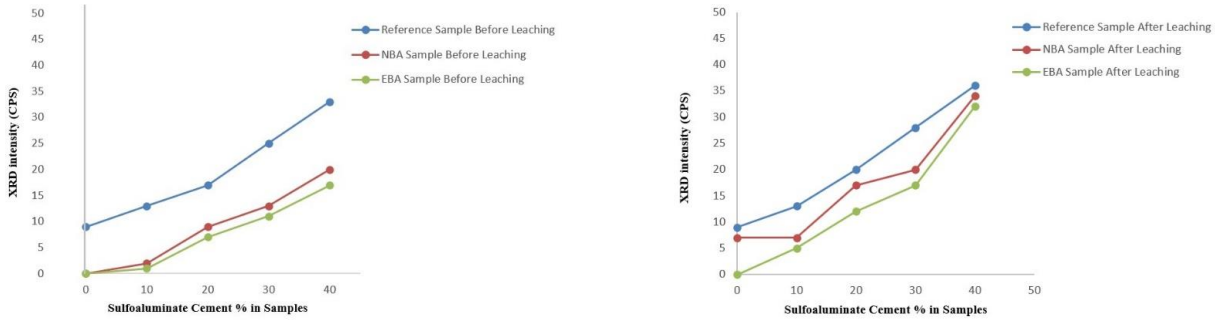

Figure 3: Selected XRD results (ettringite) for the cement paste samples before and after the standard leaching test, plotted against the percentage SAC-content in cement mixed with DM water, NBA or EBA solutions.

Neutron activation methods were used to measure the elemental mass fractions of the two different cements, and the solidified samples with different SAC ratios before and after leaching. The two nuclear methods complement each other since PGAA gives the results of major elemental composition of the samples, including the H, B and Cl content, while NAA, besides Ca, Fe and Na as major components gives the mass fraction of about 25 trace elements. The two cements (pure OPC vs. pure SAC; see Table 1) chemically show major differences between their Ca (45.2 m% vs. 27.9 m%) and Si (9.62 m% vs. 2.84 m%) content, and in their Fe (2.46 m% vs. 0.72 m%) cc., with all three elements being relatively higher in the OPC samples. Compared to that, SAC has relatively higher amounts of Al (13.3 vs. 2.76 m%), S (9.02 vs. 1.29 m%), B (167.2 vs. 37.3 µg/g) and Cl (1157.9 vs. 231.1 µg/g). As the SAC ratio is increased in the mixed cement samples, the above changes in the elemental content can nicely be followed.

PGAA		Si	Ti	Al	Fe	Mn	Ca	S	H	B	Cl		
Pure_OPC	m%	9.62	0.17	2.76	2.46	0.29	45.2	1.29	0.11	0.00373	0.02311		
	Rel.Unc. %	2.4	4.1	2.2	2.6	2.4	1.5	2.3	1.8	1.3	2.2		
PureSac	m%	2.84	0.23	13.3	0.72	0.10	27.9	9.02	0.05	0.01672	0.11579		
	Rel.Unc. %	2.7	2.3	1.6	3.3	2.4	1.9	1.9	1.8	0.9	1.5		
NAA		As	Ba	Br	Ce	Co	Cr	Cs	Eu	Hf	K	La	Na
Q81_PureOPC	mg/kg	13.6	224	2.73	21.6	5.84	295	0.45	0.40	2.03	1914	11.2	979
	Rel.Unc	3.3%	3.2%	3.9%	4.1%	1.9%	2.0%	6.3%	2.0%	2.5%	3.6%	1.9%	1.9%
Q82_PureSAC	mg/kg	3.2	857	4.74	6.48	17.5	339			1.33	3516	4.37	5394
	Rel.Unc	12%	2.3%	7.5%	6.5%	1.8%	2.2%			3.9%	4.4%	3.0%	1.8%
NAA		Nd	Sb	Sc	Sm	Sr	Ta	Tb	Th	Tm	W	Yb	Zn
Q81_PureOPC	mg/kg		13	4.46	1.42	176	0.48	0.27	3.40	0.39	5.54	0.79	217
	Rel.Unc		1.8%	1.9%	2.4%	9.2%	2.9%	3.3%	2.1%	10.0%	4.4%	3.0%	1.9%
Q82_PureSAC	mg/kg	14700	351	0.79	0.6	1574			0.99		8.88		562
	Rel.Unc	1.8%	1.8%	2.0%	11%	2.7%			5.8%		7.6%		2.0%

Table 1: PGAA and NAA results of the pure ordinary Portland cement (OPC) and pure sulfoaluminate cement (SAC).

The NBA and EBA solutions also influences the elemental composition of the borated samples. The enriched Boron cement paste samples, before leaching, compared to the normal and reference samples show higher Fe, Na and B content, and have slightly higher Ce, Co, Cr, La, Nd, Sc, Sm, Th, Yb, and Zn trace element content. In contrast the Si, Ca, and H content of the enriched samples is lower and their Al, Ti and Cl content much less, in fact below the detection limit of PGAA (Table 2), than in the normal and reference samples.

PGAA m%	Si	Al	Fe	S	Ca	Ti	H	B	Cl		
MN0	7.38	1.80	1.75	0.99	31.6	0.14	2.58	1.200	0.01265		
ME0	6.43		2.02	0.66	28.4		2.24	5.694			
MR0	7.27	2.40	1.85	0.97	34.3	0.15	2.93	0.0036	0.01615		
MN1	6.66	2.64	1.55	1.26	30.6	0.15	2.69	1.196	0.02069		
ME1	6.41		2.83	1.45	26.1		2.21	5.542			
MR1	6.53	2.93	1.67	1.46	31.3	0.14	3.17	0.0059	0.02241		
MN2	6.06	3.43	1.14	1.87	29.3	0.15	2.79	1.209	0.03101		
ME2	5.82		2.66	1.91	26.1		2.30	5.611			
MR2	6.08	3.74	1.56	1.96	30.5	0.13	3.10	0.0065	0.02923		
NAA mg/kg	As	Ba	Ce	Co	Cr	Cs	Eu	Hf	La	Lu	Na
MN0	10.8	185	17.6	4.5	238		0.35	1.55	8.26		31285
ME0	10.98	193	20.4	5.1	261	0.32	0.34	2.13	9.42	0.13	35205
MR0	10.5	165	16.9	4.34	225	0.32	0.31	1.54	8.53		733
MN1	9.8	227	17.1	6.27	254	0.4	0.33	1.52	7.8	0.1	32051
ME1	9.3	236	19.1	6.98	279	0.4	0.33	1.55	8.7	0.1	35339
MR1	9.28	236	16.9	5.96	247	0.38	0.31	1.57	7.94	0.10	1063
MN2	9.8	282	17.6	7.57	275	0.5	0.33	1.52	8.0		33527
ME2	8.1	296	17.9	8.16	291	0.51	0.32	1.43	8.48		36850
MR2	8.09	251	14.7	6.54	234	0.38	0.26	1.45	6.97	0.09	1353
NAA mg/kg	Nd	Rb	Sb	Sc	Sm	Sr	Ta	Tb	Th	Yb	Zn
MN0			10.0	3.54	1.54		0.38	0.21	2.59		176
ME0	9.83	5.4	10.12	4.01	1.61		0.48	0.23	2.83	0.72	190
MR0	7.93	5.84	9.59	3.36	1.48	141	0.37	0.22	2.53	0.68	162
MN1	7.71		34.8	3.49	1.33	244	0.33	0.22	2.60	0.62	212
ME1	7.85	6.4	36.5	3.81	1.33	274	0.39	0.26	2.66	0.76	233
MR1	7.72		35.5	3.38	1.33	226	0.40	0.22	2.58	0.68	208
MN2	7.03		63.3	3.32	1.17	418			2.38		251
ME2	7.99		62.4	3.55	1.30	389	0.40		2.47	0.76	267
MR2	6.73	5.84	58.1	2.88	1.10	337	0.36	0.19	2.19	0.59	223

Table 2: PGAA and NAA results of the normal, enriched and reference cement paste samples with 0%, 10% and 20 % SAC before leaching.

After leaching of the cement paste samples, the decrease of Na and the fluid mobile trace elements content are most visible (B, Ba, Cs) (Figure 4).

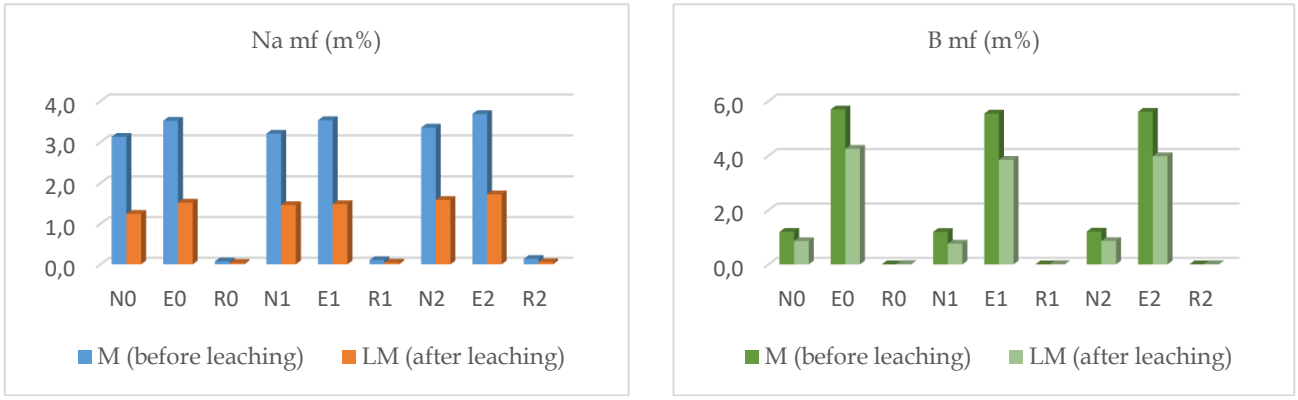

Figure 4: Na and B content decreases with leaching

ICP-OES investigations were performed on the aqueous solutions (from the leaching process) using a Perkin Elmer Avio 200 apparatus. The elements: Sr, Mg, Na, Al, B, Ca, K, Si and Ba were measured in radial view (the measurement setting characteristic of the instrument) without dilution and Y was used as the internal standard. Boron is usually assumed to provide the best measure of the extent of cement paste sample reaction because of its high solubility. Based on the standard procedure, the cumulative fraction of leached boron was calculated based on the ASTM C1308-08_2021 methods. Plotting the Cumulative Fraction Leached (CFL) values versus the cumulative time (Figure 5) can provide a straightforward graphical comparison of leaching data from the various solidified cementitious samples.

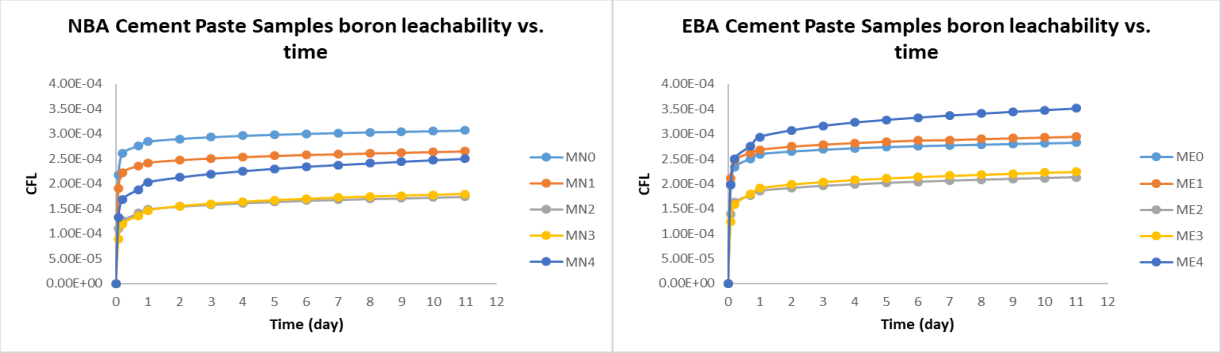

Figure 5: Cumulative fraction leached of boron from the different cementitious waste forms: (left) natural boric acid solution, (right) enriched boric acid solution. The numbers 0-4 signify how many tens of % SAC was in the cement sample.

In the case of the NBA and EBA solutions, the measured values are of the same order of magnitude, but the values and time dependence are somewhat different. The magnitude of the difference is consistent with the SAC content. As long as the cementitious system does not contain SAC, typically 10% higher CFL can be measured in the NBA sample time dependence. As the fraction of SAC increases, the trend reverses and the amount of leached boron also increases. A 50% higher CFL value was measured in the EBA sample series containing 40% SAC. The lowest amount of leached boron belongs to the cement mixture containing 20% SAC for both enriched and natural boric acid containing samples.

ICP-MS investigations were also carried out on the aqueous solutions (from the leaching tests) using an Inductively Coupled Plasma Sector Field Mass Spectrometer (ICP-SF-MS) Element2 apparatus produced by Thermo-Finnigan, Bremen, Germany. The boron-10 and boron-11 isotopic abundances are presented in Figure 6 for EBA and NBA cement paste samples, respectively. In the case of the NBA samples, the measured values indicate a constant or slightly increasing abundance of boron-11 isotope with time. In the case of the leachates of the EBA samples, there is a clear decreasing abundance of boron-10 isotope with time for all samples.

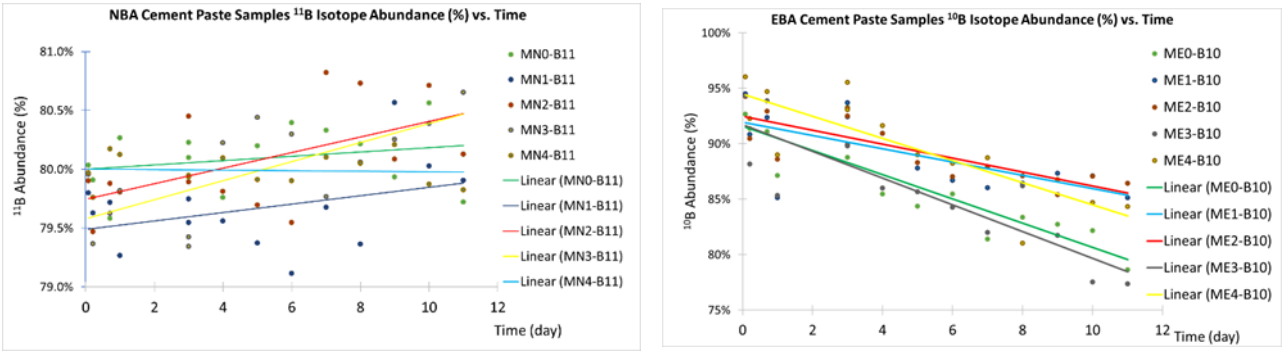

Figure 6: Time dependence of the Boron isotope abundance in the leached liquid from the different cementitious waste forms: (left) B-11 from natural boric acid solution, (right) B-10 from enriched boric acid solution.

At each initial boron concentration, the solidified specimens made with EBA show lower boron leachability than those made with NBA. This phenomenon is related to the chemical speciation of boric acid, $B(OH)_4^-$. However, in the NBA simulated liquid wastes, the $B(OH)_4^-/B_5O_6(OH)_4^-$ ratio is lower than in the EBA liquid waste. Thus, the more abundant isotope (^{11}B) has a lower possibility to locate in the interchangeable tetrahedral borate coordinates of the liquid phase and subsequently has lower possibility of substituting in the above-mentioned sites of the cement paste. The unsubstituted ^{11}B-containing ions and molecules can release from the cementitious matrix effectively when the solidified specimens get contacted with water. These phenomena are supported by the observations in Figure 6, where after a rapid release of boron from the specimens' surface during the first day (surface wash-off), the abundance of released ^{10}B decreases in time, whereas the total boron leaching increases continuously due to the ^{11}B release.

Conclusions

Based on the results of mechanical tests and CFL of boron measurements, it can be concluded that the most ideal composition could be the 20% SAC – 80% OPC to bind the boric acid. Even though adding more and more SAC could provide a chemically more favourable composition (more and more ettringite based on XRD results which can incorporate boron), the physical stability of the samples with higher SAC contents is retarded (e.g. lower compressive strength and higher boron leaching). From the SEM and XRD measurements, it was furthermore confirmed that adding boric acid to the mixture retards the stability of the hardened cement pastes. It was also concluded that NBA and EBA cement pastes behave differently during leaching tests (confirmed by primarily XRD, ICP-OES, ICP-MS analysis and neutron activation methods) due to the fact that EBA and NBA liquid wastes mostly contain boron in $\boldsymbol{B(OH)_4^-}$ and $\boldsymbol{B_5O_6(OH)_4^-}$ ions, but in different mass ratios which affects the chemical reactions of the solutions with cement clinker.

Remark

* Mojtaba Rostamiparsa and Iklaga Gabriel from ELTE were involved in the project, in the frame of *Stipendium Hungaricum Scholarships*.

Related publications

[1] M. Rostamiparsa, I. Tolnai, O. Czompoly, M. Fabian, M. Hegedus, Gy. Falus, Cs. Szabo, M. Ovari, Cs. Tobi, P. Konya, P. Volgyesi, Zs. Szabo-Krausz: *The geochemical role of B-10 enriched boric acid in cemented liquid radioactive wastes*, Journal of Radioanalytical and Nuclear Chemistry **332**, 2543-2557 (2023)

[2] M. Fabian, I. Tolnai, Z. Kis, V. Szilagyi*: Characterization of simulated liquid radioactive waste in a new type of cement mixture,* ACS Omega **7,** 36108-36116 (2022)

CHARACTERISATION OF THE AEROSOL PARTICLES RELATED TO DOMESTIC WOOD AND WASTE COMBUSTION

Veronika Groma, Endre Börcsök, Ottó Czömpöly, Szilvia Kugler and János Osán

Objective

Domestic combustion (heating, cooking) is a significant air pollution source, especially during the heating season. Moreover, the share of wood combustion in the total energy production is supposed to grow in the near future due to rising energy prices and the recently experienced energy shortage crisis in Europe. Based on our previous work [1], it is assumable that illegal incineration can also be identified as a source, even in an urban environment. Our goal is to develop a method that allows the identification of waste combustion as a source of ambient aerosols from short-term (few hours) sampling. For this purpose, we look for elemental/ionic tracers together with size information of the particles which can be characteristic for the sources of the aerosols. The aim of this research is to determine markers for waste burning as an emission source based on laboratory combustion experiments. These markers are expected to be suitable for determining the contribution of this source using an appropriate receptor model which is able to identify and quantify the apportionment of the air pollutants.

Methods

Laboratory experiments were performed at the premises of the Centre for Energy Research in collaboration with Aerosol d.o.o. (Slovenia). A conventional stove widely used in Hungary for domestic heating was set up, to which a flue-gas outlet tube was connected in order to direct the flue gas to the monitoring and sampling instruments through diluters and driers. Various conventional solid fuels (firewood, forest wood and brown coal) as well as various domestic wastes (used parkette and rubber) were incinerated separately. Particle number size distribution (in the range of 10 nm – 10 µm) was measured by a Scanning Mobility Particle Sizer (SMPS) and an Optical Particle Counter (OPC). The $PM_{2.5}$ mass concentration was recorded by a Tapered Element Oscillating Microbalance (TEOM) and Elemental Carbon (EC) was monitored by an aethalometer (Magee Scientific AE42-7) coupled with a CO_2 monitor. Size-fractionated and $PM_{2.5}$ aerosol sampling was carried out using cascade impactors on Si wafers and filter packs with cyclones. These samples were used for off-line analysis by Raman spectroscopy and the DRI standardized thermal/optical reflectance method for elemental and organic carbon (EC and OC, respectively) and gas chromatography – mass spectrometry for levoglucosan (LGS). Total-reflection X-ray fluorescence (TXRF) analysis was used for the determination of size-resolved element concentrations.

Results

Based on the complex aerosol parameter measurements made in the successful laboratory combustion experiments, certain aerosol characteristics of the smoke from different fuels could be established. In the case of the tested conventional fuels, the particle number size distribution was found to be unimodal with a maximum between 100-300 nm, while in the case of rubber, additional smaller, but significant peaks were detected at around 50 nm and 1 µm. Based on the results of the size-fractionated elemental analysis, it was found that for firewood and forest wood burning, the K, Cl, Br and V emissions are significant in the size ranges below 1 µm, while for brown coal there is an order of magnitude higher S emission compared to other conventional fuels. During the burning of rubber a high concentration of Ca was detected in the size range of 2-4 µm. The LGS and total carbon (TC) concentration in the flue gas, as well as the percent shares of OC in the TC are summarized in Table 1. Based on the Raman analysis of the size-fractionated samples collected with the impactor, we found that for burning of waste materials (parkette and rubber) the OC proportion in the total TC is maximal in the 250 nm size mode. It is hence found that different materials have quite different smoke signatures, as also shown in Table 1.

Table 1: Results of organic compound analysis related to various fuel burning emissions

Fuel	Total Carbon (mg/m³)	Proportion of OC in TC (%)	LGS (mg/m³)
Brown coal	336.4	99.7	1.5
Forest (wet) wood	125.7	93.1	14.8
Dry wood	294.5	98.8	17.9
Parkette (waste)	101.3	71.7	11.8
Rubber tire (waste)	188.6	53.0	0.8

Remaining work

We plan to continue laboratory experiments to characterize other waste fuel's smoke emission. After that, field campaigns are planned to study the contribution of waste incineration in urban and rural environments.

Related publication

[1] V. Groma, B. Alföldy, E. Börcsök, O. Czömpöly, P. Füri, Horváthné A. Kéri, G. Kovács, S. Török, J. Osán: *Sources and health effects of fine and ultrafine aerosol particles in an urban environment,* Atmos. Pollut. Res. **13,** 101302 (2022) https://doi.org/10.1016/j.apr.2021.101302

POWER-TO-GAS FACILITY SITE SELECTION METHOD BY GIS AND MCDM

Tamás Soha, Bálint Hartmann

Objective

The objective is to create the first complex, spatial-focused site suitability and site selection method for Power-to-Gas (PtG) facilities. This report represents the PhD research of the first author.

Methods

A Geographical Information System (GIS)-based methodology is presented, considering public utility services as power, gas and water networks, besides other common site suitability criteria. These factors were weighted by a Multi-Criteria Decision-Making (MCDM) process, namely AHP, to find the possible PtG sites in a study area. It was assumed that PtG facilities receive biogas as a CO_2 source from several biogas plants through dedicated pipelines.

Results

Results indicate that 2.5% of the 7,250 km² region is suitable to host PtG facilities (Fig 1). To produce 142 million m³ CH_4 per year, altogether 92.4 MW electrolyser capacity is required, which can be distributed in the region in a decentralized manner. The capital expenditure assessment showed that centralized scenarios are 16.6–26.3% less cost intensive than a totally decentralized system of PtG plants.

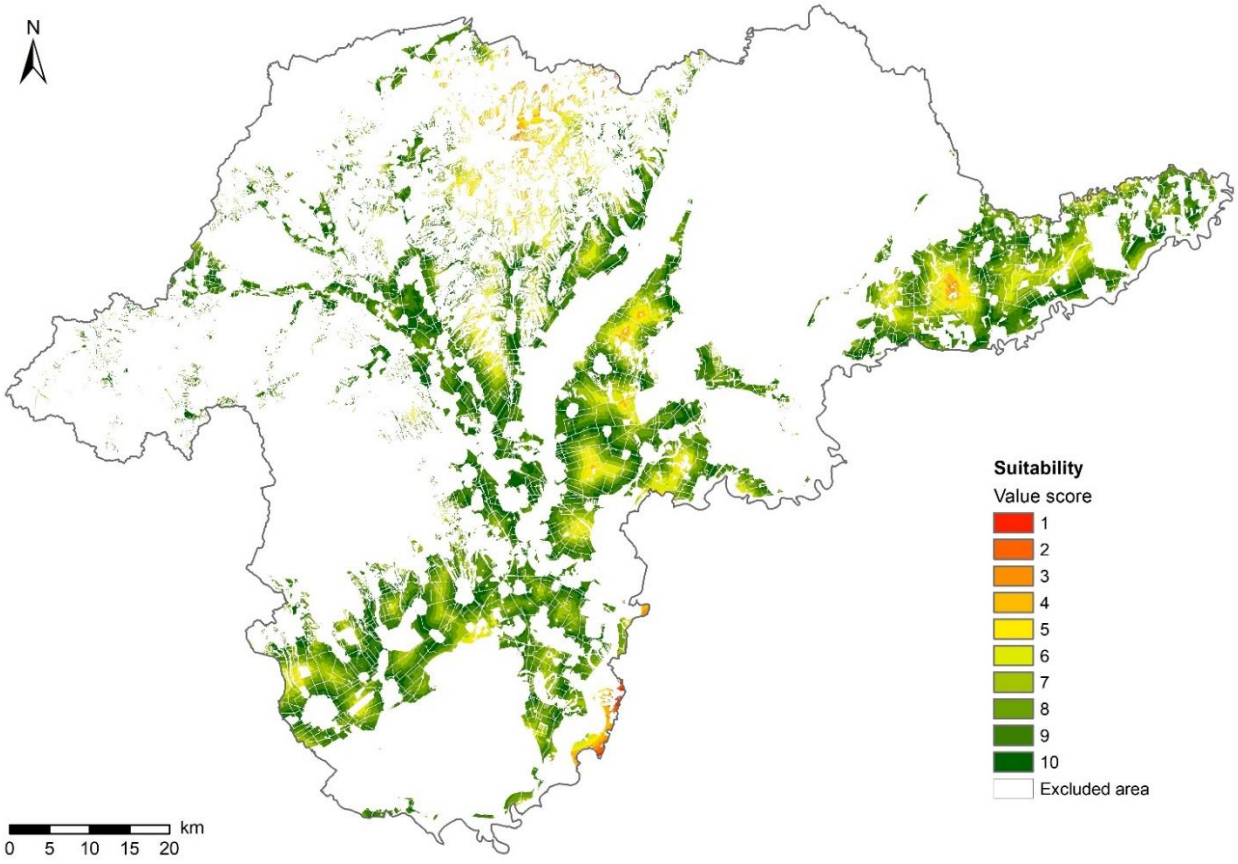

Figure 1: PtG site suitability map of the study area, Borsod-Abaúj-Zemplén county in Hungary.

Remaining work

The results have already been published [1], and the PhD dissertation was expected to be finished in December 2022.

Related publication

[1] T. Soha, B. Hartmann: *Complex power-to-gas plant site selection by multi-criteria decision-making and GIS*, Energy Conversion and Management: X **13,** 100168 (2022)

DEVELOPMENT OF A PHOTOVOLTAIC POWER OUTPUT FORECASTING MODEL

Bálint Sinkovics

Objective

In light of the proliferation of dispersed photovoltaic entities this study aimed to present a local photovoltaic power output prediction method. In case of a single rooftop system energy production, local environmental conditions can't be negligible, but the spatial-temporal resolution of recent methods are limited. The author filled in this gap and developed a forecast algorithm using space-time kriging to map sparse numerical irradiance prediction to specific sites. The value of global irradiance at a local point is primarily determined by it's diurnal cycle and cloud movements. While the former one is a deterministic parameter, the level of cloud covering notably affects the local estimation process. To handle this aspect the forecasting model considers the cloud covering. The extension of the concept enables to predict solar irradiance locally with high spatio-temporal resolution and to support monitoring stations over the local power grid area of interest.

The main objectives of the thesis work were the following:

- Review of modelling options for environmental parameters affecting photovoltaic power generation,
- Determining the critical spatial-temporal resolution of weather parameters,
- Modelling of the selected weather parameter(s) at the specified resolution using a proprietary methodology.

Methods

The spatio-temporal kriging method was used to determine the value of global radiation for a given geographical location. It is used to estimate the global irradiance of a geographic point using 1) historical data from meteorological stations in its vicinity to reveal the correlations and time-lags between each station pair, 2) spatially and temporally sparse Numerical Weather Prediction data, which were fitted to the geographical point of interest.

The structure of the proposed forecasting model is depicted by Fig. 1. Firstly, cross correlation of each station pair was determined, and all the days were clustered to 3 categories considering cloud covering: clear-sky, overcast, partly cloudy days. It was expected that as the distance between meteorological station pairs increases, the standard deviation in the time lag caused by cloud movements will also increase. This relationship defined a critical distance within which weather data are only relevant for forecasting. Based on the results so far, the kriging model predicted global irradiance for a given geographic point and was then converted to production using a PV physical model.

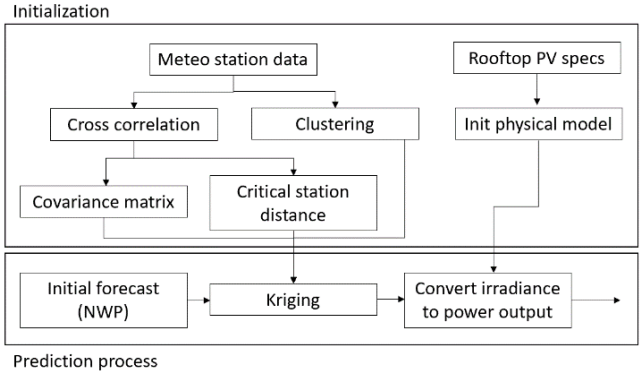

Figure 1: Proposed forecast model structure

Results

A significant correlation relationship between the data of two measurement points was observed with a time lag depending on the geographical distance. To validate this point the data of seven meteorological stations (Püspökszilágy, Bp. Zoo, Bp. Ferihegy, Bp. Pestszentlőrinc, Martonvásár, Aszód, Tápiószele) were paired in all possible ways to determine the time delay between each measurement point as a function of geographical distance. Then, using the data of all pairs of stations, the critical geographical distance beyond which the correlation between the two points is considered too weak was determined by clustering, the resulting distance being 40km.

On the basis of the spatio-temporal relationships determined, spatio-temporal kriging was used to define the global radiation value for the geographical location of the reference PV system. In this process, the kriging model determined the linear combination of nearby measurements, where the weights of the linear combinations depend on the relative positions of the measurement locations and indirectly on the value of the measurements. Based on the statistical relationships extracted from the historical measurement data, the data of a numerical prediction model were refined using kriging. The resulting, geographically corrected global irradiance data can be used as input data for a photovoltaic power plant physical model to determine the true value of the production.

SIMULATION OF ELECTRICAL SYSTEM MODELS WITH A LARGE NUMBER OF ELEMENTS USING ARTIFICIAL INTELLIGENCE AND PARALLEL PROGRAMMING

Barancsuk Lilla

Objective

Power grids are large complex networks whose dynamics, stability and vulnerability are intensively studied; new challenges arise with the increase of distributed renewable energy resources. The dynamics of electrical grids is highly affected by desynchronization between nodes, which can start an avalanche-like cascade of line failures causing massive outages. The objective of this work is to model the networks and investigate their vulnerability using Kuramoto-like synchronization models.

Methods

Modelling power systems in detail leads to an increased computational cost, as a much larger number of nodes (in the order of millions) needs to be dealt with than in the traditional power grid models. The Kuramoto model is a set of coupled nonlinear ordinary differential equations that describes the power grid as an ensemble of coupled oscillators and is widely used for investigating the synchronization properties of networks. The modelling of the power grid by the Kuramoto model consists in the solution of a system of such equations where each equation corresponds to a node in the power grid leading to a solution of a number of equations by the millions. To be able to efficiently handle the model, we numerically solved the second order Kuramoto equations on a Graphics Processing Unit (GPU), and simulated cascades as threshold line failures. Our solution uses a special memory layout for the network graph, and we studied different numerical solvers supplied by boost's *odeint* library (https://www.boost.org/doc/libs/1_63_0/libs/numeric/odeint/doc/html/index.html - It represents a C++ library), which we compared in terms of precision and performance [1]. My contribution was the implementation and analysis of line failures and simulated cascades for GPU. The combination of swing equations with line threshold failures also allows us to describe the dynamical avalanche-like blackout failures in different HV power-grid networks.

Results

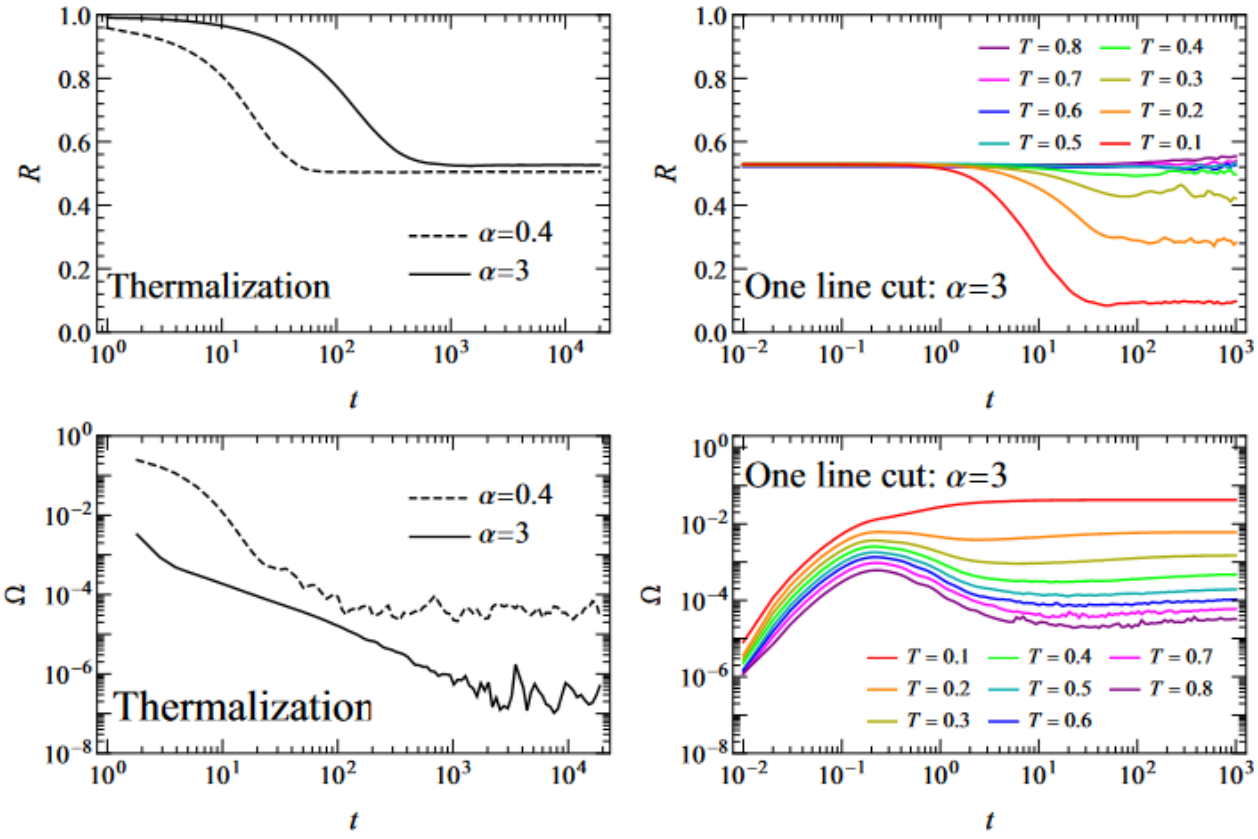

Figure 1: The thermalization dynamics and the effect of one followed line cut after the thermalization process. Meaning of symbols: a: global coupling constant; R: Kuramoto order parameter (measures network synchronization); Ω: standard deviation of node angular frequencies (measures network desynchronization); t: line cut threshold

We compared the stability and blackout statistics for two networks, the US-HV and the EU HV networks. We showed that nonuniversal power-law size and duration distributions emerge below the first-order transitions of the Kuramoto model, thus we see an example for hybrid transition known in other branches of physics [2]. The results show that the damping feedback plays a role of slowing down the dynamics, and enlarging the frequency spread at the same time. The networks exhibit a hysteresis behaviour. One random line cut can even trigger non-universal power-law cascade line failures leading to Dragon King events that can be observed in the vicinity. The EU-HV network seems to be more resilient than the US-HV network.

Remaining work

Further research will focus on extending the code for more complex network behaviour, e.g., local feature analysis.

Related publications

[1] D. Shengfeng, G. Odor, B. Hartmann, and L. Barancsuk: *Critical synchronization dynamics on power-grids,* In APS March Meeting Abstracts, vol. 2022, pp. N00-226. (2022)

[2] L. Barancsuk: *Solving the Kuramoto Oscillator Model of Power Grids on GPU,* In: GPU Day 2021 Book of Abstracts, pp. 6-7. , 2 p. (2021)

LIFE-TIME CONSIDERING CONTROL

Pál Szentannai, Tamás Fekete, Tibor Szűcs, Bálint Pudleiner

Objective

Increasing the service life-time of large scale power plants does significantly improve their benefits both from economic and ecological aspects. The target of the current project was to serve this by means of developing a generally applicable control scheme that also considers its effects on structural integrity.

Methods

After surveying the published results, based on them, we advanced by setting up a generally applicable control scheme that fulfills the Life-Time Considering Control (LTCC) requirements (Fig. 1). Further, all its components were realized by their mathematical formulations. For this, the "Process" was modelled by our in-house dynamic model of a pressurized water nuclear power plant, and both components of the "Structural Integrity Assessment" block were described by well-chosen calculations from the literature. The primary method for evaluating the different control algorithms was numerical simulation.

Results

Besides developing the generally applicable LTCC scheme (Fig. 1), it was realized for enabling numerical simulations and test runs. The first results clearly show that a significant reduction in the life-time consumption of the instationary control actions can be achieved by practically negligible loss in the control performance (Fig. 2).

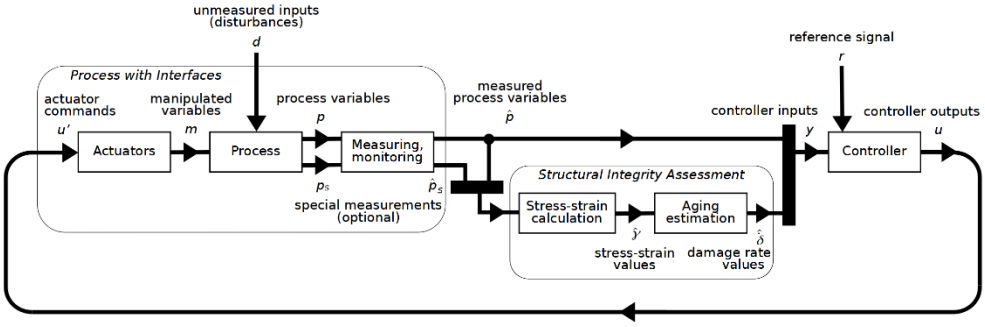

Figure 1: General structure of Life-Time Considering Control

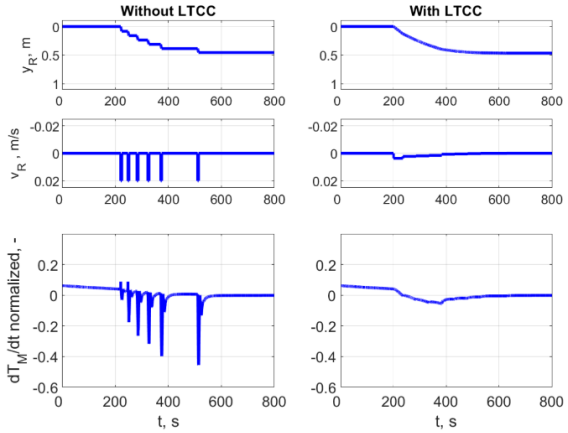

Figure 2: Simulated cases without LTCC (left column) and with LTCC (right column). The differences in the resulted thermal stress of the same load change procedure are visible in the two bottom figures. (Thermal stress is the major cause of life-time consumption. The first and second figures show the y_R positions and v_R velocities of the control rods.)

Remaining work

For developing the optimal control algorithm, a methodology is needed for finding the theoretically possible best performance (regarding reference tracking). Further, the "Structural Integrity Assessment" block must be improved by numerically cheap, though accurate algorithms.

Related publications

[1] P. Szentannai and T. Fekete: *Integrated optimization of process control and its effect on structural integrity – A systematic review*, Engineering Failure Analysis, p. 106101, Feb. 2022.

[2] P. Szentannai and T. Fekete: *Modeling and minimizing the effects of control actions on structural integrity*, 19th MNT Nuclear Symposium, Sep 29–30 2022, Budapest

TRENDS IN HUNGARY'S ENERGY MIX AND POSSIBLE NPP RESPONSES

Pál Szentannai, Tamás Fekete, Bálint Hartmann, Katalin Kulacsy

Objective

The Centre for Energy Research is a technical support organization to the operator of the existing (and later probably also of the new) units of Paks Nuclear Power Plant (NPP). Looking ahead and giving a well-established estimate of the future environment for our partners is one of the internally driven obligations of our research centre. Further, we see the radical changes that have been happening on the source side of the electricity system due to the rolling back of large-sized fossil-fuelled power plants and the coming to the front of uncontrollable renewables. Because of these, we first wanted to give an exact overview of the trends and expectations covering the upcoming two decades. Then, their consequences on large-sized power plants, including NPPs were studied, with special consideration for their structural integrity and fuel issues. Finally, the control systems were investigated as the main actors in managing the load changes properly.

Methods

In the first part of the research work, we made an overview and an estimate of the source-side composition and export-import relationships of the Hungarian electricity system. To start this, we did a literature review. It covered the scientific literature and also the available actual publications coming from several parties like the Hungarian and European governmental sector, power plant operators and owners, and other stakeholders. Throughout the evaluation of these resources, together with our own simulations, we were able to formulate the most plausible scenarios for the area and time span in question.

Structural integrity of major structural elements of the power plants is severely affected by the ageing of their structural materials. Safety limits are determined through model calculations with adequate predictive power. Numerical calculations have been performed using Finite Element Analysis (FEA) codes.

Estimating the behaviour of fuel rods was carried out based on experimental data and models found in the literature.

The control structures and algorithms were gathered by an intensive literature survey covering both scientific papers and community-made brochures and recommendations. The high number of versatile solutions was then synthesized and structured to get a systematic overview of the possible known approaches. Throughout this, the impact on structural integrity and fuel properties was also investigated and included in the structured overview. Further, the requirements set by the electricity network were understood and represented in a clear and uniform manner.

Results

An estimate on the future state of the Hungarian power system can be found in the Network Development Plan prepared by MAVIR, the Hungarian Transmission System Operator. The current methodology of the preparation of the Network Development Plan includes a detailed analysis on future scenarios of generation and consumption, which are called "behavioural analysis" scenarios. These scenarios take into consideration conceptual ideas, the macroeconomic environment, the regulatory environment, national policies and the effects of changing technological trends. The actual Network Development Plan considers two such scenarios, #1 as "Controllable and green power system" and #2 as "Boosting the economy through renewable energy investments".

Scenario #1 considers a longer lasting economic crisis, where residential and business investments are only returning slowly to their previous levels. New technologies also spread slowly, but electrification still remains an influential factor. Residential electricity generation is expected to increase, but the process is slowing down due to the abolishment of current net-metering and settlement rules. The latter trend requires and motivates maintaining and increasing flexible generation units, as without significant investment in such units, operation of the power system would be corrupted by the boom of solar generation. Controllable capacities should be extended in terms of both aFRR and mFRR (automatic and manual frequency restoration reserve, respectively).

Scenario #2 considers a faster recovery from the economic crisis, allowing national and EU-level decarbonization goals to remain as a centerpiece of the energy policy through more intensive finance of investments. The scenario expects major technological changes, which would affect the nature of the load curve as well. Residential electricity generation is expected to steadily increase, which necessitates the reservation of significant volumes of balancing reserves not only from national but regional sources.

System operators of Hungary will face important challenges. In case of Scenario #1, approximately half of the generation capacity will be based on renewable sources (55% in 2027, 54% in 2032), while in case of Scenario #2, renewable capacities still provide half of the total installed portfolio (57% and 55%).

The Network Development Plan sets the boundary conditions for balancing capacities including the following ones:

- The current aFRR capabilities of power plants will decrease by approx. 50% as new standardized balancing products will be introduced.

- Capabilities of balancing groups (aggregators) will remain at the same level, even with the appearance of new standardized balancing products with faster reaction times.
- All newly constructed power plants will be capable of providing balancing capacities as per the requirements of the Operational Guidelines.
- New energy storage installations are expected to provide 240 and 280 MW of aFRR capability by 2027 and 2032, respectively.
- 150 MW of power-to-hydrogen capacity is assumed by 2030, half of which would be capable of providing aFRR service.

Achievements in structural integrity can be summarized as follows. Load-following operation is accompanied by a significant increase in the number and amplitude of operating transients, which then results in accelerated ageing of structural materials. Material ageing is an umbrella concept as ageing is an extremely complex and multifaceted phenomenon. A deeper scientific understanding and description of ageing is still an unresolved issue. At macro-scale, material ageing results in a permanent decrease in the energy absorbing capacity of structural materials and other adverse changes in their microstructure. More frequent dynamic loads accelerate material ageing. The key ageing mechanisms affecting structural materials in NPP units are: (1) neutron-assisted ageing, (2) thermal-mechanical fatigue, (3) thermal ageing, (4) chemical ageing –e.g., corrosion, diffusion-assisted ageing, etc.–. Material ageing effects become dominant after a long period of operation –several decades– and eventually ageing limits the technically allowable lifetime of a unit. Comparing load-following with steady-state operation, neutron assisted ageing and thermomechanical fatigue in the load-following mode can increase significantly for the four ageing mechanisms mentioned above. This implies that –on the one hand– the introduction of load-following mode should be preceded by careful structural integrity calculations. On the other hand, it is recommended to introduce a control system optimizing the trade-off between time required to reach the load target and the power dissipated during the process.

The **most relevant phenomena occurring in fuel rods specific to load-follow** are cladding fatigue (studied earlier at the Centre) and burst Fission Gas Release (FGR). Burst FGR is due either to the growth and interlinkage of grain-boundary bubbles (which requires time at high temperature) to form a tunnel to the free volume, or to fuel micro-cracking (which occurs due to stresses). In both cases it is the gas accumulated over time on grain boundaries that is released, the phenomenon is therefore only relevant above a certain burnup. According to experiments and several models reported in the literature, burst FGR is only significant (>1-2%) above fuel centerline temperatures of 1450-1600 °C, when bubble interlinkage can take place. Safety analyses performed at the Centre for VVER-440 and VVER-1200 reactors show that fuel centerline temperatures never exceed 1660 °C in normal operation, but this temperature occurs at the beginning of life when there is no gas on the boundaries yet. By the time gas accumulates, the calculated maximum temperature goes down to or below 1400 °C, so no significant burst release occurs. However, experimentalists also describe a small burst FGR of maximum 2% that occurs during transients involving temperatures around the normal operation temperatures of the pellet rim, i.e., possibly during load-follow. This release is due to stress-induced micro-cracking and empties the bubbles affected by the crack, which do not contribute to any further release until they fill up again with gas, as shown by measurements. The release was of 1.5% at a burnup of 28 MWd/kgU, 1.8% at 49 MWd/kgU and up to 2% at 58 MWd/kgU, which extrapolates to 2.3% at a maximum pellet average burnup of approximately 80 MWd/kgU. The fission gas release of a VVER-1200 fuel rod with such a maximum pellet average burnup is approximately 14% corresponding to an inner pressure of 14.5 MPa. Accordingly, micro-cracking would increase it conservatively to 17% corresponding to an inner pressure of 17.5 MPa. This is still safely below the design limit of 21 MPa, so no constraint has to be imposed on load-follow operations due to fuel micro-cracking.

The **control system** of the plant is the one responsible for managing any load changes required by the consumer, the electricity network. Accordingly, it has the capabilities, thus also the responsibility for doing that in such a way that also considers its effects on structural integrity and fuel rod integrity. This approach is a rather new one, as classical control philosophy cannot integrally consider these side-effects besides the direct control target.

Modern control theory does offer all tools for realizing the so-called Life-Time Considering Control (LTCC); however, its application in large-sized power plants must be carried out in a rather mindful way. This action, namely, requires a deep and comprehensive knowledge of (i) plant dynamics, (ii) structural integrity, (iii) fuel rod behaviour, and (iv) control theory. Model-based controllers in a predictive manner are the most advisable and mostly applied algorithms; hence besides careful design of the control topology, the development of a dynamic model of the plant is also essential. Further, this model also has to incorporate all phenomena to be considered, such as the structural integrity of the well-chosen critical parts. In the present work such a control strategy for pressurized water NPPs was developed and tested via numerical simulations. The results clearly show that a significant improvement in the reduction of loss of life-time can be achieved even without any noticeable reduction of the control performance (Fig. 1).

In the case of the above simulations, the setpoint for the load changes had to be strictly followed throughout the transient, which is expressed keeping the realized lines very close to the reference for the power output. (See the continuous and dashed lines in both upermost diagrams in Fig. 1.) It is important to emphasize that the tolerance for the output power in real life is much less strict. The definition of these tolerances may vary from country to country; however, they can be grouped into just a few types. Note that applying the right scheme of tolerances is of very high importance when developing the final control setup to avoid setting too strict expectations against the controller and resulting in unaffordable consequences on the structural integrity side.

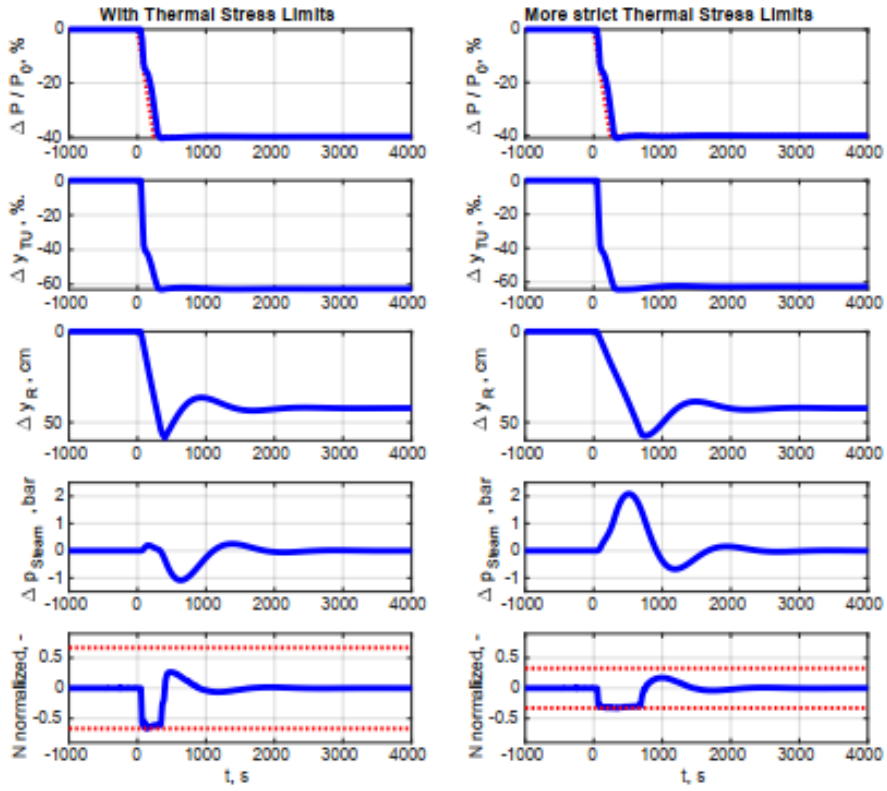

Figure 1: Load change managed by Life-Time Considering Control (LTCC) with a broader stress limit range (left column) and narrower stress limit range (right column). Note that the mechanical stress (bottom diagrams) on the reactor side during the transient was kept in a narrower band without decreasing the electrical power ramp rate (top diagrams). The model-based controller did this by utilizing the dynamic properties of the NPP. Diagrams in rows 2 to 4 show this by indicating the positions of the main steam valve and the control rods, followed by the resulting main steam pressures, respectively.

Finally, it is to be pointed out that load-follow operation even in NPPs is indeed an existing possibility. It was studied by others in depth, especially in Germany and France. Based on many years' experiences, the relative ramp rates of NPPs is ranged close to those of conventional power plants, as shown in the left diagram of Fig. 2. However, also considering the generally very big rated power values of NPPs, the same capabilities expressed in real ramp rates, that is, in MW/min, NPPs definitely outperform the other power plants, as visible in the right diagram of Fig. 2.

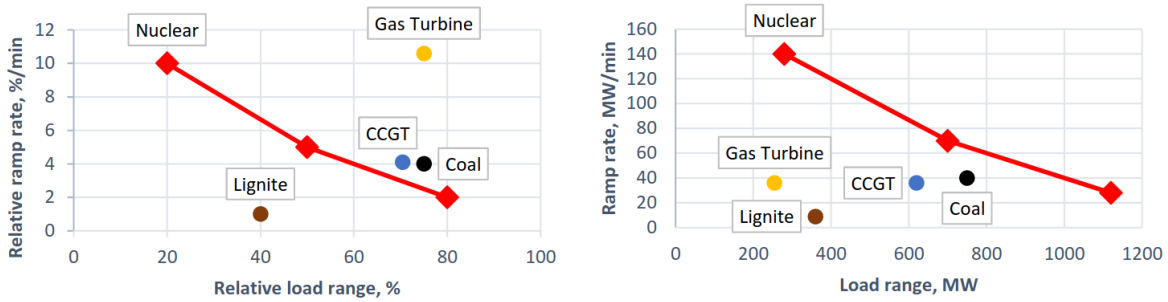

Figure 2: Typical, practically allowable ramp rates and ranges of load changes of different power plant types. Left diagram: relative values; right diagram: absolute values. (For NPPs three different Ramp Rate – Load Range pairs are widely known and applied.)

Remaining work

The requirements on the electricity network side should be further refined and actualized. All model parts should be made numerically more effective. Also, the future results should be implemented and tested via dynamic simulations. The tools and codes resulted from the present project can also be used in such a direct way that all existing controllers will be kept, only their parameters will be tuned for also considering their effects on structural integrity.

Related publication

[1] P. Szentannai and T. Fekete: *Integrated optimization of process control and its effect on structural integrity – A systematic review,* Engineering Failure Analysis, p. 106101, Feb. 2022.

ELIMINATION OF OXACILLIN, AND ITS TOXICITY AND ANTIBACTERIAL ACTIVITY BY USING IONIZING RADIATION

Erzsébet Takács, Jianlong Wang Libing Chu, Tünde Tóth, Krisztina Kovács, Anikó Bezsenyi, László Szabó, Renáta Homlok, László Wojnárovits

Objective

The presence of poorly biodegradable, recalcitrant organic molecules like antibiotics in surface waters is a general problem nowadays. Pollution by antibiotics can lead to the development of antibiotic resistant bacteria and the spread of antibiotic resistant genes in different water matrices. In our work, electron beam and γ irradiation induced degradation of a frequently used antibiotic, oxacillin (Fig. 1) was studied in detail, monitoring the chemical and biochemical characteristics of the degradation products and comparing them with those of cloxacillin (Fig. 1) [1].

Methods

Degradation of our selected antibiotic, oxacillin was studied in 0.1 mmol dm^{-3} concentration using ionizing irradiation. Pulse radiolysis experiments were carried out using 800 ns pulses of electrons accelerated to 4 MeV energy and using a 20 Gy/pulse (J kg^{-1}/pulse) dose. A panoramic type ^{60}Co facility with 1.8 PBq activity was used in the steady-state γ-radiolysis experiments. The dose rate of the ^{60}Co measured with ethanol-chlorobenzene dosimetry was 2 kGy h^{-1}.

Various methods were used in order to get a comprehensive picture about the degradation processes. The optical absorption spectra were taken using a JASCO 550 UV−Vis spectrophotometer with 1 cm light path. Oxidation and mineralization were characterized by Chemical Oxygen Demand (COD) and Total Organic Carbon (TOC) content measurements using Behrotest TRS 200 and Shimadzu TOC-L CSH/CSN equipment, respectively. According to DIN EN 1899-1 (1998), ISO 8192 (1986) and DIN EN ISO 11348-2:199, Biochemical Oxygen Demand (BOD), Oxygen Uptake Rate (OUR) and acute toxicity test TOX (using *Vibrio fischeri* as a test organism) measurements were carried out to monitor the change of biodegradability and toxicity as a function of the applied dose, respectively. The presence of hydrogen peroxide (H_2O_2) formed in the radiolysis of the water matrix disturbs these measurement; thus its removal is an important sample preparation step by adding catalase enzyme or MnO_2. The antibacterial potency of unirradiated (untreated) and irradiated samples were investigated in agar diffusion tests using a *Staphylococcus aureus* strain (B.01755) from the National Collection of Agricultural and Industrial Microorganisms (NCAIM).

Results

Oxacillin is a poorly biodegradable antibiotic. However it does not exert toxicity to *Vibrio fischeri* luminescent bacterium and it is non-toxic to the mixed microbial community of a biodegradation unit in a wastewater treatment plant. However, the microbes cannot use it as nutrient source since they are not able to decompose it.

During irradiation of aerated aqueous solutions the main reactants, the hydroxyl radicals, predominantly attack the bicyclic ß-lactam part of oxacillin and induce the degradation of this pharmacophore responsible for the antibiotic effect. Oxacillin and cloxacillin have the same fused bicyclic system. The difference between the two antibiotics is at the benzene ring: cloxacillin has a Cl atom on this ring. Because the reaction mainly takes place on the ß-lactam part, and not at the aromatic ring, the degradation characteristics of the two antibiotics are highly similar. Under anaerobic conditions, the hydrated electrons attack the carbonyl groups possessing strong electron deficiency in both oxacillin and cloxacillin. This reaction may also induce the degradation of the double ring system.

Our experiments clearly show that ~50% COD and ~25% TOC removal occurs in the 0 - 4 kGy dose range. At 1 kGy dose practically all of the original oxacillin molecules undergo transformation. The results reflect gradual degradation; first, the molecules transform to slightly oxidized derivatives (mainly hydroxylated derivatives of the original molecules) and then, very slowly, mineralize to small inorganic molecules (CO_2, H_2O, NH_3, etc.). When it was irradiated with relatively low absorbed doses (0.5 – 1 kGy), the solution became easily biodegradable (BOD_5/COD ratio is above 0.4) and the degradation products were utilized by the microbes. This low dose is adequate to eliminate the antibacterial activity of both oxacillin and cloxacillin.

According to our calculations, in a real wastewater matrix, a 0.5 - 1 kGy absorbed dose is sufficient to destroy the majority of harmful molecules, and to decrease the toxicity and reduce the antibacterial activity. Ionizing radiation, when combined with the conventional methods as a post-treatment, is a promising and economical technology for wastewater treatment plants.

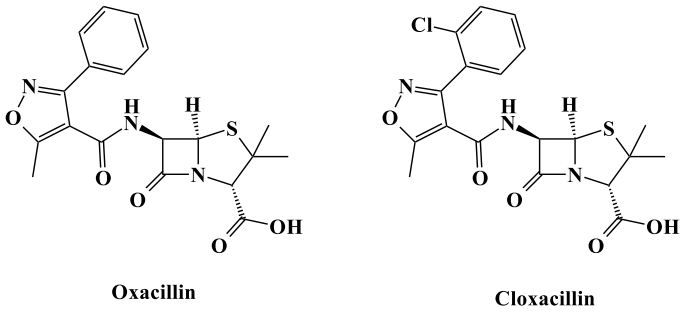

Figure 1: The chemical structure of Oxacillin and Cloxacillin

Remaining work

This project has been completed.

Related publications

[1] E. Takács, J. Wang, L. Chu, T. Tóth, K. Kovács, A. Bezsenyi, L. Szabó, R. Homlok, L. Wojnárovits: *Elimination of oxacillin, its toxicity and antibacterial activity by using ionizing radiation,* Chemosphere **286**, 131467 (2022)

[2] L. Wojnárovits, J. Wang, L. Chu, T. Tóth, K. Kovács, A. Bezsenyi, L. Szabó, R. Homlok, E. Takács: *Matrix effect on the hydroxyl radical induced degradation of β-lactam and tetracycline type antibiotics*, Radiation Physics and Chemistry **193**, 109980 (2022)

[3] L. Wojnárovits, J. Wang, L. Chu, E. Takács: *Rate constants of chlorine atom reactions with organic molecules in aqueous solutions, an overview,* Environ. Sci. Pollut. Res. **29,** 55492 (2022)

[4] Gy. Sági, SD. Pillai, E. Takács L. Wojnárovits: *Pharmaceutical Waste Management by Ionizing Technology,* in: Shima Shayanfar, Suresh D. Pillai (Eds) Ionizing Radiation Technologies: Managing and Extracting Value from Wastes. pp 229-241 (2022)

RELATIONSHIP OF AIRBORNE SARS-COV-2 RNA TO INDOOR AEROSOL IN HOSPITAL WARDS

Veronika Groma, Szilvia Kugler, Árpád Farkas, Péter Füri, Balázs Madas, János Osán

Objective

Since the COVID-19 pandemic started, a lot of attention has been drawn towards the emission, transport, infection properties, collection, detection, and particle sizing of the SARS-CoV-2 virus. But still, a lot of challenges and obstacles exist. For instance, aerosol sampling in the environment of patients treated in a hospital must be done in a way that doesn't disturb the work of the hospital staff nor the patients' calm and recovery. The first studies highlighted that SARS-CoV-2 spreads through direct human-to-human droplet transmission, by indirect means such as contact with contaminated objects or surfaces and by airborne transmission. Floating aerosol particles proved to play an essential role in airborne transmission of SARS-CoV-2 viruses. Therefore, their size-fractionated collection and analysis would be invaluable. Aerosol sampling in COVID departments, however, is not straightforward, especially in the sub-500-nm size range. The primary objective of the present study was to quantify the SARS-CoV-2 RNA prevalence in a hospital ward, and in a specific High-Dependency Unit (HDU), for a wide size range in many fractions from the ultrafine mode (particulate matter of nanoscale size) up to coarse mode (aerodynamic diameter of aerosol particles ranging from 2.5 to 10 μm), for many different patient groups, hence allowing a statistical evaluation. Based on this, our aim was to determine the characteristic size range of airborne SARS-CoV-2 RNA and its possible change over time due to the progression of the disease. By determining the distribution of the particle number concentration with high time resolution, our second aim was to study the effect of particle mass fluctuations due to indoor human activity and the relationship between the number of SARS-CoV-2 RNA copies and the aerosol particle number/mass concentration in hospital wards.

Methods

Measurements were performed in two different hospital wards. At the Pulmonology Hospital of Törökbálint (hereafter Hospital A) only one, whilst at the Department of Pulmonology of Semmelweis University (hereafter Hospital B) three patients were treated at the same time in the wards studied. While in Hospital A a normal pulmonary patient room was sampled, in Hospital B a high-intensity non-invasive ventilation unit (HDU) was sampled. The aerosol sampling and monitoring instruments were installed as close as possible to the patient on the nightstand beside the bed, at the height of the lying patients' heads at both hospitals. In Hospital A only one patient, whilst in Hospital B nineteen patients were studied. This allowed us to study both the time evolution of virus concentration for a single patient and differences of virus concentrations resulting from multiple patients with different degrees of disease severity. As the patients changed within a short time, there were only 3–4 consecutive days when the same patients were in the ward, but the type of non-invasive respiratory support might have changed, according to the improvement or worsening of the clinical condition of the patients. Thus, we could define 7 groups of measurement days for statistical analysis, which are numbered as A1 and from B1 to B6. The HDU department was cleaned regularly according to the local protocol, prior to the start of the measurement each day. Measurements lasted for 8 hours each day. During the sampling period, the variant of concern (VOC) of SARS-CoV-2 was alpha VOC for Hospital A and included periods of alpha and delta VOC for Hospital B.

An in-house built May-type cascade impactor was used to sample size-fractionated aerosol particles. Two versions of the impactor were used; a 7 stage basic version, which has aerodynamic cut-off diameters of 16, 8, 4, 2, 1, 0.5 and 0.25 μm for stages 1 to 7, respectively at 20 L/min sampling flowrate, whilst the 9 stage in-house developed extended version is suitable for collecting further size fractions with cutoff diameters of 0.18 and 0.07 μm (stages 8 and 9 respectively). No sampling was performed on stages 1 and 2, since particles larger than 10 μm aerodynamic diameter are beyond the range of PM_{10}. In Hospital B, 22 sample sets were collected (5 stages each, altogether 110 samples), while in Hospital A, only 6 sample sets (7 stages each, altogether 42 samples). Simultaneously with the 8-h impactor samplings, an optical particle counter (OPC) (GRIMM PAS 1.109) was used to measure the indoor particle mass concentration of PM_1, $PM_{2.5}$ and PM_{10} (particle matter with an aerodynamic diameter less than 1, 2.5 and 10 μm, respectively) with a time resolution of 1 minute. Simultaneous sampling by the impactor and OPC allowed the analysis of any possible correlation between the size distribution of the aerosol and the SARS-CoV-2 RNA concentration in aerosol particles for each patient group. Since the OPC data are obtained at a high time resolution, and the values are influenced also by the outdoor air quality, first a preprocessing of the PM mass concentration data measured by OPC was applied for each 8-h sampling period.

Size-fractionated PM samples were collected onto presterilized gelatin filters (Sartorius) at stages 3 to 7/9 of the impactor. The gelatin filters were removed and placed in a clean and sterile holder and were forwarded within 12-72 hours for virus testing, which is an acceptable time frame for specimen transportation and storage. The gelatin filters were dissolved in 600 μl RAV1 buffer of the NucleoSpin RNA Virus kit (Macharey-Nagel, Düren, Germany), and the isolation of viral RNA was carried out following the kit's protocol. Only samples with at least 10 copies of the N2 gene sequence for a given aerosol size gelatin were used for statistical analysis.

Results

The number of SARS-CoV-2 RNA copies was found to be highly variable in the studied size fractions. In the case of Hospital A, 25 out of the 42 samples (59.5%) within the six sample sets were determined to be positive of which 19 (45.2%) samples were quantifiable for SARS-CoV-2 RNA. The size variation of the number of copies shows a bimodal distribution in all cases except for one day (28th April 2021), while the locations of maxima vary in size from day to day. The average concentration of gene number N2 of SARS-CoV-2 ranged between 18 and 184 copies/m^3 between 70 nm and 8 µm during the measurements.

In the case of Hospital B, 65 out of the 110 samples (59.1%) were found to be positive, of which 35 (32.8%) were quantifiable, but only over a narrower size range (250 nm–8 µm). For this size interval, the total number of SARS-CoV-2 varied in the range of 0.9–59.9 copies/m^3 on average, covering the most active 8 hours of patient care at the HDU. We could obtain quantitative information for only two patient groups (B1 and B4), where the number of SARS-CoV-2 RNA copies could be determined for all days and over the entire size range. A unimodal size distribution was found to be typical in all cases, for which the maximum varied within the 1–4 µm diameter range. No clear time trend in size distribution was observed during any of the 4-day periods [1, 2].

To investigate the significance of the aerosol load status of the wards, a correlation analysis was performed between the PM mass concentration increment and the number of SARS-CoV-2 RNA N2 copies in each size range (PM10, PM2.5 and PM1). Those periods were evaluated for which at least 80% of samples were quantifiable by PCR (i.e., A1, B1, and B4 groups). SARS-CoV-2 copies were summed for all impactor stages within the size range studied (i.e., stages (9, 8), 7, 6 for PM1; all stages for PM10). The results are plotted in Fig. 1.

The most important difference between the two sites in terms of sampling is that the extended version of the May impactor was used at Hospital A, which allowed us the collection of particles below 250 nm. As the number of SARS-CoV-2 in this size range was remarkably high on certain days, it should be emphasized that the further investigation of this size range is strongly recommended. This is also confirmed by the correlation analysis results, since a more accurate conformity is found if the smallest size ranges (stages 8 and 9) are taken into account. According to different studies, the median/mean equivalent spherical diameter of SARS-CoV-2 (without the spikes) was between 60-140 nm. Since in the last two stages of the extended impactor the sampled particles were 70-250 nm in size, the detected RNA sequences could originate from virions contained in very small, eventually dried out droplets, unattached virions or merely virus fragments.

A strong linear relationship between particle mass and number of Covid genes detected was found for the smaller (PM1 and PM2.5) size ranges, while it was moderate for the larger (total, under 10 µm) size range. In general, the aerosol sources in hospital wards can basically be due to (i) the mixing of outdoor particles due to room ventilation, (ii) the emission of people by breathing and speaking, etc., (iii) resuspension as a result of patient or staff activities, and (iv) the direct and indirect particle emission of machines (respirator apparatus) operating in the room. Since the effect of outdoor sources was eliminated, and the quantity of particles emitted during breathing by the hospital staff wearing masks and by patients even with respiratory support was found to be orders of magnitude smaller than the concentration fluctuations due to human activities, it can be stated that the resuspension effect of inside movements are determinant for indoor PM concentration increase. Although, patients are the primary source of airborne SARS-CoV-2 RNA, these virus laden particles are transmitted to the surfaces by direct contact or by sedimentation. Since resuspension of all particles are significant, it can be concluded that the medical staff activities (such as movement and treatment) could result in an excess of virus-laden aerosol particles in the indoor atmosphere. It is worth noting, however, that the virus detection method used in this work cannot distinguish between viable and non-viable viruses/virions.

The slope of the linear regression lines (Fig. 1) was generally much higher for Hospital A than for Hospital B, while it was most similar (same magnitude) in case of PM2.5 at Hospital B for different patient groups. The resulting similarity in the dependence of viral content of the two smaller size range (PM_1 and $PM_{2.5}$) increments under identical site layout and measurement setup conditions (B1 and B4 patient groups at Hospital B) suggests that the viral content of the indoor air is proportional to the increase in particle number concentration caused by indoor activities, taking into account that the characteristics of viral emission of each individual person is highly variable [1, 2].

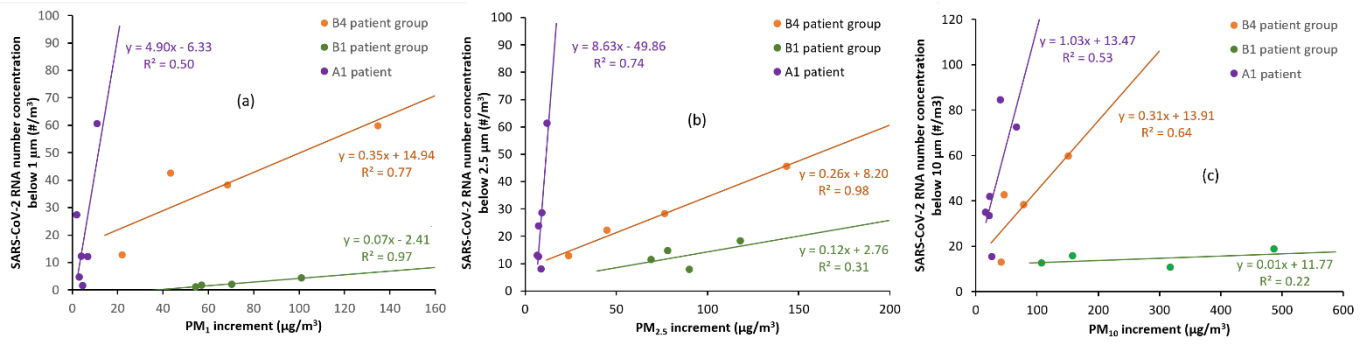

Figure 1: PM vs SARS-CoV-2 number concentrations for three measurement periods (A1, B1, and B4 patient groups) for the a) below 1 µm, b) below 2.5 µm and c) below 10 µm size ranges and the fitted linear regression lines

Remaining work

To measure the relation of indoor aerosol characteristics and size-fractionated SARS-CoV-2 RNA in the home environments of infected persons.

Related publications

[1] Sz. Kugler, Á. Farkas, P. Füri, V. Groma, J. Osán, A. Nagy, T. Erdélyi, A. Horváth, V. Müller, R. Szántó-Egész, A. Micsinai and B. Madas: *Comparison of aerosol size distribution and size fractionated SARS-CoV-2 concentration in different patient rooms*, International Aerosol Conference, Athens, Greece, 4-9 September 2022, SS2-P1-008 (2022)

[2] V. Groma, Sz. Kugler, Á. Farkas, P. Füri, B. Madas, A. Nagy, T. Erdélyi, A. Horváth, V. Müller, R. Szántó-Egész, A. Micsinai, G. Gálffy and J. Osán: *Size distribution and relationship of airborne SARS-CoV-2 RNA to indoor aerosol in hospital ward environments*, Scientific Reports **13**, 3566 (2023)

INCREASING THE STABILITY OF POWER SYSTEMS WITH HIGH RENEWABLE ENERGY SHARE BY THE USE OF COUPLED OSCILLATORS

Bálint Hartmann, Géza Ódor, Shengfeng Deng

Objective

Power-grids are among the largest man-made complex systems, staying in the synchronization state of billions of nodes. Formerly power-law tailed cascade size distributions have been found by outage statistics and Direct Current (DC) models. The spread of renewable resources poses unprecedented pressure on system stability. Our aim is to show how this can be modelled by Kuramoto-like synchronization models, which describe the real power flow in Alternating Current (AC) systems.

Methods

In the second year of the project, state-of-the-art description of the Kuramoto model was created, and numerical algorithms were implemented on graphical processors to solve the differential equation system. To further decrease computational times, the conventional Runge-Kutta-4 solver was replaced with adaptive steppers (e.g. Bulirsch-Stoer). The outage database for later simulations was also assembled.

Results

The European grid was found dynamically more robust than the US grid, however, based on their topological properties, both represent a transition between vulnerable and robust systems. The phase order parameter showed crossover-like synchronization transition as the function of global coupling. Another important result was that the system could even show a more synchronized state after the blackout cascade, near the region of critical couplings and thresholds. This suggests that stability of the grid increases after the loss of vulnerable edges near criticality, within certain parameter value ranges, which resembles the process known in literature as "intentional islanding".

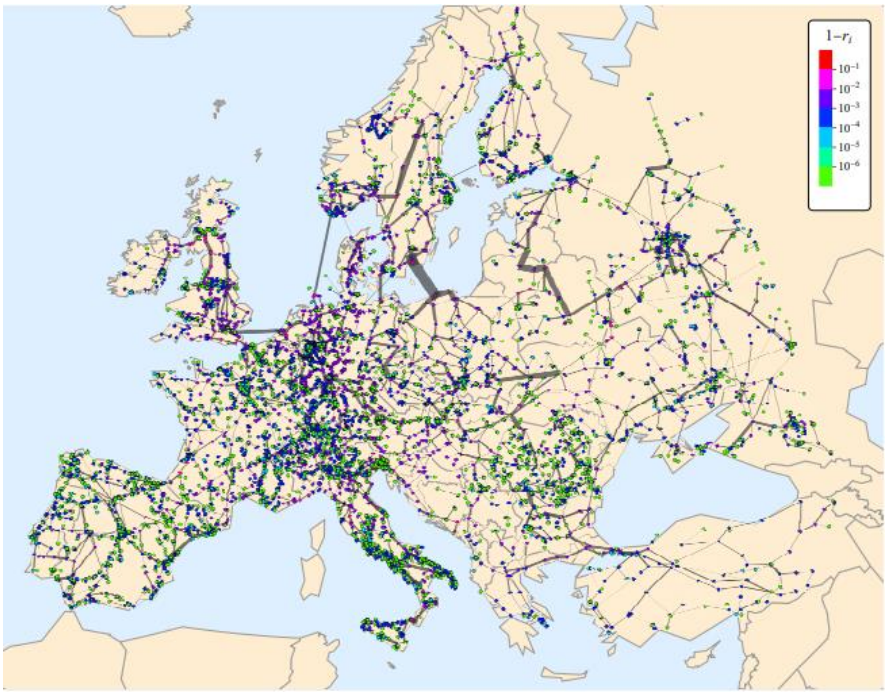

Figure 1: Local Kuramoto results encoded by the colour map as 1− ri. Red corresponds to low local synchronization, green to high synchronization. The width of grey edges is proportional to the amplitude of the power flow.

Related publications

[1] G. Ódor and S. Deng: *Synchronization Transition of the Second-Order Kuramoto Model on Lattices*, Entropy **25**, e25010164 (2023)

[2] G. Ódor, S. Deng, B. Hartmann, J. Kelling: *Synchronization dynamics on power grids in Europe and the United States*, Phys. Rev. E. **106**, 034311 (2022)

[3] S. Deng, G. Ódor, B. Hartmann, L. Barancsuk, J. Kelling: *Critical synchronization dynamics on power-grids*, APS March Meeting 2022, Chicago, USA (2022)

SYNTHESIS AND STRUCTURAL CHARACTERIZATION OF NASICON-TYPE MATERIALS

Margit Fábián, Dávid M. Gyimes, István Tolnai

Objective

A reduction of the dependence of modern society on fossil fuels is an urgent issue. To be able to replace fossil fuels by alternative energy sources like wind or solar energy, the storage of electric power from these renewable sources in rechargeable batteries should be greatly improved. Modern Li-batteries have safety problems and narrow operating temperature ranges. Thus, currently they cannot meet the growing demand for higher energy storage density, charging speed and cost reduction, and further improvements in their design and operation are needed. Besides lithium-ion batteries, sodium-ion batteries have also been rapidly developed recently, which is fortunate due to the fact that sodium is cheaper than lithium and widely available from the oceans. Based on the Nobel-laureate Goodenough's idea, the new type of glassy/amorphous solids is a potential candidate for preparing all solid-state, safe, and rechargeable batteries with high ionic conductivity, energy density and long duration thermal and chemical stability. Our work mainly focuses on the development and structural characterization of a solid Natrium Super Ionic Conductor (NASICON)-type electrolyte, with a potential application in a stationary energy storage system. The NASICON materials with the formula of $Na_{1+x}Zr_2P_{3-x}Si_xO_{12}$ where $0 < x < 3$, were discovered by Goodenough.

Methods

The NASICON solid electrolytes were prepared by a solid-state reaction method in ambient air. Analytical grade Na_2CO_3, Na_3PO_4, ZrO_2, SiO_2 and $NH_4H_2PO_4$ commercial powders were used to prepare the samples. The basic NASICON composition was then doped with ZnO or TiO_2.

Stoichiometric amounts of starting materials were weighed and the mixtures of reactants were thoroughly mixed by ball milling. The homogenized mixture was calcinated at 500 °C (undoped samples), 500 °C (Ti-doped samples) and at 700 °C (Zn-doped samples). The calcinated powders were pressed to 10/20 mm diameter pellets. The last step of the preparation was high temperature sintering at 1100 °C. Regarding the raw materials, we used two types of procedures to obtain the basic NaSiCON composition: 1) $Na_3PO_4 + 2ZrO_2 + 2SiO_2 = Na_3Zr_2Si_2PO_{12}$ (in the Table 1, series 1) (labeled PO in Table 1) and 2) $1{,}5Na_2CO_3 + NH_4H_2PO_4 + 2ZrO_2 + 2SiO_2 = Na_3Zr_2Si_2PO_{12}$ (in the Table 1, series 2 (labeled CO in Table 1).). The formula was $Na_3Zr_{2-y}Si_2PO_{12}$, where the "y" is the proportion of the dopant ions (Ti, Zn). The eight prepared and studied samples are presented in the Table 1.

The density was measured using an AccuPyc II 1340 pycnometer and the porosities were calculated from the density data. X-Ray Diffraction (XRD) measurements were performed using a Bruker AXS D8 Discover diffractometer. We used the Diffrac.EVA program and the International Centre for Diffraction Data Powder Diffraction File (ICDD PDF) database for phase identification. Neutron Diffraction (ND) experiments were performed using monochromatic neutrons (λ_0=1.069 Å) at the 2-axis Position Sensitive Detector diffractometer of Budapest Neutron Centre in the momentum transfer range Q=0.45-10 $Å^{-1}$. Microscopic X-Ray Fluorescence (μXRF) investigations were also performed on the samples. Morphology and shape information are derived from the detection of secondary electrons in Scanning Electron Microscopy (SEM) and elemental analytical information from Energy-dispersive X-ray Spectroscopy (EDX).

Table 1: The composition of the prepared and studied samples

Nr.	Name	Composition
1.0	**NASI-PO**	**$Na_3Zr_2Si_2PO_{12}$**
1.1	**NASI-PO-0,1Ti**	**$Na_3Zr_{1.9}Ti_{0,1}Si_2PO_{12}$**
1.2	**NASI-PO-0,025Ti**	**$Na_3Zr_{1.975}Ti_{0.025}Si_2PO_{12}$**
1.3	**NASI-PO-0,05Ti**	**$Na_3Zr_{1.95}Ti_{0.05}Si_2PO_{12}$**
2.0	**NASI-CO**	**$Na_3Zr_2Si_2PO_{12}$**
2.1	**NASI-CO-0,1Ti**	**$Na_3Zr_{1.9}Ti_{0.1}Si_2PO_{12}$**
2.2	**NASI-CO-0,2Zn**	**$Na_3Zr_{1.8}Zn_{0.2}Si_2PO_{12}$**
2.3	**NASI-CO-0,25Zn**	**$Na_3Zr_{1.75}Zn_{0.25}Si_2PO_{12}$**

Results

The theoretical density of the NASICON-type materials is 3.27 g/cm^3. For the basic, undoped samples, we obtained good density data (3.30 g/cm^3), but for the Ti-doped samples the density data were lower than expected (2.95 g/cm^3). In correspondence with the density data, the porosity-values also changed. The porosity was higher (17.27%) than the optimum – 6.5% - obtained from the literature data, which causes difficulty in measuring the conductivity. Both Ti-, and Zn-dopants had lower values of porosity than for basic sample; it was 9.2% and 7.95%, respectively. The higher porosity produced the

segregation of zirconia at the grain boundary, which caused a decrease in the ionic conductivity. Conductivity is significantly affected by the formation of grain boundaries which is caused by the high porosity.

In a determination of the crystalline phases present (based on the XRD analysis), the formation of both monoclinic-NASICON/PDF 01-084-1200 (identified from the PDF Database- from ICDD: The International Centre for Diffraction data) (which increases the ion conductivity) and monoclinic-ZrO_2/PDF 01-089-9066 (which significantly reduces the ion conductivity) were verified. The quantitative phase analysis results were 94%NASICON/6%ZrO_2 phases for the undoped NASICON samples. The quantitative phase calculation results for the Ti-doped samples show a change to 60%NASICON/40%ZrO_2, and in the Zn-doped samples, we identified a ratio of 89%NASICON/11%ZrO_2. For both the Ti- and Zn-doped samples, no other phase(s) could be identified.

To prove the presence of the doping (Ti, Zn) elements we used the XRF method. The measurements show that the dopants are in the prepared samples, but with this method we cannot find other information on their position in the lattice. In Figure 1, the Ti-α peaks are just below 5 keV and the Zn peaks below 10 keV.

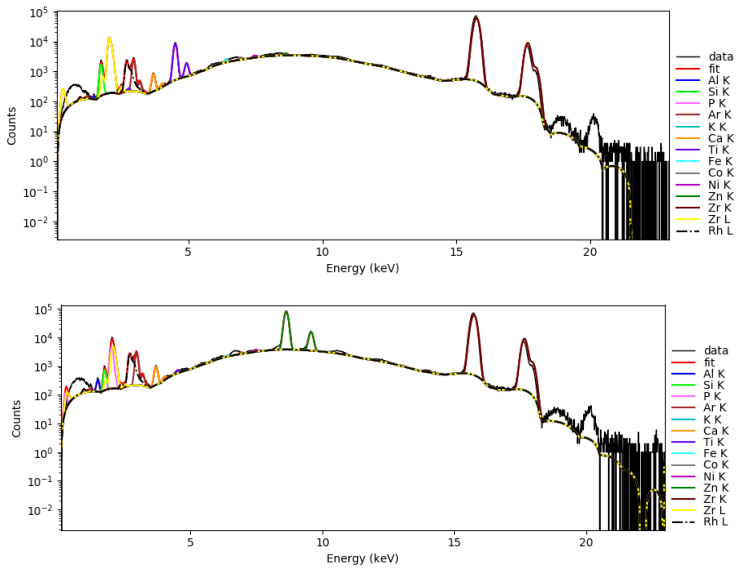

Figure 1: XRF spectras of NASI-PO-0,1Ti (above) and NASI-CO-0,2Zn (below) samples

The profiles of the neutron structure factors (S(Q)'s) of the investigated samples are different from the X-ray diffraction profiles since the scattering abilities of the constituent elements are different for X-rays and for neutrons. Significant differences can be observed between the basic and doped samples, but within a dopant series, the characters of the spectra are similar. From X-ray diffraction we obtained evidence of mixed crystalline phases, and in the case of neutron diffraction, both amorphous and crystalline phases can be identified as indicated by the broad distributions. The evaluation of the neutron diffraction data is still in progress.

Since the porosity data and diffraction results indicated inhomogeneities in the structure, an attempt was made to directly prove the presence of these inhomogeneities using local analytical methods by performing SEM investigations. Detailed SEM/EDX results contain images and major elemental composition for selected positions. Figure 2 shows the SEM backscattered electron image and the corresponding EDX elemental maps on sample NASI-PO-0,1Ti. The inhomogeneity is most apparent in the complementary distributions of Si and P, but is also evident in Zr.

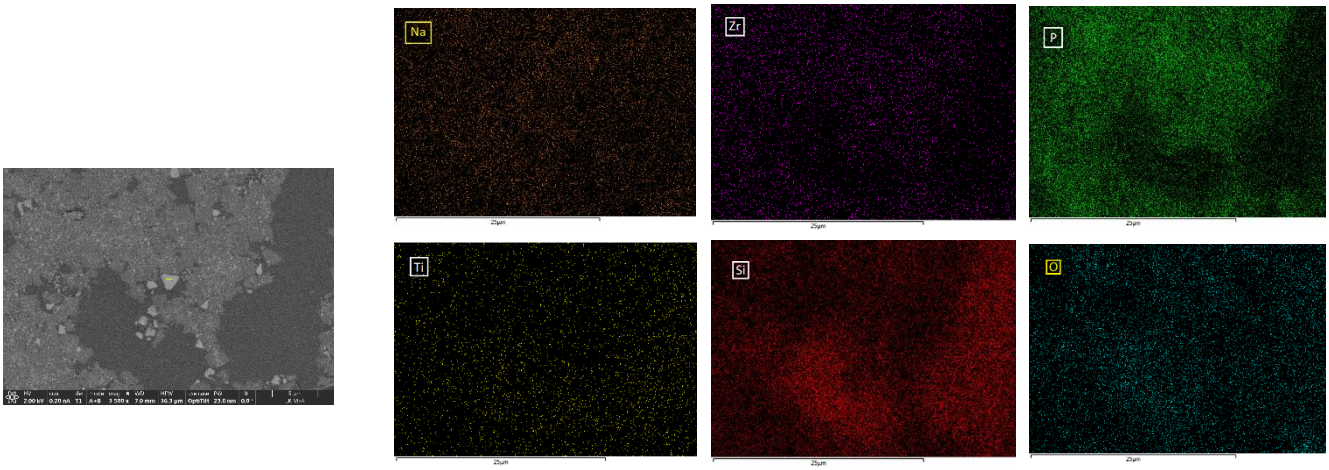

Figure 2: SEM backscattered electron image and the corresponding EDX elemental maps on sample NASI-PO-0,1Ti

The high porosity data and SEM observations carried out on the NASICON samples showed the heterogeneous nature of the samples. All investigated samples have too porous a structure, which makes them unsuitable for conductivity measurements (due to high electrical resistance).

Remaining work

The further development of the sample preparation method is necessary to produce high-density samples, which can be suitable for conductivity measurements.

Related publication

[1] D. M. Gyimes: *Nátrium alapú szilárd elektrolitok előállítása és szerkezetvizsgálatuk, (Preparation of sodium-based solid electrolytes and their structural analysis);* MSc thesis; thesis defence in January 2023; Budapest University of Technology and Economics, Faculty of Chemical Technology and Biotechnology.

V. NUCLEAR ANALYSIS AND CHEMISTRY

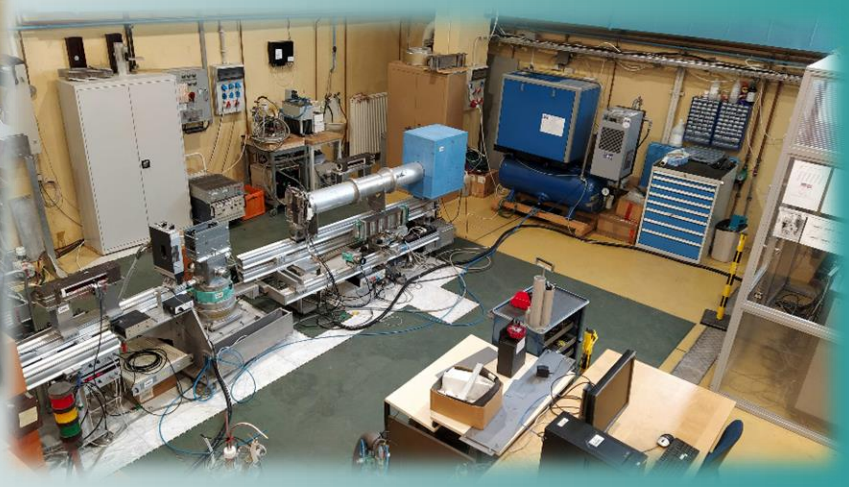

CHARACTERIZATION OF ELECTRONIC WASTE BY NUCLEAR ANALYTICAL AND IMAGING TECHNIQUES

Noémi Buczkó, Boglárka Maróti, László Szentmiklósi

Objective

The recycling of electric and electronic waste is an important aspect of the planned circular economy. This work aims at the comprehensive elemental analysis of electronic waste from discarded personal computers. An analytical methodology needs to be developed for the determination of the amount of valuable and/or hazardous elements in such waste and for the calibration of field-deployable instruments, e.g. the Portable XRF (pXRF) Spectrometer.

Methods

Neutron-based element-analytical techniques such as Prompt Gamma neutron Activation Analysis (PGAA), Instrumental Neutron Activation Analysis (INAA), and in-beam Neutron Activation Analysis (in-beam NAA) were combined with imaging techniques and Monte Carlo N-Particle Transport (MCNP) simulations.

Results

A combination of PGAA, in-beam NAA, and INAA was found to be suitable to quantify the most valuable and/or hazardous elements present in memory cards. PGAA successfully identified most of the major and minor components and some trace elements (e.g. H, B, C, Si, Cl, Cu, Ag, Ni, Ca, Ti, Br, Gd, Cd, and Sb). In-beam NAA measurements can lower the detection limit of some valuable or hazardous elements (e.g. Au, Br, Sb, W, etc.). INAA was suitable to measure the Au, Ag, Sb, Co, Sc, Sr, Hf, La, Ce, Eu, Tb, Br, Cr, and Yb in low concentrations, all of which have great importance in the circular economy or are considered as a hazardous element. The joint interpretation of analytical and imaging methods helped to reveal the spatial location of individual elements. The element ratios measured by each method were in agreement. However, the raw concentrations measured with PGAA were systematically higher than those from INAA. The reasons for the differences were identified, and corrections were applied to the measurements.

MCNP simulations were completed to determine the neutron self-shielding correction factors of powdered waste samples when irradiated in the No 17 vertical channel of the Reactor for INAA measurements or measured in the guided cold neutron beam of the PGAA station. In the case of PGAA a non-detectable main component results in an overestimation of measured concentrations for all elements. Oxygen, the presumed main component of memory cards was not measurable with PGAA under typical conditions. An assumed oxygen concentration was estimated, and the concentrations of other elements were corrected. The in-beam NAA method was successfully further developed to measure absolute concentrations with the measurement of the effective neutron flux. These concentrations were also used for the corrections of PGAA results. The results of the different techniques with these corrections show good agreement.

With pXRF, the following elements were semi-quantitatively determined: Al, Si, Ti, Ni, Cu, Sb, Sn, Pb, and Ag. The measured concentrations were significantly different from those measured by the nuclear analytical techniques. Since there is no matrix-matched factory calibration method available in the evaluation software of the handheld XRF device, a new matrix-matched calibration is being established to make the analysis practical and economical. Furthermore, the analysis of other wastes such as LEDs, Li batteries, solar cells, etc. has also been started.

Remaining work

Implementing a matrix-matched calibration to the handheld XRF spectrometer. Further MCNP computer simulations are ongoing to determine the neutron self-shielding during in-beam NAA measurements and compare them to the other results.

The knowledge will be utilized within the recently started Remade@ARI EU-funded project, which aims at establishing a distributed competence and infrastructure centre in Materials Development for Recycling (https://remade-project.eu/).

Related publications

[1] N. A. Buczkó, B. Maróti, K. Gméling, L. Szentmiklósi: *Neutron-Based Elemental Composition Analysis of Waste Computer Memory Cards*, In: I. Jószai (szerk.) Őszi Radiokémiai Napok, 2022.10.17-19. ISBN 978-615-6018-13-7, pp. 45-50., Balatonszárszó, abstract and oral presentation

[2] N. A. Buczkó, B. Maróti and L. Szentmiklósi: *Characterization of Electronic Waste with Neutron and X-Ray Based Element Analysis Techniques*, 8th International k_0-Users' Workshop, 6 – 10 June 2022, Ljubljana, Slovenia (oral presentation, in English)

SEMICONDUCTOR/METAL HYBRID HETEROSTRUCTURES BASED ON NANOPARTICLES

*Dávid Kovács, András Deák, Zsolt E. Horváth, György Z. Radnóczi, Tímea Benkó, Gergely Nagy, Attila Sulyok, Dániel Zámbó**

Objective

Figure 1: Lab-built lyophilizer

Synthesis and characterization of colloidal semiconductor particles have been in the focus of the research aiming at the fabrication of novel photocatalysts with tunable optical properties. Upon illuminating a semiconductor nanoparticle, photoexcited charge carriers (electrons and holes) are generated which can be utilized in various photocatalytic processes. However, these charge carriers can vanish in the femtosecond to nanosecond time range due to their recombination or relaxation. This work aims to investigate the combination of semiconductor nanoparticles (consisting of p-type Cu_2O) and noble metal nanoparticles (Au) in terms of morphology, optical and photocatalytic properties to exploit the charge carrier separation mechanisms emerging in hybrid semiconductor/metal nanoparticles under UV illumination. Due to the alignment of the Fermi level of the metal component positioned inside the band gap of the Cu_2O (ca. 2.17-2.30 eV), photoexcited carriers are expected to be separated spatially, accompanied by the extension of their lifetime, thus boosting up their catalytic performance. We designed colloidal model systems, in which the nanocrystal morphology, composition and surface chemistry are under powerful synthetic control. Ensuring a uniform size, shape and crystal structure for pristine Cu_2O, Au nanograin-decorated Cu_2O, and Au nanorod/Cu_2O core-shell nanoparticles allowed us to reveal the effect of gold within the multicomponent particles on the optical and photocatalytic properties [1]. Using the well-defined nanoparticle building blocks, highly porous assembled aerogel structures were fabricated in monolithic as well as supported forms by using flash-freezing and subsequent lyophilization [2].

Methods

The main research questions within the framework of the project were the following:

- How does the presence of gold modify the optical and photocatalytic properties of cuprous oxide nanoparticles?
- What is the effect of the position of the gold nanoparticles on the above-mentioned properties if the size, shape and composition (*i.e.* Cu:Au atomic ratio) are kept identical in the hybrid nanoparticles?

To reveal these questions, firstly, Cu_2O nanoparticles with octahedral shape were wet-chemically synthesized. Cu_2O was chosen due to its abundant and non-toxic nature and the availability of its methods of synthesis at ambient conditions. Nevertheless, controlling the size and shape was found to be challenging, when following the literature protocols. Hence, in-depth optimization and upscaling of the synthesis were required. Cu_2O nano-octahedra with an average edge length of 136 nm were successfully prepared without applying surfactants or stabilizer additives. In the second step, gold nanorods (AuNRs) with average length of 81 nm and width of 28 nm were overgrown with Cu_2O to prepare AuNR@Cu_2O core/shell particles having the same octahedral morphology and size (137 nm) as the pristine Cu_2O octahedra. After determining the Cu:Au atomic ratio in the AuNR@Cu_2O particles using SEM-EDX, pristine Cu_2O octahedra were wet-chemically decorated with small Au nanograins to obtain octahedra possessing the same Cu:Au ratio as well as size and shape. Hence, we prepared the three model systems (Figure 1) in which the effect of the presence and location of gold can be systematically investigated.

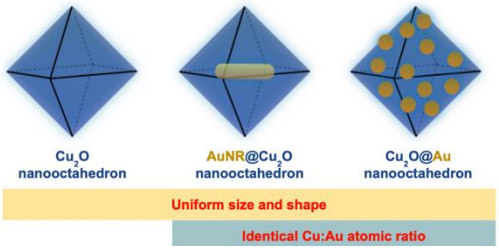

Figure 2: Schematics of the nanoparticle model systems

Extinction, absorption, photoluminescence emission spectra and fluorescence lifetime of the nanoparticle solutions were investigated via optical spectroscopy (UV-Vis-NIR) and spectrofluorometry (UV-Vis). Scanning and Transmission Electron Microscopy (SEM and TEM-EDX) and X-Ray Diffraction (XRD) revealed the morphology, elemental distribution, fine structure, and the dominant crystal facets of the particles. X-ray Photoelectron Spectroscopy (XPS) was used to investigate the chemical states of the particle surfaces. Degradation of an organic dye (methyl orange) was investigated in the photocatalytic test measurements under UV light illumination. Highly concentrated nanoparticle solutions were used to fabricate so-called cryoaerogel structures, which required the design and building in our lab of a freeze-drier. Upon flash-freezing of the nanoparticle solutions at cryogenic temperatures (-197°C or -113°C), the growing ice-crystals press the nanoparticles into sheet-like, highly porous, interconnected structures. Lyophilization allows the replacement of the ice-template with air, resulting in self-supported (monolithic) or supported (conductive substrate-supported) cryoaerogels.

Results

Figure 3 demonstrates the size and shape uniformity of the synthesized nanoparticles determined by SEM as well as their elemental maps (STEM-EDX) showing the position of the gold. All three types of particles have octahedral shape and the AuNR@Cu_2O core-shell particles contain only one Au nanorod in the middle of each octahedron. The surface of Cu_2O is decorated with tiny Au grains (~7 nm) in the case of Cu_2O@Au. The Cu:Au atomic ratio is identical for AuNR@Cu_2O and Cu_2O@Au. For the first time, these model systems with precise morphological and composition control were successfully synthesized.

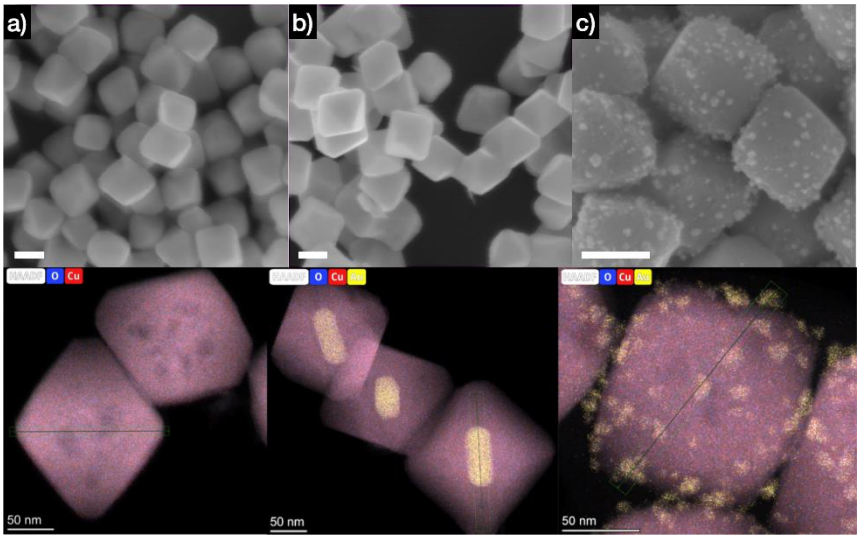

Figure 3: Morphology and elemental maps of Cu_2O (a), AuR@Cu_2O (b) and Cu_2O@Au (c) nanooctahedra. Scale bars in the SEM images are 100 nm. Upper row: SEM images, bottom row: STEM images and EDX elemental maps.

The dominant crystal facets of all samples were identified with XRD (Figure 4a). Octahedral particles are enclosed with (111) facets and the contribution of gold can be observed for AuNR@Cu_2O. The lack of diffraction related to the gold for the Cu_2O@Au nanoparticles can be attributed to the small grain sizes of the deposited metal. Importantly, the samples show solely the Cu_2O-related diffraction peaks; oxidation (and thus the formation of CuO) is not detected. To further exclude the presence of CuO, XPS measurements were carried out on freshly prepared samples stored under an inert atmosphere (Figure 4b). It can be concluded that the main oxidation state of the copper is Cu^+ in all samples (green fitted curves in Figure 4b). Hence, the synthetic procedures are robust and reliable. A small contribution of $Cu(OH)_2$ can be anticipated in all samples at 935.5 eV, and is detected (red fitted curve in Figure 4b). While gold was not detectable by XPS in the AuR@Cu_2O sample due to the thick Cu_2O around the nanorods, Au nanograins on the octahedron surface gave a strong signal for Cu_2O@Au.

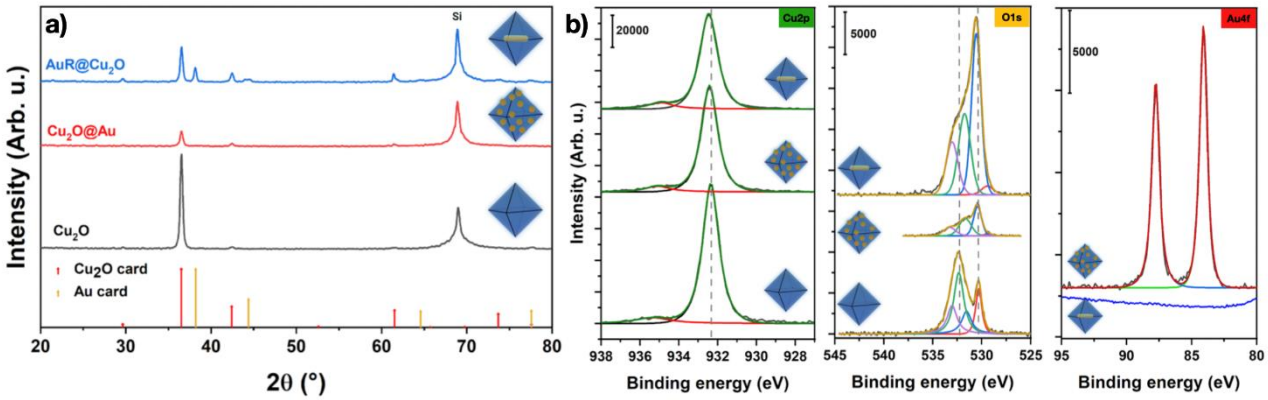

Figure 4: X-ray diffractograms (a) and XPS spectra (b) in the binding energy range of $Cu2p_{3/2}$, O1s and Au4f for all systems

The optical properties were investigated with various spectroscopy methods. Figure 5 summarizes the measured extinction, absorption and photoluminescence (PL) spectra as well as the measured PL lifetime decay. The pristine Cu_2O nanooctahedra shows a narrow extinction peak centred at 505 nm, which corresponds to the band-edge of the semiconductor and the scattering of the Cu_2O particles. This peak slightly redshifts and broadens due to the Au nanograins on the Cu_2O facets, indicating the presence of gold on the surface. AuNR@Cu_2O has a complex optical response covering the whole Ultraviolet–Near–Infrared (VIS-NIR) wavelength range. These peaks correspond to the Cu_2O band-edge absorption, the transversal plasmon mode of the embedded AuNR, the coupled Cu_2O-Au mode and the extensively shifted longitudinal plasmon mode of the nanorod, respectively. Eliminating the scattering from these spectra (measured with an integrating sphere) revealed the contribution of the band-edge absorption and the gold-related features (Figure 5b). Photoluminescence spectra measured

under UV-light excitation (320 nm) show the radiative recombination of the charge carriers emitting at 510 nm. This radiative pathway is suppressed upon introducing gold, that is, the emission intensity decreases and the contribution of a trap-state mode (at around 585 nm) increases. The fluorescence lifetime belonging to the radiative recombination also shortens from 6.4 ns to 5.0 ns for Cu_2O@Au and AuNR@Cu_2O. These observations imply an enhanced charge-carrier separation for gold-containing octahedra.

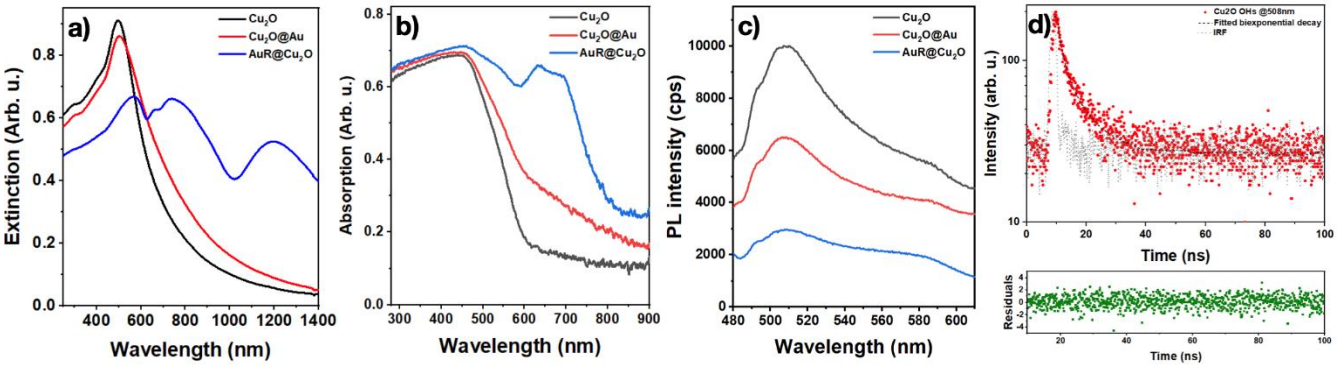

Figure 5: Extinction (a), absorption (b) and photoluminescence (c) spectra of the colloidal nanoparticle solutions (d). A representative fluorescence lifetime decay curve measured at the PL peak of Cu_2O (average lifetime = 6.25 ns calculated by fitting the decay curve with a biexponential function).

The photocatalytic activity of the synthesized nanoparticles was investigated based on the time-resolved degradation of methyl orange (MO) under UV illumination in aqueous phase. As Figure 6(b) shows, MO does not show degradation without the catalyst in the investigated time window (6 hrs in total). While pristine Cu_2O nanooctahedra were not active under the experimental conditions, the presence of Au drastically improved the photocatalytic activity of the samples. Figure 6b shows an enhanced degradation performance for Cu_2O@Au nanoparticles and AuNR@Cu_2O as well, with a final degradation of 82.2% and 68.2%, respectively. It has to be emphasized that the experiments were carried out using a commercial UV flashlight (equipped with a single LED emitting at *ca.* 400 nm) well below the peak of the MO photo absorbance at 470 nm (see Fig. 6(a)). Hence our hybrid particles open up a method towards cheap and easy-to-use photocatalytic applications.

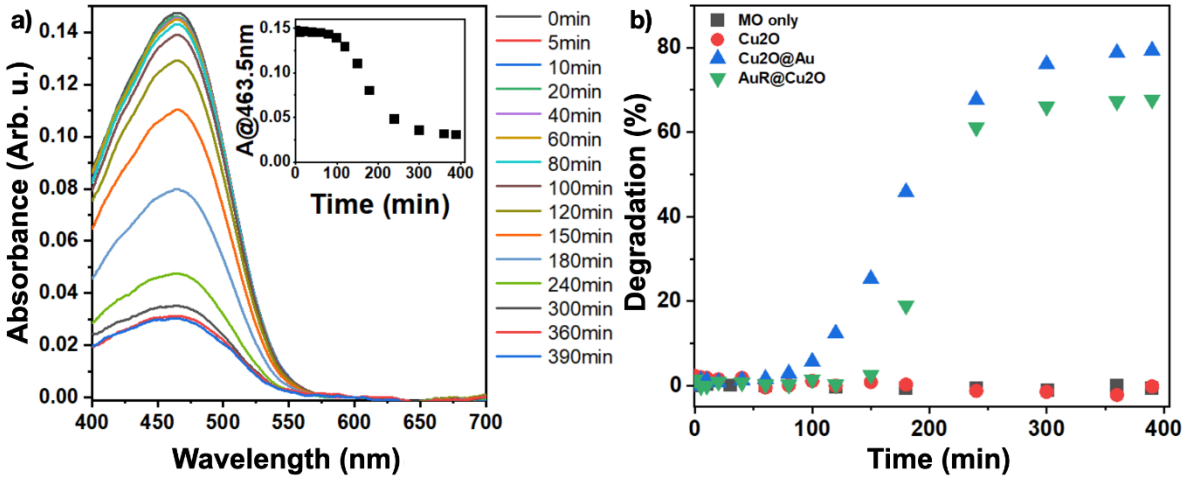

Figure 6: (a) Time-dependent absorption spectra of methyl orange in the presence of Cu_2O@Au nanooctahedra (decreasing absorption in time) (b) Degradation of the dye in the absence or presence of the different photocatalysts

Highly porous aerogel structures were also fabricated from the nanoparticle solutions. The colloid solutions were highly concentrated (up to *ca.* 20-30 g/L for Cu_2O) followed by a rapid freezing step at cryogenic or low temperature (in liquid N_2 (-197°C) or isopentane (-113°C)). Depending on the approach, monolithic aerogels or cryoaerogel coatings were prepared on conductive substrates (ITO-coated glass or carbon) after the gentle lyophilization of the frozen samples in vacuum. Figure 7 shows some examples of the monolithic aerogels and their structure (panel a-c) and the preparation method and porous structure of supported cryoaerogel coatings (panels d-e). In all cases, the nanoparticles retained their original morphology and optical properties.

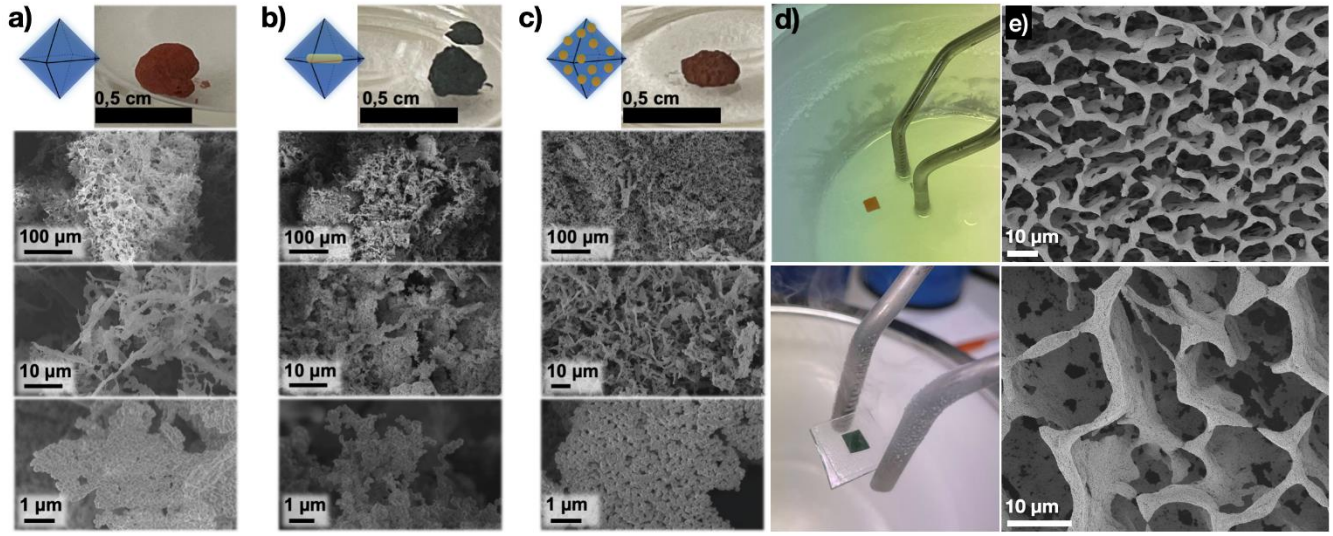

Figure 7: Appearance and macro-, micro- and nanostructure of monolithic (a-c) and supported (d-e) cryoaerogels

We have successfully synthesized multicomponent semiconductor/metal nanoparticle model systems and characterized their morphology, crystallinity, composition, surface chemistry as well as their optical properties. Au nanorods and nanograins proved to be sufficient to drastically enhance the photocatalytic activity of cuprous oxide due to the spatial separation of the photoexcited carriers upon UV illumination. Highly porous nanoparticle cryoaerogels were fabricated from the nanocrystal building blocks, which offers a promising novel platform for liquid- and gas-phase photocatalytic applications in the future.

Remaining work

Although the hybrid nanoparticles show a greatly enhanced photocatalytic activity compared to the pristine Cu_2O, degradation of the dye molecules starts only after a certain period of time. This implies the presence of a competing process, which might be the degradation of surface-attached ethanol. We aim to address this observation as well as to investigate the morphology of the particles upon illumination to exclude their structural change and photodegradation. Additionally, further photocatalytic applications are planned to be tested including gas-phase degradation reactions. Preparation of the manuscript is in progress and will be submitted soon.

Related publications

[1] D. Kovács, A. Deák, GZ. Radnóczi, ZE. Horváth, A. Sulyok, R. Schiller, O.Czömpöly, D. Zámbó: *Position of Gold Dictates the Photophysical and Photocatalytic Properties of Cu_2O in Cu_2O/Au Multicomponent Nanoparticles.* J. Mater. Chem. C **2023**, 10.1039.D3TC01213A. https://doi.org/10.1039/D3TC01213A.

[2] D. Kovács: *Multicomponent Copper(I) Oxide/Gold Nanoparticles and their Assembly*, Master Thesis, Eötvös Lóránd University, Faculty of Science (2022)

DESIGN AND DEVELOPMENT OF THE NEUTRON INSTRUMENTATION SUITE OF BNC

Márton Markó, Gyula Török, Tamás Veres

Objective

Our goal was the design and development of neutron instrumentation at the BNC.

Methods

The aim of the work was to improve and increase capability of the neutron scattering instrument suite of the Budapest Neutron Centre (BNC). For optimization we used analytical and Monte-Carlo simulations. With the help of these methods we designed the replacement of two instruments coming from the BERII reactor decommissioned in Berlin, Germany. The V14 magnetized horizontal reflectometer will replace the old REF reflectometer and a new Direct TOF spectrometer will be built at the position of the Yellow Submarine small angle scattering instrument. For the replacement we redesigned the neutron guide system of the cold guide hall of BNC and developed a new double monochromator system for the V14 instrument. Apart from the instrument replacement, we further developed the ATHOS strain scanner to get higher spatial resolution with better accuracy.

Results

The V14 reflectometer is planned to be installed at the present position of the REF vertical reflectometer at the cold neutron hall of the BNC. The planned date of the installation of the instrument was delayed due to the late arrival of it. To adapt the instrument to the horizontal guide geometry as it was in Berlin we developed a new phase-space transformer double monochromator to use the whole cross section of the existing vertical guide (1st guide of the Cold neutron hall. (Figure 1.) The publication is in progress [1].

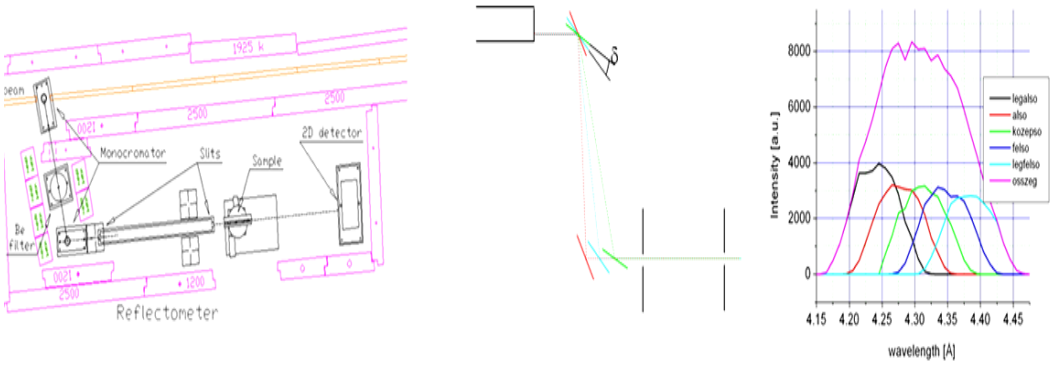

Figure 4: Planned phase-space transformer monochromator system for the V14 instrument. Left: arrangement of the instrument, middle: monochromator arrangement, the first monochromators move vertically into position and reflect the neutrons to the second ones placed behind each other in the same horizontal plane. Right: The wavelength distributions reflected by the different monochromator pairs.

The NEAT direct geometry spectrometer is a neutron scattering instrument for investigation of the low energy excitations in the soft matter. The instrument will arrive in the next years. Due to the length and the needed phase space of the instrument the cold neutron hall had to be completely redesigned taking into account the needs of NEAT, GINA, FSANS and Yellow Submarine SANS instruments. The new layout of the guide system can be seen in figure 2.

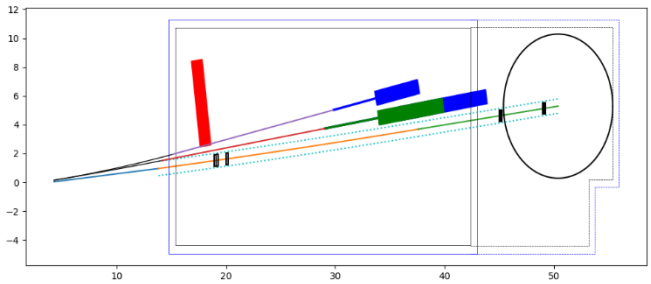

Figure 5: Schematic drawing of the 2nd and 3rd cold beamline of the BNC. Dashed gray and blue lines: extension of the present guide hall; red box: Gina reflectometer; blue: FSANS; green and blue boxes: Yellow Submarine (original size and extended to 7m length; black ellipse in the new hall: NEAT; dashed green line: shielding of the neat guide.

The Neutron Spectroscopy Department is taking part in the EASI-STRESS project that has the goal of standardization of the different strain-stress measurement on structural material [2, 3, 4]. We are developing the ATHOS spectrometer to be a strain scanner. In the previous work period we changed the whole electronic system. This year we developed the control and data treatment software of the instruments, improved the spatial resolution and accuracy of the measurement and designed a new 3D sample positioning system and an accurate beam defining system.

Remaining work

The new monochromator of V14 has to be produced, and the instrument has to be installed and commissioned.

The optimization of the new guide arrangement in the cold neutron hall of BNC has to be finished using McStas and Vitess MonteCarlo packages.

The full 3D movement table, beam defining and sample positioning system of the Athos instrument has to be installed and commissioned.

Related publications

[1] T. Veres, M. Markó, L. Bottyán: *Phase space transformer double monochromator*, (under publication)

[2] Gy Török: *Neutron scattering with low and medium flux neutron sources –Processes Detections and Applications* IAEA-TECDOC-1961 ISBN 978-92-0-116721-7 (paperback) , ISBN 978-92-0-116621-0 (PDF)

[3] IAEA Consultancy Meeting to Finalize the Proposal for Coordinated Research Project on Neutron Beam Instrumentation. Vienna 12-15 Sept. 2022

[4] Gy Török: Lecture: *Neutron Scattering Techniques and Budapest Neutron Centre Facilities,* 1st International Symposium on Environment-friendly Energy Materials in Mianyang, China, from September 16 to 17, 2022

STUDIES OF LIQUID AND COLLOID SYSTEMS BY SMALL ANGLE NEUTRON SCATTERING

László Almásy

Objective

Knowledge of the structure of matter at the nanometre length scale is important for understanding the properties and behaviour of soft condensed matter systems consisting of two or more phases, in which the interactions between the phases and components are governed by intermolecular forces, and the structure and dynamics of the colloid sized regions obey the laws of statistical physics. The size range from one to hundreds of nanometres can be efficiently studied by scattering methods, of which the Small-Angle Neutron Scattering (SANS) stands out by its versatility and suitability for a broad variety of materials. The research activity in this project focussed on the studies of liquid and colloid systems utilizing mainly the method of small angle neutron and X-ray scattering. An important part of our activity was the collaboration with external researchers on performing various experiments on the SANS diffractometer *Yellow Submarine*.

Results

Aqueous solutions of ionic liquids

Aqueous solutions of two prototypical ionic liquids (ILs), [BMIM][BF_4] and [BMIM][TfO], were investigated by UV Raman spectroscopy and SANS in the water-rich domain, where strong heterogeneities at mesoscopic length scales were expected. Analysing Raman data by a differential method, the solute-correlated (SC) spectrum was extracted from the OH stretching profiles, emphasizing specific hydration features of the anions and the molecular structuring of the interfacial water. In these microheterogeneous IL/water mixtures, IL aggregates coexist with bulk water domains (Fig. 1). The organization of the interfacial water was found to be different in the [BMIM][BF_4] and [BMIM][TfO] solutions, due to specific anion–water interactions. On the one hand, in the case of [BMIM][BF_4], which forms weaker hydrogen bonds with water, the aggregation strongly depends on the concentration, as reflected by local changes in the interfacial water. On the other hand, stronger water–anion hydrogen bonds and more persistent hydration layers were observed for [BMIM][TfO], which likely prevent changes in IL aggregates. The SANS data evidences the occurrence of significant concentration fluctuations for all of the systems, which appears as a rather general phenomenon that can be ascribed to the presence of IL aggregation, mainly induced by the cation-driven hydrophobic interactions [1].

The nanometre-range heterogeneity occurring in solutions of ionic liquids with a moderately hydrophobic anion, such as [BMIM][BF_4] is in strong contrast with the homogeneous structure of aqueous solutions of ILs with weakly hydrophilic anions, such as [BMIM][Cl]. This difference appears to be the reason for the different pore templating properties of these substances when used as co-solvents in preparation of porous silica materials: silica made by the sol–gel process using tetraethoxysilan (TEOS) as the silica precursor, with [BMIM][BF_4] has a nearly five times larger pore size than silica made in a similar acid-catalysed synthesis, but using [BMIM][Cl] as co-solvent [2].

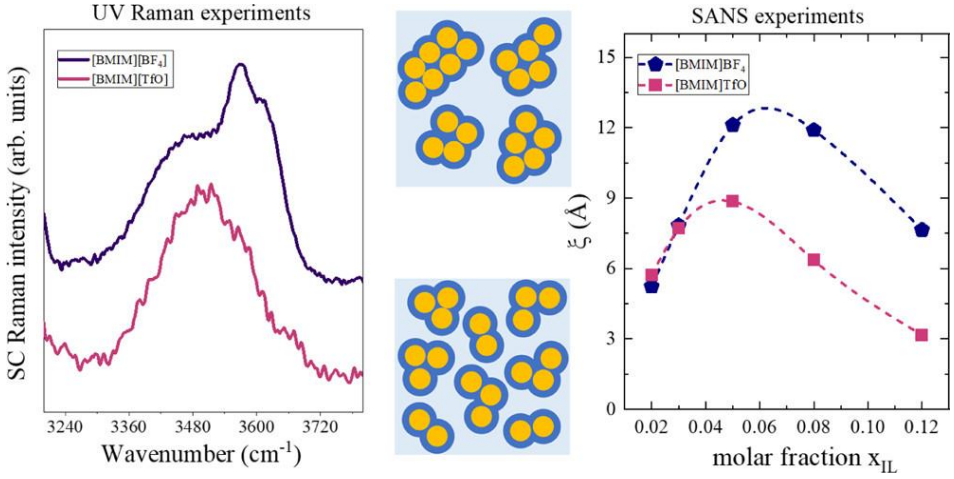

Figure 1: Raman (left) and SANS (right) results on aqueous IL mixtures. The middle panel shows a schematic representation of the molecular distribution (involving IL aggregates, bulk, and interfacial water) suggested for the [BMIM][BF_4] (top) and [BMIM][TfO](bottom) / water mixtures. Yellow: ion pair; dark blue: interfacial water; light blue: water. The [BMIM][BF_4] / water are more heterogeneous and contain a smaller amount of interfacial water.

Polyethylene glycol – water mixtures: a comprehensive structural study

Aqueous solutions of polyethylene glycol (PEG) have been studied by SANS over a broad range of polymer molecular masses and concentrations. The conformation and the interactions of the polymer chains were modelled by a Gaussian chain form factor combined with a random phase approximation, which provided good fits to the SANS data over a broad range of

polymer concentrations and molecular weights. Polyethylene glycol, in the molecular mass range of 0.4–20 kDa in water at a physiological temperature T = 37 °C, behaves like a random coil in nearly theta solvent conditions. The results obtained serve as a reference for the description of complex colloid mixtures with PEG used in various applications [3].

Amyloid disruption under the influence of a natural surfactant: small angle scattering, AFM and fluorescence study

The amyloidogenic self-assembly of many peptides and proteins largely depends on external conditions. The amyloid aggregation of insulin has been studied in the presence of a natural, cholesterol-based detergent, Chobimalt, using a combination of different experimental techniques, such as ThT fluorescence assay, CD, Atomic Force Microscopy (AFM), SANS, and Small Angle X-ray Scattering (SAXS) [4]. While at the lowest Chobimalt concentration (insulin to Chobimalt molar ratio of 1:0.004) the formation of insulin fibrils was not affected, the gradual increase of Chobimalt concentration (up to molar ratio of 1:4) led to a significant increase in ThT fluorescence, evidencing the destruction of the fibrils. Kinetic studies also confirmed the dose-dependent behaviour of fibril morphology. Depending on the concentration of Chobimalt, either (i) no effect, or (ii) significantly, ~10-times prolonged lag-phases were observed. An increase in the Chobimalt concentrations also triggers the formation of insulin fibrils with sharply altered morphological appearance. AFM, SANS and SAXS data show that the fibrils appear to be more flexible and wavy-like with a tendency to form circles (Fig. 2).

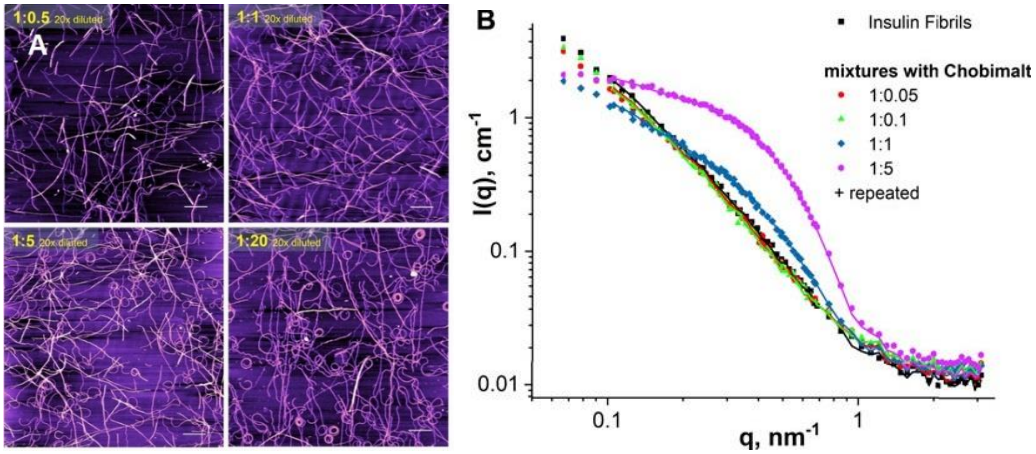

Figure 2: AFM images of insulin amyloids and SANS data of mixed amyloid – Chobimalt solutions

Further results of experiments performed with the SANS instrument Yellow Submarine

Investigations conducted on the instrument have resulted in several publications in 2022, comprising research on novel carbon-reinforced polymer composites [5], covalently bound boron-containing silica aerogels [6], pressure induced modifications of detonation nanodiamonds [7] and aluminium alloys under deep cryogenic treatment [8].

Related publications

[1] C. Bottari, L. Almásy, B. Rossi, B. Bracco, M. Paolantoni and A. Mele: *Interfacial Water and Microheterogeneity in Aqueous Solutions of Ionic Liquids*, Journal of Physical Chemistry B **126**, 4299 (2022)

[2] A.-M. Putz, A. Len, L. Trif, Zs. E. Horváth and L. Almásy: *Imidazolium Ionic Liquids as Designer Solvents Confined in Silica Nanopores*, Gels **8**, 388 (2022)

[3] L. Almásy, O.P. Artykulnyi, V.I. Petrenko, O.I. Ivankov, L.A. Bulavin, M. Yan and V.M. Haramus: *Structure and Intermolecular Interactions in Aqueous Solutions of Polyethylene Glycol,* Molecules **8,** 2573 (2022)

[4] K. Siposova, V.I. Petrenko, I. Garcarova, D. Sedlakova, L. Almásy, O.A. Kyzyma, M. Kriechbaum and A. Musatov: *The intriguing dose-dependent effect of selected amphiphilic compounds on insulin amyloid aggregation: Focus on a cholesterol-based detergent, Chobimalt,* Frontiers in Molecular Biosciences **9,** 955282 (2022)

[5] R. Petrény, L. Almásy and L. Mészáros: *Investigation of the interphase structure in polyamide 6–matrix, multi-scale composites,* Composites Science and Technology **225**, 109489 (2022)

[6] K.E. Yorov, A.P. Zhdanov, R.K. Kamilov, A.E. Baranchikov, G.P. Kopitsa, O.I. Pokrovskiy, A.L. Popov, O.S. Ivanova, L. Almásy, Yu.G. Kolyagin, K.Yu. Zhizhin and V.K. Ivanov: *$[B_{10}H_{10}]^{2-}$ Nanoclusters Covalently Immobilized to Hybrid SiO_2 Aerogels for Slow Neutron Shielding Applications,* ACS Applied Nano Materials **5**, 11529-11538 (2022)

[7] O.V. Tomchuk, M.V. Avdeev, V.L. Aksenov, O.I. Ivankov, A. Len, V.A. Turchenko, Y.L Zabulonov and L.A. Bulavin: *Regulation of nanoporous structure of detonation nanodiamond powders by pressure: SANS study*, Fullerenes, Nanotubes and Carbon Nanosctructures **30,** 171 (2022)

[8] M. Jovičević-Klug, L. Tegg, P. Jovičević-Klug, G. Dražić, L. Almásy, B. Lim, J.M. Cairney and B. Podgornik: *Multiscale modification of aluminum alloys with deep cryogenic treatment for advanced properties*, Journal of Materials Research and Technology **21**, 3062-3073 (2022)

[9] B. Fehér, J. Mihály, A. Demeter, L. Almásy, A. Wacha, Z. Varga, I. Varga, J.S. Pedersen, A. Bóta: *Advancement of Fluorescent and Structural Properties of Bovine Serum Albumin-Gold Bioconjugates in Normal and Heavy Water with pH Conditioning and Ageing,* Nanomaterials **12**, 390 (2022)

TECHNOLOGICAL EXAMINATIONS OF ANCIENT CERAMICS USING SMALL ANGLE NEUTRON SCATTERING

Katalin Bajnok, John Gait, Adél Len

Objective

Methodological developments and improvements have been carried out using Small Angle Neutron Scattering (SANS), in order to characterise and better understand several technological steps of the production technology of archaeological pottery wares. In the first instance, SANS was used to identify a range of pottery forming techniques, while the second project was focussing on determining the maximum firing temperature of archaeological ceramics.

Results

Identifying pottery forming techniques

The archaeological pottery small-angle neutron scattering project (Arch_SANS) made progress with instrumental and analytical developments, using a range of purpose made experimental vessels. A prototype sample holder was designed and tested, enabling large fine-textured pottery sherds to be analysed. Measurements of the experimental samples were completed, along with a new 2D scattering evaluation software, developed by Nicolas Hugot (summer intern from Institut Polytechnique de Paris). Processing and evaluation of the full data set was begun, and confirm that SANS can be used to measure the orientation of clay-sized particles that are too small to be effectively measured using tomographic techniques. A successful application to the ELKH Proof of Concept (PoC) competition was made, which will enable the techniques to be demonstrated through archaeological case studies.

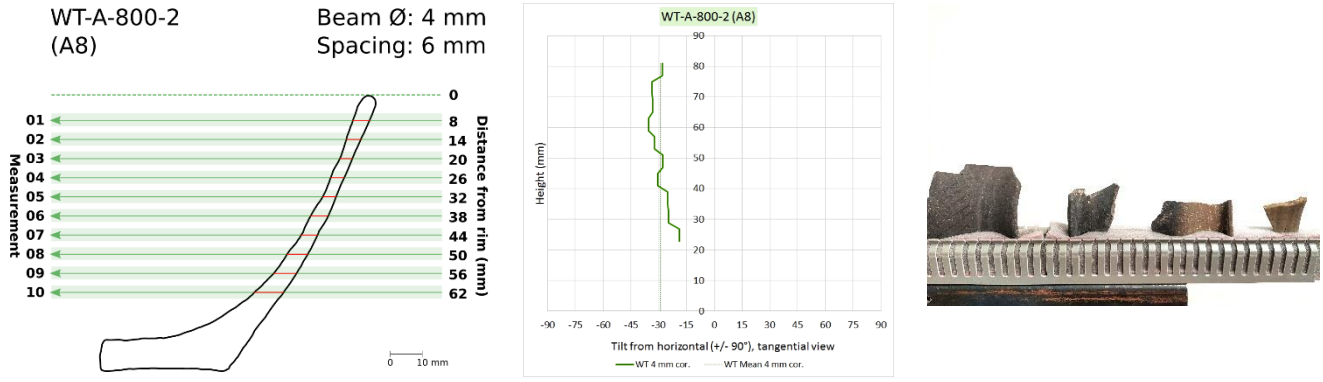

Figure 6: SANS measurements were carried out to identify ancient pottery forming techniques. ***a–b)*** *a series of vertical measurements on a wheel-thrown experimental pottery sample display how the orientation pattern may vary within a vessel;* ***c)*** *the first archaeological pottery samples of 5–6th century Pannonia were measured by SANS*

Examining the firing conditions of archaeological ceramics

In the previous years a new protocol has been developed for determining the maximum firing temperature of archaeological ceramics using SANS [1]. This year a total of 39 archaeological pottery samples have been analysed by SANS. The relationships between certain vessel functions and firing temperatures, and additionally, between certain workshop areas and consistent firing technology was found.

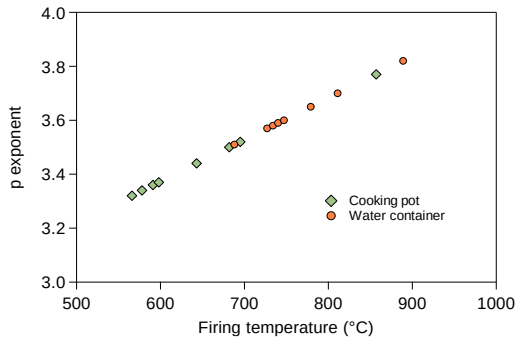

Figure 7: The maximum firing temperature of archaeological ceramic samples are presented against the exponent p *value obtained by SANS. We found that most vessels used for containing liquids were fired at a higher temperature than those used as cooking pots*

Related publication

[1] A. Len, K. Bajnok and J. Füzi: *Small-Angle Neutron Scattering for Cultural Heritage Studies*, in V. Venuti and S. D'Amico (Eds.) Handbook of Cultural Heritage Analysis. Springer International Publishing (2022) pp. 189-210.

HERITAGE SCIENCE APPLICATIONS OF NUCLEAR ANALYTICAL AND STRUCTURAL STUDIES

Zsolt Kasztovszky, Zoltán Kis, John Gait, Zoltán Kovács, Veronika Szilágyi, Katalin Bajnok, Ildikó Harsányi, Boglárka Maróti, Adél Len, László Szentmiklósi, László Rosta, Katalin Gméling, György Káli

Objective

Various objects of our Cultural Heritage made of different kinds of materials (such as rocks and minerals, metals, ceramics, and glass) have been investigated with the available, mostly non-destructive methods, to obtain information on their provenance, production technology, current condition, or authenticity.

Methods

The applied methods utilize the non-destructive and partly destructive neutron-based instruments of the BNC, such as Prompt-gamma Activation Analysis (PGAA), Neutron-Induced Prompt Gamma-ray Spectroscopy (NIPS)-NORMA, Radiography (RAD), or Neutron Activation Analysis (NAA) as well as complementary Scanning Electron Microscopy with Energy Dispersive Spectroscopy (SEM-EDS), portable XRF Spectrometer (pXRF), Near Infrared (NIR)- and Raman Spectroscopy.

Results

Several particular multi-technique studies have been conducted to investigate objects made of rocks, metals, ceramics, and glass, in collaboration with the Hungarian National Museum, the Museum of Fine Arts, the Museum of Ethnography, the Eötvös University and the Institute for Nuclear Research (ATOMKI). Through IPERION HS projects, European partners have joined some interesting projects. A methodological paper about the applicability of PGAA has been published [1]. Our colleagues made significant contributions to the Springer Handbook of Cultural Heritage Analysis [20-21].

Archaeological pottery tomographic analysis

The archaeological pottery tomographic analysis project has made significant progress with methodological and analytical developments, using a range of purpose-made experimental vessels. The project has successfully demonstrated how both neutron tomography and X-ray microtomography may be used to quantitatively evaluate the orientation of particles and voids in coarse- and medium-textured pottery fabrics and using this information, to determine pottery-forming techniques. The results from this experimental stage have recently been published [25] and, in addition, a successful application was made to the ELKH Proof of Concept (PoC) grant to enable the developed techniques to be applied to the first archaeological case studies.

Provenance study of a pre-Columbian ritual mask (in cooperation with the Museum of Ethnography, ELKH TTK, and ATOMKI)

Non-destructive methods have been used to verify the authenticity of this property of the Museum of Ethnography. The wooden support as well as the cover of the mask were analyzed. An attempt was made on the provenance identification of the turquoise inlay, using pXRF [2].

The provenance of ancient Egyptian figurines (in cooperation with the Museum of Fine Arts)

Twenty Egyptian figurines supposed to be made of lapis lazuli have been studied with PGAA, NIR- and Raman-spectroscopy. The aim was to check if they were made of lapis lazuli and also to identify their raw material source. Some pieces were found to be non-lapis lazuli, and the provenance identification was partly inconclusive. An MSc student from ELTE also joined this research [22-23].

Study of folk pottery

Three white folk pottery samples were selected from the collection of the Museum of Ethnography, for destructive microscopic investigations. The optical microscopic thin sections were subjected to detailed fabric analysis. To chemically characterize the resulting fabric groups, a limited set of samples is going to be investigated by PGAA and NAA.

Study of Late Roman and Early Migration Period pottery production

Petrographic, SEM-EDS, and Small Angle Neutron Scattering (SANS) analyses were carried out on archaeological pottery of various Trans-Danubian archaeological sites from the late Roman to early Medieval periods. We aimed to identify long-distance, regional and local production centres, and examine the technological choices made during the pottery making [19].

Non-destructive study of Bronze Age defensive and offensive weapons (in cooperation with the Hungarian National Museum, OTKA project, Gábor Tarbay, NKFIH PD_134910)

On-site handheld XRF measurements were performed in the Hungarian National Museum on gold armlets and crescent-shaped terminals. Based on the results the objects can be classified into three Hartmann groups [13]. Within an OTKA project, we studied the production techniques and alloy types of Late Bronze Age weapons found in the Trans-Danubian Region [15] to draw conclusions about their possible origins. During the analyses, a long-suspicious Late Bronze Age fibula with atypical characteristics was identified as a modern forgery using the XRF technique [12].

Large facility analytical studies of polished and ground stone artefacts for the reconstruction of Prehistoric trans-regional trade routes in the Carpathian Basin (OTKA project, Zsolt Kasztovszky, NKFIH K 131814)

In the 3rd project year, about 150 stone tools from Hungarian Museums and also geological raw materials have been analyzed by SEM-EDX and PGAA to identify the most important outcrops and trade roots. The most significant archaeological excavations that we studied were Polgár-Csőszhalom, Öcsöd-Kováshalom, Aggtelek-Baradla, and Alsónyék [8-11].

Within the IPERION HS project, several users' experiments have been performed either with the presence of the users or as "remote experiments". Several papers about the study of late Roman and Byzantine glass have been published [3-7].

Related publications

[1] Zs. Kasztovszky, B. Maróti, L. Szentmiklósi, K. Gméling: *Applicability of prompt-gamma activation analysis to determine elemental compositions of silicate-based cultural heritage objects and their raw materials*, Journal of Cultural Heritage **55,** 356–368 (2022).

[2] J. Gyarmati, B. Maróti, Zs. Kasztovszky, B. Döncző, Z. Szikszai, L. E. Aradi, J. Mihály, G. Koch, V. Szilágyi: *Hidden behind the mask: An authentication study on the Aztec mask of the Museum of Ethnography, Budapest, Hungary*, Forensic Science International **333,** 111236 (2022)

[3] R. Bugoi, A. Tarlea, V. Szilágyi, I. Harsányi, L. Cliante, Zs. Kasztovszky: *Colour and beauty at the Black Sea coast: archaeometric analyses of selected small finds from Histria*, Romanian Reports in Physics **74**, 802 (2022)

[4] R. Bugoi, G. Talmatchi, V. Szilagyi, I. Harsanyi, D. Cristea-Stan, S. Botan, Zs. Kasztovszky: *PGAA analyses on Roman glass finds from Tomis*, Romanian Journal of Physics **66,** (5–6) (2021).

[5] R. Bugoi, A. Tarlea, V. Szilagyi, I. Harsanyi, L. Cliante, Zs. Kasztovszky: *Chemical analyses on late antique glass finds from Histria, Romania* Archaeometry **64** 744–758 (2021)

[6] R. Bugoi, A. Tarlea, V. Szilagyi, I. Harsanyi, L. Cliante, I. Achim, Zs. Kasztovszky: *Shedding Light on Roman Glass Consumption on the Western Coast of the Black Sea*, Materials **15:2,** Paper: 403, 15 p. (2022)

[7] R. Bugoi, G. Talmatchi, V. Szilagyi, I. Harsanyi, D. Cristea-Stan, S. Botan, Zs. Kasztovszky: *An archaeometric perspective on selected Roman and Late Antique glass finds from Dobrudja*, Nuclear Instruments & Methods In Physics Research Section B-Beam Interactions With Materials And Atoms **511,** 84-90 (2022)

[8] G. Szakmány, K. Fehér, Zs. Kasztovszky, T. Sági: *Archaeometric analyses of adze-blades from Nuku Hiva, Marquesas Islands*, Archeometriai Műhely, **XVIII (1)**, 75–88 (2021)

[9] K. T. Biró, Gy. Szakmány, V. Szilágyi, Z. Kovács, Zs. Kasztovszky, Zsolt, I. Harsányi: *The first greenstone axe in Hungary*, In: Dobrescu, Roxana; Boroneanț, Adina; Doboș, Adrian (szerk.) Scripta praehistorica. Miscellanea in honorem Mariae Bitiri dicata, Suceava, Románia: Editura Cetatea de Scaun pp. 517-528. , 12 p. (2021)

[10] K. T. Biró, Zs. Kasztovszky, A. Mester: *New-old obsidian nucleus depot find from Besenyőd, NE Hungary*, In: T. Biró, Katalin; Markó, András (szerk.) Beyond the Glass Mountains: Papers Presented for the 2019 International Obsidian Conference 27-29 May 2019, Sárospatak, Budapest, Magyarország: Magyar Nemzeti Múzeum pp. 95-108, 14 p. (2021)

[11] G. Bóka, A. Gyucha, , I. Oláh, M. Stibrányi, M. Pethe, Zs. Kasztovszky, P. Medgyesi: *Egy különleges megalitikus lelet az Alföldről. A kevermesi sztélé kutatásának előzetes eredményei*. Magyar Régészet, **10(4)**, 9–17. (2021) http://doi.org/10.36245/mr.2021.4.4

[12] J. G. Tarbay, B. Maróti: *Sárgazréz bross: késő bronzkori hegedű alakú fibula hamisítványa Esztergom-Dunapartról*, Archeometriai Műhely, 2021/XVIII./2. 135-142.

[13] J. G. Tarbay, B. Maróti: *Handheld XRF analysis of gold armlets with crescent-shaped terminals from the Prehistoric Collection of the Hungarian National Museum*, Communicationes Archæologicæ Hungariæ. **2020,** 71-78 (2022)

[14] J. G. Tarbay, B. Maróti: *Late Bronze Age Swords With Leaded Hilt From Hungary*, CommArchHung, submitted

[15] D. Walter, V. Szilágyi: *Late Sarmatian pottery workshop in Nagymágocs–Paptanya / Késő szarmata fazekasműhely Nagymágocs–Paptanyán*, Archeometriai Műhely XIX/2 113–124. (2022) doi: 10.55023/issn.1786-271X.2022-009

[16] A. Ridovics, B. Bajnóczi, B. Maróti, Zs. Kasztovszky: *Sugárzó szépség – uránüvegek a Magyar Nemzeti Múzeum gyűjteményében / Radiating beauty – uranium glasses in the collection of the Hungarian National Museum*, Archeometriai Műhely XIX/2 189–208. (2022) doi: 10.55023/issn.1786-271X.2022-014

[17] B. Borgers, C. Ionescu, Á. Gál, F. Neubauer, C. Von Hagke, M. Auer, V. Szilágyi, Zs. Kasztovszky, K. Gméling, I. Harsányi, L. Barbu-Tudoran: , *Production technology and knowledge transfer of calcite-tempered grey ware bowls from 2nd- to 5th-century CE Noricum (Austria)*, Archaeometry, **2022;** 1–18. (2022) https://doi.org/10.1111/arcm.12823

[18] L. Szentmiklósi, B. Maróti, Sz. Csákvári, T. Calligaro: *Position-Sensitive Bulk and Surface Element Analysis of Decorated Porcelain Artifacts,* Materials **15**, 5106 (2022). https://doi.org/10.3390/ma15155106

[19] K. Bajnok, Z. Kovács, J. Gait, B. Maróti, P. Csippán, I. Harsányi, D. Párkányi, P. Skriba, D. Winger, U. von Freeden, T. Vida, Gy. Szakmány: *Integrated petrographic and geochemical analysis of the Langobard age pottery of Szólád, Western Hungary*, Archaeological and Anthropological Sciences **14:13** (2022) https://doi.org/10.1007/s12520-021-01467-1

[20] Zs. Kasztovszky: *Large Facilities and Cultural Heritage Research*, in Handbook of Cultural Heritage Analysis, Eds. Sebastiano D'Amico, Valentina Venuti, Springer 2022, pp. 13-22. https://doi.org/10.1007/978-3-030-60016-7

[21] Zs. Kasztovszky, C. Stieghorst, H. Heather Chen-Mayer, R. A. Livingston, R. M. Lindstrom: *Prompt-Gamma Activation Analysis and Its Application to Cultural Heritage*, in Handbook Of Cultural Heritage Analysis, Eds. Sebastiano D'Amico, Valentina Venuti, Springer (2022), pp. 95-144. https://doi.org/10.1007/978-3-030-60016-7

[22] Sz. Sándor, J. Zöldföldi, É. Liptay, F. J. Kevély, Zs. Kasztovszky: *Roncsolásmentes analitikai módszerek alkalmazása lápisz lazuliból készült régészeti leletek eredetvizsgálatára*, Őszi Radiokémiai Napok, Balatonszárszó, 2022. október 17-19.

[23] S. Szende: *Roncsolásmentes analitikai módszerek alkalmazása régészeti leletek eredetvizsgálatára,* TDK dolgozat, ELTE TTK, Budapest (2022)

[24] J. G. Tarbay, B. Maróti, Z. Kis, P. Barkóczy: *Analysis of Lead Segregation in a Late Bronze Age Socketed Axe from the Biatorbágy-Herceghalom Hoard,* OREA, submitted

[25] J. Gait, K. Bajnok, V. Szilágyi, I. Szenti, Á. Kukovecz, Z. Kis: *Quantitative 3D orientation analysis of particles and voids to differentiate hand-built pottery forming techniques using X-ray microtomography and neutron tomography*, Archaeological and Anthropological Sciences **14(12)**, 223 (2022) https://doi.org/10.1007/s12520-022-01688-y

APPLICATIONS OF NUCLEAR AND X-RAY ANALYTICAL TECHNIQUES TO CHEMISTRY, MATERIAL AND NUCLEAR SCIENCES

Boglárka Maróti, László Szentmiklósi, Ildikó Harsányi, Katalin Gméling

Objective

We determined the elemental compositions of various kinds of samples using PGAA, PGAI, NAA, and portable XRF methods. The data obtained were useful in catalysis, material, and heritage science. The dissemination of these state of art methods for students of numerous universities was also our task.

Methods

- Prompt Gamma Activation Analysis (PGAA) and Neutron Activation Analysis (NAA) to determine the bulk elemental composition, portable X-ray Fluorescence (pXRF) to determine the elemental composition of near-surface regions,
- Education of university students, laboratory exercises.

Results

We have published the results of a user measurement on the composition determination of different Ni-Ti dental arch wires [1]. PGAA data justified the applicability of the tested material to *in vivo* applications.

To prepare the facility for the analysis of moisture-sensitive samples and further reduce the hydrogen background related to the humidity of the air, we upgraded the PGAA sample chamber to allow inert gas flushing (Fig 1a). We have also worked out a packaging technique where the Teflon bag itself was filled up with inert gas, in this case, nitrogen. The applied heat-sealing kept the N_2 gas contained even 20 days after the experiments (Fig.1b).

This development has been utilized to analyse the hydrogen contents of layered lithium-nickel-cobalt-manganese oxides (NCM, $LiNi_aCo_bMn_cO_2$) which are promising cathode materials for lithium-ion batteries. We quantified the variable amounts of hydrogen compared to the cobalt signal. The first results were part of a poster presentation [2].

a)

b)

Figure 1: improvements to facilitate the measurement of moisture-sensitive samples by PGAA

The same new feature could be utilized when the feasibility of an industrial request was assessed to measure ppm levels of H in steel. A pair of H-loaded and baked samples were measured under identical experimental conditions. We concluded that the best achievable detection limit is 30 ppm and it is not determined anymore by the hydrogen background, but by the spectral interferences of the numerous small, but unexplored peaks of the Fe matrix with the Hydrogen peak at 2223 keV.

We have collaborated with NIST to assess the feasibility of eventual certification measurements at our PGAA station, since the NIST reactor is presently out of service. A NIST internal report has been prepared, suggesting that the modification of the experimental procedure and the evaluation can reduce the standard deviation of the results to the required level.

In an internal collaboration, the local H contents of "slim" Zr nuclear fuel cladding was profiled along the long axis with PGAI scanning, and the results were cross-checked with the hot extraction method [4].

We have started the transition of our gamma-spectrum evaluations from Hypermet-PC to Hyperlab. This latter is compatible with the new capabilities of our ORTEC DSPEC 502 spectrometer, e.g. 64k spectrum bins. Intercomparison tests were made, and the detector calibration curves for efficiency, non-linearity, and FWHM were established for both the PGAA and NIPS stations.

Educational activities were also ongoing. We hosted David Knezevic from Serbia in the framework of the ARIEL nuclear physics project, as well as two scientists from Poland as IAEA-delegated research fellows. Lab training and lecture series for students of ELTE and BME were also completed.

Related publications

[1] A. Nespoli, F. Passaretti, L. Szentmiklósi, B. Maróti, E. Placidi, M. Cassetta, R. Y. Yada, D. H. Farrar, K. V. Tian: *Biomedical NiTi and β-Ti Alloys: From Composition, Microstructure and Thermo-Mechanics to Appl.*, Metals **12**, 406 (2022)

[2] S. Oswald, R. Wilhelm, L. Szentmiklósi, B. Maróti, I. Harsányi, H. A. Gasteiger: *Effect of Washing on Nickel-Rich NCMs.* IBA 2022 – International Battery Association Hybrid Conference, poster presentation

[3] Rick Paul (NIST), László Szentmiklósi (Budapest Neutron Centre): *Determination of Hydrogen, Carbon, Nitrogen, and Sulfur in SRM 2776 Furnace Coke by PGAA at the Budapest Neutron Centre (BNC)*, Report of Analysis, October 24, 2022

[4] Z. Kis: *H/Zr arány hossztengely-menti eloszlásának roncsolásmentes mérése fűtőelemburkolaton PGAI módszerrel*. Kutatási jelentés, 9 old. (2022), EK-NAL 2022/75, EK-TFO-2022-751-08-01-M0

STRUCTURAL ASPECTS OF IRON- AND TIN-BASED MATERIAL SYSTEMS STUDIED BY MÖSSBAUER SPECTROSCOPY AND OTHER METHODS

Zoltán Klencsár, Sándor Stichleutner, Maria Gracheva, Károly Lázár

Objective

We aim to gain insights into the structure, composition and relevant properties of various iron- and tin-based materials of interest, such as the products of an electric explosion of amorphous alloy ribbons, Sn-Fe-Ni-Co quaternary alloys, clays, ferrihydrite nanocolloid suspensions and iron citrate solutions.

Methods

Besides Mössbauer Spectroscopy (MS), we have also utilized other complementary methods such as magnetization measurements, High-Resolution Transmission Electron Microscopy (HRTEM), Scanning Electron Microscopy (SEM) and X-Ray Diffractometry (XRD).

Results

The products of an electric explosion of amorphous alloy ribbons ($Fe_{45}Co_{45}Zr_7B_3$ HITPERM, $Fe_{73.5}Si_{15.5}B_7Nb_3Cu_1$ FINEMET and bulk amorphous $Fe_{71.6}Mn_{0.6}Si_{3.4}C_{12.3}B_{12.2}$) in water and in ethylene glycol were studied with SEM, XRD, HRTEM and Mössbauer spectroscopy. Strong chemical interactions with the cooling media were revealed by identifying the products. The original amorphous state was barely retained only in the bulk amorphous sample [1].

Long-term transformations of ferrihydrite aqueous nanocolloid suspensions, prepared with different surfactants used as stabilizing agents, were studied using ^{57}Fe Mössbauer spectroscopy, TEM/HRTEM and Field Cooling Zero Field Cooling (FC/ZFC) magnetization measurements [2]. A slow transformation of ferrihydrite to goethite and hematite, occurring on the time scale of years, was evidenced. The results indicate that the type of the utilized surfactant can have a strong influence on the rate of the transformation. Among the surfactants used, polyethylene glycol polymer with a mean molecular mass of 1500 g/mol was shown to be the most effective in preserving the initial structure and size of the ferrihydrite colloid particles. Studies on the uptake of iron from the suspensions by plant roots [2,3] revealed that the end product, hematite, can be more effective in restoring plant Fe deficiency than ferrihydrite.

Sn-Fe-Ni-Co quaternary alloys, prepared either by Direct Current (DC) or Pulse Plating (PP) electrodeposition in the composition range of 37–44 at% Sn, 35–39 at% Fe, 6–8 at% Ni and 13–17 at% Co, were characterized by XRD, ^{57}Fe and ^{119}Sn Mössbauer spectroscopy, SEM-EDX and magnetization measurements [4]. XRD revealed the amorphous character of the quaternary alloy deposits. The dominant ferromagnetic character of the deposits was shown by magnetization and Mössbauer spectroscopy measurements. Pronounced magnetic anisotropy was found in all quaternary alloy deposits, evidenced by considerable differences in magnetization curves measured parallel or perpendicular to the applied fields, clearly indicating that the parallel direction is the easy axis of magnetization. Dependence of saturation magnetization on deposition current density showed a correlation with occurrence of the ferromagnetic phase, determined from the ^{57}Fe and ^{119}Sn Mössbauer measurements. The differences found between the magnetization curves of DC and PP deposits can be associated with differences in the short-range ordering of these alloys.

The structure of the novel Sn(II/IV)-bentonite, successfully produced from Ca-bentonite via the ion exchange method using a $SnCl_2$ aqueous solution under aerobic conditions, was investigated by XRF, XRPD, XPS, ^{119}Sn and ^{57}Fe Mössbauer spectroscopy [5,6]. ^{119}Sn Mössbauer spectroscopy and XPS definitely revealed both Sn^{II} and Sn^{IV} ions in Sn-bentonite. At least a quarter of the tin in the Sn(II/IV)-bentonite is in the Sn^{II} state, which was attributed to tin in the interlayer space, while Sn^{IV} is located partly in the octahedral position and partly in the interlayer space of montmorillonite. Removal of $^{99m}TcO_4^-$ from aqueous and artificial urine media was successful with the use of this novel Sn(II/IV)-bentonite, which can be a useful sorbent for radioactive waste management to reduce accumulation of wastewater in the future.

Iron(III) citrate transformations during the photodegradation in solution and after foliar application on leaves were investigated by ^{57}Fe Mössbauer spectroscopy [7,8]. Highly acidic conditions led to a complete reduction of Fe together with the formation of Fe^{II} citrate and hexaaqua complexes in equal concentration. At higher pH, the only product of the photodegradation was Fe^{II} citrate, which was later reoxidized and polymerized.

A series of clay samples originating from the perspective nuclear waste host rock (Boda Claystone) were analysed with emphasis on the determination of the Fe^{2+}/Fe^{3+} ratio in them. Iron ions were located in the illite and chlorite minerals, as well as in hematite. The relative percentages of Fe^{2+} and Fe^{3+} in the layered silicates were on average 55% and 30%, along with 15% of the iron being associated with the hematite [9].

Overviews on the potential applications of Mössbauer spectroscopy on model catalysts [10], on industrial catalysts [11] and on nanomaterials [12] were also presented.

Related publications

[1] K. Lázár, L.K. Varga, V. Kovács-Kis, S. Stichleutner, A. Tegze, Z. Klencsár: *Electric explosion of amorphous iron alloy ribbons in water and in ethylene glycol,* J. of Materials Research (2022), https://doi.org/10.1557/s43578-022-00771-3

[2] M. Gracheva, Z. Klencsár, V. Kovács Kis, K.A. Béres, Z. May, V. Halasy, A. Singh, F. Fodor, Á. Solti, L.F. Kiss, Tolnai, G., Z. Homonnay, K. Kovács: *Iron nanoparticles for plant nutrition: Synthesis, transformation, and utilization by the roots of Cucumis sativus,* Journal of Materials Research (2022), https://doi.org/10.1557/s43578-022-00686-z

[3] A. Singh, V. Kovács Kis, M. Gracheva, Á. Keresztes, K. Kovács, G. Tolnai, Z. Homonnay, F. Fodor, Z. Klencsár, Á. Solti: *Apoplast utilisation of nanohaematite in the roots of Cucumis sativus: SII-P7 - Improving Fe availability in soils,* In: Thomine, Sébastien (eds.) Abstract Book of the 20th International Symposium on Iron Nutrition and Interactions in Plants, p. 29 (2022).

[4] E. Kuzmann, I. Felner, L. Sziráki, S. Stichleutner, Z. Homonnay, M.R. El-Sharif, C.U. Chisholm: *Magnetic Anisotropy and Microstructure in Electrodeposited Quaternary Sn-Fe-Ni-Co Alloys with Amorphous Character,* Materials **15**, 3015 (2022) https://doi.org/10.3390/ma15093015

[5] E.M. Kovács, D. Buzetzky, M. Soha, T. Fodor, P. Kónya, S. Stichleutner, S. Kubuki, E. Kuzmann, J. Kónya, N.M. Nagy: *Preparation and structure analyses of Sn-bentonite for pertechnetate removal,* Process Safety and Environmental Protection **168**, 133-141 (2022) https://doi.org/10.1016/j.psep.2022.09.075

[6] E.M. Kovács, D. Buzetzky, M. Soha, T. Fodor, P. Kónya, S. Stichleutner, S. Kubuki, E. Kuzmann, J. Kónya, N.M. Nagy: *Sn-bentonit előállítása és szerkezetvizsgálata pertechnetát megkötéséhez,* Őszi Radiokémiai Napok 2022, 17-19 October, 2022, Balatonszárszó, Hungary, Conf. Program and Book of Abstracts, pp. 22-23 (2022)

[7] M. Gracheva, Z. Homonnay, F. Fodor, Á. Solti, K. Kovács: *New Aspects of the Photodegradation of Iron(III) Citrate: Spectroscopic Studies and Plant Related Factors,* Őszi Radiokémiai Napok 2022, 17-19 October, 2022, Balatonszárszó, Hungary, Conference Program and Book of Abstracts, ISBN 978-615-6018-13-7, pp. 80-85 (2022).

[8] M. Gracheva, Z. Homonnay, Á. Solti, A. Singh, F. Fodor, V. B. Marosi, K. Kovács: *Photodegradation of Iron(III) Citrate, the International Symposium on the Industrial Applications of the Mössbauer Effect,* Book of Abstracts ISIAME 2022, 49 (2022)

[9] K. Lázár, S. Stichleutner: *Summarizing report on determination of Fe^{2+}/Fe^{3+} ratios on Boda claystone samples,* (Contract with Mecsekérc Ltd., 2022).

[10] K. Lázár: *Study of catalysts with Mössbauer spectroscopy – outline of some recent trends.* Part C: Bulk oxides, Fenton and Fisher-Tropsch catalysts. Mössbauer Effect Reference and Data Journal **45**, 19-26 (2022)

[11] K. Lázár: *Study of industrial catalysts and catalytic processes by Mössbauer spectroscopy,* International Symposium on the Industrial Applications of the Mössbauer Effect, 11-16 September 2022, Olomouc, Czech Republic (invited talk)

[12] I.V. Alenkina, M.V. Ushakov, P.C. Morais, R.K. Selvan, E. Kuzmann, Z. Klencsár, I. Felner, Z. Homonnay, M.I. Oshtrakh: *Mössbauer Spectroscopy with a High Velocity Resolution in the Studies of Nanomaterials,* Nanomaterials **12**, 3748 (2022) https://doi.org/10.3390/nano12213748

PHOTOCATALYTIC PROPERTIES OF BIOMIMETIC SEMICONDUCTOR PHOTONIC NANOARCHITECTURES BASED ON BUTTERFLY WINGS

Gábor Piszter, Krisztián Kertész, Gergely Nagy, Zsófia Baji, Zsolt Bálint, Krisztina Kovács, Kornél Fél, Tünde Tóth, József Sándor Pap, László Péter Biró

Objective

The aim of the project was to investigate the optical, structural, and photocatalytic properties of several butterflies with particular attention to the ZnO layers deposited on their wings. The structural colour of the ZnO thin films originated from naturally tuned photonic nanoarchitecture templates, from deep blue to greenish blue. The photocatalytic efficiency of the conformal ZnO nanoarchitectures was tested in the degradation reaction of rhodamine B, methylene blue, and methyl orange dyes under visible light illumination. The possibility of bandgap energy tuning was investigated by the controlled application of gold and alloyed gold/silver nanoparticles on the surface of the wing scale nanoarchitectures, the favourable results of which may open the way to the use of TiO_2-based biotemplates for photocatalysis in the future.

Methods

The photonic nanoarchitectures of four *Morpho* species: *M. menelaus*, *M. portis, M. rhetenor helena*, and *M. sulkowskyi* were investigated and modified. Atomic Layer Deposition (ALD) of 10, 15, and 20 nm thick ZnO layers was carried out at 100 °C as the wing samples are thermally sensitive. Scanning electron microscope images were taken from the cross section of the resulting biotemplated structures which had been prepared under cryogenic conditions. Optical reflectance measurements were conducted using a fibre optic Avantes system consisting of an AvaSpec-HERO spectrophotometer, a stabilized UV–Vis light source, a normal-incidence probe and an integrating sphere for light collection. The photocatalytic activity was evaluated based on the decomposition of rhodamine B (RhB), methylene blue (MB), or methyl orange (MO) in unbuffered ultrapure aqueous solutions upon illumination. The 15×15 mm glass and the different ZnO samples were placed vertically in 20 ml of the solutions in a glass cuvette with magnetic stirring. A heat free 300 W xenon lamp was used for illumination, while the rate of degradation was followed by an Agilent Cary 60 UV–Vis spectrophotometer equipped with an immersion probe. The gold and alloyed silver/gold nanoparticle sols were produced by the citrate assisted Turkevich method in an aqueous medium and were applied on butterfly wings using laboratory micropipettes preceded by ethanol pre-treatment. The relevant intermediates from degradation of MO and RhB were separated and identified using Agilent 1200 Liquid Chromatograph (LC) and Agilent 6410 quadrupole mass spectrometer (MS/MS) devices. The isocratic separation was implemented by a reverse phase C18 column (Phenomenex EVO C18 100A, 2.6 µm, 100 × 3 mm). The eluents were ammonium acetate and acetonitrile. The flow rate was 0.3 mL/min. The optimal MS parameters were as follows: gas temperature 350 °C, gas flow 12 L/min, nebulizer 25 psi, capillary voltage ±3500 V and fragmentor voltage 140 V in positive ionization mode. In MS/MS fragmentation N_2 was used as collision gas.

Results

Previously, we used conformal atomic layer deposition of ZnO on the wings of various butterfly species (*Arhopala asopia*, *Morpho sulkowskyi*, *Polyommatus icarus*) possessing structural colours extending from the near UV to the blue wavelength range, to test the effects arising from the nanostructured surfaces and from the presence of different types of photonic nanoarchitectures (Fig. 1A). The decomposition of RhB upon visible light illumination demonstrated the photocatalytic activity for all ZnO-coated butterfly wings [1]. The best reaction rate of decomposing RhB was found in 15 nm ZnO coated *M. sulkowskyi* wing (Fig. 1B), the reflectance of which had the highest overlap with the absorption band of the dye, and it also had the highest reflectance intensity (Fig. 1A).

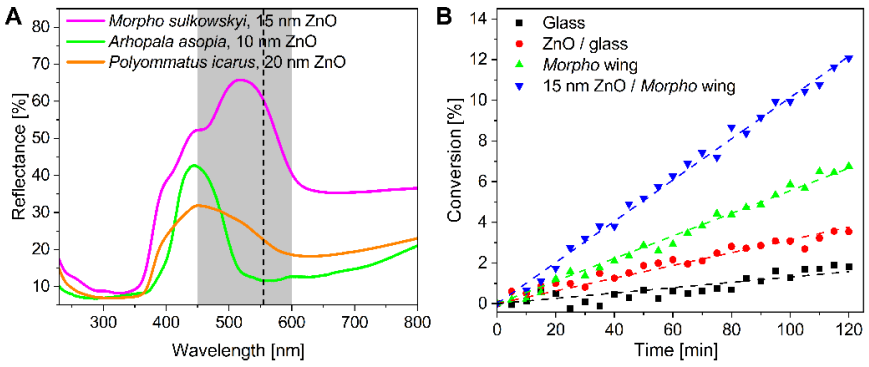

Figure 1: (A) Reflectance of butterfly wing samples conformally covered by ZnO thin films. The grey band marks the RhB absorption range, while the dashed line indicates the absorption maximum. (B) Reaction rate versus time for bare glass, 15 nm ZnO covered glass, pristine M. sulkowskyi *wing, and 15 nm ZnO covered* M. sulkowskyi *wing [1].*

As a continuation, this year we followed two directions. First, we expanded the list of investigated butterflies by using the available colour variations, from deep blue to greenish blue, of the most effective photonic nanoarchitecture type found in *Morpho* butterflies [1] as biotemplates for the ZnO semiconductor thin films. We examined the photocatalytic activity of the naturally tuned samples by decomposing different types of test dyes while monitoring the degradation products by UV-vis spectrophotometry and identifying them *ex situ* by Mass Spectrometry (MS).

The other planned direction was the application of TiO_2-based thin films on the photonic nanoarchitectures of butterflies using ALD. TiO_2 has a low cost and high photochemical stability, it is widely used and studied as a photocatalyst, but it has a wide band gap that requires UV light excitation for photocatalysis. The photocatalytic activity of TiO_2 under visible light illumination can be triggered by plasmonic properties of noble metals (Au, Ag, Pt, etc.), the application of which was not investigated on biotemplated nanostructures before. Therefore, we developed the protocol of applying gold and alloyed silver/gold nanoparticle solutions on butterfly wings and examined their optical properties in detail. In this way, we gained universal knowledge that can be used for the doping of biotemplated semiconductor thin films by nanoparticle sols in future experiments and may achieve efficient photocatalysis using visible light illumination [2].

The investigation of sodium citrate-based gold and alloyed silver/gold nanoparticle sols on the optical properties of the butterfly wings possessing blue structural colour showed that the effect of drop-drying water (solvent), sodium citrate (solute), and plasmonic metallic nanoparticles can be separated [2]. The gold and alloyed silver/gold nanoparticles caused significant redshift of the reflectance maximum (Figs. 2A&B). The magnitude of the redshift was higher for the gold nanoparticles, which had the characteristic absorption band at a longer wavelength compared to the absorption band of the alloyed silver/gold nanoparticles. The redshift increased with the increasing concentration of the metallic nanoparticles (Fig. 2B), but the coalescence of the nanoparticles has to be avoided as this can replace the photonic properties by bulk metallic behaviour. The above results were interpreted as the presence of hybridization between the photonic nanoarchitecture and the metallic nanoparticles with plasmonic properties where the optical properties of the new type of hybrid photonic nanoarchitectures (consisting of butterfly wing nanoarchitectures and plasmonic nanoparticles) are different from those of the components (Fig. 2C). Based on these results, we hope to show in the future that TiO_2-based biotemplated samples can be coated with metallic nanoparticles which will tune their band gap energy to the visible light wavelength range.

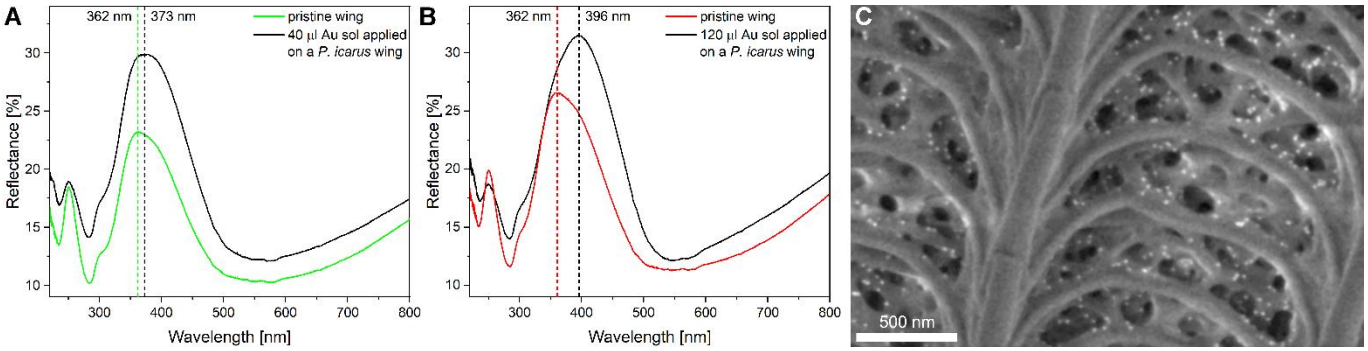

Figure 2: Integrating sphere reflectance spectra (A) in pristine state and after the application of 40 µl of gold nanoparticle sol and complete drying; (B) in pristine state and after the application of 120 µl of gold nanoparticle sol and complete drying. (C) Scanning electron micrograph of wing scale after the application of 120 µl of gold nanoparticle sol. One may note the presence of bright dots in the SEM image, which represent metallic nanoparticles covering the surface of the photonic nanoarchitecture.

From the previously presented experiment [1], the photonic nanoarchitecture of *Morpho sulkowskyi* butterfly coated with 15 nm ZnO showed the most promising photocatalytic activity. Furthermore, we found that the overlap of the blue and red edges with the absorption band of the dye plays an important role in the photocatalytic activity. Therefore, we extended our investigations to four *Morpho* species with similar photonic nanoarchitectures but with different hue of structural colours, and to other dyes to be decomposed, to investigate the effect of optical and structural tuning of the biotemplates and how it affects the photocatalytic performance on different dyes.

The wings of the *Morpho* specimens were prepared for electron microscopy using cryogenic cleavage to have access to the inside of the cover scales and the resulting cross-sections were investigated in SEM. Both pristine and ZnO coated samples were examined, where the deposited ZnO thin film was clearly visible on the surface of the wing scale nanoarchitecture (Fig. 3A, bottom panel), and its thickness was precisely measurable. The 20 nm deposition images showed that the smallest structural elements of the photonic nanoarchitectures were well-preserved even when the thickest coating was applied.

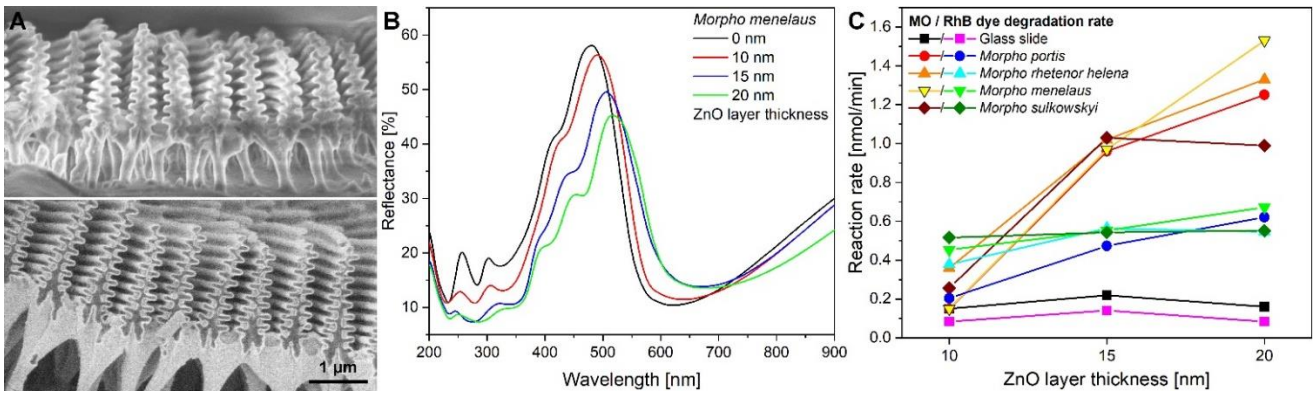

Figure 3: (A) SEM micrograph of a Morpho rhetenor helena *cover scale nanoarchitecture in pristine state (top) and with 20 nm ZnO coating (bottom); (B) Reflectance spectra of* Morpho menelaus *wings with different ZnO coating thicknesses; (C) Photocatalytic reaction rate of four investigated species using two different dyes to be decomposed as a function of ZnO coating thickness. Glass slides with ZnO coating were used as a reference. One may note that decomposition of methyl orange (MO) was more efficient with the same structures compared to rhodamine B (RhB).*

The structural colour of the wings was changed by the deposited ZnO layer which was displayed by the shift of the main peak in the reflectance spectrum (Fig. 3B). In this way, the optical properties of the biotemplates could be tuned, which also affected their photocatalytic performance. To investigate this, three kinds of dyes were used in visible light driven decomposition measurements with pristine and ZnO coated butterfly wings: rhodamine B (RhB), methylene blue (MB), and methyl orange (MO) (the results with RhB and MO are shown in Fig. 3C). The photodecomposition rates were referenced to that of ZnO coated glass slides with the same layer thicknesses (10-15-20 nm). The decomposition of MB was almost independent from the applied layer thickness and a modest two-fold increase of the photocatalytic activity was achieved compared to the coated glass samples. Using RhB, no dependence was found between the performance and the thickness of the deposited ZnO on glass slides and on *M. sulkowskyi* wings, while a linear relationship was found in the other three butterfly species (Fig. 3C). According to the mass spectroscopy analysis, the RhB undergoes gradual de-alkylation, until losing its four N-alkyl groups, in accordance with literature findings. When MO was used, a considerable enhancement of the reaction rate for 15 and 20 nm thicknesses was observed, but much less for 10 nm. This seeming threshold was probably due to an inhomogeneous or nonconformal ZnO coating at this deposited thickness. We measured almost a ten-fold increase of the photocatalytic activity when the 20 nm ZnO coated *M. menelaus* wing was compared to the similarly coated glass slide (Fig. 3C). For the *M. sulkowskyi* wing, the 20 nm layer produced too big a shift of the structural colour relative to the absorption band of the MO, resulting in a saturating behaviour. In this case, the MS analysis revealed that the decomposition route involves de-methylated intermediates that undergo further degradation via the scission of the diazenyl chromophore group. A similar reaction rate was observed for all the other investigated species when MO was decomposed, while the photocatalytic activity was also dependent on the ZnO thickness as the wings with 20 nm ZnO were the most efficient, except for *M. sulkowskyi* with a peak at 15 nm. This may be the result of the high spectral overlap between the ZnO coated *Morpho* butterflies' wing reflectance and the absorption spectrum of MO as both have peak wavelength around 500 nm which will be further studied in the future.

In addition to the publications cited above, the results of the joint work were presented at two international conferences, were shown on the cover page of Photonics [2], were published on the websites of ELKH and the Committee on Biophysics of the Hungarian Academy of Sciences. A radio interview was recorded and broadcast by Klubrádió and a clip by Novum at M5 was presented on this topic.

Remaining work

According to our plans, the photocatalytic activity of TiO_2-based biotemplated samples will be explored, similar to what was shown in our results for ZnO. Here, we plan to utilize the knowledge which we have gained about the homogeneous deposition of metallic nanoparticles, which may allow the use of visible light for photocatalysis when a TiO_2 coating is applied on the butterfly wings. Thanks to the support of the Centre for Energy Research, we will continue this fruitful collaboration started here in two new projects with external funding (OTKA PD 143037 and TKP2021-NKTA-05), for which the starting point was the current KKT-139 project.

Related publications

[1] G. Piszter, K. Kertész, G. Nagy, Z. Baji, Z. E. Horváth, Z. Bálint, J. S. Pap, L. P. Biró: *Spectral tuning of biotemplated ZnO photonic nanoarchitectures for photocatalytic applications,* Royal Society Open Science **9**, 220090 (2022)

[2] K. Kertész, G. Piszter, Z. E. Horváth, D. Zámbó, A. Deák, L. P Biró: *Effect of Plasmonic Au and Ag/Au Nanoparticles and Sodium Citrate on the Optical Properties of Chitin-Based Photonic Nanoarchitectures in Butterfly Wing Scales,* Photonics **9,** 553 (2022)

[3] G. Piszter, G. Nagy, K. Kertész, Z. Baji, K. Kovács, Z. Bálint, Z. E. Horváth, J. S. Pap, L. P. Biró: *Investigating the Effect of Reflectance Tuning on Photocatalytic Dye Degradation with Biotemplated ZnO Photonic Nanoarchitectures Based on Morpho Butterfly Wings,* Materials **16**, 3584 (2023)

NEUTRON AND X-RAY RADIOGRAPHY AND TOMOGRAPHY AT THE BUDAPEST NEUTRON CENTRE

Zoltán Kis, László Horváth, László Szentmiklósi

Objective:

We develop and use imaging instrumentation and methodology at the Budapest Neutron Centre (BNC).

Methods

Energy filtered neutron and X-ray imaging in 2D and 3D, volume rendering

Results

We finished the installation of the rotating *neutron beam filter* drum at the RAD station (*Fig.1 a*), and the tests of its remote-control system were completed. It also provides computer-controlled beam formation in the thermal, epithermal, and fast energy regimes. One of the successful extreme tests is seen in *Fig.1 b* showing the fast neutron setup (i.e., 10 mm Mirrobor plate + 250 mm Pb layers in the beam) for a sample built with an 8 mm Fe sheet + 50 mm Pb tile + 20-100 mm thick steel stair-steps. *Fig.1 c* clearly shows the gap (5 mm wide, 25, or 50 mm long along the beam) between the Pb tiles, which can be imaged even in the case when 60-80 mm thick steel is also in the beam. We finished the planning of the *detailed construction and technical requirements for NORMA*, which will serve as a firm basis for the improvement of the station in the next year.

Imaging and Prompt-gamma Activation Imaging (PGAI) measurements in the investigation of the *effect of borate concentration on the cementation* of radioactive evaporator-concentrates provided data for the optimization of the B/Ca mixing ratio. The chemical and mechanical properties were tested for nine cementitious samples, consisting of three cement compositions, each with three borate concentrations [1]. The simulated liquid waste with the higher boron concentrations, which was solidified with a newly developed cement composition (OXY-B), shows a homogeneous boron distribution in the volume of the cement cylinder, both before and after leaching (*Fig.1 d-e)*. The cement mixtures named OXY and OXY-B developed in this application were effective for the cementation of the simulated borate evaporator concentrates.

In co-operation with Politecnico di Milano, several campaigns of *thermal neutron tomography of lead battery plates* were carried out. The task was to determine the feasibility of neutron imaging because X-ray imaging has limitations in characterizing these Pb-based objects. 3D slices of all three objects are shown in *Fig.1 f*. The results show brighter and darker areas, the spatial localizations of which are rather different for each of the three samples. The darkest spots mark areas where material discontinuities (voids) or very low amounts of material are found. The Pb-alloy paste material regions show distinct behaviour for the samples with different ageing. For the PM8-F sample, there are larger regions with higher attenuation coefficient values in the middle part of the paste between the grid supports, while, in contrast, for the PM8-4 and PM8-9 samples these regions can be found in the very close vicinity to the grid supports. Based on experience we suspect the presence of hydrogen-containing material in the paste, which diffuses during the aging processes.

Seeing future trends and requests from different partners, we have started to test the feasibility of using neutron imaging to detect *thin layers of lubricant materials* in different mock-up samples. Some results are shown in *Fig.1 g-h* for a steel-in-aluminum and a steel-in-Teflon sample. A 0.05-0.1 mm thick lubricant layer, shown in red, between the components is very well detectable in cases where the scattering effect of the hydrogen-containing structural part is absent.

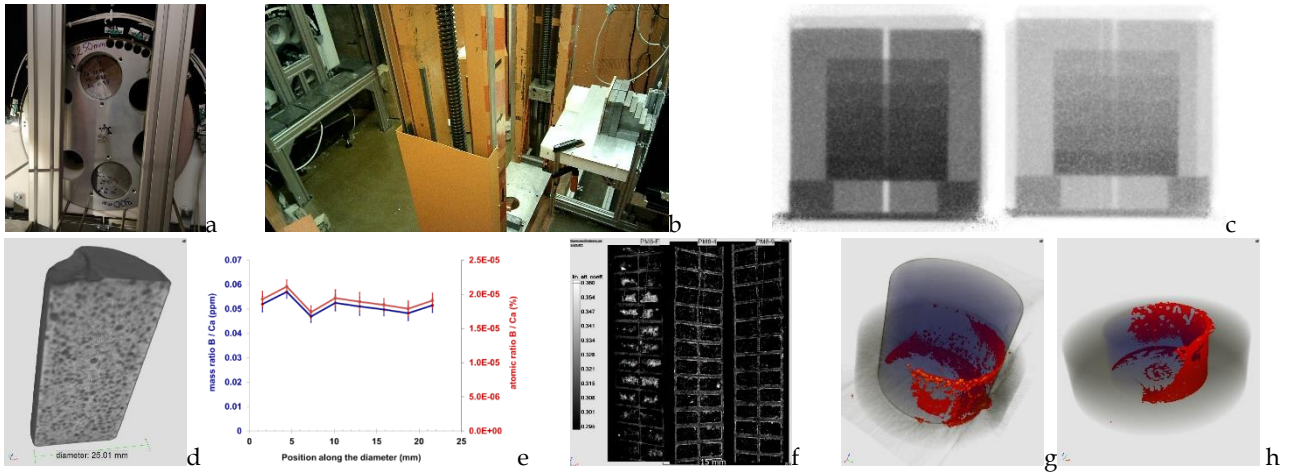

Figure 1: Neutron imaging results: see text for further information

Related publication

[1] M. Fabian, I. Tolnai, Z. Kis, V. Szilagyi: *Characterization of Simulated Liquid Radioactive Waste in a New Type of Cement Mixture.* ACS Omega **7:41** 36108–36116 (2022), https://doi.org/10.1021/acsomega.2c05507

MOLECULAR DYNAMICS STUDIES: (1) ODD-EVEN EFFECT IN N-ALKANE SYSTEMS AND (2) CORRELATION BETWEEN STRUCTURE AND DYNAMICS OF CO_2 CONFINED IN MG-MOF-74 AND THE ROLE OF INTER-CRYSTALLINE SPACE

Indu Dhiman, Marcella C Berg, Loukas Petridis, Jeremy C Smith, Siddharth Gautam, David R Cole

Objective

In the first section, we study the alternation in various properties of n - alkanes (C_nH_{2n+2}) as a function of carbon content n, which is is termed the 'odd-even effect'. Here, we report a comprehensive Molecular Dynamics (MD) simulation study on n - alkane systems carried out with n ranging between 3 (propane) and 8 (octane), examining the odd-even effect on melting point, density, intramolecular conformational ordering, and on translational and rotational motion.

In the second section, our main focus is to understand the dynamic behaviour of CO_2 in Mg based MOF-74. One of the most critical environmental challenges today is the capturing of CO_2, one of the main atmospheric components contributing towards climate change. We want to address the questions: how does a difference in the adsorbed amounts of CO_2 affect it's dynamics within Mg-MOF-74, and what role can inter-crystalline spacing play in the diffusivity of CO_2.

Methods

Classical molecular dynamics simulations were carried out using DL-POLY 4.10, which is a general purpose software with a molecular dynamics simulation package containing a highly efficient set of methods and algorithms. This is advantageous to study transport modelling, study confinement effects, and mechanical shearing behaviour, too.

Results

1. Our simulations show the presence of an odd-even behaviour in rotational and translational dynamics, below and above the melting point, respectively. The results highlight the role of both molecular shape and the variation in density and their interplay in the origins of the odd-even effect. Detailed calculations of several properties from the same simulation data helps us see correlations between the odd-even alterations in different properties and thus helps understand the origin of the odd-even effect. It can be concluded from the results reported here that both the molecular shape and density of alkanes play a significant role in the origin of the odd-even effect.

2. We report on an MD simulation study at 300K, of CO_2 confined in Mg-MOF-74 with inter-crystalline spacing of different widths. Six strong sites of CO_2 adsorption are found at the periphery of the Mg-MOF-74 pores in addition to a relatively weak adsorption at the pore centre. On insertion of inter-crystalline spacing into the simulation, additional sites of strong adsorption are seen close to the pore opening, which delocalize as the inter-crystalline space is further widened, while adsorption in the pore centre grows. This adsorption redistribution has important implications for the dynamics of CO_2. With wider inter-crystalline spacing, anomalous loading dependence of translational diffusivity is observed. In general, inter-crystalline spacing suppresses the rotational motion of CO_2. Translational motion, however, exhibits an enhancement on introduction of inter-crystalline space but gets suppressed when the space is widened.

Remaining work

To further extend this work, we aim to perform simulations on ionic liquid systems, wherein due to the absence of long-range ordering, an odd–even phenomenon is not expected in dynamic behaviour in an amorphous state. This work is also helpful for technological applications requiring novel materials with structural sensitivity.

Related publications

[1] I. Dhiman, M. C. Berg, L. Petridis, J. C. Smith, S. Gautam: *Dynamic odd–even effect in n-alkane systems: a molecular dynamics study,* Physical Chemistry Chemical Physics, https://doi.org/10.1039/D2CP02760G

[2] I. Dhiman, M. C. Berg, D. R. Cole, S. Gautam: Correlation between structure and dynamics of CO2 confined in Mg-MOF-74 and the role of inter-crystalline space: A molecular dynamics simulation study, Applied Surface Science **612,** 155909 (2023) https://doi.org/10.1016/j.apsusc.2022.155909

EXTENDING THE RELIABILITY OF TENSILE TESTS WITH A NOVEL EVALUATION FRAMEWORK

Tamás Fekete, Levente Tatár, Dániel Antók, Péter Bereczki

Objective

The tensile test is one of the most widely used engineering tests, codified in numerous national and international standards. The basic theoretical model generally used for evaluation of the test is extremely simple. The basic results of a tensile test (yield strength, ultimate tensile strength) are widely used for design and verification. This over-simplifying approximation may be enough for some simple cases assuming that the safety factor is large enough. For more complicated cases, where small-scale yielding is permitted, assessment needs an accurate description of the plasticity. With a clip gauge type extensometer and simple analytical formulae, the elastic-plastic flow curve can be reliably described until necking. These formulae cannot describe the post-necking behaviour of the specimen.

Simple approaches are not sufficient for safety calculations of large-scale, high-load, complex engineering structures. In such cases, the Structural Integrity (SI) approach, which often includes plasticity, must be used. This requires a more accurate and complete description of material properties, than can be achieved with simple analytical formulae.

A framework created for determination of a stress-strain curve based on traditional measurements (force, extensometer) complemented by optical measurements has been presented in [1] and [2]. Main elements of the framework are measurements and simulations.

Methods

The measurements are performed on a Gleeble 3800 thermomechanical simulator. Cylindrical specimens and specimens with square cross section were used. They were equipped with a clip gauge extensometer. Most important data provided by the testing machine were force, strain (measured by extensometer) and a triggering signal.

For specimens with square cross section regular patterns were created at two sides of the specimens. A dual camera system was used for taking pictures of the specimen during the test. Both cameras were triggered by the same triggering signal.

Digital Twins (DT) of the measurements were developed for simulation of the tests. Figure 1 presents an overview of the process. Specimen contours and mapping of the grid were obtained from pictures. With these data the stress-strain curve can be extended over the validity of measurements by extensometer. Since the stress field becomes triaxial, a correction has to be applied to the curve. Validity of such curves can be verified and further developed by Finite Element (FE) computations.

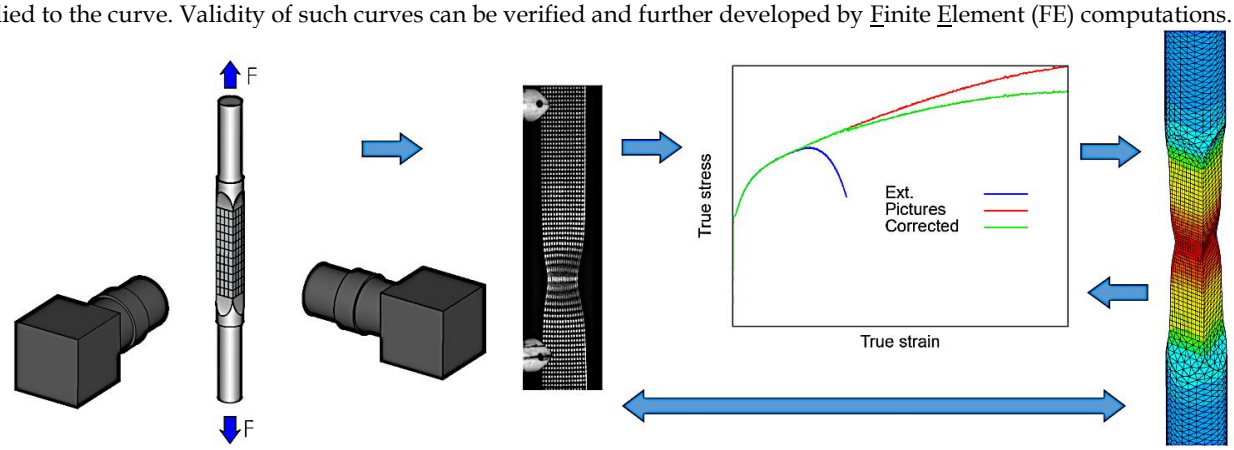

Figure 1: Overview of the process

Results

From pictures taken during the test contours to be used for extending the true strain true stress curves were determined by a multistep procedure. Extraction of the contours consisted in oversampling the original picture, then a slight blurring followed by thresholding and vectorising. The real dimensions of the curves were obtained by using the laws of geometric optics. Adjacent averaging has been applied to raw curves for smoothing and for specimens where necking was present an analytical "bell-shaped" curve was fitted to the smoothed curves. Based on this formula, the radius of the curvature at the minimal cross section has been determined. For cylindrical specimens, the Bridgman correction formula has been used (1).

$$\sigma_{eq} = \frac{\sigma}{\left(1+\frac{2R}{a}\right)\cdot \ln\left(1+\frac{a}{2R}\right)} \tag{1}$$

In this formula σ is the axial stress in the minimal cross-section ($\sigma = F/S$), σ_{eq} is the von Mises equivalent stress,

a is the minimal radius, R is the curvature radius at the lowest point of necking conform Figure 2.

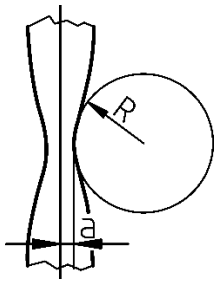

Figure 2: Notations used for Bridgman correction

For specimens with square cross section, we used the Choung-Cho formula. The formula computes a corrective factor, based on the exponent of the Ludwik formula $\sigma = \sigma_y + K \cdot (\varepsilon_{pl})^n$. It can be written as:

$$\sigma_{eq} = \varsigma(\varepsilon_{pl}, n) \cdot \sigma \,, \tag{2}$$

where $\varsigma(\varepsilon_{pl}, n)$ is the correction factor computed using the equivalent plastic strain ε_{pl} and the Ludwik exponent n. More details are presented in [3].

For the square specimens it could be clearly observed that the deformation of the specimen is different in different directions, meaning that the material is anisotropic. Another important observation is that the curvature radiuses are different for different contours.

The DTs of the tensile tests are FE models created with the MSC Marc-Mentat FE system. Axial symmetric models were used for the cylindrical specimens, while for specimens with square cross-section we used 3D models. Von Mises plasticity theory was used with multilinear strain-hardening plasticity. We considered homogeneous and isotropic material. Large strain–large displacement kinematics was used in updated Lagrangian setting.

The Bridgman formula is quite adequate for cylindrical, the Choung-Cho formula for specimens with square cross-section. However, mainly at the end of the process there are significant differences between measurements and simulations. Figure 3 shows the force-thickness reduction curve obtained on a square cross-section test specimen, and the results of the simulation using the uncorrected flow curve and the simulation using the Choung-Cho corrected flow curve.

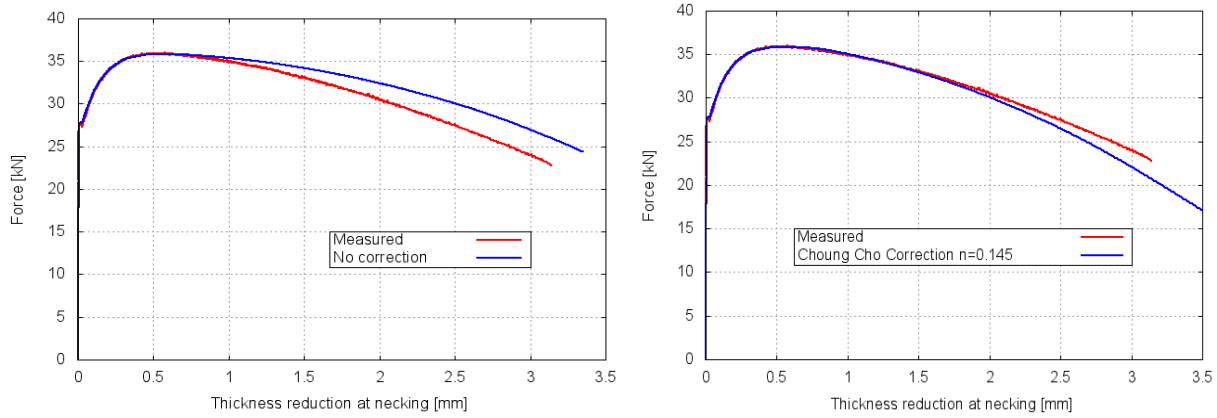

Figure 3: Measured and simulated curves: (left) original flow curve, (right) Choung-Cho corrected flow curve with n=0.145

Remaining work

When evaluating the measurements, the results are averaged over the anisotropy of the materials and the FE models use isotropic material properties. A possible direction of further development would be to incorporate anisotropy and material damage into the calculation models.

Related publications

[1] T. Fekete, D. Antók, L. Tatár, P. Bereczki, E. Kocsó: *Evaluation Framework for Tensile Measurements*, EK-CER progress report 2021.

[2] D. Antók, T. Fekete, L. Tatár, P. Bereczki: *Evaluation Framework for Tensile Measurements, based on Full-Field Deformation Measurements and Digital Twins*, In: ICSI 2021 The 4th International Conference on Structural Integrity, Structural Integrity Procedia **37,** 796–803 (2022)

[3] D. Antók, T. Fekete., L. Tatár, P. Bereczki: *Extending reliability of FEM simulations, based on optically assisted tensile tests and digital twins*, In: 23 European Conference on Fracture - ECF23, Structural Integrity Procedia **42,** 1684–1691 (2022)

INVESTIGATION OF IRON SELF-DIFFUSION IN FERH THIN FILM USING NEUTRON REFLECTOMETRY

Daniel Merkel

Objective

The aim of the ongoing experiment is to determine the diffusion coefficient and activation energy of the iron self-diffusion in the special BCC A1 and special FCC B2 structure FeRh thin film.

Methods

$[^{nat}Fe_{51}Rh_{49}(63\ Å)/^{57}Fe_{51}Rh_{49}(46\ Å)]_{10}$ isotope-periodic multilayer was prepared on MgO (001) substrate by molecular beam epitaxy technique. The substrate was held at 200 °C during the deposition process. The samples were annealed at temperature ranging from 250 °C to 550 °C for 30 min to 90 min under high vacuum circumstances.

Based on the isotope sensitivity of neutron scattering, the diffusion parameters can be obtained from the variation of the Bragg-peak in the reflectometry pattern.

Results

Neutron reflectometry measurements were carried out on isotope periodic FeRh thin film after several annealing steps. The as deposited sample exhibits A1 FCC structure, which turns to BCC B2 structure after annealing. This mechanism is governed by atomic diffusion, which smears out the adjacent isotope interfaces, resulting in a decrease in the isotope periodic Bragg-peak. The neutron reflectivity curves after low temperature heat treatments are shown in Figure 1.

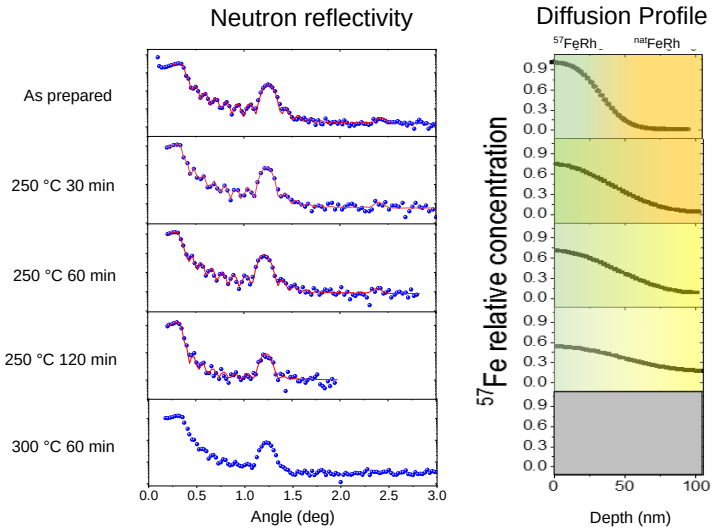

Figure 1: Neutron reflectivity spectra taken from FeRh thin film in as deposited state (A1 structure) and after various temperature and time annealing treatments. On the right, the Fe diffusion profile is shown in an adjacent isotope bilayer.

In order to determine the diffusion processes, one has to take into account that the Fe self-diffusion parameters are different in A1 and B2 structure, and during annealing these two phases can be presented simultaneously. Therefore, a series of neutron reflectometry experiments with an initially homogenous B2 structure FeRh were carried out. The B2 structure remains during heat treatment and makes it possible to extract the diffusion coefficient and activation energy of iron atoms in this phase. Knowing the iron diffusion in the B2 phase, we can use it in the A1/B2 mixed phase diffusion and determine also the Fe self-diffusion in A1 phase.

Remaining work

In order to finish this work, we have to perform further neutron reflectometry measurements on a few more annealing temperatures. The proper evaluation of the several reflectograms needs to be done. The results of this work will be published in 2023.

INVESTIGATION OF NI-TI MULTILAYERS USING GRAZING INCIDENCE SMALL ANGLE NEUTRON AND X-RAY SCATTERING

Tamás Veres, Szilárd Sajti, László Bottyán

Objective

The aim of the experiments is to determine the in- and out-of-plane correlation properties of Ni-Ti multilayers used in neutron optics and to improve the interpretation of grazing incidence scattering patterns.

Methods

Ni-Ti multilayers were prepared on borofloat glass substrate by sputtering. Grazing Incidence Small Angle Scattering (GISAS) measurements were performed using neutrons for Supermirror (SM) samples and X-rays for periodic ones ($[Ni(Mo)(85\ Å)/Ti_i(75\ Å)]_{25}$). The Resonant Diffuse Scattering (RDS) was described within the Distorted Wave Born Approximation.

Results

Experimental GISAXS data of Ni-Ti periodic multilayers of period, bilayer thickness and roughness of 50, 160Å and 5-15 Å, respectively, were collected at different grazing angles of incidence. Interface roughness correlation in multilayers have usually been derived from different cuts of GISAS patterns. The diffuse scattering was investigated outside the limit of the extensively used small roughness approximation, $q_z\sigma << 1$. We have shown that in large roughness case the use of the above mentioned approximation leads to erroneous assumption of a frequency dependence of the roughness replication and false values of coherence length. The appearence of local minima in the width of the scattering pattern at the RDS peaks (Fig. 1a), a phenomenon that have been interpreted by a spatial frequency dependence of roughness replication may be a mere consequence of the breakdown of the Small Roughness Approximation (SRA) condition. The experimental results (on a Ni-Ti multilayer of rather ordinary roughness) show, that in the correct calculations, the assumption of spatial-frequency independent roughness replication was sufficient to characterize the GISAXS pattern without assuming a complex spatial frequency dependent roughness replication.

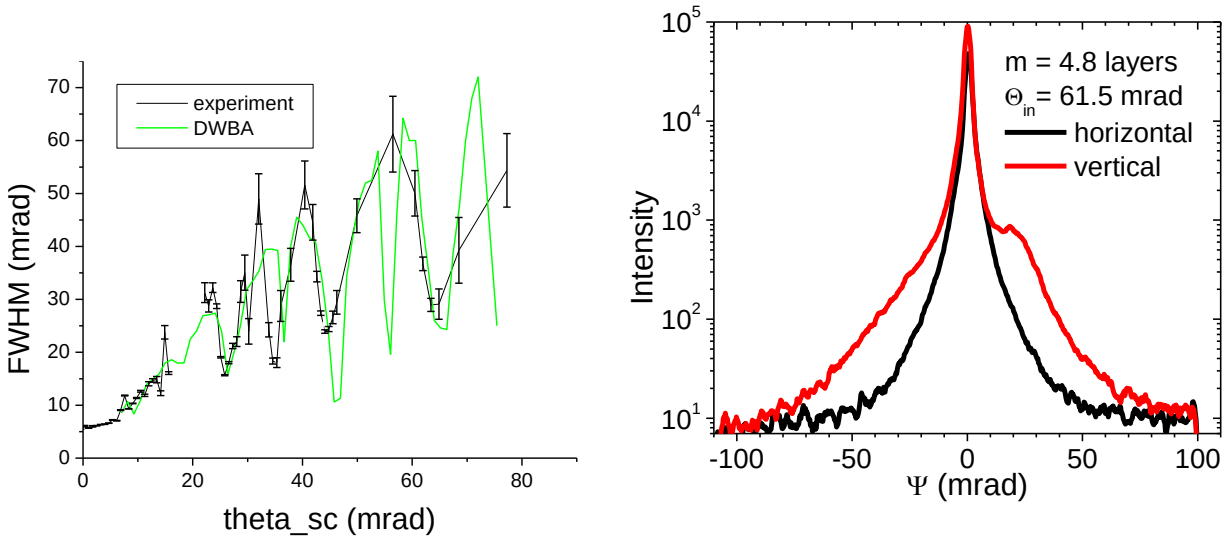

Figure 1: a) Measured and calculated widths of the sample-plane-parallel cuts of the GISAXS pattern as a function of scattering angle for the periodic multilayer, as detailed in the text. b) Asymmetric cut of GISANS from neutron SM which reveals the asymmetry in the growth of the thinnest layers (contributing to the reflectivity near to the SM critical angle) and also the roughness anisotropy of the same layers.

GISANS measurements were performed on neutron SMs. Line scans of a GISANS detector image at a given exit angle provide the correlation properties of the layers of a given thickness and the corresponding depth in the SM structure. The scattering patterns reveal an anisotropic roughness and the direction of the roughness replication deviates from the sample perpendicular.

Remaining work

The results of this work will be published in 2023.

PROTOTYPE ACCELERATOR-DRIVEN COMPACT NEUTRON SOURCE

Peter Zagyvai, Dávid Hajdú

Objective

Cooperation with Mirrotron Ltd., a major contributor of the international scientific neutron community, has started to establish a Compact Neutron Source (CNS) driven by a moderate proton accelerator unit at the Martonvásár campus of Mirrotron several years ago. Involvement of representatives of the Environmental Physics Laboratory (EPL) of EK was aimed on issues in relation to obtaining regulatory licences for the facility.

Methods

Stochastic Monte Carlo N-Particle Transport (MCNP) modelling calculations were performed on determining the prompt gamma dose field generated by incidentally diverted proton particles absorbed in the copper accelerator tube representing regularly occurring (planned) and accident exposure scenarios. For the planned scenario an average beam loss of 3% was assumed, the emergency case was defined as complete (100%) diversion of the proton beam into the tube wall for 1 s before the interlock of the accelerator cuts the beam. Fluence-to-dose conversion factors were taken from ICRP 116 publication [1] for interpreting cases with and without an additional heavy concrete slab cover above the accelerator channel, under the first floor where continuously occupied working area of non-radiation workers was designed. Prompt gamma library of copper was taken from the paper of M.J. Kenny [2]. This analysis will be included in the licensing documentation of the CNS to be submitted to the Hungarian Atomic Energy Authority (OAH).

In addition to theoretical planning, initial experiments were performed with samples of concrete slabs manufactured by Mirrotron for shielding around the joining section of the proton accelerator tube into the target chamber of the CNS where dose field of gamma and scattered neutron particles will be present during the pulsed mode operation of the system. Gamma dose field measurements were arranged and implemented at the "Pavilon" gamma irradiation facility [3] of the EK campus regularly with a major ^{137}Cs-source used for calibration and testing of radiation detectors with the authentication of the Hungarian metrological authority. As Figure 1 shows, the slabs were arranged either normal or parallel to the collimated photon beam in the experiment, in the latter case a certain number of the photons could traverse a thinner attenuating layer than in the former one.

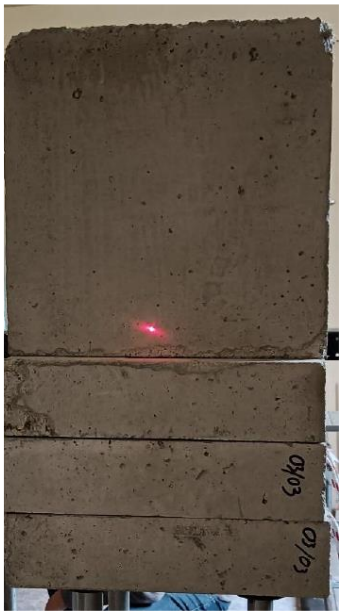

Figure 1: Concrete slabs for attenuation tests showing the laser-induced focal point of the gamma beam

Results

MCNP modelling shows temporarily elevated gamma dose rates in the rooms intended to be occupied by non-radiation workers of the Martonvásár campus building. Their annual dose constraint is likely to be accepted as 50 μSv. The dose consequence of the worst-case accidental scenario was significantly lower than that of the "regular" beam loss assumption.

The dose field at the first floor working area of non-radiation workers is shown in Figure 2.

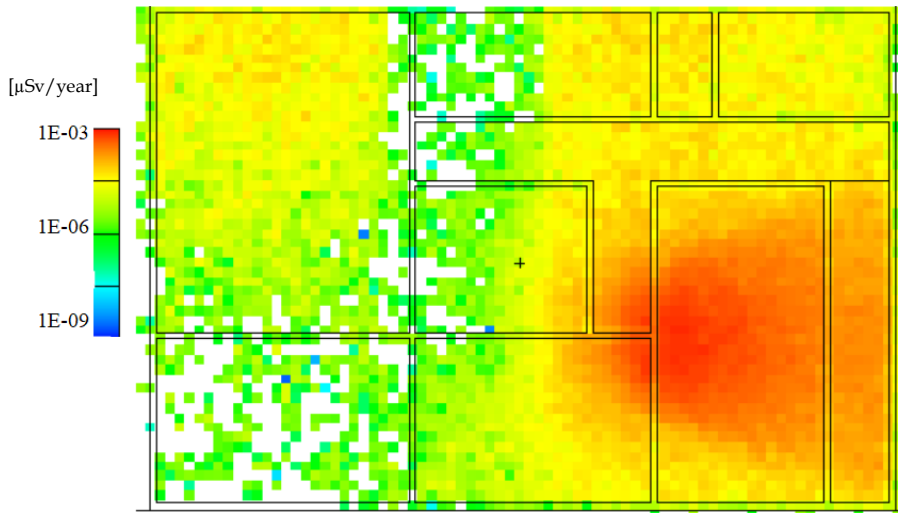

Figure 2: Assumed external doses for one working year (2000 hours) with 3% beam loss on the floor above the accelerator covered with heavy concrete slab

The highest estimated dose was calculated as 0.8 nSv per year which is quite favourable in comparison to the dose constraint. If the additional concrete slab cover is omitted, this value would reach 220 µSv per year with the same conservative estimate of residence time in the exposed area.

The experimental study of the attenuation characteristics of cast concrete blocks measuring the actual attenuated gamma dose rate with authenticated dose detectors showed the significance of the roughness of the concrete surfaces. Briefly, the arrangements when the irradiating beam arrived parallel with the gaps between the slab surfaces gave 3.3 times higher doses than the arrangements with surfaces normal to the beam. This experience underlines the requirement of "chicane"-type attachment of slabs and/or the application of a suitable (e.g. boronated silicon) gap filling.

Remaining work

Further modelling and shielding design work is necessary for compiling and submitting the Workplace Radiation Ordinance and the Radiation Protection Description documents of CNS to get a licence approval from OAH.

Related publications

[1] N. Petoussi-Henss et al.: *Conversion Coefficients for Radiological Protection Quantities for External Radiation Exposures,* ICRP Publication 116, Ann. ICRP **40** (2-5) 1–257 (2010)

[2] M. J. Kenny et al.: *Proton induced γ-ray yields,* Nuclear Instruments and Methods **168:(1–3),** 115–120 (1980)

[3] https://www.iki.kfki.hu/radsec/irradfac/page5_2.html

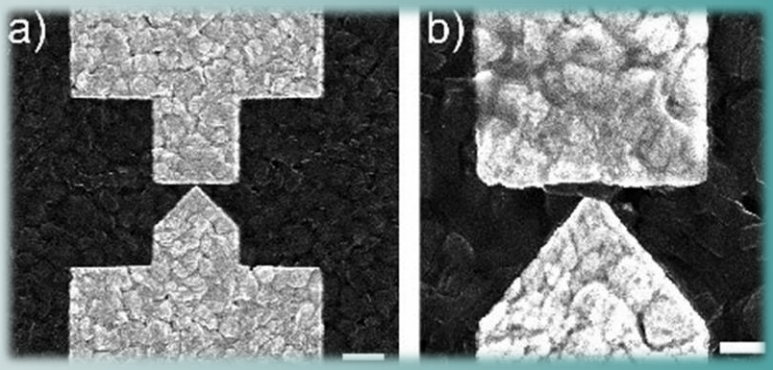

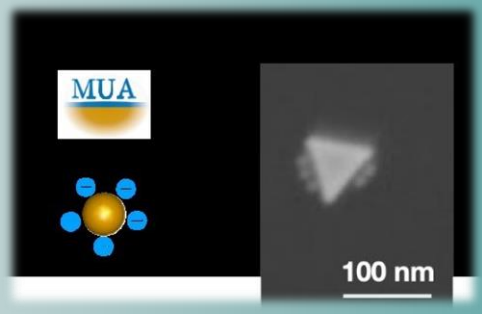

VII. RESEARCH AND DEVELOPMENT IN INSTITUTE OF TECHNICAL PHYSICS AND MATERIAL SCIENCES

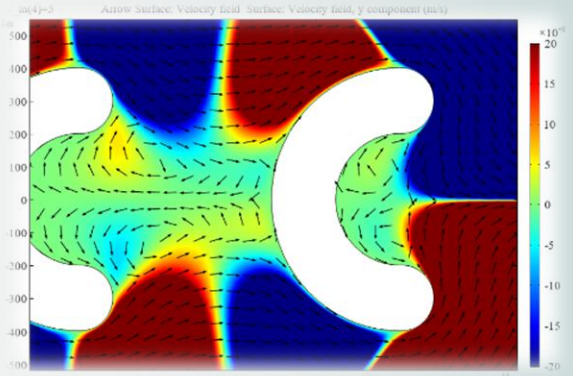

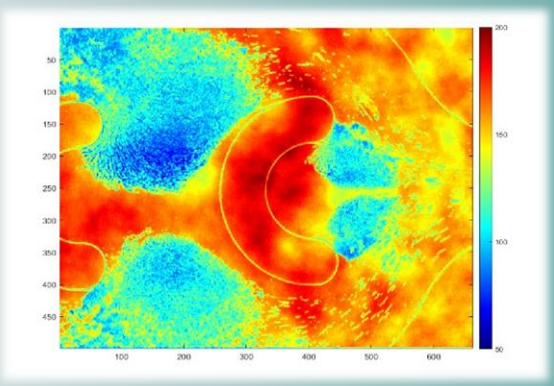

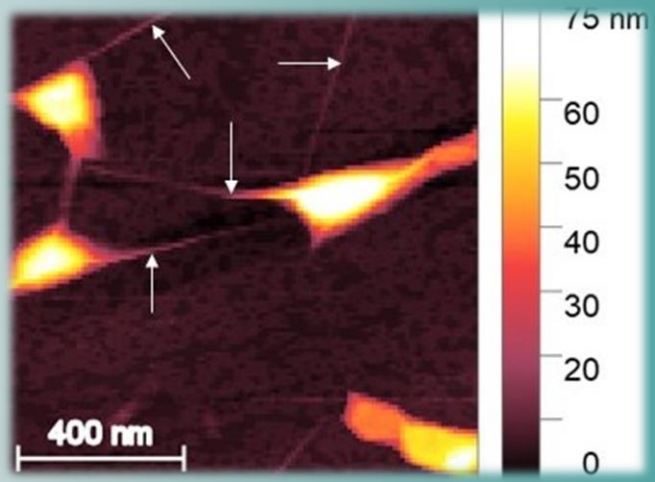

ULTRA-SMALL PT NANOCLUSTERS ON 2D MoS_2 FOR HIGHLY EFFICIENT HYDROGEN EVOLUTION

OTKA KKP 138144, OKTA 132896, TKP2021-NKTA-05, H2020-SGA-FET-GRAPHENE-2019-881603 Graphene Flagship Core3

T. Ollár, A. Koós, P. Kun, P. Vancsó, P. Nemes-Incze, J. S. Pap, L. Tapasztó

Large-scale and environmentally friendly production of hydrogen requires highly active, stable and cost-efficient catalysts. While platinum is known as the most efficient catalyst for hydrogen evolution, its high costs and scarcity strongly limit its practical use in large-scale applications. To overcome this, extensive efforts have been focused on replacing platinum with cheaper, more abundant materials, as well as on reducing the Pt content of catalysts, while maintaining the outstanding activity and stability. Among the most successful approaches are those based on improving Pt atom utilization efficiency through improving dispersion, which is maximized in Pt Single Atom Catalysts (SACs). Indeed, such catalysts were able to reach the activity of commercial Pt/C catalysts, with two orders of magnitude lower Pt loadings of order of μg/cm². However, SACs represent the end of the road in terms of catalyst design for approaches relying on dispersion. To further reduce the Pt loading, without losing activity, one needs to design Pt structures that outperform the intrinsic activity of conventional Pt nanoparticles and Pt SACs.

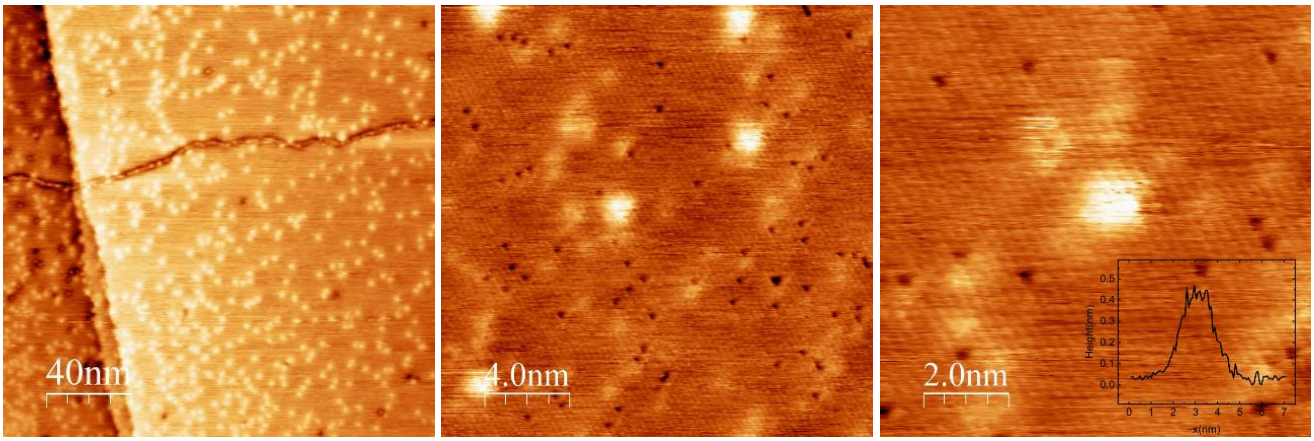

Figure 1: Scanning tunnelling microscopy images of small (~ 1 nm) Pt clusters (bright dots) deposited on 2D MoS_2 crystals. The dark spots in the atomic resolution STM images correspond ot S atom vacancies of the MoS_2 support, acting as anchor sites for Pt clusters.

Distorted Pt structures were shown to host reaction sites of increased intrinsic activity. However, this comes at the price of a substantially reduced stability. Therefore, engineering novel Pt structures is a continuous compromise between increasing activity and preserving stability. Metal-support interaction emerged as an efficient tool for engineering catalytic performance. Enhanced metal-support interactions clearly boost the stability and durability of supported metal catalysts, and it can also substantially influence their activity and selectivity. Pt/MoS_2 systems emerge as a promising candidate for realizing an increased metal-support interaction, due to the strong affinity between Pt and S. This, combined with a relatively large lattice mismatch can give rise to novel Pt structures emerging from the competition of adhesion (Pt-S) and cohesion (Pt-Pt) that holds the promise for a simultaneous enhancement of activity and stability. We have observed that the catalytic performance of the Pt/MoS_2 system can be substantially improved by realizing small Pt clusters that interact more strongly with the MoS_2 support. Such small Pt clusters were grown by an electrochemical deposition on CVD grown MoS_2 single and few layers, grown on graphite. STM investigation reveal a high-density decoration of MoS_2 surface by ultra-small (~1 nm) Pt clusters, as well as a high density of sulphur vacancy type defects in the 2D MoS_2 crystals. Such defect sites act as anchors for Pt clusters hindering their aggregation and enabling the stabilization of ultra-small Pt clusters at high density (Fig. 1).

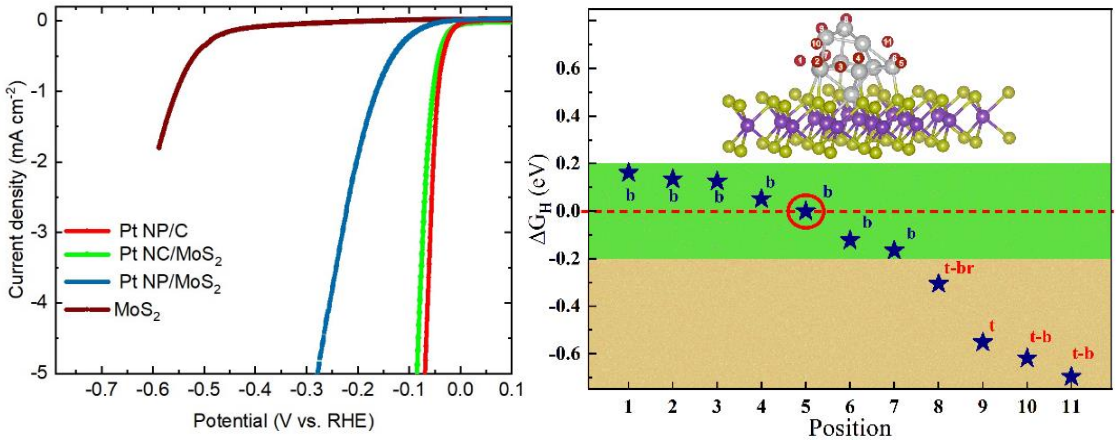

Figure 2: Linear sweep voltammetry measurements on various samples revealing the Pt nanoclusters on MoS_2 can closely approach the activity of commercial Pt-C catalysts at orders of magnitude lower Pt content (left). Theoretical model of Pt nanoclusters on MoS_2 and the corresponding H adsorption free energies, indicating the presence of highly active sites at the interface/perimeter of the Pt cluster.

2D MoS_2 crystals decorated with such small Pt clusters display exceptionally high catalytic activity towards hydrogen evolution. Such ultra-fine clusters perform much better than larger (~5 nm) Pt nanoparticles deposited on MoS_2, even though the Pt content is three orders of magnitude lower for samples comprising small Pt clusters (Fig. 2.a). Most importantly small Pt clusters on MoS_2 samples closely approach the activity of commercial Pt-C catalysts, again a three orders of magnitude lower Pt content. We attribute the observed outstanding efficiency of our catalyst to a strongly increased Pt/MoS_2 interaction, leading to: (1) the stabilization of ultra-fine Pt clusters all over the MoS_2 basal plane, (2) deformation of Pt clusters morphology into a quasi-flat (bilayer) structure, in order to take better advantage of Pt-S interactions, and (3) a spectacular increase of the intrinsic activity of Pt sites, allowing a four orders of magnitude reduction of Pt loading, compared to commercial Pt/C catalysts, without losing activity or stability. Detailed simulations of hydrogen adsorption free energies revealed that the most active sites are on the Pt atoms directly adhering to the MoS_2 surface (Fig. 2b), indicating strong synergistic effects at the origin of the outstanding catalytic performance.

IDENTIFYING STACKING FAULTS AND DOMAIN WALLS IN RHOMBOHEDRAL GRAPHITE BY SCANNING TUNNELLING MICROSCOPY

LP2017-9/2017, OTKA KKP 138144, TKP2021-NKTA-05, H2020-SGA-FET-GRAPHENE-2019-881603 Graphene Flagship Core3

K. Kandrai, K. Márity, Z. Tajkov, M. Szendrő, A. Pálinkás, P. Kun, P. Vancsó, L. Tapasztó and P. Nemes-Incze

Materials having a flat band [1] at the Fermi level can host a variety of emergent many body ground states. One such system is Rhombohedral Graphite (RG), which is a rare form of graphite (Fig. 1.a). Previously we have shown that rhombohedral graphite hosts strong interactions [2], in its surface flat band. Being one of the simplest materials with a flat surface band, we have a chance to understand the complete defect structure of the material. In most experiments one can disregard vacancies and other point defects [3], because their density is smaller than 10^9 cm^{-2}. This leaves lateral domains walls and stacking faults as the main defects we need to consider.

We have explored both types of defects using Scanning Tunnelling Microscopy (STM) measurements on thick (>6 graphene layers) RG samples. In Fig. 1. we present a representative measurement on a 17-layer thick sample showing a domain wall between the hexagonal and rhombohedral areas. The rhombohedral region is apparent only if we measure the tunnelling conductance at the Fermi level and plot it on a map (Fig. 1.d).

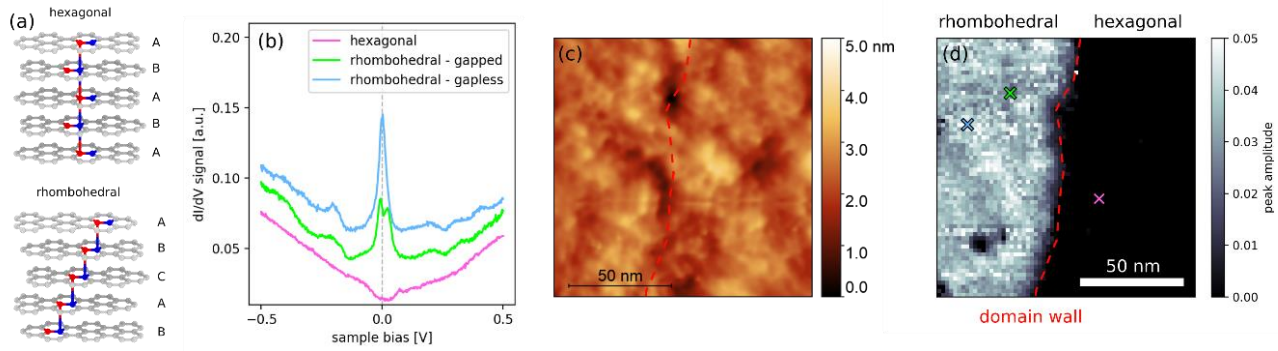

Figure 1: ***(a)*** *Stacking arrangement of the graphene layers in hexagonal and rhombohedral graphite.* ***(b)*** *Characteristic tunnelling spectroscopy measurements of the LDOS on the surface of the two graphite phases. The surface flat band shows up as a large LDOS peak at 0 V sample bias and hosts a gapped and gapless, degenerate ground state at low temperature (9 K).* ***(c)*** *STM topographic map of a 17-layer RG surface.* ***(d)*** *Map of the surface state peak intensity in the same area as (c). The surface shows a lateral domain wall between rhombohedral / hexagonal regions, made clear by the presence / absence of the surface state.*

Besides lateral domain walls, graphite samples can have stacking faults, where one layer switches the stacking configuration of the crystal, from hexagonal to rhombohedral or vice versa. Raman spectroscopy is well suited [3, 4] to identify areas of RG in exfoliated samples, but is not particularly sensitive to small perturbations of the stacking sequence, such as twins.

In our STM investigation of RG we have identified that the bulk bands of RG can be used to identify the number of rhombohedrally stacked graphene layers in a sample. By measuring the top surface of an RG crystal, the bulk bands show up as peaks in the dI/dV signal, which is a measure of the Local Density of States (LDOS). The energy spacing between these peaks decreases monotonically as the number of graphene layers increases in the crystal. An example of this can be seen in Fig. 2.a, with the calculated LDOS in Fig. 2.b. Thus, by measuring the LDOS of the top layer we gain information on the crystal structure deep inside the sample. This allows us to ensure that the sample we are measuring does not contain stacking faults within the measured area, because such a defect will change the energy of the bulk bands in a stepwise fashion. In the area presented in Fig. 2.d, the bulk band shows a smooth modulation over the surface, in correlation with the local doping (2.c).

These results are the starting points to explore the local electronic structure of lateral domain walls. Furthermore, STM measurements of the bulk bands in the surface LDOS will allow for an unprecedented understanding of the defect structure of RG, aiding further exploration of this exciting quantum material.

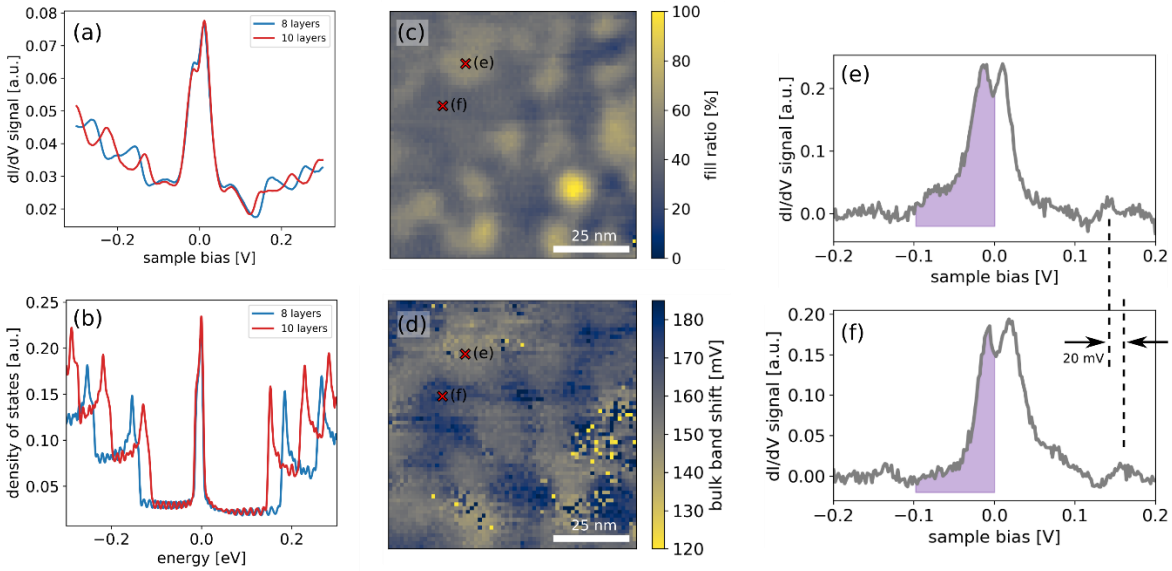

Figure 2: ***(a)*** *Tunnelling spectroscopy measurement on an 8-layer and 10-layer RG crystal on SiO_2.* ***(b)*** *Calculated LDOS.* ***(c)*** *Map of the spectral weight below the Fermi level (0 sample bias), as a measure of the local doping of the sample.* ***(d)*** *Position in sample bias of the first bulk state of the sample, tracked across the same area as in* ***(c)****, shows no step-like changes. Individual spectra shown in* ***(e, f)*** *are marked by red crosses. The spectra in* ***(e)*** *and* ***(f)*** *show a 20 mV shift in the first bulk state due to changes in the local doping.*

Related publications

[1] N. Regnault, et al.: *Catalogue of flat-band stoichiometric materials,* Nature **603,** 824–828 (2022)

[2] I. Hagymási, et al.: *Observation of competing, correlated ground states in the flat band of rhombohedral graphite, Science* Advances **8**, eabo6879 (2022)

[3] F. Joucken, et al.: *Direct Visualization of Native Defects in Graphite and Their Effect on the Electronic Properties of Bernal-Stacked Bilayer Graphene,* Nano Lett. **21,** 7100–7108 (2021)

[4] A. Torche, F. Mauri, J.-C. Charlier & M. Calandra: *First-principles determination of the Raman fingerprint of rhombohedral graphite,* Phys. Rev. Mater. **1,** 041001 (2017)

TOPOLOGICAL PHASE DIAGRAM OF $ZrTe_5$ MONO AND BILAYERS

LP2017-9/2017, OTKA KKP 138144, TKP2021-NKTA-05,
H2020-SGA-FET-GRAPHENE-2019-881603 Graphene Flagship Core3

Z. Tajkov, D. Nagy (ELTE), K. Kandrai, J. Koltai (ELTE), L. Tapasztó and P. Nemes-Incze

The concept of time reversal invariant topological insulators has been a paradigm shift in solid-state physics and the controllable topological phase transition in two-dimensional materials has been a long-sought goal. The transition-metal pentatelluride $ZrTe_5$ lies at the boundary of the weak and strong topological phases, making tuning by mechanical deformation a viable avenue to realizing transitions between topological phases. This material has received substantial interest due to its numerous exotic properties, such as the planar Hall effect, anomalous Hall effect and chiral magnetic effect. However, most studies have focused on the bulk material, with very few [1] experimental results on monolayers, even though in the single layer the crystal is predicted to be a large gap 2D topological insulator. [2]

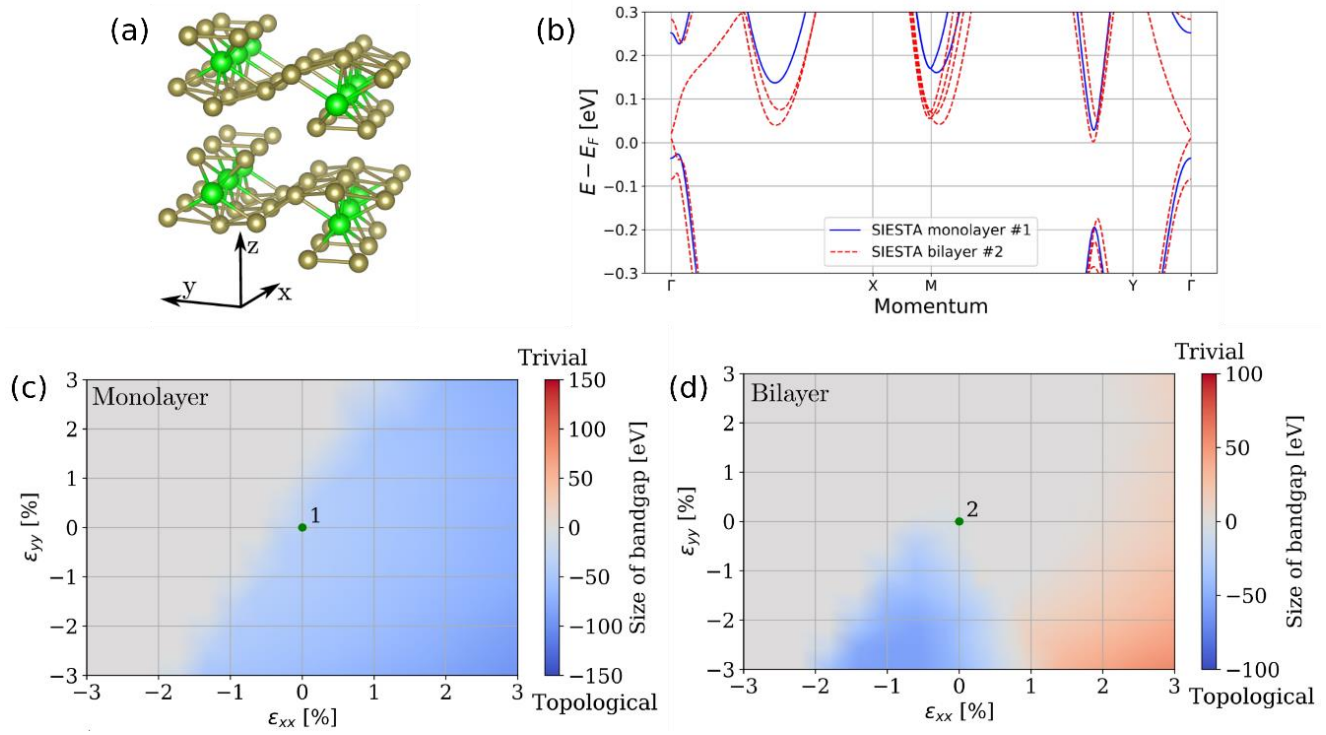

*Figure 1: Topological phases of mono and bilayer $ZrTe_5$. **(a)** Crystal structure of $ZrTe_5$, showing two van der Waals monolayers, extending along the x, y plane. **(b)** Band structure of the monolayer and bilayer. Density plot of the band gap for the monolayer **(c)** and bilayer **(d)**. Red and blue colours represent the topological character of the gap (see also ref. 3) as a function of biaxial in plane (ε_{xx}) and out of plane (ε_{xy}) strain.*

Previously, we have examined the topological phase transition in a bulk crystal, via STM measurements and *ab initio* calculations [3]. Here we explore the topological phase diagram of monolayer and bilayer $ZrTe_5$ crystals under mechanical deformations, using *ab initio* calculations. The band structure of mono- and bilayers of $ZrTe_5$ is plotted in Fig. 1b, showing a 70 meV topological gap for the monolayer, in agreement with the previous prediction by Weng et al. In the bulk, changes to the interlayer spacing is a key parameter in shaping the topology of the band structure. This is reflected in the topological phase diagrams shown in Fig. 1, where the gap closes for modest strain in the van der Waals interlayer separation. As a function of in-plane biaxial deformation, the bilayer shows a transition from a trivial insulator to a topological insulator at experimentally achievable strains of a few %. At the same time, in the monolayer case there is no trivial-topological phase transition, only a closure of the topological gap for small (<1%) compressive strain. Thus, from a perspective of tuning topological phases via strain, bilayers of $ZrTe_5$ represent a unique platform realizing the topological-trivial insulator transition.

Since the preparation of monolayers and bilayers is still a challenge, we also examine the exfoliation of $ZrTe_5$ onto gold substrates (see Fig. 2). We conclude that this method is unviable, as opposed to other 2D tellurides [4] due to strong attraction of the first layer to gold which destroys its crystalline structure. Thus, in future experiments it is worth exploring the exfoliation of $ZrTe_5$ onto other clean metal surfaces [5], where the adhesion to the metal does not compromise the crystal structure of the material.

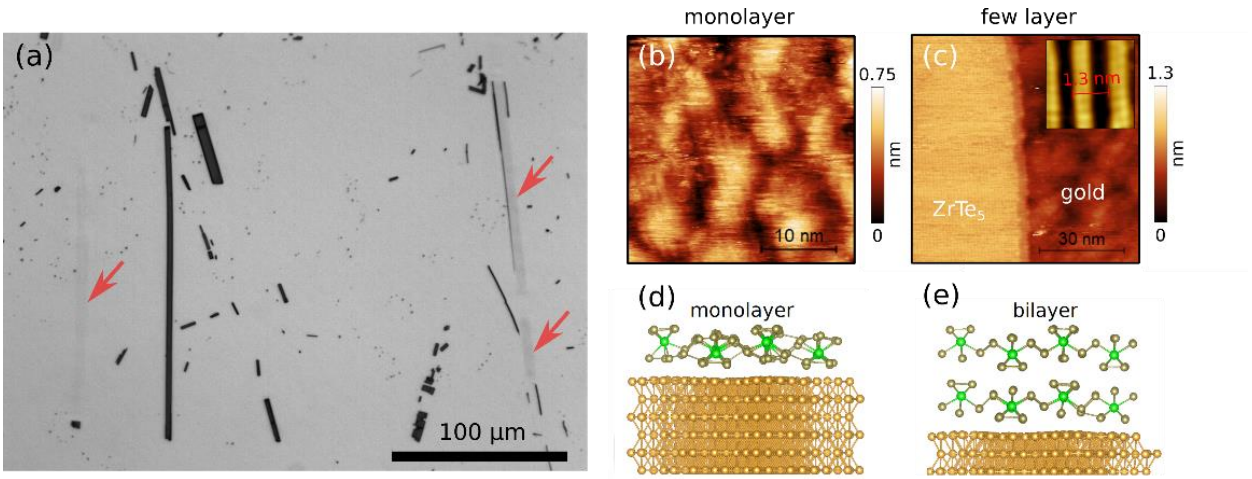

Figure 2: ***(a)*** *Optical microscopy image of exfoliated $ZrTe_5$ on a gold substrate. Red arrows mark areas with the smallest optical contrast, possibly monolayers.* ***(b)*** *Representative STM topographic image of a low contrast area, showing a disordered structure with only slight hints of unit cell periodicity.* ***(c)*** *STM topographic image of a few-layer area, showing a well resolved atomic contrast on top of the crystal.* ***(d)*** *Relaxed ab-initio model of an adsorbed $ZrTe_5$ layer on a gold (111) surface.* ***(e)*** *Calculation for a bilayer $ZrTe_5$. The crystalline structure of the monolayer is destroyed by the strong adhesion to the gold substrate, while in the bilayer case the top monolayer is unaffected.*

Related publications

[1] W. Z. Zhuo, et al.: *Thickness-dependent electronic structure in layered $ZrTe_5$ down to the two-dimensional limit,* Phys. Rev. B **106,** 085428 (2022)

[2] H. Weng, X. Dai, & Z. Fang: *Transition-Metal Pentatelluride $ZrTe_5$ and $HfTe_5$: A Paradigm for Large-Gap Quantum Spin Hall Insulators,* Phys. Rev. X **4,** 011002 (2014)

[3] Z. Tajkov, et al: *Revealing the topological phase diagram of $ZrTe_5$ using the complex strain fields of microbubbles,* npj Computational Materials **8,** 177 (2022)

[4] G. Z. Magda, et al.: *Exfoliation of large-area transition metal chalcogenide single layers,* Sci. Rep. **5,** 14714 (2015)

[5] J. Shim, et al.: *Controlled crack propagation for atomic precision handling of wafer-scale two-dimensional materials,* Science **362,** 665–670 (2018)

GRAPHENE-ENCAPSULATED SILVER NANOPARTICLES FOR PLASMONIC VAPOUR SENSING

OTKA K134258, MTA János Bolyai Research Scholarships

G. Piszter, Gy. Molnár, A. Pálinkás, Z. Osváth

Noble metal nanoparticles (NPs) are widely used for chemical and biological sensing because of their Local Surface Plasmon Resonance (LSPR) and surface-enhanced Raman scattering properties. The LSPR produces sharp spectral absorption, which can be used to detect changes in the molecular environment near the surfaces of NPs by spectral shift detection. In this work, we fabricated Ag NPs and graphene–silver nanoparticle hybrids directly on Highly Oriented Pyrolytic Graphite (HOPG) substrates as follows. Ag films of 7 nm thickness were evaporated onto HOPG and then covered with Chemical Vapour Deposition (CVD)-grown graphene. The transfer process yielded a graphene coverage of 40-50%. To form nanoparticles, both bare and graphene-covered Ag thin films were annealed at 400 °C under an inert gas atmosphere for 1.5 h. The obtained samples (samples #1 and #2) were characterized by tapping-mode Atomic Force Microscopy (AFM), as well as Scanning Electron Microscopy (SEM), see Fig. 1.

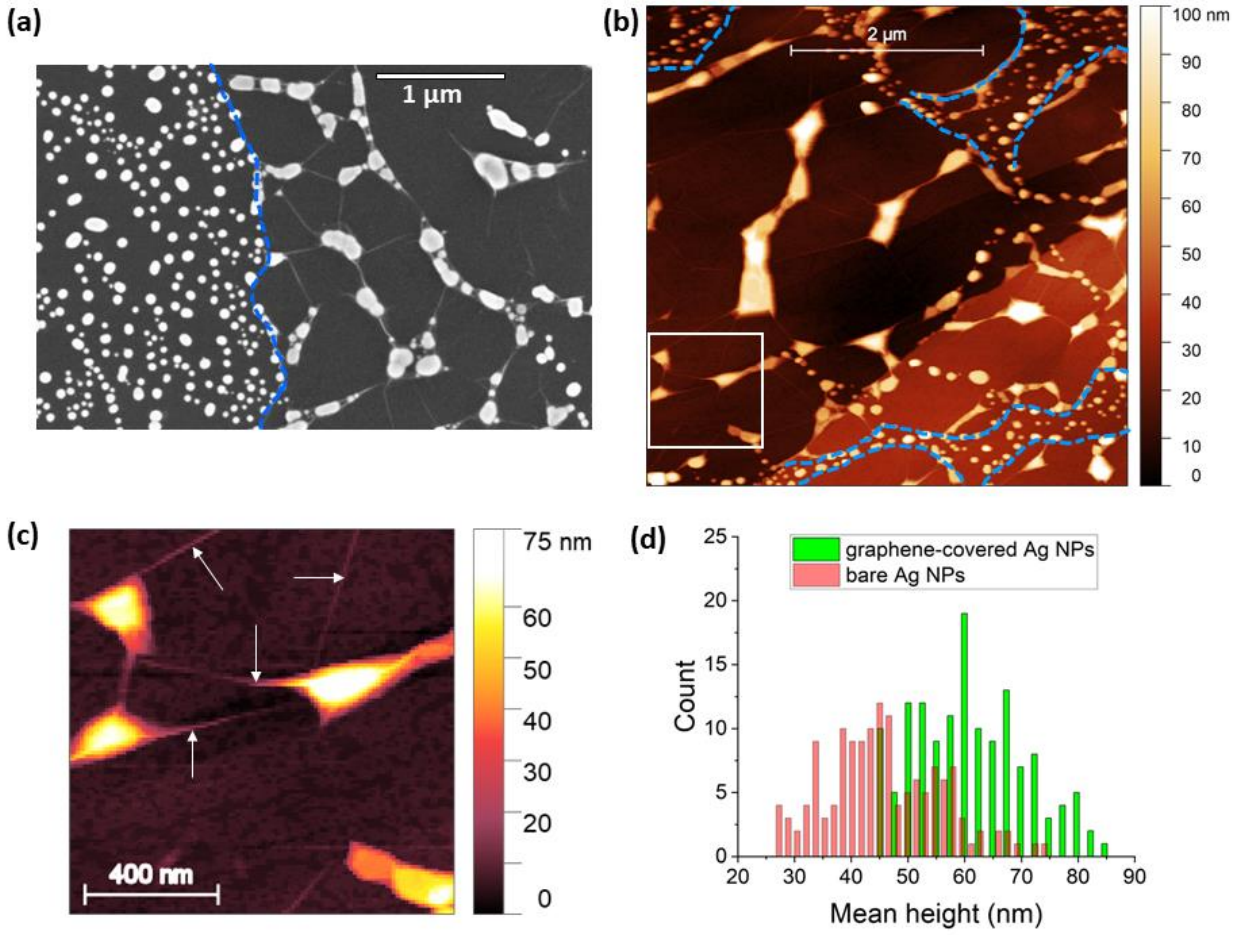

*Figure 1: **(a)** SEM image of bare Ag NPs (left) and Ag NPs covered with graphene (right). The edge of graphene is marked with a blue dashed line as a guide for the eye. **(b)** AFM image of graphene-encapsulated Ag NPs. Discontinuities in the graphene overlayer and areas with bare Ag NPs are demarcated with blue dashed lines. Several graphene-covered nanoparticles are demarcated with a white square and shown in the enlarged image in **(c)**. Here, wrinkling of the graphene overlayer is observed (arrows). **(d)** The mean height distribution of graphene-covered (green) and bare Ag NPs (red) was measured on 142 NPs in both cases.*

We investigated the effect of point defects on the sensing properties of graphene-covered Ag NPs. Therefore, we introduced defects in sample #2 by exposing it to O_2 plasma for 5 seconds. Such plasma treatment induced individual, point-like defects (vacancies) in the graphene overlayer, located several nanometres apart from each other. UV-Visible reflectance spectroscopy was used to measure the shift of the LSPR upon exposure to acetone, ethanol, 2-propanol, toluene, and water vapours. Since the LSPR shifts are rather small changes compared to the LSPR intensity, it is more convenient to use the *reflectance change* spectra (Fig. 2) defined as $\Delta R = (R/R_0)\times 100\% R_0$.

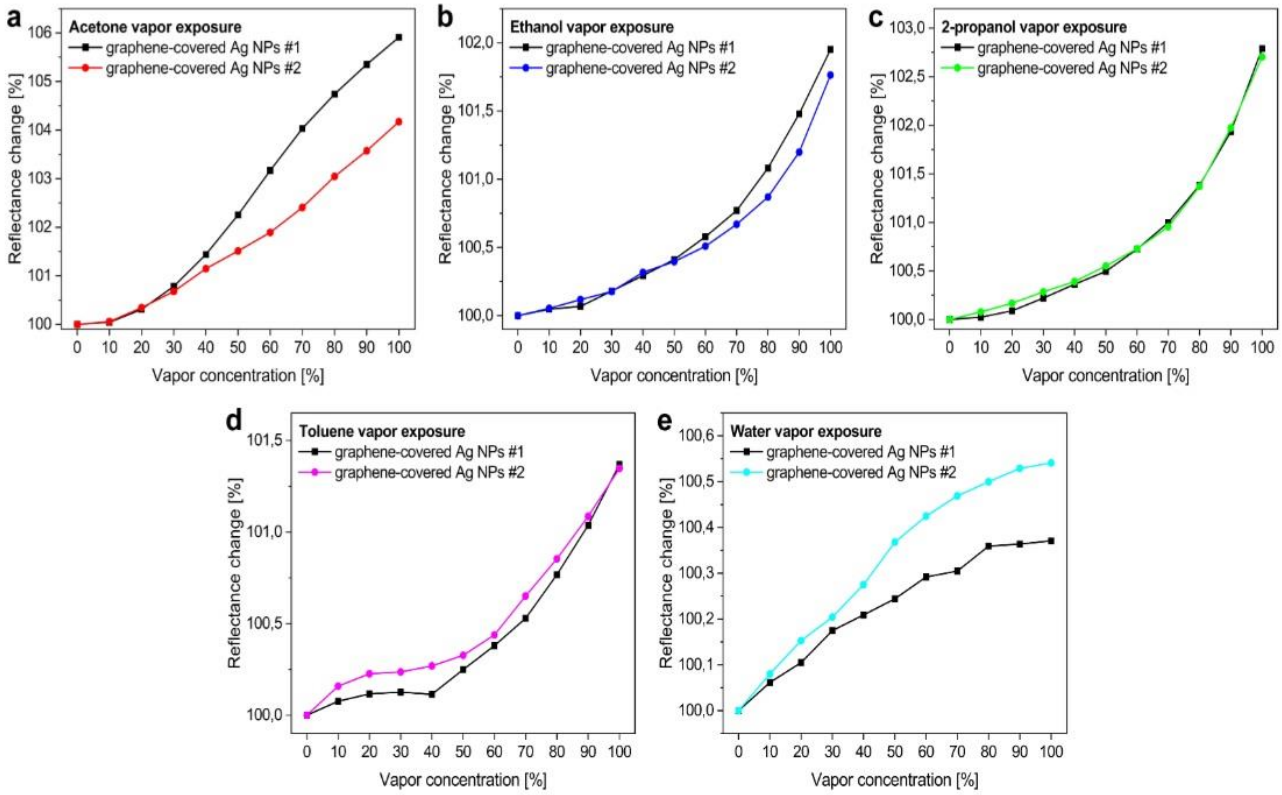

Figure 2: Maximal peak intensities in the reflectance change spectra as a function of vapour concentration. For each applied vapour, the optical responses of samples #1 and #2 are compared. (a) acetone, (b) ethanol, (c) 2-propanol, (d) toluene, and (e) water vapours were applied.

We showed that the prepared hybrid nanostructures displayed pronounced optical responses upon exposure to organic vapours. The observed concentration-dependent shifts in the LSPR were substance-specific, as demonstrated in Figure 2. One can observe that there are differences in the maximal responses of the two samples, especially for acetone, water, and toluene. The defected graphene overlayer (sample #2) increases the sensitivity to water and toluene. This agrees with recent calculations showing that toluene and water molecules adsorb better to graphene with defects. In comparison, exposure to ethanol and 2-propanol results in similar optical responses, while acetone even gives a reduced signal on defected graphene. These findings can be useful in tuning the selectivity in sensing volatile organic compounds.

Related publication

[1] G. Pisztler, G. Molnár, A. Pálinkás, Z. Osváth: *Graphene-Encapsulated Silver Nanoparticles for Plasmonic Vapor Sensing,* Nanomaterials ***12*(14),** 2473 (2022) https://doi.org/10.3390/nano12142473

SPECTRAL ENGINEERING OF HYBRID BIOTEMPLATED PHOTONIC/PHOTOCATALYTIC NANOARCHITECTURES

G. Piszter, K. Kertész, D. Kovács, D. Zámbó, Zs. Baji, L. Illés, G. Nagy, J. S. Pap, Zs. Bálint, and L. P. Biró

Heterogenous photocatalysis is a light driven process that enables transformation of the abundant and environmentally safe sunlight into much needed chemical processes to achieve, for example, water purification. For this purpose, supported catalysts are needed, which can be used in a continuous-flow regime. To enhance the efficiency of the purification process, the properties of the used catalysts have to be tuneable in a way to fit the characteristics of the pollutant to be removed. For this type of application, the photocatalyst has to be cheap and, in order to allow avoidance of the use of UV transparent materials with prohibitive prices, preferably, able to operate with visible light.

Due to their nanostructure, butterfly wings offer a support with a large specific surface that can be produced in a cheap and environmentally safe way, onto which different nanoparticles (NP) can be immobilized and eventually coated by a few nanometres of semiconductor material to enhance their photocatalytic effect. An additional benefit may arise from the photonic-crystal-type (PhC) structures in the butterfly wings.

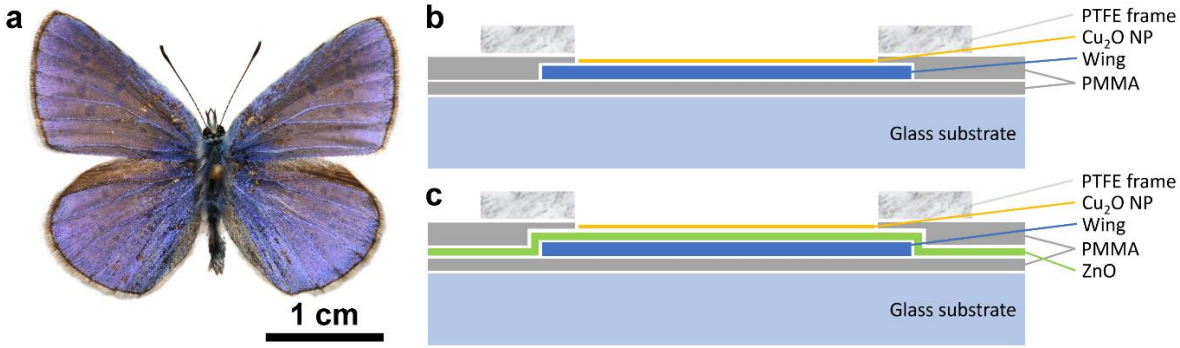

*Figure 1: Common blue butterfly and typical sample structures used. (**a**) Dorsal wing surfaces of a male specimen; (**b**) Type-1 sample structure without 15 nm ZnO layer on the butterfly wing before the Cu_2O deposition; (c) Type-2 sample structure with 15 nm ZnO layer deposited by ALD on the butterfly wing before the Cu_2O deposition.*

Here, photonic nanoarchitectures of biological origin with hierarchical organization from nanometres to centimetres were applied as biotemplates. The blue wing surface of laboratory reared male Common Blue (*Polyommatus icarus*) butterflies were used in combination with Atomic Layer Deposition (ALD) of conformal ZnO coating and deposited octahedral Cu_2O NPs to explore the possibilities of engineering the optical and photocatalytic properties of hybrid photonic nanoarchitectures (Fig. 1).

Type-1 and type-2 samples were prepared similarly, the only difference was the additional base layer of 15 nm ZnO under the Cu_2O NPs: the wings were glued to glass substrates, were pretreated in ethanol overnight, then the different amounts of Cu_2O sols were added carefully to the dry samples. Half of the samples were coated with an additional 5 nm ZnO cover layer to immobilize the Cu_2O NPs.

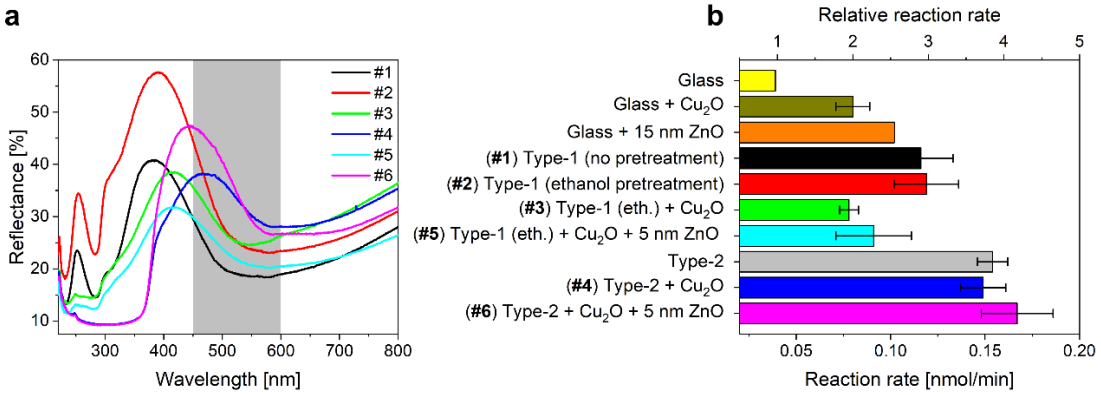

*Figure 2: (**a**) Reflectance spectra of the wing samples used in the photocatalytic experiments in as prepared state: (**1**) type-1 sample, without ethanol pretreatment; (**2**) type-1 sample with ethanol pretreatment; (**3**) type-1 sample with 120 µl of Cu_2O sol drop dried; (**4**) type-2 sample with 120 µl of Cu_2O sol drop dried; (**5**) type-1 sample with 120 µl of Cu_2O sol drop dried followed by the deposition of 5 nm of ZnO; (**6**) type-2 sample with 120 µl of Cu_2O sol drop dried followed by the deposition of 5 nm of ZnO. The grey-shaded area marks the rhodamine B absorption band. (**b**) Absolute and relative reaction rates of the samples used to characterize the photocatalytic efficiency of the biotemplated photonic/photocatalytic nanoarchitectures.*

The samples were characterized by UV-visible reflectance spectroscopy, and their photocatalytic performance was benchmarked by comparing the initial decomposition rates of rhodamine B (Fig. 2) under visible light illumination. The relative reaction rates may be helpful in comparing the individual effects of the various components of the more complex biotemplated photonic nanoarchitectures that proved to have the best efficiency in the photodegradation of the dye. The reaction rate on bare glass was taken as unity.

Cu_2O NPs alone or on the butterfly wings, covered by 5 nm thick layer of ZnO, showed poor performance. Butterfly wings, or ZnO coated butterfly wings with 15 nm ALD layer showed a 3 to 3.5 times enhancement as compared to bare glass. The best performance of almost 4.3 times increase was obtained for the conformally coated wings by 15 nm ZnO, deposited with Cu_2O NPs followed by conformal coating with an additional 5 nm of ZnO by ALD. The above results demonstrate that properly chosen photonic nanoarchitectures of biologic origin—from the large "library" of such structures—in combination with well-chosen photocatalyst(s) can significantly enhance the efficiency of complex, hybrid biotemplated photonic/photocatalytic surfaces. Taken together, our findings suggest that the reason for the enhanced efficiency is complex; both the fast carrier separation at Cu_2O–ZnO p-n heterojunctions and the slow light effect of the photonic nanoarchitecture are contributors.

EFFECT OF PLASMONIC AU AND AG/AU NANOPARTICLES AND SODIUM CITRATE ON THE OPTICAL PROPERTIES OF CHITIN-BASED PHOTONIC NANOARCHITECTURES IN BUTTERFLY WING SCALES

K. Kertész, G. Piszter, Z. E. Horváth, D. Zámbó, A. Deák, and L. P. Biró

Photocatalysis on non-toxic, stable metallic nanoparticles (NPs) such as Au or Ag/Au alloys, which offer the possibility to tune the wavelength range where photoexcitation is occurring, is ideal to be used for clean and safe technology. To be able to exploit this advantage, the metallic NPs must be supported on a substrate, which will provide a large specific surface area, possibly by micro- and nanostructuring, and can be produced in a cheap and environmentally friendly way. Photonic-crystal-type (PhC) structures, in particular inverse opal type nanoarchitectures, are used to host various catalytic NPs. These hybrid nanoarchitectures (PhC + NP) exhibit a lot of potential for harnessing solar radiation for catalytic purposes. PhC-type nanoarchitectures of biologic origin can be found on the wings of butterflies exhibiting structural coloration. Using this cheap substrate, the simplest way of producing nanocomposites of metallic NPs in PhC nanoarchitectures in butterfly wing scales is the application of colloidal sols of metallic NPs on the flat butterfly wing. In this process, the effect of three major sol components has to be taken into account: the effect of water, the metallic Au and alloyed Ag/Au NPs, and the sodium citrate used for the formation/stabilization of the NPs. Here, the impact of these three components on the optical properties of the natural photonic nanoarchitectures is discussed.

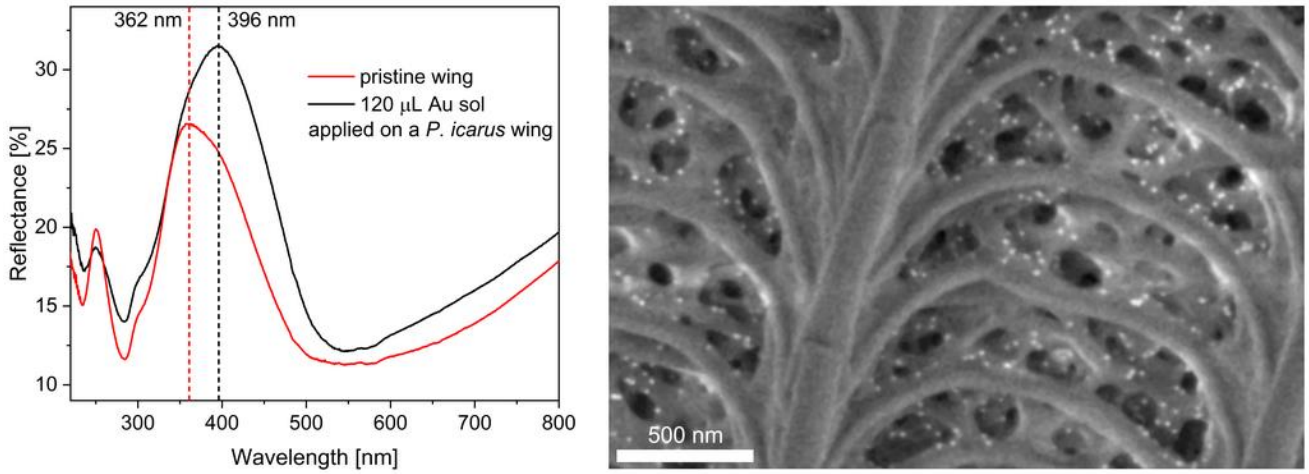

*Figure 1: **(a)** Integrating sphere reflectance measurements of the Polyommatus icarus wing in pristine state before the application of the sol and after the application of 120 µL of Au sol and complete drying; **(b)** Scanning electron micrograph of a scale of the Polyommatus icarus wing after the application of 120 µL of Au NP sol and complete drying. One may note the presence of bright dots in the image, which represent the Au NPs.*

The butterfly wing scales, with the NPs, integrated into the photonic nanoarchitecture, as seen in Fig. 1.b, behave like a complex nanocomposite, which inherits its properties from both components. As the composite is made up dominantly of the chitin-based biologic photonic nanoarchitecture, its properties are primarily determined by photonic nanoarchitectures of the butterfly wing scales. See pristine and shifted reflectance in Fig. 1.a.

For a detailed analysis, a total of 40 samples were prepared and subjected to different treatments. One may observe that Polylactic Acid (PLA) gluing produced a slight blueshift in the spectral position of the reflectance maximum, but on average, the amplitude of the reflectance maximum in normal incidence did not change significantly (Fig. 2.b). The subsequent water immersion for 8 h, followed by overnight drying, did not produce modifications of the spectral position and the amplitude of the reflectance maximum. The drop-drying of sodium citrate solution returned the spectral position of the reflectance maximum to that of the pristine state (redshift) but produced a significant increase in the amplitude of the normal incidence reflectance. The removal of the dried citrate by immersing the samples for 8 h in water and measuring them after overnight drying in air eliminated the redshift in the spectral position but preserved the increased amplitude of the reflectance.

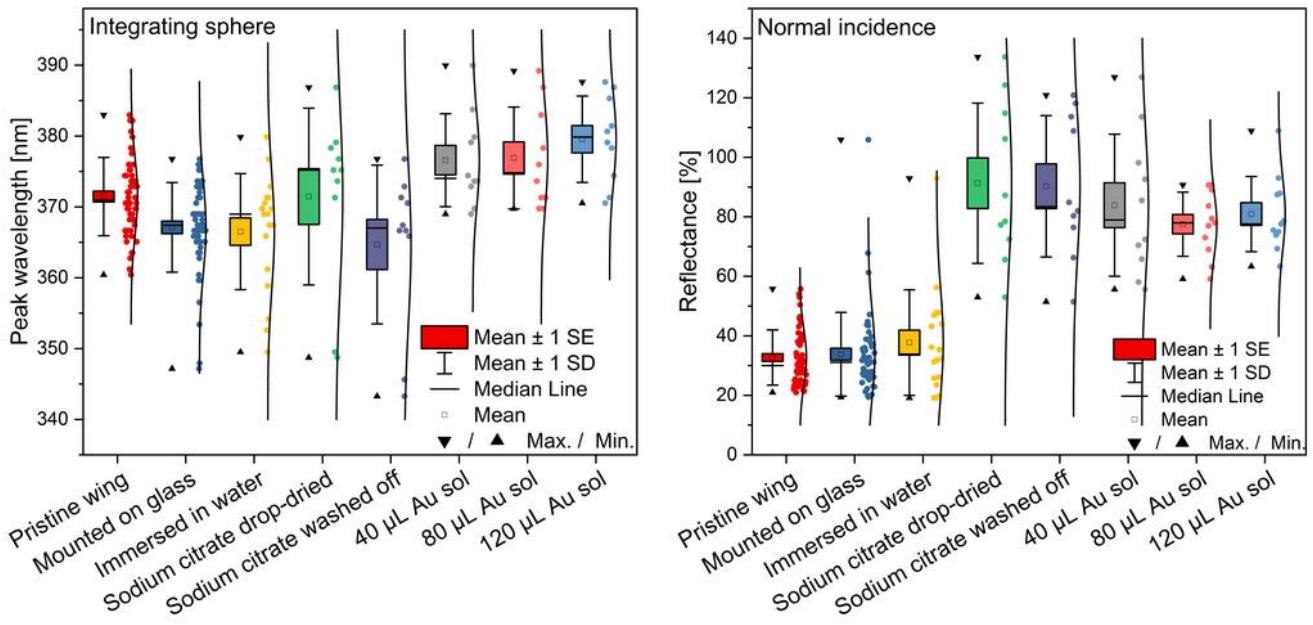

*Figure 2: Statistical presentation of the changes in optical properties of male Polyommatus Icarus wings mounted on glass substrate by PLA. **(a)** Integrating sphere measurement of the spectral position of the blue reflectance maximum after the different treatments of the wings; **(b)** normal incidence measurement of the amplitude of the blue reflectance maximum after the different treatments of the wings.*

When Au NP sol in sodium citrate solution was applied on the water-immersed and dried butterfly wings, the observed effects presented the characteristics of the citrate solution application, but an additional redshift was produced, and the increase in the amplitude of the normal incidence reflectance maximum was slightly smaller.

In addition, we used ethanol to facilitate the penetration of deionized water inside the photonic nanoarchitecture, the major effect measured after drying is the increase of normal incidence reflectance caused by the flattening of the wing scales towards the wing membrane which is a persistent effect.

CONTACT ANGLE DETERMINATION BY THE CAPILLARY BRIDGE PROBE METHOD: FROM PERFECT WETTING TO HYDROPHOBIC SURFACES

OTKA FK 128901

N. Nagy

The developed indirect Capillary Bridge Probe method combines the accuracy of the Wilhelmy method and the general usability of the sessile drop method without their limitations. The method is based on the use of a liquid bridge as a probe: the capillary bridge of the test liquid is stretched between the base of a cylinder and the investigated surface under equilibrium conditions. The advancing contact angle on the sample can be measured during the stepwise or slow (quasi-static) decrease of the bridge length. The receding contact angle is determined during the retraction of the cylinder (Fig. 1).

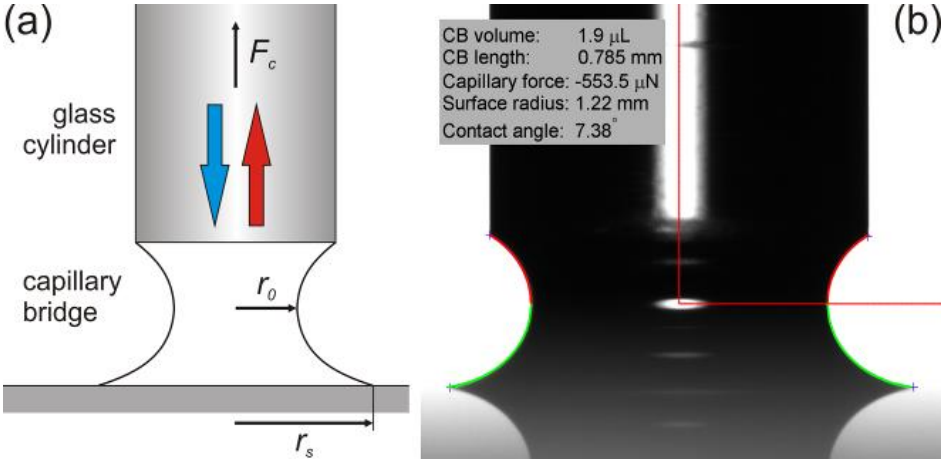

Figure 1: a) Schematics of a capillary bridge (Fc: capillary force; r_0: neck radius; r_s: contact line radius on the sample surface). b) Captured and evaluated image of a water capillary bridge on a glass surface. The diameter of the glass cylinder is 2 mm. The blue crosses designate the corners of the bridge's silhouette, the red and green curves show calculated profile.

The contact angle is calculated from Delaunay's analytical solution, while the three necessary parameters are the measured capillary force (F_c), the radius of neck or haunch (r_0), and the radius of the contact line (r_s) on the investigated surface. The latter two parameters are obtained from the automated analysis of the captured image of the liquid bridge. The radius of the upper contact line (r_c) is constant since it pins on the rim of the cylinder.

A typical measured graph and determined contact angles are plotted in Fig. 2. The measurement was carried out on a clean stoichiometric Si_3N_4 surface. The attractive (negative) capillary force decreases with the decreasing bridge length, and it shows hysteresis (Fig. 2.a). This hysteresis results in the contact angle hysteresis in Fig. 2.b. The advancing contact angle is stable, while the receding values show decreasing character (similarly to the results of evaporating drop measurements).

As a demonstration of a unique property of the method, perfect wetting situations were also characterized. The graphs shown in Fig. 3 were measured on a super hydrophilic acid-treated glass surface. The capillary force and the contact angle do not exhibit hysteretic character. However, a novel phenomenon can be observed in Fig. 3.b. The contact line starts to advance again during the retraction and the corresponding (readvancing) contact angles are much lower than the advancing and receding values. In this phase, the readvancing contact line finds prewetted surface, this is the reason of the low determined values. [1]

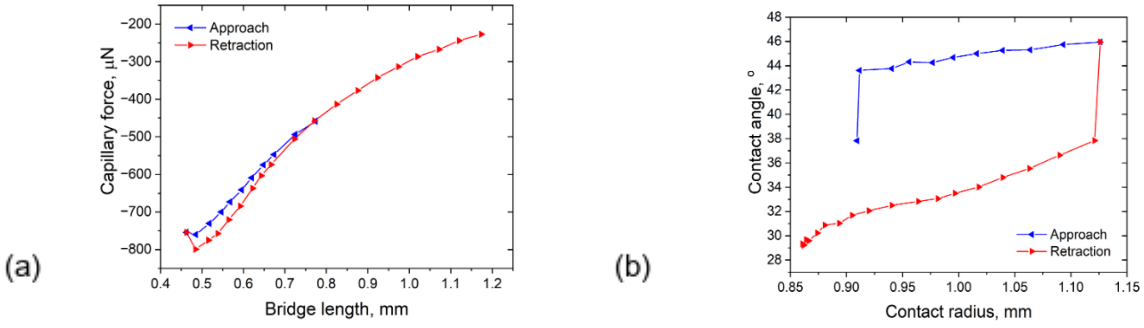

Figure 2: (a) Capillary force as a function of bridge length measured on a hydrophilic Si_3N_4 surface. (b) Determined contact angles as a function of the contact radius. The force hysteresis results in contact angle hysteresis.

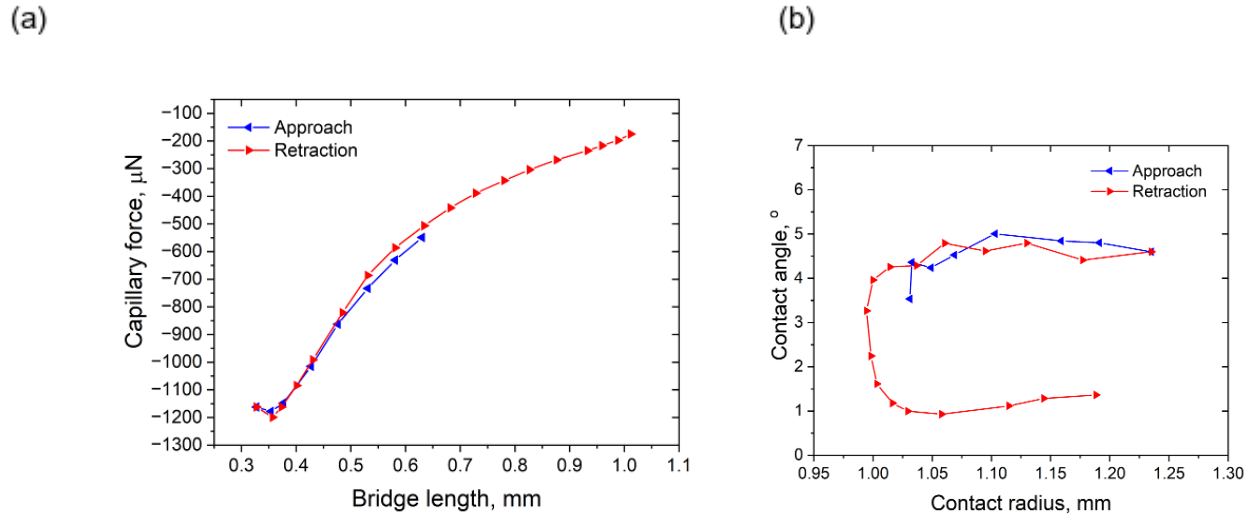

Figure 3: (a) Capillary force as a function of bridge length measured on an acid-treated superhydrophilic glass surface. (b) Contact angles vs. the contact radius. The contact line starts to advance again during the retraction and the readvancing contact angles are much lower.

Hydrophobic surfaces can be characterized with high sensitivity, as it was demonstrated on Polytetrafluoroethylene (PTFE) surfaces. The graphs in Fig. 4 show hysteresis of capillary force and contact angle, as well. Sessile drop measurements did not show any contact angle hysteresis. [2]

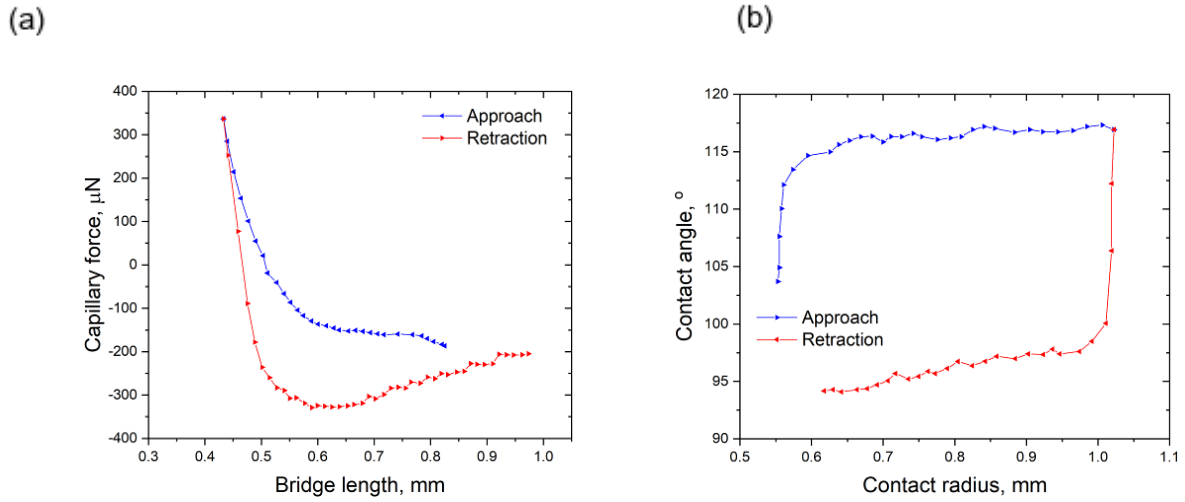

Figure 4: (a) Capillary force vs. bridge length measured on a hydrophobic PTFE surface. The capillary force changes its sign during the approach and retraction. (b) Contact angles as a function of the contact radius.

Related publications

[1] N. Nagy: *Contact Angle Determination on Hydrophilic and Superhydrophilic Surfaces by Using r–θ-Type Capillary Bridges,* Langmuir **35:(15),** 5202-5212 (2019)

[2] N. Nagy: *Capillary Bridges on Hydrophobic Surfaces: Analytical Contact Angle Determination,* Langmuir **38:(19),** 6201-6208 (2022)

MAPPING AND MODELLING OF THE OPTICAL PROPERTIES OF THIN FILMS DEVELOPED ON FERRITE GRAINS BY COLOUR ETCHING

TKP2021-EGA-04, OTKA K 131515, EMPIR POLight

J. B. Renkó, A. Romanenko, P. J. Szabó, A. Sulyok, P. Petrik, A. Bonyár

Etching methods in metallography are used to develop the grain structure at the surface. The etchant reacts with the material at the surface to change its topography, making individual grains visible. Colour etchants are less common than chemical etchants, mainly because the saline solutions used in colour etching are less aggressive. The layer grows in both directions relative to the original plane of the sample. As the film grows, each grain undergoes a cyclic colour change. Although these colour etching methods are widely used, the chemical processes involved are not or only partially explored. In this investigation we have mapped the individual grains using focused-beam ellipsometry, and compared the results with complementary methods (Fig. 1). We have shown that the refractive index varies depending on the crystallographic orientation of the grains in the same way as the etching speed. The refractive index is inhomogeneous in depth with larger values at the interface between the layer and the substrate. This finding correlates well with compositional depth profile revealed by X-ray photoelectron spectroscopy. This work was a significant contribution to relate the colours to the crystallographic orientations of the individual grains. [1]

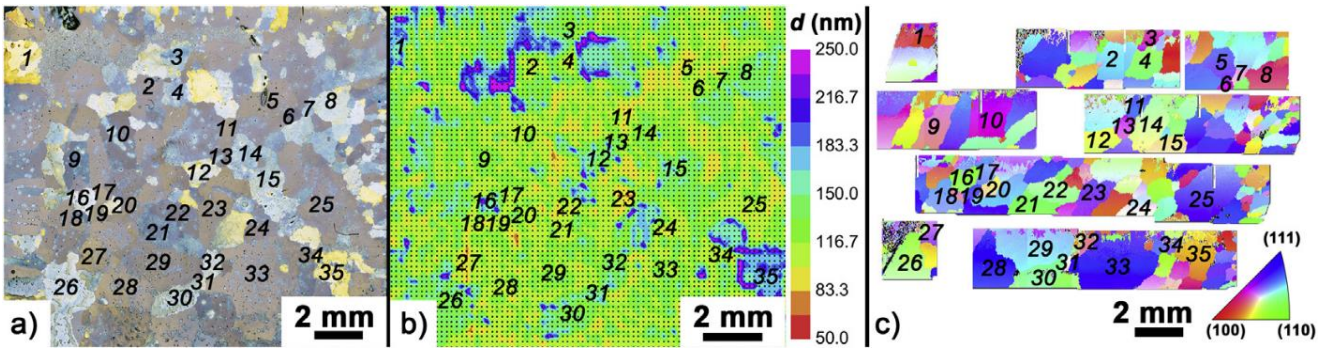

Figure 1: a) Optical microscope image of the colour etched ferritic steel specimen (60 s in Beraha-I). The numbers represent labels of the grains for further investigation. b) The layer thickness map determined by spectroscopic ellipsometry (using a Cauchy dispersion). c) The inverse pole figures of the same area from Electron Backscatter Diffraction (EBSD).

Related publication

[1] J.B. Renkó, A. Romanenko, P.J. Szabó, A. Sulyok, P. Petrik, A. Bonyár: *Analysis of structural and chemical inhomogeneity of thin films developed on ferrite grains by colour etching with Beraha-I type etchant with spectroscopic ellipsometry and XPS,* Journal of Materials Research and Technology **18,** 2822–2830 (2022) https://doi.org/10.1016/j.jmrt.2022.03.159

HIGH-SENSITIVITY ELLIPSOMETRY FOR IN-SITU CHARACTERIZATION OF INTERFACE PHENOMENA

TKP2021-EGA-04, OTKA K 131515, EMPIR POLight

P. Petrik

Taking advantage of the high sensitivity and the nondestructive nature of spectroscopic ellipsometry, interface processes were investigated in highly relevant research topics. It has been shown that the hot electrons created by plasmon excitation in gold (Fig. 1.a) occupy the top few nanometres of the layer, and they have a different dispersion than the thermalized electrons of the bulk layer [1].

Hydrocarbon adsorption on the surface of highly oriented pyrolytic graphite was measured by spectroscopic ellipsometry on time scales of more than two months (Fig. 1.b) and a few hours (not shown here, see [2]). It was shown that monolayer adsorption can be followed by this technique, as verified and analyzed by tapping mode methods.

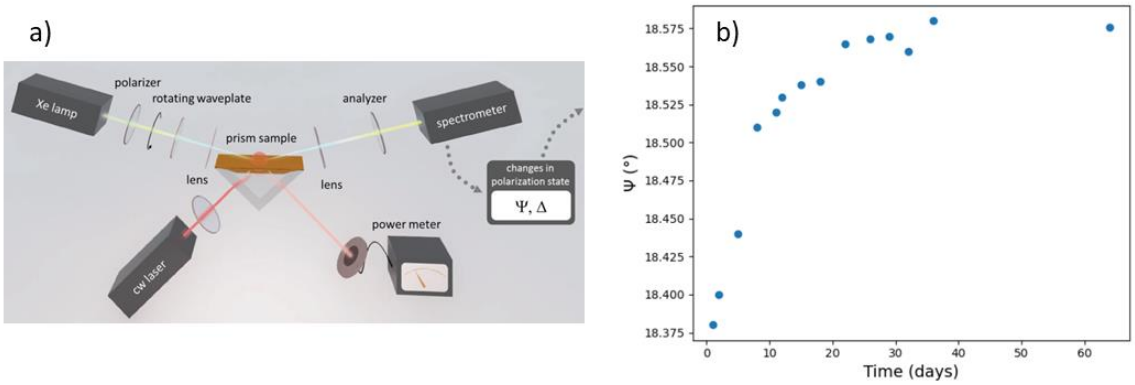

Figure 1: a) Experimental setup to measure hot electrons during plasmon excitation in a thin gold layer. The plasmons are generated by a laser illumination the layer from the substrate side, whereas the ellipsometry measurement it performed at the gold/air interface during the excitation. b) Ellipsometry measurement during hydrocarbon adsorption on highly oriented pyrolytic graphite. ($\Psi=\tan^{-1}(|r_p/r_s|)$, where r_p and r_s denote the complex reflection coefficients of light polarized parallel and perpendicular to the plane of incidence, respectively.

Related publications

[1] J. Budai, Z. Pápa, P. Petrik, P. Dombi: *Ultrasensitive probing of plasmonic hot electron occupancies,* Nat Commun. **13,** 6695 (2022) https://doi.org/10.1038/s41467-022-34554-5

[2] A. Pálinkás, G. Kálvin, P. Vancsó, K. Kandrai, M. Szendrő, G. Németh, M. Németh, Á. Pekker, J.S. Pap, P. Petrik, K. Kamarás, L. Tapasztó, P. Nemes-Incze: *The composition and structure of the ubiquitous hydrocarbon contamination on van der Waals materials*, Nat Commun. **13,** 6770 (2022) https://doi.org/10.1038/s41467-022-34641-7

ELLIPSOMETRY MONITORING OF SENSOR PROCESSES BASED ON GOLD NANOPARTICLE BONDED PROTEINS

OTKA K 131515 and OTKA NNE131269

Z. Labadi, C. Bakos, M. Szucs, A. Bonyar, D. Mukherjee, H. Jankovics, F. Vonderviszt and P. Petrik

Monitoring and reducing pollution is one of the most important challenges. To achieve this goal, techniques that allow accurate and easy measurement of pollutants are essential. Unfortunately, in the case of heavy metal pollutants, there are currently no inexpensive, field-applicable methods available that let us easily and accurately determine the concentration of ions that pose a health risk.

In this work we examine selective heavy metal sensor structures based on specific modified proteins deposited onto conductive surface and the sensing process itself is based on electrochemistry. Our previous results [1,2] show the feasibility of the modified protein-based sensor structures for ppm range monitoring of Ni and As contaminations in natural waters. Combining SEM, and voltammetry data with in-situ Spectroscopic Ellipsometry (SE) measurements provides deeper understanding of the sensing processes.

The first step of the process is the preparation of proteins with genetic modification that introduces selective nickel or arsenic binding domains. For this purpose, bacterial flagellar filaments were used. These are natural protein nanotubes, which are formed by self-assembly from thousands of flagellin subunits. Their variable middle portion that forms the D3 domain exposed on the surface of the filaments and was engineered to create a metal-binding site. This work was done at University of Pannonia, and details are given in [1].

SE is a sensitive non-destructive method to monitor interfaces. Three consecutive steps of the building of the sensor structure are monitored by SE: (1) the deposition of gold nanoparticles onto a gold substrate, (2) the binding of modified proteins on gold nanoparticles and (3) selective binding of Ni or As contaminant on the modified proteins. These processes are monitored by independent physical and chemical characterization methods (SEM, AFM, cyclic voltammetry) as well while SE gives independent in situ monitoring data. The main advantage of SE is its sub-nanometre thickness sensitivity together with spectroscopic data in the 190-1700 nm range (i.e., 0.7-6.5 eV photon energy), plus second-range time resolution.

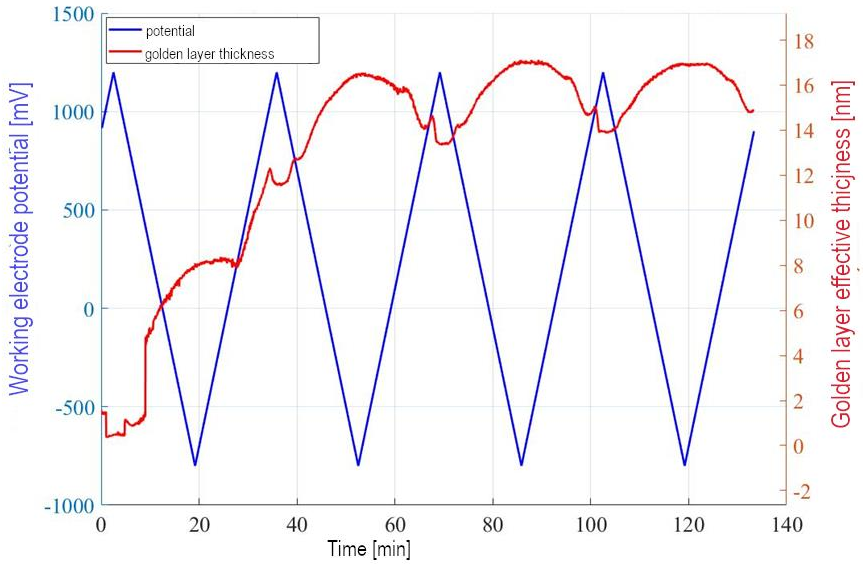

Figure 1: Equivalent layer thickness of Au nanoparticles determined by SE as a function of time (red curve). Blue graph represents the applied potential as a function of time.

Deposition of gold nanoparticles took place from 0.2mmol/l $HAuCl_4$ solution in 10mM/L HEPES (4-(2-hidroxietil)-1-piperazin-ethaensulphonic acid) pH=7.0 buffer while the substrate electrode went through potential cycles between -0,6 and 1,2V versus saturated calomel electrode. Simultaneous SE spectra were measured throughout the cycles. Evaluation of SE spectra was made using a three-layer optical model (vacuum evaporated gold, followed by a surface roughness layer and a nanoparticle layer, both characterized as mixture of water and gold using the Sellmeier model). Fig. 1 shows the measured Au nanoparticle layer thicknesses. Golden nanoparticle deposition takes place in cycles synchronous with the potential change and the deposition takes place in the 0 – 1V potential range. Fig. 2 shows the SEM micrographs of the surface after 10 cycle deposition. Full coverage with an approx. 100nm surface roughness is observable. This surface was used to immobilize the protein filaments.

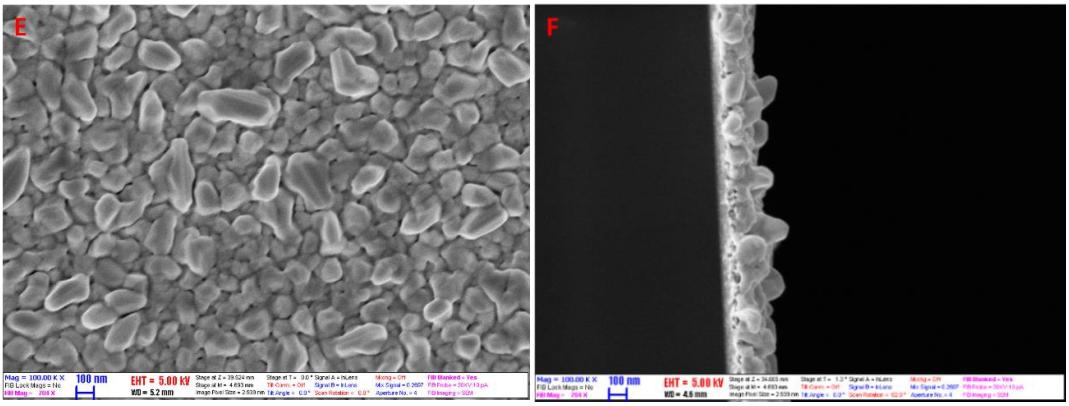

Figure 2: SEM micrographs of golden nanoparticles deposited onto evaporated gold in 10 cycles and cross-sectional view of sample

Protein immobilization was carried out from 1mM/L protein solution in 10mM/L HEPES pH=7.0 buffer applying potential cycles between -0.6 – 0.7V. Fig. 3 shows the protein filament coverage on the surface after 10 cycles. It has to be noted that the protein coverage remained relatively low, and preferably should be increased by the cycle number and/or the protein concentration.

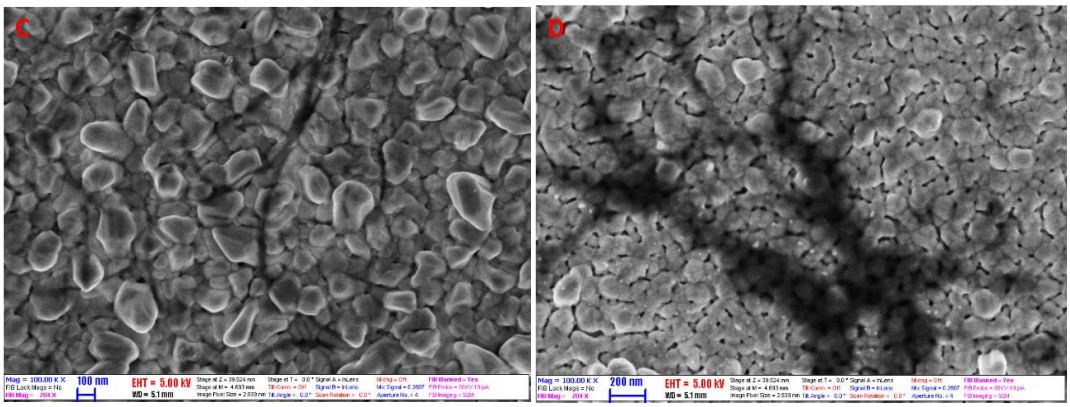

Figure 3: Protein filament coverage on the surface after 10 cycles

The protein immobilization was also followed by SE using a three-layer model (gold nanoparticle layer, rough surface layer and a protein/solvent layer characterized by different Au, water and protein contents respectively. Fig 4 shows the amount of accumulated protein at the surface as a function of time (cycles). The protein irreversibly accumulates in the middle layer (rough gold) and its amount increases with time.

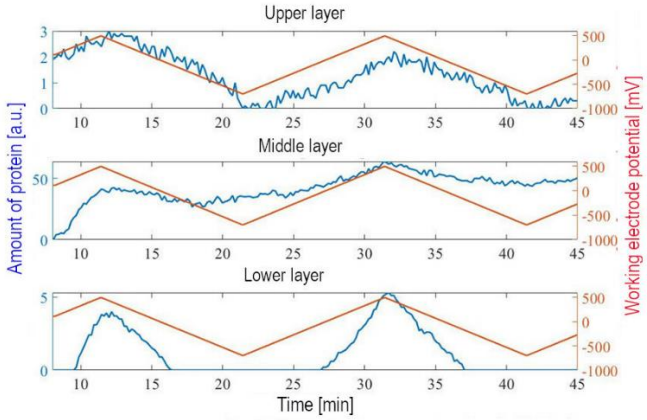

Figure 4: Protein content calculated from three-layer ellipsometry model (blue curves). Red curves represent the potential cycles.

The sensor surfaces prepared with immobilized protein were characterized for Ni ion interaction. 150mM HEPES solution was contaminated with increasing concentration of Ni ions and cyclic voltammograms were measured on them using our electrode covered with filaments. Fig. 5 shows the voltammograms taken at increasing amount of Ni. As it can be seen in Fig. 5, a redox process is observable in the presence of Ni.

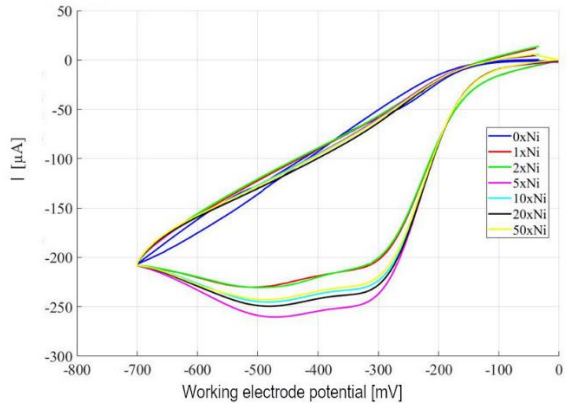

Figure 5: Cyclic voltammograms of filament covered golden surfaces in the presence of Ni contamination. Ni concentrations are expressed in the multiples of 1µmol/L concentration (i.e. at the United States Environmental Protection Agency (EPA) health limit for tap water)

Figure 6 shows the integral of the peaks as a function of the Ni concentration (curve belonging to Ni free sample was chosen as baseline). The integral values show only slight increasing tendency with increasing Ni, which can be explained by the low partial coverage of the surface and the saturation of Ni binding points.

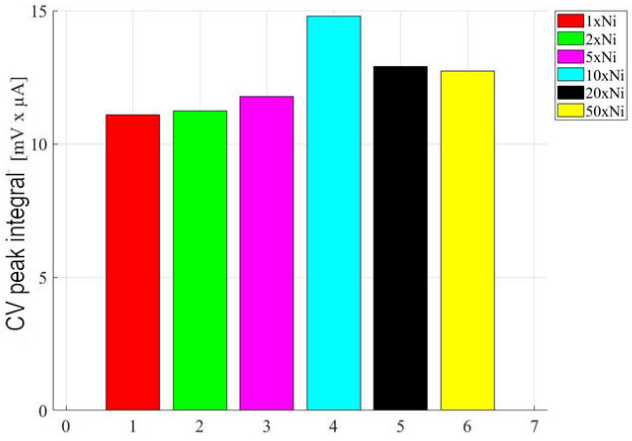

Figure 6: Integral of the curves measured on Ni contaminated samples as a function of the Ni concentration.

Protein flagellar filaments were successfully immobilized on golden nanoparticle covered electrode surface. The golden nanoparticle formation and the protein binding was successfully monitored by in situ Spectroscopic Ellipsometry. Genetically engineered bacterial flagellar filaments were successfully tested as sensor layers for measuring Ni concentration in aqueous solution at 1µmol concentration.

Related publications

[1] Z. Labadi: *Sensing Layer for Ni Detection in Water Created by Immobilization of Bioengineered Flagellar Nanotubes on Gold Surfaces,* Acs Biomaterials-Science & Engineering **6,7,** 3811-3820 (2020)

[2] H. Jankovics: *Flagellin-based electrochemical sensing layer for arsenic detection in water,* Scientific Reports **11(1),** 3497 (2021)

SURFACE SODIFICATION AND SELF-ASSEMBLY OF GOLD NANOPRISMS

OTKA FK FK128327

A. Deák

Controlled surface modification of nanoparticles could enable the preparation of nanoscale objects that feature different surface-regions on the same particle, covered by different types of molecules. Such "multifunctional" particles have application potential especially in the fields of biomedicine and sensorics. In our recent work we investigated the controlled surface modification of gold nanoprisms with the aim to cover the tip/edge and face regions of the particles with different types of molecules. [1]

The prisms were prepared *via* a seed-mediated wet chemical synthesis route, surface modification was achieved using thiolated molecules, as thiols show high affinity towards gold surfaces. The original Cetyltrimethylammonium chloride (CTAC) capping ligand layer is partially replaced by cysteamine or Mercaptolhexadecil cetyltrimethylammonium bromide (MTAB) when their respective concentration is kept low. By monitoring the time-evolution of the dipolar plasmon resonance mode of the gold nanoprisms, concentration levels could be identified where the thiols preferentially bind to the edges/tips of the prisms. In a second step the remaining surface of the prisms was covered by a thiolated Polyethylene Glycol (PEG) moiety. Whereas the tip/edge replacement of the original CTAC capping layer by the thiols induced a significant blueshift of the dipolar plasmon resonance as a result of decreasing effective refractive index in the optical near-field, PEG injected into the same system results only in a minor redshift. This indicates the successful preparation of binary, thiol/PEG surface modified nanoprisms.

The self-assembly behaviour of the prisms was also tested, using Mercaptoundecanoic acid (MUA) surface modified nanospheres. MUA renders the nanospheres negatively charged, while both cysteamine and MTAB provide a positive surface charge. As PEG is a neutral polymer, it is expected that the oppositely charged nanoparticles will heteroaggregate as dictated by the electric double layer interaction between them. When performing such a heteroaggregatation experiment, no plasmon coupling related clear indication of the heteroaggregation is found, but SEM images reveal that spheres preferentially accumulate at the sides of the prisms.

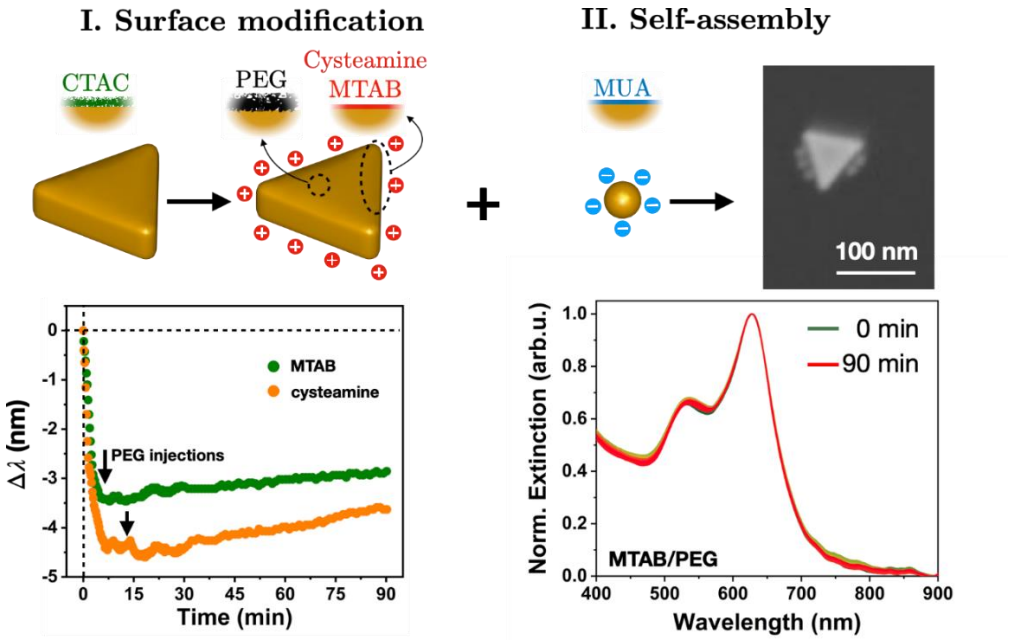

Figure 1: Sketch of the binary surface modified gold nanoprisms and the blueshift of the dipolar plasmon resonance mode upon sequentially adding the thiol and the thiolated PEG (left). Self-assembly of the MTAB/PEG binary surface modified nanoprisms with MUA coated nanospheres - only minor spectral changes are observed, but spheres accumulate at the prism edges (right)

Related publication

[1] D. Zámbó, D. Kovács, G. Südi, A. Deák: *Surface Modification of Gold Nanoprisms and their Self-assembly with Nanospheres,* Part & Part Syst Charact, 2200197 (2022)

MAKYOH IMAGING AND TOPOGRAPHY

F. Riesz

Makyoh imaging, named after the Japanese 'magic mirror', denotes an optical imaging mechanism, where a plane (or more generally, spherical) wave is reflected from a nearly flat mirror, causing intensity variations in a far-field screen image because of the local deflections. The intensity distribution reflects the mirror height map. The first application of this principle was probably the Oriental magic mirror; a modern application is Makyoh topography, used mostly for the visualization of surface defects or texture of semiconductor wafers. In the ancient magic mirror, but often also in semiconductor technology, the flatness deviations of the mirror surface are caused by mechanical pattern transfer of the back relief of the mirror plate (or wafer—see Fig. 1.a). We have modelled the role of this pattern transfer in Makyoh imaging [1]. Following the earlier studies, the convolution by a Gaussian was used for modelling the process mechanically; it was also shown that front-face deformations of semiconductor wafers induced by localized backside contamination particles during polishing can also be well approximated by the Gaussian curve, thus making the analysis more transparent (Fig. 1.b). Because of the convolution, the front face topography will have specific properties, which are reflected also in the Makyoh image. The Makyoh image formation was modelled by a full theory incorporating the effects of surface gradients on the intensity and Gaussian curvature, unlike previous approaches which used the linear approximation (Laplacian contrast). The main global features, inferred from our model, are the following: (1) the amplitude parameter of the Gaussian has a linear scaling effect on the front-face topography, this is equivalent to the scaling of the screen distance; (2) the convolution has a symmetrizing effect on the shapes as well as decreases the astigmatism of the reflected beams, this effect is characterized by the width of the Gaussian; (3) the nonlinearity of the imaging is reduced and (4) a minimum (local) focal distance (caustic limit) is imposed.

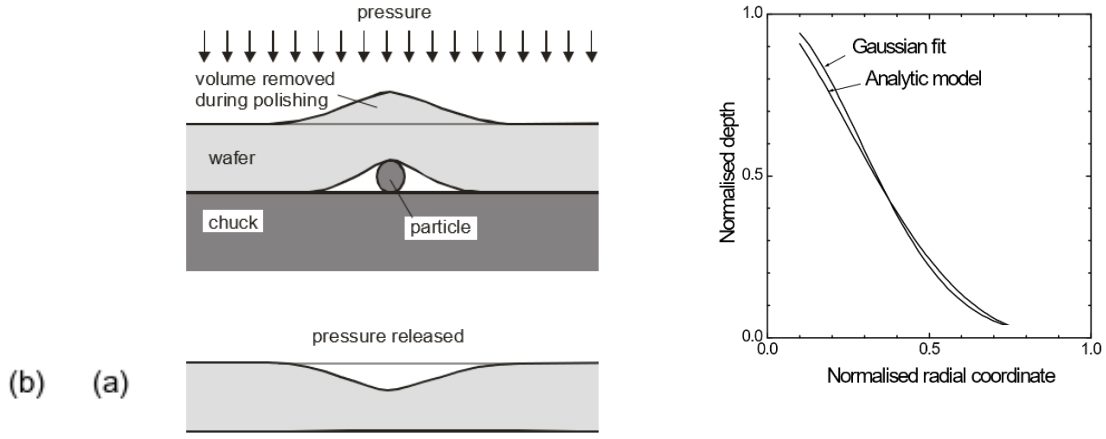

Figure 1: a) Scheme of the formation of a front-face depression induced by a contaminant particle in a semiconductor wafer during polishing. b) Deformation profile of the depression: analytic plate-theory modelling and the Gaussian fit.

In the linear case (valid if the screen distance is much larger than the front surface's local curvature radii) the whole optomechanical process is equivalent to the convolution by a LoG (Laplace of Gaussian) function; this is a standard edge-detection method in image processing. Another result of the past year is the proposal of a novel approach for the imaging of the ancient mirror: the *visual image* of the back relief pattern, rather than its topography is compared to the Makyoh image. The visual image depends on the environmental illumination conditions and surface reflection properties, but it can be stated the both images are essentially emphasise edges (gradient changes) of the back relief, thus their correspondence can be established, especially if the Makyoh imaging is in the nonlinear region (that is, the bright areas are strongly focused and their width is reduced).

Related publication

[1] F. Riesz: *Modelling of the backside pattern transfer in magic mirror (Makyoh) imaging,* Journal of Optics, **25(2),** 025602 (2023)

STRUCTURAL INVESTIGATION OF WIDE BANDGAP SEMICONDUCTORS PREPARED BY SPUTTERING

TKP2021-NKTA-05

M. Gajdics, B. Pécz

Recently wide bandgap (Eg > 4 eV) semiconductors, such as AlN and Ga_2O_3 have received considerable interest. These materials have a wide range of potential applications, i.e. electronic devices, such as diodes and transistors, optoelectronic devices, such as UV photodiodes and photodetectors, and gas detection systems. The aim of this research is the structural investigation of sputter deposited AlN and Ga_2O_3 thin films.

Gallium oxide films were deposited on sapphire substrates by radio frequency sputtering at room temperature (Fig. 1). The applied pressure was $p = 2 \cdot 10^{-2}$ mbar and the DC potential was 1400 V. Sputtering was carried out using Ar, Ar^+O_2 and Ar^+H_2 gas mixtures, the gas flow for O_2 and H_2 was 1 sccm. The AlN films were prepared by HiPIMS (High-Power Impulse Magnetron Sputtering) using an average power of 200 W, frequency of 1 kHz and pulse width of 100 µs. The N_2 concentration was varied during deposition to create a microcombinatoric film with changing composition. The structure of the films was studied by X-ray diffraction and transmission electron microscopy. The composition and refractive index was determined by energy dispersive spectroscopy and spectroscopic ellipsometry, respectively. The as-deposited Ga_2O_3 films were found to have an amorphous structure and a slightly sub stoichiometric composition ($Ga_2O_{2.9}$ for Ar and Ar^+H_2, $Ga_2O_{2.95}$ for Ar^+O_2). In order to have a crystalline material, the samples were annealed at 900 ^{0}C for 1 hour in air, using 5 ^{0}C/min heating rate. As a result of the heat treatment, X-ray diffraction peaks of the crystalline β-Ga_2O_3 phase appeared on the diffractograms (Fig. 1.a). The reflections can be indexed as (-201) and its multiples, which indicates that the film has preferential texture.

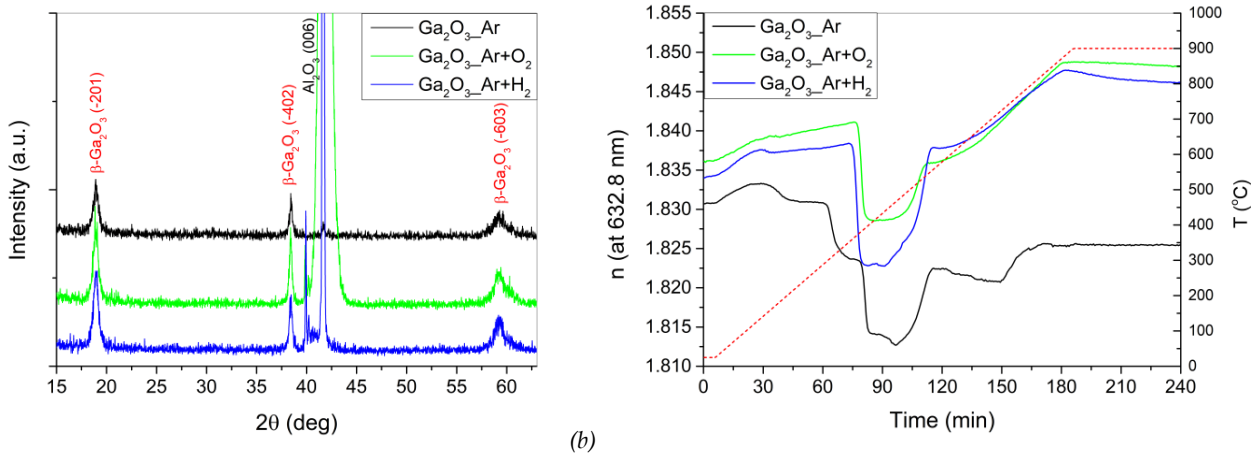

Figure 1: (a) X-ray diffraction patterns of the annealed Ga_2O_3 films showing peaks of β Ga_2O_3. (b) Variation of the refractive indices (at 632.8 nm) during annealing determined by in-situ ellipsometry measurement

The applied gas mixture apparently does not influence the crystallization of the material. After the annealing in air, the films show the Ga_2O_3 stoichiometry. Variation of the refractive index was observed during the heat treatment (Fig. 1.b), which may be indicative to phase transformations. Temperature dependence of the refractive index is similar to all the studied samples, i.e. changes occur in the same temperature ranges. Composition of the gas mixture only has a minor effect on the value of the refractive index. To further study the phase transitions additional annealing experiments and X-ray measurements are currently underway. EDS measurements of AlN thin films prepared using different N_2 flow rates show that samples with excess nitrogen cannot be manufactured under these conditions.

Nevertheless, sub-stoichiometric films can be prepared and the N concentration has a significant effect on the structure of the sample. The stoichiometric film is made up of crystalline AlN phase, with the decrease of the N concentration the fraction of the crystalline phase decreases, and at some point a completely amorphous film forms. With further decrease of N concentration, crystalline Al appears in the sample (Fig. 2).

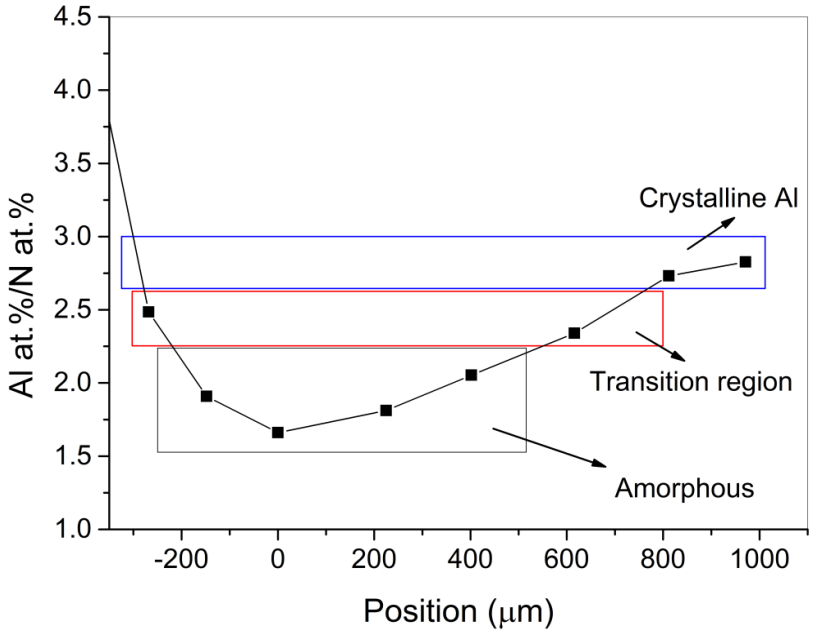

Figure 2: Al/N atomic ratio as a function of position on a microcombinatoric AlN film. Different composition results in different crystal structures, the rectangles show the different composition regions with different structure.

ROLE OF TEM IN THE DEVELOPMENT OF QUBITS. SIQUOS: SUPERCONDUCTING SILICON QUBIT IN CMOS TECHNOLOGY

2019-2.1.7-ERA-NET-2022-00032

J. L. Lábár, B. Pécz, F. Chiodi (2C2N-Paris Saclay), F. Nemouchi (CEA-Grenoble), Z. Zhang (Uppsala University), S. Zhang (Uppsala University), F. Lefloch (CEA-Grenoble)

Qubits are the basic units of quantum computing and communication. Physical implementation of a qubit needs a system with *two energy levels* that can be manipulated separately. One of the several implementations is based on usage of superconductors. A superconducting qubit is an *artificial atom*, where the energy levels are assessed by the quantized resonance frequencies of an LC resonator. The qubit consists of a capacitively shunted inductor, where the inductance is provided by a *superconducting weak link (*Josephson junction: JJ, controlled by microwave signal). In an *anharmonic* oscillator the energy level spacings are different, so we can manipulate the *first two, independently* from the others. One variant of the superconducting qubits is a *Gatemon*, where energy levels are controlled by electrostatic potential of gate. Anharmonicity is introduced by the JJ.

The aim of SIQUOS is to realise and study a Si gatemon qubit, a gate tuneable transmon qubit composed of a Si Josephson Field-Effect Transistor (JoFET) coupled to a microwave resonator. It represents a valid integrable and scalable alternative to fully metallic superconducting qubits.

SIQUOS focuses on the Si JoFET, i.e., a Si transistor with superconducting source and drain (S&D) contacts, whose non-dissipative supercurrent can be modulated by an electrostatic gate. CMOS-compatible metal silicides as well as heavily boron (B) doped Si will be used as the superconducting S&D contacts. A comprehensive investigation of the superconductor/Si (S/Sm) interface by means of structural, chemical and low-temperature electronic transport characterisation is being performed. The first and foremost objective of SIQUOS is to optimise the S/Sm interface transparency so as to allow for the transfer of correlated charge carriers from the superconducting contacts into the Si channel and to reach large, reproducible supercurrents. The second objective is to realise Si JoFETs, demonstrating the gate tuneability of the Josephson supercurrent. Thereupon, the third and final objective is to integrate Si JoFETs in a transmon geometry including on-chip capacitors and resonators, and to realise the manipulation of quantum states in Si-gatemon devices.

The heart of a CMOS Si gatemon is a JoFET that has superconducting source and drain (Fig. 1). The superconductor can be a metal-silicide (PtSi in the figure) or a highly boron-doped Si.

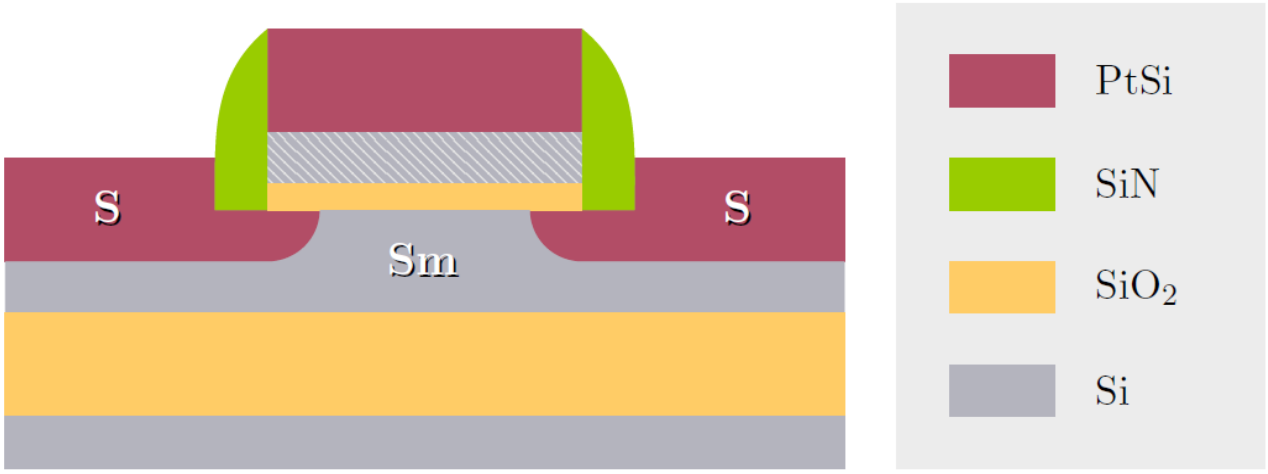

Figure 1: A Josephson field effect transistor (JoFET) that has superconducting source and drain

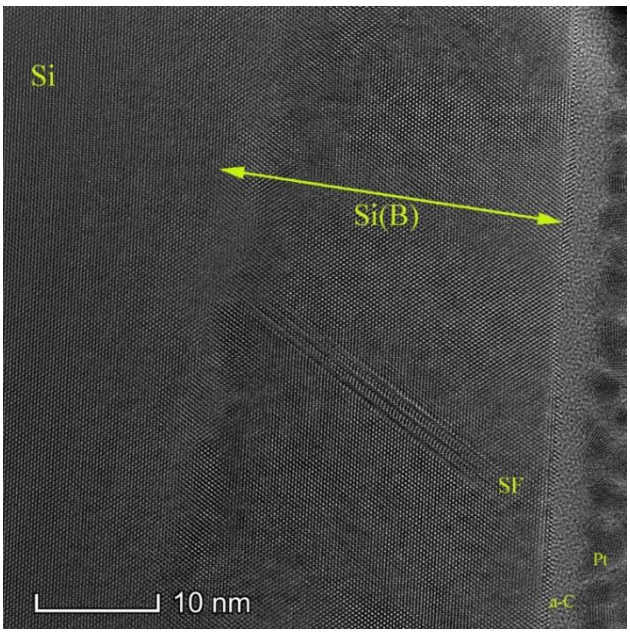

Figure 2: HRTEM image of a supersaturated, Boron doped Silicon (Si:B) layer

Quality depends on exact sizes, on crystallographic phases and their orientation and on the crystallographic quality of the interface at the *atomic level*. Here comes *electron microscopy (TEM) for characterization*. Si(B) needs a boron concentration above the equilibrium level. It is reached by a special technique: gas immersion laser doping. There is a *need to check* the depth of doping, the flatness of the interface and the concentration of B in Si. Cross section samples were prepared by FIB for HRTEM. Concentration of substitutionally positioned B was determined from the strain measured from HRTEM images (Fig. 2).

A new method was also developed for the measurement of strain from 4D-ED. The first tests seem to be useful for determining connection between strained state (measured at room temperature) and superconductivity (measured at a few tens of mK temperature). Publication of the results is expected in 2023.

This work was supported by the QUANTERA project SIQUOS and by National Research, Development and Innovation Office under the contract 2019-2.1.7-ERA-NET-2022-00032. The QuantERA II Program has received funding from the European Union's Horizon 2020 research and innovation program under Grant Agreement No 101017733. Microscope facility provided by VEKOP-2.3.3-15-2016-00002 project of the European Structural and Investment Funds was used for this study.

COMBINATORIAL MAPPING OF MICROSTRUCTURE AND MORPHOLOGY IN CU-MN FILMS

K. Hajagos Nagy, F. Misják, Gy. Radnóczi

The scaling down of advanced semiconductor devices is a serious challenge for industrial technologies. Size reduction amplifies the effects of various diffusion related problems (e.g. electromigration) and some previously well-functioning solutions (e.g. TaN diffusion barriers) cannot be integrated in the new technologies. In interconnect design the use of self-organized processes has emerged as a solution, which involves the formation of a diffusion barrier from the interconnect material i.e. an alloyed Cu layer at the Cu/dielectric interface as a result of annealing or chemical reaction. The Cu-Mn alloy is a promising candidate for a number of diffusion barrier applications needed for Cu interconnects [1].

Mapping the Cu-Mn thin film system may help in the search for optimal technological parameters. Previously, we found three one-phase regions in the system at room temperature: fcc Cu(Mn) solid solution, amorphous Cu-Mn alloy and α-Mn(Cu) solid solution. Between these intervals two phase regions exist, where an amorphous grain boundary layer covers the solid solution grains [2]. For the successful application of Cu-Mn films the changes of microstructure and morphology within the phase regions has to be known in more detail. This can be effectively investigated using combinatorial samples, where one of the growth parameters changes continuously as a function of distance on the sample.

50 nm thick Cu-Mn combinatorial films were grown by DC magnetron sputtering on amorphous carbon foils using Sáfrán's micro-combinatorial method [3]. The composition changed linearly between 0-100 at% Mn. The microstructure of the films was investigated in a Philips CM-20 transmission electron microscope by light and dark field imaging and selected area electron diffraction. The composition was verified by Energy Dispersive X-ray Spectroscopy (EDS) measurement. Diffraction patterns were evaluated using the Process Diffraction program.

Combinatorial samples offer an effective way of investigating the effect of composition on microstructure and morphology. Fig. 1 shows the characteristic microstructure and morphology of the five phase regions in lateral bright field images and Selected Area Electron Diffraction (SAED) patterns. The grain size of the fcc Cu(Mn) solid solution is bimodal, it decreases from 10-50 nm to 5-10 nm in the 0-35 at% Mn content interval. The α-Mn(Cu) solid solution has a more uniform grain size, it decreases from 10-20 nm to 5-10 nm from pure Mn to 70 at% Mn content. Calibrating the diffraction patterns by an internal standard (MnO) allowed us to determine the correlation between the composition and lattice parameter of the α-Mn(Cu) solid solution. The lattice parameter increases linearly with Cu content: $a_{\alpha-Mn(Cu)} = a_{Mn} + c_{Cu} \cdot 1{,}046$ (in Å), where $a_{Mn} = 8{,}912$ Å and c_{Cu} is the Cu concentration in at%. In the amorphous region, two types of short-range order are likely: fcc Cu(Mn) based below 50 at% Mn content and α-Mn(Cu) based over 50 at% Mn content.

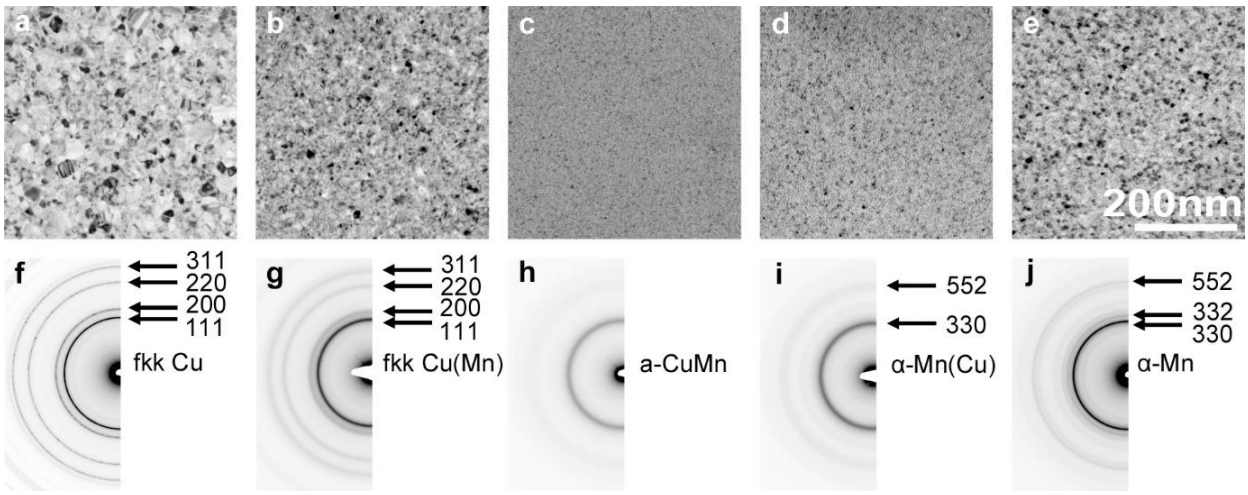

Figure 1: Morphology and microstructure of Cu-Mn films in each phase interval in lateral bright field images (a-e) and SAED patterns (f-j). Pure Cu film (a,f), Cu-based two-phase film (30 at% Mn) (b,g), amorphous film (50 at% Mn) (c,h), Mn-based two-phase film (80 at%Mn) (d,i) and pure Mn film (e,j).

Related publications

[1] J. Gambino: *Process Technology for Copper Interconnects Handbook of Thin Film Deposition,* (Fourth Edition) Elsevier Inc. 147-194 (2018)

[2] F. Misják, K.H. Nagy, P. Lobotka, and G. Radnóczi: *J. Electron scattering mechanisms in Cu-Mn films for interconnect applications,* Appl. Phys. **116,** (2014)

[3] G. Sáfrán: "*One-sample concept*" *micro-combinatory for high throughput TEM of binary films*, Ultramicroscopy **187,** 50 (2018)

BACTERICIDAL AND VIRUCIDAL PROPERTIES OF ZRN-CU NANOSTRUCTURED COATINGS DEPOSITED BY AN INDUSTRIAL PVD SYSTEM

Zs. Czigány, K. Balázsi, S. Behrangi (Masaryk University), I. Sedláček (Masaryk University), J. Štěrba (University of South Bohemia), G. Suková (Masaryk University), V. Buršíková (Masaryk University), P. Souček (Masaryk University), V. Sochora (SHM, s.r.o.) and P. Vašina (Masaryk University)

Pathogenic microbes such as bacteria and viruses spread through contaminated surfaces. Most of these microorganisms are viable for a long time, so they spread from surfaces to the living organism and cause disease. ZrN-Cu nanocomposites with different Cu content were produced in a Physical Vapour Deposition (PVD) device and their ability to kill bacteria and viruses (SARS-CoV-2) was investigated as a function of Cu content and exposure time. The layers were grown in an industrial equipment (SHM s.r.o. Šumperk, Czech Republic) using a hybrid process, combining electric arc evaporation (Zr) and magnetron sputtering (Cu) in a reactive medium. The Zr target is made of Zr702 alloy (99.2 wt% Zr; 4.5 wt% Hf; 0.8 wt% Fe, Cr, O, C).

The cylindrical copper target (99.95 wt%) was 96 mm in diameter and 445 mm long. We varied the power of the magnetron between 0.5 kW and 3 kW to control the Cu content. Additional growth parameters: N_2 pressure 1.5 Pa, substrate bias 50 V, heating current 150 A, substrate temperature 400°C, layer growth time 60 min. Below 6 at% copper content, only fcc ZrN phase is present, which suggests that copper is incorporated into the ZrN structure on the Zr sites. At higher copper content, however, copper forms a separate crystalline phase, which can be observed both in electron diffraction patterns and elemental maps (Fig. 1). Hardness and elastic constant decreased with increasing copper content. The copper content also affected the antibacterial properties. The antibacterial effect was excellent against Escherichia coli and Pseudomonas aeruginosa, especially in the case of 12 at%Cu content and treatment longer than 40 minutes. However, the antiviral effect of the coatings was not significant.

In conclusion, hard and wear-resistant ZrNCu coatings may be suitable for the development of antibacterial coatings that prevent the spread of pathogens on surfaces that people often touch. The optimal Cu content can be set between 12 and 25 at%, taking into account the trade-off between antibacterial effect and mechanical properties [1].

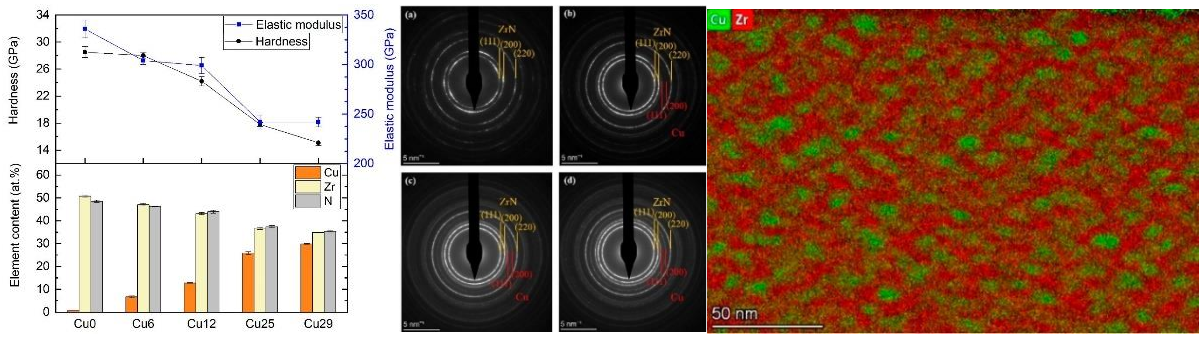

Figure 1: Left panel: composition and mechanical properties of ZrN-Cu nanocomposites. Middle panel: SAED patterns of (a) Cu6; (b) Cu12; (c) Cu25; and (d) Cu29 samples. Right panel: Combined Zr and Cu elemental maps of ZrN-Cu29 film.

Related publication

[1] S. Behrangi, I. Sedláček, J. Štěrba, G. Suková, Zs. Czigány, V. Buršíková, P. Souček, V. Sochora, K. Balázsi, P. Vašina: *Assessment of bactericidal and virucidal properties of some ZrN-Cu nanostructured coatings deposited by an industrial PVD system,* Coatings **12,** 1330 (2022)

SYNTHESIS AND CHARACTERIZATION OF THE CERAMIC REFRACTORY METAL HIGH ENTROPY NITRIDE THIN FILMS FROM CR-HF-MO-TA-W SYSTEM

Zs. Czigány, K. Balázsi, T. Stasiak (Masaryk University), P. Souček (Masaryk University), V. Buršíková (Masaryk University), N. Koutná (TU Wien), P. Vašina (Masaryk University)

High Entropy Alloys (HEA) and their nitrides were produced by reactive sputtering using Cr, segmented Mo-W and Hf-Ta targets. The purpose of the study is to determine the effect of the production parameters on the microstructure and mechanical properties of these innovative, multi-component layers. The layers were grown in pure and N_2-containing Ar gas at room temperature and at 750°C. The combined concentration of the metallic elements was stabilized with a saturation value below 50% as a function of the nitrogen injection, with a high nitrogen injection. In the case of the layers grown in argon, a single-phase body-centred cubic (bcc; a0 = 3.174 Å) structure was created (Fig. 1).

An amorphous structure was obtained at a low nitrogen injection, while a NaCl-type face centred cubic nitride phase (fcc; a0 = 4.186–4.268 Å) was formed at a high N_2 injection (Fig. 1). The lattice parameter of the fcc nitride phase increases with increasing nitrogen flow, in agreement with the values predicted by ab-initio calculations. The experimental lattice parameters of the RT samples lie between the values calculated for the composition $(CrHfMoTaW)N_{0.75}$ and $(CrHfMoTaW)N_{0.5}$, where the former composition is energetically more advantageous.

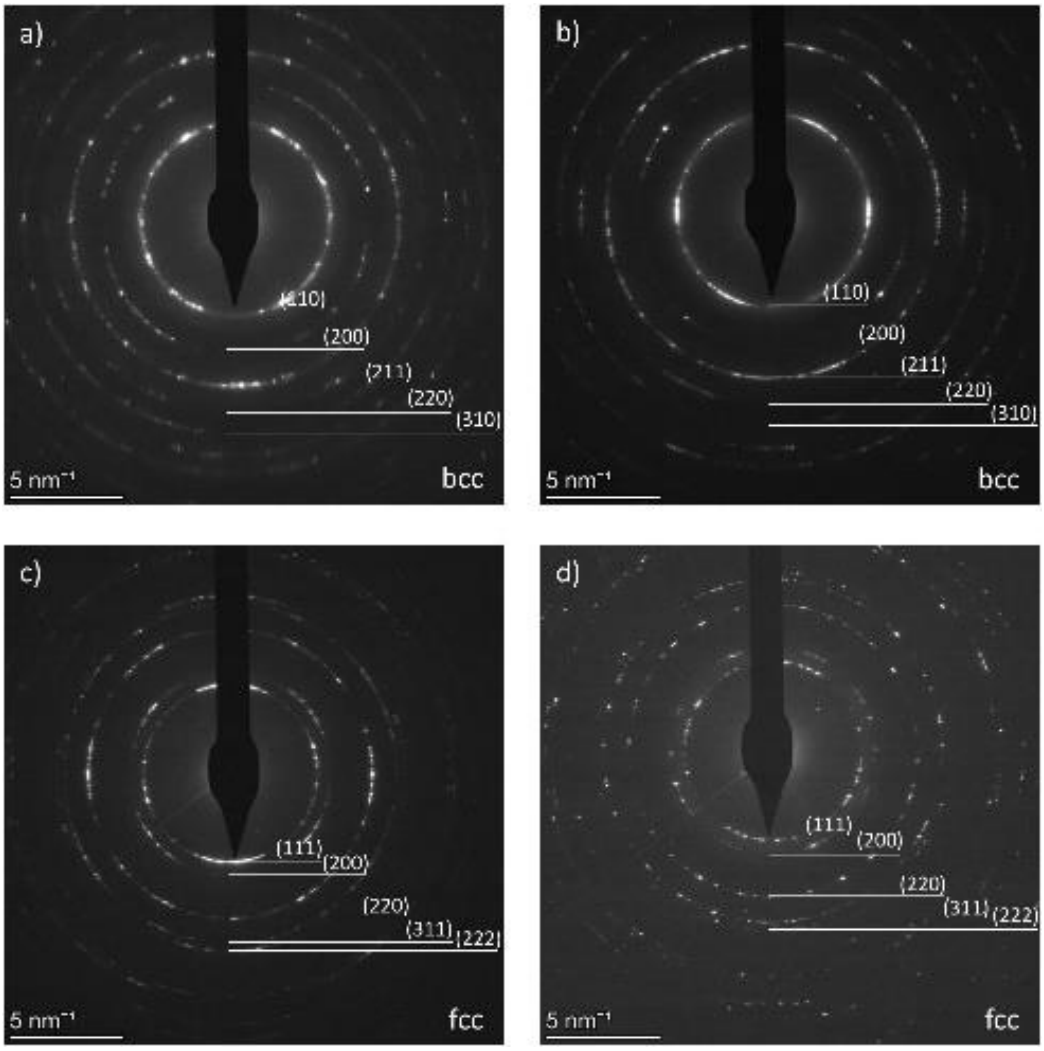

Figure 1: SAED patterns of coating: (a) RT without nitrogen flow, (b) HT without nitrogen flow, (c) RT under 20 sccm nitrogen flow, (d) HT under 20 sccm nitrogen flow.

The cross-sectional morphology of the amorphous sample was homogeneous, while the samples with the majority fcc nitride phase showed a characteristic columnar morphology (Fig. 2). In addition, the elemental maps show a multilayered structure (due to rotation of the sample holder) and that the columns are separated by amorphous walls that are poor in molybdenum and nitrogen. The values of hardness and Young's modulus were 20.3 GPa and 471 GPa, respectively, for the fcc nitride coating. The experimental values of the Young's modulus showed a good agreement with the values of the Young's modulus in the [100] direction obtained by ab-initio calculations. The results of our research showed that coatings consisting of bcc and fcc phases with favourable mechanical properties (e.g. high Young's modulus) can be produced by magnetron sputtering.

Furthermore, the results contribute to the understanding of the effect of nitrogen flow on microstructural characteristics (such as crystallite size, vacancy formation, and lattice parameter change) [1].

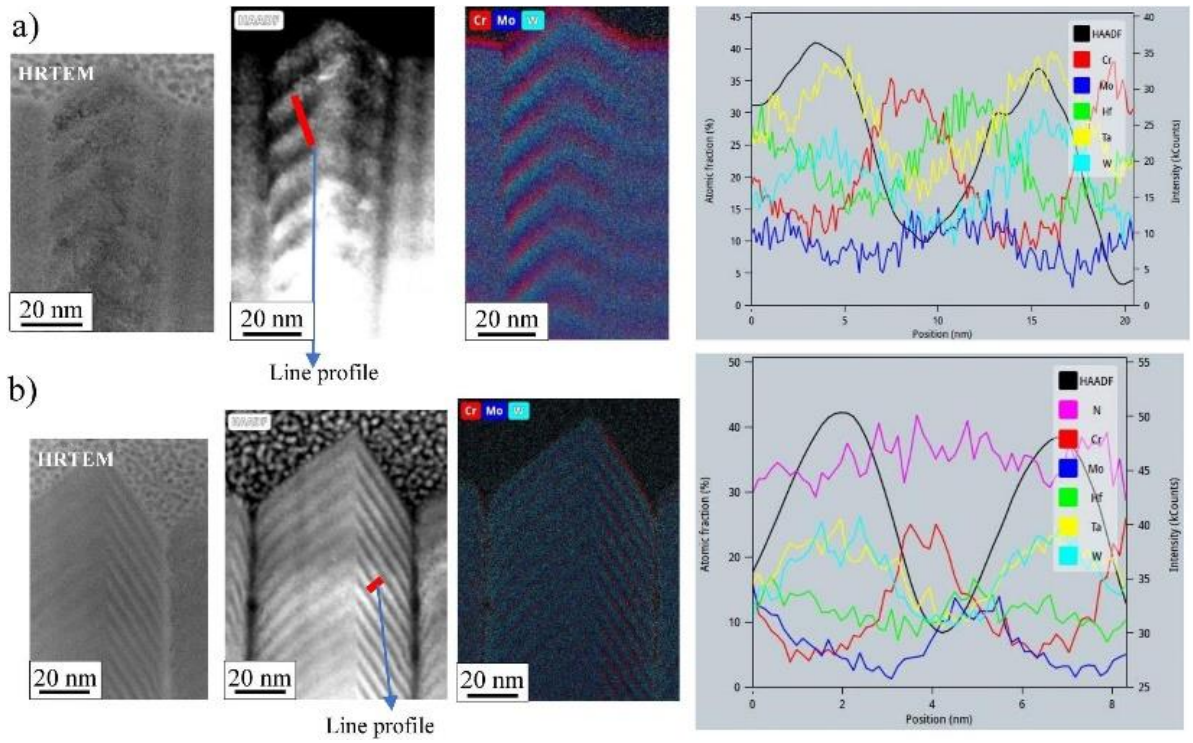

Figure 2: HRTEM and STEM HAADF images combined with EDX elemental map (Cr, Mo, W) and line profile of layer showing all elements. (a) metallic coating deposited at RT without nitrogen flow, (b) nitride coating deposited at HT under 20 sccm nitrogen flow.

The first promising experimental experience obtained on the Cr-Hf-Mo-Ta-W system confirm the possibility of the formation of multi-component metallic bcc and multi-component fcc nitride phases and represent a starting point for further optimization of the growth conditions and chemical composition in order to achieve excellent mechanical properties.

Related publication

[1] T. Stasiak, P. Souček, V. Buršíková, N. Koutná, Zs. Czigány, K. Balázsi, P. Vašina: *Synthesis and characterization of the ceramic refractory metal high entropy nitride thin films from Cr-Hf-Mo-Ta-W system,* Surface and Coatings Technology **449,** 128987 (2022)

PROBING THE ONSET OF WURTZITE PHASE FORMATION IN (V,AL)N THIN FILMS BY TRANSMISSION ELECTRON MICROSCOPY AND ATOM PROBE TOMOGRAPHY

Zs. Czigány, M. Hans (RWTH Aachen), D. Neuß (RWTH Aachen), J. A. Sälker (RWTH Aachen), H. Rueß (RWTH Aachen), J. Krause (RWTH Aachen), G. K. Nayak (Montanuniversität Leoben), D. Holec (Montanuniversität Leoben), J. M. Schneider (RWTH Aachen)

The thermal decomposition mechanisms of single-phase, metastable cubic (V,Al)N thin films grown at 440 °C by high-power pulsed magnetron sputtering were systematically investigated by vacuum heat treatment at 600-900 °C after deposition [1]. During growth, a columnar microstructure was formed in the layers. The beginning of the spinodal phase separation, during which cubic AlN separates into V- and Al-rich cubic nitride phases with the same structure, can be detected after heat treatment at 700 °C. Furthermore, both transmission electron microscopy and atom probe tomography measurements provide evidence for diffusion of aluminium to grain boundaries and triple junctions at this temperature.

According to ab initio calculations, the activation energy of volume diffusion of aluminium is 25% lower than that of vanadium, which explains the formation of Al-rich regions. It is reasonable to assume that these Al-rich regions are precursors for the formation of wurtzite AlN, which can be clearly identified after heat treatment at 800 °C by both microscopy (Fig. 1) and tomography. The significantly larger equilibrium volume of quartzite AlN compared to the cubic AlN phase explains that the formation of the wurtzite phase is limited exclusively to the triple junctions and grain boundaries. In contrast, twin boundaries are rich in vanadium.

Interestingly, the formation of the wurtzite phase at grain boundaries and triple junctions can be detected by resistivity measurements, while X-ray diffraction and nanoindentation are less sensitive to the formation of the minority phase. Thus, the latter methods clearly confirm its formation only after heat treatment at temperatures above 900 °C. Therefore, it is evident that previously reported formation temperatures for wurtzite AlN in transition metal aluminium nitrides, determined by non-nanometer-scale chemical and structural methods, are overestimates.

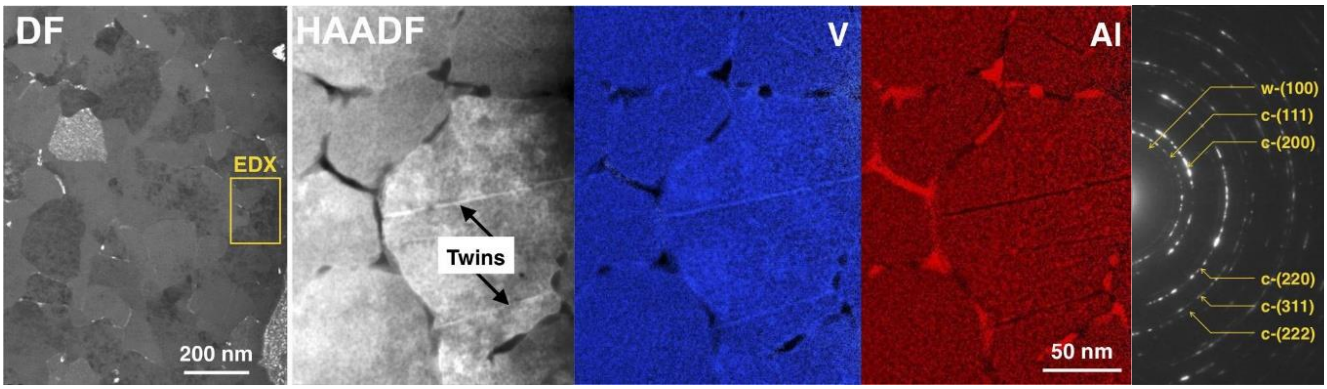

Figure 1: Plan-view DF image of VAlN film annealed at 800°C, taken with the wurtzite (100) reflections. HAADF and STEM-EDX elemental maps (Al and V) of the region of interest indicated in the DF. Elemental maps indicate Al diffusion into grain boundaries and triple junctions. In contrast, twin boundaries are rich in vanadium. The electron diffraction pattern (right) proves formation of wurtzite phase that is located at grain boundaries and triple junctions in DF.

Related publication

[1] M. Hans, Zs. Czigány, D. Neuß, J. A. Sälker, H. Rueß, J. Krause, G.K. Nayak, D. Holec, J. M. Schneider: *Probing the onset of wurtzite phase formation in (V,Al)N thin films by transmission electron microscopy and atom probe tomography,* Surf. Coat. Technol. **442,** 128235 (2022)

INVESTIGATION OF LITHIUM NIOBATE NANOCRYSTALS SYNTHESIZED ON DIFFERENT ROUTES

T. Kolonits, L. Kocsor (Wigner FK, ELTE), G. Dravecz (Wigner FK), L. Péter (Wigner FK)

Within the framework of a collaboration between the Thin Film Physics Department, the Wigner Research Centre for Physics and the Eötvös University (ELTE), the synthesis of lithium niobate nanocrystals was investigated. Lithium niobate is an excellent optical material with outstanding electro- and acousto-optical, nonlinear optical, and photorefractive properties. Since its first single crystal growth realized more than 50 years ago, a progress has also been made in the production of nanopowders in the last decades. In the present study two synthetisation routes were investigated: solvothermal synthesis (a bottom-up method) and wet condition ground milling (a top-down one).

The solvothermal synthesis using different organic media is an easy and effective way for producing nanoparticles at relatively low temperature. The organic medium, acting as stabilizer can control the growth of the particles and prevent their agglomeration. In our study [1] four polyol media were used: ethylene glycol, diethylene glycol, triethylene glycol and glycerol. The reaction was performed through the following process:

$$Nb_2O_5 + 2LiOH \rightarrow 2LiNbO_3 + H_2O \quad (1)$$

Our results [1] suggest that the reaction goes through two consecutive steps. First, LiOH reacts with Nb_2O_5 on the surface of the nanoparticles, forming the Li-rich Li_3NbO_4 phase:

$$Nb_2O_5 + 6LiOH \rightarrow 2Li_3NbO_4 + 3H_2O \quad (2)$$

Then, the second step is that the Li_2O already incorporated to the peripheral Li_3NbO_4 phase penetrates further into the Nb_2O_5 particle and forms lithium niobate:

$$Li_3NbO_4 + Nb_2O_5 \rightarrow 3LiNbO_3 \quad (3)$$

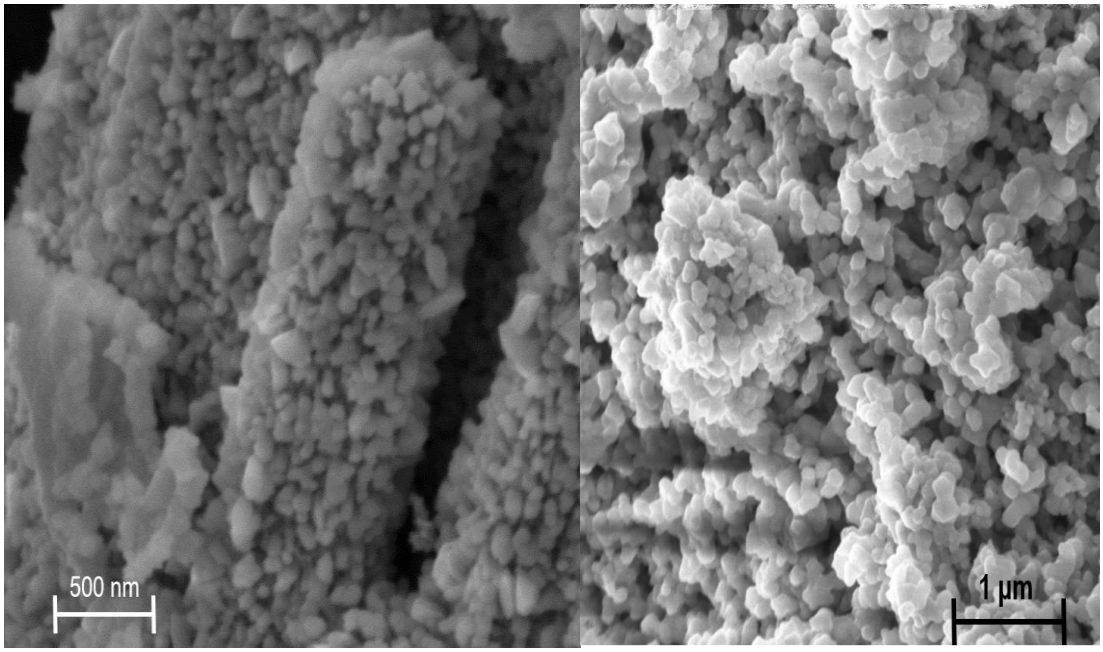

Figure 1: End product of the solvothermal reaction. Left without- and right with pre-milling of Nb_2O_5.

Nb_2O_5 was pretreated by milling the raw material down to 300-500 nm in particle diameter using a planetary mill. Without this treatment, the product retained the original columnar structure of Nb_2O_5 and the $LiNbO_3$ formation could only be completed on its surface as it can be seen on Fig. 1. The effects of the polyol media, the reaction time and the Li excess were investigated. As a conclusion, the best yield and the most homogeneous lithium niobate phase could be prepared by using diethylene glycol medium with a Li/Nb ratio of 1.5 and a 72-hour reaction time.

Planetary milling as a top-down method was also investigated. During this study [2] congruent lithium niobate prepared by sintering was grounded under wet conditions in a planetary mill in order to produce nanocrystals. The aim was to prove that this method is more efficient than using a shaker mill. The particle size was monitored by SEM and dynamic light scattering with a good correspondence.

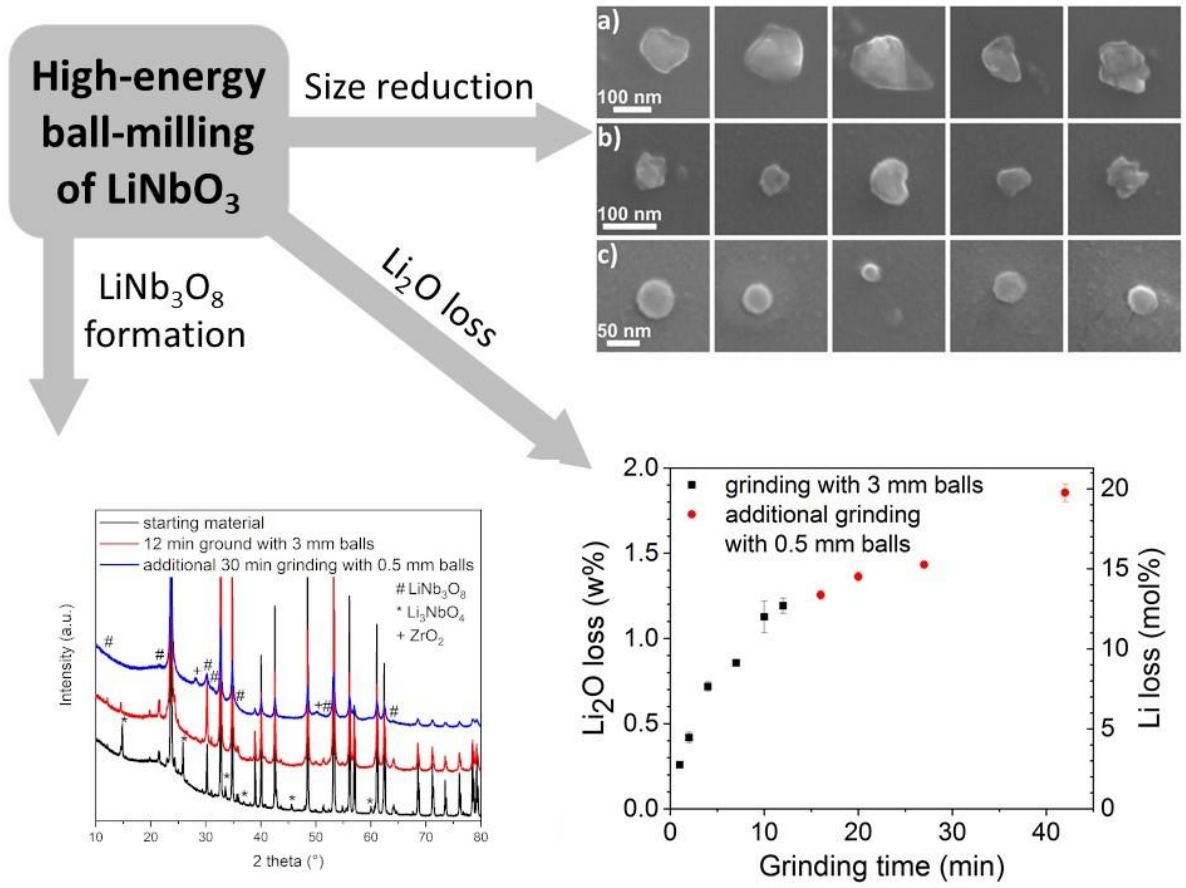

Figure 2: The morphology of the ball-milled $LiNbO_3$ nanoparticles, the X-Ray diffraction phase analysis and the calculated LiO_2 loss

It was shown, that already the first phase of ball-milling in the planetary mill by using balls of 3 mm diameter resulted in particles with 100 nm < D <150 nm after 12 min effective milling time, as opposed to the shaker mill where the minimum diameter was several hundred nanometre after several hours. X-Ray diffraction has shown, that the final size of the crystals could be reduced to about 12–15 nm. Hence, it is obvious that the particles seen in the SEM images (Fig. 2) are composed of several crystallites.

As a correlation with the particle size reduction, X-ray diffractometry revealed the formation of a lithium-deficient $LiNb_3O_8$ phase (Fig. 2) as a Li_2O loss during the milling process. The presence of $LiNb_3O_8$ was confirmed by means of Raman spectroscopy. The amount of Li_2O loss was also determined by titration in a good agreement with the other methods. Correlation was revealed between the composition change of the nanopowder and the total surface area of the particle assembly calculated from dynamic light scattering measurements (Fig. 2).

Related publications

[1] G. Dravecz, T. Kolonits, L. Péter: *Formation of $LiNbO_3$ Nanocrystals Using the Solvothermal Method,* Crystals **13(1),** 77 (2023)

[2] L. Kocsor, L. Kovács, L. Bencs, T. Kolonits, K. Lengyel, G. Bazsó, Zs. Kis, L. Péter: *Lithium oxide loss of lithium niobate nanocrystals during high-energy ball-milling,* Journal of Alloys and Compounds **909,** 164713 (2022)

DESIGN AND CORROSION RESISTANCE OF TUNGSTEN CARBIDE-RICH COATING LAYERS

A. S. Rácz, Zs. Fogarassy, Zs. Kerner, M. Menyhárd

Tungsten carbide is known for its superior hardness and good chemical resistance. In this work tungsten-carbide-rich coating layers have been produced by irradiating C/W multilayer of various structures (with individual layer thicknesses from 10 to 20 nm) by argon and xenon ions. The range of energies and fluences varied between 40-110 keV, and 0.07 - 6x10^{16} ions/cm^2, respectively. The component in-depth distributions have been determined by Auger-Electron Spectroscopy (AES) depth profiling.

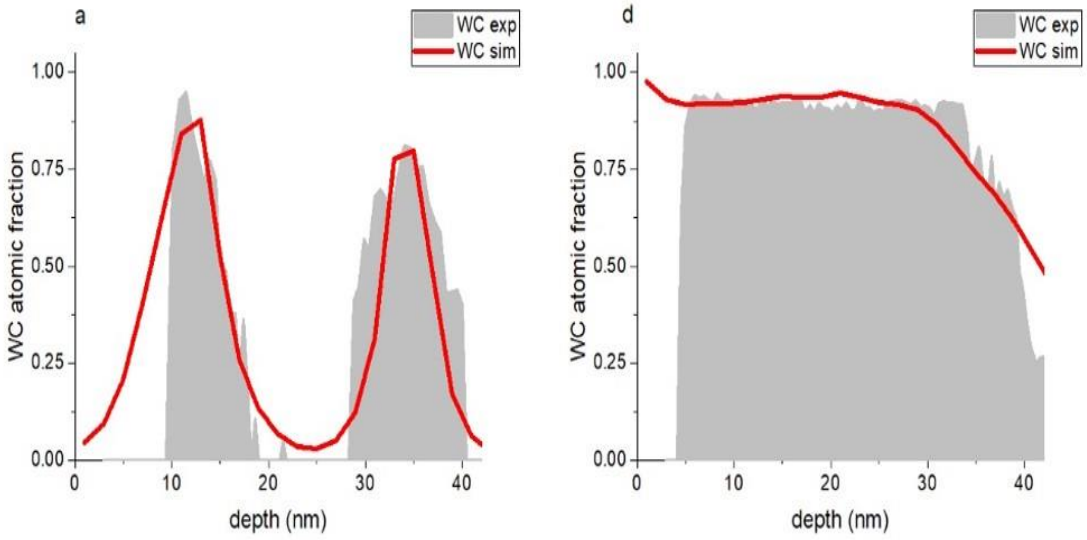

Figure 1: Comparison of measured WC distribution with that of calculated for sample of C 10nm / W 24.5 nm / C 9.1 nm // Si substrate, irradiated by 120 keV Xe$^+$ applying various fluences

It has been shown that the growth of the WC-rich layer started at the interfaces and with increasing fluence the separately growing layers coalesced. For predicting the WC in-depth distributions TRIDYN simulation has been applied. This simulation is based on the description of binary collisions and describes the ballistic mixing, which is usual for systems having low average atomic number (<20). We show that adapting parametrizations the simulations were able to estimate the in-depth distribution of the elements after ion irradiation.

The amount of carbide has been calculated applying a simple model. The agreement between the experimental and simulated depth profiles has been tested for a rich dataset differing in layer structures, projectiles, ion fluences and energies. An example is shown in Fig. 1. The good agreement enables the design of the WC-rich layers and also enables the significant decrease of the experimental work [1].

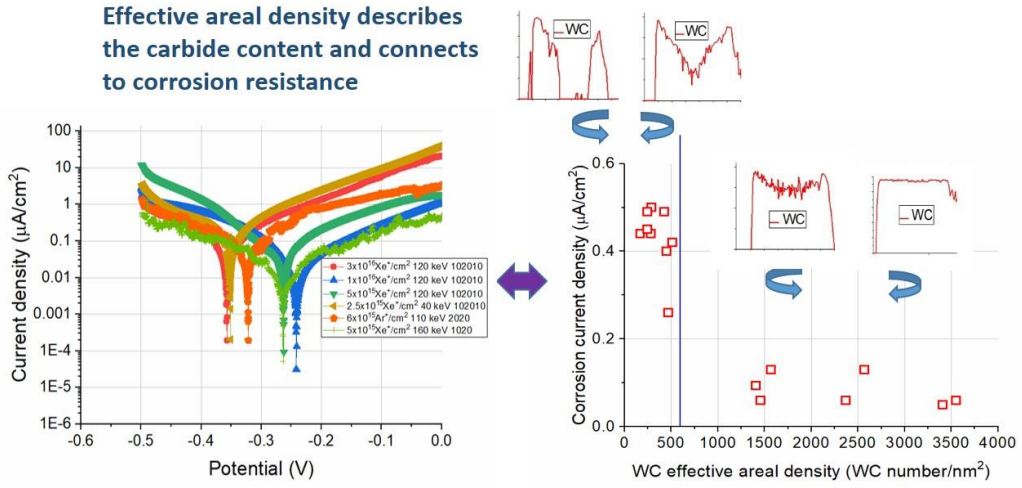

Figure 2: The measured Tafel curves in 3.5 wt% NaCl solution and the connection between the WC effective areal densities and corrosion current densities

The corrosion resistance of the samples has been tested by potentiodynamic corrosion test in 3.5 wt% NaCl solution. The test has shown that the irradiated samples had better corrosion resistive properties than that of a WC cermet. For quantifying the protectivity of the systems the term WC effective areal density has been introduced which can be calculated from the carbide in-depth distributions.

If the effective areal density was in the range of 0–550 WC (number/nm^2) the corrosion current density was 0.5 (μA/cm^2) ± 35%, while if the effective areal density was higher than 1200 WC (number/nm^2) the corrosion current density was 0.08 (μA/cm^2) ± 36% (Fig. 2).

As the effective areal density values can be calculated also from the TRIDYN simulations, the fast and cheap design of these corrosion protective layers is possible.

The EU H2020 Project No. 824096 "RADIATE", HZDR-Dresden and project funding of Centre for Energy Research is highly acknowledged.

Related publication

[1] A.S. Racz, Z. Fogarassy, U. Kentsch, P. Panjan, M. Menyhárd: *Design and production of tungsten-carbide rich coating layers,* Applied Surface Science **586,** 152818 (2022)

A COMBINATORIAL STUDY OF THE RF SPUTTERING PROCESS AND THE PROPERTIES OF SILICON-OXYNITRIDE THIN FILM SYSTEM UNDER VARIABLE REACTIVE GAS INJECTION

OTKA K143216, KDP 2021 Cooperative Doctoral Program

N. Hegedüs, Cs. Balázsi, T. Kolonits, D. Olasz, Gy. Sáfrán, M. Serényi, K. Balázsi

Pure silicon dioxide (SiO_2) and silicon nitride (SiN) have long been used in electronics technology and are produced by a number of proven technologies such as RF sputtering. In its complex form, amorphous silicon oxynitride (SiON) is a chemically very stable material with a refractive index of between 1.45 and 2.05, depending on the oxygen and nitrogen content. This wide range of refractive index is very useful in optoelectronic applications. The application of SiON technology is limited because the composition of the composite layer and thus its refractive index is particularly sensitive to small changes in sputtering parameters, especially the oxygen content of the plasma gas [1].

Our aim is to efficiently investigate the sputtering process itself and the properties of the Si-O-N thin film system over the whole compositional range. To achieve this, we have developed and applied a combinatorial layer growth method with variable reactive gas-injection [2, 3]. Instead of producing and testing a large number of individual samples with different compositions, we have therefore chosen a more efficient combinatorial solution. In a single 25 mm long sample, an amorphous silicon-oxynitride layer of variable properties was grown by reactive RF sputtering, that included the complete transition from oxide to nitride. Two different target voltages (1.62kV and 1.95kV) were used to sputter layers of different thicknesses. The variation of optical properties and layer thickness was investigated by Spectroscopic Ellipsometry (SE) measurements, while the elemental composition was studied by Energy Dispersive Spectrometry (EDS).

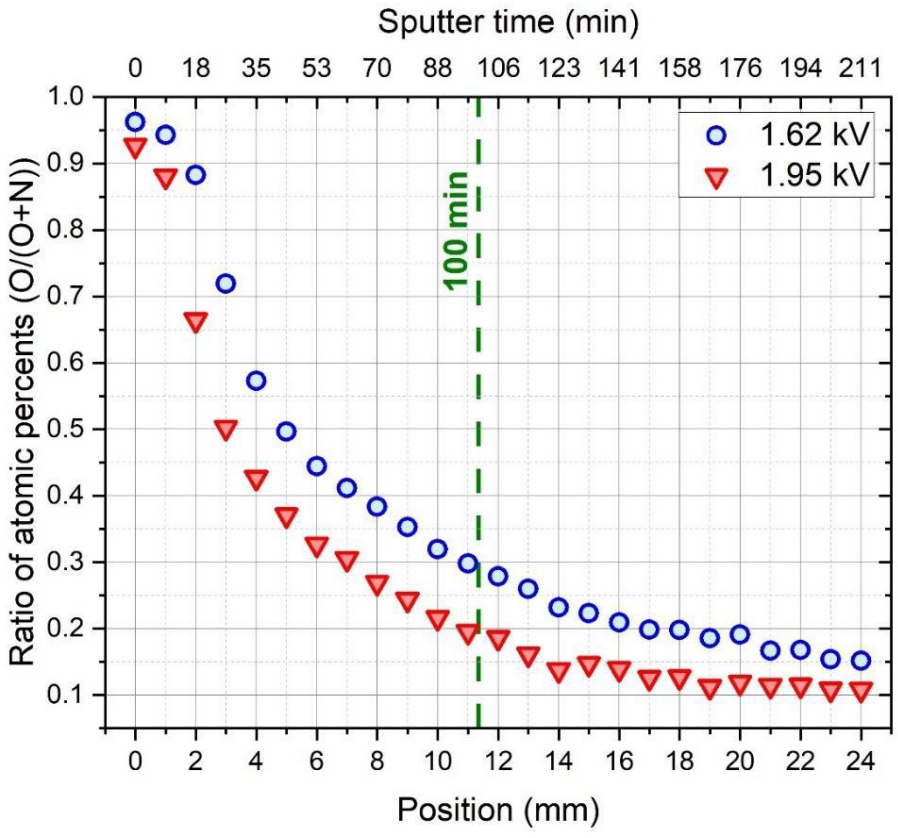

Figure 1: Atomic concentrations (O/O+N) measured by EDS in Si-O-N samples of varying composition sputtered at 1.62 and 1.95 kV as a function of distance along the sample

Fig. 1 clearly shows a remarkable effect of partial pressures of O and N reactive gases on the layer composition. O/O+N decreases with the oxygen depletion in the reactive gas mixture and as well with the DC voltage as measured along the sample.

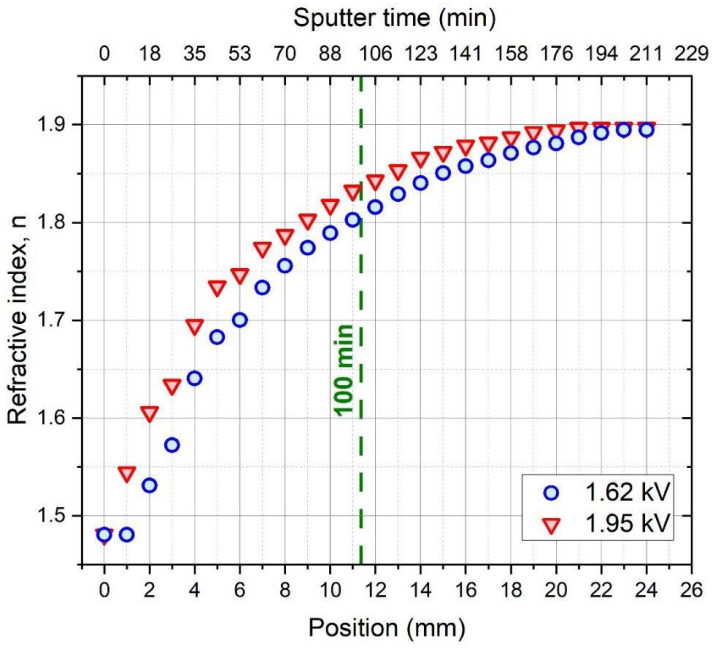

Figure 2: Refractive index (n) variation of samples sputtered at 1.62 and 1.95 kV of varying O/O+N composition measured along the substrate by spectroscopic ellipsometry

In Fig. 2, we have shown that the refractive index (n) of the layer can be tuned in the range 1.48-1.89 by varying the partial pressure of oxygen injected into the chamber, in accordance with the compositional variation. It is clear that the refractive index increases as the O content decreases, indicating an SiOx–SiOxNy–SiNx transition in the composition-spread samples. From the data on the composition of the layer, the typical physical parameters of the process were determined using the Berg model [4, 5] developed for reactive sputtering. A new approach was introduced in the modelling - a metallic Si target sputtered with a uniform nitrogen and variable oxygen gas flow was considered as an oxygen gas sputtered SiN target [6]. According to the calculations detailed in the publication, the sputtering gas temperature can increase by up to 40 °C during the growth of the oxygen-rich layer due to the exothermic nature of the oxidation.

Our variable gas-induced combinatorial layer growth method and the correlations found between sputtering parameters, layer composition and refractive index, in agreement with the model developed, allow us to produce silicon-oxynitride layers with exactly the designed optical properties. This experimental technique, moreover, allows the growth of thin films with gradient refractive indexes required for some specific applications.

This research was supported by the Cooperative Doctoral Program of the Ministry of Innovation and Technology, KDP-2021, Doctoral Student Scholarship Programme, funded by the National Research, Development and Innovation Fund. The research was also supported by the OTKA grant K143216.

Related publications

[1] M. Serényi, M. Rácz and T. Lohner: Vacuum **285(61),** 245-249 (2001)

[2] G. Sáfrán: "*One-sample concept*" *micro-combinatory for high throughput TEM of binary films*, Ultramicroscopy **187,** 50 (2018)

[3] G. Sáfrán, N. Szász, G. Dobrik, B. Kalas, M. Serényi: *Smart gas dosage by a peristaltic pump for reactive RF sputtering of composition spread combinatorial hafnium-oxy-nitride layers,* Vacuum **182,** 109675 (2020)

[4] S. Berg, H.-O. Blom, T. Larsson and C. Nender: Journal of Vacuum 291 Science & Technology A: Vacuum, Surfaces, and Films **5(2),** 202-207 (1987)

[5] S. Berg and T. Nyberg: *Fundamental understanding and modeling of reactive sputtering processes,* Materials Thin Solid Films **476(293),** 215-230 (2005)

[6] N. Hegedűs, Cs. Balázsi , T. Kolonits , D. Olasz, G. Sáfrán, M. Serényi and K. Balázsi: Materials **15,** 6313 (2022)

INDENTATION SIZE EFFECT IN EXCEPTIONALLY HARD ALCU THIN FILMS

OTKA K143216, KDP 2021 Cooperative Doctoral Program

D. Olasz, Gy. Sáfrán, N. Szász, G. Huhn (ELTE), N. Q. Chinh (ELTE)

We investigated the correlations between the structure and mechanical properties of the AlCu thin film system by efficient combinatorial methods: in a single experiment, 15 adjacent bands of 12x1 mm², ~1.7 um thick samples of varying composition representing the whole concentration range (Al_xCu_{1-x}, $0 \le x \le 1$) were deposited on a 25x12 mm² Si substrate using dual DC magnetron sputtering. Composition-dependent mechanical properties of the samples, such as hardness and deformation mechanisms, have been determined by nanoindentation, and composition, structure and morphology by microscopic methods (SEM, TEM) [1].

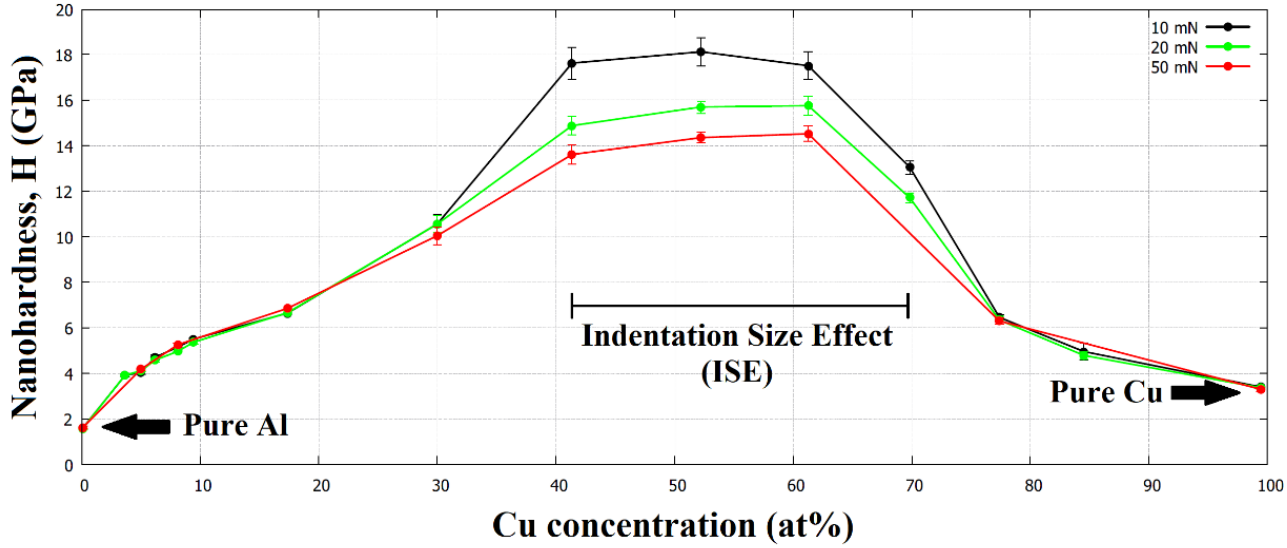

Figure 1: Hardness of AlCu alloy thin films as a function of composition, measured at three maximum indentation forces (10, 20 and 50 mN)

Fig. 1 shows the hardness (H) of the layers as a function of copper concentration. It is observed that the hardness of pure Al layer is 1.6 GPa, which is significantly higher than the hardness of bulk Al (~0.3 GPa). Even in the presence of a low alloying concentration of 3.7 at% Cu, the strength of the layer increases significantly to 3.9 GPa. The maximum strength value of ~16 GPa, which is 10 times harder than the pure Al thin film, is reached in the concentration range of ~40-60 at% Cu. This extraordinary strength is not only twice that of the hardest AlCu thin film reported in the literature, H=8 GPa [2], but also comparable to that of the hard coating materials used in industry. Fig. 1 shows that at the edges of the diagram, at low alloy concentrations, different indentation forces - 10, 20, 50 mN - result in practically identical H values, while in the medium ~40-70 at% Cu concentration range, lower indentation forces are associated with higher H values. This phenomenon is the Indentation Size Effect (ISE), which is well-known for pure bulk Al and Cu materials. In contrast, our measurements showed the absence of ISE in the pure- and low alloying concentration materials.

The absence of ISE at low alloying concentrations can be explained by the microstructure. In our present films, even the pure Al and Cu layers are characterized by very fine grain size (~ 100 nm), which brings to the fore another deformation mechanism, grain boundary sliding. AFM and SEM measurements revealed the formation of pile-ups around the indentation marks (Fig. 2), what also confirms the enhanced activity of the grain boundary sliding.

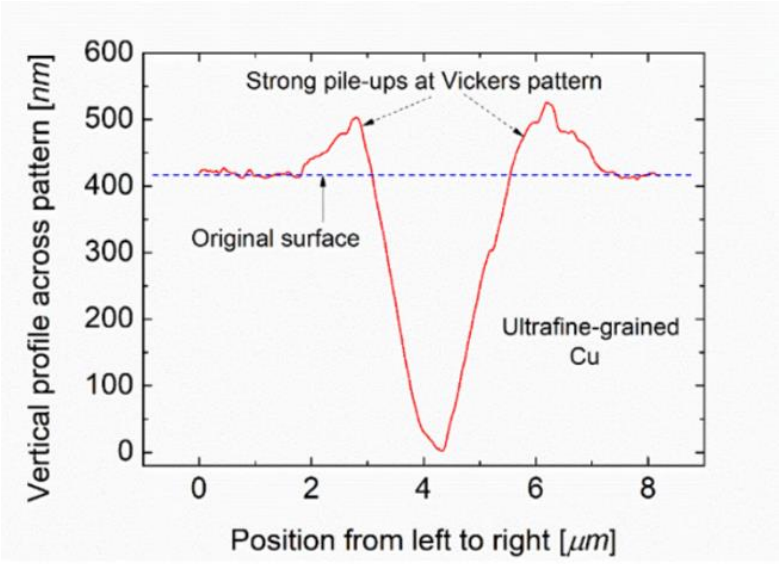

Figure 2: For a pure Cu layer, the vertical profile of the indentation trace determined by AFM. The "pile-up" phenomenon is clearly visible at the edge of the trace.

On the other hand, in the ~40-70 at% Cu range, the nanoindentation load-displacement (P-h) curves (Fig. 3.a) at a maximum indentation force of 50 mN clearly show a step-like behaviour, indicating a non-continuous deformation.

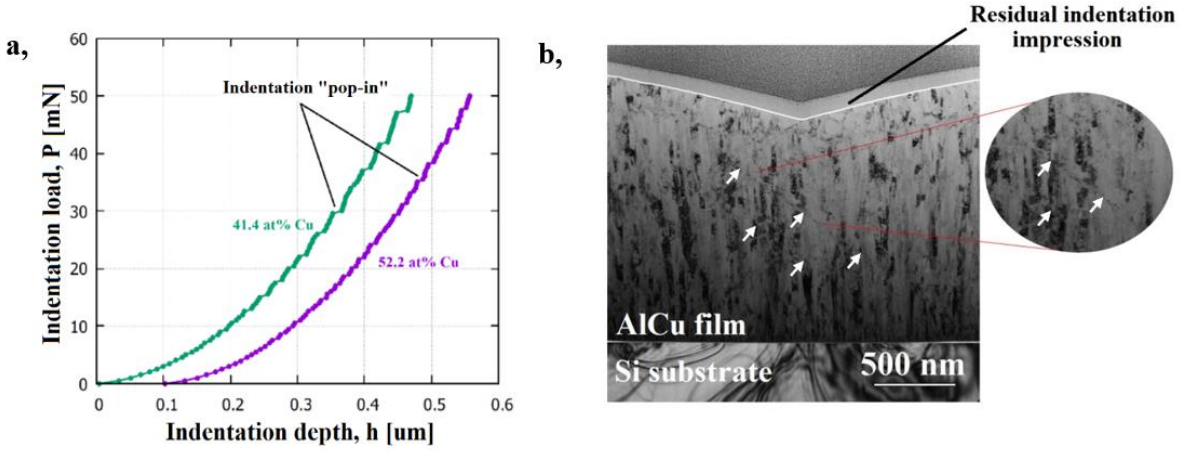

Figure 3: (a) "Step-like" indentation curves showing a "pop-in" phenomenon at a maximum indentation force of 50 mN. (b) Cross-sectional TEM image of an indented layer containing 52.2 at% Cu. Arrows indicate the two deformation bands around the indentation.

The cross-sectional TEM image in figure Fig. 3.b shows the layer with 52.2 at% Cu exhibiting a fine columnar morphology. Arrows mark deformation bands found under the indentation, running at an angle of about 45°. The measured step-like indentation behaviour ("pop-in") can be explained by the formation and propagation of these shear bands. [1, 2]

Related publications

[1] D. Olasz, Gy. Sáfrán, N. Szász, G. Huhn, N. Q. Chinh: *Indentation size effect in exceptionally hard AlCu thin films,* Materials Letters **330,** 133409 (2023)

[2] M Draissia, H Boudemagh and M Y Debli: *Structure and Hardness of the Sputtered Al-Cu Thin Films System,* Phys. Scr. **69,** 348 (2004)

STRUCTURE DETERMINATION USING CORRECTED DIFFRACTION INTENSITIES: EXTENSION OF THE EWALD CORRECTION METHOD

OTKA K143216; Doctoral School of Physics ELTE

E. Dódony, B. Rudd, I. Dódony (NanoLab) and Gy. Sáfrán

Today, with the development of nanotechnology, it is increasingly important to understand the materials of modern devices at the atomic level. Transmission Electron Microscopy (TEM) is one of the most important tools for this. The structure of the sample is determined by a combined analysis of high-resolution (HRTEM) images and Electron Diffraction (ED) patterns obtained by TEM. The HRTEM images and ED patterns require a preliminary correction for deviations from the projected charge density and the structure factor (F^2_{hkl}) squared as determined by scattering theory. The deviation between the high-resolution images and the projected-charge-density is due to the signal transfer characteristics of the electron microscope. The detected intensities differ from the ideal F^2_{hkl} proportional values if, due to experimental conditions, the Ewald sphere is deflected from the detector plane. To determine a crystal structure, it is necessary to know the square of the structure factors (F^2_{hkl}), so the diffracted intensities $I_{exp_{hkl}}$. In the ED pattern, the intensity of the reflections differs from this as a function of the distance between the Ewald sphere at the given reflections and the reciprocal plane. Cowley described the equation in 1992 [1] for the effect of the Ewald sphere on the diffraction intensities:

$$I_{exp_{hkl}} = I_{hkl} * E_{w_{hkl}}$$

$$E_{w_{hkl}} = \frac{\sin\frac{\pi\lambda t}{2d^2_{hkl}}}{\frac{\pi\lambda t}{2d^2_{hkl}}}$$

where $I_{exp_{hkl}}$ is the experimentally measured intensity of the reflection at the Miller index hkl, $I_{hkl} = F^2_{hkl}$ and $E_{w_{hkl}}$ is the Ewald sphere effect on the intensity I_{hkl} at a given value of d_{hkl} as a function of λ wavelength and sample thickness t.

Thus, the intensities measured in the experimental image can be corrected by the reciprocal of $E_{w_{hkl}}$ to obtain the theoretical F^2_{hkl} values ($I_{hkl} = \frac{I_{exp_{hkl}}}{E_{w_{hkl}}}$).

While several computer programs (e.g. CRISP) are available for the correction of HRTEM images, no such program has been developed for the Ewald correction of diffraction patterns. When correcting diffraction patterns in some cases up to a few hundred reflections have to be corrected separately, which is a very time consuming task. To ease this task, a computer program has been developed that performs the correction for the whole diffraction image, given the wavelength λ, the microscope constant K, the centre of the Laue zone, the position of the direct beam, and the d-value of the reflection in the zero-order Laue zone furthest from the direct beam. By extending Cowley's theory [1, 2], we provide a solution for the case when the centre of the Laue zone is not on the optical axis. The method also works for cases that are a few degrees off the zone axis (~0.8° in cases ~5° depending on the structure). It is of great advantage, for example, when working with radiation-sensitive material and there is no time for precise orientation of the crystal. Fig. 1.a and 1.b illustrate the oriented and the misaligned cases.

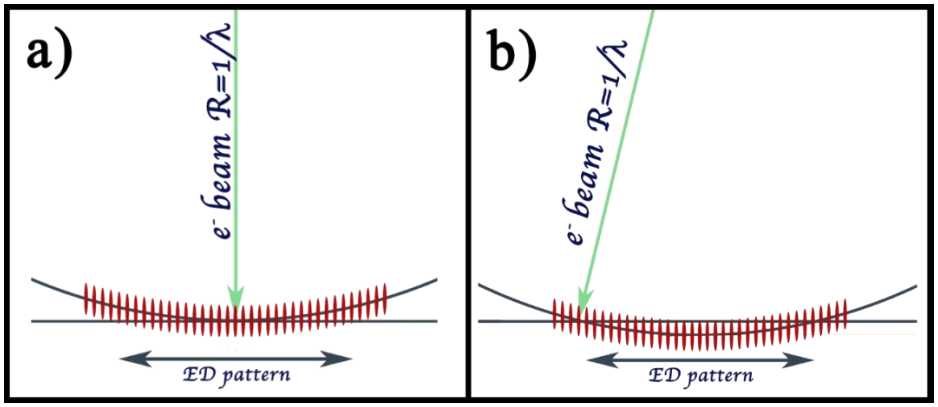

Figure 1: (a) In the oriented case the detector plain is tangent with the Ewald sphere, the centre of the Laue-zone coincides with the location of the direct beam. Correction is done by applying $\frac{1}{E_{w_{hkl}}}$ on the diffracted intensities. (b) In the slightly misaligned case the detector plain intersects the Ewald sphere, the centre of the Laue zone (at the lowest point of the sphere) doesn't coincides with the location of the direct beam.

For the correction we have to use a different function from $\frac{1}{E_{w_{hkl}}} \rightarrow \frac{1}{E_{w,tilt_{hkl}}}$.

The $\frac{1}{E_{w_{hkl}}}$ correction function was extended to the slightly misaligned case through a simple idea. When searching for the new $\frac{1}{E_{w,tilt_{hkl}}}$ function we had an idea, that the same correction is applicable at a given reciprocal space in the misaligned case as in the aligned, where the distance between sphere and plane are the same. So we related every reciprocal lattice point $d^*_{hkl,tilt}$ in the misaligned case to the d^*_{hkl} in the aligned case where the distance between the Ewald sphere and the detector plane are the same and used the correction calculated with d^*_{hkl} for the aligned case at the place $d^*_{hkl,tilt}$. The correctness of the new procedure was verified on diffraction images that are deviated from the zone axis.

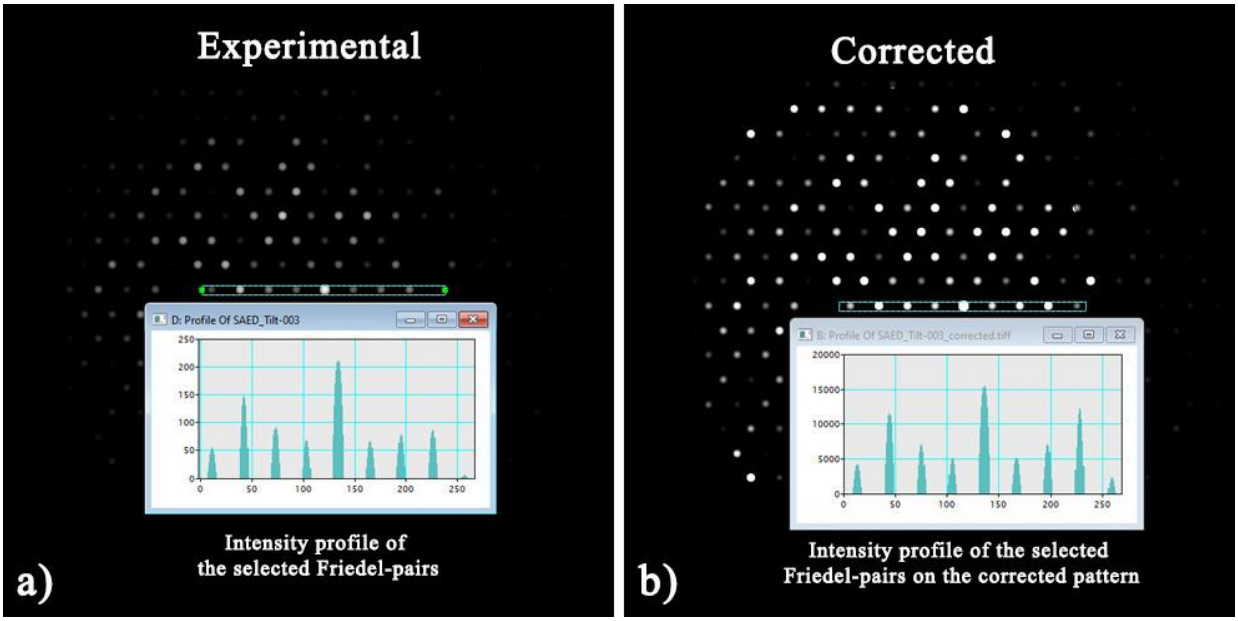

Figure 2: (a) The intensity ratios of the Friedel pairs in the experimental diffraction pattern are different from 1 (misaligned orientation), (b) the intensities of the Friedel pairs in the software corrected pattern are nearly identical. As a result, the Ewald correction can be extended to the misaligned cases.

We examined the intensity ratios of the Friedel pairs before and after correction. In the well-oriented case, the Friedel pairs have the same intensity, so if the ratio of Friedel pairs approaches one by applying the new correction function, we know that the correlation is correct. This check was performed for different orientations of apatite, of which the case tilted out of the [001] zone axis is shown in Fig. 2. It clearly shows that after the correction the ratio of the Friedel pair intensities is close to one, while before the correction it was far from one. (This was true for all the orientations tested.) Therefore, we can conclude that the extended procedure works.

With the computer program we have developed, it is possible to perform a fast Ewald correction of the experimental electron diffraction patterns, thus ensuring that the I_{hkl} theoretical intensity dataset needed to determine unknown structures is easily accessible. The program can also be applied to cases with small deviations from the zone axis (~0.8° in cases up to ~5°). This is an advantage when working with beam-sensitive materials or in post-processing if the sample is not perfectly oriented but you want to use the I_{hkl} intensity set of the SAED pattern.

Related publications

[1] J. M. Cowley: *Electron Diffraction Techniques,* Oxford Uni. Press. Vol. 1. 1992

[2] X. Zou: *Electron Crystallography of Inorganic Structures – Theory and Practice,* Chemical Communications, Stockholm University, 1995

MICROSTRUCTURE INVESTIGATION OF NANOCRYSTALLINE MATERIALS USING ELECTRON DIFFRACTION BASED RIETVELD ANALYSIS – APPROXIMATION OF INSTRUMENTAL BROADENING

OTKA K125100, VEKOP-2.3.3-15-2016-00002

V. Kovács Kis, Zs. Czigány, Zs. Kovács (ELTE)

Rietveld analysis [1] is commonly used for the evaluation of XRD and neutron powder diffraction patterns providing quantitative data on phase composition, crystal structure and microstructure parameters, such as crystallite size, anisotropic shape, preferred orientation, microstrain. However, this full pattern fitting method is less used for Electron Powder Diffraction (EPD) patterns, mostly because the contribution of dynamical scattering of electrons to the detected intensity distribution hampers direct interpretation of diffraction pattern. Another difficulty is concerning the large variability of electron optics, which requires standardized measurements to control e.g. instrumental broadening in electron diffraction. So far, the number of papers presenting results based on Rietveld analysis of EPD does not exceed 25, however, this method has a great potential in nanoparticle and thin film analysis, as yields quantitative and statistically representative information on nanostructured materials. Indeed, to achieve accuracy and reproducibility of EPD similar to that of the other diffraction methods, and to obtain as small instrumental broadening of diffraction peaks as possible, strict control on lens currents of the electron microscope is needed [2].

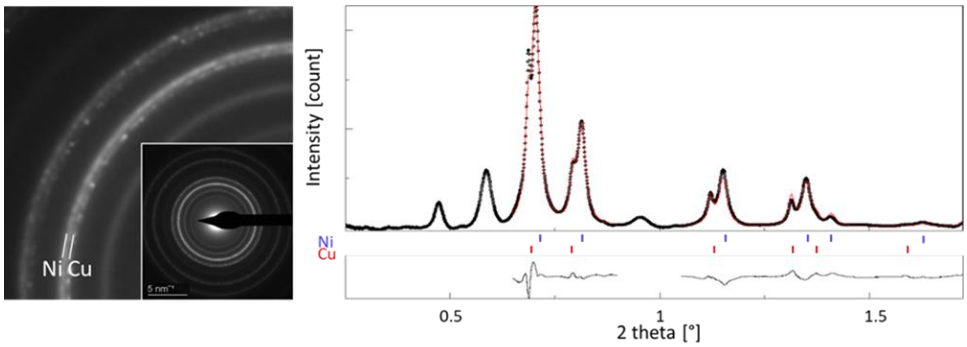

Figure 1: SAED of a Cu-Ni thin film deposited at 150 °C using DC magnetron sputtering (left) and corresponding integrated intensity profile (right). Black dots are measurement data and red line is the fitted curve. Bragg positions of Cu and Ni and difference curve of the fitted regions are also plotted.

To measure and reproduce the instrumental broadening parameters for EPD Rietveld analysis, a three-step procedure was proposed [3], which comprises subsequent XRD and EPD measurements of two different calibration samples. We propose a novel, single step in TEM (Transmission Electron Microscope) procedure, which allows to obtain the instrumental broadening function of the TEM directly from a single measurement, without the need of an additional X-ray diffraction measurement. Using graphene calibration standard and applying properly controlled acquisition conditions on a spherical aberration corrected microscope, we achieved an instrumental broadening of ±0.01 Å in terms of interplanar spacing. The shape of the diffraction peaks is modelled as function of scattering angle using the Caglioti relation [4], and the obtained parameters for instrumental broadening can be directly applied in Rietveld analysis of electron diffraction data of the analysed specimen. During peak shape analysis, instrumental broadening parameters of the TEM are controlled separately from nanostructure related peak broadening effects, which contributes to a higher reliability of nanostructure information extracted from electron diffraction patterns. The potential of the proposed procedure is demonstrated through the Rietveld analysis of hematite nanopowder and two-component Cu-Ni nanocrystalline thin film specimens (Fig. 1).

Related publications

[1] H.M. Rietveld: *Line Profiles of Neutron Powder–Diffraction Peaks for Structure Refinement,* Acta Crystallogr **22,** 151–152 (1967)

[2] Zs. Czigány & V.K. Kis: *Acquisition and evaluation procedure to improve the accuracy of SAED,* Microsc. Res. Tech. 1–13. (2022)

[3] P. Boullay, L. Lutterotti, D. Chateigner, & L. Sicard: *Fast microstructure and phase analyses of nanopowders using combined analysis of transmission electron microscopy scattering patterns,* Acta Crystallogr **A70,** 448–456 (2014)

[4] G. Caglioti, A. Paoletti, & F. P. Ricci: Choice of collimators for a crystal spectrometer for neutron diffraction, Nucl Instrum **3,** 223–228 (1958)

BIPHASIC IRON UPTAKE FROM NANO-HAEMATITE PARTICLES BY ROOTS

OTKA K115784, VEKOP-2.3.3-15-2016-00002

V. Kovács Kis, Z. Klencsár, Á. Keresztes (ELTE), F. Pankaczi (ELTE), F. Fodor(ELTE), Á. Solti (ELTE)

Nanoscale Fe containing particles can penetrate the root apoplast. Nevertheless, cell wall size exclusion questions that for Fe mobilisation, a close contact between the membrane integrating Ferric Reductase Oxidase (FRO) enzymes and Fe containing particles is required. Haematite nanoparticle suspension, size of 10–20 nm, characterized by ^{57}Fe Mossbauer spectroscopy, TEM, ICP and SAED was subjected to Fe utilisation by the flavin secreting model plant cucumber (*Cucumis sativus*). Alterations in the structure and distribution of the particles were revealed by ^{57}Fe.

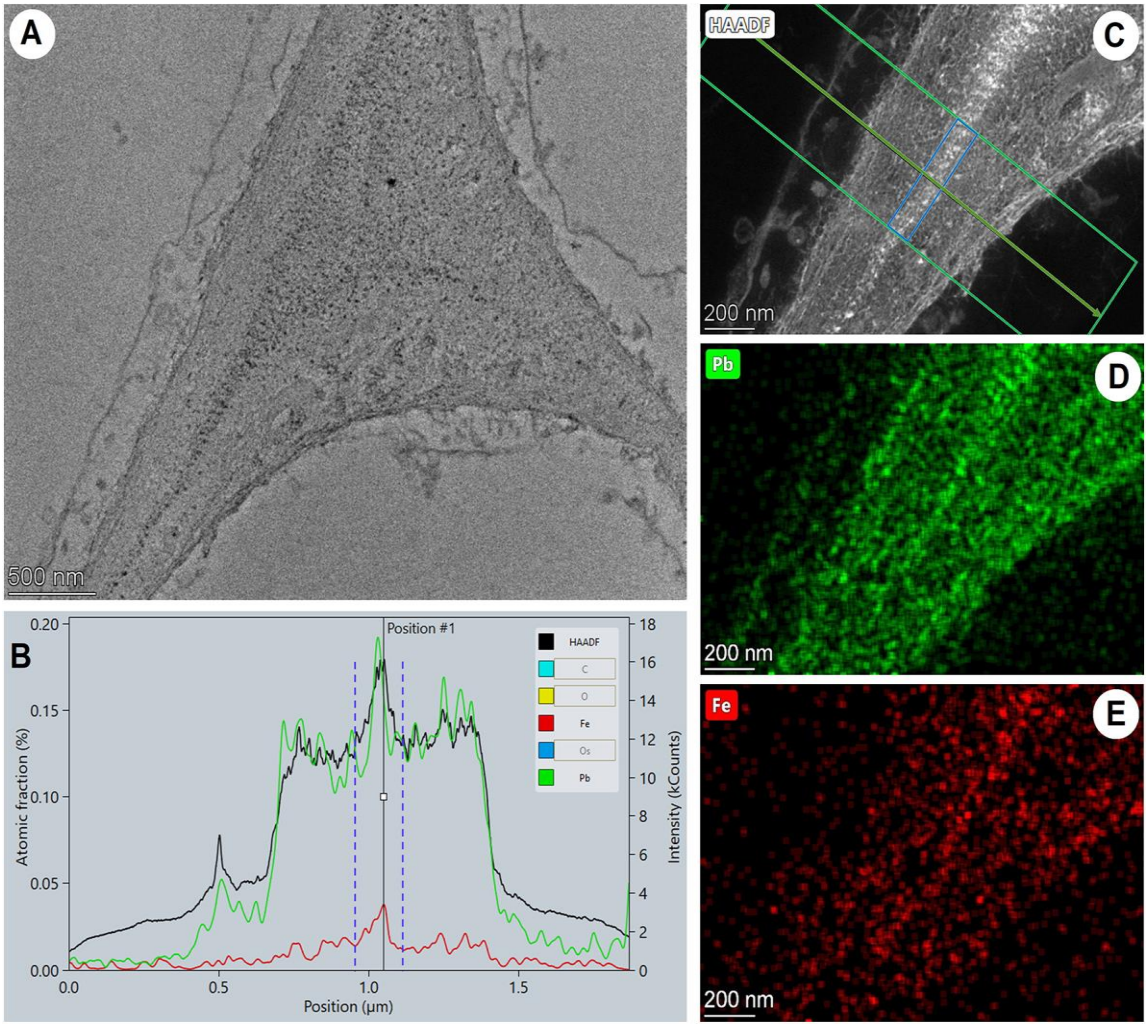

Figure 1: Transmission electron micrograph of a three-cell junction (A) and High-Angle Annular Dark-Field (HAADF) image (B) of the root tip meristem cells of NH treated plants. Energy dispersive X-ray spectroscopy (EDS) line profile analysis (B) performed by merging data applying a 300 pixel integration width perpendicular to the line indicated on (C). Elemental distribution maps of Pb as for contrasting material (D) and Fe (E) was created based on the Pb La1 and Fe Ka peaks (10.55 and 6.40 keV, respectively). Area of the line profile between dashed lines on (B) is the region marked by blue box on (C), which coincides with the middle lamella in the two-cell junction. In this area large number of high atomic number particles (bright spots) are seen, and, according to EDS line profile analysis, besides the contrasting material Pb, is characterized by elevated concentration of Fe.

TEM analysis revealed aggregates of electron dense particles in the middle lamellae between adjacent cell walls in the Nanohaematite (NH) treated sample (Fig. 1.a-c) with elevated iron content (Fig. 1). EDS elemental mapping (Fig. 1.b, Fig. 1.d-e) revealed that abundance of both Fe and Pb (this latter originated from the contrasting material) was higher in the middle lamella between the adjacent cell walls across the root tip. In contrast to NH treated samples, accumulation of Fe was not observed in the control samples.

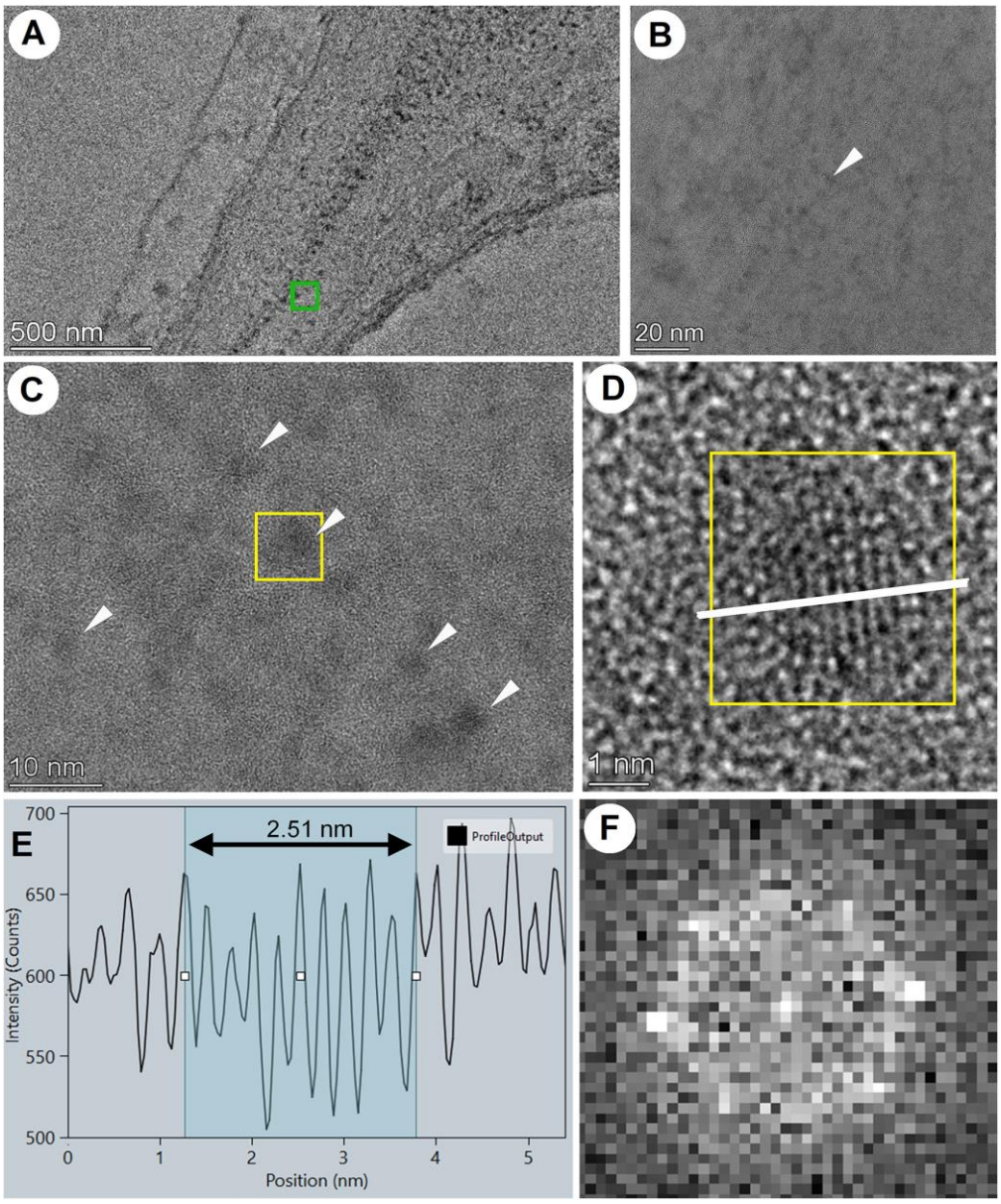

Figure 2: High-resolution transmission electron micrographs (HRTEM; A–C) of the root tip meristem cells of NH treated plants. Subdivision B is a high-resolution site indicated by a green square on subdivision A (sample is identical to 3A). Bar on (A) equal to 500 nm. Electron dense particles, pointed by arrowheads, accumulated in the middle lamella of the cell wall at two-cell junctions. HRTEM indicate the presence of several separate electron dense particles (C). Atomic resolution image of an individual particle proves crystalline structure (D), the measured periodicity is 2.51 nm, typical to haematite d(110) interplanar spacing (E). Fourier transform support unambiguously haematite nanoparticle in [001] zone axis orientation (F).

HRTEM analysis of NH treated roots indicates accumulation of particles at the interfaces of the middle lamella and the adjacent walls (Fig. 2.a-c), which corresponds to the linearly arranged high average atomic number particles observed on the HAADF images (Fig 2.c). Based on the interplanar spacing values measured on the Fourier transforms, these nanoparticles were identified as haematite (Fig. 2.d-f). Size analysis of the particles indicated a diameter of 1.96 ± 0.28 nm for the particles, where no particles were detected above the diameter of 2.85 nm.

Biological utilisation of Fe resulted in a suppression of Fe deficiency responses (expression of *CsFRO 1, 2* & *3* and *RIBOFLAVIN A1*; *CsRIBA1* genes and root ferric chelate reductase activity). Haematite nanoparticles were stacked in the middle lamella of the apoplast. Fe mobilisation is evidenced by the reduction in the particle size. Fe release from nanoparticles does not require a contact with the plasma membrane. Parallel suppression in the *CsFRO 1&3* and *CsRIBA1* transcript amounts support that flavin biosynthesis is an inclusive Fe deficiency response involved in the reduction-based Fe utilisation of *Cucumis sativus* roots. CsFRO2 is suggested to play a role in the intracellular Fe homeostasis [1].

Related publication

[1] A. Singh, M. Gracheva, V. Kovács Kis, Á. Keresztes, M. Sági-Kazár, B. Müller, F. Pankaczi, W. Ahmad, K. Kovács, Z. May, et al:. *Apoplast utilisation of nanohaematite initiates parallel suppression of RIBA1 and FRO1&3 in Cucumis sativus,* Nanoimpact **29,** 100444 (2023)

BIORESORBABLE AND BIOCOMPATIBLE BIOMINERALIZED CARBONATED AMORPHOUS CALCIUM PHOSPHATE LOADED BIOPOLYMER COMPOSITES

OTKA PD131934

M. Furko

The aim of this research work is to develop biomineralized bioceramic/biopolymer composite coatings onto implant materials. Amorphous or nanocrystalline Calcium Phosphates (ACPs) and their combination with biopolymers are innovative types of resorbable coatings for load bearing implants that can promote the integration of metallic implants into human bodies. In addition, they are advantageous form of the various calcium phosphate phases since they have faster dissolution rate than that of crystalline hydroxyapatite. Owing to the biomineral additions (Mg, Zn, Sr) in optimized concentrations, the base CP particles became more similar to the mineral phase in human bones (dCP). We investigated the effect of bioactive mineral addition on the morphology and chemical characteristic of the powder, as well as we prepared carbonated Amorphous Calcium Phosphate - Polycaprolactone (cACP-PCL) composite thin layers to implant surfaces and studied their biodegradability characteristic by corrosion measurements.

Fig. 1 shows the difference in morphology of cACP powder and the biomineralized cACP powder. The biomineralization caused a slight decrease in the particle size and the particles tended to agglomerate into larger blocks, while in the cACP, disordered, mainly needle-like microstructure formed.

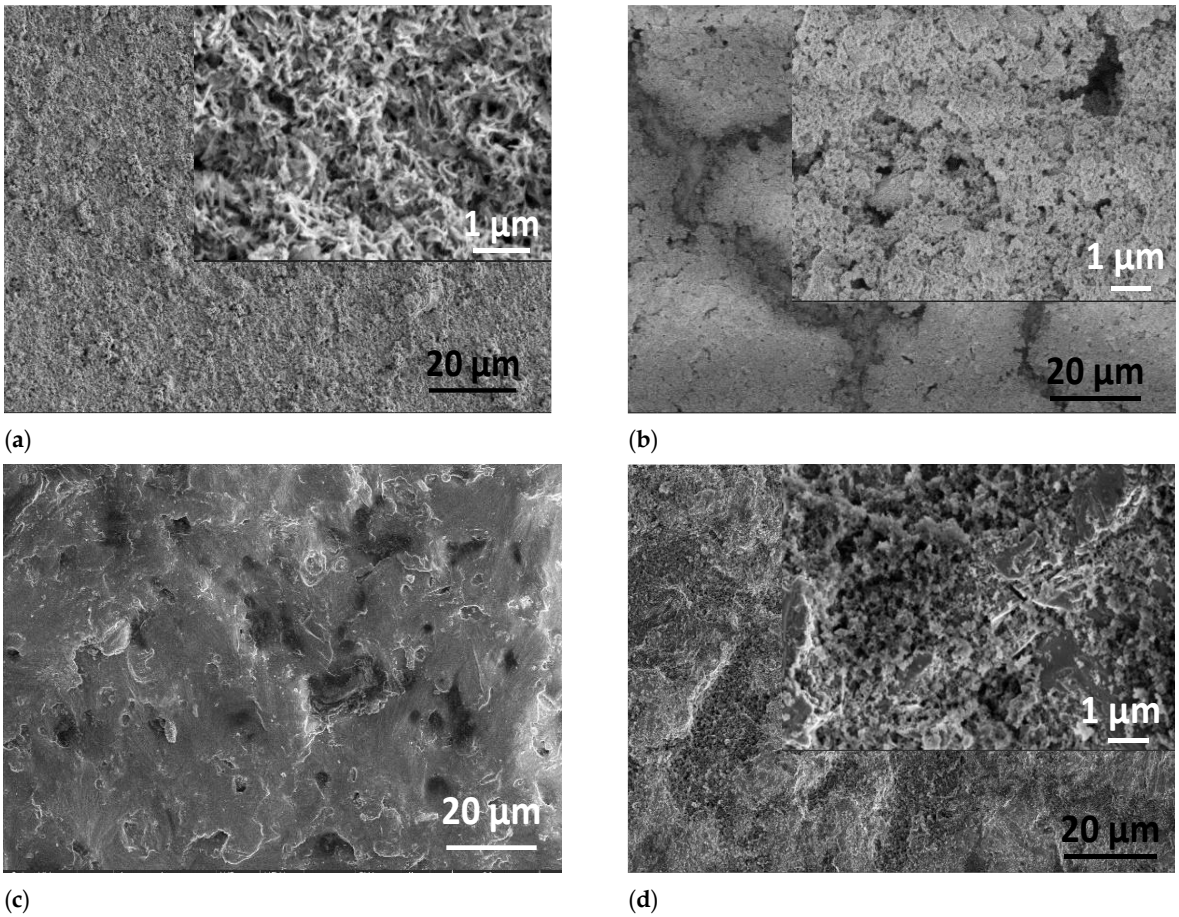

Figure 1: SEM images of calcium phosphate cACP powder coating (a) biomineralized cACP powder coating (b) PCL thin layer (c) biomineralized cACP-PCL thin layer (d)

The SEM image of PCL coating (Fig. 1.c) reveals that the layer is very thin and contains numerous holes through which the substrate surface emerges. The surface of polymer layer is smooth and the polymer particles has glass-like amorphous feature. Incorporating the cACP particles into PCL matrix increased the adherence of the coating since it acts as a natural bioadhesive on the surface. The microstructure of cACP added PCL thin film noticeably differ from the powder coatings. It contains larger agglomerates and blocks along with smaller particles such causing rougher surface with larger surface area that is advantageous to the bone cell attachment. The biodegradable properties of different thin layers were evaluated by potentiodynamic polarization curves.

As it is visible in Fig. 2, the shape and characteristic of the curves is quite similar in all cases and did not change noticeably over time. The difference appears in the values of corrosion currents and corrosion potentials of different samples which corresponds to their corrosion rates.

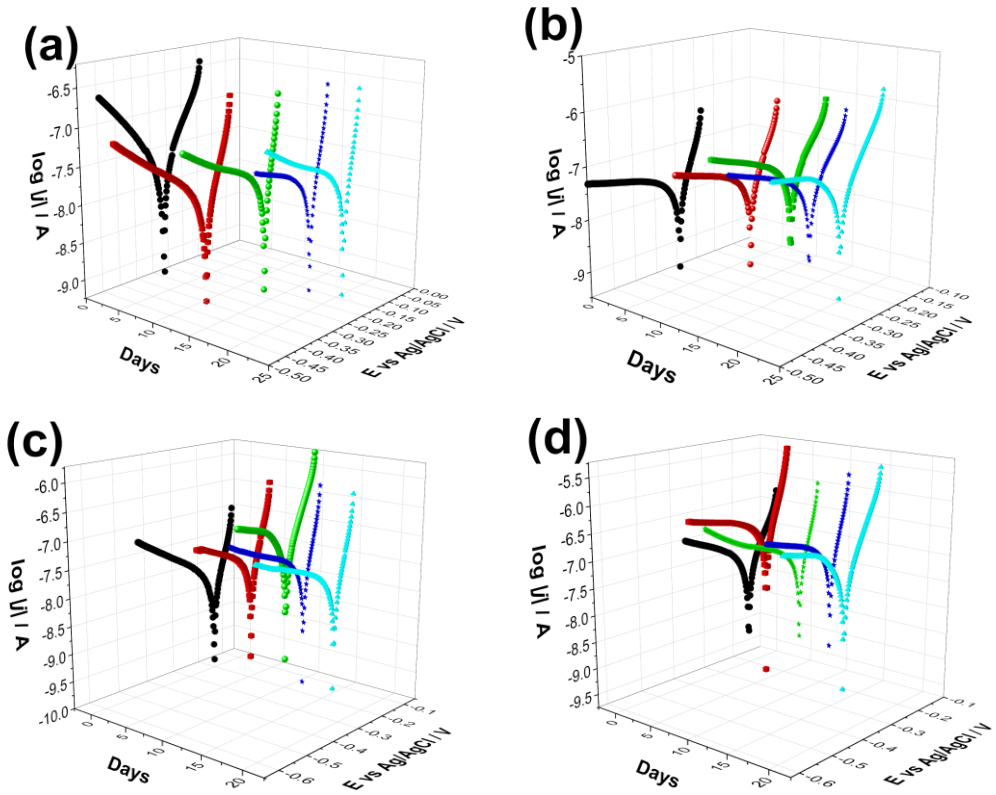

Figure 2: Potentiodynamic polarization curves recorded on uncoated Ti6Al4V alloy (a) on CP thin coating (b) on dCP thin coating (c) as well as on dCP-PCL composite thin layer. The measurements were repeated several times over a two-week period in Phosphate Buffered Solution (PBS) in ambient condition. The potential scanning rate is 1 mV s^{-1} in each case.

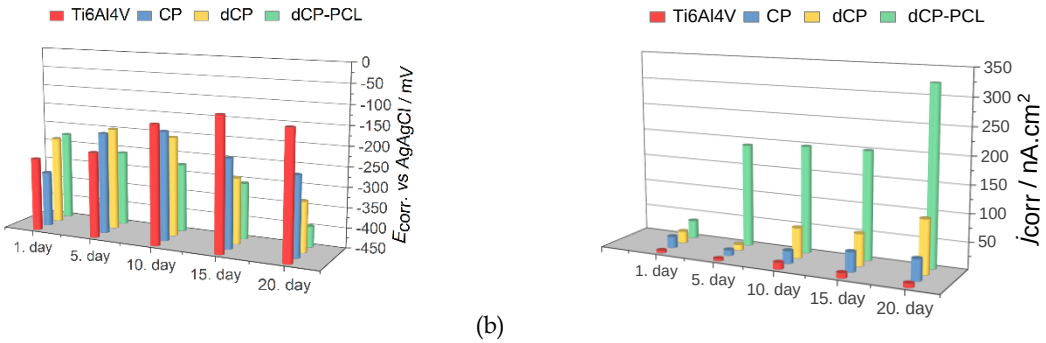

(a) (b)

Figure 3: Electrochemical parameters: E_{corr} (a) j_{corr} (b) derived from the potentio-dynamic curves in Figure 2

The corrosion potential ($E_{corr.}$) values shifted to slightly more positive potentials as time passed for the substrate material, which indicates surface passivation. The corrosion potentials of cACP and biomineralized cACP thin coatings slightly decreased over the whole immersion period. The corrosion current density values hardly changed with immersion time in the case of uncoated implant, however, in the cases of powder and composite thin layers, the j_{corr} showed a steady and slightly slow increasing tendency over the investigated immersion time. The highest j_{corr} values were measured for the cACP-PCL composite layer, that supports its increased biodegradability.

Al_2O_3 PREPARED FROM THE OXIDIZED ALN POWDER BY HOT ISOSTATIC PRESSED AND PRESSURELESS POST-SINTERING

K. Balázsi, D. Varanasi, M. Furkó, Cs. Balázsi

Aluminium nitride (AlN) is an alternative refractory ceramic material being used in various range of applications such as optics, electronics and computer circuits for its unique thermal and electrical properties. It has a really high degree of thermal stability and wear resistance while exhibiting a low density. The effect of the pressureless post-sintering in hydrogen on the structural and mechanical properties of the hot isostatic pressed alumina (Al_2O_3) ceramics prepared by oxidized AlN powder has been studied as the potential substrates for integrated circuits.

The micrometre size AlN powder (H.C. Starck GMBH, Berlin) has been oxidized in air at 900° C and sintered by Hot Isostatic Pressing (HIP) at 1700 °C, 20 MPa nitrogen atmosphere for 5 h (Fig. 1). Pressureless Sintering (PS) has been applied for all HIP sintered samples in H_2 gas at 1800° C for 10 h. Transmission (TEM, Jeol 3010) and scanning (SEM, Thermo Fisher) electron microscopy were used for detailed structural analysis. HIT300 (Anthon-Paar) nanoindenter was used for the nanomechanical testing.

Based on the structural characterizations, the oxidation caused a core–shell AlN/Al_2O_3 structure and the amount of Al_2O_3 increased with increasing of the oxidation time of the AlN powder. AlN powder before oxidation showed mainly globular character with average grain size of~1 µm The processing method is influencing the obtained microstructure, reduces the grain size and increases the densification of final sintered ceramic. Te increasing of the oxidization time above 10 h caused the formation of pores on the surface of the AlN, indicating the creation of Al_2O_3 oxide phase. Hot Isostatic Pressing (HIP) has unique advantages in promoting the compactness of parts, eliminating void defects, reducing segregation and improving the mechanical properties of the ceramics. The presence of α-Al_2O_3 phase has been only observed. The subsequent PS sintering effected the grain growth from 1 µm to ~ 5 µm at 1800 °C for 10 h. The PS sintered Al_2O_3 has been consisted from the non-uniform morphology and the grain size has been still around 5 µm. The structure of oxidizes ceramics compared to non-oxidized reference showed the smoother surface. The improvement of the mechanical properties of Al_2O_3 can be expected potential ceramics for novel engine or other applications. The hardness values of post-sintered samples have been increased to 17–18 GPa having apparent densities between 3.11 and 3.39 g/cm^3.

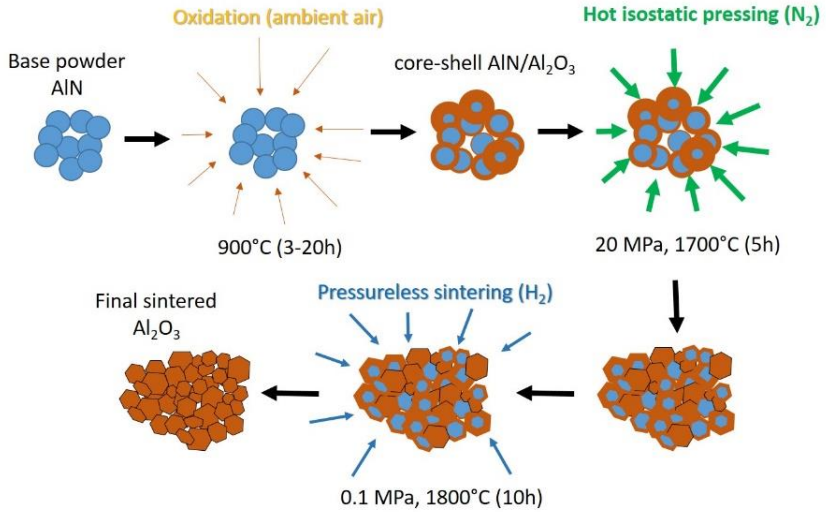

Figure 1: Experimental procedure of Al_2O_3 sintered sample preparation from AlN powder

Bulk sintered Al_2O_3 has been prepared by oxidization of AlN powder and combined sintering process, the hot isostatic pressing (HIP) in N_2 and pressureless sintering (PS) in the atmosphere. Both sintering methods (HIP followed by PS) of oxidized AlN powder without sintering additives has been successfully developed for the first time [1]. The micrometre sized AlN has been oxidized between 3 and 20 h in ambient atmosphere. The volume of Al_2O_3 phase increased with the increasing of oxidation time of AlN powder. High temperature HIP sintering transformed θ-Al_2O_3 and only two major phases α-Al_2O_3 and minor AlN have been stabilized. PS post-sintering in 1800 °C for 10 h caused the phase transformation to α-Al_2O_3 which had effect on the apparent density and hardness of PS sintered ceramics. The highest apparent densities 3.11–3.39 g/cm3 (78–85% relative densities) and highest hardness values (17–18 GPa) have been measured for PS sintered α-Al_2O_3 prepared from base powder oxidized between 3 and 10 h.

Related publication

[1] K. Balázsi, D. Varanasi, Zs. E. Horváth, M. Furkó, F. S. Cinar & C. Balázsi: *Effect of the pressureless post-sintering on the hot isostatic pressed Al_2O_3 prepared from the oxidized AlN powder,* Scientifc Reports **12,** 8250 (2022)

VO_2 LAYERS WITH HIGH RESISTIVE SWITCHING RATIO BY ATOMIC LAYER DEPOSITION

2019-2.1.11-TÉT-2020-00189

Zs. Baji, L. Pósa, Gy. Molnár, Z. Szabó, M. Volom, A. K. Kjara Surca, G. Drazic*, J. Volk*
**National Institute for Chemistry, Ljubljana, Slovenia*

The atomic layer deposition of vanadium oxides has been in the focus of much research effort. Vanadium oxides are much-researched materials due to the wide range of applications from microelectronics, smart electrochromic and thermochromic windows, metamaterials, gas sensors, programmable critical thermal sensors to battery energy storage. VO_2 is in the centre of most research due to its reversible transition at 68°C, where the crystalline structure of the material reorganises from monoclinic to tetragonal rutile structure coupled by dramatic changes both in the electrical and optical properties. Therefore, all the optical and electrical properties of the material may be controlled through this Semiconductor Metal Transition (SMT). This quality makes VO_2 an excellent material for resistive switching.

The atomic layer deposition of vanadium oxides has been in the focus of much research effort. With atomic layer deposition, a number of precursors and different reactions can be used for this purpose, but there are some substantial difficulties with all of them. The present work aims at the comprehensive investigation of the atomic layer deposition of VO_2 with the TEMAV precursor. Water, formalin and oxygen plasma were used as oxidants at deposition temperatures between 200°C and 350°C.

All the deposited films were examined with AFM SEM and XRD, and they all proved to be very smooth with RMS roughness's between 2-5 nm. The XRD showed no peaks typical of vanadium oxide, therefore they all the layers were amorphous. According to the results of the structural and electrical characterisation, the deposition with water vapour at 200°C was ideal for the preparation of resistively switching VO_2. The crystallinity of the layers was improved with annealing, for which procedure oxygen, nitrogen and hydrogen atmospheres were investigated, and different temperatures and annealing lengths were examined. The optimal layers were prepared with the post deposition annealing of 3 hours in oxygen rich atmosphere at 500°C. This layer is shown in Fig. 1.b, and it can be seen, that the layer is dense with large crystallites.

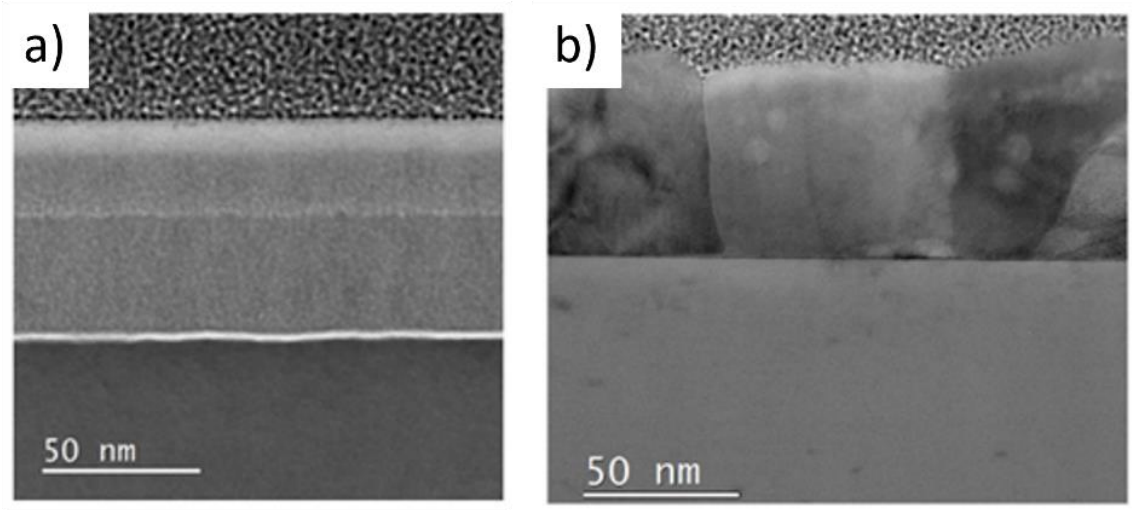

Figure 1: STEM image of as deposited vanadium oxide (200°C) film with water as an oxidant before (a) and after (b) annealing in O_2 for 3 hours at 500°C

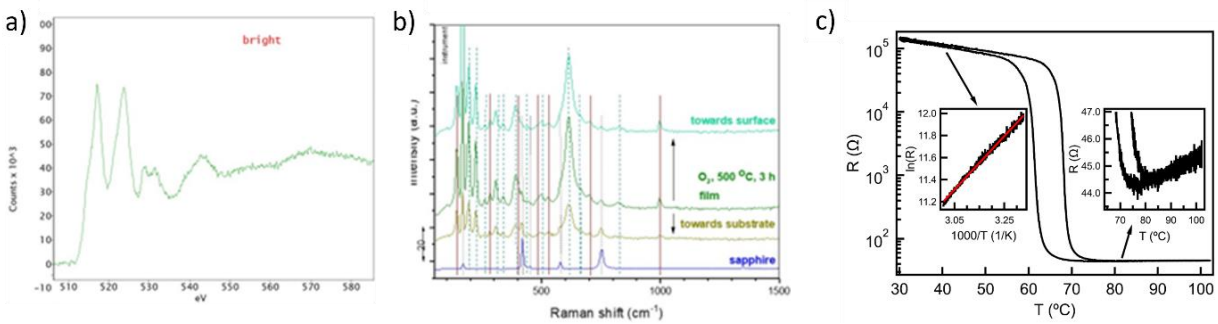

Figure 2: Electron Energy Loss Spectroscopy (EELS) (a), Raman (b) and temperature dependent resistance (c) spectrum of the VO_2 film

Electron Energy Loss Spectroscopy (EELS) and Raman measurements also proved that the films are monoclinic VO_2. The EELS spectrum showed the typical shoulder for VO_2 at the Vanadium peak at 515 eV, and the characteristic double peak of the Oxygen around 530eV (Fig. 2.a). The Raman measurement also found only the peaks corresponding to VO_2 (Fig. 2.b). The electrical properties of the films were measured by Hall technique at room temperature, and after being heated to the phase transition temperature. The optimal layer showed the required phase transition, with its resistance dropping by three orders of magnitude at the transition temperature. The free electron mobility rose from 0.18 cm^2/Vs to 15.4 cm^2/Vs, while the carrier concentration increased from $3.5*10^{18}\,cm^{-3}$ to $2.9*10^{19}\,cm^{-3}$. Therefore, the drop in resistivity in our layers is due to a combination of increasing mobility and carrier concentration. It is widely stated that the phase transition is a result of the rearrangement of the V-V bond lengths, which are alternately shorter and longer in the monoclinic structure, to the equidistant shorter lengths of the rutile phase, thus the sharp decrease of the V-O distance and the overlapping of the oxygen 2*p* and vanadium 3*d* orbitals resulting in both the *d* and π orbitals being partially occupied at the Fermi level, and ultimately in a metallic behaviour.

The temperature dependent resistance was measured between 1 mm diameter Ti/Au ohmic contacts dots separated by 2mm. During the electrical resistance measurement triangular voltage signal was applied with 20 mV amplitude, while the current was monitored by a current amplifier. The layer showed ohmic behaviour with linear I(V) characteristics, thus the resistance could be determined by linear fit. The R(T) trace shows a several orders of magnitude jump around Tc=68 °C, characteristic to VO_2 (Fig. 2.c). The resistance switching ratio between 30 °C and 100 °C exceeds 3100. At low temperature, the layer exhibits semiconducting behaviour with an E_{gap}=418 meV band gap energy (see left inset), which is in good agreement with the literature values. Above the phase transition temperature, the sample shows an increasing resistance with the temperature, referring to metallic phase (see right inset). Due to the hysteretic behaviour, the layer transforms back to the semiconductor state at lower temperature (T_c=61 °C) during the cooling process. In summary, vanadium-oxide layers with the desired stoichiometry (VO_2) were successfully synthesized by atomic layer deposition and a post-annealing step. The layer showed a distinct switching property around the critical temperature with an R_{OFF}/R_{ON} ratio of over 3000 providing an attractive active layer for volatile memristor devices.

INTERPLAY OF THERMAL AND ELECTRONIC EFFECTS IN THE MOTT TRANSITION OF ULTRASMALL VO_2 PHASE CHANGE MEMORY DEVICES

OTKAK 128534, OTKA K 143282, János Bolyai Research Scholarship, ÚNKP Postdoctoral Scholarship, Cooperative Doctoral Programme

L. Pósa, P. Hornung, N. T. Török, S. Arjmandabasi, Gy. Molnár, Zs. Baji, A. Halbritter*, and J. Volk*

**Department of Physics, BME, Budapest, Hungary*

VO_2 has been studied for decades due to its Metal-Insulator Transition (MIT) at T ≈ 68 °C. This first order phase transition is accompanied by the structural transformation from low-temperature, semiconducting monoclinic to high-temperature, metallic tetragonal phase. This near room temperature phase transition was exploited in the field of neuromorphic computing, taking advantage of the volatile resistive switching characteristics of VO_2 devices. However, the underlying switching mechanism exhibits remarkable complexity both in the temporal and spatial domain. The description of these phenomena mostly requires complex modelling tools, like a percolation network model. We aimed to lessen the complexity of the physical operation in VO_2 resistive switches by focusing the switching to a nanometre-sized well defined active volume. We established devices with an ultra-small (≈ 30 nm) spacing between the contacting electrodes and anticipate that these devices are already describable by the formation and disappearance of a single metallic spot instead of more complex spatial patterns. This simplified arrangement facilitates the device modelling, providing further insight into the details of the local electronic and thermal processes.

Our devices were fabricated in lateral arrangement by depositing Ti/Au metal electrodes onto a Si/SiO_2 substrate covered by VO_x layer (see the SEM image in Fig. 1.a). The gold top electrodes (light grey) were patterned by electron beam lithography, realizing an asymmetric structure with triangular electrode on one side and rectangular one on the other. At the narrowest spot the separation of the two electrodes is ≈ 30 nm. The VO_2 layer (dark grey) was produced by the thermal oxidation of a pure, 100 nm thick V layer at 400 °C for 4.5 h under 0.1 mbar sparse air. According to Electron Energy Loss Spectroscopy (EELS) measurements the topmost 30-50 nm thick part of the oxidized VO_x layer contains VO_2 grains, whereas the bottom 170-190 nm thick part is V_2O_5. The presence of VO_2 at the surface region is also supported by the temperature dependent electrical resistance measurement. The device shows pronounced phase change characteristic, shown in Fig. 1.c. The resistance switching ratio between 30 °C and 100 °C exceeds 600. We anticipate that the discrete jumps in the R(T) curve during the transition are related to the involvement of only a few VO_2 grains in the electrical transport. The electrically induced phase transition could be also triggered by applying triangular voltage signals to the device.

To identify the contribution of the thermal and electronic effects in the device operation, we studied the scaling of the switching parameters as well as the detailed evolution of the device resistance with the base temperature and bias voltage. Fig. 1.d shows I(V) characteristics recorded at different temperatures between 30.4 °C and 66 °C. The set voltages (V_{set}) show a very clear decreasing tendency as the temperature increases, whereas the current right before the switching (I_{set}) is nearly temperature independent. Accordingly, the switching power ($P_{set}=V_{set}\cdot I_{set}$) also shows decreasing trend, however, it does not reach the zero power value at Tc=66.2 °C. Consequently, these trends can not be qualitatively described by either the pure thermally or electrically triggered MIT.

To gain further insight the underlying physical mechanisms performed a detailed analysis of the R(V) curves to determine the conduction phenomena. The high electric-field induced carrier generation can produce a finite slope of the R(V) curve around zero bias, which is presented in the measured data (see dashed linen in Fig 1.e). Several conduction mechanisms were applied to describe the nonlinear I(V) behaviour of VO_2 layers, which all can be summarized in the following form:

$$R(V_{bias},T) \approx R_0(T) \cdot \exp\left[-(V_{bias}/V_c)^{\alpha}\right],$$

where $R_0(T)$ is the temperature dependent low voltage resistance shown in Fig. 1.c, V_{bias} is the voltage drop on the device, V_c is a characteristic voltage, whereas the α exponent specifies the conduction mechanism. The dominant conduction mechanism was determined by fitting the ln(−ln(R/R0)) vs. ln(Vbias) curves to a line (see inset of Fig. 1.e), whose slope, the α parameter were close to unity at all temperatures referring to Zener conduction.

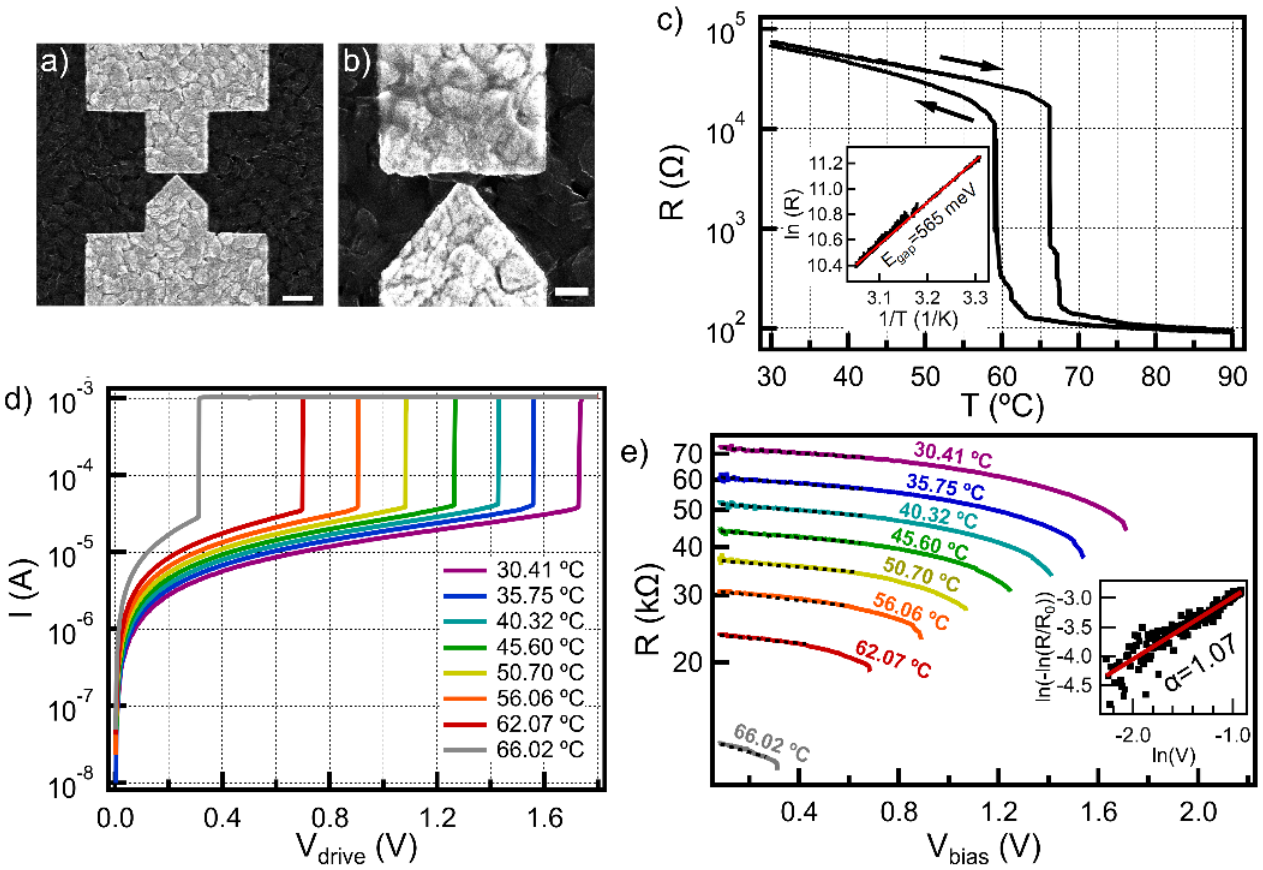

Figure 1: Scanning Electron Microscopy (SEM) image of the device before (a) and after (b) performing the electrical measurements. The scale bar in the initial a) SEM image indicates 500 nm, whereas in panel b) it indicates 200 nm. c) Temperature dependent resistance shows very sharp phase transition, characteristic to VO_2. The arrows indicate the direction of the hysteresis loop. d) Current-voltage characteristics recorded at different base temperatures. The resistive switching occurs at decreasing voltages as the temperature increases. e) R(V) traces measured at different temperatures. All traces show the similar nonlinear current behaviour at low bias voltage (see dashed lines). The inset shows the $\ln(-\ln(R/R_0))$ vs. $\ln(V)$ relation at 56.06 °C base temperature whose slope determines the a exponent, introduced in the equation above.

To better understand the contribution of nonlinear electronic phenomena to switching mechanism, we performed steady-state finite element simulations in COMSOL Multiphysics implementing the exact geometry of the device. The layer structure of the model with the most relevant dimensions is schematically presented in Fig. 2.a, mimicking the result of the TEM and EELS measurements. Fig. 2.a. also shows the considered heat conduction mechanisms (marked by coloured arrows) and thermal boundary conditions (marked by dashed black line). We considered a thermal boundary conductance at the VO_2/Ti interface (h_{th}, purple arrow).

To demonstrate that neglecting either the thermal or the electronic phenomena leads to insufficient description, we plotted a measured R(V) trace at 35.75 °C (black curve) with its best fittings with either a purely thermal or purely electronic model, (Fig. 2.c). The red trace shows the result when the field dependence was eliminated from the model (i.e. $\rho(E,T) = \rho_0(T)$) and the resistance changes solely due to the self-heating effect. Similarly, we simulated the field dependent resistance, assuming no self-heating effect (blue curve). Both models give a poor fit to the measured data. In contrast, Fig. 2.d shows the results of the electrothermal simulation at different base temperatures (black circles with line) using the temperature and electric field dependent resistivity. The measured R(V) curves (coloured curves) are well fitted by the simulation, all of them have correct slope at low bias and follow the same high bias nonlinearity due to the self-heating. The combined electrothermal simulation gives a remarkably precise agreement with the experimental observations. [1]

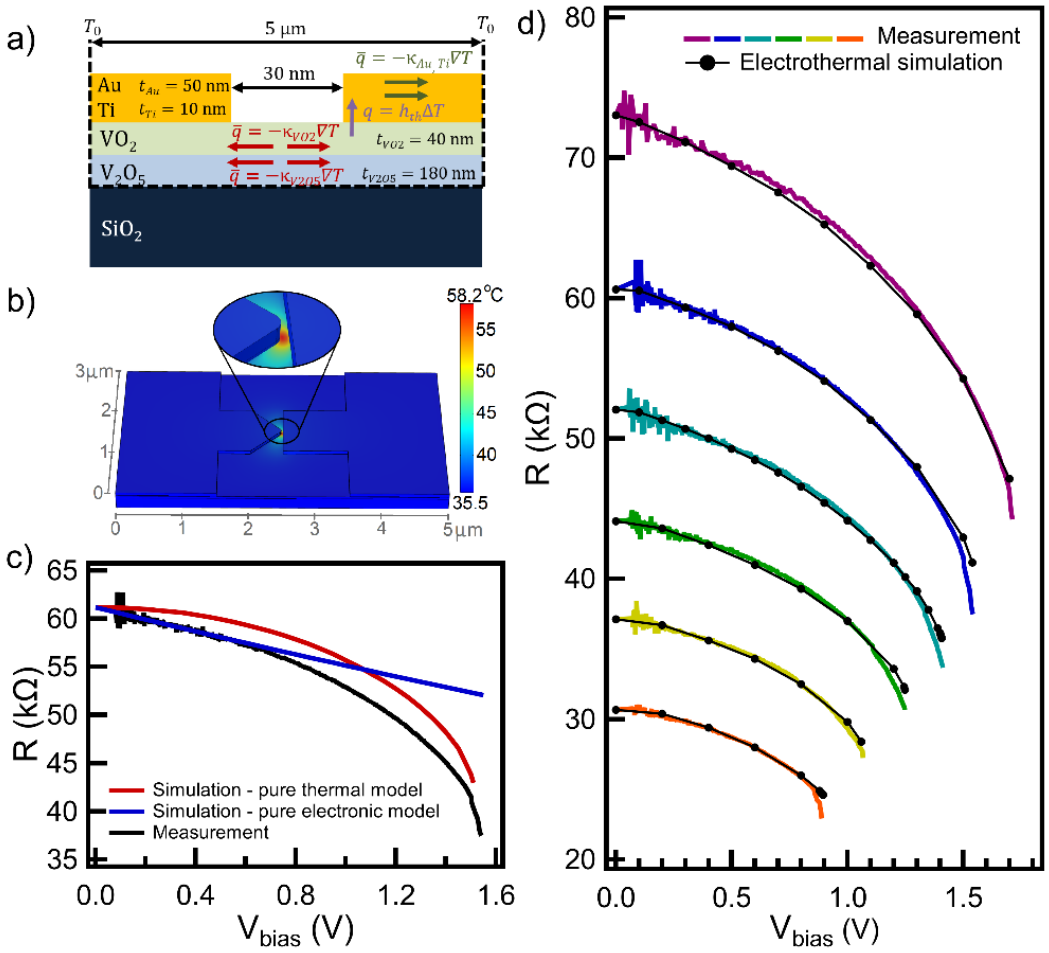

Figure 2: a) Schematic of the thermal model of the device, introducing the most relevant geometry parameters and the heat transfer mechanisms with the corresponding heat equations. b) The simulated temperature profile with V_{bias} = 1.5 V and T_0 = 35.75 °C, showing the realistic device geometry. The magnified view of the gap shows the focused ultra-small active region. c) Results of pure thermal and pure electronic simulation. The thermal model (red curve) cannot reproduce the initial decreasing tendency of the R(V) curve due to the negligible Joule heating. The pure electronic model (blue curve) has a constant nonlinearity due to the lack of Joule heating and diverges from the measured R(V) curve (black) at higher bias. d) Measured (coloured curves) and simulated R(V) characteristics (black curves) using the electrothermal model. The simulated traces show very good agreement with the measurement at each base temperature between 30.41 °C and 56.06 °C.

Related publication

[1] L. Posa, P. Hornung, T. N. Torok, S. Arjmandabasi, Gy. Molnar, Zs. Baji, G. Dražić, A. Halbritter, J. Volk: *Interplay of thermal and electronic effects in the Mott transition of ultrasmall VO_2 phase change memory devices,* submitted to ACS Applied Nano Materials

ALGAN/GAN HETEROSTRUCTURE BASED 3-DIMENSIONAL FORCE SENSORS

TKP2021-NVA-03

P. L. Neumann, J. Radó, J. M. Bozorádi, J. Volk

Tactile sensing is an essential physical-electrical gateway in sensing technology. Creating such sensors is a complex challenge if the goal is to reproduce human-like sensations. Classical MEMS tactile sensor solutions in typical environmental conditions exist few types, but harsh conditions such as space technology or high-temperature range are not solved yet. One proposed material complex is the GaN/AlGaN system.

In this project, a novel AlGaN/GaN heterostructure-based 3D force sensor is proposed. The principle of operation is similar to its Si counterpart: a thin membrane is deformed upon applying a loading force on the Si micro-stick formed on the backside of the membrane (Fig. 1.a). Local strains in four positions of the membrane are measured by semiconductor gauges (Fig. 1.b). By collecting the electrical signals, both the magnitude and the direction of the force can be determined. However, in contrast to conventional Si piezoresistive devices, mechanical strain influences the density of the 2-dimensional electron-gas (2DEG) at the AlGaN/GaN interface by changing the magnitude of the discontinuity in the polarisation vector between the AlGaN barrier and GaN channel layer, that means the external strain could be a proportional modulation factor to the density of the carrier concentration.

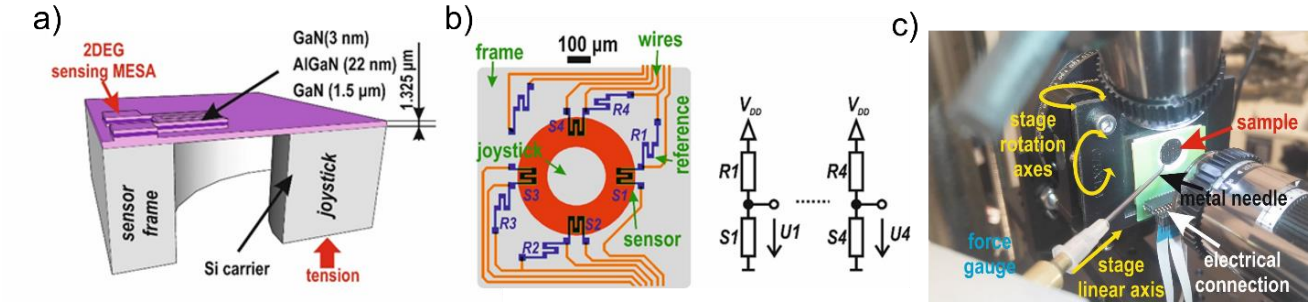

Figure 1: The cross-section shows the quarter of the prepared MESA structure containing the 2DEG layer (a). Top view of the 2DEG force sensor with the sensor elements (S1-S4), the reference elements (R1-R4) and its equivalent circuit (b). Wire-bonded force sensor mounted on a three degrees of freedom vertical sample stage and loaded from the actuator side with a load cell needle and monitored by a USB camera (c).

The mechanical and electromechanical measurements were carried out using a purpose-built system with three degrees of freedom sample holder (Fig. 1.c). The external loading was performed with a medical needle mounted on a force gauge (Andilog Centor Easy). During the alignment and testing, the position of the force gauge and the needle was precisely controlled by translational actuators (ThorLabs) and visually monitored by a USB camera (Dino-Lite Edge). A LabView software-controlled data acquisition module (NI USB 6211 DAQ) was used to power (V_{DD}) the wire-bonded 2DEG force sensor and to collect its response signals (U_1-U_4). The signals were filtered to reduce the noise.

Numerical simulation was carried out by COMSOL Finite Element Method to determine the volumetric strain map in the AlGaN/GaN membrane, which predicts the possible 2DEG modulation to sense the force strength and direction. The simulated object geometry was the same as the original design. Fig. 2 shows the analytically calculated volumetric strain under an applied load of 10 mN. In normal loading direction, pointing to the centre of the Si microstick, the resulting strain is circularly symmetric and shows absolute minimum (ε_{min}=-296 ‰) and maximum (ε_{max}=311 ‰) values close to the outer edge and to the root of the microstick, respectively (Fig. 2.a). That can assume the sensor elements on the membrane will show conformity between its output signals' directions and values. In contrast, for a load force at an oblique angle φ= 45° (where φ is the angle with respect to the normal direction), the simulation result shows a significant asymmetry of the volumetric strain building up in the membrane (Fig. 2.b). The simulation results predict that the asymmetric out voltage will be on the sensor element in the force direction and symmetrical one in the perpendicular direction, but the lower 2DEG modulation effect will be lower.

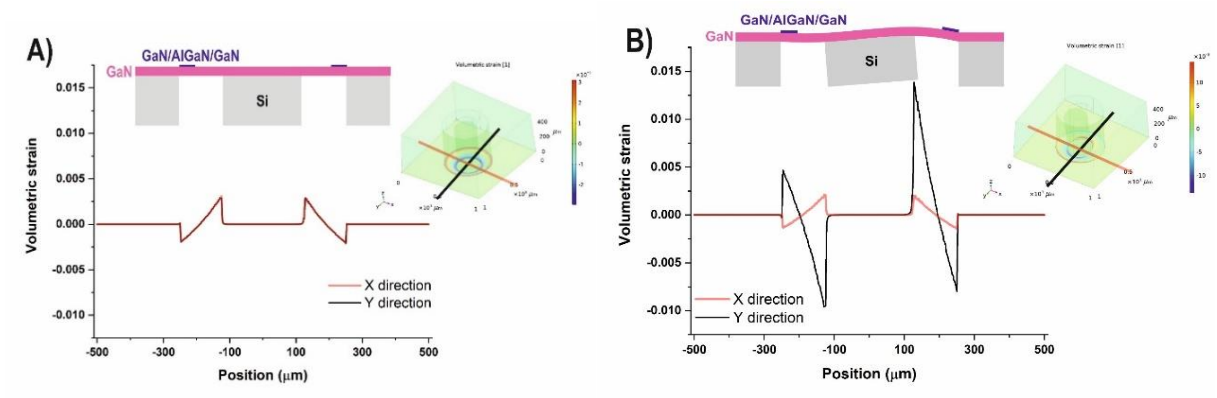

Figure 2: Simulation results of the volumetric strain for normal (φ= 0°) (A) and oblique (φ= 45°) (B) load force, where φ is the angle with respect to the normal direction. The inset shows the simulation results of the deflection and the volumetric strain, indicating the locations of the line cuts.

In the electromechanical experiment, the sensitivity of the force sensor on normal force load was investigated (Fig. 3.a). All four bridges show almost the same voltage response upon increasing load. The sensitivity from the plotted curves is approx. 100 mV/N/V. This value is more than one order higher than the Si base force sensor case, where this sensitivity was ~9 mV/N/V. The recorded voltage signals gave a fast response (< 0.2 s) on the applied load. The response examination was followed by a dynamic normal tension analysis, in which load pulses with increasing magnitude. The individual sensor bridges showed increasing voltage pulses with increasing load and ran roughly together since the stress and the arising strain at the position of the symmetrically arranged MESA elements are similar. In the next experiment, the load force angle was set to φ= 45° (Fig. 3.b) and increased, and then the measured signals trends split in the direction of load force as expected in the simulations. A further plan is to get an accurate tensile sensor for harsh environments is to investigate the temperature sensing and dependency, the direction decoding from the recognized response of the voltage divider, and the matrix arrangement of the sensors to obtain redundancy information for the precise touching information. [1]

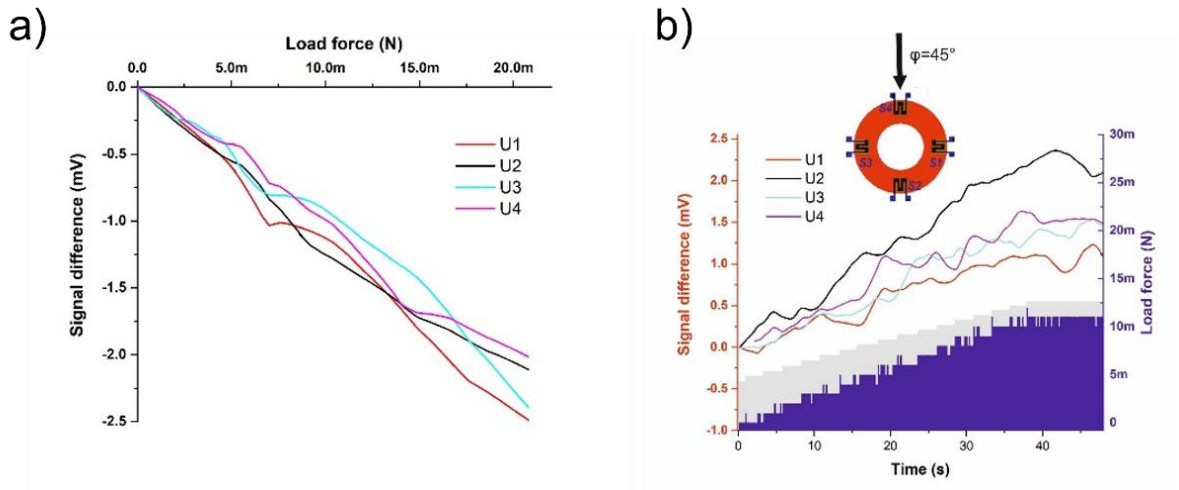

Figure 3: Normal load force response signals of the sensor outputs (a). For a better visualization, at the beginning of the measurement, a reference voltage was taken for each bridge, and only the change as a function of time upon increasing load pulses is shown. Sensor output signal for increasing φ=45° load force as a function of time (b). The grey region represents the needle displacement (total step length ≈ 950 μm).

Related publication

[1] P.L. Neumann, J. Radó, J.M. Bozorádi, J. Volk: *AlGaN/GaN Heterostructure Based 3-Dimensional Force Sensors*, submitted to Micro and Nano Engineering Journal

WEARABLE GAS SENSORS FOR EMERGENCY AND EXTREME CONDITIONS

Thematic Excellence Programme TKP2021-NVA-03

F. Bíró, I. Bársony, Cs. Dücső

Gas sensor applications for wearable devices

In the „ Chemical gas sensors" workpackage of the TKP2021-NVA-03 „Environmental monitoring sensors for emergency and extreme conditions" project we plan to develop wearable gas sensors for detection dangerous gases carry high risk during natural or industrial disaster management (time frame: April 1. 2022 – March 31. 2026). Two families of gas sensors are considered: **1) low cost solid-state chemoresistive sensors** for simple alarming and development of sensor KIT to provide a standard tool for characterize their gas sensing layers and **2) moderate cost optical sensor for more accurate concentration measurements**. The primary goal is the recognition of methane leakage; however, detection of other risky gases will also be investigated.

Microhotplates for chemoresitive sensor

We exploit our previously developed microhotplate structure as the carrier of the gas sensitive material. Regardless the operation principle, these sensors operate at elevated temperatures between 100 – 500°C. The basis of the sensors is a newly developed small diameter (150 μm) microhotplate exhibiting ±1% temperature uniformity on the heated area below 550°C. The stability of the heater is 5000 hours at least at the operation temperature of 530°C, thereby in pulsed mode operation ca. 5 years operation can be achieved. The power dissipation at 500°C is 27mW/1.5V, so the chip can be utilized in portable or wearable devices for personal safety. A utility model protection was given for the microhotplate design in 2021 (*Microheater with uniform surface temperature,* U 20 001150, registration number 5279).

The sensor KIT will be developed by the mid of the project. It comprises two chips: i) a three element sensor chip and a ii) dedicated masking element chip what enables the end-user laboratories to easy adapt their deposition technique by selectively form their sensing layers on the heated area and test its functionality. In 2022 we elaborated the concept and designed the appropriate processing technology including the necessary photomask set.

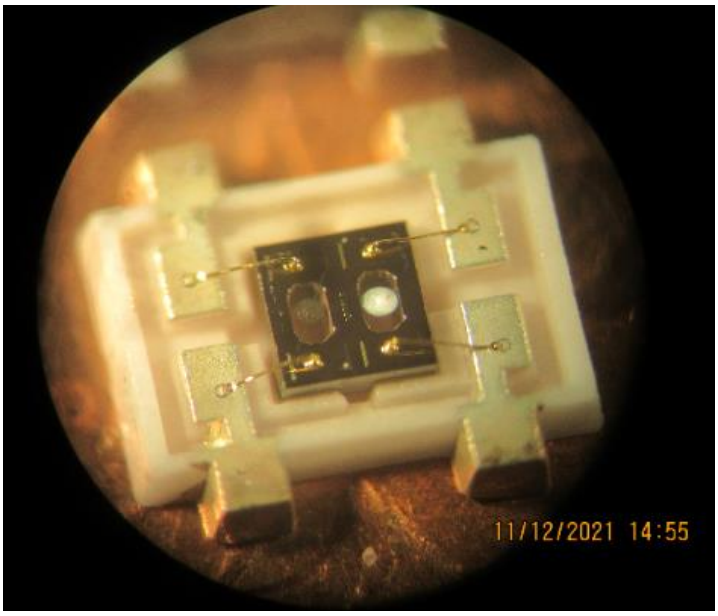

Figure 1: Gas sensor chips in laser micromilled ceramic headers. In this sample the hotplate is covered with catalyst (black on the optical image) and reference suspensions (white) dropped on hotplates (The size of both chips is 1x1mm^2. The same hotplates structure forms the basis of the chemoresistive devices.

Optical gas sensing

We have been investigating the construction and capability of methane detection by non-dispersive operation principle in the mid infrared region. The goal is to develop a complete setup consists of MEMS elements, such as microheaters and reflectors for IR source, optical channels and detectors. Test setup was built from commercial components, whereas the electronics was constructed in modular form for **driving the IR source** and the **appropriate read-out**. Adequate optical systems were constructed to ensure high IR intensity projection on the detector and improve the achievable signal-to-noise ratio with the

applied pathway (30 mm). The preliminary results show that the construction is capable to detect methane in the 500 – 50000 ppm concentration range with the accuracy of 1-10%. Nevertheless, in order to minimize device size and eliminate the thermal effects, we plan to adapt digitized detector chips and elaborate the best sensing methodology. The final goal is to fabricate the smallest possible device composed of our micromachied components and a commercially available detector chip.

Microcalorimeters

Having in hand the **stable heaters** we now focus on other applications also. In cooperation with the University Debrecen we have already started to develop a **micro-calorimetric measuring method** to investigate thermally indicated physical-chemical phenomena in thin films. [1-3]

Related publications

[1] F. Bíró, A. Deák, Cs. Dücső, Z. Hajnal: "*Microheater with uniform surface temperature*", Utility model: U 20 001150, registration number 527

[2] F. Bíró, A. Deák, I. Bársony, N. Samotev, Cs. Dücső: *An analytical method to design annular microfilaments with uniform temperature,* Microsystem Technologies (0946-7076 1432-1858): **28 (11)**, 2511-2528 (2022)

[3] L. Harasztosi, I. A. Szabó, F. Biró, R. Gy. Kiss, G. Battistig: *Microcalorimeter development and calibration based on a twin microheater platform,* Proceedings of the 8th International Conference on Sensors and Electronic Instrumentation Advances, Korfu: International Frequency Sensor Association (IFSA) Publishing, 112-116 (2022)

3D MEMS FORCE SENSOR FOR TISSUE RECOGNITION

H2020-ECSEL-2017-2-783132 "POSITION-II, 2018-2.1.6-NEMZ-ECSEL-2018-00001

J. M. Bozorádi, Cs. Dücső, P. Fürjes

Laparoscopic devices have been widely used in the past decades during surgical procedures. Currently they are the golden standard in minimal invasive surgery. Combining these devices with robotic platforms, most notably the Da Vinci system, is more and more common. Minimally Invasive (robotic) Surgery (MIS) offers several advantages for the patients, although the lack of sensory feedback for the surgeon is also a barrier in its progress. Collecting immediate multi-parametric information about the physical and anatomic conditions of tissues is crucial for the operator to precisely control the robotic actions or support the tissue recognition and pathologic characterization. Smart devices with integrated MEMS force sensors can provide such feedback and improve the safety of these interventions or help in on-site pathologic decisions.

Our goal was to develop a novel device with integrated micromachined 3D force sensors to provide tactile information about the different organs and tissues touched. Piezoresistive force sensory units were integrated with dedicated readout electronics and precisely controlled linear motors solving the accurate tissue deformation to provide more information about the mechanical (elastic) parameters of the analysed materials. In the present work we demonstrate the complex, automatized measurement system – as well as hardware and software solutions – which is capable of implementing in vitro mechanical tissue characterization and thus provides elastomeric and pathological data (see Fig. 1).

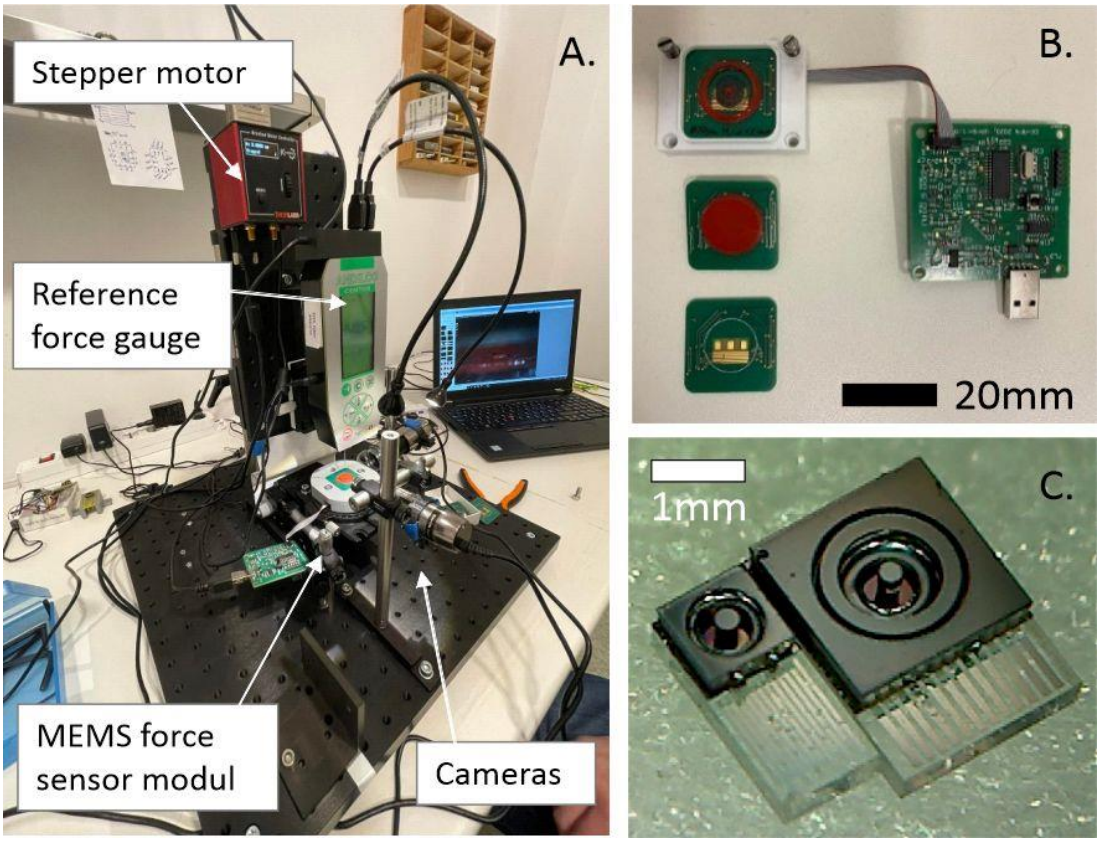

Figure 1: Measurement setup developed for mechanical characterization of elastomers and tissues (A.). The device contains dedicated electronics (B.) for readout and processing the signals of the integrated piezoresistive MEMS 3D force sensors (C.).

We designed and manufactured 3D piezoresistive force sensors by silicon micromachining technology and mechanically integrated in the appropriate biocompatible packaging and elastic coverage. Application specific readout electronics were also elaborated to solve the analog-digital signal conversion, initialization, noise filtering and the communication with a LabVIEW data acquisition user interface. A custom built Thorlabs stage equipped with a nanometre precision stepper motor and controlled by the LabVIEW based driver interface was used for actuation. Preliminary calibration tests were accomplished to evaluate and compare the force signals of the integrated MEMS sensors to a reference Andilog force gauge as the function of the material deformation.

Tactile measurements were implemented on artificial samples and real animal tissues to prove the feasibility of the device for biomechanical screening during Minimal Invasive Surgery or pathological analysis. The applicability of the setup was proved by differentiation the mechanical behaviour – calculated elastic parameters (Young-modulus) – of various

polydimethylsiloxane (PDMS) elastomer samples as the function of their curing agent / elastomer mixing ratios. The elastic properties of the PDMS samples were similar to the commonly published values. After calibration and setup of the packaged MEMS sensors real bovine gastric samples were also characterised and its elastic parameters were also calculated (see Fig. 2).

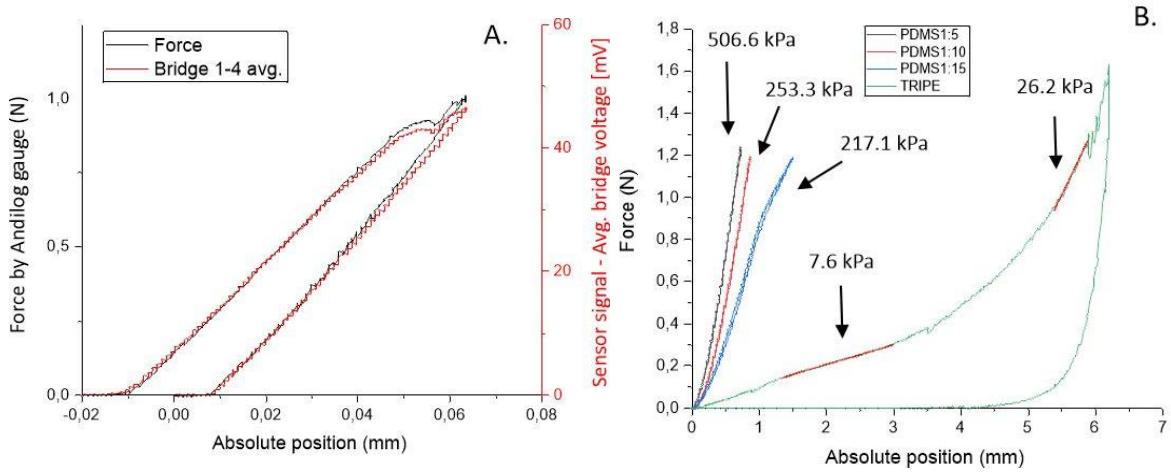

Fig. 2: Deformation dependent signal of the piezoresistive MEMS sensors calibrated by reference force gauge (A) and the measured force values during the deformation of different PDMS samples and real tissue material (bovine gastric) and the calculated elastic parameters (Young-modulus) (B).

The results also demonstrate the deformation dependent and hysteretic behaviour of the artificial viscoelastic and biological samples also, as the Young modulus is continuously changing during the loading procedure (between the values of 7,6 kPa and 26,2 kPa in case tripe). Both of these values were validated and confirmed by different literatures, which correlates with the hardening phenomena of real tissues experienced by surgeons during stapling procedures. On the basis of the results both a compact measurement setup and a prototype electronics were developed for in vitro human tissue measurements. [1-3]

Related publications

[1] J. Radó, R. Dekker; M. C. Louwerse, V. A. Henneken, M. Peters, P. Fürjes, Cs. Dücső: *Force Sensor Chip With High Lateral Resolution for Artificial Skin and Surgical Applications,* IEEE Sensors Journal, **22 (19),** 18359 – 18365 (2022)

[2] P. Fürjes: *Tactile sensing and tissue recognition in Minimal Invasive Surgery - Smart laparoscopes and surgery robots,* SEB2022 – Sustainable Electronics & Bioanalytics Workshop 2022, Tallinn, Estonia, 2022 (invited keynote)

[3] J. M. Bozorádi, A. Nagy, J. Radó, P. Földesy, I. Bársony, G. Papp, Cs. Dücső, P. Fürjes: *Characterisation tissue elasticity by MEMS force sensors*, MNE-ES 2022 - Micro and Nano Engineering (MNE) & Eurosensors 2022 Conferences, Leuven, Belgium, 2022

MICROFLUIDIC METHODS FOR PARTICLE AND CELL MANIPULATION – FILTERING, SORTING, CAPTURING

Thematic Excellence Program TKP2021-EGA-04

A. Bányai, P. Hermann, O. Hakkel, E. L. Tóth, P. Fürjes

In several diagnostic applications, the main goal is to develop **microfluidic cartridge** for certain subtasks of **sample preparation and handling**, which then can be integrated into an optical or electro-chemical measurement instrument. The integrated Lab-on-a-Chip cartridge must include transport and filtration of the liquid sample, positioning of bacteria in the detection chamber over the sensing layer. Hydrodynamic principle based **microfluidic filters and lateral concentrating structures** were developed and evaluated by their filtration efficiency for different particle sizes, and by the target loss ratio in the size range of bacteria.

Filtration efficiencies of crossflow type microfilters for E.Coli separation

Crossflow filtration is a pressure-controlled separation method for size dependent segregation of fine particles, microorganism, spores or even micelles. It is a preferred technology in the food industry to remove bacteria or in healthcare for high-throughput plasma filtration. In contrast to dead-end filtration processes, the filter surface is parallel to the liquid flow in case of crossflow separation, thereby significantly reducing the possibility of clogging. The particle separation in these crossflow systems is based on the pore size, although the filtration process is sensitive to the flow rate, transmembrane pressure, membrane resistance, layer resistance, and particle size distribution in the suspension.

Crossflow microfluidic systems with parallel filter structure were parameterized and designed to optimize the separation efficiency and the amount of the target in the filtrate. For preliminary tests multi-disperse fluorescent beads (with 2 µm, 6 µm, 16 µm diameters) were used as a model representing the particles and cells in urine. The target E.coli was initially modelled with 1.97 µm diameter polystyrene beads before applying GFP-labeled E. coli bacteria. The trajectories of the fluorescent beads and GFP-E.colis, the developing compaction layer on the filter's surface and consequently the degree of target loss were characterized by fluorescent microscopy. The efficiency of the filtration was determined by particle counting by Bürker chamber and by Luna-II imaging based cell counter also. The columnar and weir type filter architectures were compared: the latter was considered more advanced.

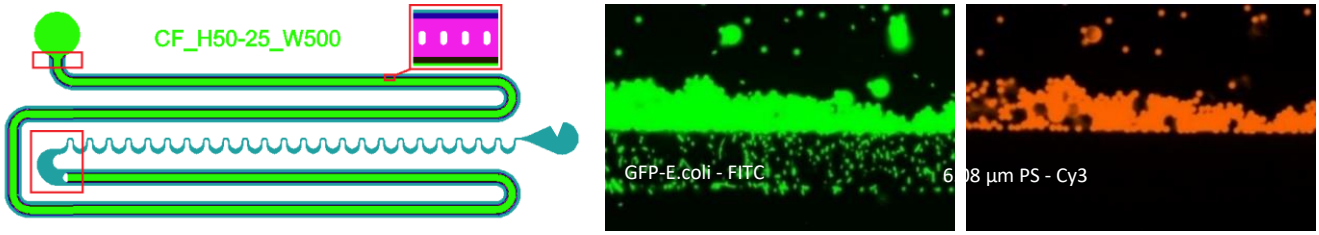

Figure 1: Crossflow filter architecture (left) and the structure of the compaction layer during filtration (right)

Lateral focusing model particles and real cell samples

After filtering every larger component of the urine sample, the permeated bacteria must be vertically and possibly laterally focused in the detection chamber in order to achieve high trapping efficiency on the functionalized surface. The inertial focusing phenomenon was investigated, which can be used as a passive method for sample preparation and target manipulation in case of particulate suspensions. Asymmetric channel geometry was designed to apply additional inertial forces besides lift forces to promote laterally ordered particles to achieve sheathless focusing or size dependent sorting. In these channels secondary flow – counter rotating Dean vortices – also promotes lateral focusing further to a single point beside the inertial forces. The parameter dependence of the fluidics were determined with the ratio of particle size (a) and the hydrodynamic channel diameter (D_h): $a/D_h > 0.07$, above which successful focusing is expected. The evolving hydrodynamic forces were tailored with altered channel parameters (width and height), and different flow rates, to get a better understanding of smaller beads' lateral migration. The behaviour of the microfluidic system was tested by using artificial fluorescent beads with different sizes (diameter of 15.8 µm – 6.08 µm – 1.97 µm beads) and real samples as GFP-modified E. coli, red blood cells, yeast cells and HeLa tumour cells also.

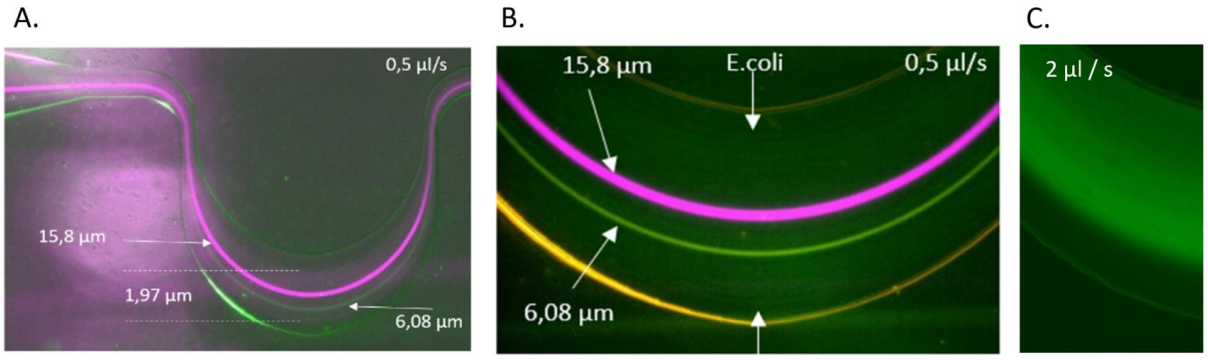

Figure 2: Lateral focusing in pressurized flow with different particle sizes. A.) Lateral focusing of beads at 0.5 µl/s flow rate: 15.8 and 6.08 µm beads, and concentration of 1.97 µm beads at the end of the lateral focusing unit. B.) E.coli could not be focused in the very same structure, shape: stick, dimensions: 0.5 and 2 µm. C.) E.coli concentration at decreased channel height (15 µm), and increased flow rate (2 µl/s).

Computational Fluid Dynamics (CFD) simulation was also performed using COMSOL Multiphysics (version 5.3a) to analyse and predict particle movement in the specially designed microchannels. Finite Element Modelling (FEM) is applied to numerically calculate the Navier-Stokes equation considering laminar flow due to the low Reynolds number regime. Particle tracing module was used to calculate particle trajectories in the pre-solved velocity field. Dean vortices evolving in curvature are visualised in Fig. 3 and the Poincare map represents the calculated positions of the particles at the outer surface of the microfluidic systems.

The position and extent of the focused region were investigated using polystyrene fluorescent beads with different bead diameters (Ø = 0.5 – 16.5 µm) at flow rates 0.5 – 2 µL/s. Size-dependent focusing generated a precise map of the equilibrium positions of the spherical beads at the end of the periodically altering channels. Comparing them with the four types of living cells – E.coli – RBC – Saccharomyces cerevisiae – HeLa cells – they gave a good benchmark for focusing multi-dimensional particles and cells (see Fig. 4).

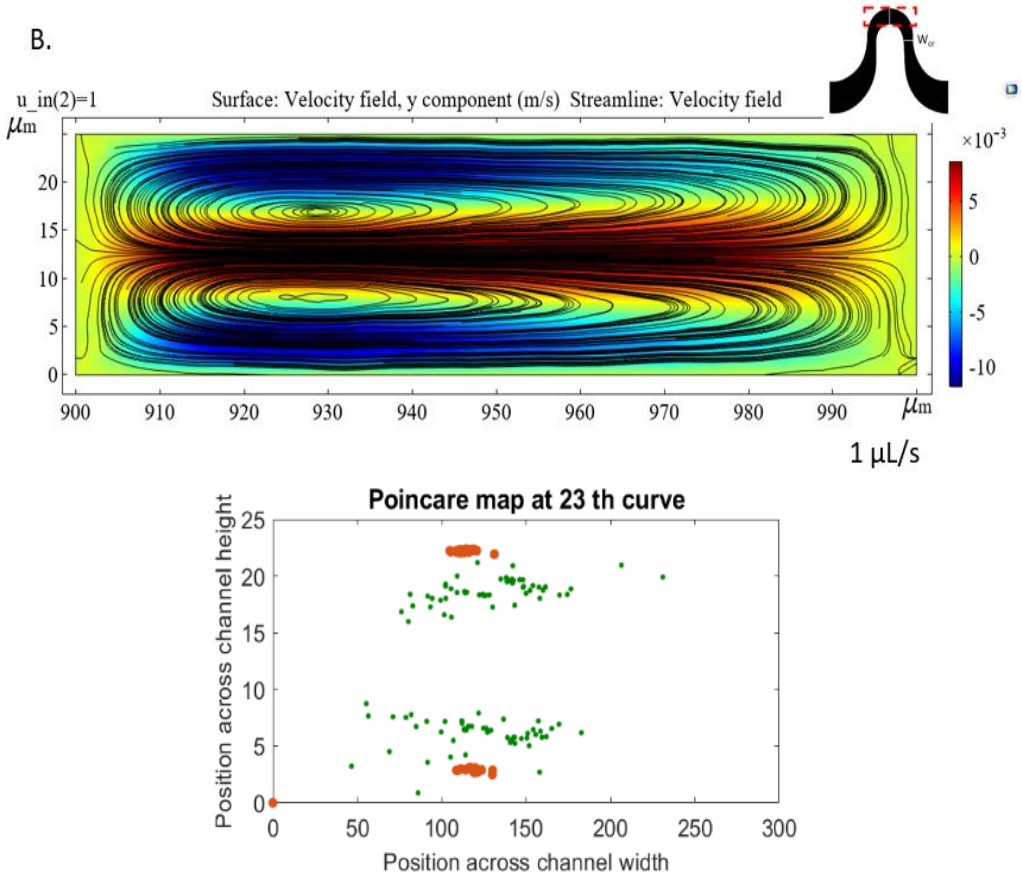

Figure 3: Dean vortices evolving in the curvatures (up) can be visualised by Finite Element Modelling. The Poincare-map (down) shows the equilibrium positions of the model beads (diameters: 15.8 µm and 6.08 µm) in the channel cross-section. The presence of the Dean vortices depicted in the smaller bend in the channel cross-section.

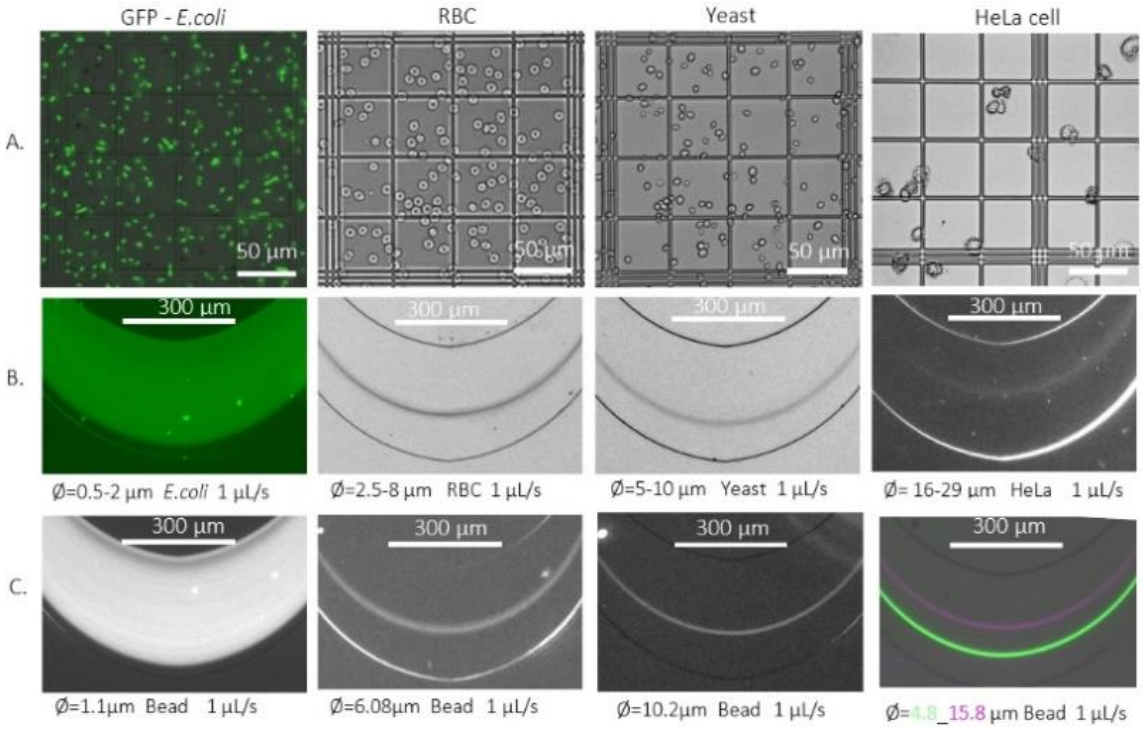

Figure 4: Lateral focusing of biological cells and their rigid model beads at 1 µL/s flow rate. The size and morphology of the applied biological sample (A), and their lateral positions (B) were studied. In (C) are the polystyrene bead profiles that best describes the lateral focusing position and profile of the given cell sizes.

Single cell trapping and viability testing

In vitro testing of cell populations or individual cells in artificial systems that model their real environment is highly prospective from a biomedical and environmental point of view. Specially designed microfluidic systems allow the development of such a controllable chemical environment that is comparable to the size of cells. The application of such Organ-on-chip devices, which integrate sensing functions, can be a significant step in the research of pharmaceutical agents, but also in facilitating the spread of personalized medicine. Cell trapping and fluorescent dying are powerful tools that enable the investigation of cell viability and proliferation in microfluidic structures.

A microfluidic system capable of trapping cells individually was created and the viability of yeast cells was investigated. The microfluidic chip had narrowing channels with the dimensions compatible with the size of cells and being capable of trapping yeast cells (diameter: 5-10 µm). The optimal concentration of cell suspension was determined to ensure the trapping of individual cells in the traps, thus conducting single-cell tests. After the cells were trapped a fungicide solution (50 mg/l Penconazole - $C_{13}H_{15}C_{l2}N_3$ - Syngenta TOPAS 100 EC) was injected into the fluidic channels and then the dead cells were dyed with propidium iodide fluorescent dye (see Fig. 5). Concentration dependent physiological effect on fungi was observed by fluorescent microscopy and compared to the results of optical spectroscopy. The established microfluidic system has been proved capable of trapping individual cells and observing their physiological processes in artificial chemical environment.

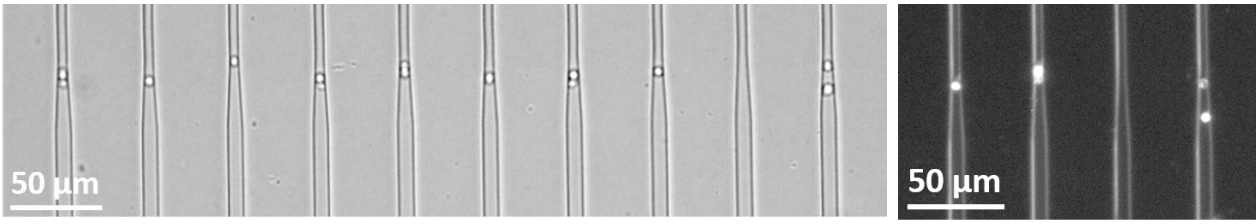

Figure 5: Captured cells in microfluidic systems (left) and dyed with propidium iodide in fungicide chemical environment (right)

Magnetophoretic trapping in microfluidic system

Immunomagnetic separation methods based MEMS systems are quite straightforward for high-volume particle separation for bioanalytical applications. In this work different microfluidic channel geometries and secondary morphological inhomogeneities were applied to modulate the local magnetic trapping efficiency. The effect of the combined magnetophoretic and hydrodynamic phenomena was analysed experimentally and by finite element modelling to optimise the trapping pattern and to increase the local distribution of captured beads at higher flow rates.

The high-volume flow-through magnetophoretic separation method was tested in specially designed microfluidic devices. Permanent neodymium magnets, attached from the bottom side of the channel ensured the magnetic flux. The applied channel

heights (25, 50 µm) and morphological inhomogeneities – as secondary columns and walls (C-shape, D-shape, Zig-zag) in the middle of the channel – were varied to modulate the location dependent trapping efficiency and to form proposed lateral pattern of the magnetic beads (Ø= 2.8 µm) even at higher flow rates (0.5-1-2 µL/s).

The trapping pattern of magnetic beads were recorded, and the experimental results were compared to FEM simulations performed by COMSOL Multiphysics software. The combined effects of the superpositioned magnetophoretic and hydrodynamic processes were investigated – considering the flow velocity field evolving in the chamber around the built in inhomogeneities. Based on the developing local concentration distribution of the magnetic beads the applicability of the multi-domain finite element model was proved to represent and predict the trapping behaviour of the magnetic beads realistically at even higher flow rates. [1-6]

25µm_1µl/s_2.8µm_ H: 10x4x2 mm³_N52

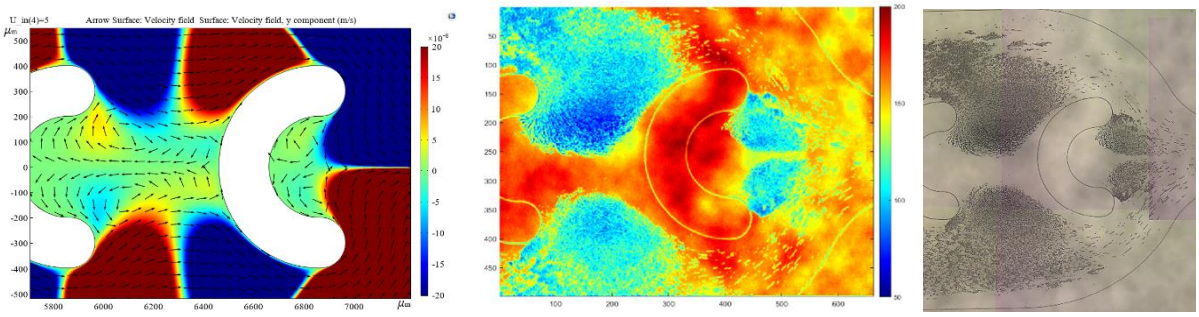

Figure 6: Flow velocity distribution (left) determines the magnetophoretic trapping of ferromagnetic particles in the microfluidic systems (right)

Related publications

[1] A. Bányai, M. Varga, P. Fürjes: *Filtration efficiencies of crossflow type microfilters for E.Coli separation,* Mátrafüred International Meeting on Chemical Sensors 2022, Visegrád, Hungary, 2022

[2] A. Bányai, E. L. Tóth, M. Varga, P. Fürjes: *Geometry-Dependent Efficiency of Dean-Flow Affected Lateral Particle Focusing and Separation in Periodically Inhomogeneous Microfluidic Channels,* Sensors **22 (9),** 3474 (2022)

[3] E. Farkas, R. Tarr, T. Gerecsei, A. Saftics, K. D. Kovács, B. Stercz, J. Domokos, B. Peter, S. Kurunczi, I. Szekacs, A. Bonyár, A. Bányai, P. Fürjes, Sz. Ruszkai-Szaniszló, M. Varga, B. Szabó, E. Ostorházi, D. Szabó, R. Horváth: *Development and In-Depth Characterization of Bacteria Repellent and Bacteria Adhesive Antibody-Coated Surfaces using Optical Waveguide Biosensing,* Biosensors 12 : 2 Paper: **56 ,** 20 (2022)

[4] L. Bató, P. Fürjes: *A fluorescent detection method to measure the diffusion coefficients of proteins in a free-diffusion based microfluidic system,* Lab-on-a-Chip and Microfluidics Europe 2022 Conference, Rotterdam, The Netherlands, 2022

[5] L. Bató, P. Fürjes: *Microfluidic device for single cell trapping and viability testing,* Mátrafüred International Meeting on Chemical Sensors 2022, Visegrád, Hungary, 2022

[6] A. Bányai, E. L. Tóth, P. Fürjes: *Effects of channel morphology on magnetophoretic separation in microfluidic particle trapping,* Lab-on-a-Chip and Microfluidics Europe 2022 Conference, Rotterdam, The Netherlands, 2022

DEVELOPMENT OF NEAR INFRARED LEDS AND SPECTROSCOPIC APPLICATIONS

Moore4Medical, ECSEL Innovation Actions ECSEL-2019-1-IA-876190

B. Beiler, K. Pankász, F. Bíró, J. M. Bozorádi, Cs. Dücső, P. Fürjes, Z. Szabó

Infrared spectroscopy is a very popular measurement technique especially in food industry, pharmaceutical industry and agriculture for the detection and measurement of organic materials. The -OH, -NH and -CH functional groups found in organic substances can frequently be detected by spectroscopy through absorbance measurements at the resonance wavelength of valence-bond vibrations. The measured wavelengths are 4-2.5 µm, while the signal to noise ratio of photon detectors is low due to thermal noise at room temperature. The 1st-3rd harmonic absorption bands are located in the range of the Near Infrared (NIR), where smaller signals can be measured effectively in practice. NIR LEDs have narrow wavelength, therefore they are suitable for measurements at given wavelength. Further advantages of LEDs compared to incandescent lamps are their small dimensions, high efficiency, and low power consumption, which is critical in small handheld devices.

GaInAsP/InP is an ideal material system for the fabrication of double heterostructure devices as the emission wavelength is easily tuneable between 950-1650 nm. As InP has higher bandgap than the lattice-matched GaInAsP active layer the absorption losses inside the device structure can be minimized. In order to tune the emission wavelength of the LED, the composition of the semiconductor light-emitting layer has to be properly set. Our high quality single peak LED chips (1220nm) have a stable market with a business partners as SENOP Oy (Fi) and Anton Paar Ltd. (At).

Development multiple wavelength or broadband IR-LED

In the cases when a broader emission-peak is preferred for spectroscopic applications, multiple solutions are known. One of them is where the primary light coming from the active layer of the diode excites the second smaller band gap epitaxial layer producing secondary light by photoluminescence. The partly transmitted primary and the secondary light together result in a broader spectrum. Our research group has already demonstrated the method by integrating one active and one photoluminescent layer using Liquid Phase Epitaxy (LPE). Specific InGaAsP/InP layer structures were grown by LPE to fabricate wide emission-spectrum near-infrared LEDs. The final multilayer structure could be achievable in two consecutive LPE growth steps: by growing 2 InGaAsP photoluminescent layers with the emission peaks of ca. 1320 nm and 1500 nm first and by growing other photoluminescent (1650 nm) and the active (1220 nm) layers in the second step.

Samples were characterized by optical transmittance and photoluminescence measurements right after each LPE growth steps. The derivative transmittance spectrum shows information about the optical band gap, thickness and quality of the grown layers. The photoluminescence-intensity of the layers depends on the thickness of the InP separation layers due to the optical and charge carrier coupling, too. Scanning electron microscope was used to measure layer thicknesses and to verify epitaxial crystal formation. The LED chips were characterized electrically and optically as well. The I-V curves showed the expected diode characteristics while the four emission peaks appeared on the emission spectrum. The slightly unbalanced emission spectrum can be improved by precisely adjusted layer thicknesses. The integrated emitted optical power is ca. 1/3 of the optical power of the standard 1220 nm LED. This loss is due to the energy difference of the primary and secondary photons but implies high conversion efficiency. [1]

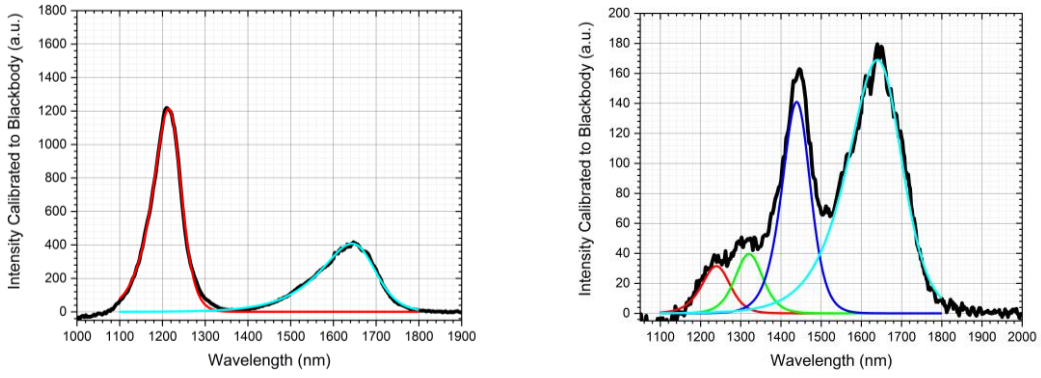

Figure 1: Optical radiation spectra of different multi-layered IR-LED structures (combinations of 2 (left) and 4 (right) wavelengths)

Related publication

[1] Z. Szabó, V. Rakovics, B. Beiler, P. Fürjes: *Wide emission-spectrum NIR-LED based on in-chip efficient photon-recycling*, ICEL 2022 – 13th International Conference of Electroluminescence and Optoelectronic Devices, London, UK, 2022

PLATE READER-COMPATIBLE MICROFLUIDIC CHAMBERS FOR FLUORESCENT SPECTROSCOPY

Horizon Europe Marie Skłodowska-Curie Actions 101065044 - POC-TDM

D. Bereczki, A. Füredi, P. Fürjes

Fluorescence spectroscopy is a widespread method to measure concentrations of specific drug molecules such as Active Pharmaceutical Ingredients (APIs) or their impurities. It is also commonly used to determine the content of components in biological samples and to characterize the mechanism of reactions between proteins and small-molecule drugs. The emitted fluorescent wavelength and the intensity can be characteristic signals of a chosen molecule conformation and concentration by fluorescent spectroscopy. Plate readers or benchtop spectrophotometers are appropriate for screening these molecules. To analyze reduced sample volume, a device-compatible microfluidic cuvette should be applied. Considering UV-VIS range excitation, a proper material selection for the microfluidic system is crucial to ensure appropriate sensitivity. To reduce the sample volume a plate reader-compatible microfluidic system was designed and fabricated by soft lithography. For increased sensitivity, the geometric parameters of the microfluidic structure were optimized by modifying the chamber diameter and depth.

For VIS range excitation, the spectral fluorescent properties of the well-known Alexa Fluor 350 dye were screened by Tecan Spark Plate Reader in both microplate and the manufactured microfluidic chip. The applied glass window material was suitable for excitation above 350 nm. The signal intensity and linearity were tested by applying well-designed microfluidic chambers for 20 µl sample volume and compared to conventional microplate-based spectrophotometric methods. To characterize the applicability of the specific cuvette in the UV excitation range, window materials – glass and fused silica – were compared by analysing the fluorescent emission spectra of G-1™ PLUS (Vitrolife) cell culture media containing 5 mg/mL Human Serum Albumin (HSA). Consequently, advanced sensitivity and excellent linearity were achieved by using a well-designed microfluidic cuvette and the plate reader-compatible structure, what is appropriate to determine the concentration of APIs having fluorescent characteristics in the UV-VIS range. [1-2]

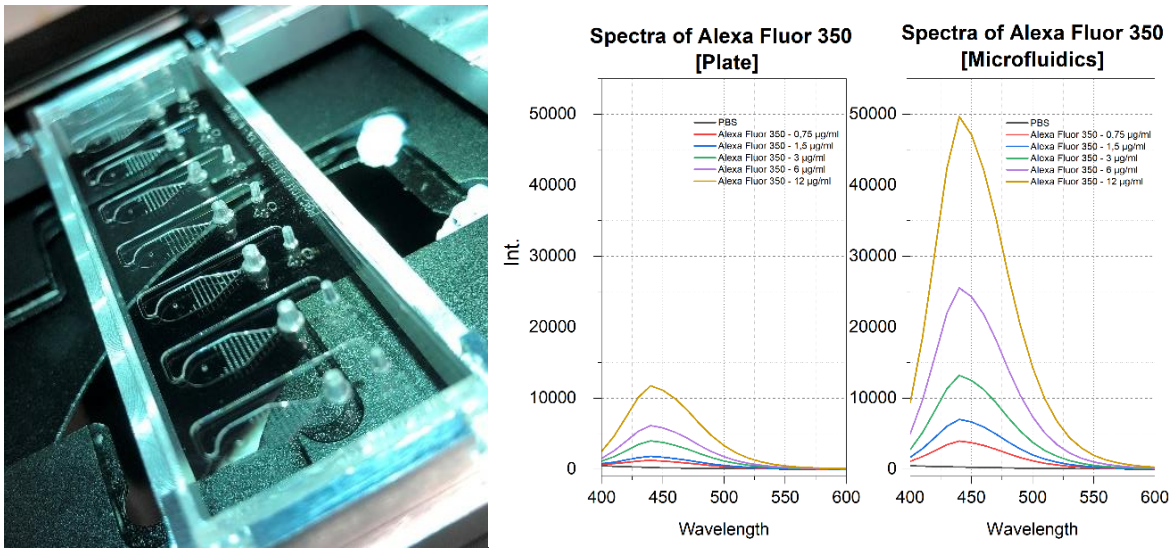

Figure 1: Plate Reader-compatible microfluidic cuvette (A) and optical spectra of Alexa Fluor 350 dye (B) compared in a plate and in microfluidic chip – measured in 5 different concentrations (0,75-12 µg/ml)

Related publications

[1] D. Bereczki, A. Füredi, P. Fürjes: *Plate reader compatible microfluidic cuvette for UV-excited fluorescent spectroscopy,* Lab-on-a-Chip and Microfluidics Europe 2022 Conference, Rotterdam, The Netherlands, 2022

[2] D. Bereczki, A. Füredi, P. Fürjes: *Plate reader compatible microfluidic chambers for fluorescent spectroscopy,* Mátrafüred International Meeting on Chemical Sensors 2022, Visegrád, Hungary, 2022

CHARACTERIZATION OF THE DISSOLUTION OF WATER MICRODROPLETS IN OIL

LP2012-26/2012 Lendület, OTKA ERC_HU 117755, and OTKA KKP129936

T. Gerecsei, R. Ungai-Salánki, A. Saftics, I. Derényi (ELTE), R. Horváth, B. Szabó (ELTE)

The main objectives are to develop highly sensitive and reliable label-free high-content optical methods. Water in oil emulsions have a wide range of applications from chemical technology to microfluidics, where the stability of water droplets is of paramount importance. Here, using an accessible and easily reproducible experimental setup we describe and characterize the dissolution of water in oil, which renders nanolitre-sized droplets unstable, resulting in their shrinkage and disappearance in a time scale of hours. This process has applicability in creating miniature reactors for crystallization. We generated nanolitre-sized water droplets dispersed in oil and observed that they gradually shrank and disappeared in a few hours. Using an easily reproducible and low-cost setup based on a spinning Petri dish to generate the nanolitre scale droplets and an inverted microscope to observe them (Fig. 1), we monitored the contact radius and the volume of droplets, without the need for specialized droplet printing equipment [1].

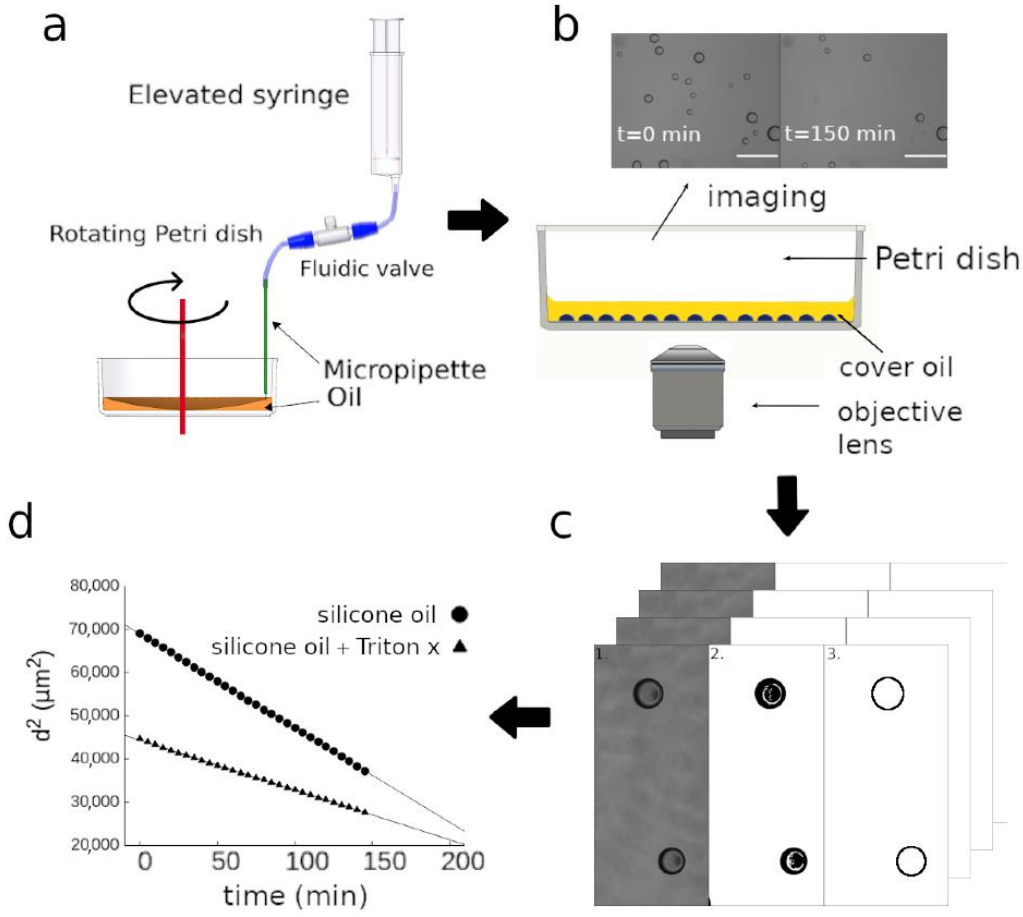

Figure 1: The workflow of droplet diameter measurements. (a): The droplets are generated by a water-filled micropipette immersed in a rotating Petri dish containing oil. (b): The Petri dish with the w/o emulsion is placed on an inverted microscope and images are taken in time-lapse mode. Scale bars indicate 100 µm. (c): Image stacks are segmented to detect and track the droplets. (d): Diameter of droplets is automatically measured to plot the curves of droplet dissolution.

Related publication

[1] T. Gerecsei, R. Ungai-Salánki, A. Saftics, I. Derényi, R. Horvath, B. Szabó: *Characterization of the dissolution of water microdroplets in oil*, Colloids and Interfaces **6,** (2022)

DEVELOPMENT AND IN-DEPTH CHARACTERIZATION OF BACTERIA REPELLENT AND BACTERIA ADHESIVE ANTIBODY-COATED SURFACES USING OPTICAL WAVEGUIDE BIOSENSING

LP2012-26/2012 Lendület, OTKA ERC_HU 117755, TKP2021-EGA-04, OTKA KKP129936 and OTKA PD 131543

E. Farkas, R. Tarr, T. Gerecsei, A. Saftics, K. D. Kovács, B. Stercz (SE), J. Domokos (SE), B. Péter, S. Kurunczi, I. Székács, A. Bonyár (BME), A. Bányai, P. Fürjes, Sz. Ruszkai-Szaniszló (77E), M. Varga (77E), B. Szabó (77E), E. Ostorházi (SE), D. Szabó (SE), R. Horváth

Bacteria repellent surfaces and antibody-based coatings for bacterial assays have shown a growing demand in the field of biosensors, and have crucial importance in the design of biomedical devices. We described an Optical Waveguide Lightmode Spectroscopy (OWLS)-based method supporting the development of bacteria repellent surfaces and characterize the layer structures and affinities of different antibody-based coatings for bacterial assays (Fig. 1). The best performance in the biosensor measurements was achieved by employing a polyclonal antibody in combination with protein A-based immobilization and PAcrAM-P blocking of nonspecific binding. Using this setting, a surface sensitivity of 70 cells/mm^2 was demonstrated [1].

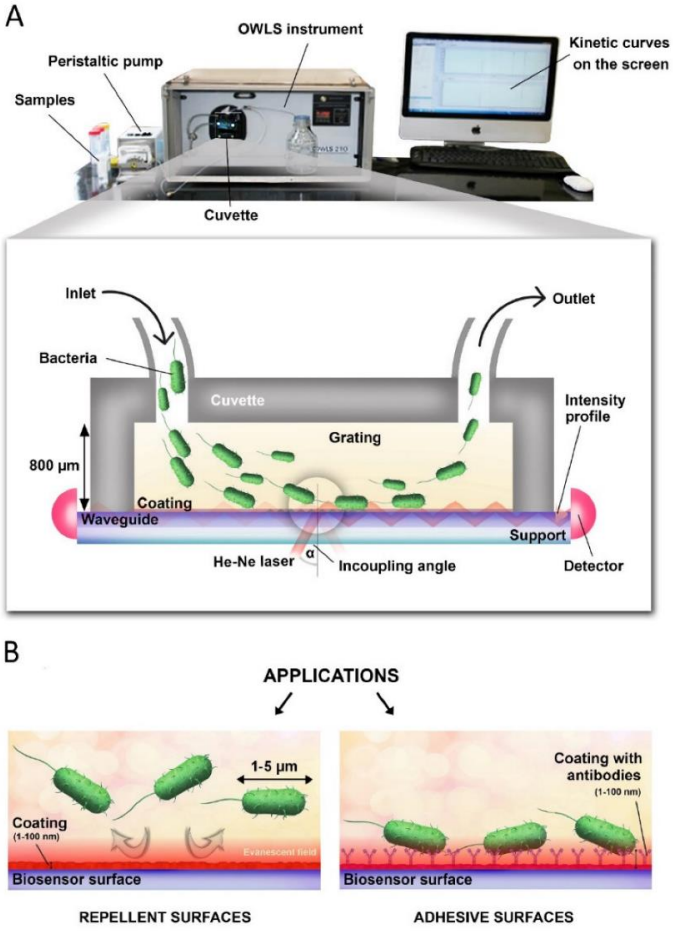

Figure 1: *(A) Cross-sectional view of the OWLS cuvette and the basics of optical detection. Laser light is coupled into an optical waveguide layer by a surface grating where it propagates by total internal reflection to a photodetector placed at the end of the waveguide. Adsorbing bacteria shift the resonant angle (a). (B) OWLS is an ideal tool for testing and developing both bacteria repellent and bacteria adhesive surfaces.*

Related publication

[1] E. Farkas, R. Tarr, T. Gerecsei, A. Saftics, K. D. Kovács, B. Stercz, J. Domokos, B. Péter, S. Kurunczi, I. Székács, A. Bonyár, A. Bányai, P. Fürjes, Sz. Ruszkai-Szaniszló, M. Varga, B. Szabó, E. Ostorházi, D. Szabó, R. Horváth: *Development and in-depth characterization of bacteria repellent and bacteria adhesive antibody-coated surfaces using optical waveguide biosensing,* Biosensors, **12,** (2022)

SINGLE-CELL ADHESIVITY DISTRIBUTION OF GLYCOCALYX DIGESTED CANCER CELLS FROM HIGH SPATIAL RESOLUTION LABEL-FREE BIOSENSOR MEASUREMENT

LP2012-26/2012 Lendület, OTKA ERC_HU 117755, TKP2021-EGA-04, OTKA KKP129936 and OTKA PD 131543

N. Kanyó, K. D. Kovács, S. V. Kovács, B. Béres, B. Péter, I. Székács, R. Horváth

The glycocalyx is a cell surface sugar layer of most cell types that greatly influences the interaction of cells with their environment. Interestingly, cancer cells have a thicker glycocalyx layer compared to healthy cells, but to date, there has been no consensus in the literature on the exact role of cell surface polysaccharides and their derivatives in cellular adhesion and signalling. In our study, a high spatial resolution label-free optical biosensor was employed to monitor the adhesivity of cancer cells both at the single-cell and population level (Fig. 1). Population-level distributions of single-cell adhesivity were first recorded and analyzed when ChrABC was added to the adhering cells. The presented results open up new directions in glycocalyx related cell adhesion research and in the development of more meaningful targeted cancer treatments affecting adhesion [1].

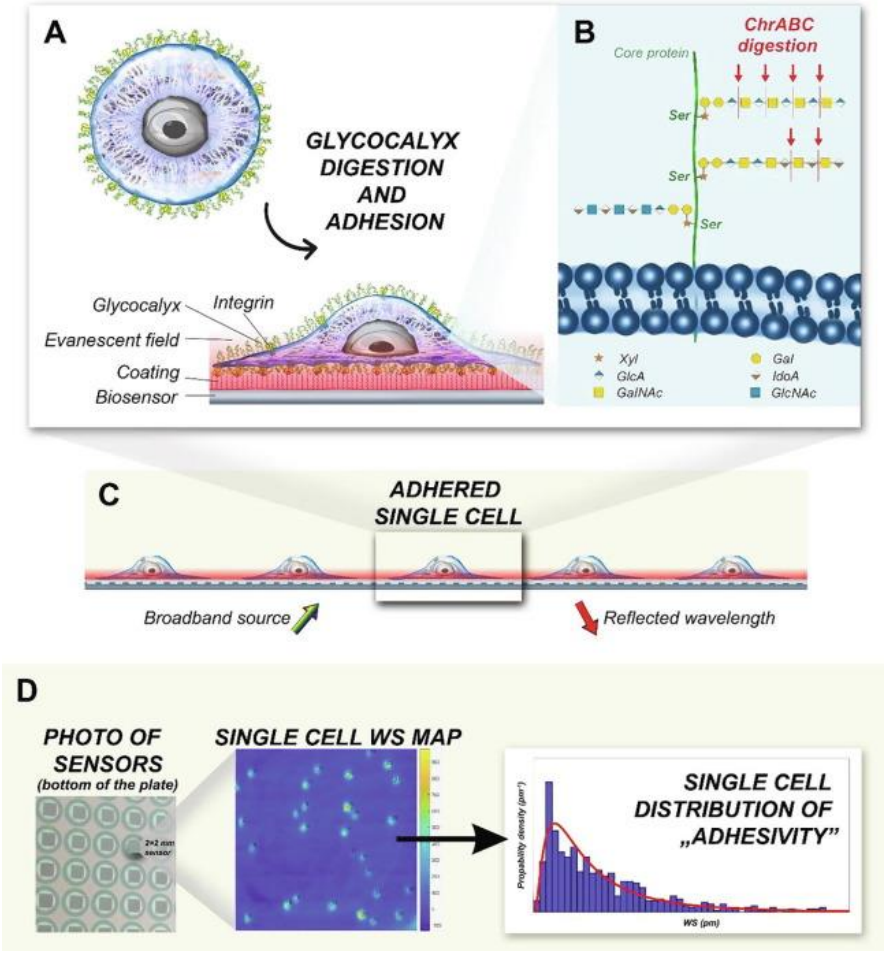

Figure 1: Schematic representation of the applied label-free method. (A) ChrABC enzyme digests the glycocalyx components of the HeLa cells. (B) Schematic illustration of the glycocalyx components. (C) With the RWG biosensor, even single-cells can be studied with high resolution. (D) The device works with 384-well microplates with 2×2 mm RWG biosensors in each well. The primary output of the device is the wavelength shift (WS) map in each well.

Related publication

[1] N. Kanyo, K. D. Kovács, S. V. Kovács, B. Béres, B. Péter, I. Székács, R. Horváth: *Single-cell adhesivity distribution of glycocalyx digested cancer cells from high spatial resolution label-free biosensor measurement,* Matrix Biology Plus **14,** (2022)

EPIGALLOCATECHIN-GALLATE TAILORS THE CELL ADHESIVITY OF FIBRONECTIN COATINGS IN OXIDATION AND CONCENTRATION-DEPENDENT MANNER

LP2012-26/2012 Lendület, OTKA ERC_HU 117755, TKP2021-EGA-04, OTKA KKP129936 and OTKA PD 131543

B. Péter, N. Kanyó, I. Székács, A. Csampai (ELTE), Sz. Bősze (ELTE), R. Horváth

Fibronectin is an extracellular matrix component that plays a significant role in many physiological processes, such as cell adhesion, growth, differentiation, and migration. In our study, we revealed the interaction between this important protein and the widely studied natural active substance green tea polyphenol epigallocatechin-gallate (EGCG) and its oxidized form. Furthermore, we investigated the kinetics of cancer cell adhesion on the polyphenol-treated fibronectin coatings. We applied a high-throughput, label-free optical biosensor capable of monitoring the above processes in real time with an excellent signal-to-noise ratio (Fig. 1) [1].

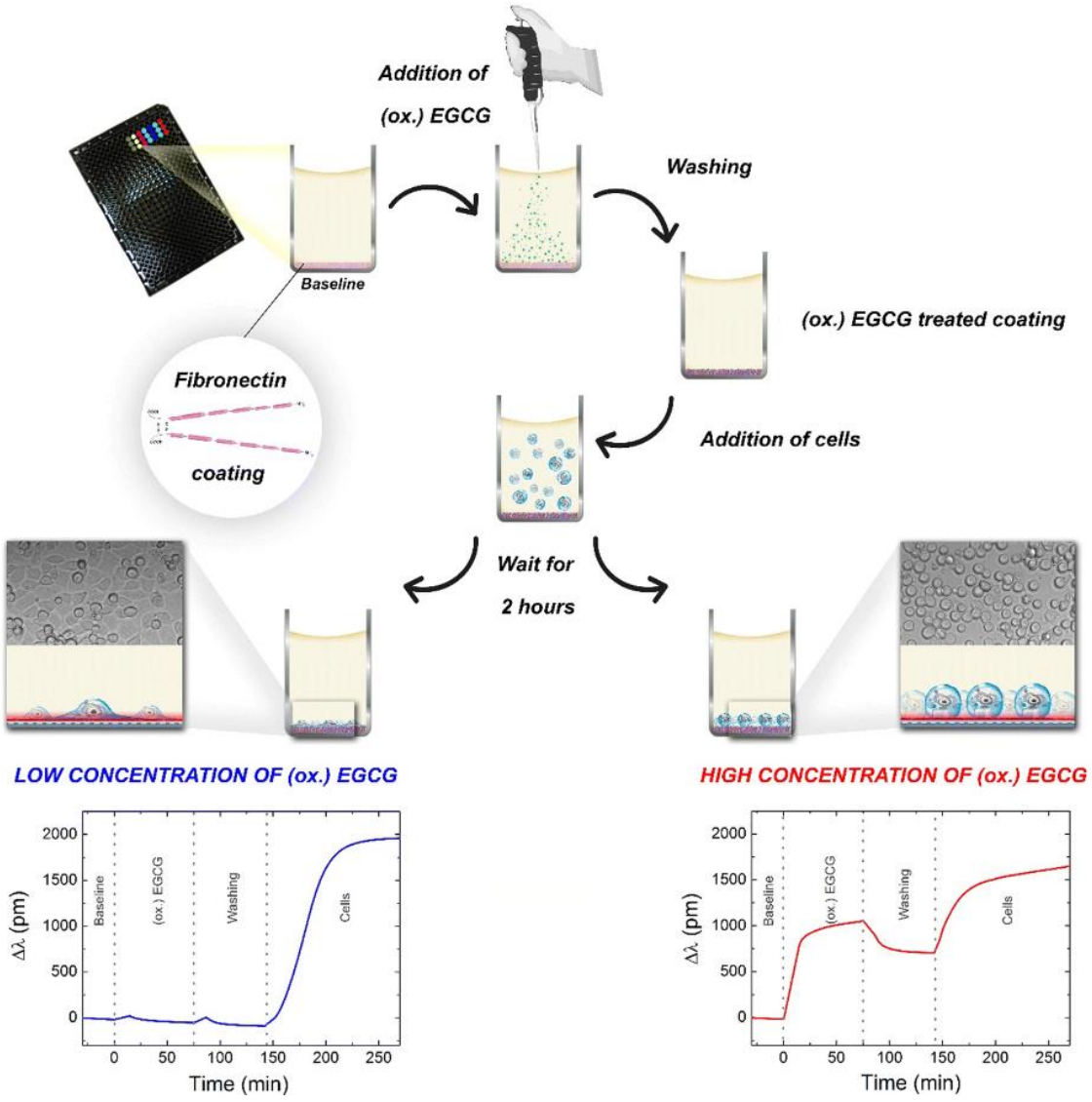

Figure 1: Schematic illustration of the measurement procedure and the typical kinetic curves obtained on the fibronectin coating

Related publication

[1] B. Péter, N. Kanyó, I. Székács, A. Csámpai, Sz. Bősze, R. Horváth: *Epigallocatechin-gallate tailors the cell adhesivity of fibronectin coatings in oxidation and concentration-dependent manner,* Materials Advances **3,** (2022)

FUNCTIONAL BLOOD CELL ANALYSIS BY LABEL-FREE BIOSENSORS AND SINGLE-CELL TECHNOLOGIES

LP2012-26/2012 Lendület, OTKA ERC_HU 117755, TKP2021-EGA-04, OTKA KKP129936, OTKA PD 134195 and OTKA PD 131543

Z. Szittner, B. Péter, S. Kurunczi, I. Székács, R. Horváth

Our aim was to summarize the current state of methods for label-free identification and functional characterization of leukocytes (Fig. 1) with biosensors and novel single cell techniques in a review article. The emphasis is on techniques on the characterizations of single cells with special attention to surface sensitive technologies. Recent developments highlighted the importance of small cell populations and individual cells both in health and disease. Nonetheless, techniques capable of analyzing single cells offer a promising tool for therapeutic approaches where characterization of individual cells is necessary to estimate their clinical therapeutic potential [1].

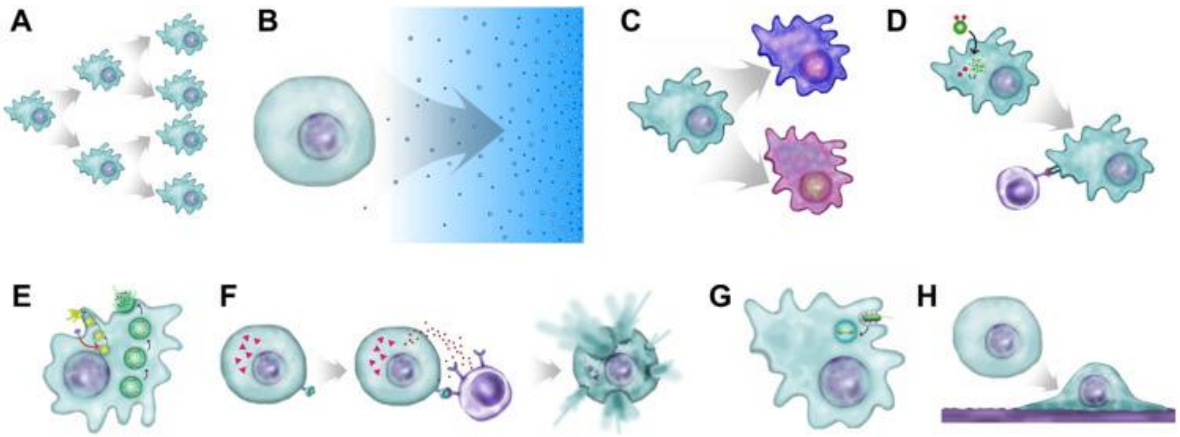

Figure 1: Examples of leukocyte functions detectable by label-free biosensors (A) proliferation (B) chemotaxis (C) cell polarization and activation (D) antigen presentation (E) degranulation and secretion (F) cytotoxicity (G) phagocytosis and (H) adhesion.

Related publication

[1] Z. Szittner, B. Péter, S. Kurunczi, I. Székács, R. Horváth: *Functional blood cell analysis by label-free biosensors and single-cell technologies,* Advances in Colloid and Interface Science **308,** (2022)

POPULATION DISTRIBUTIONS OF SINGLE-CELL ADHESION PARAMETERS DURING THE CELL CYCLE FROM HIGH-THROUGHPUT ROBOTIC FLUIDIC FORCE MICROSCOPY

LP2012-26/2012 Lendület, OTKA ERC_HU 117755, TKP2021-EGA-04 and OTKA KKP 129936

Á. G. Nagy, N. Kanyó, A. Vörös, I. Székács, A. Bonyár (BME), R. Horváth

Robotic fluidic force microscopy (FluidFM) was utilized to measure the adhesion parameters of cells in a high-throughput manner to study their population distributions in-depth. The investigated cell type was the genetically engineered HeLa Fucci construct with cell cycle-dependent expression of fluorescent proteins (Fig. 1). We first revealed that reticular adhesion can exert a higher force per unit area than canonical focal adhesions, and cells in this phase are significantly stiffer. The possible biological consequences of these findings were also discussed, together with the practical relevance of the observed population-level adhesion phenomena [1].

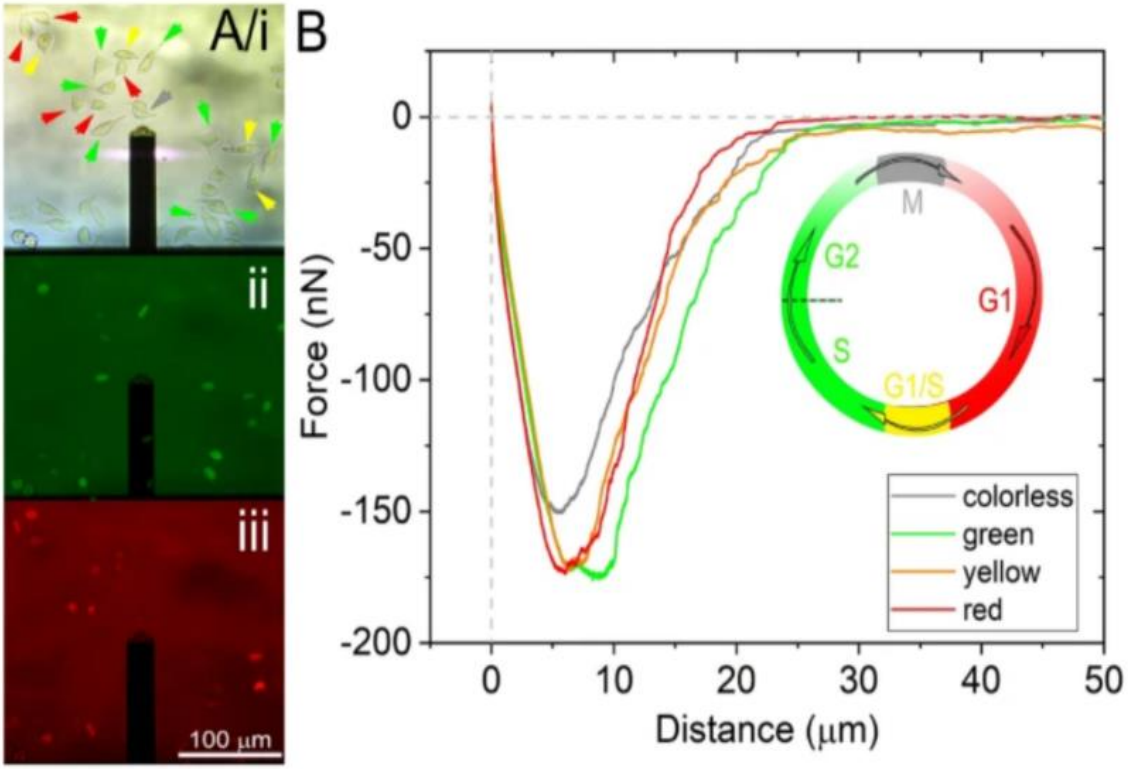

Figure 1: The Fucci construct and the actual measurement when the FluidFM cantilever is approaching the targeted cell. (A) Schematics of the HeLa Fucci cycle indicate the colours visible during the different phases. Fluorescent images were taken during the measurements on the FluidFM platform. (B) Averaged characteristic curves were obtained from each measurement belonging to different colour phases of HeLa Fucci cells.

Related publication

[1] Á.G. Nagy, N. Kanyó, A. Vörös, I. Székács, A. Bonyár (BME), R. Horváth: *Population distributions of single-cell adhesion parameters during the cell cycle from high-throughput robotic fluidic force microscopy,* Scientific Reports **12,** (2022)

CELL-SUBSTRATUM AND CELL-CELL ADHESION FORCES AND SINGLE-CELL MECHANICAL PROPERTIES IN MONO- AND MULTILAYER ASSEMBLIES FROM ROBOTIC FLUIDIC FORCE MICROSCOPY

LP2012-26/2012 Lendület, OTKA ERC_HU 117755, TKP2021-EGA-04 and OTKA KKP 129936

Á. G. Nagy, I. Székács, A. Bonyár (BME), R. Horváth

We studied the cellular adhesion maturation of epithelial Vero monolayers by measuring single-cell force-spectra with FluidFM. We found that HeLa cells adhere significantly stronger to the tight Vero monolayer than cells of the same origin. Moreover, the mechanical characteristics of Vero monolayers upon cancerous HeLa cell influence were recorded and analyzed (Fig. 1) [1].

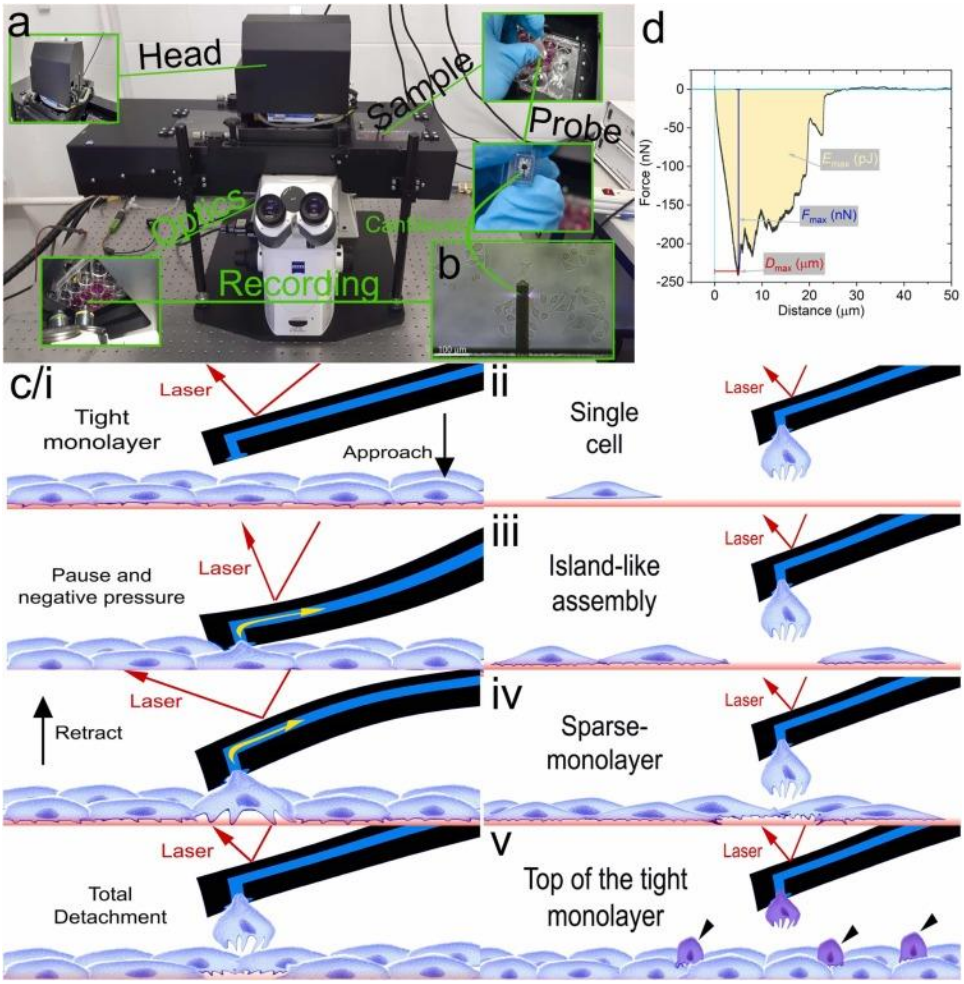

Figure 1: Schematic representation of the robotic FluidFM measurement setup and procedure. Living cell cultures on the FluidFM (a) can be observed with an optical microscope (see insert b where the cantilever is clearly visible). Under the measurement head, the large area sample stage allows multiple cell targeting in mm-cm scale areas. c) During Single Cell Force Spectroscopy (SCFS) recording, the cell from a tight cellular monolayer (i), single cells (ii), cells from island-like assemblies (iii), cells from a sparse monolayer (iv), or cells seeded on top of the tight monolayer (v, black arrowheads) are approached with the hollow FluidFM cantilever, which pauses upon contact with the targeted cell. Subsequently, suction (vacuum) is applied to attach the cell to the aperture, and the cantilever is retracted from the substrate.

Related publication

[1] Á. G. Nagy, I. Székács, A. Bonyár, R. Horvath: *Cell-substratum and cell-cell adhesion forces and single-cell mechanical properties in mono- and multilayer assemblies from robotic fluidic force microscopy,* European J. of Cell Biology **101,** (2022)

SIMPLE AND AUTOMATIC MONITORING OF CANCER CELL INVASION INTO AN EPITHELIAL MONOLAYER USING LABEL-FREE HOLOGRAPHIC MICROSCOPY

LP2012-26/2012 Lendület, OTKA ERC_HU 117755, TKP2021-EGA-04 and OTKA KKP 129936

Á. G. Nagy, I. Székács, A. Bonyár (BME), R. Horváth

The invasiveness of cancer cells describes the metastasizing capability of a primary tumour. The straightforward detection and quantification of cancer cell invasion are important to predict the survival rate of a cancer patient and to test how anti-cancer compounds influence cancer progression. Digital holographic microscopy based M4 Holomonitor (HM) is a technique that allows the label-free monitoring of cell morphological and kinetical parameters in real-time (Fig. 1). It was demonstrated that the invasion of single cancer cells is soundly observable and also quantifiable through monitoring parameters such as phase shift, optical volume, area, and motility, which parameters can easily be obtained and processed automatically. Based on the experimental data, the invasion speed of cancer cells entering the epithelial layer can be defined as the shrinking of detected single-cell volume per unit time. [1].

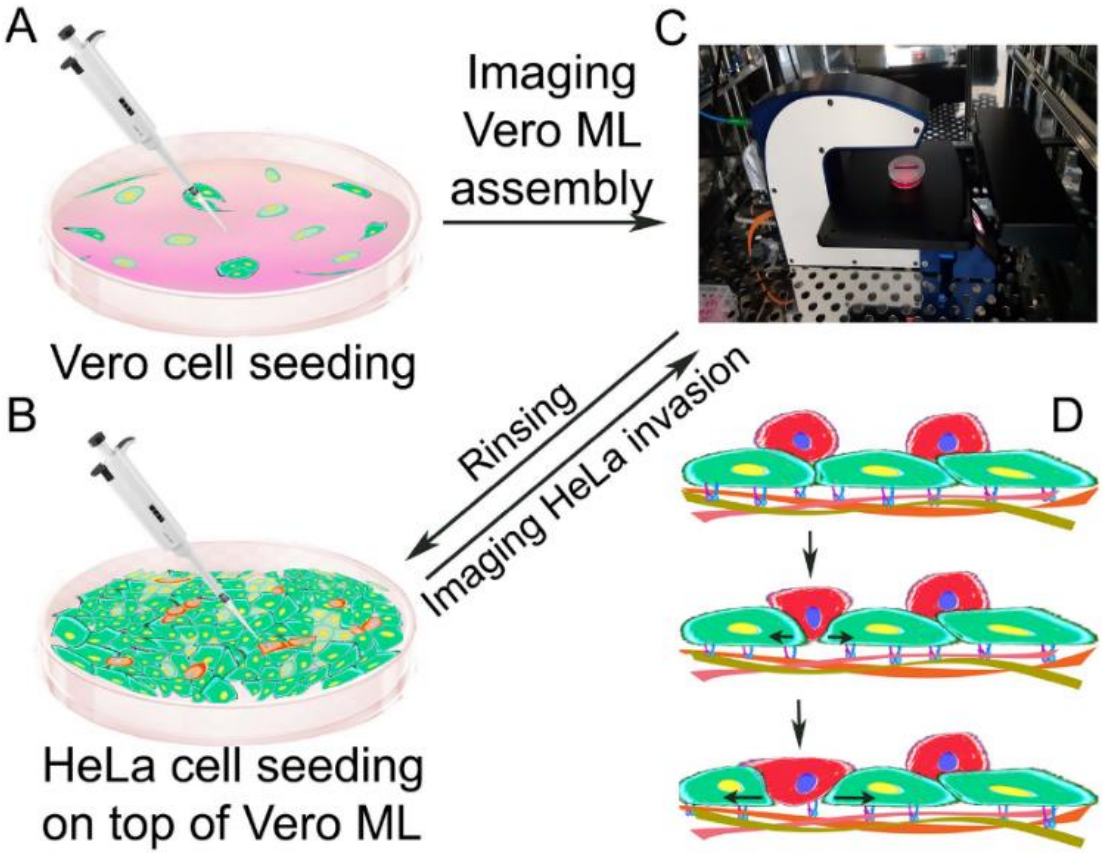

Figure 1: Schematics of experimental design, execution, and results. (A) Seeding of Vero cells (green) on gelatin-coated dish. (B) Seeding of HeLa cells (red) on top of the self-assembled 100% confluent Vero monolayer (ML). (C) Holomonitor M4 was used to image monolayer assembly and invasion for 24 h. (D) Illustration of the expected result, the HeLa cells seeded on top of the Vero monolayer infiltrate by searching for optimal invasion positions.

Related publication

[1] Á. G. Nagy, I. Székács, A. Bonyár, R. Horváth: *Simple and automatic monitoring of cancer cell invasion into an epithelial monolayer using label-free holographic microscopy,* Scientific Reports **12,** (2022)

REVIEW OF LABEL-FREE MONITORING OF BACTERIA: FROM CHALLENGING PRACTICAL APPLICATIONS TO BASIC RESEARCH PERSPECTIVES

LP2012-26/2012 Lendület, OTKA ERC_HU 117755, TKP2021-EGA-04, OTKA KKP 129936, OTKA PD 134195 and OTKA PD 131543

B. Péter, E. Farkas, S. Kurunczi, Z. Szittner, Sz. Bősze (ELTE), J. J. Ramsden (University of Buckingham, UK), I. Székács, R. Horváth

Novel biosensors already provide a fast way to detect the adhesion of whole bacteria (or parts of them), biofilm formation, and the effect of antibiotics (Fig. 1). Moreover, the detection sensitivities of recent sensor technologies are large enough to investigate molecular-scale biological processes. Usually, these measurements can be performed in real time without using labelling. Despite these excellent capabilities summarized in the present work, the application of novel, label-free sensor technologies in basic biological research is still rare; the literature is dominated by heuristic work, mostly monitoring the presence and amount of a given analyte. The aims of this review are (i) to give an overview of the present status of label-free biosensors in bacteria monitoring, and (ii) to summarize potential novel directions with biological relevancies to initiate future development. Optical, mechanical, and electrical sensing technologies are all discussed with their detailed capabilities in bacteria monitoring. [1].

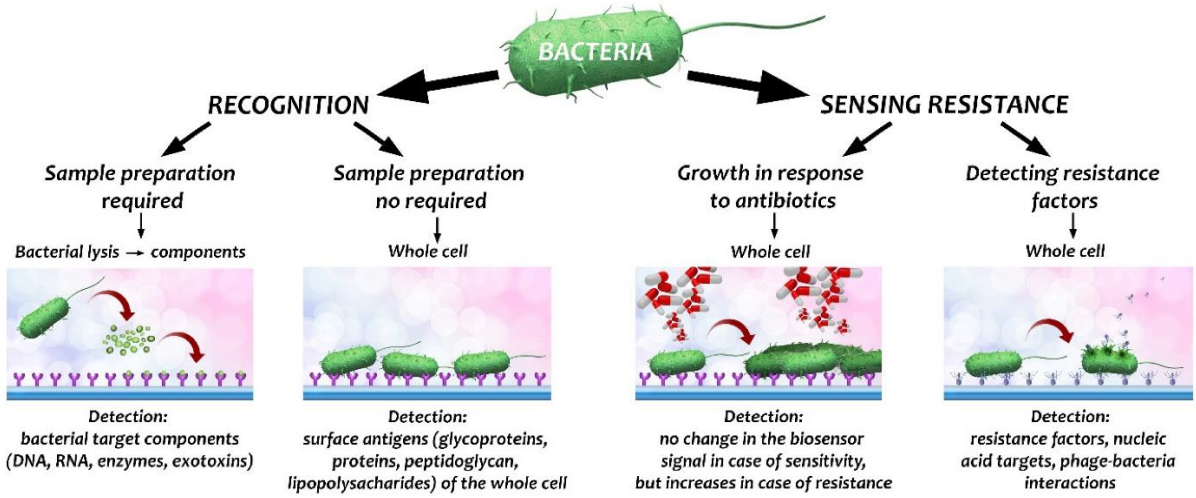

Figure 1: Summary of the strategies of recognition of bacteria and ways of resistance sensing using biosensors. Sample preparation may be needed to lyse the bacteria (or otherwise disrupt them) to liberate the target bacterial components (first column); and preparation-free whole cell-based assays are in the second column. Few biosensors can sense antibiotic resistance as well. There are two possibilities: measuring and monitoring the growth of bacteria during antibiotic treatment (third column) or measuring resistance factor adhesion or bacteriophage–bacterium interaction.

Related publication

[1] B. Péter, E. Farkas, S. Kurunczi, Z. Szittner, Sz. Bősze, J. J. Ramsden, I. Székács, R. Horváth: *Review of label-free monitoring of bacteria: From challenging practical applications to basic research perspectives,* Biosensors **12,** (2022)

PROSPECTS OF FLUIDIC FORCE MICROSCOPY AND RELATED BIOSENSORS FOR MEDICAL APPLICATIONS

LP2012-26/2012 Lendület, OTKA ERC_HU 117755, TKP2021-EGA-04, OTKA KKP 129936 and OTKA PD 131543

T. Gerecsei, B. Péter, R. Ungai-Salánki, S. Kurunczi, I. Székács, B. Szabó, R. Horváth

The biophysical characterization of cells is gaining momentum nowadays as more and more studies show that biomechanical parameters such as adhesion and stiffness carry relevance both in understanding and in diagnosing diseases. The revolution in the field sparked by atomic force microscopy has accelerated since the introduction of fluidic force microscopy roughly a decade ago. Unparalleled in versatility, it is easy to predict FluidFM to become the gold standard in single-cell manipulation (Fig. 1). It has become a common perception in biomedical sciences, especially in cancer research, hematology, and developmental biology to look at populations of cells as a distribution of various phenotypes and gene expression patterns rather than a homogeneous population of identical units. Thus, the characterization of single-cells and the identification of subpopulations has gained importance, together with the methods that can be utilized to achieve these goals. The detachment, isolation, injection, and extraction of a wide variety of cell types with high viability has been demonstrated with FluidFM and the list of applications is expected to grow. In this book chapter, we presented and summarized FluidFM and related biosensors for medical applications [1].

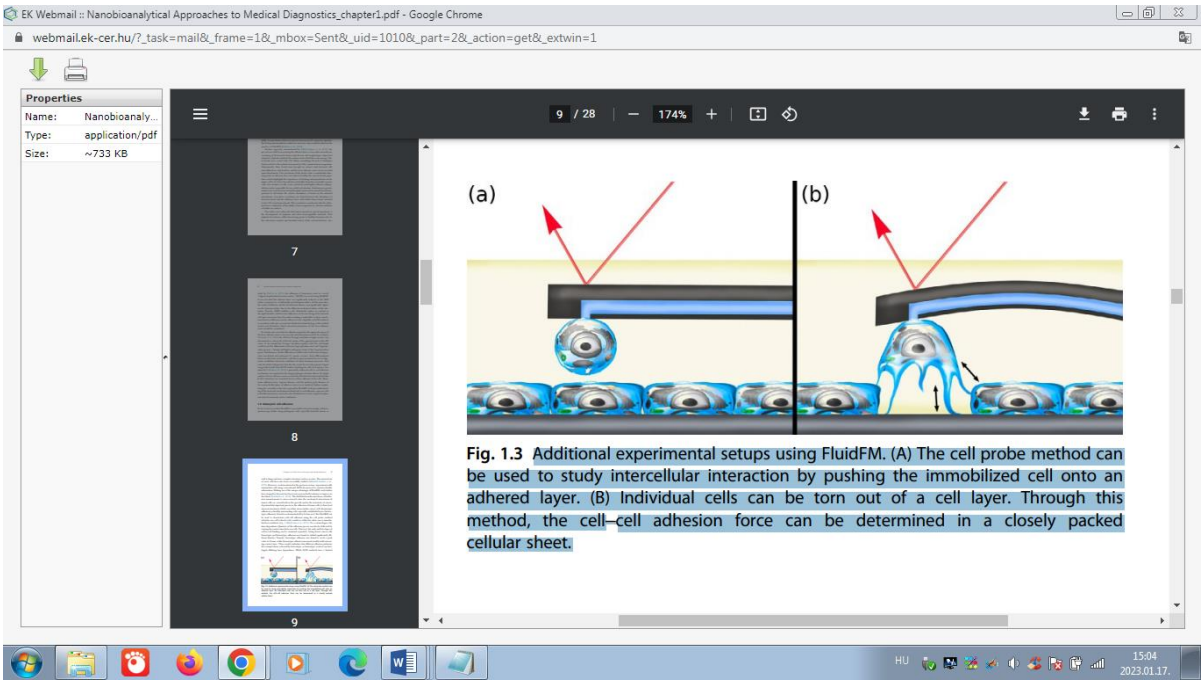

Figure 1: Experimental setups using FluidFM. (A) The cell probe method can be used to study intercellular interaction by pushing the immobilized cell onto an adhered layer. (B) Individual cells can be torn out of a cell layer. Through this method, the cell–cell adhesion force can be determined in a closely packed cellular sheet.

Related publication

[1] T. Gerecsei, B. Péter, R. Ungai-Salánki, S. Kurunczi, I. Székács, B. Szabó, R. Horváth: *Prospects of fluidic force microscopy and related biosensors for medical applications, Nanobioanalytical Approaches to Medical Diagnostics,* Woodhead Publishing Series in Biomaterials, (2022)

CYTOTOXIC EFFECTS OF ROUNDUP CLASSIC AND ITS COMPONENTS ON NE-4C AND MC3T3-E1 CELL LINES DETERMINED BY BIOCHEMICAL AND FLOW CYTOMETRIC ASSAYS

LP2012-26/2012 Lendület, OTKA ERC_HU 117755, TKP2021-EGA-04, OTKA KKP 129936

M. Oláh (MATE), E. Farkas, I. Székács, R. Horváth, A. Székács (MATE)

Cytotoxic effects of the market leading broad-spectrum, synthetic herbicide product Roundup Classic, its active ingredient glyphosate (in a form of its isopropylamine (IPA) salt) and its formulating surfactant polyethoxylated tallowamine (POE-15) were determined on two murine cell lines, a neuroectodermal stem cell-like (NE-4C) and a high alkaline phosphatase activity osteoblastic cell line (MC3T3-E1). Cytotoxicity, genotoxicity, effects on cell viability and cell cycles were examined in five flow cytometry tests (Fig. 1), the two former of which were compared by the enzymatic-assay and the alkaline single cell gel electrophoresis (Comet) assay. All of the tests indicated the NE-4C cells being more sensitive, than the MC3T3-E1 cell line to the treatments with the target compounds. Higher sensitivity differences were detected in the viability test by flow cytometry (7–9-fold), than by the MTT assay (1.5–3-fold); in the genotoxicity test by the Comet assay (3.5–403-fold), than by the DNA-damage test (9.3–158-fold); and in the apoptosis test by the Annexin V dead cell kit (1.1–12.7-fold), than by the Caspase 3/7 kit (1–6.5-fold). Cell cycle assays indicated high count of cells (~70%) in the G0/G1 phase for MC3T3-E1 cells, than in NE-4C cell (~40%) after 24 h. The order of the inhibitory potency of the target substances has unequivocally been POE-15 > Roundup Classic > > glyphosate IPA salt [1].

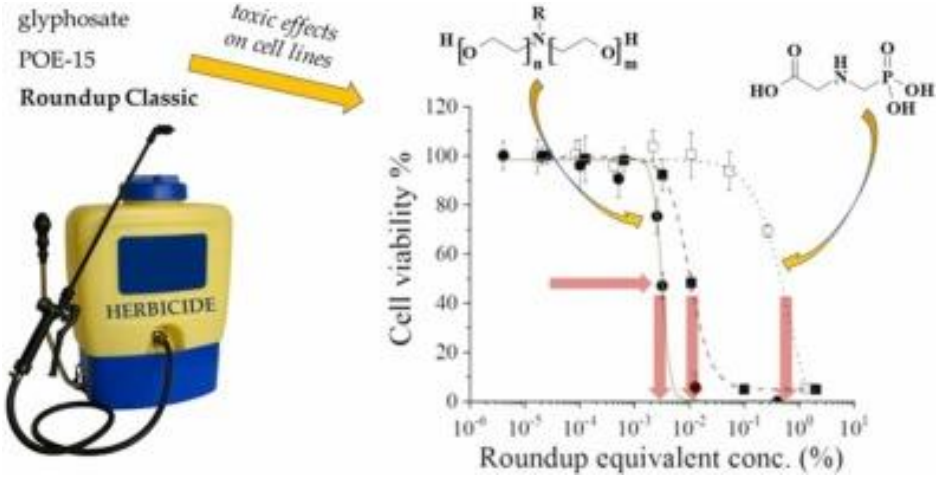

Figure 1: Examination and analysis of the cytotoxic effect of herbicides

Related publication

[1] M. Oláh, E. Farkas, I. Székács, R. Horváth, A. Székács: *Cytotoxic effects of Roundup Classic and its components on NE-4C and MC3T3-E1 cell lines determined by biochemical and flow cytometric assays,* Toxicology Reports **9,** (2022)

COMPARATIVE ASSESSMENT OF THE INHIBITORY POTENTIAL OF THE HERBICIDE GLYPHOSATE AND ITS STRUCTURAL ANALOGS ON RGD-SPECIFIC INTEGRINS USING ENZYME-LINKED IMMUNOSORBENT ASSAYS

LP2012-26/2012 Lendület, OTKA ERC_HU 117755, TKP2021-EGA-04, OTKA KKP 129936

B. Gémes (MATE), E. Takács (MATE), I. Székács, R. Horváth, A. Székács (MATE)

Transmembrane glycoprotein integrins play crucial roles in biochemical processes, and by their inhibition or activation, different signal pathways can be disrupted, leading to abnormal physiological functions. We have previously demonstrated the inhibitory effect of glyphosate herbicide's active ingredient on cell adhesion and its αvβ3 integrin antagonist effect. Therefore, it appeared particularly exciting to investigate inhibition of glyphosate and its metabolites on a wider range of Arg-Gly-Asp (RGD) binding integrins, namely αvβ3, α5β1 and αIIbβ3. Thus, the purpose of this study was to assess how extended the inhibitory effect observed for glyphosate on the integrin αvβ3 is in terms of other RGD integrins and other structurally or metabolically related derivatives of glyphosate.

Five different experimental setups using enzyme-linked immunosorbent assays were applied (Fig. 1):

(i) αvβ3 binding to a synthetic polymer containing RGD;

(ii) αvβ3 binding to its Extracellular Matrix (ECM) protein, vitronectin;

(iii) α5β1 binding to the above polymer containing RGD;

(iv) αIIbβ3 binding to its ECM protein, fibrinogen and

(v) αvβ3 binding to the SARS-CoV-2 spike protein receptor binding domain.

Total inhibition of αvβ3 binding to RGD was detected for glyphosate and its main metabolite, Aminomethylphosphonic Acid (AMPA), as well as for acetylglycine on α5β1 binding to RGD [1].

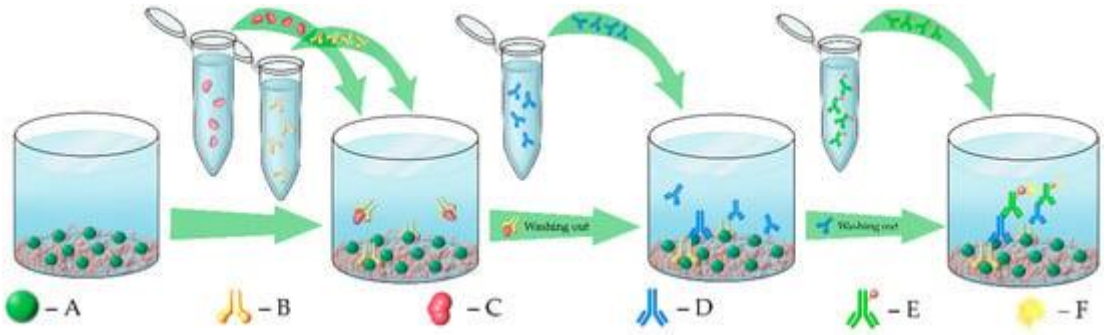

Figure 1: Schematic illustration of the Enzyme-Linked Immunosorbent Assay (ELISA)

Related publication

[1] B. Gémes, E. Takács, I. Székács, R. Horváth, A. Székács: *Comparative assessment of the inhibitory potential of the herbicide glyphosate and its structural analogs on RGD-specific integrins using enzyme-linked immunosorbent assays,* International Journal of Molecular Sciences **23,** (2022)

SINGLE-CELL TEMPORAL TRANSCRIPTOMICS FROM TINY CYTOPLASMIC BIOPSIES

LP2012-26/2012 Lendület, OTKA ERC_HU 117755, TKP2021-EGA-04, OTKA KKP 129936

R. Horváth

In a recent issue in Nature, Chen et al. [1] present Live-seq, a single-cell transcriptomic profiling method using picoliter scale single-cell cytoplasmic biopsies instead of complete cell lysis. Since the cells quickly recover and basically remain unaffected after the cytoplasmic extraction, the authors transform single-cell RNA sequencing (scRNA-seq) from an end point to a temporal analysis platform. In our recent Spotlight article, this topic and results were discussed (Fig.1) [2].

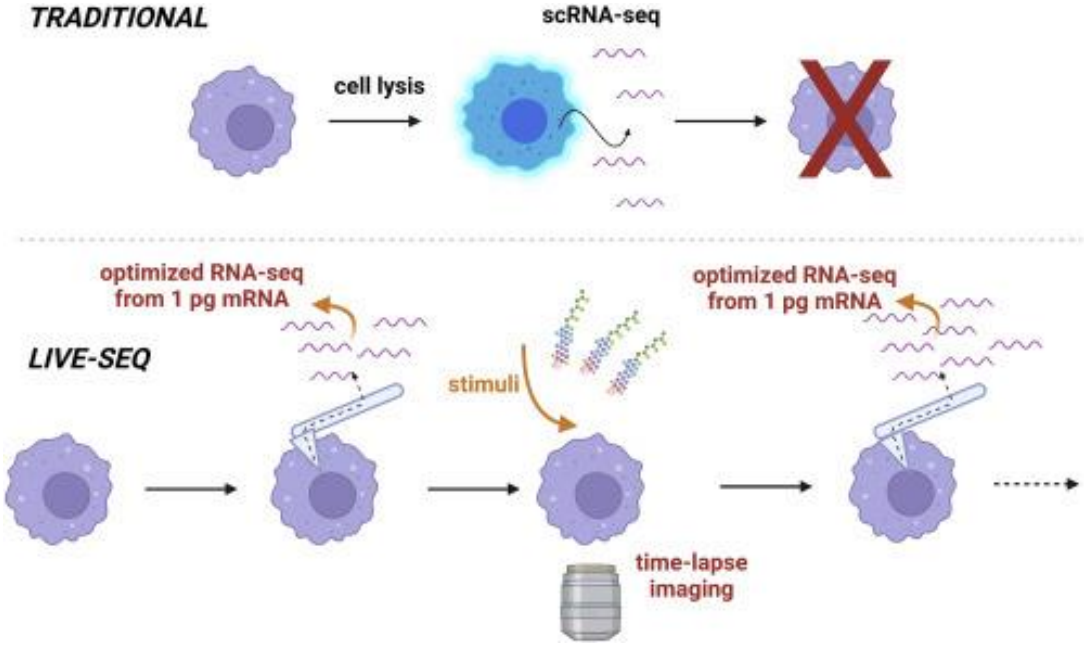

Figure 1: Schematic comparison of traditional scRNA-seq and Live-seq

Related publications

[1] W. Chen, O. Guillaume-Gentil, P.Y. Rainer, C.G. Gabelein, W. Saelens, V. Gardeux, A. Klaeger, R. Dainese, M. Zachara, T. Zambelli, et al.: *Live-seq enables temporal transcriptomic recording of single cells,* Nature **608,** (2022)

[2] R. Horváth: *Single-cell temporal transcriptomics from tiny cytoplasmic biopsies,* Cell Reports Methods **2,** (2022)

QUANTIFICATION AND STATISTICAL ANALYSIS OF TOPOLOGICAL FEATURES OF RECURSIVE TREES

OTKA PD 138571

B. Király, I. Borsos, and G. Szabó

Our recent research into the structure and properties of payoff matrices in game theory has revealed that square matrices can be decomposed as linear combinations of just a handful of fundamentally different kinds of basis matrices that each represent archetypal interaction situations. Symmetry considerations can further simplify the picture: In particular, antisymmetric matrices consist only of hierarchical and cyclic components. We applied this insight to the by definition antisymmetric adjacency matrix representation of simple directed graphs, and thus found that they can be considered as linear combinations of star-like hierarchical and rock-paper-scissors-like cyclic basis graphs. Using the expansion coefficients of the elementary matrices, we have introduced various vectors and scalar products to quantify and characterize some local and global topological properties of the underlying graphs. For example, the elements of the vector **h** count the difference between the outgoing and incoming edges of each node, and its scalar product with itself, **h**·**h**, turns out to be proportional to the weight of the graph's hierarchical component.

We decided to begin testing the applicability and the usefulness of these quantities on recursive trees, because the presence of a unique root naturally designates a unique decomposition in the otherwise linearly dependent set of all elementary cyclic matrices. Moreover, the structural properties of recursive trees allowed us to determine analytically the averages of certain quantities over the set of same-sized recursive trees by induction. We focused our efforts on a number of promising scalar products that quantify the correlations between local measures derived from the leaf structure and the hierarchical and cyclic components of the adjacency matrix. In order to find out how effectively these measures can sort graphs into groups according to their isomorphism classes, we counted the number of different values these measures can take. We found that global measures that combine fundamentally different topological features have the highest resolving power, some of them can even correctly identify all isomorphism classes for smaller recursive trees, but we have found none that can keep up with the exponential increase in the number of isomorphism classes as the size of the graphs is increased. One way to further increase the resolving power of this approach is to use two or more suitably chosen global measures simultaneously, as illustrated by the figure on this page, which shows both joint and marginal distributions of 7-node trees over the values two such measures derived from the hierarchical, cyclical, and leaf structures of the graphs can take.

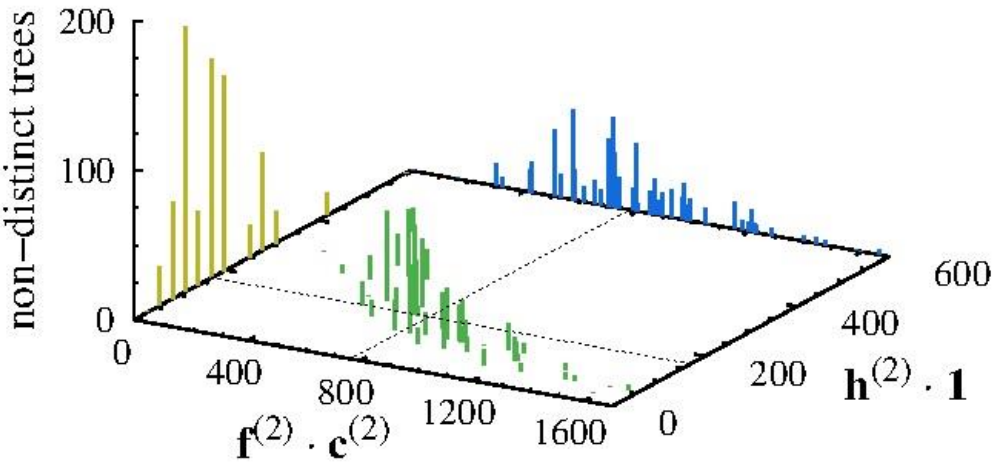

Figure 1: Distribution of the number of recursive trees characterized by two measures, h(2)·1 and f(2) c(2), for n=7. The marginal distributions are shown by vertical columns along the axes and the dash lines indicate their average values (quantitatively 168 and 770) over the whole set.

MERCENARY PUNISHMENT IN STRUCTURED POPULATIONS

OTKA K 142948

H.-W. Lee, C. Cleveland, and A. Szolnoki

Punishing those who refuse to participate in common efforts is a known and intensively studied way to maintain cooperation among self-interested agents. But this act is costly, hence punishers who are generally also engaged in the original joint venture, become vulnerable, which jeopardizes the effectiveness of this incentive. As an alternative, we may hire special players, whose only duty is to watch the population and punish defectors. Such a police-like or mercenary punishment can be maintained by a tax-based fund. If this tax is negligible, a cyclic dominance may emerge among different strategies. When this tax is relevant then this solution disappears. In the latter case, the fine level becomes a significant factor that determines whether punisher players coexist with cooperators or alternatively with defectors. The maximal average outcome can be reached at an intermediate cost value of punishment. Our observations highlight that we should take special care when such kind of punishment and accompanying tax are introduced to reach a collective goal. [1]

The payoff values of different strategies, cooperator, defector, and punisher, originated from a game are the following:

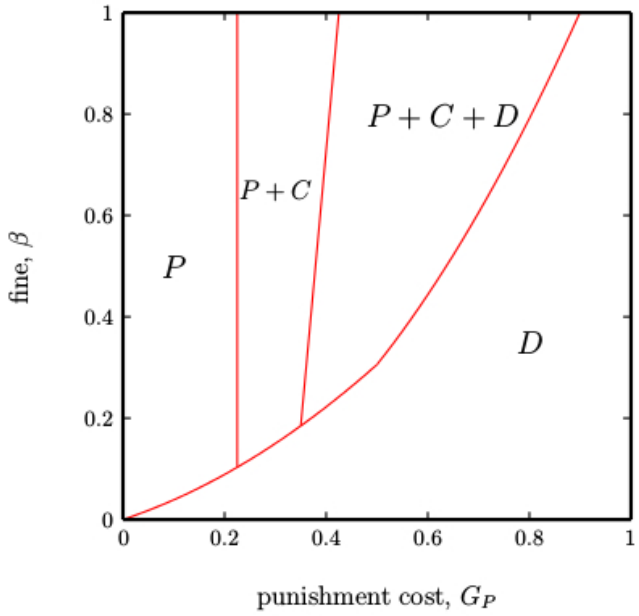

Figure 1: Schematic phase diagram on the punishment cost – penalty plane obtained at r = 3, T = 0. Despite the lack of tax, cooperators can coexist with punishers at an intermediate cost value if the fine is high enough. When we weaken punishers further by increasing the punishment cost then a cyclic dominance emerges, where C→P→D→C is the rank among competing strategies. By increasing G_P further, this delicate balance is broken and defectors prevail.

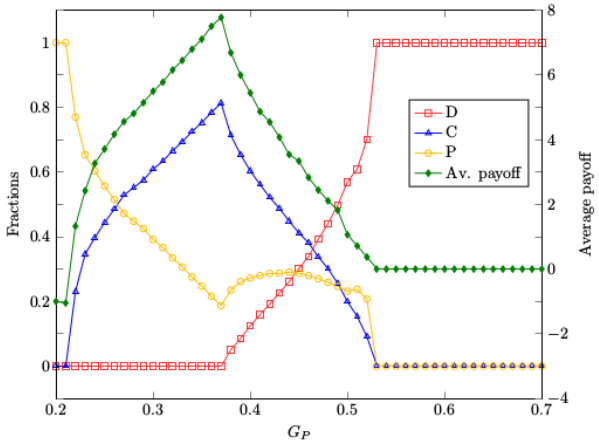

Figure 2: Cross section of the phase diagram shown in Figure 1, as obtained for β = 0.4 fine value. Depicted are stationary fractions of the three competing strategies as a function of punishment cost. As we increase G_P, the system enters to P+C solution from full P state, then P+C+D state emerges, and finally it arrives to full D state. We also plotted the average payoff values of the population, which signs that there is an optimal G_P cost level of punishers, which is necessary to reach the best collective income.

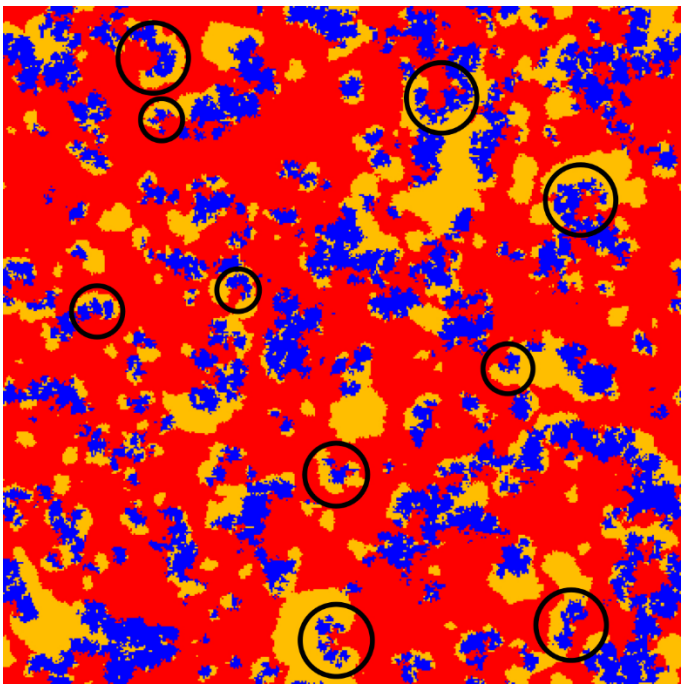

Figure 3: Characteristic distribution of competing strategies in the P+C+D phase. Blue, red, and yellow colours denote players with C, D, and P strategy respectively. The rotating spiral patterns of invasion fronts between homogeneous domains signal clearly the cyclic dominance among three competing strategies. For clarity, we marked them with black circles. The snapshot was taken at $\beta = 0.4$, $T = 0$, $G_P = 0.5$ in the stationary state where linear size was $L = 400$.

Related publication

[1] H.-W. Lee, C. Cleveland, A. Szolnoki: *Mercenary punishment in structured populations,* Appl. Math. Comput. **417,** 12679 (2022)

THE SELF-ORGANIZING IMPACT OF AVERAGED PAYOFFS ON THE EVOLUTION OF COOPERATION

A. Szolnoki and M. Perc

According to the fundamental principle of evolutionary game theory, the more successful strategy in a population should spread. Hence, during a strategy imitation process a player compares its payoff value to the payoff value held by a competing strategy. But this information is not always accurate. To avoid ambiguity a learner may therefore decide to collect a more reliable statistic by averaging the payoff values of its opponents in the neighbourhood, and makes a decision afterwards. This simple alteration of the standard microscopic protocol significantly improves the cooperation level in a population. Furthermore, the positive impact can be strengthened by increasing the role of the environment and the size of the evaluation circle. The mechanism that explains this improvement is based on a self-organizing process, which reveals the detrimental consequence of defector aggregation that remains partly hidden during face-to-face comparisons. Notably, the reported phenomenon is not limited to lattice populations but remains valid also for systems described by irregular interaction networks. [1]

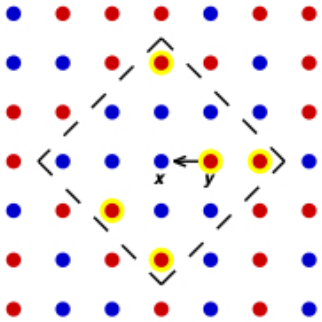

Figure 1: As a learner, a cooperator (blue) player x tries to imitate the strategy of the defector (red) neighbour player y. To calculate the imitation probability player x considers not only the Π_y payoff of player y, but also the Π_{av} averaged payoff values of ball other defector players who are within the evaluation circle. The latter players are marked by yellow background while the border of evaluation circle around player x is marked by a dashed diamond. In this particular case $l_e = 2$ is applied, which means that all players whose distance from player x are not larger than 2 may contribute to Π_{av}, hence providing a more accurate statistics about the general success of s_y strategy. To calculate the effective payoff we apply $\Pi_w = q\Pi_{av} + (1 - q)\Pi_y$, where q is the control parameter determining how strongly our learner player trusts on the alternative source of information about the success of tempting strategy.

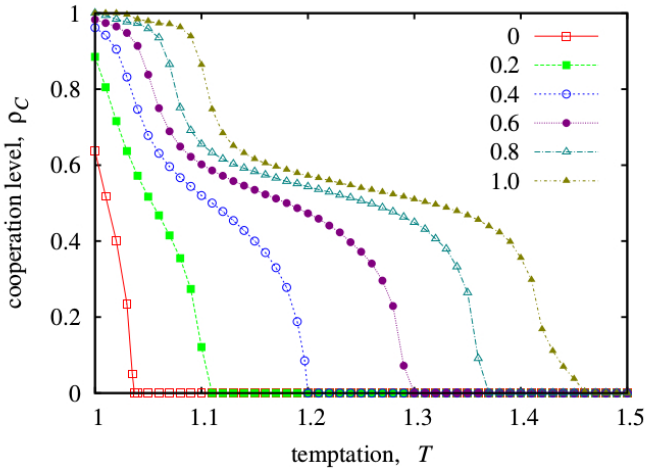

Figure 2: Cooperation level in dependence of temptation value on a square lattice for different values of q obtained at $l_e = 2$. The values of q are marked in the legend. The curves suggest that the cooperation level can be improved significantly if the learner players give greater credit to payoff information obtained from the neighbourhood instead of trusting to the neighbouring model player exclusively. In other words, it is wiser to make a decision based not only on a single information, but collecting more. By enlarging the size of the neighbourhood with the collected extra information the cooperation level can be lifted further even if the mentioned information has just a minor role on the decision making because of the small value of q. Interestingly, however, the reachable cooperation level saturates for large range of information circle.

Related publication

[1] G. Ódor, S. Deng, B. Hartmann, and J. Kelling: *Synchronization dynamics on power grids in Europe and the United States,* Phys. Rev. E **106,** 034311 (2022)

SYNCHRONIZATION DYNAMICS ON POWER GRIDS IN EUROPE AND THE UNITED STATES

ELKH SA-44/2021

G. Ódor, B. Hartmann, S. Deng, J. Kelling

Dynamical simulation of the cascade failures on the European and United States (U.S.) high-voltage power grids have been done via solving the second-order Kuramoto equation. We show that synchronization transition happens by increasing the global coupling parameter K with metastable states depending on the initial conditions so that hysteresis loops occur. We provide analytic results for the time dependence of frequency spread in the large-K approximation and by comparing it with numeri's of d= 2, 3 lattices, we find agreement in the case of ordered initial conditions. However, different Power-Law (PL) tails occur, when the fluctuations are strong.

After thermalizing the systems, we allow a single line cut failure and follow the subsequent overloads with respect to threshold values T. The probability distribution of line failures (PDFs ($p(N_f)$) of the cascade failures exhibit PL tails near the synchronization transition point K_c. Near this, the exponents of the PLs for the U.S. power grid vary with T as $1.4<\tau<2.1$, in agreement with the empirical blackout statistics, while on the European power grid we find somewhat steeper PLs characterized by $1.4<\tau<2.4$. Below K_c, we find signatures of T-dependent PLs, caused by frustrated synchronization, reminiscent of Griffiths effects. Here we also observe stability growth following the blackout cascades, similar to intentional islanding, but for $K>K_c$ this does not happen. For $T<T_c$, bumps appear in the PDFs with large mean values, known as "dragon king" blackout events. We also analyze the delaying or stabilizing effects of instantaneous feedback or increased dissipation and show how local synchronization (r_i) behaves on geographic maps. [1]

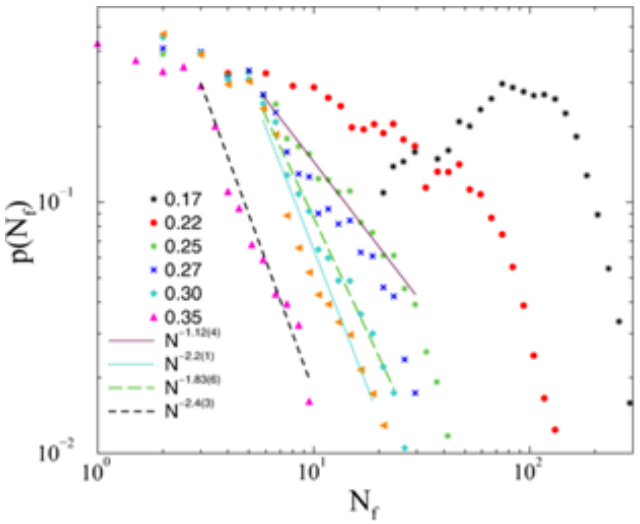

Figure 1: Probability distribution of line failures for different thresholds for K=60 shown in the legends in case of the Europe-HV power grid. Dashed lines show power-law fits for the scaling region, determined by visual inspection. One can observe dragon king bumps for low threshold values.

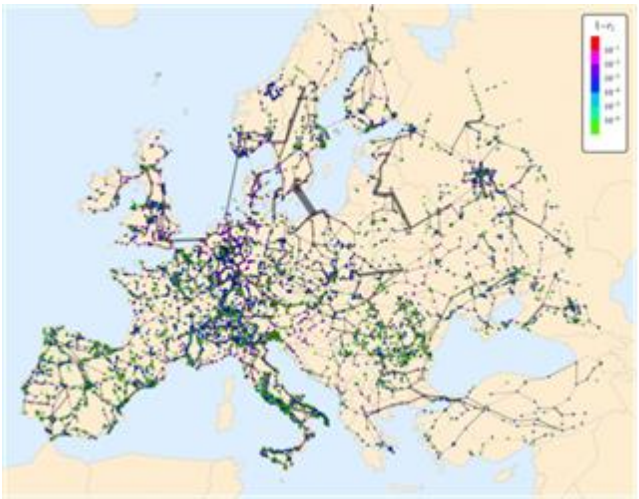

Figure 2: Local Kuramoto results encoded by the colour map as $1-r_i$. Red corresponds low local synchronization, green to high synchronization. The width of grey edges is proportional to the amplitude of the power flow.

Related publication

[1] G. Ódor, I. Papp, S. Deng, J. Kelling: *Synchronization transitions on connectome graphs with external force,* Front. Phys. Sec. Complex Physical Systems **11,** (2023)

SYNCHRONIZATION TRANSITIONS ON CONNECTOME GRAPHS WITH EXTERNAL FORCE

OTKA K 128989

G. Ódor, I. Papp, S. Deng, J. Kelling

We investigate the synchronization transition of the Shinomoto-Kuramoto model on networks of the fruit-fly and two large human connectomes. This model contains a force term (F), thus is capable of describing critical behaviour in the presence of external excitations. By numerical solution we determine the crackling noise durations with and without thermal noise and show extended non-universal scaling tails, described by the exponent $2< t_t < 2.8$, in contrast with the Hopf transition of the Kuramoto model, without the force $t_t =3.1(1)$. Comparing phase and frequency order parameters we find different transition points and fluctuations peaks as in case of the Kuramoto model related to a crossover at Widom lines. Using the local order parameter values we also determine the Hurst (phase) and b (frequency) exponents and compare them with recent experimental results, obtained by fMRI. We show that these exponents, characterizing the auto-correlations are smaller in the excited system than in the resting state and exhibit module dependence. [1]

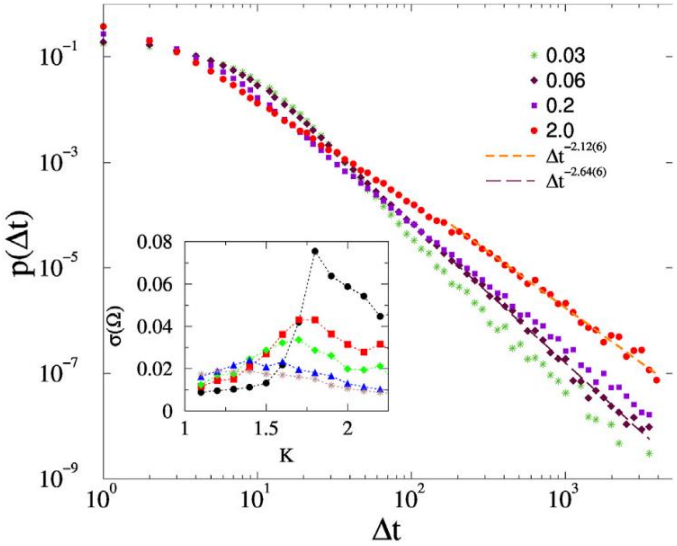

Figure 1: Avalanche duration distributions on the fruit-fly connectome for different forces, shown by the legends and at K = 1.3 global coupling. Dashed lines are PL fits for Δt > 100. The inset shows the steady state σ(Ω) as the function of K, for excitation values F = 0.001, 0.0667, 0.1, 0.2, 0.3 (top to bottom).

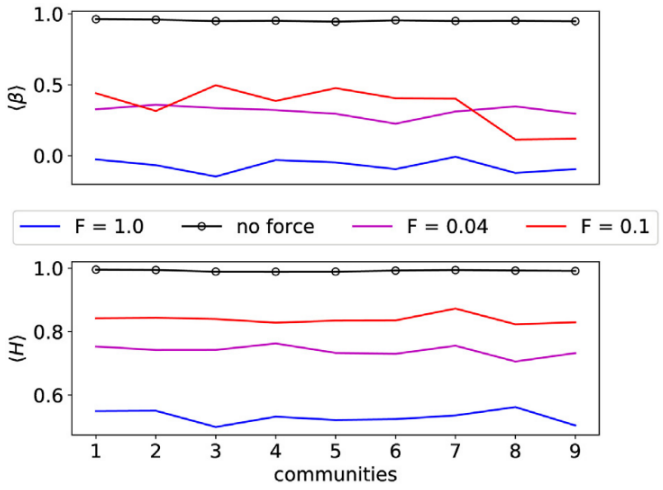

Figure 2: Hurst and beta exponents of all fruit-fly connectome communities. In the forceless case at the critical Hopf transition coupling, the H exponent is the largest for every community. With forces, these values drop for each community. This shows a resemblance with the rest and non-rest studies of different brain areas in [63], showing ⟨H⟩ ≈ 1.0 at resting state and ⟨H⟩ ≈ 0.7 at task driven states.

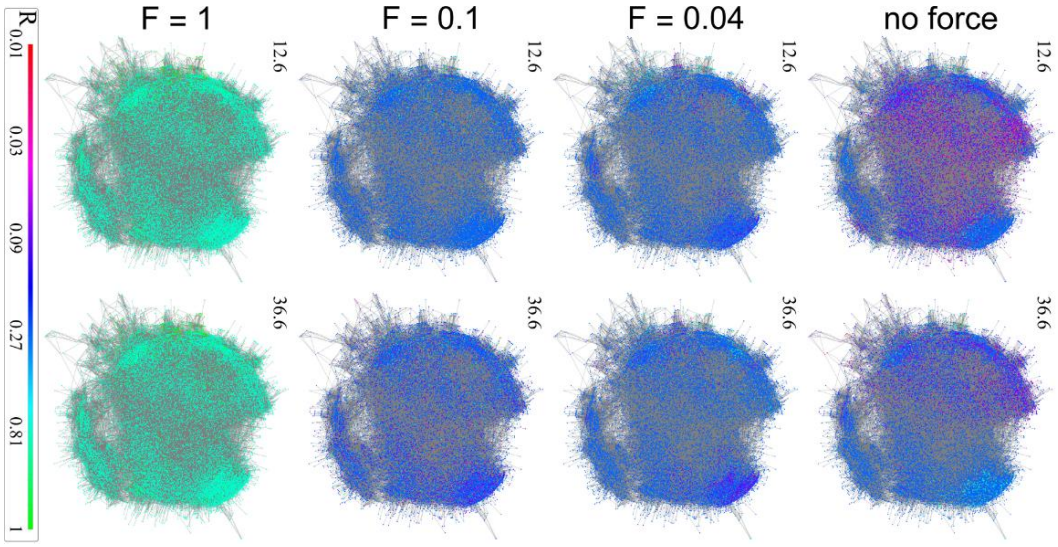

Figure 3: Here we see the evolution of the local order parameters $R_i(t)$ of a sub-graph of the fruit-fly connectome at different time steps: t = 12.6, 36.6. The right column shows R_i map without a force, left columns show the one with F = 1.0. Colour-coding at the bottom provides $R_i(t)$ for all subfigures.

Related publication

[1] S. Deng and G. Ódor: *Critical behaviour of the diffusive susceptible-infected-recovered model,* Phys. Rev E **107,** 014303 (2023)

CRITICAL BEHAVIOUR OF THE DIFFUSIVE SUSCEPTIBLE-INFECTED-RECOVERED MODEL

OTKA K 128989

S. Deng and G. Ódor

The critical behaviour of the non-diffusive Susceptible-Infected-Recovered (SIR) model on lattices had been well established in virtue of its duality symmetry. By performing simulations and scaling analyses for the diffusive (SIRD) variant on the two-dimensional lattice, we show that diffusion (D) for all agents, while rendering this symmetry destroyed, constitutes a singular perturbation that induces asymptotically distinct dynamical and stationary critical behaviour from the non-diffusive model. In particular, the manifested crossover behaviour in the effective mean-square radius exponents reveals that slow crossover behaviour in general diffusive multispecies reaction systems may be ascribed to the interference of multiple length scales and timescales at early times.

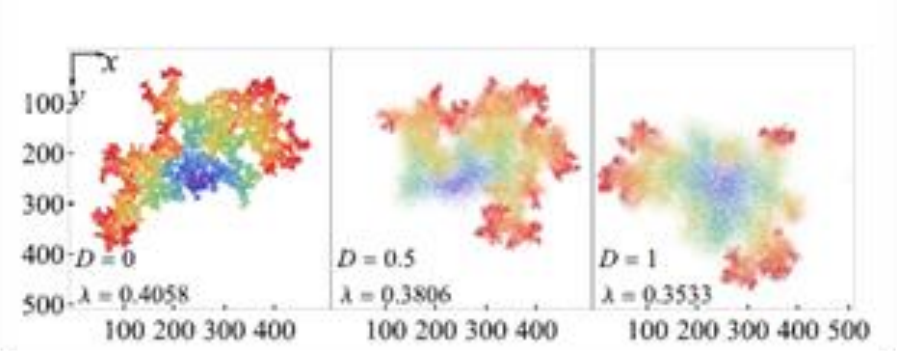

Figure 1: Snapshots for the critical SIRD process with diffusion rates D = 0, 0.5 and 1 on a 500 × 500 lattice. The S and I species are coloured in white and black. The rainbow spectrum beard by the R species, from blue to red, linearly marks their relative generating time.

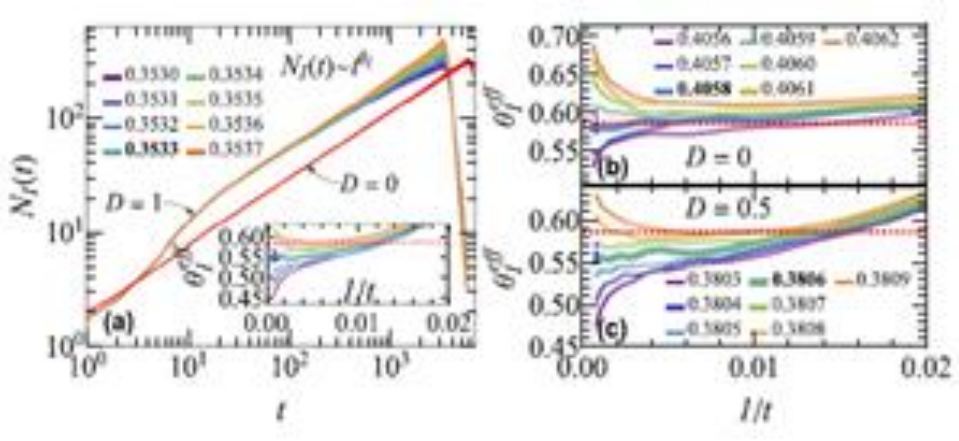

Figure 2: Growth of the I population size $N_I(t)$ from a single infectious seed on a L=4001 square lattice in the vicinity of criticality for (a) D=1, and the evolution of the corresponding effective exponent θ_{eff} in the inset, in panel (b) for D=0, and in panel (c) for D= 0.5. For comparison, the red solid line in panel (a) depicts the critical $N_I(t)$ result for D=0. The critical points, emphasized by the thick curves, are estimated at infection probabilities λ_c=0.4058(1), λ_c=0.3806(1), and λ_c =0.3533(1) for D=0, D=0.5, and D=1, respectively. The horizontal dashed red line indicates the SIR value. All results were averaged over 10^4 independent runs.

ABBREVIATIONS

AC	Alternating Current
ACP	Amorphous Calcium Phosphate
AE	Acoustic Emissions
AEKI	Institute for Atomic Energy Research
AES	Auger Electron Spectroscopy
AFM	Atomic Force Microscopy
ALD	Atomic Layer Deposition
alg	alginate
ALLEGRO	Experimental Helium Gas Cooled Fast Reactor Developed by the European V4G4
AM	Additive Manufacturing
AMPA	Aminomethylphosphonic Acid
AOP	Advanced Oxidation Processes
APC	Aerosol Particle Counter
APIs	Active Pharmaceutical Ingredients
ASTM	American Society for Testing and Materials
ATF-TS	Testing and Simulation for Advanced Technology and Accident Tolerant Fuels
ATOMKI	Institute for Nuclear Research, Debrecen
BCC	Body Centred Cubic
BCF	Boda Claystone Formation
BCP	Border Control Point
BDD	Boron Doped Diamond
BEE	Back-End Electronics frame
BES	Beam Emission Spectroscopy
BEXUS	Balloon Experiments for University Students
BF	Bright Field
BME	Budapest University of Technology and Economics
BNC	Budapest Neutron Centre
BOD	Biochemical Oxygen Demand
BRR	Budapest Research Reactor
BWR	Boiling Water Reactor
cACP	carbonated Amorphous Calcium Phosphate
CAD	Computer Aided Design
CARC	Calculations for Atmospheric Release Criteria
CDD	Context Definition Document
CDR	Critical Design Review
CDS	Ceramic Dispersion Strengthened
CEA	Commissariat à l'énergie atomique et aux énergies alternatives
CEFR	China Experimental Fast Reactor
CERIC	Central European Research Infrastructure Consortium
CETS	Central European Training School
CFD	Computational Fluid Dynamics
CFL	Cumulative Fractions of boron Leaching
CFU	Colony Forming Unit
CH	Cultural Heritage
CMOS	Complementary Metal-Oxide Semiconductor
CNS	Compact Neutron Source
COD	Chemical Oxygen Demand
CP	Calcium Phosphate
CPE	Controlled Potential Electrolysis
CRP	Coordinated Research Project
CSA	Charge Sensitive Amplifier
CSD	Control and Shutdown Device
CTAC	Cetyltrimethylammonium chloride
CV	Cyclic Voltammetry, Central Vector
CVD	Chemical Vapour Deposition
DBA	Design Basis Accident
DC	Drop-Casting, Direct Current
DCC	Direct Current Converter
DEC	Design Extension Condition
DEM	Digital Elevation Model
DEMO	DEMOnstration Power Station

DF	Dark Field
DG INTPA	Directorate General for International Partnerships
DHR	Decay Heat Removal
DHR HXs	Decay Heat Removal Heat exchangers
DLR	German Aerospace Centre
DM	Demineralized
DMS	Disruption Mitigation Systems
DNA	Deoxyribonucleic acid
DoF	Depth of Field
DP	Deposition Precipitation
DPA	Displacement per Atom
dpm	disintegration per minute
DPM	Digital Processing Module
DRM	Dry Reforming of Methane
DRIFTS	Diffuse Reflectance Fourier Transform Infrared Spectroscopy
DT	Digital Twin
EAD	European Active Dosimeter
EB	Electron Beam
EBA	Enriched Boric Acid
EBS	Engineered Barrier System
EBSD	Electron Backscatter Diffraction
EC	Elemental Carbon, European Commission
ECCS	Emergency Core Cooling System
ECM	Extracellular Matrix
ECR	Electron Cyclotron Resonance
ECSS	European Cooperation for Space Standardization
ED	Electron Diffraction
EDM	Erosion Deposition Monitor
EDS	Energy Dispersive X-ray Spectroscopy
EDX	Energy-dispersive X-ray Spectroscopy
EELS	Electron Energy Loss Spectroscopy
EGCG	Epigallocatechin-gallate
EGSE	Earth Ground Support Equipment
EIS	Electrochemical Impedance Spectroscopy
EK	Centre for Energy Research (Hungarian acronym)
ELISA	Enzyme-Linked Immunosorbent Assay
ELKH	Eötvös Loránd Research Network (Hungarian acronym)
ELKH TTK	Research Centre for Natural Sciences
ELTE	Eötvös Loránd University, Budapest (Hungarian acronym)
EM	electromagnetic, Engineering Model
EMR	Electron Magnetic Resonance
ENEN	European Nuclear Education Network, (Belgium)
EOL	End Of Life
EPA	Environmental Protection Agency (United States)
EPD	Electron Powder Diffraction
EPP	Equatorial Port Plug
EPL	Environmental Physics Laboratory, EK
EP&R	Emergency Preparedness and Response
EPR	Electron Paramagnetic Resonance, Evolutionary Power Reactor
ERO	Earth Return Orbiter
ESA	European Space Agency
ETE	Embrittlement Trend Evaluation
EU	European Union
EURAD	European Joint Programme on Radioactive Waste Management
EURATOM	European Atomic Energy Community
FAIR	Findable, Accessible, Interoperable, Reusable
FC	Faraday Cup
FC/ZFC	Field Cooling Zero Field Cooling
FCC	Face Centred Cubic
FE	Finite Element
FEA	Finite Element Analysis
FEE	Front-End Electronics frame
FEM	Finite Element Method
FFT	Fast Fourier Transform

FGR	Fission Gas Release
FIB	Focus Ion Beam
FKKL	EK Laboratory of Surface Chemistry and Catalysis (Hungarian acronym)
FL	MFA Photonics Laboratory (Hungarian acronym)
FluidFM	Fluidic Force Microscopy
FMI	Finish Meteorological Institute
fMRI	functional Magnetic Resonance Imaging
FPL	Fusion Plasma Physics Department, EK
FRR	Frequency Restoration Reserve
FSANS	Focusing Small Angle Neutron Scattering
FTL	Fusion Technology Department, EK
FT-IR	Fourier-transform Infrared Spectroscopy
FTO	Fluorine-doped Tin Oxide
FWHM	Full width at half maximum
GC	Glassy Carbon, Gas Chromatograph
GFP	Green Fluorescent Polymer
GFR	Gas-Cooled Fast Reactor
GINA	Grazing Incidence Neutron Apparatus
GIS	Geographical Information System
GISAS	Grazing Incidence Small Angle Scattering
GM	Geiger–Müller
GPS	Global Positioning System
GPU	Graphics Processing Unit
GUI	Graphical User Interface
GV	Gauge Volume
HAADF	High-angle Annular Dark-field
HALO	Habitation and Logistics
HDU	High-Dependency Unit
HEA	High Entropy Alloy
HER	Hydrogen Evolving Reaction
HIP	Hot Isostatic Pressing
HiPIMS	High-Power Impulse Magnetron Sputtering
HLW	High-level Radioactive Waste
HM	Holomonitor
HOPG	Highly Oriented Pyrolytic Graphite
HPGe	High-purity Germanium
HPSI	High Pressure Safety Injection
HRTEM	High Resolution Transmission Electron Microscopy
HSA	Human Serum Albumin
HT	High Temperature
HUNOR	Hungarian to Orbit Astronaut Program
HV	High Voltage
HZP	Hot Zero Power
IAEA	International Atomic Energy Agency
IC	Ion Chromatography
ICDD PDF	International Centre for Diffraction Data Powder Diffraction File
ICP-MS	Inductively Coupled Plasma Mass Spectrometry
ICP-OES	Inductively Coupled Plasma Optical Emission Spectrometry
IDA	Internal Dosimeter Array
iHIBP	imaging Heavy Ion Beam Probe
ILs	Ionic liquids
ILW	Intermediate Level Radioactive Waste
INAA	Instrumental Neutron Activation Analysis
INSC	International Nuclear Safety Cooperation
INT	Interface Electronics frame
IONPs	Iron Oxide Nanoparticles
IPERION HS	Integrating Platforms for the European Research Infrastructure ON Heritage Science
IR	Infrared, Induced Repair
ISE	Indentation Size Effect
ISS	International Space Station
ITER	International Thermonuclear Experimental Reactor
ITO	Indium Tin Oxide
IUPAC	International Union of Pure and Applied Chemistry
JAXA	Japan Aerospace Exploration Agency

JET	Joint European Torus
JJ	Josephson Junction
JoFET	Josephson Field-Effect Transistor
JUICE	JUpiter ICy moons Explorer
KIKO3DMG	Nodal Reactor Physics Calculation Code Developed in the EK
KKM	Ministry of Foreign Affairs and Trade (Hungarian acronym)
LC	Liquid Chromatograph
LCL	Latching Current Limiter
LDOS	Local Density of States
LED	Light Emitting Diode
LGS	levoglucosan
LNG	Liquefied Natural Gas
LoG	Laplace of Gaussian
LOCA	Loss of Coolant Accident
LoRaWAN	Long-Range Wide Area Network
LPE	Liquid Phase Epitaxy
LRI	Large Research Infrastructures
LSC	Liquid Scintillation Counting
LSPR	Local Surface Plasmon Resonance
LSV	Linear Sweep Voltammetry
LTCC	Life-Time Considering Control
LV	Low-Voltage
LWR	Light Water Reactor
MA	Minor Actinides
MAT	Magnetic Adaptive Testing
MB	Methylene blue
MC	Monte Carlo
MCDM	Multi-Criteria Decision-Making(
MCNP	Monte Carlo N-Particle Transport
MD	Molecular Dynamics
MEMS	Microelectromechanical System
MEST	Mobile Expert Support Team
MFA	Institute of Technical Physics and Materials Science (Hungarian acronym)
MH	Hungarian Defence Forces (Hungarian acronym)
MHX	Main Heat exchangers
MIS	Minimally Invasive Surgery
MIT	Metal-Insulator Transition
ML	Monolayer
MLI	Multilayer Insulation
MO	Methyl orange
MOX	Mixed Oxide
MPH	Material Property Handbook
MRI	Magnetic Resonance Imaging
MRR	Manufacturing Readiness Review
MS	Mössbauer Spectroscopy, Mass Spectrometry
MSR	Mars Sample Return
MTAB	Mercaptolhexadecil cetyltrimethylammonium bromide
MUA	Mercaptoundecanoic acid
MV	Medium-Voltage
MVM	Hungarian Power Companies (Hungarian acronym)
MW	Microwave
MWCNT	Multiwalled carbon nanotubes
micro-XRF	Microscopic X-Ray Fluorescence
NAA	Neutron Activation Analysis
NH	Nanohematite
NASA	National Aeronautics and Space Administration, USA
NASA/JPL	National Aeronautics and Space Administration / Jet Propulsion Laboratory
NASICON	Natrium Super Ionic Conductor
NAV	National Tax and Customs Administration (Hungarian acronym)
NBA	Natural Boric Acid
NCAIM	National Collection of Agricultural and Industrial Microorganisms
ND	Neutron Diffraction
NDA	Non-Destructive Assays
NENE	Nuclear Energy for New Europe

NDT	Non-Destructive Testing
NINE	Nuclear and INdustrial Engineering S.r.l. (Italy)
NIPS	Neutron-Induced Prompt Gamma-ray Spectroscopy
NIR	Near InfraRed
NKFIH	National Research, Development and Research Office (Hungarian acronym)
NMR	Nuclear Magnetic Resonance
NNI	Hungarian National Police, National Bureau of Investigation (Hungarian acronym)
NOMAD	Non-destructive Evaluation System for the Inspection of Operation-Induced Material Degradation in Nuclear Power Plants (EU H2020 project)
NP	Nanoparticle
NPP	Nuclear Power Plant
NRAs	National Nuclear Regulatory Authorities
NUBIKI	Nuclear Safety Research Institute (Hungarian acronym)
OAH	Hungarian Atomic Energy Authority (Hungarian acronym)
OC	Organic Carbon
ODS	Oxide Dispersion-Strengthened
OER	Oxygen Evolving Reaction
OKF	National Directorate for Disaster Management (Hungarian Acronym)
OPC	Optical Particle Counter
ORC	Organic Rankine Cycle
OS-SEM-EDX	Original Surface" Scanning Electron Microscopy with Energy Dispersive X-Ray microanalysis
OTKA	Hungarian Scientific Research Fund (Hungarian Acronym)
OUR	Oxygen Uptake Rate
OVP	Over Voltage Protection
OWLS	Optical Waveguide Lightmode Spectroscopy
O&M	Operation and Maintenance
Paks NPP	Paks Nuclear Power Plant
PC	Portland Cement
PCL	Polycaprolactone
PCM	Power Converter Module
PDFs	Probability Distribution of Failures
PDMS	Polydimethylsiloxane
PEG	Polyethylene Glycol
PEP	Particle Environment Package
PGAA	Prompt-gamma Neutron Activation Analysis
PGAI	Prompt-gamma Activation Imaging
PGAI-NT	Prompt-gamma Activation Imaging – Neutron Tomography
PhC	photonic-crystal
PIGE	Proton Induced Gamma-ray Emission
PIP	Platform Interface Plate
PIXE	Particle Induced X ray Emission
PL	Photoluminescence, Power-law
PLA	Polylactic Acid
PM	Particulate Matter
PnP	Plug and Play
PoC	Proof of Concept
PP	Pulse Plating
PRISE	Primary to secondary leak
PS	Pressureless Sintering
PtG	Power-to-Gas
PTFE	Polytetrafluoroethylene
PUMMA	Plutonium Management for More Agility
PV	Photovoltaic
PVD	Physical Vapour Deposition
pXRF	Portable XRF Spectrometer
PWM	Pulse With Modulation
PWR	Pressurized Water Reactor
R&D	Research & Development
RAD	Radiography
RADMOS	Radiation Monitoring System
RBC	Red Blood Cell

RBS	Rutherford Backscattering Spectrometry
RDS	Resonant Diffuse Scattering
REEs	Rare Earth Elements
RES	Renewable Energy Sources
RF	Radio Frequency
RG	Rhombohedral Graphite
RGD	Arginine-glycine-aspartic acid (Arg-Gly-Asp)
RI	Research Infrastructure
RMSE	Root Mean Square Error
RN	Radionuclide
RPV	Reactor Pressure Vessel
RR	Research Reactor
RRTC	Rankine-based Thermodynamic Cycle
RT	Room Temperature
RWG	Resonant Waveguide Grating
SAC	Sulfoaluminate Cement
SACs	Single Atom Catalysts
SAED	Selected Area Electron Diffraction
SANS	Small Angle Neutron Scattering
SAXS	Small Angle X-ray Scattering
SBL	Nuclear Security Department, EK
SC	Solute-Correlated
SCFS	Single Cell Force Spectroscopy
SCRAM	emergency shutdown of the reactor
SDS	Space Dosimetry System
SE	Secondary Electron, Spectroscopic Ellipsometry
SEM	Scanning Electron Microscopy
SEM-EDS	Scanning Electron Microscopy with Energy Dispersive Spectroscopy
SEM-EDX	Scanning Electron Microscopy with Energy Dispersive X-Ray microanalysis
SGTR	Steam Generator Tube Rupture
SI	Structural Integrity
SIR	Susceptible Infected Recovered
SM	Supermirror
SMPS	Scanning Mobility Particle Sizer
SMT	Semiconductor Metal Transition
SPI	Shattered Pellet Injection
SPN	Simplified Spherical Harmonics
SPS	Spark Plasma Sintering
SRA	Small Roughness Approximation
SRD	System Requirement Documents
SR XRF	Synchrotron Radiation X-Ray Fluorescence
STEM	Scanning Transmission Electron Microscope
STM	Scanning Tunnelling Microscopy
SWV	Square Wave Voltammetry
TC	total carbon
TEK	Counter Terrorism Centre (Hungarian acronym)
TEL	Telescopes Baseplate
TEM	Transmission Electron Microscopy
TEOM	Tapered Element Oscillating Microbalance
TEOS	Tetraethylorthosilicate
TÉT	Bilateral Research Program (Hungarian acronym)
TFC	Trilateral Flash Cycle
TGYE	Tryptone-glucose-yeast extract
TL	Thermoluminescent
TOC	Total Organic Carbon
TOF	Time-Of-Flight
TOF-ND	Time-of-Flight Neutron Diffraction
ToF-ERDA	Time-of-Flight Elastic Recoil Detection Analysis
TPR	Temperature Programmed Reduction
TSO	Technical Support Organization
TXRF	Total-reflection X-ray Fluorescence
UAV	Unmanned Aircraft Vehicle
UDR	Unified Digital Radio Telecommunication
UGV	Unmanned Ground Vehicle

UOX	Uranium Oxide
USB	Universal Serial Port
UV	Ultraviolet
UV-VIS	Ultraviolet-Visible (Spectroscopy)
VERONA	VVER On-Line Analysis
VOC	Variant Of Concern
VRF	MFA Thin Film Physics Department (Hungarian acronym)
VRSS	Virtual Radioactive Source System
VVER	Water-Cooled Water-Moderated Energetic Reactor, Russian acronym
XANES	X-ray Absorption Near-Edge Structure
XPS	X-ray Photoelectron Spectroscopy
XRD	X-ray Diffraction
XRF	X-ray Fluorescence Analysis
μ-XRF	Microscopic X-ray Fluorescence
XRS	X-Ray Spectrometry
XTEM	Cross-sectional Transmission Electron Microscopy
WC	Tungsten-carbide
Wigner FK	Wigner Research Centre for Physics
WPRM	Work Package Remote Maintenance
WS	Wavelength Shift

IMPRINT

Editor

László Redler

Lectors

Ferenc Szlávik
Jesse Weil

Publisher

Ákos Horváth
Tamás Belgya
Béla Pécz
Centre for Energy Research
H-1121, Budapest, Konkoly Thege M. út 29-33.
Hungary

Design

Anikó Jécsai
Tamás Szabolics

Picture credits

Centre for Energy Research

Accessibility

http://www.ek.hun-ren.hu/

Contact

Centre for Energy Research, Eötvös Loránd Research Network
Location: *KFKI Campus, Budapest Konkoly-Thege Miklós street 29-33., H-1121 Hungary*
Phone: *(+36 1) 395 91 59*
E-mail adresses: info@ek.hun-ren.hu

Centre for Energy Research

Centre for
Energy Research

KFKI Campus, Konkoly-Thege Miklós út 29-33.
Budapest H-1121, Hungary
Phone: +36 1 395 9159
www.ek.hun-ren.hu